ADVANCED STEEL CONSTRUCTION

An International Journal

Volume 19 Number 3

September 2023

CONTENTS

Technical Papers

Copyright © 2023 by :
The Hong Kong Institute of Steel Construction
Website: *http://www.hkisc.org*
ISSN 1816-112X
Science Citation Index Expanded, Materials Science Citation Index and ISI Alerting
Cover: Tower cranes in building construction @LIU Yao-Peng
e-copy of IJASC is free to download at "www.ascjournal.com" in internet and mobile apps.

ADVANCED STEEL CONSTRUCTION

VOL.19, NO.3 (2023)

ADVANCED STEEL CONSTRUCTION

an International Journal

ISSN 1816-112X

Volume 19 Number 3 *September 2023*

Editors-in-Chief

S.L. Chan, *The Hong Kong Polytechnic University, Hong Kong, China*

W.F. Chen, *University of Hawaii at Manoa, USA*

R. Zandonini, *Trento University, Italy*

ISSN 1816-112X

Science Citation Index Expanded, Materials Science Citation Index and ISI Alerting

Advanced Steel Construction
an international journal

EDITORS-IN-CHIEF

Asian Pacific, African and organizing Editor
S.L. Chan
The Hong Kong Polyt. Univ., Hong Kong, China

American Editor
W.F. Chen
Univ. of Hawaii at Manoa, USA

European Editor
R. Zandonini
Trento Univ., Italy

ASSOCIATE EDITORS

Y.P. Liu
The Hong Kong Polyt. Univ., Hong Kong, China

S.W. Liu
The Hong Kong Polyt. Univ., Hong Kong, China

INTERNATIONAL EDITORIAL BOARD

F.G. Albermani
Central Queensland Univ., Australia

I. Burgess
Univ. of Sheffield, UK

F.S.K. Bijlaard
Delft Univ. of Technology, The Netherlands

R. Bjorhovde
The Bjorhovde Group, USA

M.A. Bradford
The Univ. of New South Wales, Australia

D. Camotim
Technical Univ. of Lisbon, Portugal

C.M. Chan
Hong Kong Univ. of Science & Technology, Hong Kong, China

T.H.T. Chan
Queensland Univ. of Technology, Australia

T.M. Chan
The Hong Kong Polyt. Univ., Hong Kong, China

Z.H. Chen
Tianjin Univ., China

S.P. Chiew
Nanyang Technological Univ., Singapore

W.K. Chow
The Hong Kong Polyt. Univ., Hong Kong, China

G.G. Deierlein
Stanford Univ., California, USA

L. Dezi
Univ. of Ancona, Italy

D. Dubina
The Politehnica Univ. of Timosoara, Romania

R. Greiner
Technical Univ. of Graz, Austria

L. Gardner
Imperial College of Science, Technology and Medicine, UK

Y. Goto
Nagoya Institute of Technology, Japan

L.H. Han
Tsinghua Univ. China

S. Herion
University of Karlsruhe, Germany

G.W.M. Ho
Ove Arup & Partners Hong Kong Ltd., Hong Kong, China

B.A. Izzuddin
Imperial College of Science, Technology and Medicine, UK

J.P. Jaspart
Univ. of Liege, Belgium

S. A. Jayachandran
IIT Madras, Chennai, India

S.E. Kim
Sejong Univ., South Korea

S. Kitipornchai
The Univ., of Queensland, Australia

D. Lam
Univ. of Bradford, UK

H.F. Lam
City Univ. of Hong Kong, Hong Kong, China

G.C Li
Shenyang Jianzhu Univ., China

G.Q. Li
Tongji Univ., China

J.Y.R. Liew
National Univ. of Singapore, Singapore

E.M. Lui
Syracuse Univ., USA

Y.L. Mo
Univ. of Houston, USA

J.P. Muzeau
CUST, Clermont Ferrand, France

D.A. Nethercot
Imperial College of Science, Technology and Medicine, UK

Y.Q. Ni
The Hong Kong Polyt. Univ., Hong Kong, China

D.J. Oehlers
The Univ. of Adelaide, Australia

J.L. Peng
Yunlin Uni. of Science & Technology, Taiwan, China

K. Rasmussen
The Univ. of Sydney, Australia

J.M. Rotter
The Univ. of Edinburgh, UK

C. Scawthorn
Scawthorn Porter Associates, USA

P. Schaumann
Univ. of Hannover, Germany

Y.J. Shi
Tsinghua Univ., China

G.P. Shu
Southeast Univ. China

L. Simões da Silva
Department of Civil Engineering, University of Coimbra, Portugal

J.G. Teng
The Hong Kong Polyt. Univ., Hong Kong, China

G.S. Tong
Zhejiang Univ., China

K.C. Tsai
National Taiwan Univ., Taiwan, China

C.M. Uang
Univ. of California, USA

B. Uy
University of Western Sydney, Australia

M. Veljkovic
Univ. of Lulea, Sweden

F. Wald
Czech Technical Univ. in Prague, Czech

Y.C. Wang
The Univ. of Manchester, UK

Y.L. Xu
The Hong Kong Polyt. Univ., Hong Kong, China

D. White
Georgia Institute of Technology, USA

E. Yamaguchi
Kyushu Institute of Technology, Japan

Y.B. Yang
National Taiwan Univ., Taiwan, China

Y.Y. Yang
China Academy of Building Research, Beijing, China

B. Young
The Univ. of Hong Kong, Hong Kong, China

X.L. Zhao
Monash Univ., Australia

X.H. Zhou
Chongqing University, China

Z.H. Zhou
The Hong Kong Polyt. Univ., Hong Kong, China

S.Y. Zhu
The Hong Kong Polyt. Univ., Hong Kong, China

R.D. Ziemian
Bucknell Univ., USA

Cover: Tower cranes in building construction @LIU Yao-Peng
e-copy of IJASC is free to download at "www.ascjournal.com" in internet and mobile apps.

General Information
Advanced Steel Construction, an international journal

Aims and scope

The International Journal of Advanced Steel Construction provides a platform for the publication and rapid dissemination of original and up-to-date research and technological developments in steel construction, design and analysis. Scope of research papers published in this journal includes but is not limited to theoretical and experimental research on elements, assemblages, systems, material, design philosophy and codification, standards, fabrication, projects of innovative nature and computer techniques. The journal is specifically tailored to channel the exchange of technological know-how between researchers and practitioners. Contributions from all aspects related to the recent developments of advanced steel construction are welcome.

Disclaimer. No responsibility is assumed for any injury and / or damage to persons or property as a matter of products liability, negligence or otherwise, or from any use or operation of any methods, products, instructions or ideas contained in the material herein.

Subscription inquiries and change of address. Address all subscription inquiries and correspondence to Member Records, IJASC. Notify an address change as soon as possible. All communications should include both old and new addresses with zip codes and be accompanied by a mailing label from a recent issue. Allow six weeks for all changes to become effective.

The Hong Kong Institute of Steel Construction
HKISC
c/o Department of Civil and Environmental Engineering,
The Hong Kong Polytechnic University,
Hunghom, Kowloon, Hong Kong, China.
Tel: 852- 2766 6047 Fax: 852- 2334 6389
Email: *ceslchan@polyu.edu.hk* Website: *http://www.hkisc.org/*
ISSN 1816-112X
Science Citation Index Expanded, Materials Science Citation Index and ISI Alerting
Copyright © 2023 by:
The Hong Kong Institute of Steel Construction.

ISSN 1816-112X

Science Citation Index Expanded, Materials Science Citation Index and ISI Alerting

EDITORS-IN-CHIEF

Asian Pacific, African and organizing Editor
S.L. Chan
The Hong Kong Polyt. Univ., Hong Kong, China
Email: ceslchan@polyu.edu.hk

American Editor
W.F. Chen
Univ. of Hawaii at Manoa, USA
Email: waifah@hawaii.edu

European Editor
R. Zandonini
Trento Univ., Italy
Email: riccardo.zandonini@ing.unitn.it

Advanced Steel Construction
an international journal

VOLUME 19 NUMBER 3 September 2023

Technical Papers

Advanced Steel Construction – Vol. 19 No. 3 (2023) 185–196
DOI:10.18057/IJASC.2023.19.3.1

SEISMIC BEHAVIOR OF BUCKLING RESTRAINED BRACE WITH FULL-LENGTH OUTER RESTRAINT: EXPERIMENT AND RESTORING FORCE MODEL

Bo Yang [1, 2], Zhan-Zhong Yin [1, *] and Hong-Bo Xu [1]

[1] *School of Civil Engineering, Lanzhou University of Technology, Lanzhou 730050, China*
[2] *Architecture and Civil Engineering Institute, Guangdong University of Petrochemical Technology, Maoming 525000, China*
** (Corresponding author: E-mail: yzztianyu@126.com)*

ABSTRACT

In order to solve the instabilities, fracture failures, and difficult repairs of welded gusset plates in buckling-restrained braced frames (BRBFs) under severe earthquakes, the idea of a full-length outer restraint BRB (FLBRB) is introduced. This new brace consists of a cross-section core, two end-weakened connectors, and a full-length outer restraint. In this paper, three FLBRBs with different parameters were designed, and their mechanical behaviors were evaluated through quasi-static testing, including failure mode, stress distribution and hysteretic behavior. Besides, the refined FE models were established and compared with the test. And the simplified bilinear load-displacement model and hysteretic rule considering the degradation of unloading stiffness are proposed based on the experimental investigation and FE simulation, the simplified bilinear load-displacement model and hysteretic rule considering the degradation of unloading stiffness are proposed, as well as the formulas for calculating the stiffness of either loading or unloading. The results demonstrate that the FLBRB has good hysteresis performance as it can confine the plastic to the weakened connectors and the BRB. Furthermore, the simplified restoring force model was verified by comparing it with the experiment, indicating that the load–displacement curve of the FLBRB could be accurately predicted by the suggested theoretical formula and model. These research results can be adopted to provide theoretical foundation for the engineering application of the FLBRB.

ARTICLE HISTORY

Received: 20 September 2022
Revised: 29 January 2023
Accepted: 18 February 2023

KEYWORDS

FLBRB;
Weakened connector;
Full length outer restraint;
Quasi-static test;
Hysteretic behavior;
Restoring force model

Copyright © 2023 by The Hong Kong Institute of Steel Construction. All rights reserved.

1. Introduction

As an traditional braced frame of structural steel, special concentrically braced frames (SCBFs) have higher bearing capacity, excellent ductility, and large lateral stiffness [1]. The connection between the frame and the brace are welded with gusset plate in the conventional design, and so the stress concentration is easy to generate in the joint field, which results in the brace being over-stressed and prematurely rupture at the welded corner gusset connection [2,3]. After a severe earthquake, such a permanently damaged brace and connection are very difficult to repair or replace, resulting in a structure not being able to restore its original form and function [4-6]. Although it is typical practice to design connections subjected to axial loads only, the yield of joints and the post-buckling response of braces should be balanced in the design process [7,8].

To address the aforementioned problems, researchers have made many improvements and conducted numerous studies. Fleischman et al. [9-12] applied cast modular components to beam-to-column connectors and nodes, compared with traditional connections, these designs exhibited superior energy dissipation and excellent ductility. De Oliveira et al. [13] proposed using high-strength connectors for connection of circular hollow sections in SCBFs, and connecting to the gusset plate by bolts or pins. Gary et al. [14] proposed the yielding brace system (YBS) for SCBFs. Through special design, the shear yielding elements at one end of the brace is designed for the inelastic energy dissipation under seismic loading in this system. Subsequently, the YBS has been further tested and developed [15,16]. Federico et al. [17] proposed a similar brace system called the floating brace (FB) system. This new concept creates a strong, rigid, and flexible lateral bracing system by using a series of special shaped plates at one end of a brace. On this basis, Ward et al. [18,19] designed a ductile bracing system according to the concept of "dog bone" [20], and introduced it to SCBFs. Through their theoretical and experimental research of system, they provided corresponding design methods and suggestions. Besides, Steven et al. [21] proposed an alternative connection of the concentrically braced frames. This connection can confine the damage to a replaceable module, while realizing rapid repair and replacement. Finally, Zhao et al. [22,23] proposed a new type of joint connection, which can effectively reducing the stress response at the joints of frame through the sliding of gusset plates.

According to the commentary of the code of AISC [24], the damage of SCBFs observed in previous severe earthquakes was generally caused by insufficient ductility and corresponding brittle failures of the connections. In addition, when the braces are compressed, they will buckle in advance, leading to instability or even failure of the structure during severe earthquake [5,25].

The researchers then proposed a buckling-restrained brace (BRB) and the improvement and optimization research were carried out. Wakabayashi [26] conducted an experimental study on BRB. Then, Watanabe et al. [27] developed a BRB consisting of steel core and concrete-filled steel tube, and it was verified by tension and compression tests that the BRB had excellent energy dissipation performance. Tsai et al. [28] proposed double-core configuration BRBs that reduce the length of the connecting section at the end of the BRB to improve the stability of the regions, and tested their hysteretic response experimentally. Jia et al. [29] conducted the quasi-static test on concrete composite frame with BRB, and proposed the design suggestions to improve the stability of BRB end connection.

For the BRBs is widely used in practical construction, the fabrication materials, yield behavior, assembly and connection types of BRBs were improved, including SMA BRBs, double-stage yield BRBs, and assembled self-centering BRBs [30-33]. The corresponding design methods were optimized [34-35]. As to enhance the performance of BRBs further, Yin [36] designed an improved double-tube BRB (IBRB), which set a series of contact rings between the inner tube and the outer tube to improve the mechanical properties of the double-tube BRB. Based on the advantages and good mechanical properties of IBRBs, the author applied it to the EBFs [37]. Furthermore, Yin developed a novel assembled BRB with ductile castings (CBRBs) [38,39], which solved the brittle failures of the gusset plates in the buckling restrained brace frames (BRBFs). By changing the details and design parameters of the CBRBs, the double-stage yield of the ductile castings and BRB was realized. This formed a repairable and replaceable structural system.

Based on the research achievements mentioned above, we have designed a new buckling-restrained brace with a full-length outer restraint (FLBRB), that consists of a cross-section core, end-weakened connector, and full-length outer restraint. The characteristics are as follows. The FLBRB is connected to the frame through weakened connectors using bolt connections to replace the traditional welded gusset plates. To avoid the brittle fractures and stress concentrations in the joint field and to confine the inelastic deformation on the end-weakened connectors, these connectors are repairable and replaceable after severe earthquakes. Using the full-length outer sleeve as the buckling restraint improves the stability of the end-weakened connector and avoids the instability of the connecting section between the weakened connector and core of BRB. Each part of the FLBRB is assembled with high-strength bolts on site, forming a structure in which all components can be repaired and replaced.

In this paper, three different parameters of FLBRB were tested under axial cyclic load. We analyzed its hysteretic behavior, developed the restoring force model of the FLBRB based on theoretical analysis, and verified the

experimental results. These results demonstrated that the FLBRB has stable hysteretic behavior, while the load-displacement curve calculated by the theoretical simplified bilinear model coincides fairly with the experimental results. The above conclusions are useful for further research of FLBRB in steel frame.

2. Design of the FLBRB

2.1. Description of proposed FLBRB

The FLBRB consists of the cross-section core, end-weakened connector, and full-length outer restraint, as shown in Fig. 1. Each component is fabricated in the shop and assembled by bolts on site, thus reducing the erection time. The weakened connectors can confine the plastic deformation to this part, which relieves the stress concentration at the beam-column joint, and effectively reduce the possibility of brittle fracture at the connection between the brace and the frame.

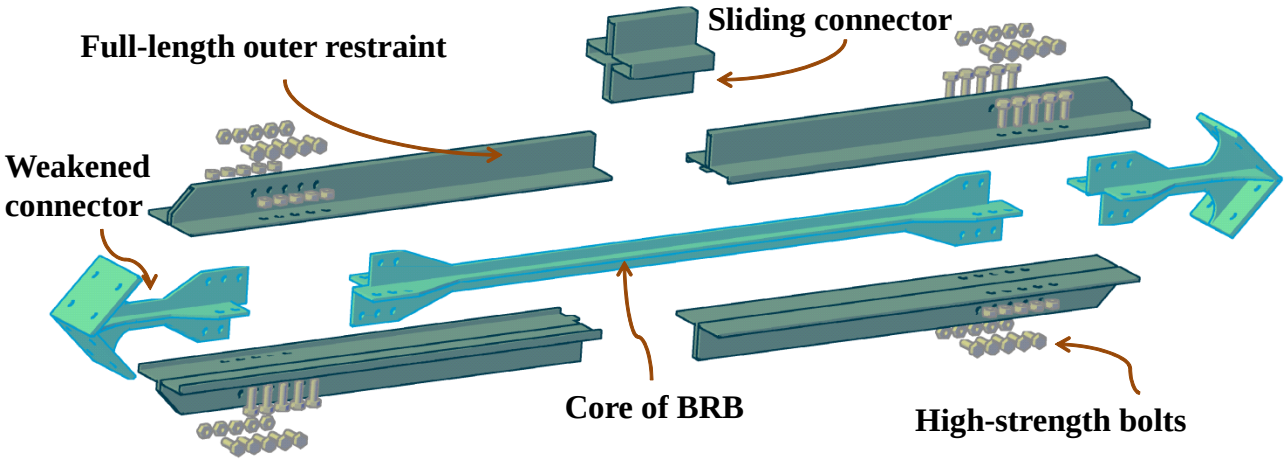

(a) Components

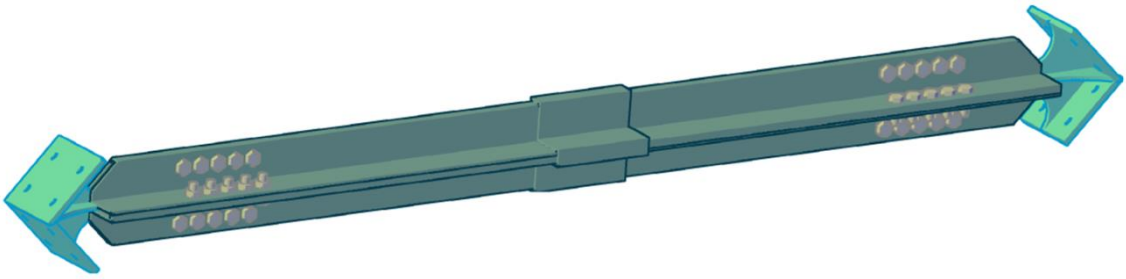

(b) Fabrication

Fig. 1 Example of a figure

2.2. Specimen design

An 11-story frame was used as a prototype. The planned dimensions are shown in Fig. 2(a). The structure was designed according to the relevant specifications, including the GB50011-2010 [40] and JGJ 99-2015 [41]. And the structure was scaled by 1/3 in consideration of the laboratory conditions.

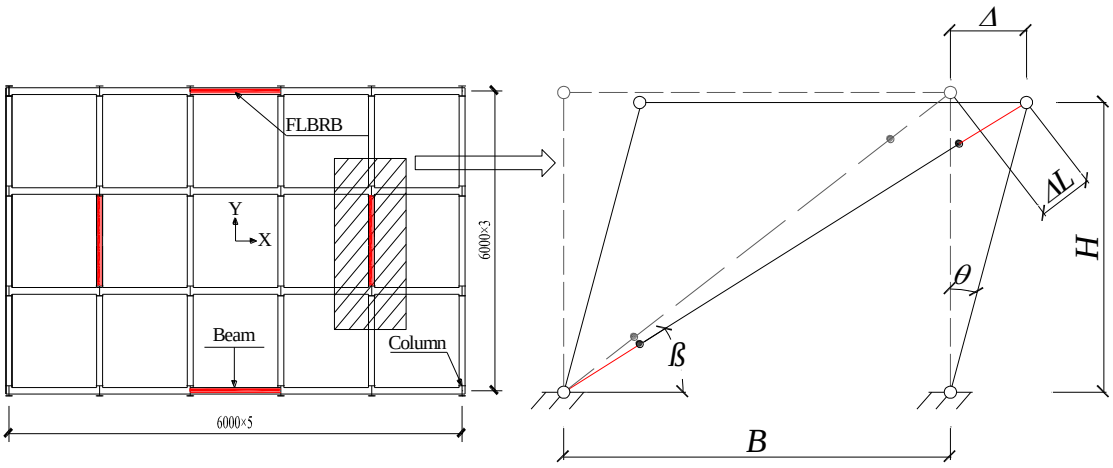

(a) Plane

(b) Schematic of one-story one-bay

Fig. 2 Schematic diagram of FLBRB frame

Fig. 2(b) gives a schematic diagram of one-story one-bay structure with FLBRB. The reasonable lateral stiffness distribution of the FLBRB and frame is an essential factor for the design of the structure. Prior to the research in this paper, the author completed the laboratory tests and numerical simulations of

the BRBFs with ductile castings (CBRBSFs). The research results showed that, when the lateral stiffness ratio is in a reasonable range [38], it is conducive to the performance of brace in CBRBFs and the maximum dissipation of seismic energy. Therefore, according to the recommended value and following steps to design:

(1) The column and beam are designed according to the design conditions including load and seismic intensity, etc. The horizontal stiffness of the frame is calculated by the following equation, which is called the D-value method:

$$K_F = 2\alpha \frac{12E_c I_c}{H^3} \tag{1}$$

where I_c and E_c are the cross-sectional moment of inertia and the Young's modulus of the column, respectively. H is the story height, α is a correction coefficient [42].

(2) Ignoring the change of the angle between the horizontal line and the FLBRB. (Fig. 2(b)). The lateral stiffness of the FLBRB is derived according to Eqs. (2) to (4):

The axial force of the FLBRB is:

$$\Delta L = \Delta \cos\beta = \frac{F\sqrt{B^2+H^2}}{E_B A_B} \Rightarrow F = \frac{E_B A_B \Delta \cos\beta}{\sqrt{B^2+H^2}} \tag{2}$$

The corresponding horizontal force of the FLBRB is:

$$F_x = F\cos\beta = \frac{E_B A_B \Delta \cos^2\beta}{\sqrt{B^2+H^2}} \tag{3}$$

The lateral stiffness of the FLBRB is:

$$K_B = F_x/\Delta = 2E_B A_B \cos^2\beta \sin\beta / H \tag{4}$$

where A_B is the cross-sectional area of the inner of FLBRB; β is the angle between the horizontal line and FLBRB; B is the span of the structure.

(3) By combining the above Eqs. (1) and (4), and defining the lateral stiffness ratio of FLBRB and frame (the recommended ratio k should be between 1.5 and 3.0), the cross-section of the FLBRB can be determined:

$$A = k \cdot K_F \cdot H / E_B \sin\beta \cos^2\beta \tag{5}$$

According to the previous the theoretical and experimental research [43,44], We found that three parameters had an obvious effect on the hysteretic performance, including the width-to-thickness ratios and the lengths of yielding segments of the weakened connectors, as well as the axial force ratio n:

$$n = p_W / p_B \tag{6}$$

where p_W and p_B are the axial tensile and compressive yield strength of the weakened connector and the core of BRB, respectively.

Thus, three FLBRB (termed FLBRB-1, FLBRB-2, and FLBRB-3) with different details (Table 1) were designed and conducted quasi-static tests. Due to limitations of test equipment and conditions, the length of a specimen is designed to be half of the original according to the principle of symmetry. The details and dimensions of the FLBRB are shown in Fig. 3. Including FLBRB-frame connection segment L_{c1}, yielding segment $L_{c2}(L_{c2'})$, transition segment $L_{c3}(L_{c3'})$, and weakened connector-BRB connection segment $L_{c4}(L_{c4'})$. The full-length sleeve as the outer restrained part is assembled by four equal angles steel, which can improve the stability at the connection between a weakened connector and BRB and restrain the buckling of the end-weakened connector [45].

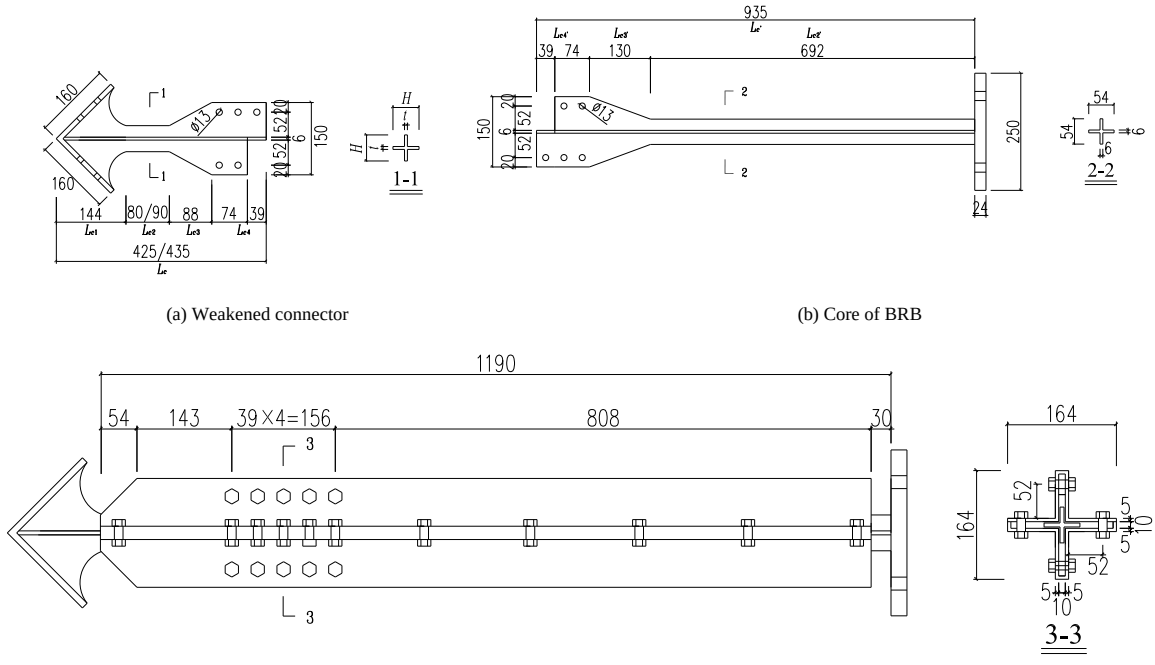

(a) Weakened connector

(b) Core of BRB

(c) FLBRB

Fig. 3 Schematic of FLBRB

Table 1
Parameters of weakened connector

Number of Specimens	Design Parameters						
	n	L_{c1}/mm	L_{c2}/mm	L_{c3}/mm	L_{c4}/mm	H/mm	t/mm
FLBRB-1	1.0	144	90	88	113	54	6
FLBRB-2	1.0		80			54	
FLBRB-3	0.8		90			43	

3. Experimental process

3.1. Coupon Tests

According to the test procedures recommended in the GB/T 228.1-2010 [46] and GB/T 2975-2018 [47]. Standard plate tensile coupons were prepared (Fig. 4) to test the steel properties, which are listed in Table 2 below.

Fig. 4 Coupon test of specimens

Table 2
Properties of steel

Specimen	Yield strength f_y/Mpa	Ultimate strength f_u/MPa	Young's modulus E/MPa	Elongation δ/%
Weakened connector	237	424	232800	26
Core of BRB	240	450	220000	25
Full length outer restraint	340	500	210500	26

3.2. Loading device and protocol

The test was conducted in the western engineering research center. The maximum output load of the vertical loading device was 2000 kN. The device consisted of a vertical loading frame and concrete reaction floor, equipped with an electro-hydraulic jack, a rigid base, and a right-angle support simulating the connection of the beam-column joint. The rigid base and right-angle support were fixed by high-strength bolts of d = 20mm. And the surrounding of the electro-hydraulic jack was restrained by the scaffolds to prevent non-axial displacement during loading, as shown in Fig. 5.

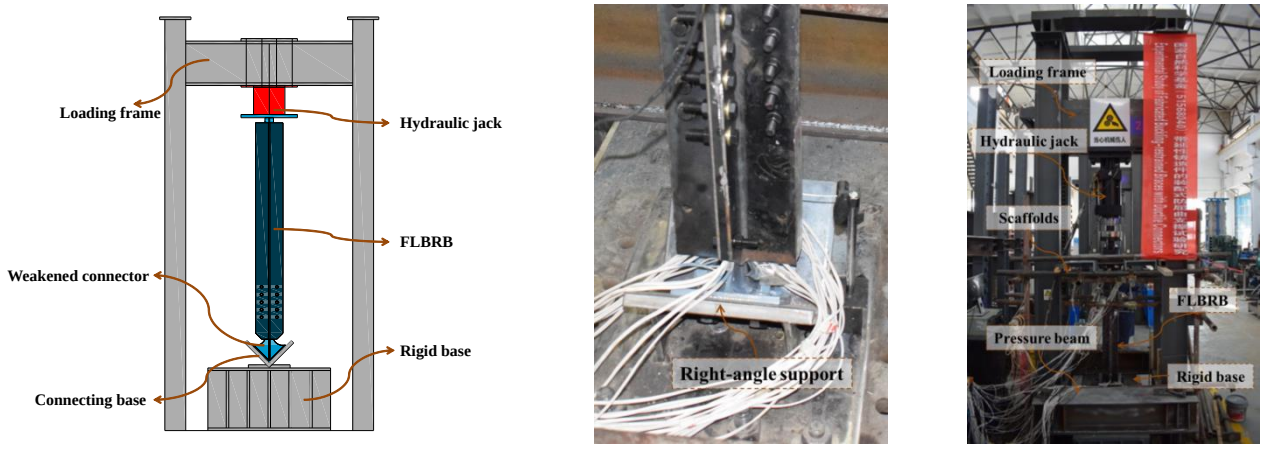

(a) Details of vertical loading device (b) Connecting base (c) On-site

Fig. 5 Loading device

The displacement loading control recommended by the specification [48] was implemented in this test. Fig. 6 showed the amplitudes of the loading, which were 1mm, 3mm and 5mm …. The test would be stopped until the specimen was damaged.

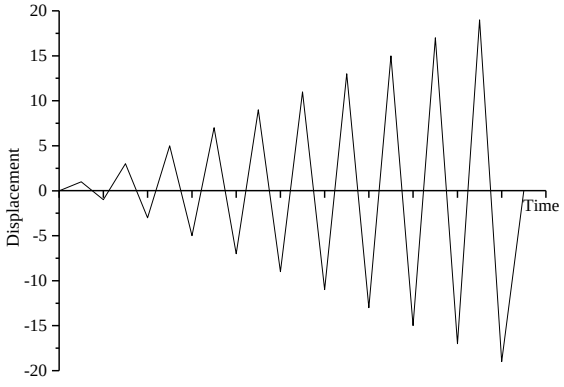

Fig. 6 Loading Protocol

3.3. Layout of measuring point

Fig. 7(a) shows the arrangements of displacement meters. Since the test adopted vertical loading, the axial deformation of FLBRB and weakening connector was measured by No. 1 and No. 2, respectively. In addition, considering the possibility of non-axial deformations of FLBRB, the Nos.2 to No.4 were arranged for measurement. And the arrangements of strain-gauge of FLBRB are illustrated in Fig. 7(b).

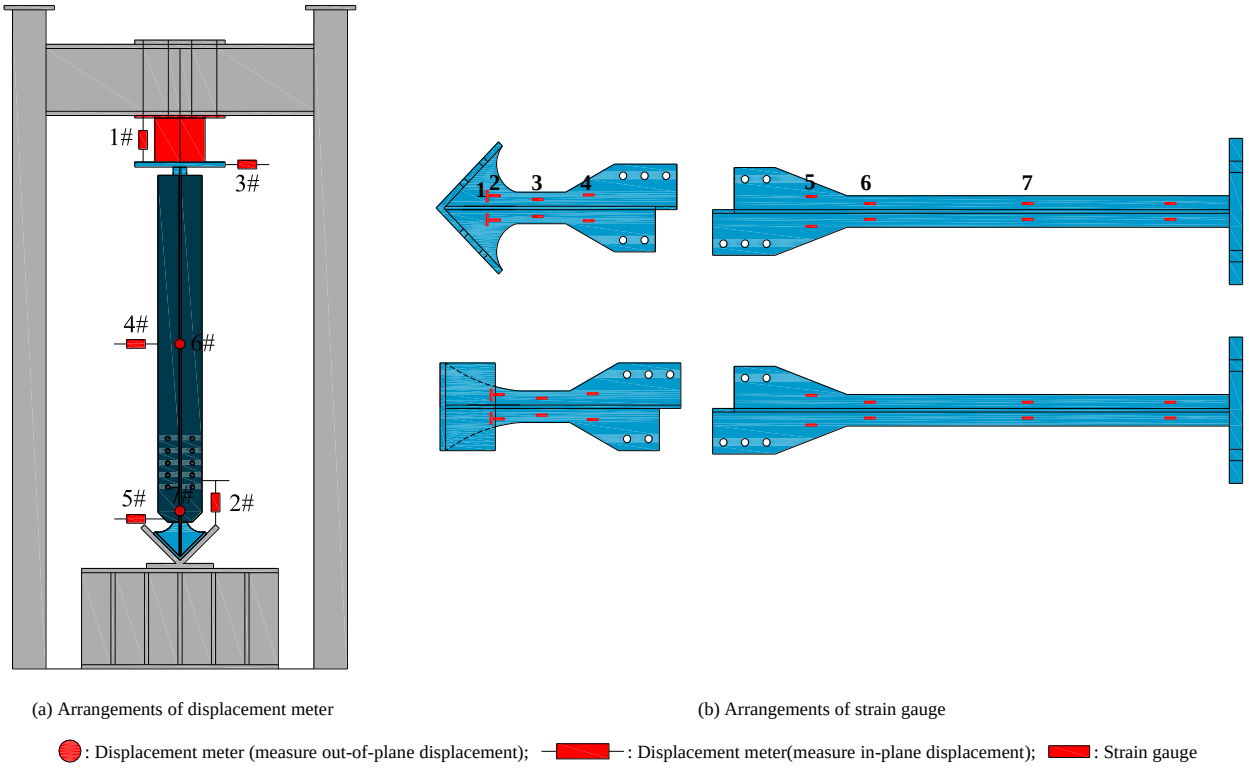

(a) Arrangements of displacement meter

(b) Arrangements of strain gauge

Fig. 7 Test point layout

3.4. Test description

The following rules were established: (1) Before the test, preloading was required to test the device as well as eliminate the installation gap of specimen; (2) Loading directions were downward positive and upward negative; and (3) θ was defined as the story drift angle of the corresponding structure with FLBRB.

Under cyclic loading, no obvious experimental phenomenon was observed before 3 mm loading displacement ($\theta=1/210$), and three specimens were in the elastic stage. Starting from 5 mm ($\theta=1/125$), closer inspection of readings of the No. 2 displacement meter showed that the connection between the weakened connector and BRB of FLBRB-1 slipped for a displacement of approximately 2 mm in the axial direction, which was also observed in the other specimens. Continuing the loading, it was found that the data of No. 1 and No. 2 displacement meters increased with the increasing test load, indicating that the weakened connector and core of BRB begin to deform in axial compression and tension. As the loading displacement approaching 7 mm ($\theta=1/90$), the yielding segment of the weakened connector reached the yield first. Further comparisons of data of displacement meters and strain gauges indicated that the elongation and compression of a weakened connector are larger than those of core of BRB. Moreover, the friction sound of the specimen was heard, and this was due to the friction between the weakened connector and the inner of the full-length outer restraint, resulting in the compression load of the specimen being greater than the tensile load.

When the loading displacement was close to 13 mm ($\theta=1/50$), the reading of Nos. 4 to 7 displacement meters changed slightly, and the core of the BRB entered the elastic-plastic stage and twisted. Subsequently, it was observed that the readings of the No. 1 and No. 2 displacement meters differed by more than 3mm, and this was attributed to the increased bolts slipping at the connection of the weakened connector and BRB. With the further increase of the loading, the friction between the weakened connector and the outer restraint intensified, resulting in the failure of some strain gauges, and the core-high-order buckling began to appear at the displacement of 17 mm ($\theta=1/40$). When the displacement finally loaded to 19 mm ($\theta=1/35$), the loading-carrying capacity of FLBRB-1 and FLBRB-2 reached the peak value, while that of FLBRB-3 began to dropped, thus the test was stopped.

3.5. Stress responses

The stress of each measuring point of the FLBRB in Fig. 7(b) was analyzed in the following description when the axial deformation of the specimen was 3mm, 7mm, 13mm and 19mm, respectively.

A significant difference among the stress responses of the three specimens was not evident. For simplicity, we took the stress data of FLBRB-1 as an example to illustrate the main characteristics of the stress distribution. As shown in Fig. 8(a), at the loading displacement of 3 mm ($\theta=1/210$), the stress of each measuring point was small. When the axial deformation increased to 7 mm ($\theta=1/90$), the stress at points Nos. 1 to 4 of the weakened connector was 132.0 MPa, 223.8 MPa, 243.6 MPa, and 237.9 MPa, respectively, which approached or exceeded the yield stress. This indicated that the weakened connector began to yield and resulted in yielding deformation, while the core of the BRB remained an elastic state, which the maximum stress response was only 168.3 MPa. As the test continued, the stress responses of the BRB and weakened connector rose with loading. When the axial deformation climbed to 13 mm ($\theta=1/50$), the stress responses of Nos. 1 to 4 were 253.2 MPa, 301.1 MPa, 323.6 MPa, and 302.4 MPa, respectively, while the maximum stress responses of Nos. 5 to 7 was 264.1 MPa. This result revealed that the plastic deformation appeared in BRB, which dissipated seismic energy with the weakened connector. It is noteworthy that the stress responses of the weakened connector (points Nos. 1 to 4) were greater than that of the core of the BRB (points Nos. 5 to 7) during the test process, as shown in Fig. 8. These results sufficiently demonstrate that the weakened connector began to yield before the BRB supplemented the energy dissipation. More importantly, the above stress responses and yield processes also satisfy the performance requirements of elastic and elastic-plastic story drift angle limited value ($\theta=1/250$ and $\theta=1/50$) recommended by the GB50011–2010.

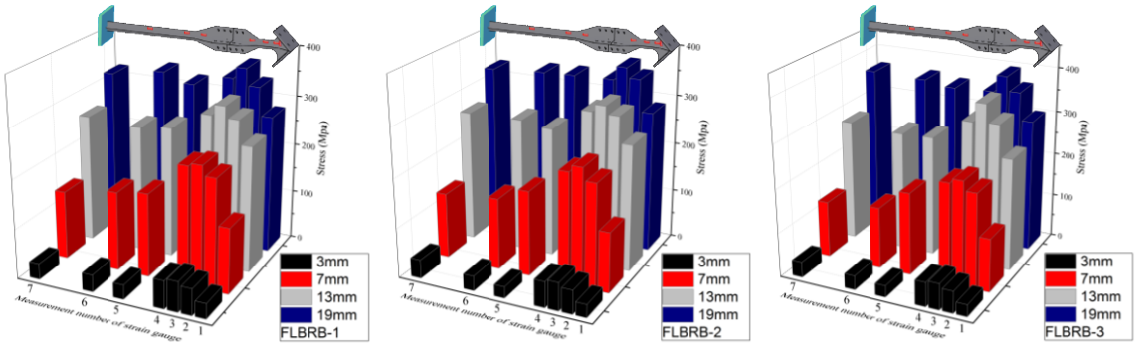

(a) FLBRB-1 (b) FLBRB-2 (c) FLBRB-3

Fig. 8 Comparison of stress responses of weakened connector and core of BRB

3.6. Failure process

The loading phenomenon and failure mode of the three specimens showing a basically consistent process during the test. At the loading level of 3 mm ($\theta=1/210$), three specimens were kept in elastic. When the axial deformation was increased to 7 mm ($\theta=1/90$), note that the strain of the weakened connector exceeded the yielding strain and had enter the plastic stage. As the axial displacement approached 13 mm ($\theta=1/50$), the stress of the core of BRB showed that it also yielded to consume energy. When the displacement expanded to 17 mm ($\theta=1/40$), the core-high-order buckling phenomenon occurred at the FLBRB, as shown in Fig. 9. Finally, the BRB and the weakened connector showed excessive deformation under axial cyclic load, especially in the FLBEB-3, for which the failure mode belongs to the fracturing due to the obvious deformation and buckling of the weakened connector. The main reason is that the smaller axial force ratio lead to premature buckling and fatigue failure at the yielding segment of the weakened connector under cyclic load. In summary, the failure process of the three specimens were ductile failures.

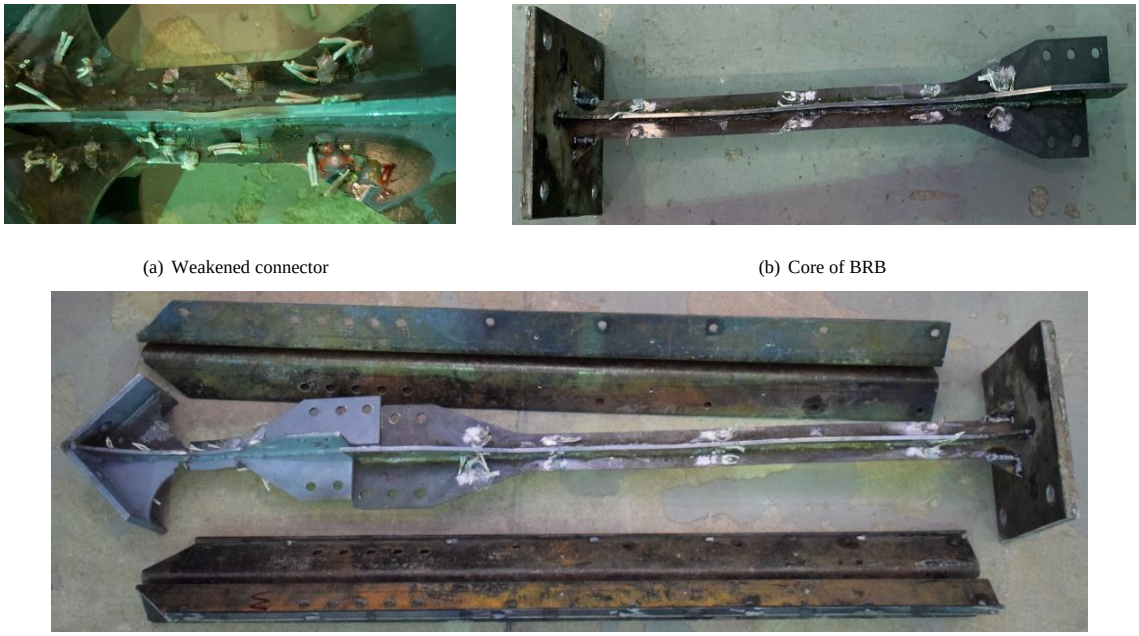

(a) Weakened connector (b) Core of BRB

(c) Disassemble the specimen

Fig. 9 Deformation of specimen

3.7. Hysteretic curve

The hysteretic curves of FLBRB-1, FLBRB-2, and FLBRB-3 are presented in Fig. 10. The load-displacement loops of three specimens had a shape of spindle and stable hysteretic capacity without obvious degradation during the loading process. The energy dissipation coefficient *E* of FLBRB-1, FLBRB-2, and FLBRB-3 were 2.38, 2.44, and 2.09, respectively, which verified that the FLBRB can effectively dissipate energy under cyclic load, and has excellent seismic behavior. What stood out in data from FLBRB-1 and FLBRB-2 was the coefficient *E* decreased with an increase in the length of the yielding segment of the weakened connector. These conclusions are consistent with the calculation of the total area of hysteretic curves.

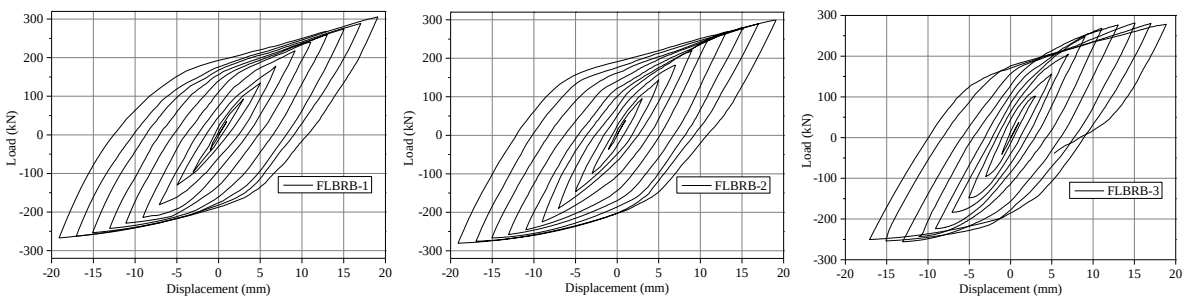

Fig. 10 Hysteretic Behavior of the FLBRB

The load-displacement curves of all specimens were similar and displayed a narrow shape during the initial stage. With the test progressed, it was observed that the area surrounded by the curve gradually increased with a increase of loading-carrying capacity, indicating that the weakening connector began to enter the phase of elastic-plastic, and the plastic energy consumption of the specimens increased steadily. When the loading reached a certain stage, another noteworthy finding was that the asymmetry between the compression and tension loading deteriorated as the friction interaction between the core of FLBRB and the inner surface of the full-length outer restraint increased.

In the later phase of the test, the loading of the specimens increased slowly and gradually achieved peak. Remarkably, the load of FLBRB-3 with the minimum axial force ratio declined significantly due to premature failure. The main cause of this result was that the axial force ratio reduced to a certain value that caused the weakened connector to become a weak component during the late stage of the experiment, which was not conducive to the energy consumption of the FLBRB. Consequently, the optimal axial force ratio was recommended in the range of 0.9 to 1.0 to ensure the bearing and hysteretic capacity of the specimen.

3.8. Skeleton curve

Fig. 11 shows skeleton curves of specimens, and related key parameters of the skeleton curves are presented in Table 3.

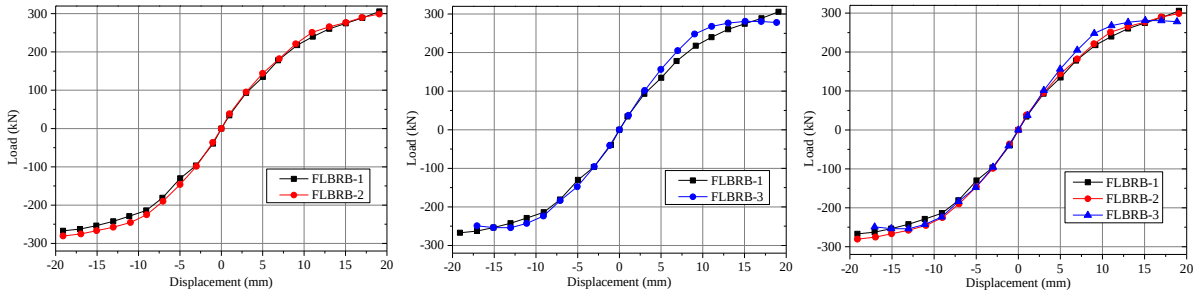

Fig. 11 Comparison of skeleton curves

A similar variation trend and loading-carrying capacity were observed from the comparison of skeleton curves. All specimens remain elastic within an axial displacement of approximately 5 mm. The initial stiffness in the positive and the negative increased linearly. Notably, the initial stiffness of FLBRB-2 was greater than that of the FLBRB-1, showing that the FLBRB-2 has higher yield load. With the progress of the test, the load increased at a slower speed and the slope of the curve decreased gradually.

For FLBRB-1 and FLBRB-3, the stiffness of FLBRB-3 degraded seriously at the later phase of test, and the ultimate strength of FLBRB-3, which has a low axial force ratio, is dramatically lower than that of FLBRB-1. This consequence further confirms the relationship between the loading-carrying capacity and axial force ratio; that is, the low axial force corresponds to a worsening energy dissipation and plasticity of the yielding segment of the weakened connector. In addition, the process of decreasing the length of the yielding segment of weakened connector is conducive to increasing the plasticity of the weakened connector and the loading-carrying capacity of the FLBRB.

4. Numerical simulation

4.1. FE modeling

Numerical simulation using Abaqus/Standard (version 6.12) was performed to investigate the yield mode and cyclic behavior of three specimens. Nonlinear material properties (Table 2) with the isotropic-kinematic hardening rules were implemented to reproduce the plastic behavior of all models.

The initial imperfection of 0.1% of the FLRBR length was imposed on the model. And the algorithm of Newton-Raphson was utilized for large displacement analyses. Besides, the 3D modeling was established using eight-node reduced integration solid element (C3D8R). And the element mesh sizes of the core of FLBRB and the full-length outer sleeve were 10 mm, and 20 mm, respectively (Fig. 12). Considering the interaction between the core of the FLBRB and the outer restraint, the hard contact and the penalty method were used for calculation of perpendicular and tangential interaction between inner and outer of the FLBRB, respectively. Applied the fixed constraint to the connection-end of the FLBRB, and the horizontal loading consistent with the test was applied at the reference point on the right side of the FLBRB, as shown in Fig. 13.

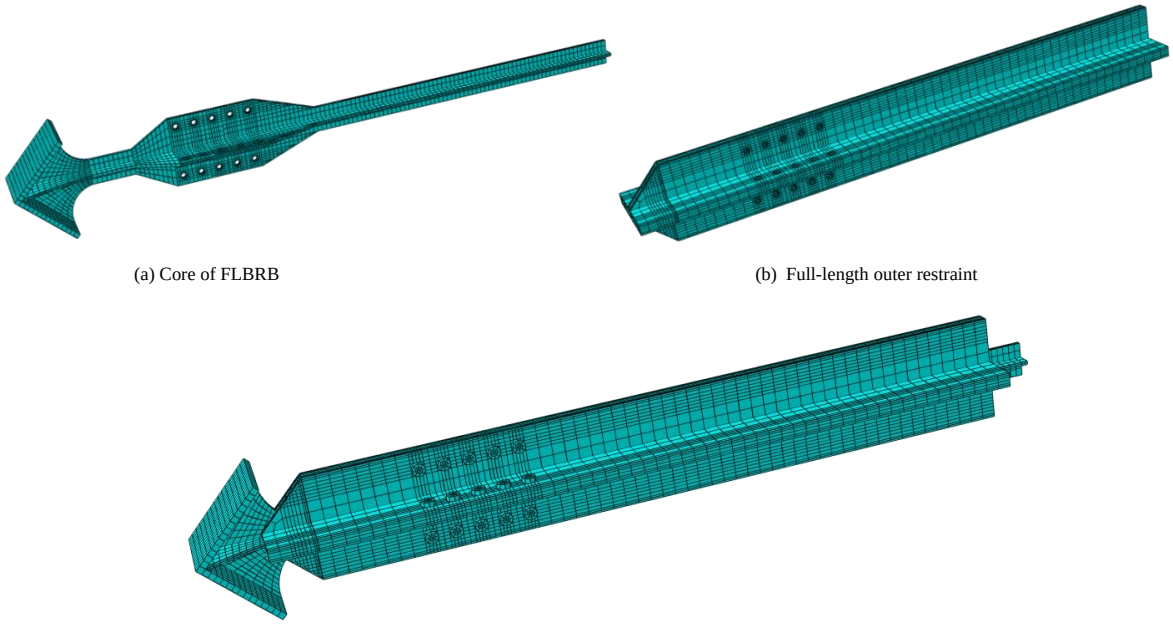

(a) Core of FLBRB

(b) Full-length outer restraint

(c) FLBRB

Fig. 12 FE model

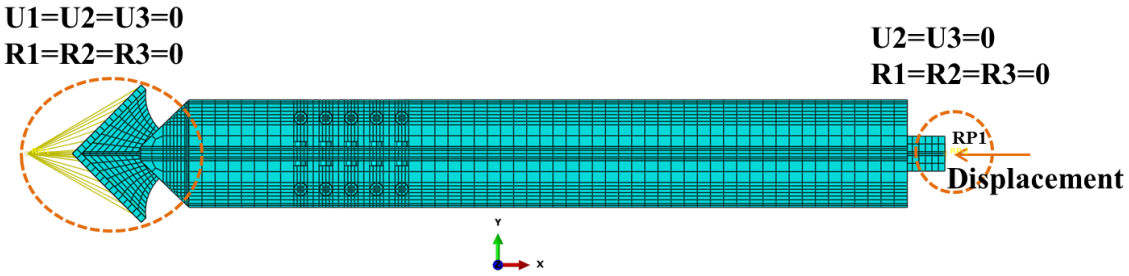

Fig. 13 Boundary constraints of FE model

4.2. Model verification

The hysteretic curve obtained from the FE of the FLBRB is shown in Fig. 14, displaying overall satisfaction between the FE and the test results. Besides, the numerical model can simulate the tension-compression asymmetric behavior well, and the maximum compression capacity is approximately larger than the maximum tension capacity by 10%. Furthermore, the prediction error of the ultimate bearing capacity was mostly less than 10% and some even within 1%, thus showing the accuracy of the refined FE model. However, there is a large error in the initial stiffness at the initial stage for the three specimens as depicted in Table 3. One of the prime reasons for the higher deviation of elastic stiffness was that the inevitable installation clearance and slipping in bolted connection resulting in inaccurate measurements of axial displacements. Nevertheless, the energy dissipation coefficients E of the experimental and FE models were both exceed 2.0, which indicated that the FLBRB has excellent energy dissipation capacity.

The stress distributions of the FLBRB with axis displacements of 3 mm, 7 mm, 13 mm, and 19 mm obtained from the FE simulation are shown in Fig. 15. Comparing with the stress response in Fig. 8 reveals that the stress value obtained from the FE simulation is consistent with the test at different loading displacements. At the initial loading stage, a weakened connector enters the plastic stage before BRB. With the test proceeding, both of BRB and weakened connector dissipate energy through plastic deformation. According to Mises stress diagram, it can be seen that the maximum stress of the FLBRB is mainly confined to the weakened connector.

As shown in Fig. 16, the similar deformation was observed in the comparison results. In addition, the failure regions of the specimens were coincident with the locations in the FE model. High-order buckling in core of BRB was well captured. In conclusion, the refined FE model provided an effective prediction for the dissipated energy, asymmetry behavior and buckling shape of the FLBRB under cyclic loading. Accordingly, the further theoretical research on FLBRB can be investigated through the FE simulated results.

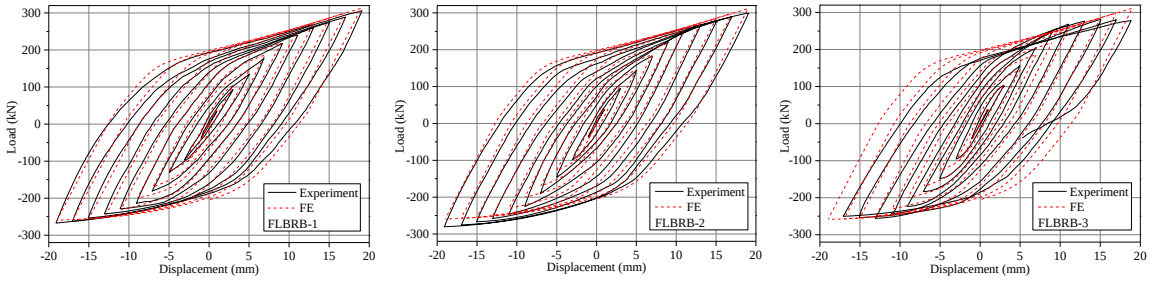

Fig. 14 Comparison of FE and experiment

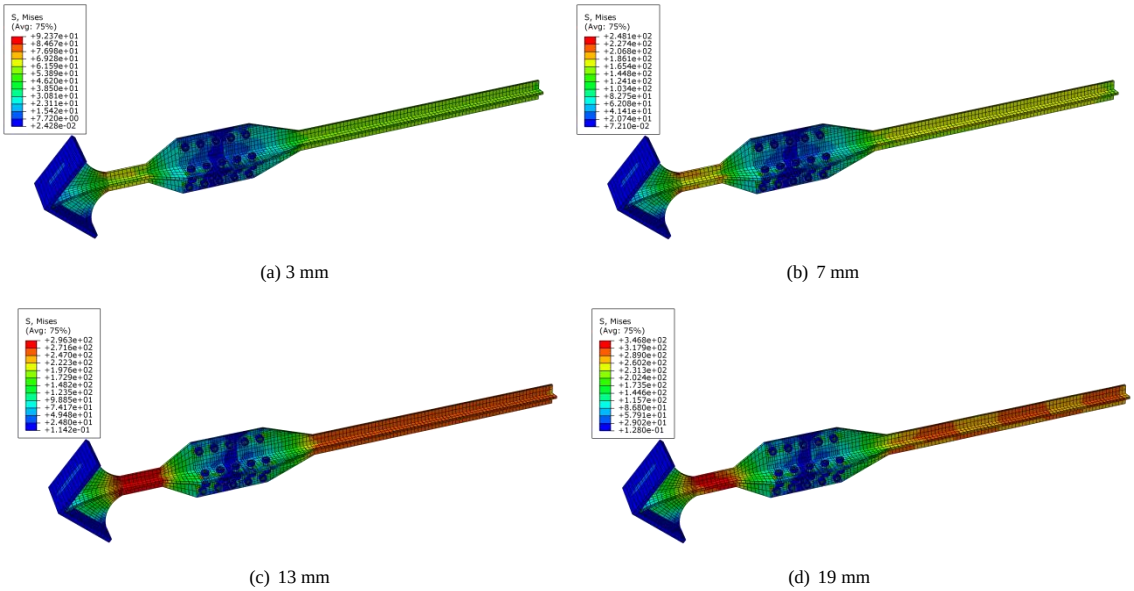

(a) 3 mm (b) 7 mm

(c) 13 mm (d) 19 mm

Fig. 15 Stress distribution of the FLBRB with different loading displacement

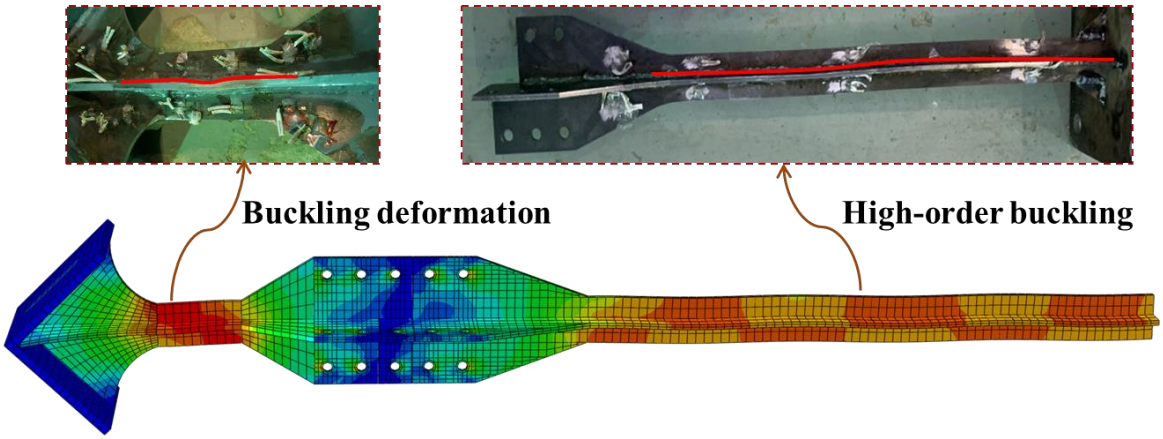

Fig. 16 Comparison of deformation

Table 3
Comparison of analysis results

			Positive		Negative	
			K_0 (kN/mm)	P_{max} (kN)	K_0 (kN/mm)	P_{max} (kN)
FLBRB-1		Test	38.68	305.664	38.5	-267.312
		FE	41.72	312.61	41.69	-260.39
		Theory	42.27	318.06	42.27	-289.14
	Error	Test-FE	7.29%	2.22%	7.65%	3.08%
		Theory-FE	1.3%	1.71%	1.37%	9.94%
		Theory-Test	8.49%	3.90%	8.92%	7.55%
FLBRB -2		Test	39.55	298.85	40.62	-280.61
		FE	42.1	311.23	42.08	-260.96
		Theory	42.48	318.86	42.48	-289.87
	Error	Test-FE	6.06%	3.98%	3.47%	7.86%
		Theory-FE	0.89%	2.39%	0.94%	9.97%
		Theory-Test	6.9%	6.28%	4.38%	3.19%
FLBRB -3		Test	37.46	281.09	38.62	-254.2
		FE	40.13	311.23	41.06	-258.56
		Theory	41.16	309.74	41.16	-281.58
	Error	Test-FE	6.65%	9.68%	5.94%	1.69%
		Theory-FE	2.5%	0.48%	0.24%	8.18%
		Theory-Test	8.99%	9.25%	6.17%	9.72%

5. Restoring force model of FLBRB

Based on the above tests and referring to the research of FLBRBs [44], the bilinear mechanical model for FLBRB was proposed through theoretical analysis, as well as the calculation for the stiffness of either loading or unloading was formulated. And the restoring force model of the FLBRB was proposed by combining the bilinear skeleton curve model and the load-unload rule, which is a reasonable calculation method for the further research of the design of a structure with FLBRB.

5.1. Bilinear mechanical model

Based on the experimental results, the axial displacement and loading-carrying capacity curve of the FLBRB can be simplified by a bilinear model. By analyzing the changing trend of the skeleton curve, it can be divided into two phases (Fig. 17) .

Phase I (Elastic stage, OA/OA'): In this stage, the whole specimen remains elastic. The load-displacement relationship changed linearly, which implies that the slope of the curve is equal to the initial stiffness of the FLBRB numerically.

Phase II (Elastic-plastic stage, AB/A'B'): The specimen enters this stage after reaching the yielding load. With the increase of displacement, the growth of load is slower than that of the Phase I, displaying obvious stiffness degradation characteristic, which is mainly caused by the yielding of the weakened connector and the BRB.

Accordingly, the simplified bilinear mechanical model needs to determine six characteristic parameters: initial stiffness K_y, yield displacement Δ_y, yield load P_y, post yield stiffness K_p, ultimate load P_u, and ultimate displacement Δ_u.

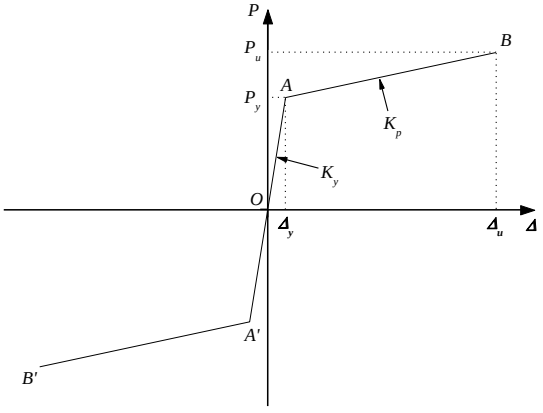

Fig. 17 Simplified Bilinear Mechanical Model

Initial stiffness K_y:

During the FLBRB design process, the equivalent stiffness is proposed to determine the initial stiffness of the specimen, which consists of weakened connector stiffness and BRB stiffness. The following Eqs. (7)-(9) were used to calculate the initial stiffness of the FLBRB based on series mechanism.

$$K_y = \frac{1}{1/K_{WC} + 1/K_{BRB}} \tag{7}$$

where K_{WC} and K_{BRB} are the elastic stiffness of the weakened connector and the BRB, respectively.

The elastic stiffness of the weakened connector K_{WC} can be obtained by Eq. (8), in which $K_{L_{c1}}$, $K_{L_{c2}}$, $K_{L_{c3}}$,and $K_{L_{c4}}$ are the stiffness of corresponding segments of L_{c1}, L_{c2}, L_{c3} and L_{c4} (as shown in Fig. 3(a)).

$$K_{WC} = \frac{1}{1/K_{L_{c1}} + 1/K_{L_{c2}} + 1/K_{L_{c3}} + 1/K_{L_{c4}}} \tag{8}$$

Similarly, elastic stiffness of the BRB can be calculated by the Eq. (9):

$$K_{BRB} = \frac{1}{1/K_{L_{c2'}} + 1/K_{L_{c3'}} + 1/K_{L_{c4'}}} \tag{9}$$

where $K_{L_{c2'}}$, $K_{L_{c3'}}$ and $K_{L_{c4'}}$ are the stiffness of corresponding segments of $L_{c2'}$, $L_{c3'}$ and $L_{c4'}$ for the core of BRB, respectively(Fig. 2(b)).

The stiffness in above Eqs. (7)-(9) can be calculated using axial stiffness formula $K = EA / L$.

Yield displacement Δ_y:

Based on the design concept of the FLBRB, the yield displacement of the FLBRB is determined by:

$$\Delta_y = \Delta_{WC,y} + \Delta_{BRB,y} = \frac{N_{WC} L_{WC}}{EA_{WC}} + \frac{N_{BRB} L_{BRB}}{EA_{BRB}} \tag{10}$$

where N_{WC} , N_{BRB}, A_{WC}, A_{BRB}, L_{WC} and L_{BRB} are the axial force, core cross-sectional area and length of the weakened connector and the BRB, respectively.

Yield load P_y:

When the FLBRB yields, the yield load is calculated according to the following equation:

$$P_y = K_y \cdot \Delta_y \tag{11}$$

Ultimate load P_u:

The strain hardening and the frictional interaction between the core of the FLBRB and the inner surface of the full-length outer restraint should be considered when calculating the ultimate load of the FLBRB, which is proposed by following Eq. (12):

$$P_u = \omega \cdot \gamma \cdot P_y \tag{12}$$

where ω is the strengthening factor of steel. According to the tests of three specimens and specified value in JGJ 99-2015, the recommended value for the Q235B steel is larger than 1.5. γ is the ratio of the maximum compression bearing capacity of the FLBRB to the maximum tensile bearing capacity. The AISC 341-16 specifies that the factor (γ) should be less than 1.3.

Ultimate displacement Δ_u:

Introducing the FLBRB incorporated into the SCBFs, the yield mechanism of the structure assumed that when the story drift angle of structure reaches the limit value specified in the GB50011-2010, the FLBRB forms a ductile failure mechanism. Ignores the deformation of the frame itself, the ultimate displacement of the FLBRB caused by the horizontal displacement of the structure can be expressed as:

$$\Delta_u = tg\theta \frac{BH}{L} \tag{13}$$

where L is the design length of FLBRB; θ is the ultimate story drift angle of the frame.

Post yield stiffness K_p:

The end weakening connector and BRB enter the elastoplastic stage successively, when the FLBRB exceeds the elastic stage. The post yield stiffness of the FLBRB can be calculated according to the following Eq. (14):

$$K_p = \frac{P_u - P_y}{\Delta_u - \Delta_y} \tag{14}$$

5.2. Bilinear mechanical model

The characteristic points of the bilinear mechanical model can be calculated according to Eqs. (7)-(14). The comparison of the theoretical skeleton curve and the test results is shown in Fig. 18 and Table 3. And there were differences of 8.71%, 5.64% and 7.58% between the theoretical initial stiffness (K_y) and the experimental initial average stiffness for three specimens, respectively, while the computed ultimate load (P_u) of the FLBRB agreed well with the tested ultimate load within a 10% difference. The result of having a larger difference in initial stiffness was possibly because of the installation clearance and slippage in the bolted connection and the discreteness of the test data. Meanwhile, the results showed the theoretical initial stiffness and ultimate load of the three specimens can be well fitted with the test, with an average difference of 7.31% and 6.65%, respectively. The results of comparison and analysis confirmed that the suggested Eqs. (7)-(14) can be used to calculate the equivalent stiffness and bearing capacity of the FLBRB.

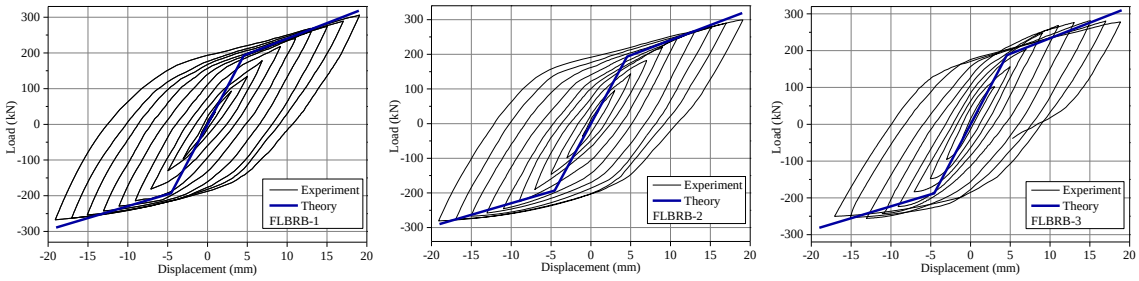

Fig. 18 Verification of the simplified bilinear mechanical model

5.3. Simplified restoring force model

On the basis of the theoretical analysis and numerical regression of FE data, the simplified restoring force model was established. According to the hysteretic curves of test, the loading phase can be divided into four typical stages: positive elasticity, positive elastic-plasticity, negative elasticity, and negative elastic-plasticity, while the unloading phase is divided into two typical stages: positive unloading and reverse unloading. Fig. 19 depicts the proposed restoring force model of the FLBRB. And the hysteresis criterion can be concluded as follows:

(1) When the loading does not reach the yield displacement Δ_y, the FLBRB is in the elastic stage, *OAB* and *OA'B'* are the positive and negative loading-unloading routes of the specimens, and K_y represents the loading and unloading stiffness. The bearing capacity was symmetrical on the whole in positive and negative loading directions.

(2) The loading route process along with the skeleton curves when the

loading exceeds the yielding load from the yielding point *A* to the *a*, the stiffness can be defined as post yield stiffness K_p. Then the unloading process reaches the point *b*, the slope of *ab* is defined as the positive unloading stiffness K_1. After that, the specimen continues reverse loading along the route *bA'c*, then unloads from point *c* towards point *d*, and the slope of *cd* is defined as the negative unloading stiffness K_2. Then continue to load and cycle until the maximum displacement.

(3) As the load over the yield load of the FLBRB, the unloading stiffness will gradually decrease with the increasing load due to the weakened connector and core of BRB yield successively. As shown in Fig. 20, fitting unloading stiffness data for each hysteretic loop to obtain the K_1 and K_2:

$$K_1 = 0.93218K_y(\Delta_1/\Delta_u)^{-0.0393} \tag{15}$$

$$K_2 = 0.90856K_y(\Delta_2/\Delta_u)^{-0.0319} \tag{16}$$

where Δ_1 and Δ_2 are the displacement corresponding to the positive and negative unloading, respectively.

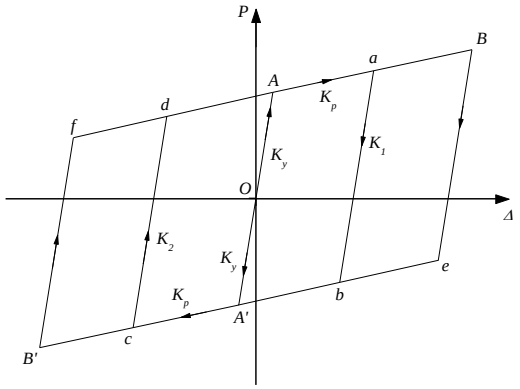

Fig. 19 Simplified restoring force model

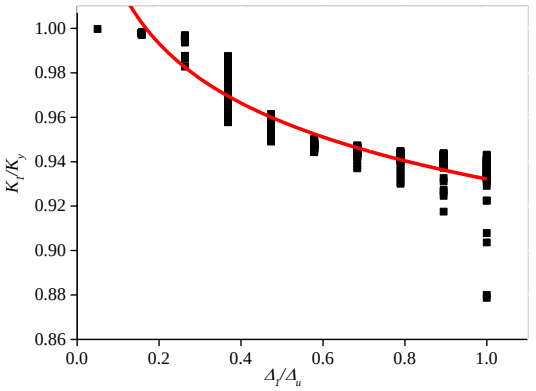

(a) Positive

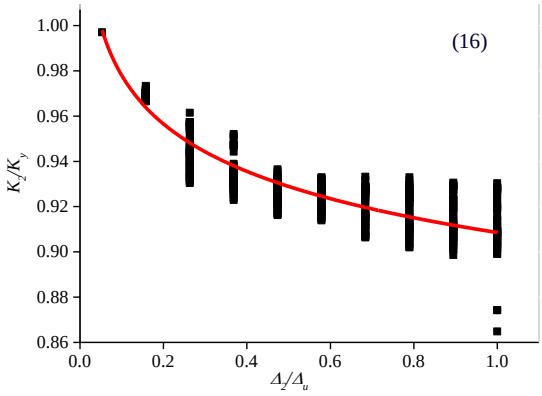

(b) Negative

Fig. 20 Fitting curve of stiffness degradation

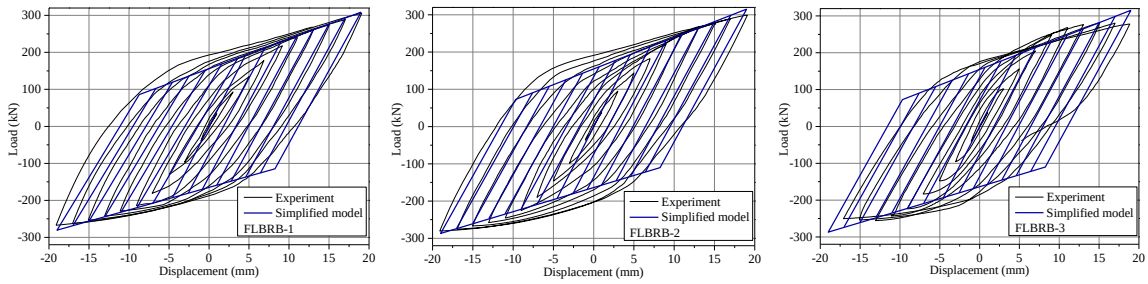

Fig. 21 Verification of restoring force model

5.4. Validation of theoretical model

To verify the theoretical restoring force model, the experimental hysteretic curves of three specimens are comparted with the calculated model, as shown in Fig. 21. A satisfactory agreement of hysteretic behaviors between the theoretical model and test results was observed, which shows that the suggested loading-unloading rule can predict the hysteresis behavior of the FLBRB. However, it can be found that the theoretical restoring force curve does not transit smoothly, mainly attributed to the simplified bilinear mechanical model adopted by the skeleton curve.

6. Conclusion

The new assembled buckling-restrained brace with a full-length outer restraint (FLBRB) was designed and tested to evaluate its hysteretic properties. The experimental results and comparisons of the test with numerical analysis were analyzed. In addition, a theoretical restoring force model was established and verified with experiments. Conclusions are listed below:

(1) The FLBRB showed excellent hysteretic property and deformation ability. The inelastic deformation was mainly concentrated in the weakened connector and BRB using the full-length outer restraint, which effectively improves the stability of the end-weakened connector and avoids the instability of the connecting section between the weakened connector and the BRB.

(2) The specimen with a bolted connection was convenient for installation and replacement. Each part of the FLBRB is assembled with high-strength bolts on site, forming a structure in which all components can be repaired and replaced.

(3) The numerical models of specimens were established, and the dissipated energy, asymmetry behavior and buckling shape of the FLBRB were verified by the tests. The result indicated that the refined FE model can simulate the behavior of the FLBRB under cyclic load well.

(4) On the basis of equivalent stiffness, a formula of the simplified bilinear skeleton model and the load-unload criterion was proposed and validated numerically and experimentally, which can be used to predict the hysteretic curve of FLBRB.

(5) The experimental and theoretical research will provide the suggestion and reference for designs and applications of the FLBRBs in the structures of buildings. Besides, further numerical simulation and test are needed to study the mechanical behaviors and the seismic performances of the structure with the FLBRB.

Acknowledgments

This study has been supported by the National Natural Science Fund of

China under grant No. 51968044, and the National Key Research and Development Program of China No. 2019YFD1101003.

References

[1] Uriz P., "Toward earthquake-resistant design of concentrically braced steel frame structures", PhD Thesis, University of California, Berkeley, CA, USA, 2005.

[2] Astaneh-Asl A., Goel S.C., and Hanson R.D., "Cyclic behavior of double angle bracing members with end gusset plates", Research Report UMEE 8287, University of Michigan, Ann Arbor, MI, USA, 1989.

[3] El-Tayem A.A., and Goel S.C., "Cyclic behavior of angle X - Bracing with welded connections", Research report UMCE 85-4, University of Michigan, Ann Arbor, MI, USA, 1985.

[4] Black R.G., Wenger W.A.B., and Popov E.P., "Inelastic buckling of steel struts under cyclic load reversals", UCB/EERC-80/40, Earthquake Engineering Research Center, University of California, Berkeley, CA, USA, 1980.

[5] Tremblay R., Filiatraul A., and Timler P., "Performance of steel structures during the 1994 Northridge earthquake", Canadian Journal of Civil Engineering, 22(2):338-360, 1995.

[6] Hsiao P.C., "Seismic Performance Evaluation of Concentrically Braced Frames", PhD Thesis, University of Washington, Seattle, WA, USA, 2012.

[7] Roeder C.W., Lehman D.E., Clark K., Powell J., Yoo J.H., Tsai K.C., Lin C.H., and Wei C.Y., "Influence of gusset plate connection and braces on the seismic performance of X-braced frames", Earthquake Engineering and Structural Dynamics, 40(4):355-374, 2011.

[8] Roeder C.W., Lumpkin E.J., and Lehman D.E., "A Balanced Design Procedure for Special Concentrically Braced Frame Connections", Journal of Constructional Steel Research, 67(11):1760-1772, 2011.

[9] Fleischman R.B., and Hoskisson B.E., "Modular Connectors for Seismic Resistant Steel Moment Frame", Advanced Technology in Structural Engineering, 103:1-9, 2000.

[10] Fleischman R.B., Li X., Pan Y., and Sumer A., "Cast Modular Panel Zone Node for Steel Special Moment Frames. I: Analytical development", Journal of Structural Engineering, 133(10):1393-1403, 2007.

[11] Fleischman R.B., Palmer N.J., Wan G., and Li X., "Cast Modular Panel Zone Node for Steel Special Moment Frames. II: Experimental Verification and System Evaluation", Journal of Structural Engineering, 133(10):1404-1414, 2007.

[12] Sumer A., Fleischman R.B., and Hoskisson B.E., "Development of a Cast Modular Connector for Seismic-Resistant Steel Frames part I: Prototype Development", AISC Engineering Journal, 44(3):195-211, 2007.

[13] De Oliveira J., Packer J., and Christopoulos C., "Cast steel connectors for circular hollow section braces under inelastic cyclic loading", Journal of Structural Engineering, 134(3):374-383, 2008.

[14] Gray M.G., Christopoulos C., and Packer J.A., "Cast steel yielding fuse for concentrically braced frames", Proceeding of the 9th US National and 10th Canadian Conference on Earthquake Engineering, July 25-29, Ottawa, ON, Canada, 2010.

[15] Gray M.G., Christopoulos C., Packer J.A., and Lignos D.G., "Development, Validation and Modeling of the new Cast Steel Yielding Brace System", Proceedings of the 20th Analysis and Computation Specialty Conference, Chicago, JOT, USA, 2012.

[16] Gray M.G., Christopoulos C., and Packer J.A., "Cast Steel Yielding Brace System for Concentrically Braced Frames: Concept Development and Experimental Validations", Journal of Structural Engineering, 140(4):1-11, 2014.

[17] Federico G., "Use of Cast Modular Components for Concentrically Braced Steel Frames", PhD Thesis, University of Arizonza, AZ, USA, 2012.

[18] Ward K.M., Fleischman R.B., and Federico G.A., "Cast modular bracing system for steel special concentrically braced frames", Engineering Structures, 45:104-116, 2012.

[19] Federico G., Fleischman R.B., and Ward K.M., "Buckling control of cast modular ductile bracing system for seismic-resistant steel frames", Journal of Constructional Steel Research, 71:74-82, 2012.

[20] Balut N., and Gioncu V., "Suggestion for an improved 'dog-bone' solution", Proceedings of the 4th International Conference on Behavior of Steel Structures in Seismic Areas, Naples, Italy, 2003.

[21] Stevens D., and Wiebe L., "Experimental Testing of a Replaceable Brace Module for Seismically Designed Concentrically Braced Steel Frames", Journal of Structural Engineering, 145(4):1-11, 2019.

[22] Zhao J.X., Chen R.B., Wang Z., and Pan Y., "Sliding corner gusset connections for improved buckling-restrained braced steel frame seismic performance: Subassemblage tests", Engineering Structures, 172:644-662, 2018.

[23] Zhao J.X., Yu H.C., Pan Y., Chen R.B., and Guo R., "Seismic performance of sliding gusset connections in buckling-restrained braced steel frame", Journal of Building Structures, 40(02):117-127, 2019.

[24] AISC 341-16. Seismic provisions for structural steel buildings, American Institute of Steel Construction, Inc, Chicago, IL, USA, 2016.

[25] Okazaki T., Dimitrios G.L., Mitsumasa M., James M.R., and Jay L., "Damage to steel buildings observed after the 2011 Tohoku earthquake", Earthquake Engineering Research Institute, 29(1_suppl):219–243, 2013.

[26] Wakabayashi M., "Experiments on the elastic-plastic behavior of bars subjected to cyclic axial loads", Proceedings of Annual Meeting, October, Japan, 1972.

[27] Watanabe A., Hitomi Y., Saeki E., Wada A., and Fujimoto M., "Properties of brace encased in buckling-restraining concrete and steel tube", Proceeding of the 9th World Conference on Earthquake Engineering, August 2-9, Toyko, Kyoto, Japan, 1988.

[28] Tsai K.C., Lai J.W., Hwang Y.C., and Lin S.L., "Research and application of double-core buckling restrained braces in Taiwan", 13th World conference on earthquake engineering, August 1-6, Vancouver, BC, Canada, 2004.

[29] Jia M.M., Li L., Hong C., Liu K., and Sun L., "Experiment of hysteretic behavior and stability performance of buckling-restrained braced composite frame", Advanced Steel Construction, 17(2):149-157, 2021.

[30] Shi, Y., Qian, H., Kang, L., Li, Z., and Xia, L., "Cyclic behavior of superelastic SMA cable and its application in an innovative self-centering BRB", Smart Materials and Structures, 30(9): 095019, 2021.

[31] Zhang, C., Zong, S., Sui, Z., and Guo, X., "Seismic performance of steel braced frames with innovative assembled self-centering buckling restrained braces with variable post-yield stiffness", Journal of Building Engineering, 64:105667, 2023.

[32] Hu, B., Min, Y., Wang, C., Xu, Q., and Keleta, Y., "Design, analysis and application of the double-stage yield buckling restrained brace", Journal of Building Engineering, 48:103980,2022.

[33] Lu, Y., Liu, Y., Wang, Y., Liu, J., and Huang, X., "Development of a novel buckling-restrained damper with additional friction energy dissipation: Component tests and structural verification", Engineering Structures, 274:115188, 2023.

[34] Yue Y.C., Bai Y.T., Wang Y., Ma X.F., Wang Y.H., and Li X.H., "Experimental behavior and design of rectangular concrete-filled tubular buckling-restrained braces", Advanced Steel Construction, 17(4):366-375, 2021.

[35] Xie L.Q., Wu J., Shi J.H., and Zhu Y.Q., "Influence of the core-restrainer clearance on the mechanical performance of sandwich buckling-restrained braces", Advanced Steel Construction, 16(1):37-46, 2020.

[36] Yin Z.Z., Chen W., Chen S.L., and Wang X.L., "Experimental study of improved double-tube buckling restrained braces", Journal of Building Structures, 35(09):90-97, 2014. (in Chinese)

[37] Yin Z.Z., Yang B., and Zhang X.B., "Design of an eccentrically buckling-restrained braced steel frame with web-bolted replaceable links", Journal of Constructional Steel Research, 192:1-18, 2022.

[38] Yin Z.Z., Yang B., and An S.Z., "Seismic Performance Analysis of Buckling-Restrained Braced Steel Frames with Ductile Castings", KSCE Journal of Civil Engineering, 25(10):1-18, 2021.

[39] Yin Z.Z., Xu D.Y., and Yang B., "Experimental study of prefabricated buckling-restrained braces with ductile casting connectors", Journal of Building Structures, 43(1):77-85, 2022. (in Chinese)

[40] GB 50011-2010. Code for Seismic Design of Buildings, China Ministry of Construction, Beijing, China.

[41] JGJ 99–2015. Technical specification for steel structure of tall building, China Ministry of Construction, Beijing, China.

[42] Bao S.H., Structural design of high-rise building, China Architecture & Building Press, Beijing, China.

[43] Li J.M., "Experimental study on buckling restrained brace with ductile connectors", MS Thesis, Lanzhou University of Technology, Lanzhou, China, 2019. (in Chinese)

[44] Yin Z.Z., Feng D.Z., Yang B., and Pan C.C., "The Seismic Performance Analysis of Double Tube Buckling Restrained Brace with Cast Steel Connectors", Advanced Steel Construction, 18(1):436-445, 2022.

[45] Xu D.Y., "Research on Mechanical Properties of Special Centrically Braced Steel Frame with the Weakened Ductile Connectors", MS Thesis, Lanzhou University of Technology, Lanzhou, China, 2020. (in Chinese)

[46] GB/T 228.1-2010. Tensile testing of metallic materials—Part 1: Room temperature test methods, General Administration of Quality Supervision, Inspection and Quarantine, Beijing, China.

[47] GB/T 2975-2018. Steel and steel products-Location and preparation of samples and test pieces for mechanical testing, State Administration for Market Regulation, Beijing, China.

[48] JGJ/T 101-2015. Specification for seismic test of buildings, China Ministry of Construction, Beijing, China.

Advanced Steel Construction – Vol. 19 No. 3 (2023) 197–208
DOI:10.18057/IJASC.2023.19.3.2

DEVELOPMENT OF ANALYTICAL MODELS FOR PREDICTING THE FLEXURAL BEHAVIOUR OF ENGINEERED CEMENTITIOUS COMPOSITES – HIGH STRENGTH STEEL COMPOSITE BEAMS

Cong-Luyen Nguyen [1, *] and Chi-King Lee [2]

[1] *The University of Danang – University of Science and Technology, Danang 550000, Vietnam*
[2] *School of Engineering and Information Technology, The University of New South Wales, Canberra, ACT 2600, Australia*
** (Corresponding author: E-mail: ncluyen@dut.udn.vn)*

ABSTRACT

This paper presents the results of three-dimensional (3D) finite element (FE) and analytical models on the prediction of the flexural behaviour of composite beams comprising high strength steel (HSS) I-section and Engineered Cementitious Composite (ECC) slab. In the FE approach, 108 composite beam models which cover a wide range of key parameters including HSS grade, ECC compressive strength, HSS section depth, ECC slab thickness, ECC slab width were generated and analysed. The flexural strength of these composite beam models was subsequently employed to validate the accuracies of some commonly used flexural strength prediction methods that are originally based on the rigid plastic analysis (RPA). It was found that these methods generally underpredicted the flexural strength of the ECC-HSS composite beams. Hence, a simple analytical model was proposed, and validation results of its accuracy showed that this simple analytical model produced more accurate predictions than the RPA methods. In order to allow designers to obtain the load-deflection curves of the beams, a full analytical model which is based on strain compatibility and force equilibrium was also developed. Validations against both FE model and test results showed that this full analytical model produced the most accurate flexural strength predictions.

ARTICLE HISTORY

Received: 26 September 2022
Revised: 16 February 2023
Accepted: 23 February 2023

KEYWORDS

Engineered cementitious Composite–high strength steel composite beams;
Flexural behaviour;
Flexural strength;
Rigid plastic analysis;
Simple analytical model;
Full analytical model

Copyright © 2023 by The Hong Kong Institute of Steel Construction. All rights reserved.

1. Introduction

High strength steel (HSS), which normally possesses yield strength of higher than 690 MPa, has been increasingly applied in structural engineering thank to its superior strength to weight ratio which enhances structural performance and leads to more sustainable design. Furthermore, advances in steel manufacturing technology also reduce the cost of HSS and increase its weldability. As a result, many studies have been dedicated in an attempt to investigate the behaviour of HSS structures in forms of bare steel structures [1-8], composite columns [9-11], connection details [12-14], encased [15-17] and composite beams [18-22].

One potential application of HSS is the construction of composite beam in which the HSS section is placed at the bottom to resist tension and normal strength concrete (NSC) is placed on top to resist compression. Nevertheless, previous studies reported that the superior yield strength of HSS section might not be fully utilized when NSC slab was used. To be more specific, the yield strain of HSS (0.35% for S690 grade) could exceed the peak compressive strain (≈0.3%) of NSC. As a result, this may lead to a premature failure of NSC-HSS composite beam when NSC slab is crushed before the HSS section is fully yielded [19-24]. When comparing the FE and test results of NSC-HSS composite beams with predicted results by the rigid plastic analysis (RPA) in terms of its flexural strength, it was found that the RPA overpredicted their test results. Note that RPA approach assumes HSS section fully yielded in its calculation of flexural strength and has been adopted by many national standards to predict the flexural strength of NSC–normal strength steel (NSS) composite beams [25,26].

In order to address such strain incompatibility issue, Engineered Cementitious Composites (ECC) was employed to replace NSC in constructing slab of HSS composite beam [18]. ECC is a form of advanced building material [27] which is well-known for its high compressive and tensile strain capacities [17,28]. The compressive strain at peak strength for almost all types of ECC exceed 0.5% which is higher than the yield strain of nearly all HSS grades employing in structural engineering. This allows ECC to work efficiently with HSS in composite beam construction. In addition, it is recently reported that ECC is capable of preventing longitudinal shear failure of composite beam if NSC slab is used in conjunction with HSS section [29]. By conducting a series of test on ECC-HSS composite beams, Nguyen and Lee [18] found that ECC-HSS composite beams showed higher strength and ductility than those constructed with NSC slab and HSS I-section. In addition, the RPA conservatively predicted the flexural strength of ECC-HSS composite beams [18]. Nevertheless, limited results obtained from the costly and time-consuming experimental study are obviously not sufficient to examine the prediction of RPA methods over the flexural capacity of ECC-HSS composite beams. Thus, in this study, the 3D FE model which has been developed and validated against the experimental results reported in authors' previous work [18] was employed to generate 108 models which cover a wide range of key parameters of the composite beams. The results of these models were then used to assess the accuracies of flexural strength predictions obtained from different methods based on RPA. Simple analytical model was subsequently developed in order to predict the flexural strength of ECC-HSS composite beams more precisely. Furthermore, a full analytical model was proposed to allow engineers to obtain the ECC-HSS composite beam's detailed responses (i.e., the load-displacement curves, flexural strength).

2. FE model used and parameter design

The FE model employed in this study, which uses the FE software ABAQUS [30], was shown to produce accurate predictions when comparing with experimental results [18] for all stages of the composite beams comprising ECC slab and HSS section under 4-point bending load. As the model development and validation processes were described with details in [18], only a summary of its key features is given here.

2.1. Key features of the FE model used

The beam cross-sectional configuration is shown in Fig. 1(a). All beams modelled are simply supported with clear span of 3100 mm and are under four-point bending. The lengths of the pure bending region and the shear span are 800 mm and 1150 mm, respectively [18]. The main structural components of the composite beam which consist of the HSS section, the ECC slab and the shear studs were modelled using eight-node hexahedral solid elements with reduced integration (C3D8R) [30]. Four-node shell elements (S4R) and three-node truss elements (T3D2) were employed to model the profiled steel sheeting (PSS) and slab reinforcement, respectively. After a mesh size sensitivity analysis [18], nominal element sizes of 40 mm and 20 mm were respectively used within the two shear spans and pure bending region. Interactions between PSS and ECC slab, between PSS and HSS section, and between shear studs and ECC slab were defined by ABAQUS's surface-to-surface contact feature. Contacts between shear studs and HSS section's top flange, between loading plates and the slab were guaranteed by tie constraints (Fig. 1(b)). Roller and pin constraints were employed to reproduce the test support conditions. Loading was applied in such a way that prescribed downward displacement was assigned to nodes located on the surfaces of two loading plates. A typical FE model is shown in Fig. 1(c). Constitutive models for different materials used were

presented in [18] and are indicated in Fig. 2(a)-(f). For ECC, damage evolution was applied when it reached its compressive strain, as indicated in Fig. 2(g). Values of all key material parameters employed in the constitutive models of the FE models are listed in Tables 1–2.

2.2. Parameter design

The following five key parameters which define the beam's cross-sectional dimensions and material properties are considered and their modelling ranges are listed below:

(1) HSS grade (S690 and S960 grades HSS)
(2) ECC compressive strength (40 MPa and 70 MPa)
(3) HSS section depth (180 mm, 230 mm and 280 mm)
(4) ECC slab thickness (140 mm, 170 mm and 200 mm)
(5) ECC slab width (600 mm, 1000 mm and 1400 mm).

Names of composite beams modelled are labelled using the format of "SW*a*-ST*b*-ID*c*-E*x*-S*y*" where "SW", "ST", "ID" respectively denotes the ECC slab width, ECC slab thickness and depth of HSS I-section (Fig. 1(a)). "E" and "S" represent the compressive strength of ECC (f'_{ECC}) and the HSS yield strength ($f_{y(HSS)}$), respectively. "*a*", "*b*", "*c*" are respectively the slab width, slab thickness and HSS section depth in mm. "*x*", "*y*" are f'_{ECC} and $f_{y(HSS)}$ in MPa, respectively. For instance, "SW600-ST140-ID180-E40-S690" refers to a beam comprising a 600 mm × 140 mm ECC slab with compressive strength of 40 MPa connected to a S690 HSS section with a depth of 180 mm. These beams were arranged with the same shear studs with shank diameter of 19 mm and stud height of 100 mm after welding, stud spacing of 100 mm, steel beam's flange width b_f of 120 mm, steel beam's flange thickness t_f of 8 mm, and steel beam's web thickness t_w of 6 mm. These were similar to the test conducted by the authors reported in [18]. It should be noted that shear connection degree η of the beam is defined by the ratio of the number of shear connectors installed in the beam (n) to the number of shear connectors required for full shear connection (n_f). Beam with $\eta \geq 1$ is considered as fully connected in shear. Otherwise, it is partially shear connected. η is affected by all of parameters mentioned above since they all have effects on the value of n_f. As the shear stud spacing was kept constant at 100 mm (n is constant) but cross-sectional dimensions and material parameters are varied among the beams (n_f is varied), η for these sets of models varied between 0.42 and 0.82. These models were divided into two subsets based on the HSS yield strength (i.e, S690 MPa and S960 MPa). Their details and flexural strength (P_{FE}) obtained from the FE modelling are listed in Table 3.

3. Comparing flexural strength obtained from FE models with RPA predictions

The RPA [31] is a reliable method in predicting the flexural strength of composite beams constructing by using NSC slab and NSS section. It uses the concept of stress blocks for the calculation of the beam's flexural strength. It has been adopted by Eurocode 4 [25] and AS2327 [26] for NSC-NSS composite beam design. However, previous studies [19-21,23] reported that the flexural strength predicted by RPA ($M_{RPA,equi}$) might not be conservative for NSC-HSS composite beams. One possible reason is that the NSC slab was crushed before the HSS section reached a high degree of yielding [18]. For NSC-HSS beam, Eurocode 4 [25] and AS2327 [26] suggest that when using the RPA, a reduction factor should be applied to account for the limited strain hardening of HSS. Hence, the flexural strength predicted by these codes, $M_{EC4/AS2327}$, is more conservative than $M_{RPA,equi}$.

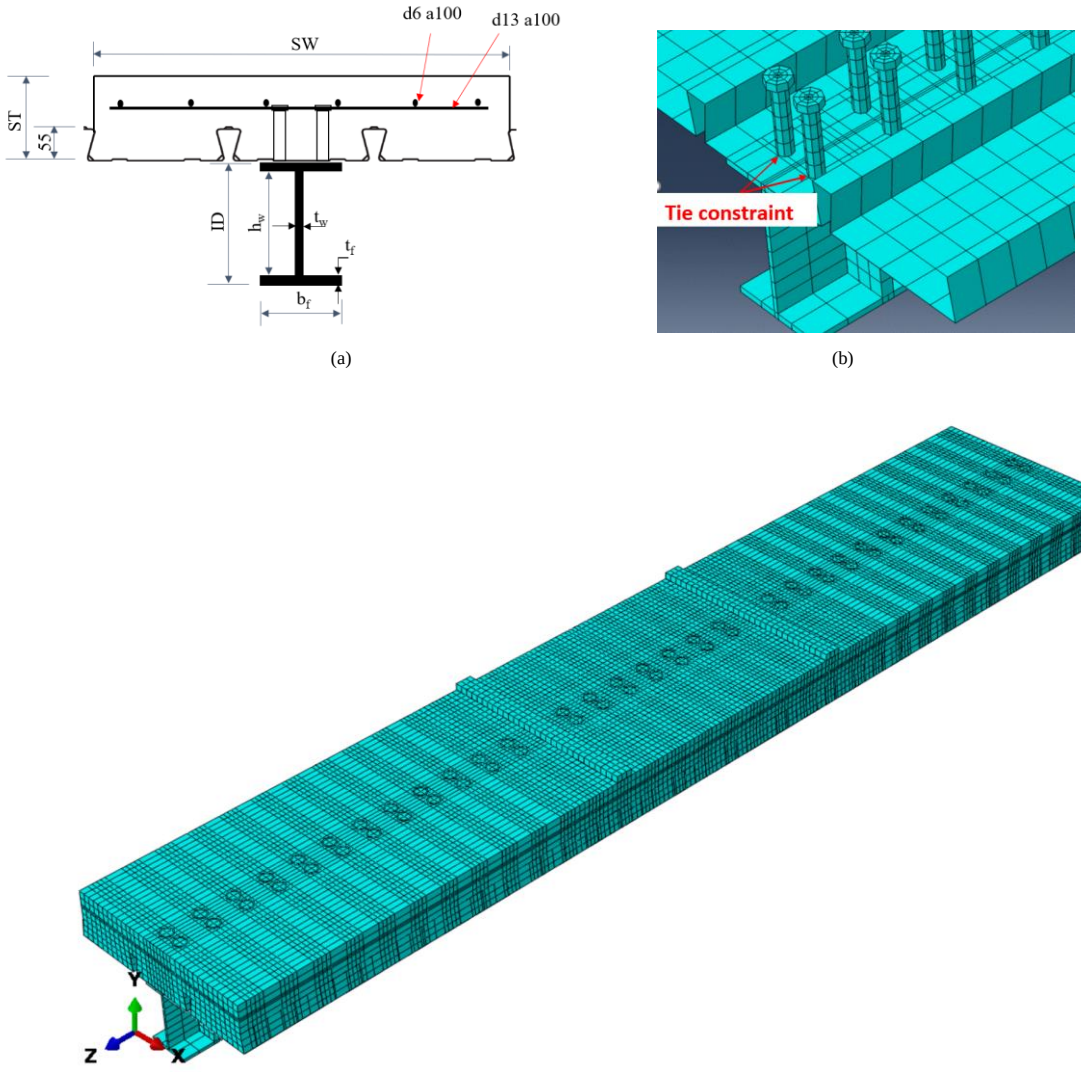

(a) (b)

(c)

Fig. 1 Beam's cross-section and FE model: (a) Cross-section configuration; (b) Shear studs meshing and contact between shear studs and steel beam; (c) Typical FE model

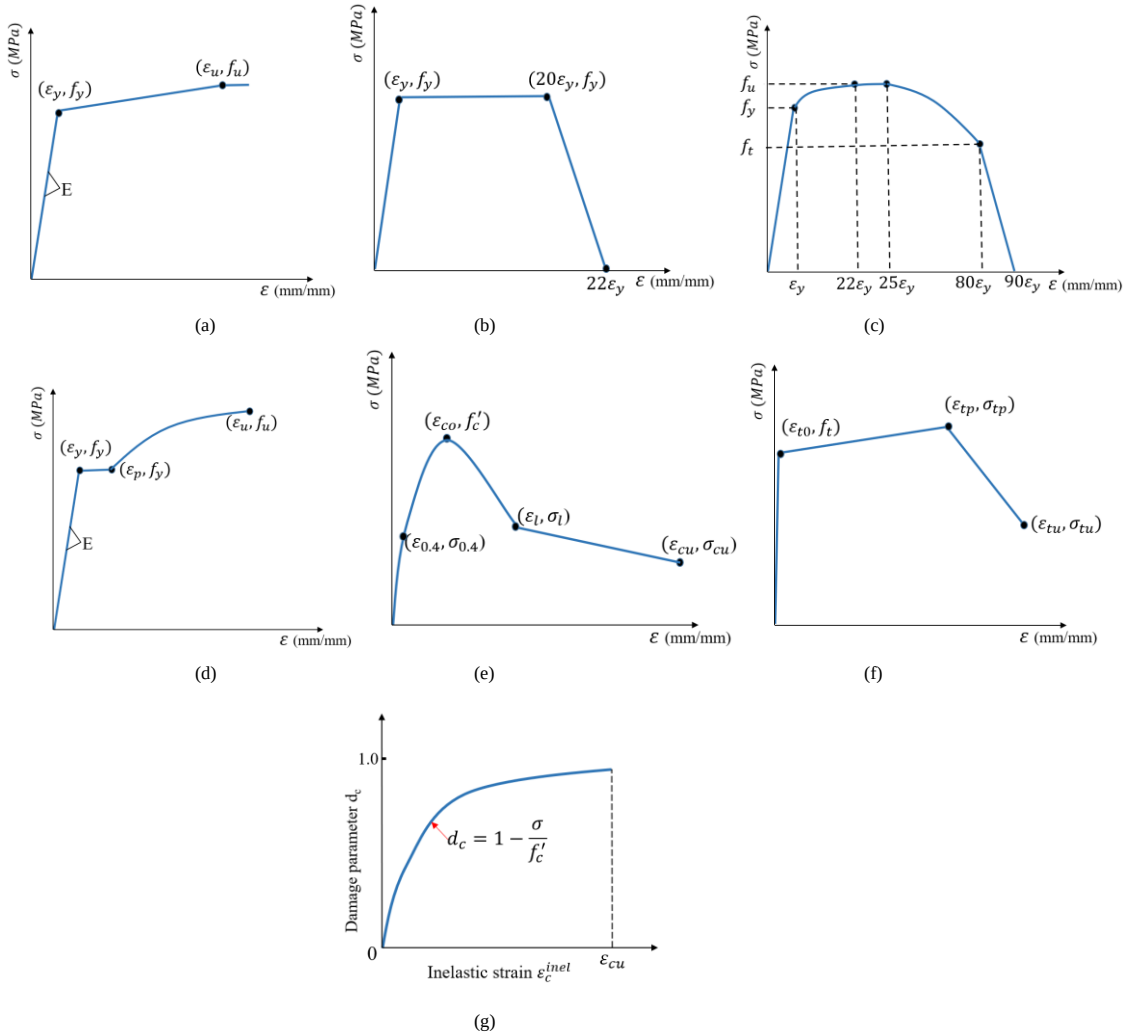

Fig. 2 Stress – strain models for materials used in the FE models: (a) HSS; (b) PSS; (c) Headed shear stud; (d) Steel reinforcement; (e) Compressive stress-strain model for ECC; (f) Tensile stress-strain model for ECC; (g) Compressive damage model for ECC

Table 1
Material properties used in the FE models

Material	E (GPa)	ε_y(%)	f_y (MPa)	ε_p(%)	ε_u(%)	f_u (MPa)	f_t (MPa)
S690	200	0.35	690	-	8.0	770	-
S960	200	0.48	960	-	5.5	980	-
Steel reinforcement	200	0.27	543	2.4	20.8	632	-
PSS	248	0.28	691	-	-	-	-
Headed shear stud	200	0.17	344	-	-	410	331

Table 2
Material properties of ECC used in the FE models

Material	E_c (GPa)	$\sigma_{0.4}$ (MPa)	$\varepsilon_{0.4}$ (%)	f'_c (MPa)	ε_{co} (%)	σ_l (MPa)	ε_l (%)	σ_{cu} (MPa)	ε_{cu} (%)	f_t (MPa)	ε_{to} (%)	σ_{tp} (MPa)	ε_{tp} (%)	σ_{tu} (MPa)	ε_{tu} (%)
ECC40	15.5	16	0.10	40	0.50	20.0	0.85	10.0	1.20	2.43	0.016	3.2	1.2	1.7	2.2
ECC70	20.5	28	0.14	70	0.53	30.0	0.95	13.5	1.40	4.40	0.021	5.3	1.0	3.0	1.7

Table 3
FE model details and their flexural strength

HSS S690 Beams (54 models)				HSS S960 Beams (54 models)			
Main dimensions	Materials	η	P_{FE} (kN)	Main dimensions	Materials	η	P_{FE} (kN)
SW600-ST140-ID180	E40-S690	0.82	604	SW600-ST140-ID180	E40-S960	0.82	712
	E70-S690	0.82	700		E70-S960	0.59	828
SW600-ST140-ID230	E40-S690	0.82	734	SW600-ST140-ID230	E40-S960	0.82	876
	E70-S690	0.74	835		E70-S960	0.54	1001
SW600-ST140-ID280	E40-S690	0.82	890	SW600-ST140-ID280	E40-S960	0.82	1014

	E70-S690	0.68	994		E70-S960	0.54	1215
SW600-ST170-ID180	E40-S690	0.71	676	SW600-ST170-ID180	E40-S960	0.61	767
	E70-S690	0.82	815		E70-S960	0.59	920
SW600-ST170-ID230	E40-S690	0.64	813	SW600-ST170-ID230	E40-S960	0.61	937
	E70-S690	0.74	955		E70-S960	0.53	1098
SW600-ST170-ID280	E40-S690	0.61	962	SW600-ST170-ID280	E40-S960	0.61	1122
	E70-S690	0.68	1110		E70-S960	0.49	1294
SW600-ST200-ID180	E40-S690	0.71	766	SW600-ST200-ID180	E40-S960	0.51	853
	E70-S690	0.82	931		E70-S960	0.59	1030
SW600-ST200-ID230	E40-S690	0.64	916	SW600-ST200-ID230	E40-S960	0.48	1038
	E70-S690	0.74	1095		E70-S960	0.53	1241
SW600-ST200-ID280	E40-S690	0.59	1044	SW600-ST200-ID280	E40-S960	0.48	1185
	E70-S690	0.68	1244		E70-S960	0.49	1395
SW1000-ST140-ID180	E40-S690	0.71	672	SW1000-ST140-ID180	E40-S960	0.51	773
	E70-S690	0.82	798		E70-S960	0.59	908
SW1000-ST140-ID230	E40-S690	0.64	819	SW1000-ST140-ID230	E40-S960	0.49	965
	E70-S690	0.74	963		E70-S960	0.53	1112
SW1000-ST140-ID280	E40-S690	0.59	975	SW1000-ST140-ID280	E40-S960	0.49	1166
	E70-S690	0.68	1106		E70-S960	0.49	1320
SW1000-ST170-ID180	E40-S690	0.71	781	SW1000-ST170-ID180	E40-S960	0.51	876
	E70-S690	0.82	947		E70-S960	0.59	1045
SW1000-ST170-ID230	E40-S690	0.65	923	SW1000-ST170-ID230	E40-S960	0.46	1038
	E70-S690	0.74	1093		E70-S960	0.53	1242
SW1000-ST170-ID280	E40-S690	0.59	1087	SW1000-ST170-ID280	E40-S960	0.42	1288
	E70-S690	0.68	1256		E70-S960	0.49	1452
SW1000-ST200-ID180	E40-S690	0.71	906	SW1000-ST200-ID180	E40-S960	0.51	994
	E70-S690	0.82	1107		E70-S960	0.59	1203
SW1000-ST200-ID230	E40-S690	0.65	1048	SW1000-ST200-ID230	E40-S960	0.46	1171
	E70-S690	0.74	1253		E70-S960	0.53	1393
SW1000-ST200-ID280	E40-S690	0.59	1205	SW1000-ST200-ID280	E40-S960	0.42	1371
	E70-S690	0.68	1418		E70-S960	0.49	1604
SW1400-ST140-ID180	E40-S690	0.71	759	SW1400-ST140-ID180	E40-S960	0.51	841
	E70-S690	0.82	906		E70-S960	0.59	1028
SW1400-ST140-ID230	E40-S690	0.65	894	SW1400-ST140-ID230	E40-S960	0.46	1042
	E70-S690	0.74	1043		E70-S960	0.53	1208
SW1400-ST140-ID280	E40-S690	0.59	1045	SW1400-ST140-ID280	E40-S960	0.42	1238
	E70-S690	0.68	1196		E70-S960	0.49	1406
SW1400-ST170-ID180	E40-S690	0.71	894	SW1400-ST170-ID180	E40-S960	0.51	998
	E70-S690	0.82	1083		E70-S960	0.59	1210
SW1400-ST170-ID230	E40-S690	0.65	1054	SW1400-ST170-ID230	E40-S960	0.46	1219
	E70-S690	0.74	1251		E70-S960	0.53	1405
SW1400-ST170-ID280	E40-S690	0.59	1208	SW1400-ST170-ID280	E40-S960	0.42	1420
	E70-S690	0.68	1415		E70-S960	0.49	1613
SW1400-ST200-ID180	E40-S690	0.71	1075	SW1400-ST200-ID180	E40-S960	0.51	1229
	E70-S690	0.82	1341		E70-S960	0.59	1457
SW1400-ST200-ID230	E40-S690	0.65	1214	SW1400-ST200-ID230	E40-S960	0.46	1338
	E70-S690	0.74	1520		E70-S960	0.53	1699
SW1400-ST200-ID280	E40-S690	0.59	1369	SW1400-ST200-ID280	E40-S960	0.42	1540
	E70-S690	0.68	1655		E70-S960	0.49	1861

For partially shear connected beams, due to the slip strain between the steel section and the slab, stress blocks of the beam will be more complicated and more complex calculation is needed to obtain $M_{RPA,equi}$. In this case, Eurocode 4 [25] adopts the following simplified method for partially shear connected beams so that

$$M_{RPA,sim} = M_{pl,a} + \eta(M_{pl,Rd} - M_{pl,a}) \quad (1)$$

In Eqn. (1), $M_{RPA,sim}$ is the flexural strength predicted by the simplified method, $M_{pl,a}$ is the moment resistance of HSS section alone while $M_{pl,Rd}$ is the

moment resistance for fully shear connected beam. In Eqn. (1), the maximum value of η is 1.0. $M_{RPA,sim}$ generally gives a more conservative prediction than $M_{RPA,equi}$.

Experimental results obtained by the authors [18] showed that when ECC with high compressive strain (>0.5%) was employed to replace NSC, the HSS section could develop a higher degree of yielding before the ECC slab was crushed. Hence, in order to study the accuracy of different prediction approaches mentioned above for a wider range of ECC-HSS composite beams, the flexural strength M_{FE} obtained from the 108 models were compared with the predictions from $M_{RPA,equi}$, $M_{RPA,sim}$ and $M_{EC4/AS2327}$.

Means and standard deviations of the ratios $M_{FE/MRPA,sim}$, $M_{FE}/M_{RPA,equi}$ and $M_{FE}/M_{EC4/AS2327}$ for all beams modelled obtained are summarized in Table 4. Fig. 3 plots the ratio $M_{FE}/M_{RPA,sim}$ against η. Fig. 3 and Table 4 show that predictions by $M_{RPA,sim}$ were more conservative than the FE predictions, even for S960 HSS section beams. On average, $M_{RPA,sim}$ overpredicted the flexural strength of the beams by 28%. The main reasons were (i) ECC was employed to replace NSC, a high degree of yielding of the HSS was achieved and (ii) the more conservative Eqn. (1) was used.

The ratio $M_{FE}/M_{RPA,equi}$ obtained for the 108 ECC-HSS beams modelled together with the experimental results obtained for ECC/NSC-HSS beams tested in [18] and those NSC-HSS beams reported in [21] and [23] are plotted in Fig. 4. Again, $M_{FE}/M_{RPA,equi}$ of most ECC-HSS beams were above unity with an average value of 1.17. This ratio is 11% lower than the average ratio for $M_{FE}/M_{RPA,sim}$ since $M_{RPA,equi}$ uses a more realistic/detailed stress block distribution for calculation. This confirmed that for most ECC-HSS beams, a high degree of yielding of the HSS section was achieved. Moreover, Fig. 4 shows that for most NSC-HSS beams studied in [18,21,23] their ratios $M_{FE}/M_{RPA,equi}$ were less than unity, especially for beams with higher η values. This reconfirmed that the RPA failed to produce conservative prediction for NSC-HSS beams, especially when shear stress was effectively transferred and produced a higher compressive strain at the top NSC slab surfaces. For $M_{FE}/M_{EC4/AS2327}$, as $M_{EC4/AS2327}$ is obtained by reducing the values of $M_{RPA,equi}$, Fig. 5 and Table 4 show that an even more conservative prediction with a mean value of 1.38 was obtained.

4. Simple analytical model for flexural strength prediction of ECC-HSS composite beams

As it is found that $M_{RPA,equi}$, $M_{RPA,sim}$ and $M_{EC4/AS2327}$ generally underpredicted the flexural strength of ECC-HSS composite beams, in order to improve the prediction accuracy, a simple analytical model which is based on the RPA method and the following assumptions is developed:

(i) There is no shear failure nor shear lag.

(ii) All contributions of ECC parts in the PSS troughs are ignored.

(iii) As ECC slab reinforcement bars provided little flexural resistance while the PPS is thin and slip between the PPS and ECC were observed before the crushing of ECC [18], their contributions are ignored.

(iv) Full compressive strength of f'_{ECC} is developed within the effective areas of the ECC slab.

The stress distributions at the beam's ultimate states corresponding to full or partial shear connection are shown in Fig. 6. Expressions of internal forces of different components are summarized in Table 5. For full shear connection, three different cases corresponding to PNA within the ECC slab, within the steel flange and within the steel web can be identified. For partial shear connection, due to bond slip, only two cases corresponding to PNA within the steel flange and within the steel web are possible. Based on Fig. 6 and Table 5, a flow chart (Fig. 7) was developed for the calculation of the flexural strength obtained by simple analytical model M_{sana}. This simple analytical method was then applied to predict the flexural strength for the 108 beams generated from FE model. They were compared with the FE modelling results M_{FE} and the three test results obtained in [18]. A summary of the comparison results obtained given in Table 6 shows that the proposed simple analytical model provided more accurate but conservative predictions (on average 13%).

5. Full analytical model for predicting of flexural behaviour of ECC-HSS composite beams

5.1. Development of full analytical model

While the simple analytical model allows engineers to obtain a quick and more accurate prediction of the flexural strength of the beam over RPA approaches, it does not produce the load – displacement curve nor allows engineers to gain more insight into the flexural behaviour of the ECC-HSS composite beams at various stages before final failure. Hence, in this section, a full analytical model is developed which allows engineers to obtain detailed behaviours the composite beams without the need to conduct any time-consuming FE modelling. This analytical model is applicable for composite beams with HSS section connected with top ECC slab in forms of either solid slab or slab with PSS.

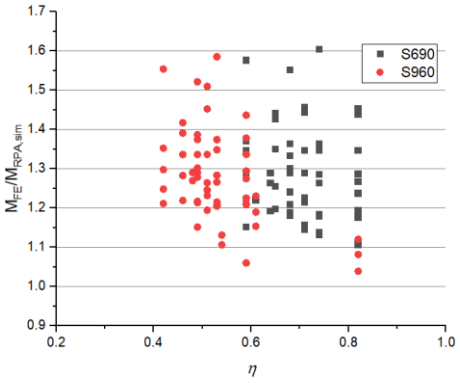

Fig. 3 $M_{FE}/M_{RPA,sim}$ versus shear connection degree for all FE modelled beams

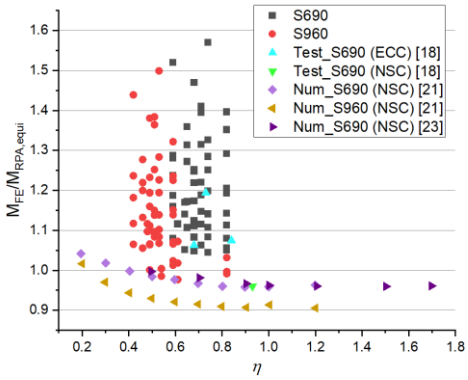

Fig. 4 $M_{FE}/M_{RPA,equi}$ obtained from all FE modelled beams and other studies [18,21,23] versus shear connection degree

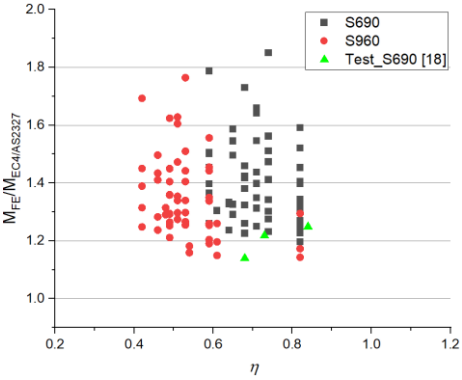

Fig. 5 $M_{FE}/M_{EC4/AS2327}$ versus shear connection degree for all FE modelled beams and experimental results from [18]

Table 4
Summary of comparison of flexural strength predictions obtained by FE model with RPA methods and EC4/AS2327

Beam group	$M_{FE}/M_{RPA,sim}$		$M_{FE}/M_{RPA,equi}$		$M_{FE}/M_{EC4/AS2327}$	
	Mean	SD	Mean	SD	Mean	SD
HSS S690 Beams (54 beams)	1.28	0.12	1.20	0.13	1.41	0.15
HSS S960 Beams (54 beams)	1.28	0.12	1.15	0.12	1.35	0.14
Overall (108 beams)	**1.28**	**0.12**	**1.17**	**0.13**	**1.38**	**0.15**

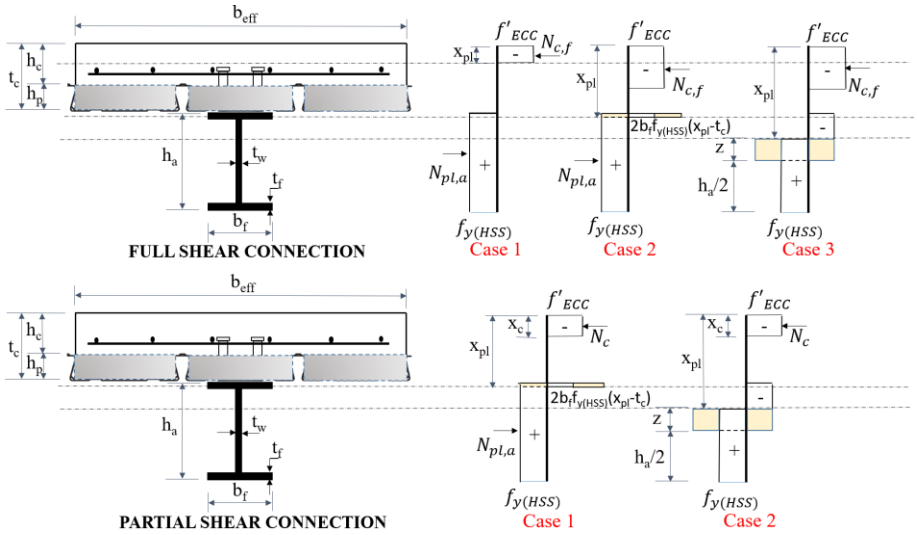

Fig. 6 Simple analytical model for calculating flexural strength of ECC-HSS composite beams

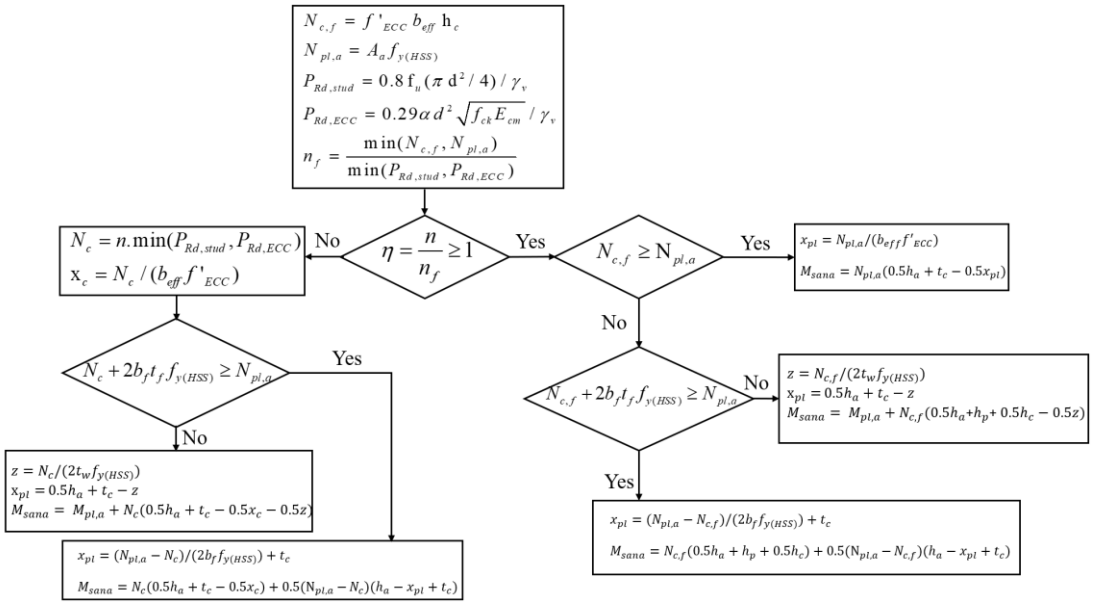

Fig. 7 Flow chart to calculate flexural strength of ECC-HSS composite beams using the simple analytical model

Table 5
Expressions for flexural strength prediction of ECC-HSS composite beams using the simple analytical model

Type of shear connection	Case		Analytical expression
Full	Case 1 (PNA in slab)	Depth of PNA	$x_{pl} = N_{pl,a} / (b_{eff} f'_{ECC})$
		Ultimate moment M_{sana}	$M_{sana} = N_{pl,a}(0.5h_a + t_c - 0.5x_{pl})$
	Case 2 (PNA in steel flange)	Depth of PNA	$x_{pl} = (N_{pl,a} - N_{c,f}) / (2b_f f_{y(HSS)}) + t_c$
		Ultimate moment M_{sana}	$M_{sana} = N_{c,f}(0.5h_a + h_p + 0.5h_c) + 0.5(N_{pl,a} - N_{c,f})(h_a - x_{pl} + t_c)$
	Case 3 (PNA in steel web)	Depth of PNA	$z = N_{c,f} / (2t_w f_{y(HSS)})$ $x_{pl} = 0.5h_a + t_c - z$
		Ultimate moment M_{sana}	$M_{sana} = M_{pl,a} + N_{c,f}(0.5h_a + h_p + 0.5h_c - 0.5z)$
Partial	Case 1 (PNA in steel flange)	Depth of PNA	$x_{pl} = (N_{pl,a} - N_c) / (2b_f f_{y(HSS)}) + t_c$
		Ultimate moment M_{sana}	$M_{sana} = N_c(0.5h_a + t_c - 0.5x_c) + 0.5(N_{pl,a} - N_c)(h_a - x_{pl} + t_c)$
	Case 2 (PNA in steel web)	Depth of PNA	$z = N_c / (2t_w f_{y(HSS)})$ $x_{pl} = 0.5h_a + t_c - z$
		Ultimate moment M_{sana}	$M_{sana} = M_{pl,a} + N_c(0.5h_a + t_c - 0.5x_c - 0.5z)$

Notes:

Compressive force acting on ECC $N_{c,f}$ (full shear connection): $N_{c,f} = f'_{ECC}\, b_{eff}\, \mathrm{h}_c$

Tensile force acting on HSS $N_{pl,a}$: $N_{pl,a} = A_a f_{y(HSS)}$

Shear resistance of headed shear stud: $P_{Rd,stud} = 0.8 \mathrm{f}_u (\pi \mathrm{d}^2 / 4) / \gamma_v$

$P_{Rd,ECC} = 0.29 \alpha d^2 \sqrt{f_{ck} E_{cm}} / \gamma_v$

Compressive force acting on ECC N_c (partial shear connection): $N_c = n.\min(P_{Rd,stud}, P_{Rd,ECC})$

Height of ECC stress block (partial shear connection): $\mathrm{x}_c = N_c / (b_{eff}\, f'_{ECC})$

Number of headed shear connections to assure full shear connection: $n_f = \dfrac{\min(N_{c,f}, N_{pl,a})}{\min(P_{Rd,stud}, P_{Rd,ECC})}$

Table 6
Summary of comparison of flexural strength obtained by simple and full analytical models with FE models and test results

Source	Beam group	M_{FE}/M_{sana}		M_{FE}/M_{fana}	
		Mean	SD	Mean	SD
FE models	HSS S690 beams (54 beams)	1.16	0.13	1.05	0.06
	HSS S960 beams (54 beams)	1.11	0.12	0.97	0.03
Experiment	Three tests from [18]	0.99	0.03	1.02	0.06
Overall (111 cases)		**1.13**	**0.13**	**1.01**	**0.06**

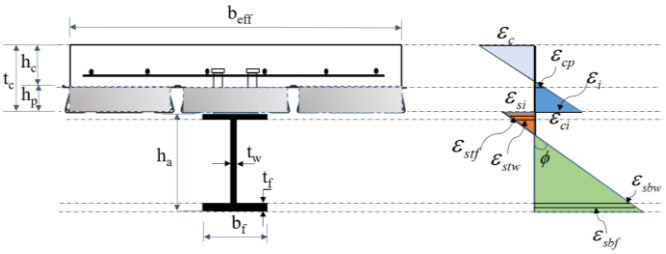

Fig. 8 Strains distributed in cross-section for full analytical model

Both full and partial shear connection are considered in this model. This analytical model is based on strain compatibility and force equilibrium of the beam's cross-section and the following assumptions were made:

(i) Strains of individual components (i.e., HSS section, ECC slab) are distributed linearly throughout the cross-section with the same curvature ϕ.

(ii) Stresses at top and bottom flanges of HSS section are constant throughout their thickness. Their values are calculated by using strains at their mid-thickness (ε_{stf} and ε_{sbf}, Fig. 8).

(iii) For slab using PSS, contribution from the ECC part in trough is ignored.

(iv) Neither plate buckling nor shear failure nor shear slag occurs.

The full analytical modelling procedure consists of four main steps and details of them are given in the following four sections.

5.1.1. Step 1: Strain distribution of the section

Strain distribution throughout the cross-section is shown in Fig. 8. The composite beam may be treated as a fully or partially shear connection by using the slip strain ε_i at the interfaces between the HSS top flange and the ECC slab such that

$$\varepsilon_i = (1-\eta)^2 \left(\frac{h_a}{2} + \frac{t_c}{2}\right)\phi \tag{2}$$

In Eqn. (2), h_a is HSS section height, t_c is the ECC slab thickness and η is the shear connection degree. In order to account for the nonlinear effect of η, slip strain is expressed as second order function of η. From Eqn. (2), for fully shear connected beam, $\eta = 1.0$ and $\varepsilon_i = 0$ (i.e., no slip between the HSS section and the ECC slab). On the other hand, if $\eta = 0$, there is no bond between the HSS section and the ECC slab so that the neutral axis of the ECC slab and HSS section will be at their corresponding mid-heights.

From Fig. 8, strains of all other components can be expressed in term of strain at the mid-thickness of HSS section's bottom flange ε_{sbf} and the beam's curvature ϕ:

$$\varepsilon_{sbw} = \varepsilon_{sbf} - \frac{t_f}{2}.\phi \tag{3}$$

$$\varepsilon_{stw} = \varepsilon_{sbf} - \left(h_a - \frac{3t_f}{2}\right).\phi \tag{4}$$

$$\varepsilon_{stf} = \varepsilon_{sbf} - \left(h_a - t_f\right).\phi \tag{5}$$

$$\varepsilon_{si} = \varepsilon_{sbf} - \left(h_a - \frac{t_f}{2}\right).\phi \tag{6}$$

$$\varepsilon_{ci} = \varepsilon_{sbf} - \left(h_a - \frac{t_f}{2}\right).\phi + \varepsilon_i \tag{7}$$

$$\varepsilon_{cp} = \varepsilon_{sbf} - \left(h_a - \frac{t_f}{2} + h_p\right).\phi + \varepsilon_i \tag{8}$$

$$\varepsilon_c = \varepsilon_{sbf} - \left(h_a - \frac{t_f}{2} + t_c\right).\phi + \varepsilon_i \tag{9}$$

In Eqns. (3) – (9), ε_{stw} and ε_{sbw} are respectively the strains at the top and bottom tips of the HSS section's web. ε_{stf} is the strain at HSS section's top flange. ε_{si} is the strain of HSS section at the interface between HSS section and ECC slab. ε_{ci} is the strain of ECC slab at the interface between HSS section and ECC slab. ε_{cp} is the strain of ECC at the tip of PSS trough while ε_c is the ECC strain at the ECC slab's top surface. t_f is the thickness of HSS section flange and h_p is the PSS trough height.

5.1.2. Steps 2: Stresses and forces of individual components

The forces acting on individual components can be calculated based on the stress distribution shown in Fig. 9. For the ECC slab, it is assumed that stress is distributed linearly throughout slab's height. As contribution from the ECC in trough is neglected, stress distribution in slab is dependent on the strain of ECC at the tip of PSS trough ε_{cp}. Based on the value of ε_{cp}, the compression force F_{cc} and tension force F_{ct} are calculated as:

$$F_{cc} = -\frac{1}{2}\sigma_c \frac{\varepsilon_c}{\phi} b_{eff} \qquad \text{if } \varepsilon_{cp} \geq 0 \tag{10}$$

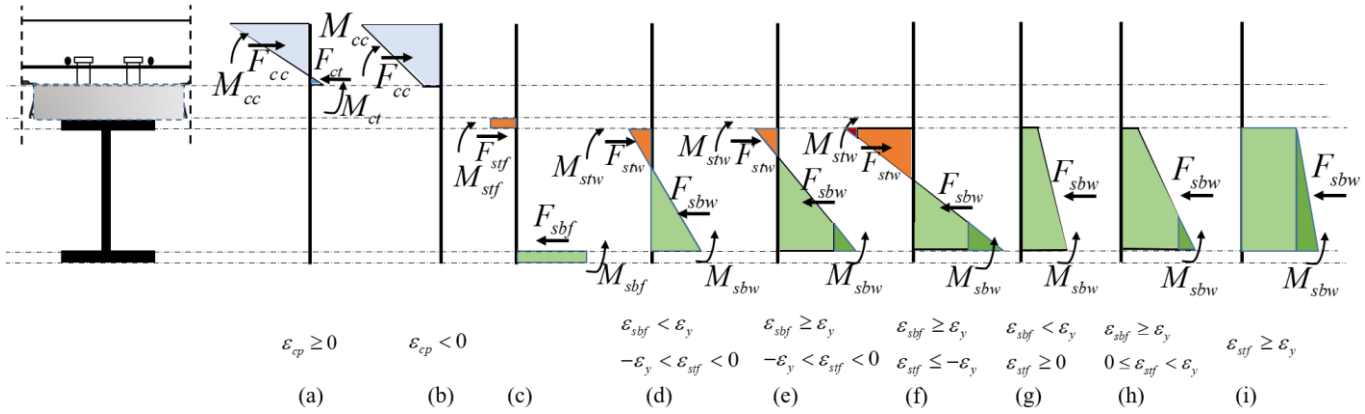

Fig. 9 Forces acting in cross-section for full analytical model

$$F_{cc} = -\frac{\sigma_c + \sigma_{cp}}{2} h_c b_{eff} \quad \text{if } \varepsilon_{cp} < 0 \tag{11}$$

$$F_{ct} = \frac{1}{2}\sigma_{cp} . \frac{\varepsilon_{cp}}{\phi} . b_{eff} \quad \text{if } \varepsilon_{cp} \geq 0 \tag{12}$$

$$F_{ct} = 0 \quad \text{if } \varepsilon_{cp} < 0 \tag{13}$$

In Eqns. (10) – (13), σ_c is the stress of ECC at the top surface of ECC slab. σ_{cp} is the stress of ECC at the tip of PSS trough. h_c is the distance from the top surface of ECC slab to the tip of PSS trough and b_{eff} is the effective width of ECC slab. For composite beam using solid slab, in Eqns. (10) – (13), ε_{cp} is replaced by the strain at the bottom of ECC slab ε_{ci} while σ_{cp} is replaced by σ_{ci}.

All stress terms used in Eqns. (10) – (13) can be calculated based on the stress – strain model of ECC shown in Figs. 2(e) and (f) by using the following equations:

For ECC in compression (Fig. 2(e)):

$$\sigma_c = \begin{cases} f'_c \frac{\varepsilon_c}{\varepsilon_{co}} \left\{ 0.8 \left(1 - \frac{\varepsilon_c}{\varepsilon_{co}} \right) + 1 \right\} & 0 \leq \varepsilon_c \leq \varepsilon_{co} \\ f'_c + \frac{(\sigma_l - f'_c)(\varepsilon_c - \varepsilon_{co})}{\varepsilon_l - \varepsilon_{co}} & \varepsilon_{co} < \varepsilon_c \leq \varepsilon_l \end{cases} \tag{14}$$

For ECC in tension (Fig. 2(f)):

$$\sigma_t = \begin{cases} \frac{f_t}{\varepsilon_{t0}} \varepsilon_t & 0 \leq \varepsilon_t \leq \varepsilon_{t0} \\ \sigma_{tp} + \frac{(\sigma_{tp} - f_t)(\varepsilon_t - \varepsilon_{t0})}{\varepsilon_{tp} - \varepsilon_{t0}} & \varepsilon_{t0} < \varepsilon_t \leq \varepsilon_{tp} \end{cases} \tag{15}$$

Forces acting on top and bottom steel flanges are then calculated by using Eqns. (16)-(17):

$$F_{sbf} = \sigma_{sbf} . b_f . t_f \tag{16}$$

$$F_{stf} = \sigma_{stf} . b_f . t_f \tag{17}$$

Forces acting on the top and bottom of steel web can be obtained by using Eqns. (18)-(25):

$$F_{sbw} = \frac{\sigma_{sbw} . \varepsilon_{sbw} . t_w}{2\phi} \quad \text{if } \varepsilon_{sbw} < \varepsilon_y \ \& \ -\varepsilon_y < \varepsilon_{stw} < 0 \tag{18}$$

$$F_{sbw} = \left(\frac{f_y \left(\varepsilon_{sbw} - \frac{\varepsilon_y}{2} \right)}{\phi} + \frac{1}{2} \frac{(\sigma_{sbw} - f_y)(\varepsilon_{sbw} - \varepsilon_y)}{\phi} \right) t_w \quad \text{if } \varepsilon_{sbw} \geq \varepsilon_y \ \& \ \varepsilon_{stw} < 0 \tag{19}$$

$$F_{sbw} = \frac{1}{2} (\sigma_{sbw} + \sigma_{stw}) (h_a - 2t_f) t_w \quad \text{if } \varepsilon_{sbw} < \varepsilon_y \ \& \ \varepsilon_{stw} \geq 0 \tag{20}$$

$$F_{sbw} = \left(\frac{f_y \left(\varepsilon_{sbw} - \frac{\varepsilon_y}{2} \right) - \frac{1}{2}\sigma_{stw} . \varepsilon_{stw}}{\phi} + \frac{1}{2} \frac{(\sigma_{sbw} - f_y)(\varepsilon_{sbw} - \varepsilon_y)}{\phi} \right) t_w \quad \text{if } \varepsilon_{sbw} \geq \varepsilon_y \ \& \ 0 \leq \varepsilon_{stw} < \varepsilon_y \tag{21}$$

$$F_{sbw} = \left(\sigma_{stw} + \frac{1}{2} (\sigma_{sbw} - \sigma_{stw}) \right) (h_a - 2t_f) t_w \quad \text{if } \varepsilon_{stw} \geq \varepsilon_y \tag{22}$$

$$F_{stw} = \left(\frac{f_y \left(\varepsilon_{stw} + \frac{\varepsilon_y}{2} \right)}{\phi} - \frac{1}{2} \frac{(\sigma_{stw} + f_y)(\varepsilon_{sbw} + \varepsilon_y)}{\phi} \right) t_w \quad \text{if } \varepsilon_{stw} \leq -\varepsilon_y \tag{23}$$

$$F_{stw} = -\frac{\sigma_{stw} . \varepsilon_{stw} . t_w}{2\phi} \quad \text{if } -\varepsilon_y < \varepsilon_{stw} < 0 \tag{24}$$

$$F_{stw} = 0 \quad \text{if } \varepsilon_{stw} \geq 0 \tag{25}$$

All stresses terms used in Eqns. (18) to (25) can be calculated using constitutive model of HSS shown in Fig. 2(a) which can be expressed as:

$$\sigma_s = \begin{cases} E_s.\varepsilon_s & \varepsilon_s \le \varepsilon_y \\ f_y + \dfrac{\left(\varepsilon_s - \varepsilon_y\right)\left(f_u - f_y\right)}{\varepsilon_u - \varepsilon_y} & \varepsilon_y < \varepsilon_s \le \varepsilon_u \end{cases} \tag{26}$$

5.1.3. Step 3: Forces equilibrium for the solution of ϕ and moment calculation

If the beam is under bending only, applying compressive and tension forces equilibrium of the cross-section implies that:

$$F_{cc} + F_{stf} + F_{stw} = F_{ct} + F_{sbw} + F_{sbf} \tag{27}$$

For any given value of ε_{sbf} which defines the strain status of the section (Eqns. (3) to (9)), Eqn. (27) is obviously a nonlinear equation for the solution of the beam's curvature ϕ. For a given value of ε_{sbf}, by starting with reasonable lower and upper estimates of ϕ, a converged solution of ϕ (i.e., corresponding to an error tolerance of 0.01% of the unbalance force) can be obtained by the standard bi-section method using MATLAB.

After the value ϕ is solved from Eqn. (27), by referring to Fig. 9 again, moment contributions from different components about the mid-thickness of the bottom flange of steel section at different stages of the beam can be calculated by using Eqns. (28) – (41).

$$M_{sbf} = 0 \tag{28}$$

$$M_{stf} = \sigma_{stf}.b_f.t_f.\left(h_a - t_f\right) \tag{29}$$

$$M_{sbw} = \frac{\sigma_{sbw}.\varepsilon_{sbw}.t_w}{2\phi}\left(\frac{\varepsilon_{sbw}}{3\phi} + \frac{t_f}{2}\right) \quad \text{if} \quad \varepsilon_{sbw} < \varepsilon_y \;\&\; -\varepsilon_y < \varepsilon_{stw} < 0 \tag{30}$$

$$M_{sbw} = \frac{f_y\left(\varepsilon_{sbw} - \varepsilon_y\right)t_w}{\phi}\left(\frac{\varepsilon_{sbw} - \varepsilon_y}{2\phi} + \frac{t_f}{2}\right) + \frac{f_y.\varepsilon_y.t_w}{2\phi}\left(\frac{3\varepsilon_{sbw} - 2\varepsilon_y}{3\phi} + \frac{t_f}{2}\right) + \frac{1}{2}\frac{\left(\sigma_{sbw} - f_y\right)\left(\varepsilon_{sbw} - \varepsilon_y\right)t_w}{\phi}\left(\frac{\varepsilon_{sbw} - \varepsilon_y}{3\phi} + \frac{t_f}{2}\right) \quad \text{if} \quad \varepsilon_{sbw} \ge \varepsilon_y \;\&\; \varepsilon_{stw} < 0 \tag{31}$$

$$M_{sbw} = \sigma_{stw}\left(h_a - 2t_f\right)t_w\left(\frac{h_a - t_f}{2}\right) + \frac{1}{2}\left(\sigma_{sbw} - \sigma_{stw}\right)\left(h_a - 2t_f\right)t_w\left(\frac{2h_a - t_f}{6}\right) \quad \text{if} \quad \varepsilon_{sbw} < \varepsilon_y \;\&\; \varepsilon_{stw} \ge 0 \tag{32}$$

$$M_{sbw} = \frac{f_y\left(\varepsilon_{sbw} - \varepsilon_y\right)t_w}{\phi}\left(\frac{\varepsilon_{sbw} - \varepsilon_y}{2\phi} + \frac{t_f}{2}\right) + \frac{f_y.\varepsilon_y.t_w}{2\phi}\left(\frac{3\varepsilon_{sbw} - 2\varepsilon_y}{3\phi} + \frac{t_f}{2}\right) - \frac{\sigma_{stw}.t_w.\varepsilon_{stw}}{2\phi}\left(\frac{\varepsilon_{stw}}{3\phi} + h_a - \frac{3t_f}{2}\right) + \frac{1}{2}\frac{\left(\sigma_{sbw} - f_y\right)\left(\varepsilon_{sbw} - \varepsilon_y\right)t_w}{\phi}\left(\frac{\varepsilon_{sbw} - \varepsilon_y}{3\phi} + \frac{t_f}{2}\right) \quad \text{if} \quad \varepsilon_{sbw} \ge \varepsilon_y \;\&\; 0 \le \varepsilon_{stw} < \varepsilon_y \tag{33}$$

$$M_{sbw} = \sigma_{stw}\left(h_a - 2t_f\right)t_w\left(\frac{h_a - t_f}{2}\right) + \frac{1}{2}\left(\sigma_{sbw} - \sigma_{stw}\right)\left(h_a - 2t_f\right)t_w\left(\frac{2h_a - t_f}{6}\right) \quad \text{if} \quad \varepsilon_{stw} \ge \varepsilon_y \tag{34}$$

$$M_{stw} = \frac{\sigma_{stw}.\varepsilon_{stw}.t_w}{2\phi}\left(h_a - \frac{3t_f}{2} - \frac{\varepsilon_{stw}}{3\phi}\right) \quad \text{if} \quad -\varepsilon_y < \varepsilon_{stw} < 0 \tag{35}$$

$$M_{stw} = -\frac{f_y\left(\varepsilon_{stw} + \varepsilon_y\right)t_w}{\phi}\left(h_a - \frac{3t_f}{2} + \frac{\varepsilon_{stw} - \varepsilon_y}{2\phi}\right) + \frac{f_y.\varepsilon_y.t_w}{2\phi}\left(h_a - \frac{3t_f}{2} + \frac{3\varepsilon_{stw} - 4\varepsilon_y}{3\phi}\right) + \frac{1}{2}\frac{\left(\sigma_{stw} + f_y\right)\left(\varepsilon_{stw} + \varepsilon_y\right)t_w}{\phi}\left(h_a - \frac{3t_f}{2} + \frac{\varepsilon_{stw} + \varepsilon_y}{3\phi}\right) \quad \text{If} \quad \varepsilon_{stw} \le -\varepsilon_y \tag{36}$$

$$M_{stw} = 0 \quad \text{if} \quad \varepsilon_{stw} \ge 0 \tag{37}$$

$$M_{cc} = \frac{\sigma_c.\varepsilon_c.b_{eff}}{2\phi}\left(h_a + t_c - \frac{t_f}{2} + \frac{\varepsilon_c}{3\phi}\right) \quad \text{if} \quad \varepsilon_{cp} \ge 0 \tag{38}$$

$$M_{cc} = \frac{\sigma_{cp}\left(\varepsilon_c - \varepsilon_{cp}\right)}{\phi}\left(h_a + t_c - \frac{t_f}{2} + \frac{\varepsilon_c - \varepsilon_{cp}}{\phi}\right)b_{eff} + \frac{\left(\sigma_c - \sigma_{cp}\right)\left(\varepsilon_c - \varepsilon_{cp}\right)b_{eff}}{2\phi}\left(h_a + t_c - \frac{t_f}{2} + \frac{\varepsilon_c - \varepsilon_{cp}}{3\phi}\right) \quad \text{if} \quad \varepsilon_{cp} < 0 \tag{39}$$

$$M_{ct} = \frac{\sigma_{cp}.\varepsilon_{cp}.b_{eff}}{2\phi}\left(h_a + h_p - \frac{t_f}{2} + \frac{\varepsilon_{cp}}{3\phi}\right) \quad \text{if} \quad \varepsilon_{cp} \geq 0 \tag{40}$$

$$M_{ct} = 0 \quad \text{if} \quad \varepsilon_{cp} < 0 \tag{41}$$

It should be noted that if solid slab is used instead of PSS, in Eqns. (39)-(41), ε_{cp} and σ_{cp} should be replaced by ε_{ci} and σ_{ci}, respectively.

5.1.4. Step 4: Effective stiffness and deflection calculation

After the moment contribution is known, internal moment in the cross-section can be calculated as:

$$M_{f\,ana} = M_{sbf} - M_{stf} + M_{sbw} - M_{stw} - M_{cc} + M_{ct} \tag{42}$$

Beam's effective bending stiffness EI_{eff} can be achieved as:

$$EI_{eff} = \frac{M_{f\,ana}}{\phi} \tag{43}$$

And the mid-span deflection δ_{max} for the beam under four-point bending can be obtained as:

$$P_{f\,ana} = \frac{M_{f\,ana}}{a} \tag{44}$$

$$\delta_{max} = \frac{P_{f\,ana}\,a\left(3L^2 - 4a^2\right)}{24EI_{eff}} \tag{45}$$

In Eqns. (44) and (45), P_{fana} is the loading corresponding to M_{fana} and a is the shear span of the beam. Obviously, expression of Eqn. (45) can be modified for other loading cases easily. In order to trace out the entire load-deformation curve, an incremental procedure is employed by starting from an initial value of $\varepsilon_{sbf} = 0$ (so that $P_{fana}=0$ and $\delta_{max}=0$). A small increment of ε_{sbf} (i.e., 0.02%) is applied incrementally so that the above four-step procedure are repeatedly applied to obtain the corresponding load and deflection.

5.2. Validation of the full analytical model

The full analytical model was validated against experimental results obtained from the three ECC-HSS composite beams (ECC40-140, ECC-70-140, ECC-40-170) tested by the authors [18]. The flexural strengths obtained from full analytical model of the three beams tested are compared against the test results in Fig. 10(a) which shows a good agreement between the analytical model and the test results. In terms of load – displacement curves, Figs. 10(b)-(d) show that the full analytical model captured the behaviours of the tested beams at different stages with the results similar to the test and FE results..

In order to further validate the accuracy and reliability of the proposed full analytical model, it was employed to predict the flexural strengths and load-deflection curves of all the 108 models generated using FE model. Examples of some selected load-deflection curve comparisons are shown in Fig. 11 for the configuration SW600-ST140-ID180 using PSS with different material properties. Fig. 11 shows that the analytical and the FE model curves are well agreed with each other. Results from another comparison example for the same configuration with solid slab are shown in Fig. 12. Furthermore, results of beams with different HSS section depths, slab thicknesses are compared in Figs. 13(a) and (b), respectively. Figs. 12 and 13 again indicate that the proposed full analytical model was able to predict the load-displacement relationship of the beams with good accuracy.

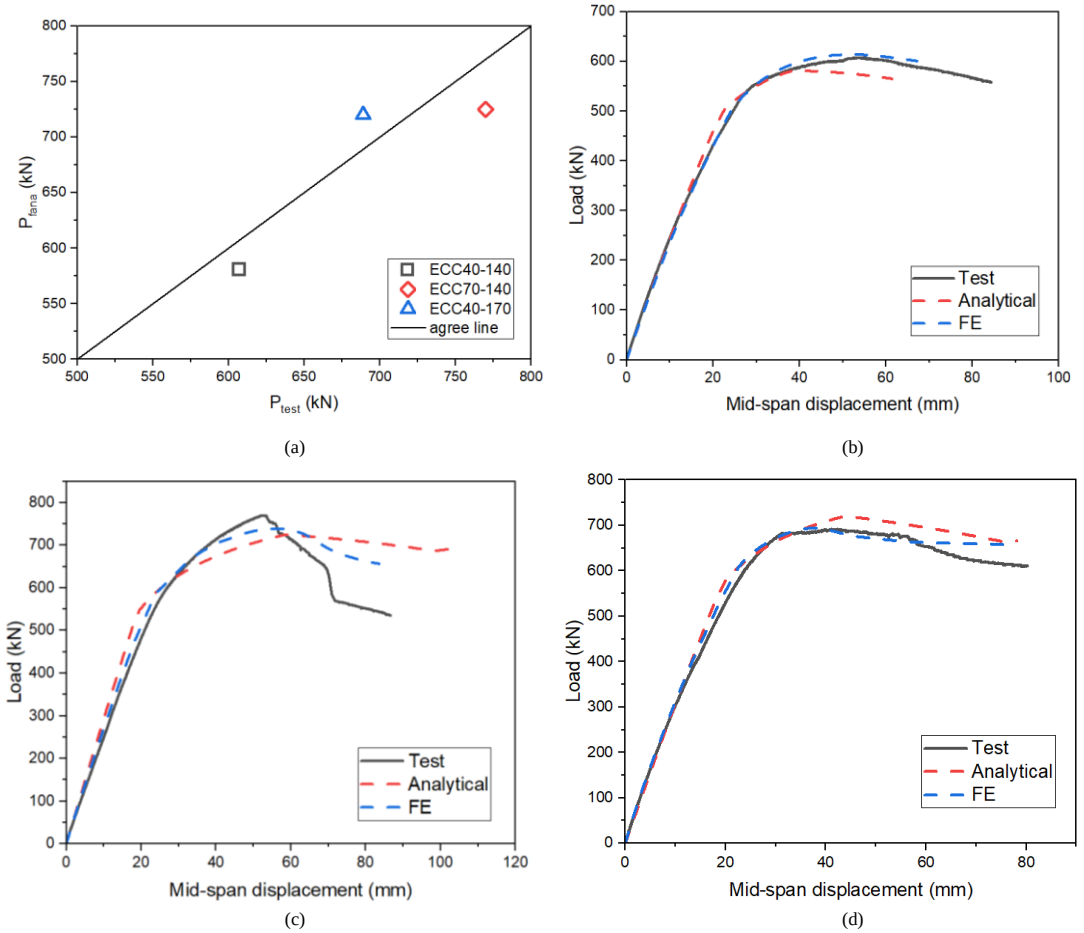

Fig. 10 Results obtained from full analytical model compared with tests and FE results in [18]: (a) Comparison of the test and full analytical model in terms of flexural strength; (b) Load – displacement curves of beam ECC40-140; (c) Load – displacement curves of beam ECC70-140; (d) Load – displacement curves of beam ECC40-170

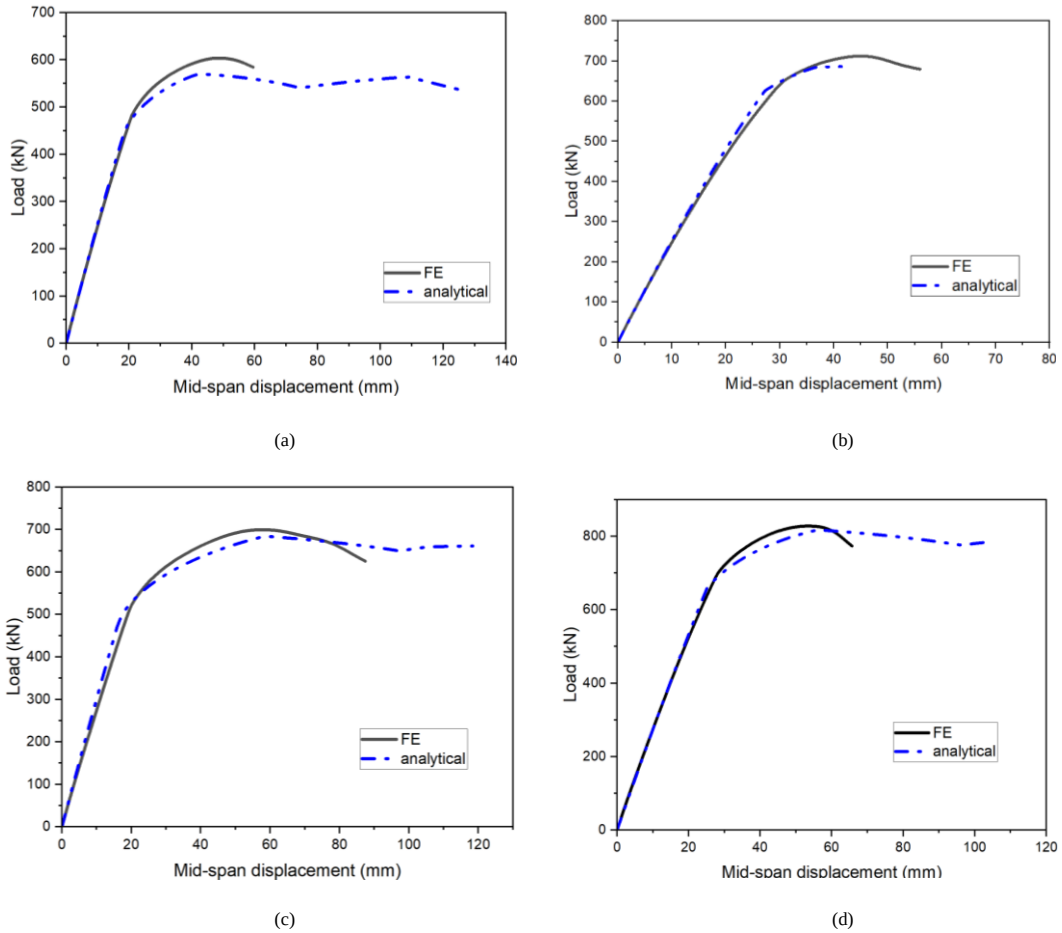

Fig. 11 Full analytical model results of beam SW600-ST140-ID180 using PSS with different material properties compared with FE model results. (a) E40-S690; (b) E40-S960; (c) E70-S690; (d) E70-S960

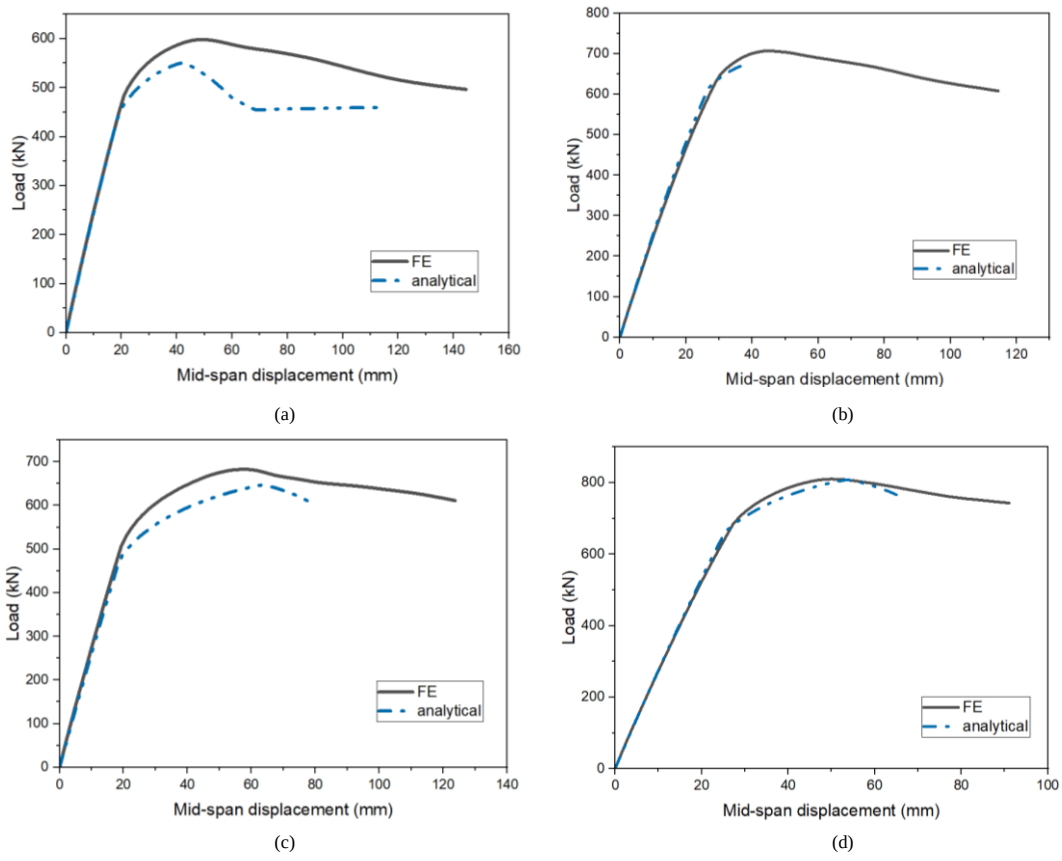

Fig. 12 Full analytical model results of beam SW600-ST140-ID180 using solid slab compared with FE model results: (a) E40-S690; (b) E40-S960; (c) E70-S690; (d) E70-S960

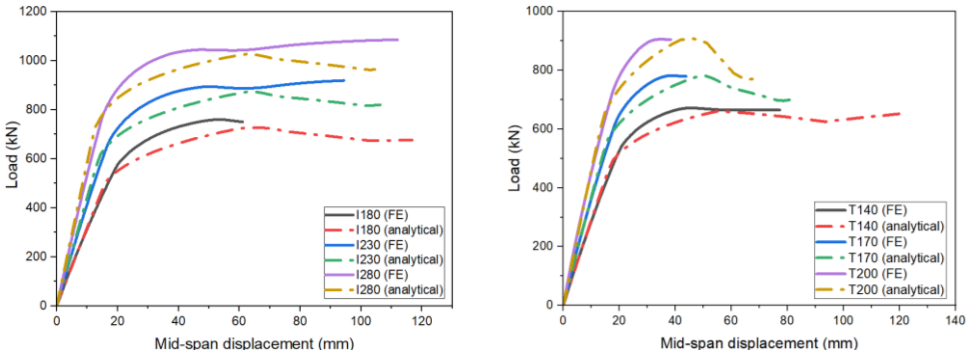

Fig. 13 Full analytical model results of different beams compared with FE model results: (a) Beams with different HSS section depths; (b) Beams with different slab thickness

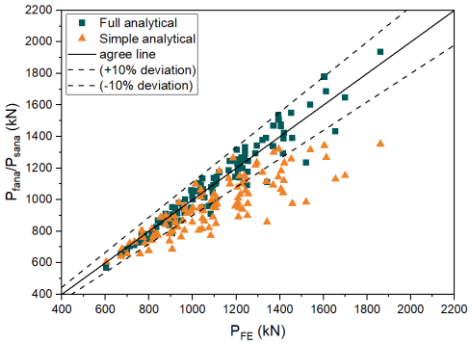

Fig. 14 Flexural strength obtained by full and simple analytical models compared with FE models

Regarding flexural strength prediction, comparisons between the simple analytical model and the full analytical model against the FE modelling results for all 108 models are plotted in Fig. 14. Fig. 14 shows that virtually all full analytical model results are within the 10% deviation lines. On the other hand, predictions by the simple analytical model have a wider scattering and generally underpredict the flexural strength. The mean and standard deviation of flexural strength prediction ratios obtained by the simple analytical model (M_{sana}) and the full analytical models (M_{fana}) for the three tested beams in [18] and the 108 FE models (M_{FE}) are summarized in Table 6. Table 6 clearly shows that the full analytical model results are more accurate and reliable than the simple analytical model results.

6. Conclusions

In this study, by using a validated 3D finite element (FE) model developed in authors' previous work [18], 108 models were generated and analysed to assess the accuracies of RPA approaches in predicting the flexural capacity of ECC-HSS composite beams. Simple and full analytical models were also developed in order to obtain the bending responses of these beams. Based on the results achieved, the following conclusions can be drawn.

(1) It is found that RPA approaches underpredicted (on average from 17% to 38%) the flexural strength of the ECC-HSS composite beams. Hence, an improved simple analytical model accounting for the higher compressive ductility of ECC was proposed. Validation with experimental and FE modelling results found that this simple analytical model produced more accurate predictions and reduced the average underprediction to 13%.

(2) In order to produce the full load-deflection curve of the beams without running any time-consuming FE model, full analytical model that is based on strain compatibility and force equilibrium was developed and validated against experimental and FE model results. Validation results show that this full analytical model produced more accurate and reliable results than the simple analytical model with prediction accuracy very close to the 3D FE modelling and tests results.

Acknowledgment

University International Postgraduate Award (UIPA) provided by UNSW Sydney for the first author to pursue his PhD are gratefully acknowledged.

This work was supported by The University of Danang, University of Science and Technology, code number of Project: T2023-02-11.

References

[1] Shi, G., et al., Local buckling of 460 MPa high strength steel welded section stub columns under axial compression. Journal of Constructional Steel Research, 2014. 100: p. 60-70.
[2] Shi, G., H. Ban, and F.S.K. Bijlaard, Tests and numerical study of ultra-high strength steel columns with end restraints. Journal of Constructional Steel Research, 2012. 70: p. 236-247.
[3] Shi, G., W. Zhou, and C. Lin, Experimental investigation on the local buckling behavior of 960 MPa high strength steel welded section stub columns. Advances in Structural Engineering, 2015. 18.
[4] Shi, G., et al., Local buckling behavior of welded stub columns with normal and high strength steels. Journal of Constructional Steel Research, 2016. 119: p. 144-153.
[5] Ban, H., et al., Experimental investigation of the overall buckling behaviour of 960MPa high strength steel columns. Journal of Constructional Steel Research, 2013. 88: p. 256-266.
[6] Rasmussen, K. and G. Hancock, Tests of high strength steel columns. Journal of Constructional Steel Research, 1995. 34: p. 27–52.
[7] Lee, C.-H., et al., Flexural strength and rotation capacity of I-shaped beams fabricated from 800-MPa steel. Journal of Structural Engineering, 2013. 139(6): p. 1043-1058.
[8] Joo, H.S., et al., Rotational capacity and optimum bracing point of high strength steel I-girders. Journal of Constructional Steel Research, 2013. 88: p. 79-89.
[9] Uy, B., Stability and ductility of high performance steel sections with concrete infill. Journal of Constructional Steel Research, 2008. 64(7-8): p. 748-754.
[10] Kim, C.-S., et al., Eccentric axial load capacity of high-strength steel-concrete composite columns of various sectional shapes. Journal of Structural Engineering, 2014. 140(4): p. 04013091.
[11] Khan, M.K.I., et al., Behaviour of engineered cementitious composite-encased stub concrete columns under axial compression. Magazine of Concrete Research, 2020. 72(19): p. 984-1005.
[12] Puthli, R. and O. Fleischer, Investigations on bolted connections for high strength steel members. Journal of constructional steel research, 2001. 57(3): p. 313-326.
[13] Može, P. and D. Beg, Investigation of high strength steel connections with several bolts in double shear. Journal of constructional steel research, 2011. 67(3): p. 333-347.
[14] Coelho, A.M.G. and F.S. Bijlaard, Experimental behaviour of high strength steel end-plate connections. Journal of Constructional Steel Research, 2007. 63(9): p. 1228-1240.
[15] Elghazouli, A. and J. Treadway, Inelastic behaviour of composite members under combined bending and axial loading. Journal of Constructional Steel Research, 2008. 64(9): p. 1008-1019.
[16] Kabir, M.I., et al., Flexural behaviour of ECC-LWC encased slender high strength steel composite beams. Journal of Constructional Steel Research, 2020. 173: p. 106253.
[17] Kabir, M.I., et al., Flexural behaviour of engineered cementitious composite encased high strength steel composite beam. ce/papers, 2019. 3(3-4): p. 713-718.
[18] Cong-Luyen Nguyen and C.K. Lee, Flexural behaviours of Engineered Cementitious Composites – High strength steel composite beams. Engineering Structures, 2021. 249.
[19] Uy, B. and R. Sloane, Behavior of composite tee beams constructed with high strength steel. Journal of Constructional Steel Research, 1998. 1: p. 203-4.
[20] Zhao, H. and Y. Yuan, Experimental studies on composite beams with high-strength steel and concrete. Steel and Composite Structures, 2010. 10(5): p. 373-383.
[21] Ban, H. and M.A. Bradford, Flexural behaviour of composite beams with high strength steel. Engineering Structures, 2013. 56: p. 1130-1141.
[22] Ban, H., et al., Available rotation capacity of composite beams with high-strength materials under sagging moment. Journal of Constructional Steel Research, 2016. 118: p. 156-168.
[23] Shamass, R. and K.A. Cashell, Behaviour of Composite Beams Made Using High Strength Steel. Structures, 2017. 12: p. 88-101.
[24] Ban, H. and M.A. Bradford, Elastoplastic cross-sectional behavior of composite beams with high-strength steel: analytical modeling. Journal of Structural Engineering, 2015. 141(10): p. 04014236.
[25] EN 1994-1-1:2004 Eurocode 4: Design of Composite Steel and Concrete Structures Part 1-1: General rules and Rules for Buildings.
[26] Standards Australia. AS 2737.1-2003. Composite Structures Part 1: Simply supported beams. Sydney: Standards Australia, 2003.
[27] Li, V.C., Engineered Cementitious Composites (ECC): Bendable Concrete for Sustainable and Resilient Infrastructure. 2019: Springer.
[28] Meng, D., et al., Mechanical behaviour of a polyvinyl alcohol fibre reinforced engineered cementitious composite (PVA-ECC) using local ingredients. Construction and Building Materials, 2017. 141: p. 259-270.
[29] Cong-Luyen Nguyen, C.K.Lee, Experimental study of flexural behaviour of high strength steel (HSS)-Engineered Cementitious Composites (ECC) composite beam with profiled steel sheeting. ce/papers, 2021. 4(2-4): p. 781-786.
[30] Abaqus, V., 6.14-1. Abaqus/standard user's manual and Abaqus CAE manual. Providence, RI, USA: Dassault Systemes Simulia Corp, 2014.
[31] Oehlers, D.J. and M.A. Bradford, Composite steel and concrete structures: fundamental behaviour: fundamental behaviour. 2013: Elsevier.

Advanced Steel Construction – Vol. 19 No. 3 (2023) 209–222
DOI:10.18057/IJASC.2023.19.3.3

THE BENDING BEHAVIOR AND FREE VIBRATION OF THE CONCRETE-STEEL COMPOSITE FLOORS

Sadiq Ahmad Afzali [1], Çağlar Özer [2], Barış Bayrak [1], Ahmad Jamshid Sadid [1], Oğuzhan Çelebi [1] and Abdulkadir Cüneyt Aydın [1, *]

[1] *Ataturk University, Engineering Faculty, Department of Civil Engineering, 25030, Erzurum, Turkey*
[2] *Ataturk University, Earthquake Research Center, Erzurum, Turkey*
** (Corresponding author: E-mail: acaydin@atauni.edu.tr)*

ABSTRACT

The paper aims to investigate the bending behavior and free vibration of the concrete-steel composite floors, including high temperatures. The inspected properties are analyzed for the maximum displacement, load capacity, energy absorption capacity, and acceleration by using bending tests for varying stud density and elevated temperatures. Withal, bolts are used as studs throughout this study. The result of bending tests implies that, decreasing the spacing of the studs and the addition of mesh reinforcement and steel fiber will increase the energy absorption and maximum load capacity of the steel composite floors. Besides, the increasing the stud density reduces the vibration response of the composite floors, and the mesh reinforcement eliminates the efficiency of the steel fiber on the vibration response of the steel composite floors. Meanwhile, increasing the steel-fiber content causes the reduction in the vibration response of the slabs exposed to high temperatures.

ARTICLE HISTORY

Received: 12 September 2022
Revised: 5 March 2023
Accepted: 3 April 2023

KEYWORDS

Composite floor;
Cold-formed steel;
Steel fiber;
Vibration;
Bending;
High temperature

Copyright © 2023 by The Hong Kong Institute of Steel Construction. All rights reserved.

1. Introduction

Steel composite floors are considered as an alternative to the commonly used conventional reinforced concrete floors. Steel composite floors are generally preferred in recreational, commercial, industrial, and residential buildings due to their fast construction process and safe and economical construction methods. Structurally, composite flooring meets all needs in terms of providing the sufficient strength and durability stipulated by the standards. Composite floors consist of steel sheets, plain or reinforced concrete, and connectors. The strength and ductility of the steel-concrete composite floors depend on various factors such as the geometry of the profiled sheeting, layout and position of the connectors used to ensure composite action between the steel sheeting, the reinforced concrete, and the thickness of the profiled sheeting [1-4]. In addition, steel composite floors, which can also be used as reinforcement elements in structural systems, can also resist bending (positive and negative moment) moments in both directions [5]. Steel sheet, which is one of the components of steel composite flooring, can be used not only as a mold but also in cases where tensile stresses are intense [6]. In addition to materials such as steel sheet, conventional concrete and studs that make up the composite flooring, it is also aimed to reduce the stresses and vibrations caused by possible bending of the flooring by using steel fiber in the flooring. Steel fibers increase the shear and bending strength after cracks occur, allowing effective stress to spread uniformly between these cracks [7]. Studs are widely used in structures to meet the shear forces between composite materials, especially at the floors. The dynamic and/or static loads result in the shear force and bending moment at the floors. In addition, it can be exposed to environmental vibration, earthquake, wind, explosions and vibration, caused by machines on the floor. Such vibrations can cause undesirable deflections and horizontal displacements in the structure. Furthermore, these vibrations negatively affect human comfort and can also damage some important equipment in the building [8]. Therefore, floor vibrations must be considered in the structural design or evaluation [9].

In recent years, the composite floors have been in great demand, due to their light weight, affordability, and ability to respond to natural disasters, such as earthquakes. However, the free or forced vibration behavior of composite floors is a very familiar phenomenon. The most common practice to improve the quality of composite floors is to identify and suppress the unwanted vibrations, as vibration can cause discomfort, serviceability problems, and direct failure of the structure. Several studies on the determination of the dynamic characteristics of the structural floor systems have been performed with an emphasis on the natural frequencies of the floor systems. Ferreira and Fasshauer [10] performed a study on the free vibration of symmetric composite plates based on an innovative numerical scheme. The results of different thickness-to-length ratios were determined and discussed in the study. Ju et al. [11] performed experimental tests to measure the natural frequencies and damping ratios of a new composite floor system. The composite floor systems consisting of steel beams and concrete slabs were examined, and the results were compared with the design codes to evaluate the serviceability of the system in three construction stages (steel erection stage, concrete casting stage, and finishing stage). Gandomkar et al. [12] experimentally and numerically investigated the effect of parameters such as screw spacing, steel profiled sheet thickness, and dry board thickness on the natural frequencies of a composite floor system by the name of profiled steel sheet dry board (PSSDB). Furthermore, Gandomkar et al. [13] measured the natural frequencies of profiled steel sheet dry board floors infilled with concrete (PSSDBS). Hector and Fernando [14] conducted an experimental study to determine the shear behavior of composite slabs according to Eurocode 4. In order to examine the shear behavior, cracks were observed with cyclic loading in composite slabs designed differently from each other. Hick et al. [15] investigated the contribution of the use of studs to the shear resistance of composite slabs formed with steel profiles with a span of 11.4 m. The results showed that the effect of stud should be considered in three-point bending tests. Costa-Neves et al. [16] specified the modes of vibration and natural frequencies of the composite steel deck floor system in a multi-story, multi-bay building. They used the system's natural frequencies to determine its comfortableness. Jarnerö et al. [17] experimentally investigated the natural frequencies, mode shapes, and damping ratio of a prefabricated timber floor system in unusual boundary conditions and different construction stages. The main concerns about composite slabs are mostly focused on the shear bond, shear resistance, flexural strength, and slip behavior, including cast screws [11, 12, 16, 17]. Holomek et al. [18] conducted a series of experiments to investigate the effects of cast screws diameters and structural element layouts on the bending capacity of composite slabs. The results showed that small-diameter screws were effective at small shear forces, while large ones were efficient at-large shear forces.

This study aims to investigate the effect of the shear stud density on the vibration response and bending behavior of the steel composite floors, including the post-fire response. Meanwhile, the spacing of the studs, steel fiber content, and the mesh reinforcement were considered as the parameters of the investigation. The high-temperature, steel fibers, stud density, and reinforcement effect with free vibration for bending are inspected, also.

2. Experimental work

2.1. Material properties and specimens

In this investigation, 18 steel-concrete composite floor models were prepared using three types of concrete mixes (conventional concrete and two types of steel fiber reinforced concrete). The concrete mixes was produced according to the Turkish Standard TS802 [19], using CEM II/A-M(P-LL) 42.5 R cement and 16 mm maximum size aggregate. The hooked steel fiber (Fig. 1a)

with the geometric dimension of length (L) = 35 mm, diameter (d) = 0.55 mm, and the aspect ratio (L/d) = 65 with a nominal tensile strength of 1.345 MPa and young's modulus of 2×105 MPa was selected according to TS/EN-14889-1 [20]. The amount of steel fiber for the steel fiber reinforced concrete (SFRC) was chosen as 30 kg/m^3 and 60 kg/m^3 of the total volume of the model. The no-fiber type reference samples presented a compressive strength as 50 MPa, where the similar strength values were 48 and 43 MPa for the samples with 30 kg/m^3 and 60 kg/m^3 steel fibers, respectively. The galvanized cold-formed steel sheet was used with the dimensions of 860x27x0.5 mm, for the floor decking of the models. M6*80 mm pan-headed bolts with EPDM bonded sealing washers were used for strengthening the shear bond between concrete and the steel sheet (Fig. 1b). To observe the stud density effect, the spans for bolt-type studs are designed for 22 and 55 cm. Furthermore, for the models, the Q188/188 mesh reinforcements (Fig. 1c) were used according to TS4559 [21].

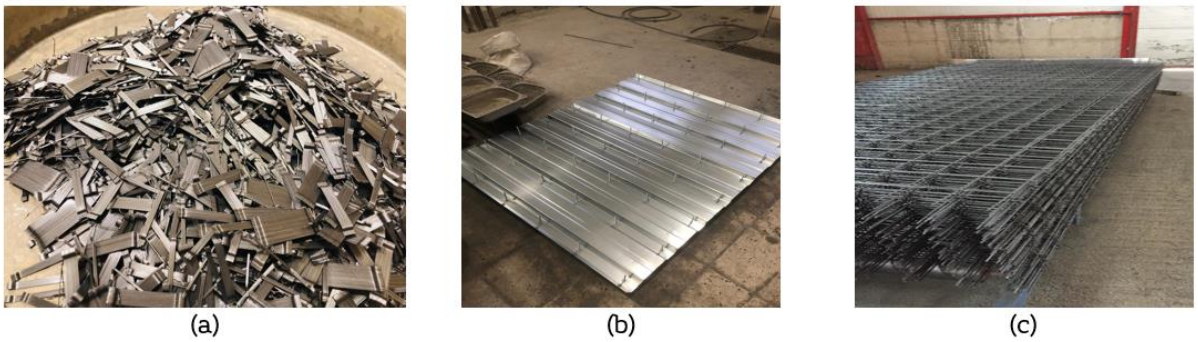

Fig. 1 Composite floor components used in the study

In this investigation, there are two groups of models. The first group of models includes 12 steel-composite floors fabricated with an aspect ratio of 0.8 (1500 mm x 1200 mm), and the second group includes 6 with an aspect ratio of 0.92 (760 mm x 700 mm). The second group of the models is designed according to high-temperature furnace for three hours of 600 ^{0}C (6 hours from room temperature to 600 ^{0}C, 3 hours at 600 ^{0}C, and 8 hours from 600 ^{0}C to room temperature). The thickness of all the models is considered as 110 mm. The type of concrete, the spacing of the bolts, and the reinforcement are the main variables of the models. The specifications and dimensions of the models are presented in Table 1 and Fig. 2.

Table 1
Properties of composite floor models

Model Code	Type of Concrete (Compressive Strength)	Steel Fiber Ratio in Concrete (Kg/m^3)	Bolts Spacing (mm)	Mesh Reinforcement
	Group 1 of Models (1500 mm x 1200 mm)			
CC22M	Conventional Concrete	0	220	With Mesh
CC55M		0	550	With Mesh
CC22		0	220	Without Mesh
CC55		0	550	Without Mesh
30SFRC22M	30 kg/m^3 SFRC	30	220	With Mesh
30SFRC55M		30	550	With Mesh
30SFRC22		30	220	Without Mesh
30SFRC55		30	550	Without Mesh
60SFRC22M	60 kg/m^3 SFRC	60	220	With Mesh
60SFRC55M		60	550	With Mesh
60SFRC22		60	220	Without Mesh
60SFRC55		60	550	Without Mesh
	Group 2 of Models (760 mm x 700 mm)			
FCC22M	Conventional Concrete	0	220	With Mesh
FCC22		0	220	Without Mesh
F30SFRC22M	30 kg/m^3 SFRC	30	220	With Mesh
F30SFRC22		30	220	Without Mesh
F60SFRC22M	60 kg/m^3 SFRC	60	220	With Mesh
F60SFRC22		60	220	Without Mesh

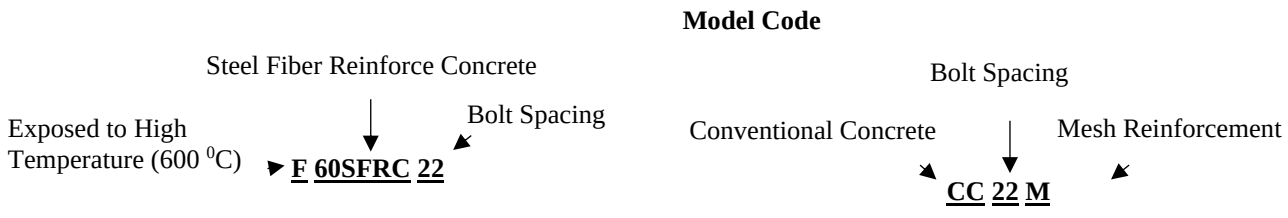

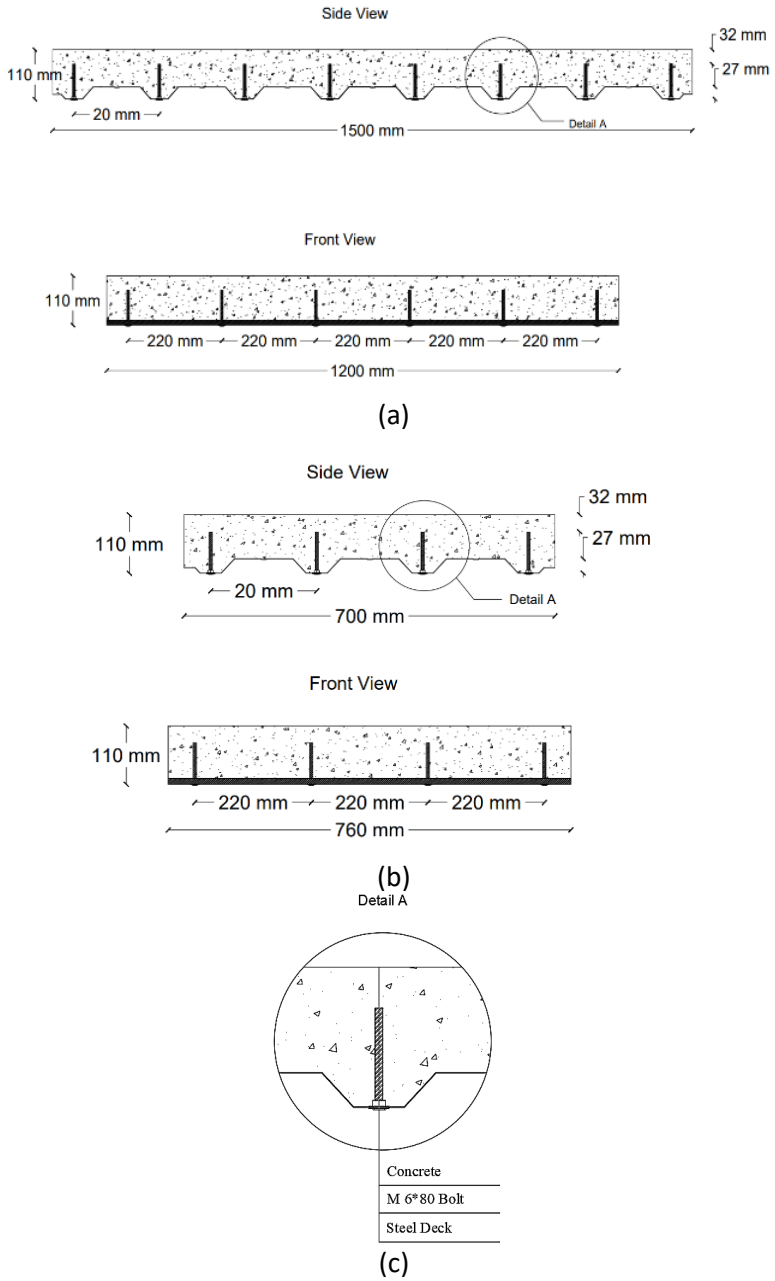

Fig. 2 Geometric dimensions of tested models (a) Group 1 (b) Group 2 (c) Composite floor bolt detail

Table 2
Concrete mixing ratios

Concrete type	Cement kg/m^3	Sand (0-4 mm) kg/m^3	Aggregate (4-16 mm) kg/m^3	Water kg/m^3	Steel fiber kg/m^3
Conventional concrete	370	448.54	1345	206.614	0
30SFRC	365.317	442.87	1328.47	204	30
60SFRC	360.64	437.2	1311.45	201.4	60

2.2. Test setup and procedure

2.2.1. Concrete experiments

As the main component of the composite floors, the concrete, with or without fibers, was tested for the mechanical properties. The concrete mixture calculation was made according to TS 802 [19] (Table 2), and a total of 18 concrete samples were prepared to be placed in 15x15x15 cm cube, 10x10x40 prism and 10x20 cylinder molds (Fig. 3a). The obtained concrete samples were kept in a curing environment at 22 °C for 28 days and subjected to compression and bending tests. The compression and bending tests were realized according to TS EN 12390-3 [22] and TS EN 12390-5 [23], respectively. Then, relevant tests were also repeated for the samples with the 30 or 60 kg/m^3 steel fibers. The placement of the studs to the steel sheet before concrete pouring is shown in Fig. 3b and after the concrete is poured, the composite floor is presented in Fig. 3c. The 28 days- compression and flexural test results of three mixtures are given in Table 3. Furthermore, the stress-strain curves of samples observed from the compressive strength tests are also shown in Fig. 4. The mean value of three samples was used while drawing the stress-strain curve.

Table 3
Hardened concrete test results

	Compressive strength			Flexural strength		
Concrete type/Sample	Conventional concrete	30SFRC	60SFRC	Conventional concrete	30SFRC	60SFRC
Sample 1	50.42	49.81	42.35	3.80	4.44	4.32
Sample 2	46.95	47.15	41.67	4.15	4.33	4.64
Sample 3	50.08	46.71	44.40	4.09	4.20	4.84
Average	49.15	47.89	42.81	4.01	4.32	4.60

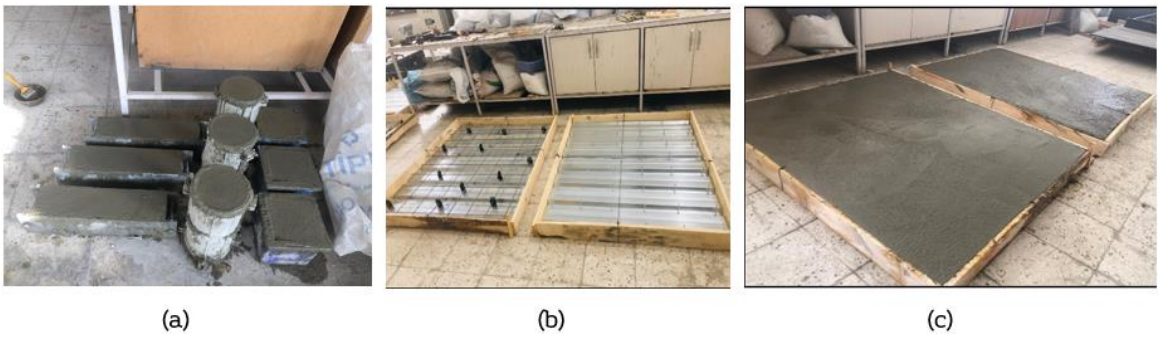

Fig. 3 Concrete mixture experiments: a) Concrete poured into cube, cylinder and prism molds b) Placement of the studs to the sheet steel without concrete c) Model composite floor

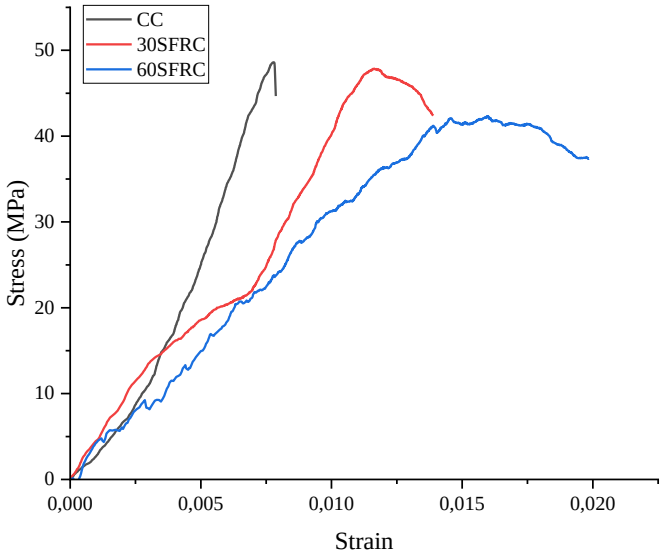

Fig. 4 Stress-strain curve of samples

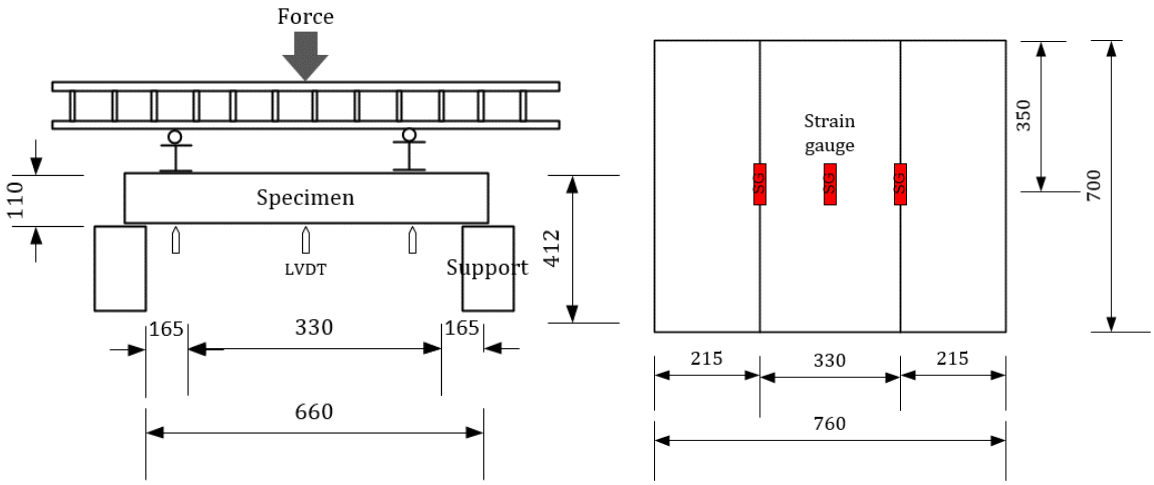

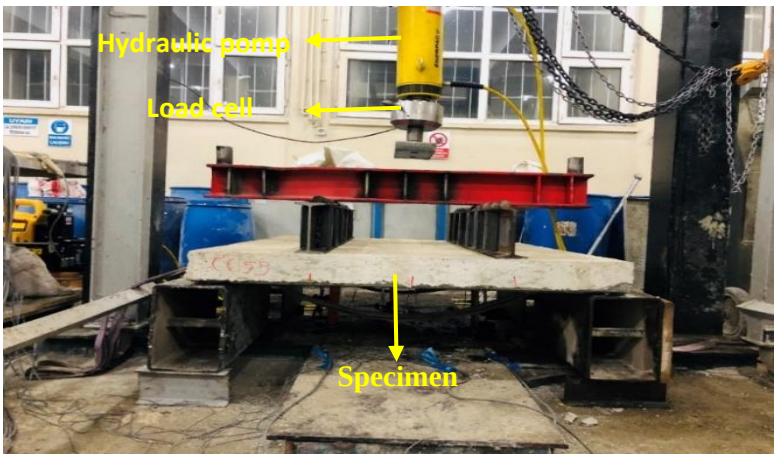

Fig. 5 The bending test setup, the positions of LVDTs, and strain gages of the models (all units are mm)

2.2.2. Bending test setup

The bending tests were to measure the bending capacities and corresponding deformations of composite floors formed with different fiber ratios and mesh reinforcements. The effects of steel fibers, stud placement, high temperature, and mesh reinforcements on the bending capacities, and the deformation abilities of the slabs were determined by bending tests. The orientation and the drawing of the experimental setup can be seen at Fig. 5. Thus, the hydraulic pump with a load capacity of 1000 KN is in a position to apply a uniform load to the entire floor resting on two horizontally placed supports (Fig. 4a). The bending tests of the models were prepared according to the Eurocode-4 [24]. To measure the vertical displacement of the models, the LVDTs (Linear Variable Displacement Transducers) were placed vertically in three positions under the floor systems. Besides, the strain gauges were attached to each model to measure the deformations of the steel sheet. Fig. 5 shows the bending test setup, the positions of LVDTs, and strain gages of the models.

2.2.3. Vibration test setup

The accelerometer tests were applied to measure possible vibrations that may occur on the samples. The effect of steel fibers, placement of studs, high-temperature, and mesh reinforcements on vibrations have been investigated, by using accelerometer data for the region where the sample would likely deflect the most (Fig. 6a). The vibration test experimentation is shown in Fig. 6b. Within the light of the literature, the digital accelerometer (CMG-5TD) was placed to area, where the moment is maximum [25]. The sensor was positioned and fixed using the provided screws to the surface of the model and connected to the PC.

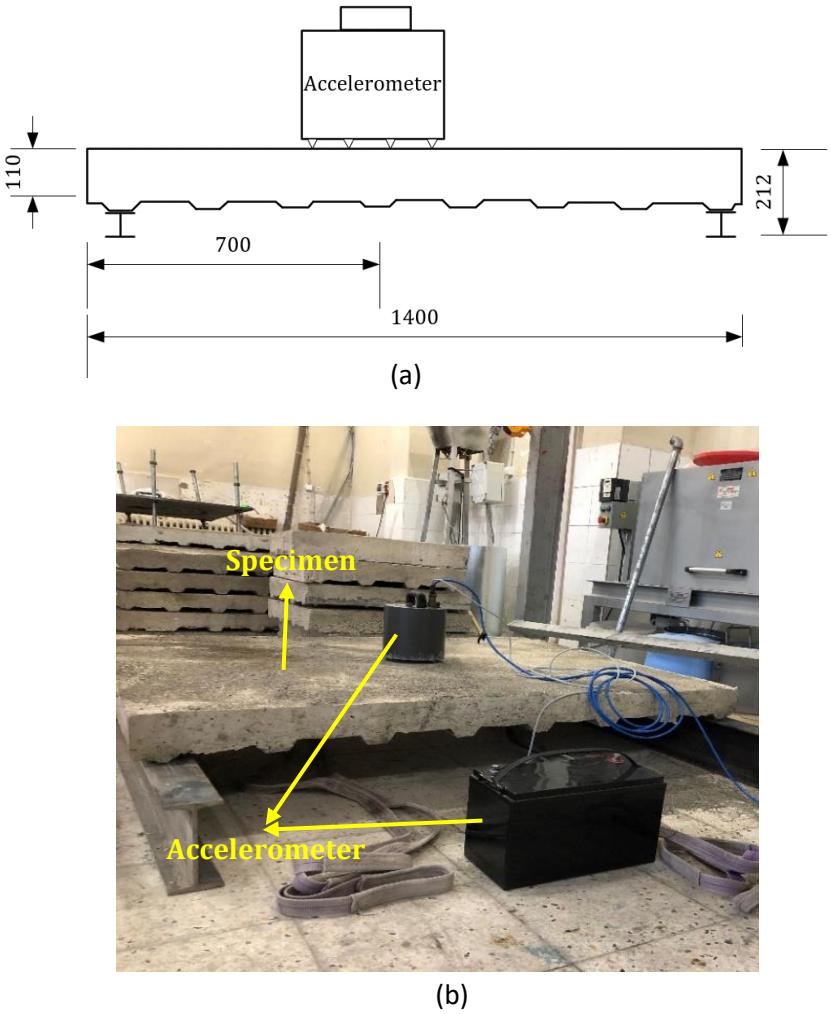

Fig. 6 The vibration test setup: a) Placement on slab of accelerometer b) Application of vibration test

2.2.4. High temperature related experiments

In this part, the models were kept at 600 °C for 3 hours to observe the changes in bending capacities and vibration parameters, when the samples with different steel fiber contents and exposed to high temperatures. For this experiment, a digitally controlled high-temperature furnace with a heating capacity of 1200 °C was used. After the models were kept at 600 °C for 3 hours. Then, they were removed from the high-temperature furnace, after getting waited to cool down to room temperature (8 hours from 600 ^{0}C to room temperature), for the vibration and bending tests. Fig. 7a and Fig. 7b shows the high-temperature furnace, and the models placed.

Fig. 7 High-temperature experiments: a) high-temperature furnace b) models in the furnace

3. Results and discussions

3.1. Bending test

3.1.1. The effect of bolt spacing on the behavior of the composite floors

Fig. 8 is obtained according to the bending test results. As shown, the decreasing stud (bolt) spacing increased the bending and energy absorption capabilities, as the fiber ratio increase.

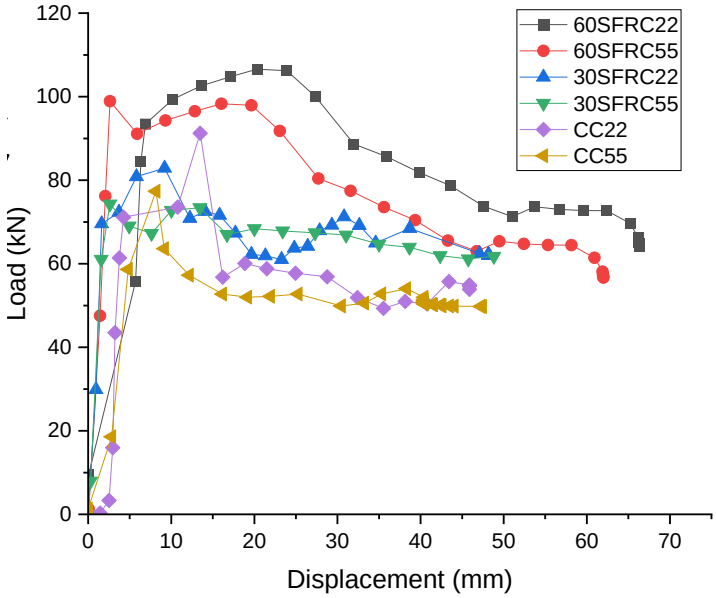

Fig. 8 Load-displacement graph for CC55, CC22, 30SFRC55, 30SFRC22, 60SFRC55 and 60SFRC22

Table 4
The effect of bolts spacing on the behavior of composite floors

Model Code	Energy Absorption (kN*mm)	Difference in Energy Absorption (%)	Maximum Load (kN)	Maximum Displacement at the center point (mm)
		CC		
CC55	2415.35	+7.46	77	8
CC22	2595.56		90	14
		30SFRC		
30SFRC55	3204	+1.62	74	2.6
30SFRC22	3256		82	9
		60SFRC		
60SFRC55	4821.51	+12.97	99	16
60SFRC22	5447.15		106	20

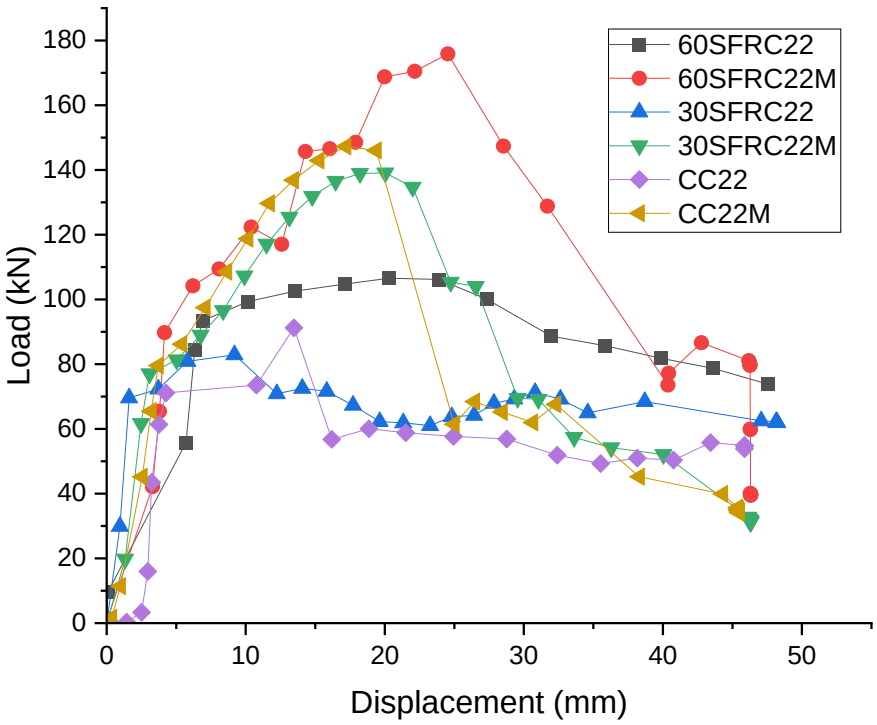

Fig. 9 Load-displacement graph for CC22 and CC22M, 30SFRC22, 30SFRC22M, 60SFRC22 and 60SFRC22M

3.1.2. The effect of mesh reinforcement on the behavior of composite floors

According to the results of the bending tests, it has been determined that the bolt spacing is at 22 cm, which has the highest bending, displacement and energy absorption capacity. Therefore, to determine the effectiveness of the mesh reinforcement, the models with a bolt spacing of 22 cm were taken as a reference in the test results. As seen in Table 5 and Fig. 9, the energy adsorption capability was increased by 43.47% for the conventional concrete models. Withal, these increments were 21.16%, and 31.34%, for the steel fiber reinforced ones with 30 kg/m^3 and 60 kg/m^3, respectively. The displacements of the CC22 and CC22M models were increased linearly in the loading interval of 0-90 kN and 0-150 kN. The displacements corresponding to the maximum load for CC22 and CC22M models were determined as 14 mm and 17 mm, respectively. Similarly, the displacement at the center points of 30SFRC22 and 30SFRC22M models increased linearly in the loading interval of 0-82 kN and 0-80 kN. The displacements corresponding to the maximum load for the 30SFRC22 and 30SFRC22M models were determined as 9 mm and 18 mm. Furthermore, the displacements of 60SFRC22 and 60SFRC22M were increased linearly in the loading interval of 0-106 kN and 0-176 kN, and the displacement corresponding to the maximum load for 60SFRC22 and 60SFRC22M were 20 mm and 24 mm, respectively.

The maximum load capacities were increased by 62.85%, 64.66%, and 65.56% for the CC, 30SFRC, and 60SFRC models. Furthermore, the displacements at the maximum load were increased by 32.96%, 216.58%, and 2.63% for the CC, 30SFRC, and 60SFRC samples. The bending tests have shown that, the use of mesh reinforcements in combination with steel fibers in composite flooring gives higher bending and displacement capability, then the ones with conventional concrete. Although, the increase in the amount of steel fiber in composite floors with mesh reinforcement did not change the bending capacity much, it was determined that, the displacement capacity decreased significantly. In addition, the after-test photos of the samples (failure mode) are shown in Fig. 10.

Table 5
The effect of mesh reinforcement on the behavior of composite floors

Model Code	Energy Absorption (kN*mm)	The difference in Energy Absorption (%)	Maximum Load (kN)	Maximum Displacement at the center point (mm)
		CC		
CC22	2595.56	+43.47	90	14
CC22M	3723.86		150	17
		30SFRC		
30SFRC22	3256	+21.16	82	9
30SFRC22M	3945.06		140	18
		60SFRC		
60SFRC22	4089.97	+31.34	106	20
60SFRC22M	5371.65		176	24

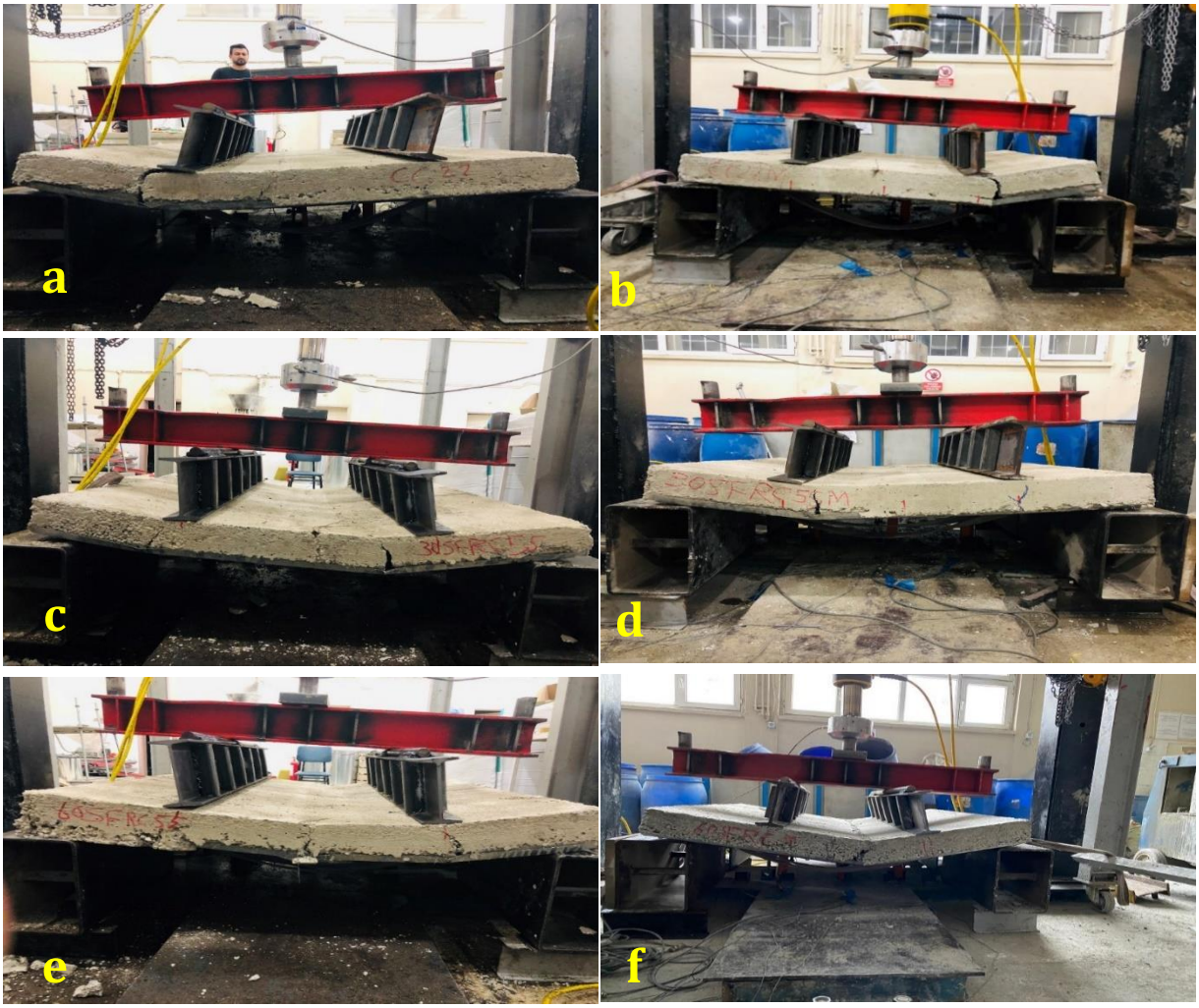

Fig. 10 Failure mode of tested samples a) CC22 b) CC22M c) 30SFRC55 d) 30SFRC55M e) 60SFRC55

3.1.3. The effect of steel fiber reinforcement on the behavior of composite floors

As seen in Table 6, when the steel-fiber is added to the mixture, the energy absorption capacity is increased by 25.45 % for the models with 30 kg/m^3 steel-fiber, where this increment was 57.58 % for the ones with 60 kg/m^3 for the steel-fibers. The maximum load capacity of the composite floors were decreased by 8.89% and increased by 17.78% for the 30SFRC and 60SFRC models. The displacements at the maximum load were decreased by 35.71% and increased by 42.86% for the 30SFRC and 60SFRC models. As expected, increasing the steel fiber content to 30 kg/m^3 resulted less load carrying capability, but greater deformation capability, when compared to conventional concrete models. Which means, more permanent deformation and more energy absorption capability without sudden collapse.

Table 6
The effect of steel fiber reinforcement on the behavior of composite floors

Model Code	Energy Absorption (KN*mm)	The difference in Energy Absorption (%)	Maximum Load (KN)	Maximum Displacement at the center point (mm)
CC22	2595.56	-	90	14
30SFRCC22	3256.00	+25.45	82	9
60SFRCC22	4089.97	+57.58	106	20

Fig. 11 shows the load displacement at the center point of the models. The displacements of the CC22, 30SFRC22, and 60SFRC22 models were increased linearly in the 0-90 kN, 0-82 kN, and 0-06 kN loading ranges. If it is desired to create composite flooring with only steel fiber reinforcement, without the use of mesh reinforcement, it is foreseen that the amount of fiber should be adjusted optimally. Because, it is obvious that the energy absorption capacity, bending strength and permanent deformation of the model with 60 kg/m^3 steel fiber content was higher than that of the one with 30 kg/m^3 steel fiber content. In addition, the permanent deformation without sudden load changes of the model containing 60 kg/m^3 steel fiber and loss of permanent deformation ability, as sudden load loss for the one with 30 kg/m^3 steel fiber indicates the optimum amount of the steel fiber.

Fig. 12 has been drawn to compare the energy absorption, load carrying, and permanent strain capacities of the Group 1 samples concerning each other.

As shown in Fig. 12a, the flooring with the highest energy absorption capacity was the model with 60 kg/m^3 steel fiber content, 22 cm bolt (stud) spacing, and no mesh reinforcement. In this case, it is understood that the steel fiber and the bolt spacing contribute significantly to the ductility of the flooring. In Fig. 12b, it is seen that the composite flooring with 60 kg/m^3 steel fiber content, mesh reinforcement and 22 cm bolt spacing has the highest load-carrying capacity. It has been determined that the increase in the amount of steel fiber, the reduction of the bolt spacing and the use of mesh reinforcement increase the load capacity of the flooring. In Fig. 12c, it is observed that the composite flooring with 60 kg/m^3 fiber content, no mesh reinforcement and 22 cm bolt spacing has the highest displacement capacity. It has also been determined that the displacements of the model, in which the steel fiber and mesh reinforcement are used together, are not much different from the displacements of the only conventional concrete-containing model.

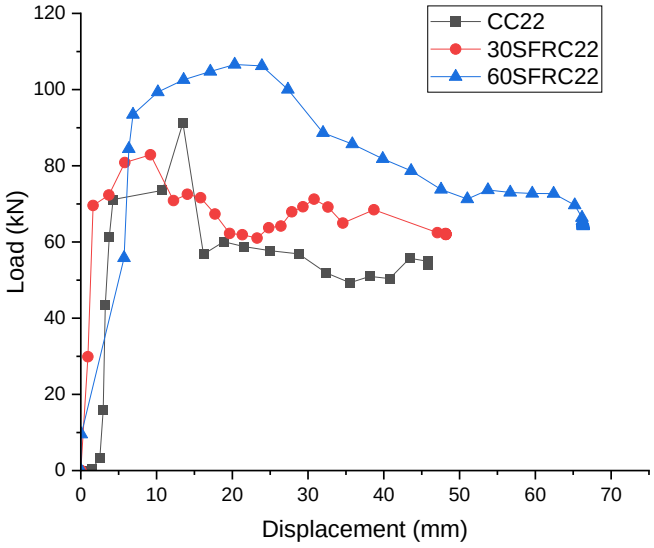

Fig. 11 Load-displacement graph for CC22, 30SFRC22 and 60SFRC22

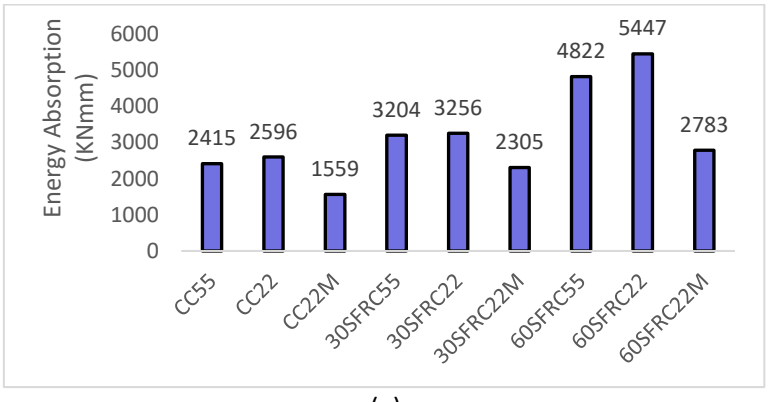

(a)

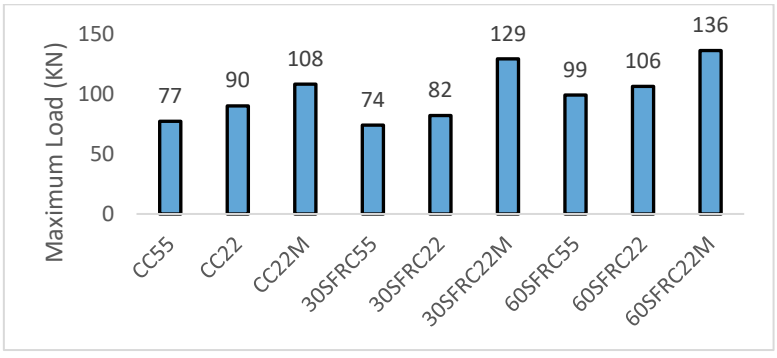

(b)

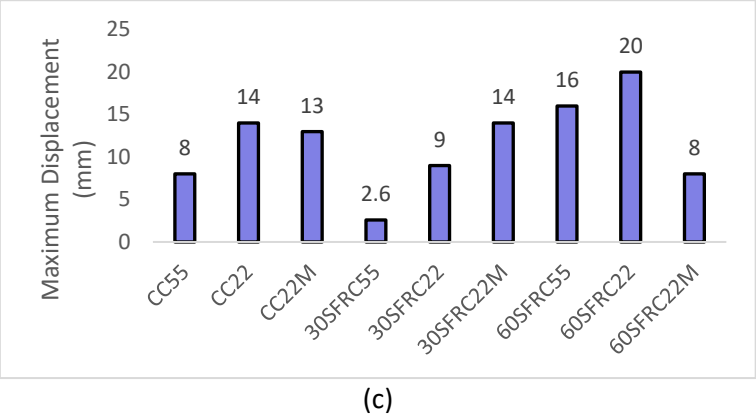

Fig. 12. Bending test results of the 1st group samples: a) energy absorption b) Capacity of load c) Capacity of displacement

3.1.4. The effect of mesh reinforcement and steel fiber reinforcement on the behavior of models exposed to high temperatures

The load-displacement graph of the models exposed to high-temperature is shown in Fig. 13. The displacements of the FCC22, FCC22M, F30SFRC22, F30SFRC22M, and F60SFRC22 models increased linearly with increasing the load up to 61 kN, 108 kN, 88 kN, 129 kN, and 105.88 kN respectively. The displacements corresponding to the maximum load of these models were determined as 20 mm, 13 mm, 14 mm, 14 mm, 19.8 mm and 8 mm.

As shown in Table 7, when the mesh reinforcement is added to the models, the effect of elevated temperature to energy absorption capacity is increased by 52.26 % in conventional concrete, by 39.07 % for the models with 30 kg/m^3 steel fibers, and by 22.92 % for the ones with 60 kg/m^3 steel fibers. After the high-temperature process, the observed maximum load was increased by for the CC model. However, the same observation for the 30SFRC, and 60SFRC models were indicated an increase by 46.59% and 28.45%, respectively. When the steel fiber is added to the concrete mixture, the energy absorption capacity is increased by 61.86% and 121.09% in 30 kg/m^3 reinforced steel fiber concrete, and 60 kg/m^3 reinforced steel fiber concrete. Besides, the maximum load capacities of the models were increased by 44.26% and 73.57% for the 30SFRC and 60 SFRC ones. Furthermore, the displacements corresponding to the maximum load were decreased by 30% and 1% for the 30SFRC and 60SFRC models, respectively.

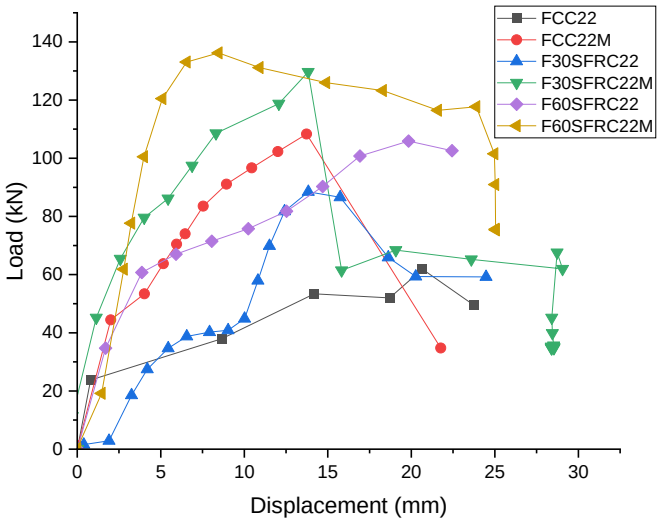

Fig. 13 Load-displacement graph for FCC22, FCC22M, F30SFRC22, F30SFRC22M, F60SFRC22, and F60SFRC22M)

Table 7
The effect of mesh reinforcement and steel fiber reinforcement on the behavior of composite floors exposed to high temperatures

Model Code	Energy Absorption Area (KN*mm)	The difference in Energy Absorption (%)	Maximum Load (KN)	Maximum Displacement at the center (mm)
		CC		
FCC22	1024	+52.26	61	20
FCC22M	1559.11		108	13
		30SFRC		
F30SFRC22	1657.46	+39.07	88	14
F30SFRC22M	2305.09		129	14
		60SFRC		
F60SFRCC22	2264	+22.92	105.88	19.8
F60SFRC22M	2783		136	8

3.2. Vibration response

In this study, the vertical vibrations were obtained by placing CMG-5TD accelerometers on the model slabs made of 30 kg/m^3 and 60 kg/m^3 steel fiber with conventional concrete with varying stud spacings. The vibrations were measured in 1st group models (1500 x 1200 mm) and 2nd group models (760x700 mm) after the high-temperature process. The vibration records, applied in 0.01 s time steps in the time history, were filtered in the frequency range of 0.5-25 Hz to obtain internal vibration data from the sample. The natural frequencies of the models were determined by using Fourier transforms (FFT) [26]. The frequency environment of the models with varying stud spacings and mesh reinforcements, for the conventional concrete were presented in Fig. 14. The 1st mode natural frequencies of the CC22, CC22M, CC55M and CC55 models were determined as 10.53, 20.44, 11.82 and 13.99 Hz, respectively. It was determined that, reducing the screw (stud) spacing from 55 cm to 22 cm, the natural frequency was reduced by 10.92% for the no-mesh model, and by 31.67% for the one with mesh. Withal, the use of mesh reinforcement was shown that, the oscillations were reduced by approximately 50% for the models with 22 cm screw spacing, and 14% for the ones with 55 cm screw spacing. The 2nd mode frequencies of the CC22, CC22M, CC55 and CC55M models were obtained as 12.95, 21.02, 17.18, and 20.8 Hz, respectively. The 3rd mode frequencies of the models were determined as 23.7 Hz. The CC55 model had the highest amplitude between the ones at the same frequency. It was noted that in this group of models, the arrangement of the mesh reinforcement and the 22 cm screw spacing present the most optimum results.

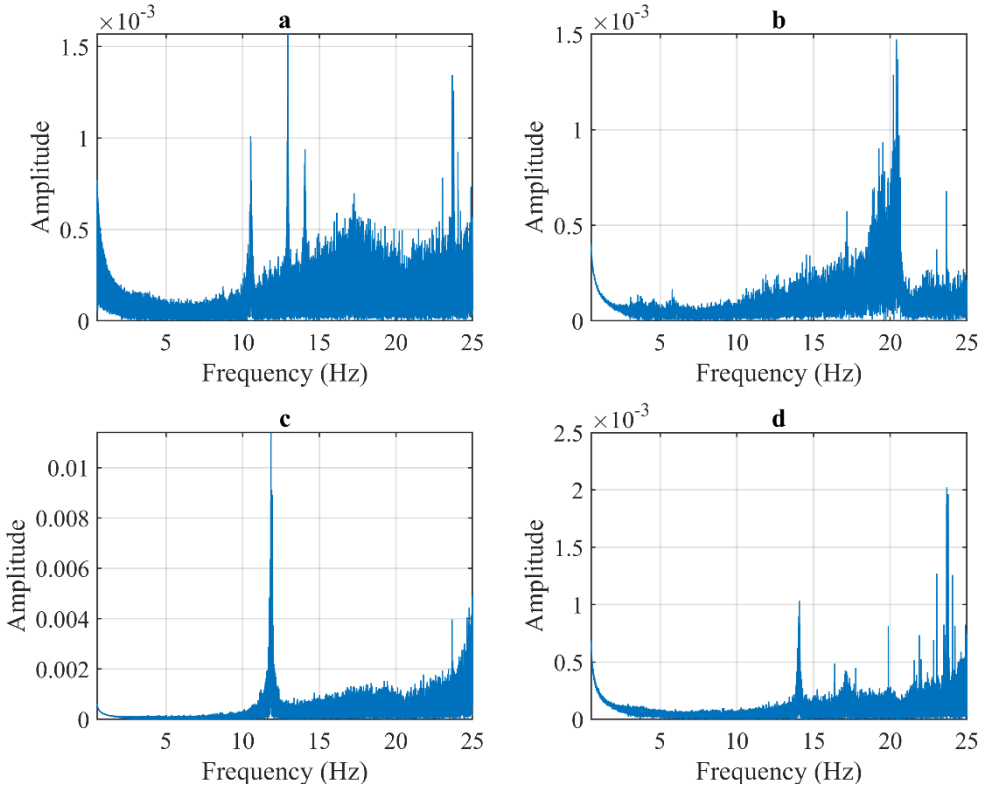

Fig. 14 Frequency of the models with conventional concrete and mesh a) CC22 b) CC22M c) CC55 d) CC55M

The frequency calculations, obtained for the models with 30 kg/m^3 fibers are presented in Fig. 15. It has been determined that, the use of 30 kg/m^3 steel fiber with 22 cm screw spacing was increased the natural frequency of the flooring from 10.53 Hz to 12.67 Hz. The natural frequency, for the model with mesh reinforcement and same screw spacing, was decreased from 20.44 Hz to 9.57 Hz with the use of 30 kg/m^3 steel fiber. A similar situation was also presented for the model with 55 cm screw spacing. In this case, the simultaneous use of mesh reinforcement and 30 kg/m^3 steel fiber showed that, the oscillation of the model was increased. In Fig. 15c, the model with the smallest amplitude in the same frequency ranges was the CC55 one. The use of 30kg/m^3 steel fiber with 55 cm screw spacing, was implied the most optimum result.

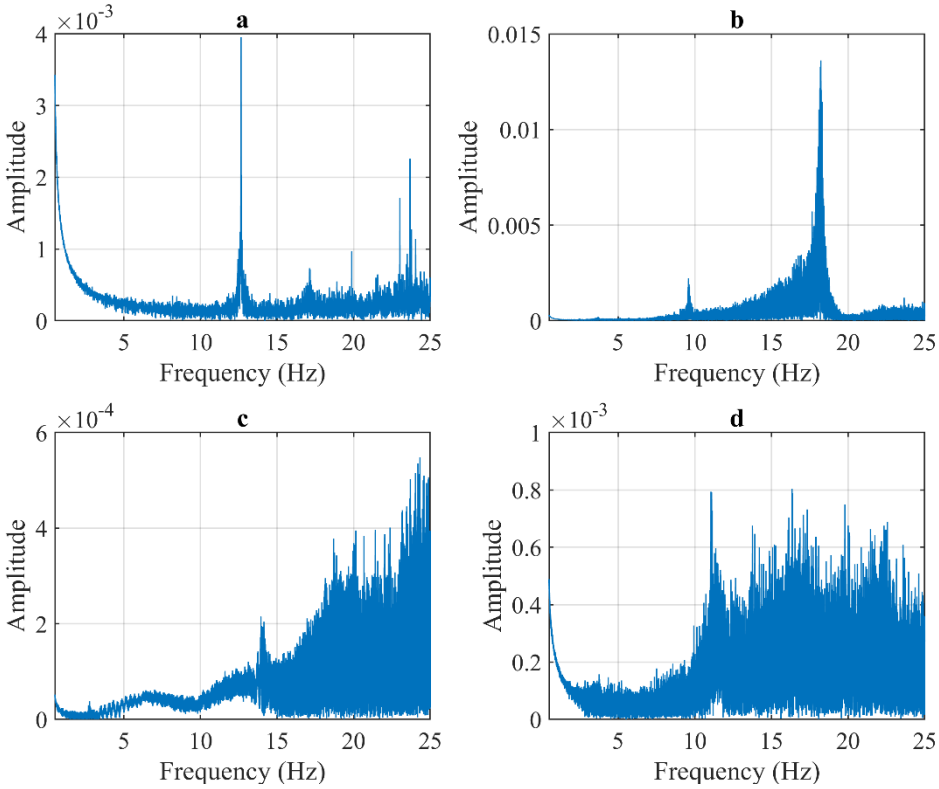

Fig. 15 Frequency of the models containing 30 kg/m^3 steel fiber a) 30SFRC22 b) 30SFRC22M c) 30SFRC55 d) 30SFRC55M

The frequency transforms, obtained for the models with 60 kg/m^3 fibers, were presented in Fig. 16. It was determined that, the dominant frequencies of the 60SFRC22 and 60SFRC22M models were 23.7 and 24.87 Hz, respectively (Fig. 16). As a result of 60 kg/m^3 steel fiber addition to the mix of the models with 22 cm screw spacing and mesh reinforcement; the oscillations were decreased about 18%. The 1st mode frequencies of the 60SFRC55 and 60SFRC55M models were 13.88 and 12.5 Hz (Fig. 16c and Fig. 16d). It was also obtained that 60 kg/m^3 steel fiber addition to the mix was implied a good result by increasing the oscillation of the models with or without mesh, but with 55 cm screw spacing. The oscillations of the models, with 22 cm screw spacing,

mesh reinforcement and 60 kg/m^3 steel fiber content, were reduced approximately 56% for 1st group samples. When 30 kg/m^3 steel fiber and mesh reinforcement were used together, the oscillations of the models were increased. However, the addition of 30 kg/m^3 or 60 kg/m^3 steel fiber with 55 cm screw spacing were reduced the oscillations approximately 25% and 24%, respectively. It was predicted that the 60SFRC22M model with 22 cm screw spacing and the 30SFRC55 model with 55 cm screw spacing were the most optimal ones for the oscillations.

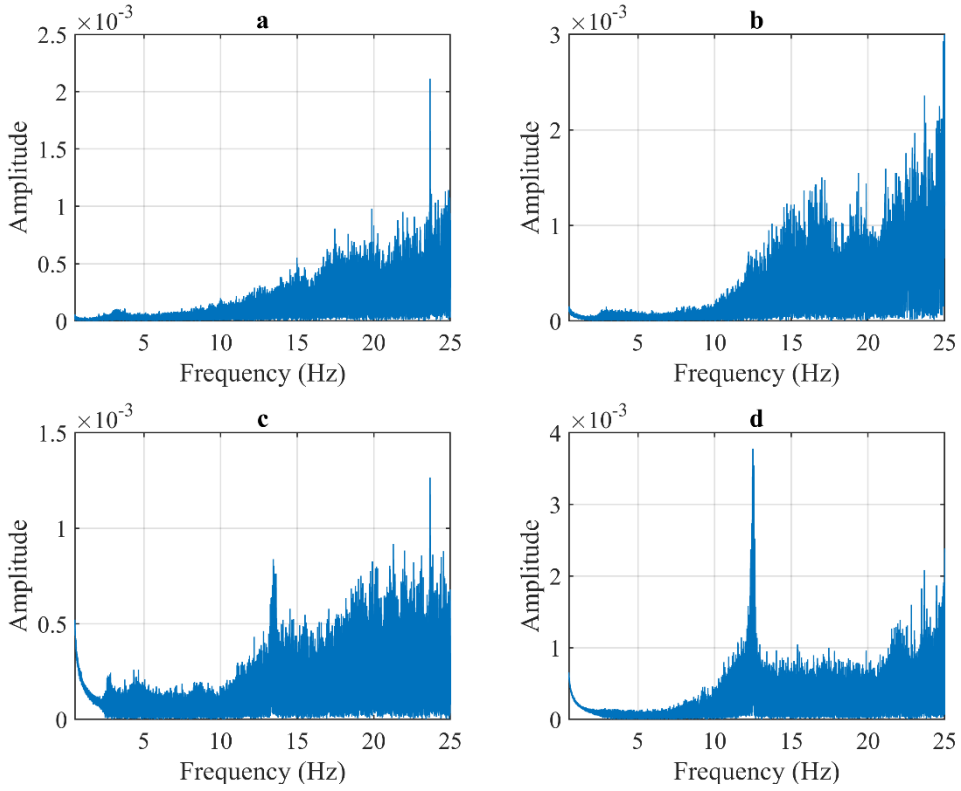

Fig. 16 Frequency of the models with 60 kg/m^3 steel fiber a) 60SFRC22 b) 60SFRC22M c) 60SFRC55 d) 60SFRC55M

The models of 760x720 mm, with 22 cm screw spacing, were inspected after high-temperature process at 600 °C for vibration analysis. Fig. 17 shows the frequency conversions of the models produced by conventional concrete, with and without mesh-reinforcement, before and after high-temperature process at 600 °C. The natural frequencies of the CC22, CC22M, FCC22 and FC22M models were 18.05, 19.07, 14.32, and 13.02 Hz, respectively. The use of mesh reinforcement before the high-temperature process was reduced the oscillations of the model and increased after the high-temperature process. It was determined that keeping the models at 600 °C increased approximately 21% and 32%, respectively, for the models with and without mesh. In addition, the oscillations, with larger amplitude content, were observed for the models after high temperature process (Fig. 17). The use of mesh was increased the oscillations of the model against high-temperature process.

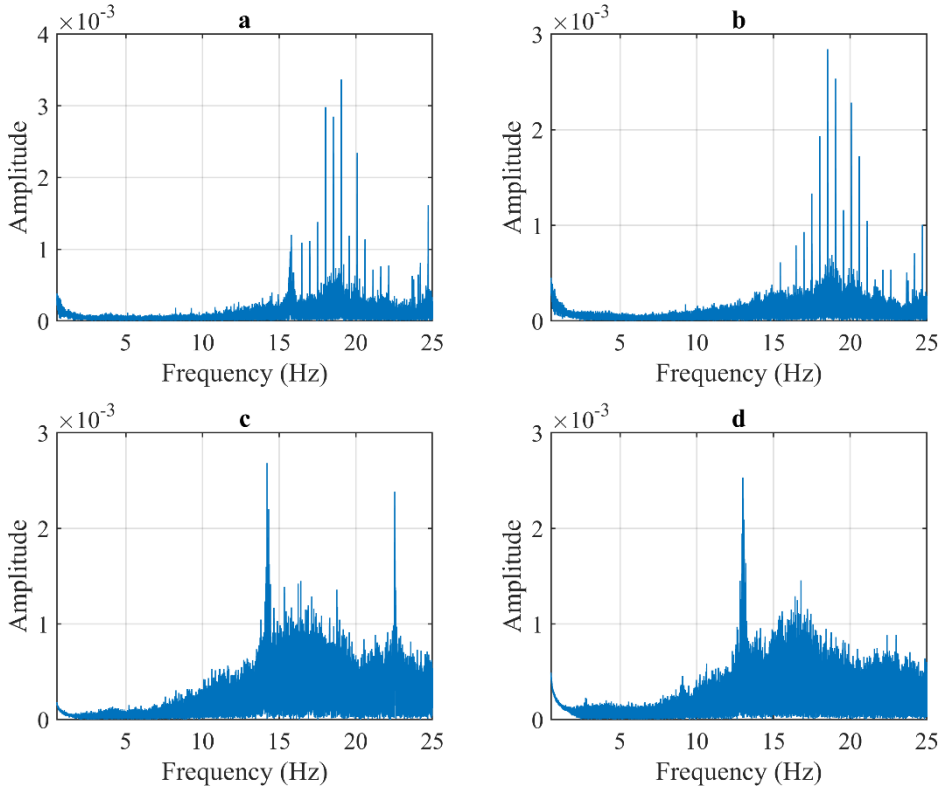

Fig. 17 Frequency of the models without steel fiber exposed to 600 °C temperature process a) CC22 b) C22M c) FCC22 d) FCC22M

The frequency conversions are presented in Fig. 18, after the high-temperature process (600 ℃) of the models with 30 kg/m^3 steel fibers. The dominant frequencies of the 30SFRCC22, 30SFRC22M, F30SFRC22, and F30SFRC22M models were determined as 18.49, 13.28, 16.09, and 16.58 Hz, respectively. The emissions were applied by the model increased by 11.2%. The amplitudes of the models were increased about 10% in the dominant frequency ranges after the high-temperature process. The use of mesh was significantly reduced the pre-heat and post-heat amplitudes of the models.

The frequency conversions are presented in Fig. 19, after the high-temperature process (600 ℃) of the models with 60 kg/m^3 steel fibers. The dominant natural frequencies of the 60SFRCC22, 60SFRC22M, F60SFRC22, and F60SFRC22M models were determined as 14.32, 13.19, 18.29, and 15.6 Hz, respectively. As a result, it was observed that 30kg/m^3 and 60 kg/m^3 steel fiber content were reduced the emissions of the models, approximately 12% and 22%, respectively. The fact that the model, which was formed by using 60kg/m^3 steel fiber and mesh reinforcement together, especially in the same frequency ranges, produced more amplitude at higher frequencies. Withal, mentioned models were also showed the highest damping capacity [27, 28].

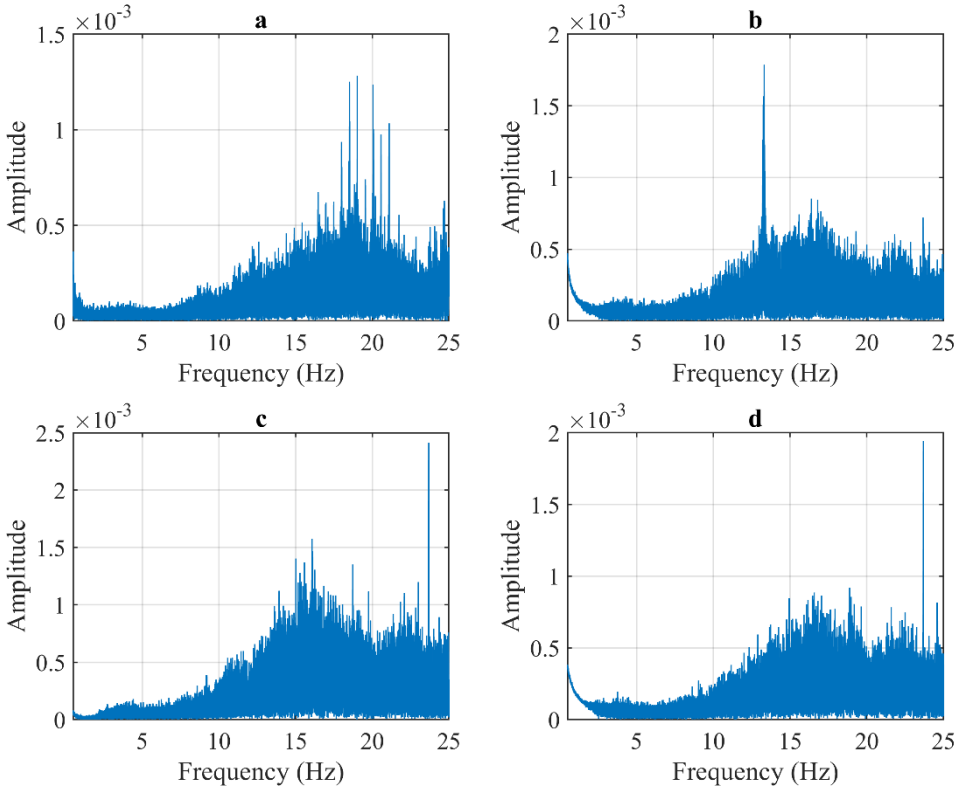

Fig. 18. Frequency of the models with 30 kg/m^3 steel fiber exposed to 600 ℃ temperature process a) 30SFRCC22 b) 30SFRC22M c) F30SFRC22 d) F30SFRC22M

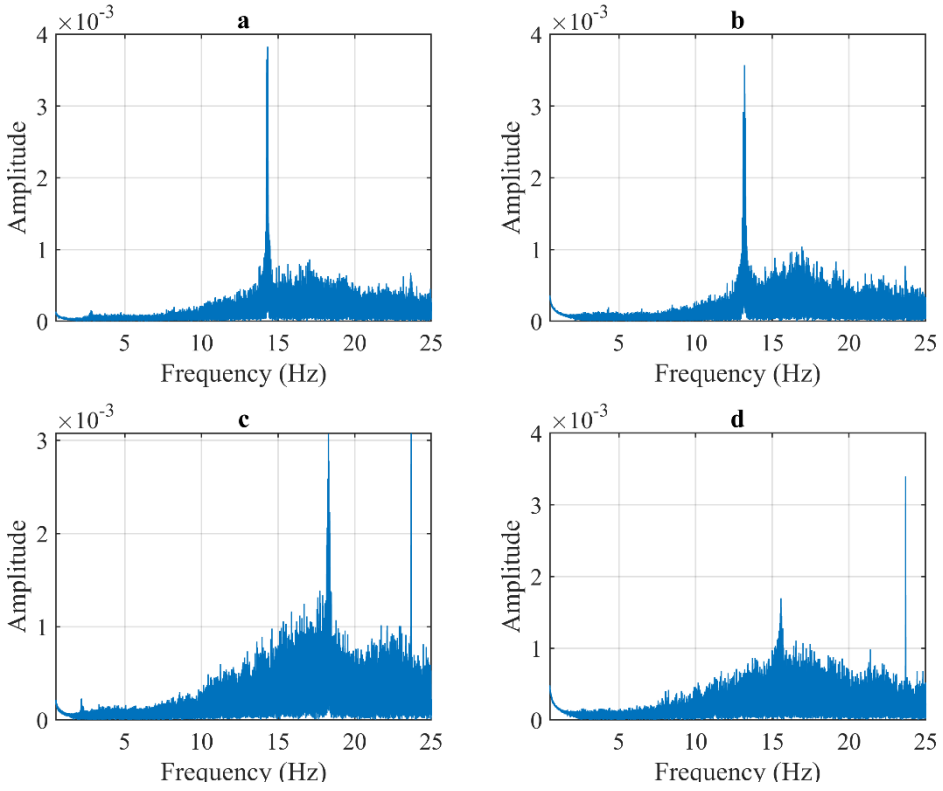

Fig. 19 Frequency of 30 kg/m^3 steel fiber models exposed to 600 ℃ temperature environment a) 60SFRCC22 b) 60SFRC22M c) F60SFRC22 d) F60SFRC22M

The acceleration response spectral curves have been designed by summing the absolute values of the data in the time history, as a result of vibration tests [29]. The response spectrum gives ideas about the maximum positive accelerations that can occur in the model. Based on the acceleration of the model at the prevailing period values, it has been interpreted to what extent the screw spacing, mesh reinforcements, and steel fibers to reduce the model vibrations.

The response spectrum acceleration graphs were presented in Fig. 20**,** for the 1st group models (1500x1200 mm), without fiber, with 30 kg/m^3, and 60 kg/m^3 fiber content. The maximum acceleration of the CC22, CC22M, CC55 and CC55M models were determined to be 0.0090, 0.0048, 0.018, and 0.0116 m/s^2, respectively. It was determined that reducing the screw spacing from 55 cm to 22 cm, was reduced the acceleration by 50.55%, and the mesh reinforcement was reduced by 46.77% for the same period step. The use of 30 kg/m^3 and 60 kg/m^3 steel fiber in composite flooring increases the reaction acceleration by approximately 44.44% and 18.91%, respectively, in the same screw spacing. In general, the use of 30 kg/m^3 steel fiber and mesh reinforcement in 22 cm and 55 cm screw spacing created high acceleration values, such as, 0.0247 m/s^2 and 0.019 m/s^2, respectively, while also reaches the highest floor vibration acceleration value of 0.056 at 55 cm screw spacing. The steel fiber content of 30 kg/m^3 were produced the highest vibration acceleration values in composite floors (Fig. 20b). The lowest vibration acceleration value in the study was 0.00468 m/s^2 in the case of 60 kg/m^3 steel fiber content and the arrangement of screws at 55 cm spacing without mesh reinforcement (Fig. 20c). Similarly, low acceleration values such as 0.0111 m/s^2 without mesh reinforcement and 0.00689 m/s^2 with mesh reinforcement were produced at 22 cm screw spacing. The test results showed that the composite floor where vibration accelerations were felt the least was 60SFRC55 and the floor where the highest vibration is felt was 30SFRC55.

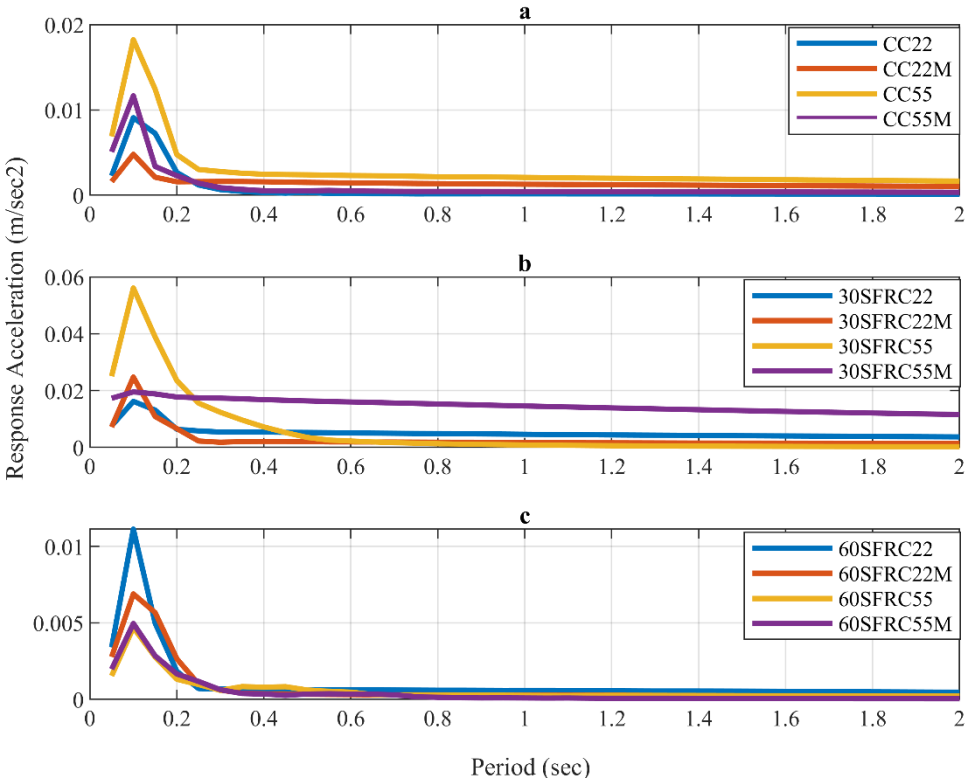

Fig. 20 Response spectra of Group 1 models a) no-fiber models b) Models with 30 kg/m^3 steel fiber c) Models with 60 kg/m^3 steel fiber.

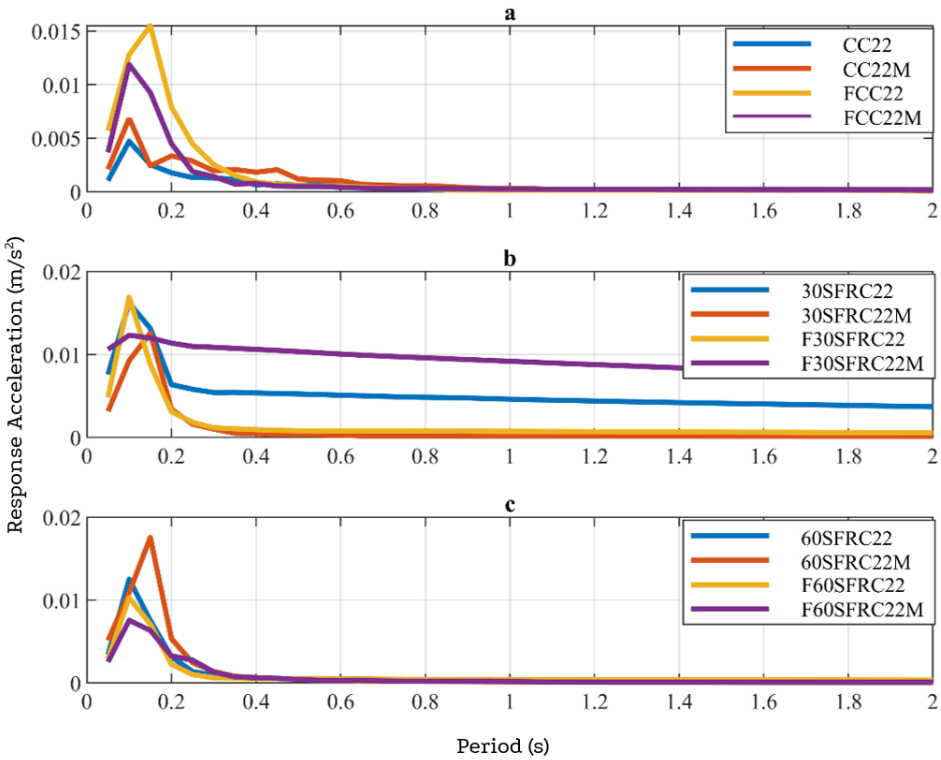

Fig. 21 Response spectra of Group 2 models a) no fiber models b) Models with 30 kg/m^3 steel fiber c) Models with 60 kg/m^3 steel fiber

The response acceleration spectra, for the 760x700 mm, no-fiber, 30 kg/m^3, and 60 kg/m^3 steel fiber models with 22 cm screw spacing and processed for 600°C (high-temperature condition), were presented in Fig. 21. This result showed that, reducing the size of models also reduces vibrations, as expected. It was observed that the same models reached vibration acceleration values of 0.0115 and 0.0119 m/s^2, respectively. The increase in vibration acceleration after heating process, corresponds to approximately 59% and 42%, respectively. It was observed that the vibration accelerations of the models without or with mesh by using 30 kg/m^3 steel fiber, were increased by 8.28% and 3.25%, respectively. The vibration accelerations of the models, without or with mesh using 60 kg/m^3 steel fiber, were decreased by 33.59% and 36.13%, respectively. Withal, the highest vibration acceleration was observed as 0.0175 m/s^2 for the 60SFRC22M model, and the lowest one was observed for the 30SFRC22 model as 0.0047 m/s^2, among the second group.

The highest vibration acceleration of the F30SFRC22M model was observed as 0.0169 m/s^2, where the lowest one was 0.0047 m/s^2. The vibration acceleration of the model CC22M was determined as 0.0069 m/s^2 before the heating process with the same screw spacing, also. In this case, if the model, with 60 kg/m^3 steel fiber, was exposed to the heating process, the vibration of the model was increased only by 9.21%. However, it was detected that the vibration acceleration of the model, without mesh, was 0.0047 m/s^2 before the heating process. Similarly, the model with 60 kg/m^3 steel fiber, was reached a great value of 0.0103 m/s^2 with an increase of 54%. This result implies that, the 60 kg/m^3 steel fiber content ensures optimum compatibility with the mesh reinforcement and minimizes floor vibrations, also.

4. Conclusion

The vibration response and the bending behavior of 18 model composite floors have been investigated in this study. The effect of bolt spacing, steel-fiber, and mesh reinforcement on the performance of the model composite floors were analyzed, experimentally. Furthermore, the effects of high-temperature on the behavior of the models were examined.

- ❖ Decreasing the spacings of the screws in the models without mesh reinforcement decreased the peak acceleration response of the steel composite floors. The affectivity of the screw spacing reduction was strikingly decreased by the fiber increase. The effectiveness values were found as 73.2%, 19.5%, and 10.8%, for the models with steel fibers, and 60 kgm^3 steel fibers, respectively.
- ❖ Using mesh reinforcement was decreased the peak acceleration response of the model composite floors manufactured with conventional concrete. However, using the steel-fiber was increased the peak acceleration response of the models.
- ❖ When the composite floors were exposed to the high-temperature, the peak acceleration response was increased for the models with conventional concrete, but started to decrease by increasing the amount of the steel fiber content.
- ❖ Decreasing the bolt spacing and adding the mesh, caused an increase in the energy absorption capacity, maximum load capacity, and maximum displacement of all the models in group 1. Meanwhile, using steel fiber has shown an increase in the energy absorption capacity of the models.
- ❖ Using the mesh and steel fiber caused an increase in the energy absorption capacity of the high-temperature exposed models (Group 2 models).
- ❖ Vibration test results show that the model vibrations were reduced by approximately 50% as a result of reducing screw spacing. It has been determined that the model vibrations are reduced by 47% in the case of using mesh reinforcement.
- ❖ The 60 kg/m^3 steel fiber content can significantly (approximately 54%) reduce possible vibrations that may occur in composite floors when used with mesh reinforcements. In addition, the use of 60 kg/m^3 steel fiber with or without mesh reinforcement in composite floors with screw spacing of 55 cm, the acceleration values were similar to composite floors formed with 22 cm screw spacing.
- ❖ The use of 60 kg/m^3 steel fiber content together with the mesh reinforcement is effective in reducing the vibrations of composite floors after the high-temperature process. The vibrations of the composite model floors prepared before the heat process and formed with conventional concrete at 22 cm screw spacing, increased by approximately 9% compared to the vibrations of the other models when exposed to high-temperature process with the addition of 60 kg/m^3 steel fiber and mesh reinforcement, and became the most recommended flooring type.
- ❖ The deformation, energy absorption capacities, floor vibrations, and the fire resistance are considered; the applicable flooring type is 60SFRC22M composite flooring with 60kg/m^3 steel fiber, 22 cm screw spacing, mesh reinforcement and traditional concrete.
- ❖ The results showed that the amount of steel fiber should be optimally adjusted for the mesh reinforcement and steel fiber to work in harmony. It is also foreseen that if a high amount of steel fiber content is used, the screw spacing should be adjusted according to this ratio.

Acknowledgment

The research is part of the Sadiq Ahmad Afzali master thesis and Ataturk University Projects FYL-2019-7293. The author would like to thank Ataturk University for funding the projects.

Declaration of competing interest

The authors declare that they have no known competing financial interests or personal relationship that could have appeared to influence the work reported in this paper.

References

[1] A. Chatteree, S. Chandra, Thin-slab casting: new possibilities, Sadhana 26 (2001) 163-178
[2] J. Qureshi, D. Lam, J. Ye, The influence of profiled sheeting thickness and shear connector's position on strength and ductility of headed shear connector, Engineering Structures 33(5) (2011) 1643-1656.https://doi.org/10.1016/j.engstruct.2011.01.035
[3] S. Gopinath, A. Prakash, R. Aahrthy, M.B. Harish, Investigations on the influence of matrix and textile on the response of textile reinforced concrete slabs under impact loading, Sādhanā 43 (2018) 1-11.https://doi.org/10.1007/s12046-018-0933-8
[4] S. Nayar, R. Gettu, Mechanistic-empirical design of fibre reinforced concrete (FRC) pavements using inelastic analysis, Sādhanā 45(1) (2020) 19.https://doi.org/10.1007/s12046-019-1255-1
[5] P.M. Choradiya, P.D. Kumbhar, Behaviour of concrete deck slab using shear connectors: A review, International Journal of Innovative Research in Science, Engineering Technology 4 (12) (2015) 12883-12892
[6] H. Wright, H. Evans, P. Harding, The use of profiled steel sheeting in floor construction, Journal of Constructional Steel Research 7(4) (1987) 279-295
[7] J.W. Luo, Behaviour and analysis of steel fibre-reinforced concrete under reversed cyclic loading, University of Toronto (Canada)2014.
[8] W.D. Varela, R.C. Battista, Control of vibrations induced by people walking on large span composite floor decks, Engineering Structures 33(9) (2011) 2485-2494.https://doi.org/10.1016/j.engstruct.2011.04.021
[9] A. Pavic, M. Willford, Vibration Serviceability of Posttensioned Concrete Floors. Post-Tensioned Concrete Floors Design Handbook, Appendix G, Technical Report 43, 2005.
[10] A. Ferreira, G. Fasshauer, Analysis of natural frequencies of composite plates by an RBF-pseudospectral method, Composite Structures 79(2) (2007) 202-210.https://doi.org/10.1016/j.compstruct.2005.12.004
[11] Y.K. Ju, D.-Y. Kim, S.-D. Kim, S.-W. Yoon, Y.-K. Lee, D.-H. Kim, Dynamic characteristics of the new composite floor system, Steel Structures 8 (2008) 347-356
[12] F.A. Gandomkar, W.H.W. Badaruzzaman, S.A. Osman, The natural frequencies of composite Profiled Steel Sheet Dry Board with Concrete infill (PSSDBC) system, Latin American Journal of Solids Structures 8 (2011) 351-372
[13] F. Gandomkar, W. Wan Badaruzzaman, S. Osman, A. Ismail, Experimental and numerical investigation of the natural frequencies of the composite profiled steel sheet dry board (PSSDB) system, Journal of the South African Institution of Civil Engineering= Joernaal van die Suid-Afrikaanse Instituut van Siviele Ingenieurswese 55(1) (2013) 11-21
[14] H. Cifuentes, F. Medina, Experimental study on shear bond behavior of composite slabs according to Eurocode 4, Journal of Constructional Steel Research 82 (2013) 99-110.https://doi.org/10.1016/j.jcsr.2012.12.009
[15] S.J. Hicks, A.L. Smith, Stud shear connectors in composite beams that support slabs with profiled steel sheeting, Structural Engineering International 24(2) (2014) 246-253.https://doi.org/10.2749/101686614X13830790993122
[16] L. Costa-Neves, J.S. da Silva, L. De Lima, S. Jordão, Multi-storey, multi-bay buildings with composite steel-deck floors under human-induced loads: The human comfort issue, Computers Structures 136 (2014) 34-46.https://doi.org/10.1016/j.compstruc.2014.01.027
[17] K. Jarnerö, A. Brandt, A. Olsson, Vibration properties of a timber floor assessed in laboratory and during construction, Engineering Structures 82 (2015) 44-54.https://doi.org/10.1016/j.engstruct.2014.10.019
[18] J. Holomek, M. Bajer, M. Vild, Cast screws as shear anchors for composite slabs, Procedia Engineering 195 (2017) 114-119
[19] TS802, Turkish Standard -Design of concrete mixes, Ankara, Turkey, (2016)
[20] TS/EN-14889-1, Fibres for concrete - Part 1: Steel fibres - Definitions, specifications and conformity, Ankara, Turkey, (2016)
[21] TS4559, Steel Mesh for Concrete, Ankara, Turkey, (2006)
[22] TS/EN/12390-3, Compressive strength of test specimens, (2019)
[23] TS/EN/12390-5, Flexural strength of test specimens, (2019)
[24] Eurocode-4, Design of composite steel concrete structures, Part 1.1: General rules and rules for buildings, European Committee for Standardization (CEN), (2004)
[25] P. Wessel, W.H. Smith, R. Scharroo, J. Luis, F. Wobbe, Generic mapping tools: improved version released, Transactions American Geophysical Union 94(45) (2013) 409-410
[26] A. Chopra, Dynamics of Structures: Theory and Applications to Earthquake Engineering, Prentice Hall, Englewood Cliffs, NJ 1995.
[27] K. Beyen, Damage identification analyses of a historic masonry structure in TF domain, Journal of Technical 32(2) (2021) 10577-10610
[28] O. Sak, K. Beyen, Damage analysis of the structures in time-frequency domain with wavelet transform method, Journal of Technical 30 (2019)
[29] S. Rajasekaran, Structural dynamics of earthquake engineering: theory and application using MATHEMATICA and MATLAB, Elsevier2009.

Advanced Steel Construction – Vol. 19 No. 3 (2023) 223–241
DOI:10.18057/IJASC.2023.19.3.4

A GENERALIZED METHOD FOR SHEAR CORRECTION FACTORS OF ARBITRARY THIN-WALLED SECTIONS

Yue-Yang Ding [1], Lun-Hua Bai [1, 2, *], Wen-Feng Chen [1], Yao-Peng Liu [1, 3] and Siu-Lai Chan [1]

[1] *Department of Civil and Environmental Engineering, The Hong Kong Polytechnic University, Hong Kong, China*
[2] *School of Transportation, Civil Engineering & Architecture, Foshan University, Foshan, China*
[3] *NIDA Technology Company Limited, Hong Kong Science Park, Shatin, N.T., Hong Kong, China*
** (Corresponding author: E-mail: bailunhua@163.com)*

ABSTRACT

Shear deformation may significantly affect the structural behaviours, especially for the structural members with small span-to-depth ratios. It is vital to consider the shear effects in the Direct Analysis Method (DAM) of thin-walled structures such that only the section capacity check is required in the evaluation of both member and system stability. However, there is lack of a general method to determine the shear correction factors of thin-walled cross-sections in various shapes and as a result DAM cannot be applied to the structures adopting these cross-sections. This paper proposes an innovative one-dimensional warping element model method to compute the shear correction factors of arbitrary thin-walled sections such as single open and closed sections, built-up sections, and large box sections with stiffeners. Also, the thin-walled cross-sections with non-uniform thickness can be considered by the proposed method. Several examples are investigated to validate the accuracy and efficiency of the proposed method against the analytical solution, conventional warping area element method and section analysis in ANSYS. Thus, this work provides a simple and practical method for direct analysis of thin-walled structures made of complex cross-sections with consideration of shear deformation.

ARTICLE HISTORY

Received: 2 February 2022
Revised: 13 September 2022
Accepted: 21 October 2022

KEYWORDS

Shear correction factor;
Thin-walled section;
Built-up section;
Taper plate;
One-dimensional warping element

Copyright © 2023 by The Hong Kong Institute of Steel Construction. All rights reserved.

1. Introduction

Thin-walled members are widely used in the construction of building and bridge structures owing to their advantages of light weight, material saving, excellent stiffness and high strength. When the thin-walled members with a relatively small span-to-depth ratio are adopted in the engineering structures such as box girder bridges and long-span spatial structures (Bai *et al.* 2021; Shen *et al*. 2019; Ljubinkovic *et al*. 2019; Liu *et al*. 2018), the influence of shear deformation increases and therefore the beam-column elements based on the Euler-Bernoulli theory cannot provide accurate prediction. To this point, the beam-column elements based on Timoshenko theory considering shear deformation attract considerable attention worldwide (Saritas *et al.* 2009; Dikaros *et al.* 2016; Ding *et al.* 2018; Franza *et al.* 2020; Wang *et al.* 2014; Tao *et al.* 2014; Zhuge *et al.* 2020; Bai *et al.* 2020; Du *et al*. 2019; Tang *et al*. 2022). It is vital to consider the shear effects in the Direct Analysis Method (DAM) of thin-walled structures for better prediction of structural behaviours such that only the section capacity check is required in the evaluation of both member and system stability (Du *et al*. 2019; Tang *et al*. 2022) without use of the conventional effective length method (ELM). The ELM is based on linear analysis with many limitations as discussed by Chan *et al.* (2005). However, there is lack of general method to determine the shear correction factors of thin-walled cross-sections in various shapes when using Timoshenko beam-column elements and as a result DAM cannot be applied to this kind of structures with the cross-sections in various shapes.

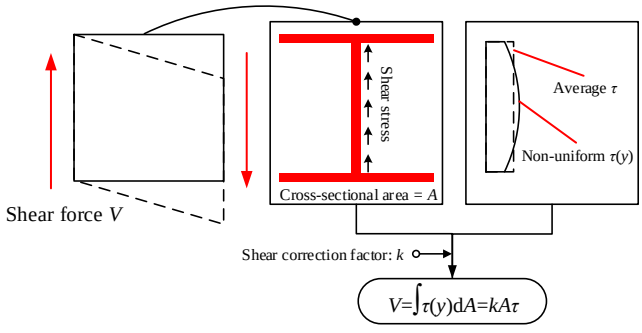

Fig. 1 Shear correction factor for non-uniformly distributed shear stress

The shear correction factor is widely used to represent the non-uniformly distributed shear stresses in a cross-section when using a beam-column model for global structural analysis. As illustrated in Fig. 1, the actual shear effect can be replaced by average shear stress multiplying by shear correction factor and the cross-sectional area.

For thin-walled members with a small span-to-depth ratio, the Timoshenko beam-column model allowing for shear deformations has been continuously improved, including the force-based and displacement-based elements. Du *et al.* (2019) proposed a novel flexibility-based beam-column element considering both shear deformation and member initial imperfection, as well as material nonlinearity by the fiber section method. Bai *et al.* (2020) presented a mixed beam-column element considering shear deformation for taper I-section member. Based on the point precise element (PEP) proposed by Chan *et al*. 1994, Tang *et al.* (2022) put forward an improved PEP element considering shear deformation and member initial imperfection. The mentioned new Timoshenko beam-column models provide excellent results. Paolo *et al.* (2018, 2021) proposed a mixed 3D beam element to consider shear deformation based on the warping displacement field of the cross sections. However, the traditional beam-column elements cannot account for both shear deformations and initial member imperfection, which are compulsively required in direct analysis.

Extensive works on Timoshenko beam-column models are also found in conventional nonlinear analysis focused on material nonlinearity. A fiber beam model considering slab spatial composite effect proposed by Tao *et al*. (2014) is based on the Timoshenko beam-column element in the commercial software Msc.Marc. Similarly, several fiber beam-column models are proposed by Ding *et al.* (2018) for reinforced concrete coupling beam and steel link beam with consideration of nonlinear shear behaviors in Msc.Marc. Wang *et al*. (2014) adopted the commercial software ABAQUS to implement a novel beam-column element for circular concrete filled steel tube considering torsional effect.

Note that the above works are mainly for the structural members using regular shape cross-sections, in which the shear correction factors for prediction of shear effect can be determined by analytical methods. Generally speaking, the previous research on Timoshenko beam-column models which use shear correction factors to include shear effects is limited to some typical shapes such as circular sections, rectangular sections, I-shape sections, box sections and Tee sections. There is an urgent need to develop a general method for determination of shear correction factors of thin-walled sections with various shapes, complicated box sections with extensive stiffeners, built-up sections, etc. Otherwise, the Timoshenko beam-column elements with excellent performance as reported in existing literature, such as Du *et al.* (2019) and Tang *et al.* (2022), cannot be used to predict the structural behaviors of the structures with unusual shape of cross-sections when the shear deformation becomes dominant.

Previous research on shear correction factors mainly focuses on the analytical solutions for simple shape sections (Timoshenko 1921, 1970; Love 1944; Herrmann 1965; Cowper 1966; Stephen 1980, 2001; Hutchinson 2001), numerical methods for more complicated sections (Krahula 1969; Karan 1979; Schramm *et al.* 1994; Friedman *et al.* 2000; Gruttman *et al.* 1999, 2001; Dong *et al*. 2010, 2013; Fialko *et al.* 2013), and experimental study for rectangular sections (Puchegger *et al.* 2003). Generally, the analytical methods and the experimental methods are limited to single regular sections. Also, the experimental method has both cost and time implication and therefore it is limited to research purpose. The numerical methods are mainly based on the fiber section approach, in which the section should be meshed into a number of triangular or quadrilateral shape fibers. This kind of methods requires reliable meshing algorithm. For thin-walled sections in irregular shape, extensive fibers may be induced and as a result the calculation process becomes time-consuming. Most importantly, the fiber-based method cannot be applied to the sections with several discontinuous areas like compound sections, which are widely used in steel structures.

In this paper, a generalized numerical method is proposed for determination of the shear correction factors of thin-walled sections in various shapes. Both the open and closed thin-walled sections using uniform or non-uniform thickness can be taken into account. This method is also applicable to complicated box sections with extensive stiffeners and built-up sections. Karan (1979) and Gruttman (1999, 2001) introduced a simple model, i.e., a cantilever beam subjected to free-end concentrated force, to study the shear deformation of structural members. Their method is essentially a fiber-based approach, in which the cross section is simulated by several plane warping area elements as indicated in Fig. 2(a). The drawbacks as discussed above such as time-consuming and continuous sectional areas only will limit the applications of this kind of methods in more complicated cases. Thus, a new one-dimensional element method allowing for warping effect is proposed here to calculate the shear correction factors of thin-wall sections in general cases, as shown in Fig. 2(b).

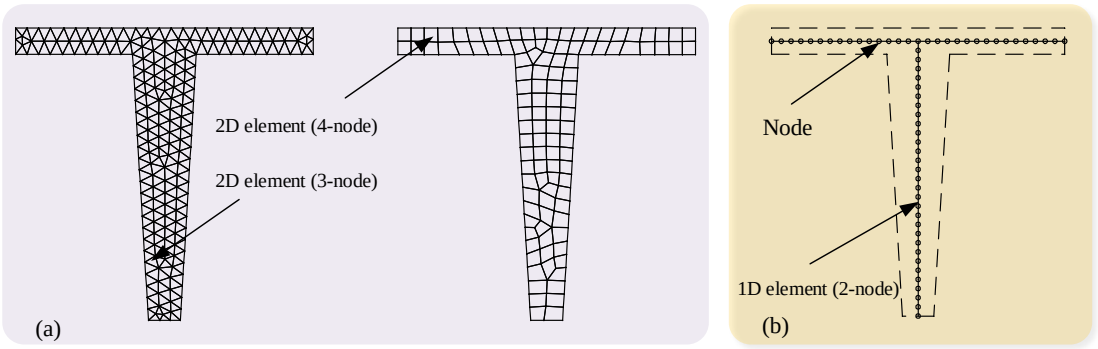

Fig. 2 Two numerical methods for shear correction factors: (a) Traditional 2D element model; (b) Proposed 1D element model

It is also found that few research is carried out on the determination of the shear correction factors of built-up sections composed of several single sections such as angles and channels connected with fasteners. An equivalent plate thickness method will be also developed to fill this gap.

In the proposed one-dimensional element model, the change of shear stress along the plate thickness is ignored as this kind of stress is not dominant in the thin-walled sections. The method is implemented in the program NIDA. Finally, several examples for the commonly used thin-walled sections are investigated for validation and demonstration.

2. One-dimensional warping element model method

The cantilever beam subjected to concentrated loads at the free end as shown in Fig. 3 is widely used to study the shear correction factors of cross sections. The force V_y is for the analysis of bending about x-axis to find shear center x_{sc} and shear correction factor k_{yy}. Similarly, the force V_x is for the analysis of the flexural behavior about y-axis to determine shear center y_{sc} and shear correction factor k_{xx}. Note that k_{xx} is along x-axis caused by V_x, while k_{yy} is along y-axis induced by V_y. The detailed derivation of proposed one-dimensional element for calculation of shear correction factors are presented as follows.

It should be noted that the cantilever beam model for derivation of shear center and shear correction factors is extensively adopted due to the shear forces along the length of the member being constant. By using this model, the displacement functions have simple forms for integral, leading to simpler element formulations than the simple beam and continuous beam models.

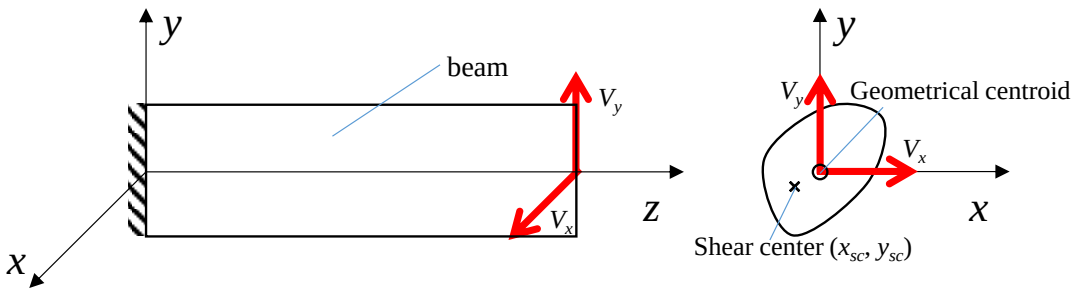

Fig. 3 Cantilever beam model for study of shear correction factors

2.1. Assumptions

The assumptions are used in this study: (1) the plane section is not required to remain plane with the consideration of the warping along the section; (2) the material is isotropic and linearly elastic; (3) the influence on the geometrical section properties due to section deformation is ignored; (4) the contribution of St. Venant torsional effect on lateral deflection is ignored; (5) the direct stress state is the same as the section subjected to pure bending moments; (6) the change of the shear stress along the plate thickness is ignored, which is acceptable for thin-walled sections; and (7) both the global and local buckling effects are ignored.

Note that, the first assumption illustrates that the cross section is not a rigid plane such that the non-uniform shear stress distribution along the cross section can be captured. The shear correction factors are widely used in conjunction with the Timoshenko beam-column elements so that the numerical efficiency of global structural analysis will be significantly enhanced. The complicated shear stress distribution has been simplified by using shear correction factors.

2.2. Shear correction factors

The displacement field of the cantilever beam as shown in Fig. 3 can be expressed as (Karan 1979):

$$u(x,y,z)=u_b+u_s$$
$$=\underbrace{\left(\frac{1}{2}Lz^2-\frac{1}{6}z^3\right)C_x}_{u_b}+\underbrace{\mu(L-z)\left[\frac{1}{2}C_x\left(x^2-y^2\right)+C_yxy\right]+a_2z+a_4}_{u_s} \quad (1)$$

$$v(x,y,z)=v_b+v_s$$
$$=\underbrace{\left(\frac{1}{2}Lz^2-\frac{1}{6}z^3\right)C_y}_{v_b}+\underbrace{\mu(L-z)\left[\frac{1}{2}C_y\left(y^2-x^2\right)+C_xxy\right]+a_1z+a_3}_{v_s} \quad (2)$$

$$w(x,y,z)=w_b+w_s$$
$$=\underbrace{-\left(Lz-\frac{1}{2}z^2\right)\left(C_xx+C_yy\right)}_{w_b}+\underbrace{\phi(x,y)-a_1y-a_2x}_{w_s} \quad (3)$$

where, u, v, and w represent the displacement along x-, y-, and z-axis, respectively; u_b, v_b, and w_b represent the displacement caused by the related bending moment; u_s, v_s, and w_s are the displacement caused by the related shear force; μ is Poisson's ratio; $\phi(x,y)$ is the warping function, and L is the length of the beam. C_x and C_y are the coefficients given by:

$$C_x=\frac{V_xI_{xx}-V_yI_{xy}}{E\left(I_{xx}I_{yy}-I_{xy}{}^2\right)} \quad (4)$$

$$C_y=\frac{V_yI_{yy}-V_xI_{xy}}{E\left(I_{xx}I_{yy}-I_{xy}{}^2\right)} \quad (5)$$

where, I_{xx} and I_{yy} are the second moment of inertia with respect to x- and y-axis, respectively; I_{xy} represents the inertia product of cross section; E is the Young's modulus of elasticity; and the constants a_1, a_2, a_3, and a_4 are related to the section shape and expressed in a general form as:

$$a_1=\frac{I_{xx}\int\phi(x,y)ydA-I_{xy}\int\phi(x,y)xdA}{I_{xx}I_{yy}-I_{xy}{}^2} \quad (6)$$

$$a_2=\frac{I_{xx}\int\phi(x,y)xdA-I_{xy}\int\phi(x,y)ydA}{I_{xx}I_{yy}-I_{xy}{}^2} \quad (7)$$

$$a_3=-\frac{\mu L}{A}\left[C_xI_{xy}+\frac{1}{2}C_y\left(I_{xx}-I_{yy}\right)\right] \quad (8)$$

$$a_4=-\frac{\mu L}{A}\left[C_yI_{xy}+\frac{1}{2}C_x\left(I_{yy}-I_{xx}\right)\right] \quad (9)$$

The coordinates of shear center of the cross section are defined as:

$$x_{sc}=\frac{M_x}{V_y}=\frac{1}{V_y}\int\left(x\tau_{zy}\big|_{V_y=const,V_x=0}-y\tau_{zx}\big|_{V_y=const,V_x=0}\right)dA \quad (10)$$

$$y_{sc}=\frac{M_y}{V_x}=\frac{1}{V_x}\int\left(y\tau_{zx}\big|_{V_x=const,V_y=0}-x\tau_{zy}\big|_{V_x=const,V_y=0}\right)dA \quad (11)$$

In the above Eqs. (10) and (11), only applying V_y to the end of the cantilever beam can obtain x_{sc}, while only applying V_x to the end of the cantilever beam can obtain y_{sc}. Totally, two loading cases should be considered. It is noted that M_x is the torsion caused by V_y while M_y is the torsion caused by V_x.

According to the theory of elasticity mechanics, the normal and shear stresses can be written as:

$$\sigma_{zz}=-E(L-z)\left(xC_x+yC_y\right) \quad (12)$$

$$\tau_{zx}=G\left\{\frac{\partial\phi(x,y)}{\partial x}-\mu\left[\frac{1}{2}C_x\left(x^2-y^2\right)+xyC_y\right]\right\} \quad (13)$$

$$\tau_{zy}=G\left\{\frac{\partial\phi(x,y)}{\partial y}-\mu\left[xyC_x-\frac{1}{2}C_y\left(x^2-y^2\right)\right]\right\} \quad (14)$$

$$\sigma_{xx}=\sigma_{yy}=\tau_{xy}=0 \quad (15)$$

in which, G is the shear modulus of elasticity of the material.

Thus, the coordinates of shear center defined in Eqs. (10) and (11) can be rewritten as:

$$x_{sc}=\frac{G}{2V_y}\int\begin{bmatrix}2x\dfrac{\partial\phi(x,y)\big|_{V_y=const,V_x=0}}{\partial y}\\-2y\dfrac{\partial\phi(x,y)\big|_{V_y=const,V_x=0}}{\partial x}\\+\mu\left(C_yx-C_xy\right)\left(x^2+y^2\right)\end{bmatrix}dA \quad (16)$$

$$y_{sc}=-\frac{G}{2V_x}\int\begin{bmatrix}2x\dfrac{\partial\phi(x,y)\big|_{V_x=const,V_y=0}}{\partial y}\\-2y\dfrac{\partial\phi(x,y)\big|_{V_x=const,V_y=0}}{\partial x}\\+\mu\left(C_yx-C_xy\right)\left(x^2+y^2\right)\end{bmatrix}dA \quad (17)$$

The average deflections caused by shear forces weighted by the lateral displacements along the longitudinal z-axis of the cantilever beam are expressed as:

$$\bar{u}_s=\frac{1}{A}\int u_sdA \quad (18)$$

$$\bar{v}_s=\frac{1}{A}\int v_sdA \quad (19)$$

Further, the average shear deformation can be expressed as:

$$\frac{d\bar{u}_s}{dz}=\frac{\partial\left(\frac{1}{A}\int u_sdA\right)}{\partial z}=\frac{1}{A}\frac{\partial\left(\int u_sdA\right)}{\partial z} \quad (20)$$

$$\frac{d\bar{v}_s}{dz}=\frac{\partial\left(\frac{1}{A}\int v_sdA\right)}{\partial z}=\frac{1}{A}\frac{\partial\left(\int v_sdA\right)}{\partial z} \quad (21)$$

Substituting Eqs. (1) to (3) into Eqs. (20) and (21), it leads to:

$$\frac{d\bar{u}_s}{dz}=\frac{V_x}{GA_{xx}}+\frac{V_y}{GA_{xy}}=\frac{V_x}{GAk_{xx}}+\frac{V_y}{GAk_{xy}} \quad (22)$$

$$\frac{d\bar{v}_s}{dz}=\frac{V_x}{GA_{yx}}+\frac{V_y}{GA_{yy}}=\frac{V_x}{GAk_{yx}}+\frac{V_y}{GAk_{yy}} \quad (23)$$

In Eqs. (22) and (23), the term $V_i/(GAk_{ii})$ represents the deflection along i-axis caused by shear force V_i, while the term $V_j/(GAk_{ij})$ represents the deflection along i-axis caused by shear force V_j. Subscript i can be x or y. Totally, there are four shear correction factors, i.e., k_{xx}, k_{xy}, k_{yx}, and k_{yy} as given in Eqs. (24) to (26). Since the shear deformation along x-axis (or y-axis) is mainly caused by the shear force along x-axis (or y-axis), the hybrid shear correction factors k_{xy} and k_{yx} are rarely adopted in the practical structural analysis using beam-column model. Thus, only k_{xx} and k_{yy} are discussed in this paper.

$$k_{xx}=\frac{I_{xx}I_{yy}-I_{xy}{}^2}{\left\{\frac{GA}{V_x}\left[I_{xx}\int x\phi(x,y)\big|_{V_x=const,V_y=0}dA-I_{xy}\int y\phi(x,y)\big|_{V_x=const,V_y=0}dA\right]-q_1\right\}} \quad (24)$$

$$k_{xy}=k_{yx}=-\frac{4(1+\mu)}{\mu}\cdot\frac{\left(I_{xx}I_{yy}-I_{xy}^{\ 2}\right)}{I_{xy}\left(I_{yy}+I_{xx}\right)} \tag{25}$$

$$k_{yy}=\frac{I_{xx}I_{yy}-I_{xy}^{\ 2}}{\left\{\frac{GA}{V_y}\left[I_{yy}\int y\phi(x,y)\big|_{V_y=const,V_x=0}\,dA-I_{xy}\int x\phi(x,y)\big|_{V_y=const,V_x=0}\,dA\right]-q_2\right\}} \tag{26}$$

in which, q_1 and q_2 are the constants given by:

$$q_1=\frac{\mu}{4(1+\mu)}\left[I_{xx}\left(I_{yy}-I_{xx}\right)-2I_{xy}^{\ 2}\right] \tag{27}$$

$$q_2=\frac{\mu}{4(1+\mu)}\left[I_{yy}\left(I_{xx}-I_{yy}\right)-2I_{xy}^{\ 2}\right] \tag{28}$$

From Eqs. (24) and (26), the shear correction factors depended on the section properties (A, I_{xx}, I_{yy}, and I_{xy}), material properties (shear modulus of elasticity G and Poisson's ratio μ), and warping function $\phi(x,y)$. Thus, once the warping function $\phi(x,y)$ is known, the shear correction factors can be determined accordingly. This paper proposes a numerical method to determine the solution of the warping function $\phi(x,y)$.

2.3. Warping function for one-dimensional element

This Section introduces a finite element method to obtain the solution of warping function $\phi(x,y)$ as shown in Eqs. (24) and (26).

Based on the conventional fiber-based approach, a section can be represented by a number of area elements allowing for warping effect as shown in Fig. 2(a). The value of $\phi(x,y)$ at each node of the plane element is denoted as ϕ_i. Thus, the $\phi(x,y)$ at the any location of the element can be interpolated by:

$$\phi=\sum_{i=1}^{n}N_i(\xi,\eta)\phi_i \tag{29}$$

Using theory of iso-parametric element, the coordinates of the element can be expressed as:

$$x=\sum_{i=1}^{n}N_i(\xi,\eta)x_i \tag{30}$$

$$y=\sum_{i=1}^{n}N_i(\xi,\eta)y_i \tag{31}$$

where, ξ and η are the natural coordinates as seen in Fig. 3(a); n is the number of nodes of the element; and $N_i(\xi,\eta)$ is the shape function which will be introduced in the followings.

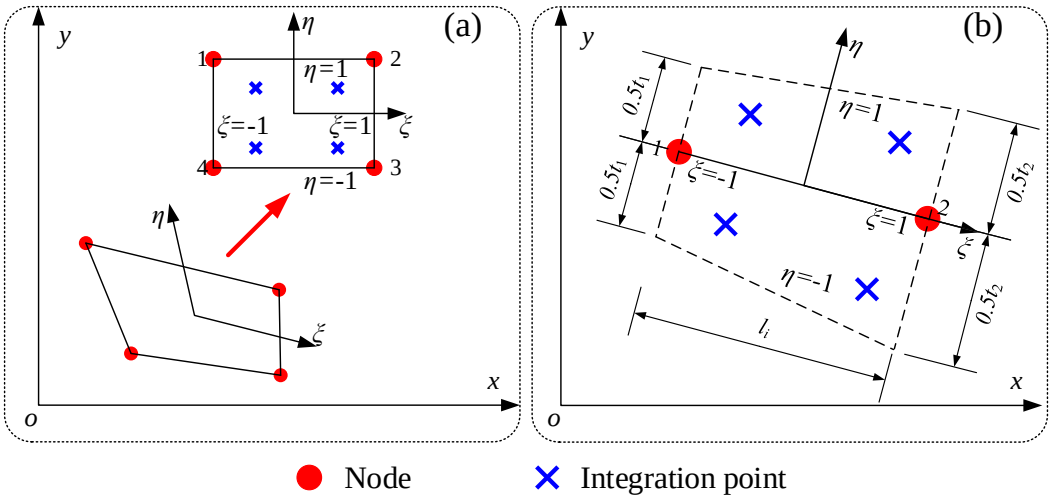

Fig. 4 Iso-parametric elements: (a) Conventional plane warping area element; and (b) Proposed one-dimensional warping element

In this paper, a one-dimensional warping element as shown in Fig. 4(b) is proposed to achieve modelling simplicity and computational efficiency. A thin-walled section can be represented by several two-node segments modelled by the proposed element. For comparison and verification purposes, a conventional plane warping area element with four nodes as shown in Fig. 4(a) is also developed here.

In the proposed element, the coordinates of the two nodes are denoted as (x_1, y_1) and (x_2, y_2). For thin-walled sections with non-uniform thickness, the thickness of the thin-walled segment at the first end is assumed as t_1 while the other end is t_2. As the linear form of $N_i(\xi,\eta)$ is adopted, the coordinates at any location in the one-dimensional warping element can be expressed as:

$$\begin{aligned}x&=\sum_{i=1}^{2}N_i(\xi)x_i+\sum_{i=1}^{2}H_i(\xi,\eta)t_i\sin\theta_i\\&=\frac{1-\xi}{2}x_1+\frac{1+\xi}{2}x_2-\frac{1-\xi}{2}\frac{\eta}{2}t_1\sin\theta_i-\frac{1+\xi}{2}\frac{\eta}{2}t_2\sin\theta_i\end{aligned} \tag{32}$$

$$\begin{aligned}y&=\sum_{i=1}^{2}N_i(\xi)y_i+\sum_{i=1}^{2}H_i(\xi,\eta)t_i\cos\theta_i\\&=\frac{1-\xi}{2}y_1+\frac{1+\xi}{2}y_2+\frac{1-\xi}{2}\frac{\eta}{2}t_1\cos\theta_i+\frac{1+\xi}{2}\frac{\eta}{2}t_2\cos\theta_i\end{aligned} \tag{33}$$

Note that $N_i(\xi)$ and $H_i(\xi,\eta)$ are two special forms of $N_i(\xi,\eta)$ for the proposed element, θ_i is angle of the i^{th} one-dimensional warping element.

Due to the change of the shear stress along the plate thickness is ignored, the warping displacement not related with the thickness term can be expressed as:

$$\phi=\sum_{i=1}^{2}N_i(\xi)\phi_i=\frac{1-\xi}{2}\phi_1+\frac{1+\xi}{2}\phi_2 \tag{34}$$

By differentiating Eq. (34), it gives:

$$\begin{cases}\dfrac{\partial\phi(x,y)}{\partial x}=\displaystyle\sum_{i=1}^{2}\frac{\partial N_i(\xi)}{\partial x}\phi_i=\frac{(x_1-x_2)}{l_i}\phi_1+\frac{(-x_1+x_2)}{l_i}\phi_2\\[2ex]\dfrac{\partial\phi(x,y)}{\partial y}=\displaystyle\sum_{i=1}^{2}\frac{\partial N_i(\xi)}{\partial y}\phi_i=\frac{(y_1-y_2)}{l_i}\phi_1+\frac{(-y_1+y_2)}{l_i}\phi_2\end{cases} \tag{35}$$

$$\sin\theta_i=\frac{y_2-y_1}{l_i},\quad\cos\theta_i=\frac{x_2-x_1}{l_i},\quad l_i=\sqrt{(x_2-x_1)^2+(y_2-y_1)^2} \tag{36}$$

2.4. Stiffness matrix and load vector

The energy method is adopted here to derive the element stiffness matrix. From Section 2.3, the basic unknowns of the section are the warping displacements at two ends, i.e. $\boldsymbol{\Delta}_{si}=\{\phi_1,\ \phi_2\}^T$. The total potential energy of the proposed element is expressed as:

$$\Pi_{si} = U_{si} - W_{si} \tag{37}$$

in which, U_{si} represents the strain energy and W_{si} is the work done by external loads. They are given by:

$$\begin{aligned} U_{si} &= \frac{1}{2}\int\left(\sigma_{zz}\varepsilon_{zz} + \tau_{zy}\gamma_{zy} + \tau_{zx}\gamma_{zx}\right)dV_i \\ &= \frac{1}{6}GL^3\int\left(C_x x + C_y y\right)^2 dA_i + \frac{1}{2}GL^3\int\left[\left(\frac{\partial\phi(x,y)}{\partial x} - C_1\right)^2 + \left(\frac{\partial\phi(x,y)}{\partial y} - C_2\right)^2\right]dA_i \end{aligned} \tag{38}$$

$$\begin{aligned} W_{si} &= V_{x,i}\bar{u}\big|_{z=L} + V_{y,i}\bar{v}\big|_{z=L} = V_{x,i}\left(\frac{1}{3}C_x L^3 + a_2 L + a_4\right) + V_{y,i}\left(\frac{1}{3}C_y L^3 + a_1 L + a_3\right) \\ &= V_x\frac{\int dA_i}{A}\left(\frac{1}{3}C_x L^3 + a_2 L + a_4\right) + V_y\frac{\int dA_i}{A}\left(\frac{1}{3}C_y L^3 + a_1 L + a_3\right) \end{aligned} \tag{39}$$

where, A_i is the area of the i^{th} element. The constants C_1 and C_2 are given by:

$$C_1 = \mu\left[\frac{1}{2}C_x\left(x^2 - y^2\right) + xyC_y\right] \tag{40}$$

$$C_2 = \mu\left[\frac{1}{2}C_y\left(y^2 - x^2\right) + xyC_x\right] \tag{41}$$

By using the principle of stationary potential energy, we have:

$$\frac{\partial\Pi_{si}}{\partial\phi_i} = 0,\ i = 1,\ 2 \tag{42}$$

Thus, the element stiffness matrix $\mathbf{k_e}$ can be obtained as:

$$\mathbf{k_e} = \left[k_{ij}\right] = \left[\frac{\partial^2\Pi_{si}}{\partial\phi_i\partial\phi_j}\right] = \left[G\int_{-1}^{1}\int_{-1}^{1}\left(\frac{\partial N_i}{\partial x}\frac{\partial N_j}{\partial x} + \frac{\partial N_i}{\partial y}\frac{\partial N_j}{\partial y}\right)\left|\mathbf{J_F}\right|d\xi d\eta\right] \tag{43}$$
$$\left(i = 1,2 \text{ and } j = 1,2\right)$$

where, $\mathbf{J_F}$ is the Jacobi matrix which is calculated as:

$$\begin{aligned} J_F &= \begin{bmatrix} \frac{\partial x}{\partial\xi} & \frac{\partial y}{\partial\xi} \\ \frac{\partial x}{\partial\eta} & \frac{\partial y}{\partial\eta} \end{bmatrix} \\ &= \begin{bmatrix} \frac{x_2}{2} - \frac{x_1}{2} + \eta t_1\frac{\sin\theta_i}{4} - \eta t_2\frac{\sin\theta_i}{4} & \frac{y_2}{2} - \frac{y_1}{2} - \eta t_1\frac{\cos\theta_i}{4} + \eta t_2\frac{\cos\theta_i}{4} \\ \left(-\frac{1-\xi}{4}t_1 - \frac{1+\xi}{4}t_2\right)\sin\theta_i & \left(\frac{1-\xi}{4}t_1 + \frac{1+\xi}{4}t_2\right)\cos\theta_i \end{bmatrix} \end{aligned} \tag{44}$$

Note that the well-known Gauss-Legendre 2×2 Integral scheme as listed in Table 1 has been adopted in this paper to determine the element stiffness matrix. It should be pointed out that the proposed warping element allowing for non-uniform thickness has not been reported in previous study.

Table 1
Gauss-Legendre 2×2 Integration Scheme

Integral variable	Integration point	Weight
ξ	+0.774596692	1.0
	-0.774596692	1.0
η	+0.774596692	1.0
	-0.774596692	1.0

Then, the load vector $\mathbf{f_{es}}$ of the element is expressed as:

$$\begin{aligned} \mathbf{f_{es}} &= \left\{f_{esi}\right\} = \left\{-\frac{\partial\Pi_{si}}{\partial\phi_i} + \sum_{i=1}^{2}k_{ij}\phi_j\right\} \\ &= \left\{G\int_{-1}^{1}\int_{-1}^{1}\left(C_1\frac{\partial N_i}{\partial x} + C_2\frac{\partial N_i}{\partial y}\right)\left|\mathbf{J_F}\right|d\xi d\eta + E\int_{-1}^{1}\int_{-1}^{1}N_i\left(xC_x + yC_y\right)\left|\mathbf{J_F}\right|d\xi d\eta\right\} \\ &\left(i = 1,2\right) \end{aligned} \tag{45}$$

The system stiffness matrix $\mathbf{K}$ can be formed by assembling all element stiffness $\mathbf{k_e}$ while the total load vector $\mathbf{F_s}$ is formed by all element load vector $\mathbf{f_{es}}$. Finally, the equilibrium equations of the section can be written as:

$$\mathbf{K\Delta_s} = \mathbf{F_s} \tag{46}$$

in which, $\mathbf{\Delta_s} = \left\{\phi_{s1},\ \phi_{s2},\ ...,\ \phi_{sm}\right\}^T$ is the warping displacements of the section represented by several proposed elements, and subscript m is the number of nodes of the section. Thus, the conventional linear solvers can be used to solve the system of equations in Eq. (46). After that, the shear correction factors can be calculated by Eqs. (24) and (26) using the warping displacements $\mathbf{\Delta_s}$.

For isotropic material, it has $G=E/[2(1+\mu)]$. From Eqs. (43) and (45), the material properties such as Young's modulus E and shear modulus G can be eliminated in Eq. (46) when only one isotropic material is adopted in the section concerned. Thus, the warping displacements $\mathbf{\Delta_s}$ will be affected by Poisson's ratio only in regard to material properties.

3. Modelling of built-up thin-walled sections

Nowadays, the built-up sections composed of several single sections such as angles and channels connected with fasteners such as screws, bolts, and clinches have been extensively used for economic design and fast construction. It is clear that the section properties such as A, I_{xx}, I_{yy}, and I_{xy} of the built-up section will be not less than the summation of the individual sections. Normally, the second moment of inertia I_{xx} and I_{yy} of the built-up section will be significantly increased due to composite action. Note that there is few research on the shear correction factors of built-up sections. Because the numerical method proposed in Section 0 is only for the cross sections in a continuous domain, an additional procedure is introduced in this Section so that the built-up sections with several discontinuous domains can be converted to a single continuous one.

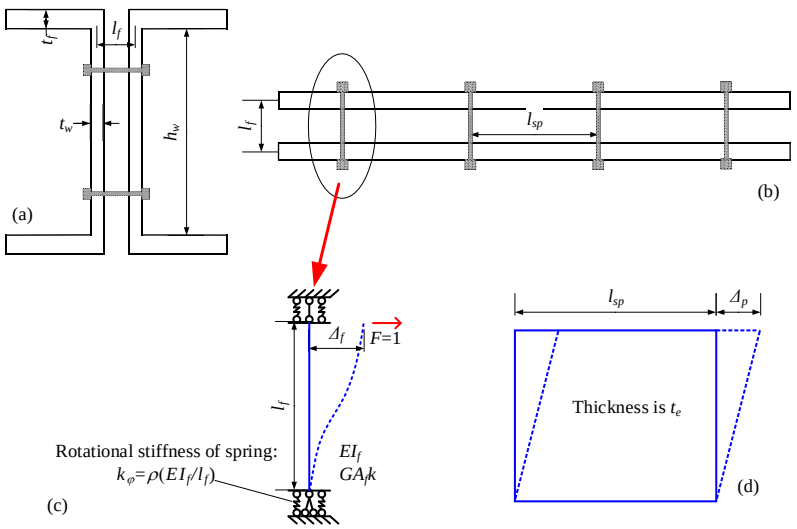

Fig. 5 Model for calculation of equivalent thickness of built-up section: (a) Section view; (b) Plan view; (c) Modeling of the fastener; and (d) Equivalent plate for the fastener

In this paper, an analytical method is proposed to convert the discrete fasteners to plates connecting the individual parts, leading that a built-up section can be treated as a single section with continuous domain. By using this method, an equivalent plate thickness should be determined for the plate representing the associated fastener. A double-channel section as shown in Fig. 5(a) and (b). is adopted here to demonstrate the proposed analytical method. The discrete fastener is treated as a beam with two ends constrained by springs as shown in Fig. 5(c). The rotational stiffness of the spring is expressed as:

$$k_\varphi = \rho \frac{EI_f}{l_f} \tag{47}$$

where, ρ is a rigidity coefficient; E is Young's Modulus; I_f is the second moment of inertia of the fastener; l_f is the length. In Fig. 5, A_f is the sectional-area of the fastener; l_{sp} is the longitudinal spacing between the adjacent fasteners, t_f is the thickness of the flange, t_w is the thickness of the connected web, and h_w is the height of the web.

Applying a virtual unit force F at one end of the fastener as indicated in Fig. 5(c), the energy of the fastener can be written as:

$$\begin{aligned} U_f &= \frac{l_f^3}{24EI} + \frac{l_f}{2GA_f k_f} + 2\times\frac{1}{2}\times\frac{l_f}{2}\times\frac{l_f}{2k_\varphi} \\ &= \frac{l_f^3}{24EI_f} + \frac{l_f}{2GA_f k_f} + \frac{l_f^3}{4\rho EI_f} \end{aligned} \tag{48}$$

where, k_f is the shear correction factors of the solid section of the fastener. For circular section, k_f is taken as 0.9.

The shear strain of the equivalent steel plate is expressed as:

$$\gamma = \frac{F}{Gl_{sp}t_e} \tag{49}$$

where, t_e is the thickness of the equivalent plate to be determined. The shear strain energy of the plate can be written as:

$$U_p = \frac{1}{2}G\gamma^2 l_f l_{sp} t_e = \frac{1}{2}G\left(\frac{F}{Gl_{sp}t_e}\right)^2 l_f l_{sp} t_e = \frac{l_f}{2Gl_{sp}t_e} \tag{50}$$

According to the principle of conservation of energy, U_p should be equal to U_f. Thus, the equivalent plate thickness t_e can be derived as:

$$t_e = \frac{1}{l_{sp}\left[\dfrac{l_f^2}{24(1+\mu)I_f} + \dfrac{1}{A_f k_f} + \dfrac{l_f^2}{4\rho(1+\mu)I_f}\right]} \tag{51}$$

For fully fixed end condition, i.e. $\rho\to\infty$, the upper bound of t_e can be obtained from Eq. (47):

$$t_{e,\max} = \frac{1}{l_{sp}\left[\dfrac{l_f^2}{24(1+\mu)I_f} + \dfrac{1}{A_f k_f}\right]} \tag{52}$$

As the stiffness of the constraint spring does not equal to zero, a lower bound of t_e can also be derived. As shown in Fig. 5, the fastener is subjected to the constraints provided by the web of the channel. It is noted that the influences of the flange of the channel to the constraint spring are ignored. Thus, a simple model as shown in Fig. 6 is proposed for representation of the lath cut from the web. The stiffness of the lath per unit width can be written as:

$$D_l = \frac{Et_w^3}{12(1-\mu^2)} \tag{53}$$

Therefore, the corresponding rigidity coefficient ρ of the spring is expressed as:

$$\begin{aligned} \rho &= k_\varphi \frac{l_f}{EI_f} = \frac{2M_1}{\theta'}\frac{l_f}{EI_f} = \frac{4D_l\left(\dfrac{h_w}{N_r}\right)}{l_{sp}}\frac{l_f}{EI_f} \\ &= \frac{Et_w^3}{12(1-\mu^2)}\frac{4}{l_{sp}}\frac{h_w}{N_r}\frac{l_f}{EI_f} = \frac{t_w^3 h_w l_f}{3(1-\mu^2)l_{sp}N_r I_f} \end{aligned} \tag{54}$$

where, N_r is the number of fasteners at a section, h_w/N_r represents the width of the lath cut from the web for supporting one fastener. From Eq. (50), the lower bound of t_e can be obtained as:

$$t_{e,\min} = \frac{1}{l_{sp}\left[\dfrac{l_f^2}{24(1+\mu)I_f} + \dfrac{1}{A_f k_f} + \dfrac{3(1-\mu)l_f l_{sp} N_r}{4t_w^3 h_w}\right]} \tag{55}$$

As t_e is relatively small and mainly for maintaining the domain continuity of the cross section, its contribution on section properties such as A, I_{xx}, I_{yy}, and I_{xy} is ignored here. However, it may influence the shear flow and then shear correction factors of the built-up section. The upper bound $t_{e,\max}$ provides the maximum shear correction factors, while the lower bound $t_{e,\min}$ gives the minimum shear correction factors. The verification and discussion of Eqs. (48) to (55) will be illustrated in a worked example in Section 5.6.

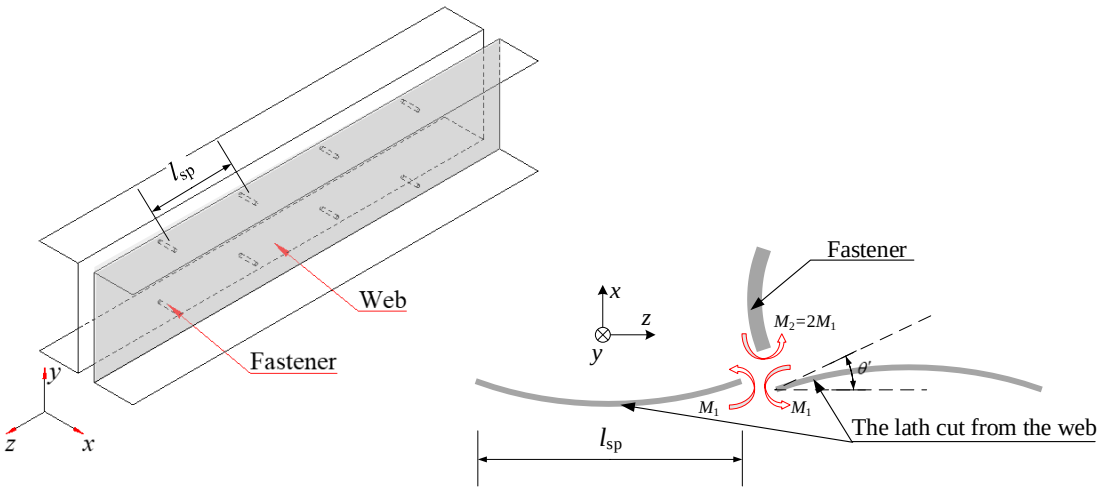

Fig. 6 The lath cut from the web and the constraint actions

4. Numerical implementation

From Eqs. (24) and (26), the basic section properties such as A, I_{xx}, I_{yy}, and I_{xy} should be calculated before determining the shear correction factors. These basic section properties can be easily obtained by summing A_i, $I_{i,xx}$, $I_{i,yy}$, and $I_{i,xy}$

of all elements. The subscript i means the contributions of the i^{th} one-dimensional warping element to the section properties. More specifically, they can be computed as:

$$A_i = \int l_i dt = \frac{l_i (t_{i1} + t_{i2})}{2} \tag{56}$$

$$I_{i,xx} = \int y^2 dA_i = \frac{1}{3} A_i \left(y_{i1}^{\ 2} + y_{i1} y_{i2} + y_{i2}^{\ 2} \right) + \frac{1}{48} A_i \left(t_{i1} + t_{i2} \right)^2 \cos \theta_i^2 \tag{57}$$

$$I_{i,yy} = \int x^2 dA_i = \frac{1}{3} A_i \left(x_{i1}^{\ 2} + x_{i1} x_{i2} + x_{i2}^{\ 2} \right) + \frac{1}{48} A_i \left(t_{i1} + t_{i2} \right)^2 \sin \theta_i^2 \tag{58}$$

$$I_{i,xy} = \int xy dA_i = \frac{1}{6} A_i \left(2x_{i1} y_{i1} + x_{i1} y_{i2} + x_{i2} y_{i1} + 2x_{i2} y_{i2} \right) - \frac{1}{48} A_i \left(t_{i1} + t_{i2} \right)^2 \sin \theta_i \cos \theta_i \tag{59}$$

where, (x_{i1}, y_{i1}) and (x_{i2}, y_{i2}) are the coordinates of the element two ends by referring to the centroid.

Fig. 7 shows the flowchart of the procedure to find the shear center and the shear correction factors based on the proposed method introduced in Section 2 and 3. The method is implemented in the program NIDA (2021). The verification examples in the next Section are then prepared by using the program NIDA.

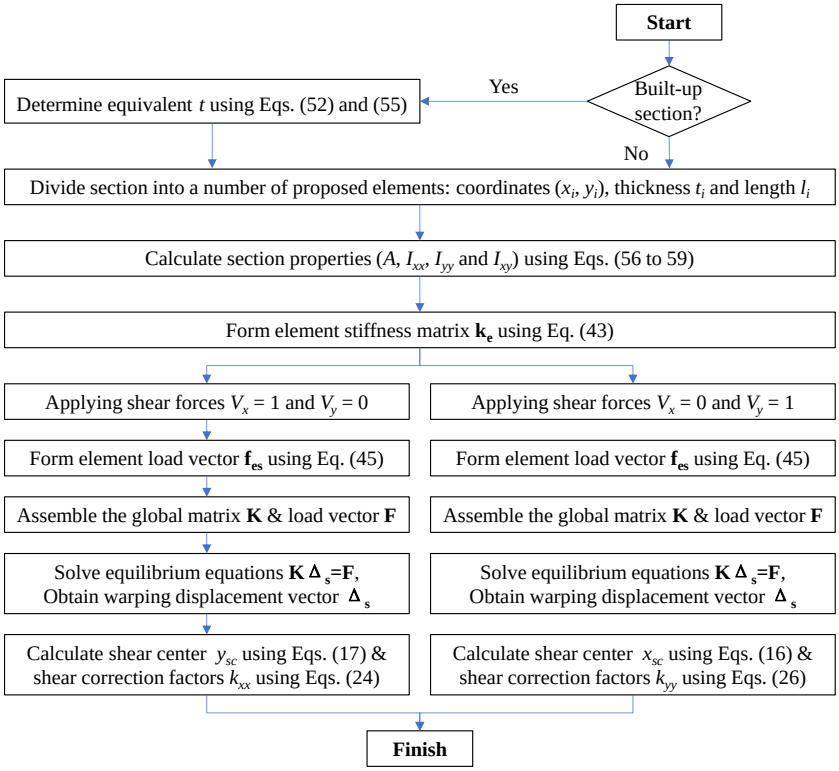

Fig. 7 Flowchart for calculation of shear correction factors

5. Verification examples

To validate the accuracy and the efficiency of the proposed method, six examples are investigated here with consideration of single sections in regular shape, open and closed thin-walled sections, complex sections with non-uniform thickness, built-up sections. The results predicted by the proposed element will be verified against the analytical solution, conventional warping area element method and the section analysis in commercial software ANSYS based on fiber section approach. Further, an example is provided at the end to demonstrate the influence of shear correction factors and the application of the proposed method in conjunction with the Direct Analysis Method.

5.1. Example 1 – Rectangular and trapezoidal sections

The rectangular sections are the simplest and widely used cross sections, as shown in Fig. 8. The analytical solution for the shear correction factors of rectangular sections with consideration of Poisson effect has been well-developed by [21]Herrmann (1965). To verify the performance of the proposed element in sections with non-uniform thickness, the trapezoidal sections are also studied here.

In this example, the rectangular sections with different height-to-width (h/b) ratios equal to 10, 5, 2, 1, 0.5 and 0.25 are studied. The rectangular section is divided into a number of the proposed 1D warping elements along the height. To study the mesh sensitivity, the Poisson's ratio is assumed as 0 and the results are shown in Fig. 9. It is observed that the shear correction factors vary with the increase of the number of elements. Clearly, 20 elements per segment can lead to convergent results for the shear correction factors. Also, the rectangular sections with different h/b ratios show the same trend. Thus, it is recommended at least 20 elements should be used for each segment of the thin-wall sections to get an accurate result.

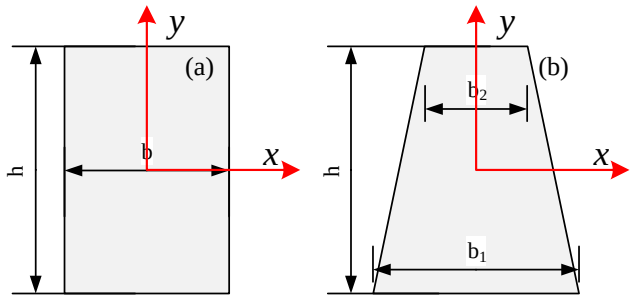

Fig. 8 Simple plate sections: (a) Rectangular; and (b) Trapezoidal

Further, the influence of Poisson effect is studied to investigate the accuracy of the present method. An analytical formula including Poisson's ratio proposed by Leonard[23] in 1965 is adopted here for the validation. The shear correction factor along one axis of the rectangular section can be calculated by:

$$k = \frac{10(1+\mu)}{12+11\mu} \tag{60}$$

To study the Poisson effect on shear correct factors, different Poisson's ratios (i.e. 0, 0.2, 0.25, 0.3, 0.5) in related commonly used materials in building and bridge structures are assumed for the above rectangular sections. The shear correction factors predicted by the proposed method are listed in Table 2 against the results obtained by the analytical solution from Eq. (60) and the element Plane82 in software ANSYS. It can be seen that the results from present study agree well with the analytical solution. As the change of Poisson's ratio does not affect the result from ANSYS, it can be concluded that the section analysis method in ANSYS cannot consider the Poisson effect.

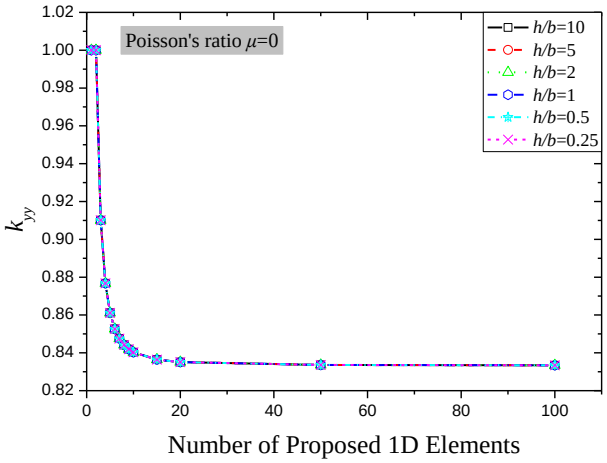

Fig. 9 Mesh sensitivity study for rectangular section

Table 2
Shear correction factors of rectangular sections

Poisson's ratio	① Analytical	② ANSYS	③ Present	Diff (③-①)/① (%)	Diff (③-②)/② (%)
0	0.8333	0.8333	0.8334	0.012	0.012
0.20	0.8451	0.8333	0.8451	0	1.416
0.25	0.8475	0.8333	0.8475	0	1.704
0.30	0.8497	0.8333	0.8497	0	1.968
0.50	0.8571	0.8333	0.8572	0.012	2.868

To study the sections with non-uniform thickness, the trapezoidal sections as shown in Fig. 7(b) with h/b_1 equal to 1, 2, 3 and 4 are also investigated. For simplicity, the h/b_2 ratios for different h/b_1 ratios are kept as 10. The results from present study are given in Table 3 against the results from traditional warping area element method and ANSYS. It can be seen that the proposed method can provide accurate shear correction factors when $h/b_1 \geq 2$.

Table 3
Shear correction factors of trapezoidal sections

h/b_1	①Warping area element	② ANSYS	③Present	Diff (③-①)/① (%)	Diff (③-②)/② (%)
1	0.7849	0.7818	0.8361	6.523	6.946
2	0.8313	0.8197	0.8425	1.347	2.782
3	0.8411	0.8270	0.8437	0.309	2.019
4	0.8441	0.8298	0.8458	0.201	1.928

5.2. Example 2 – Typical open sections

This example investigates the shear center and shear correction factors of several commonly used steel open sections such as unequal I-section, Tee, angle, channel and z sections by the proposed numerical method. To study the influence of plate thickness, the section classification according to Hong Kong Steel Code (CoPSC 2011) as shown in Table 4 is adopted. Poisson's ratio is taken as 0 and 0.3 for all sections. The value of 0.3 represents steel material. For comparison purpose, the results from ANSYS using Plane82 element are also presented. The shear correction factors and shear centers obtained from the present method are listed in Table 5 to Table 9 against the results from ANSYS.

It can be concluded that as the plate thickness decreases, the difference tends to be smaller. It may be caused not only by the assumption of ignoring the nonuniform shear stress along the plate thickness but also the overlapped effect (Fig. 11) by using the one-dimensional warping element. The overall agreement between the proposed method and ANSYS can be observed within 10% difference which meets the requirements of engineering. Also, since ANSYS cannot consider the Poisson effect, the results predicted by the presented method with Poisson's ratio = 0 agree well with ANSYS, especially for Tee, Angle and Zee sections.

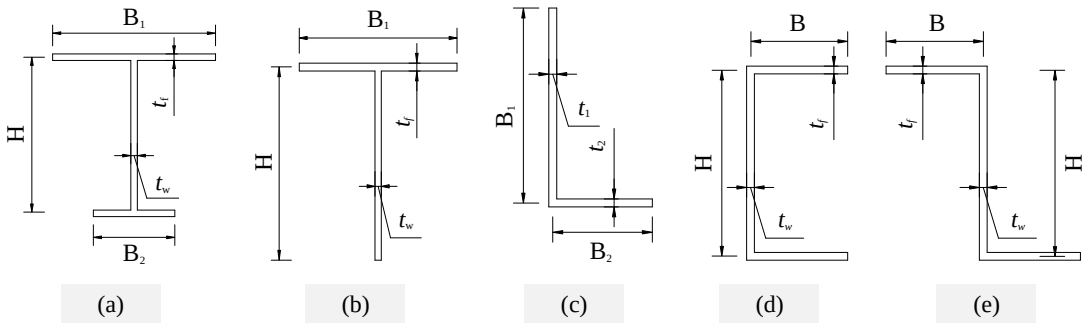

Fig. 10 Open sections: (a) Unequal I; (b) Tee; (c) Angle; (d) Channel; and (e) Z-shape

Table 4
The *b/t* ratios for the section classification in CoPSC 2011

Ratio	Class 1 Plastic	Class 2 Compact	Class 3 Semi-compact	Class 4 Slender
b/t	8	9	13	>13

Table 5
Shear center and shear correction factors of Unequal I-section

$B_1 \times B_2 \times H \times t_f \times t_w$(m)	Parameter	①ANSYS (μ=0)	②Present (μ=0)	③Present (μ=0.3)	Diff (②-①)/① (%)	Diff (③-①)/① (%)
Class 1: 0.4×0.2×0.4×0.05×0.05	y_{sc} (m)	0.1100	0.1140	0.1208	3.611	9.818
	k_{xx}	0.4577	0.4205	0.4205	-8.118	-8.128
	k_{yy}	0.4098	0.3660	0.3667	-10.691	-10.517

Class 3: 0.4×0.2×0.4×0.02×0.02	y_{sc} (m)	0.1142	0.1153	0.1222	0.963	7.005
	k_{xx}	0.4258	0.4109	0.4110	-3.495	-3.476
	k_{yy}	0.3792	0.3632	0.3638	-4.210	-4.061
Class 4: 0.4×0.2×0.4×0.01×0.01	y_{sc} (m)	0.1150	0.1155	0.1224	0.427	6.435
	k_{xx}	0.4170	0.4096	0.4097	-1.786	-1.751
	k_{yy}	0.3706	0.3628	0.3634	-2.093	-1.943

Table 6
Shear center and shear correction factors of Tee section

B×H×t_f×t_w(m)	Parameter	①ANSYS (μ=0)	②Present (μ=0)	③Present (μ=0.3)	Diff (②-①)/① (%)	Diff (③-①)/① (%)
Class 1: 0.4×0.4×0.05×0.05	y_{sc} (m)	0.0975	0.0985	0.0886	0.986	-9.128
	k_{xx}	0.459	0.4298	0.4178	-6.362	-8.976
	k_{yy}	0.4355	0.3980	0.3943	-8.606	-9.460
Class 3: 0.4×0.4×0.02×0.02	y_{sc} (m)	0.0975	0.0998	0.0886	2.308	-9.128
	k_{xx}	0.459	0.4188	0.4178	-8.768	-8.976
	k_{yy}	0.4355	0.3939	0.3943	-9.559	-9.460
Class 4: 0.4×0.4×0.01×0.01	y_{sc} (m)	0.1004	0.0999	0.0899	-0.461	-10.458
	k_{xx}	0.423	0.4181	0.4055	-1.169	-4.137
	k_{yy}	0.4002	0.3942	0.3895	-1.490	-2.674

Table 7
Shear center and shear correction factors of Angle section

B_1×B_2×t_1×t_2(m)	Parameter	①ANSYS (μ=0)	②Present (μ=0)	③Present (μ=0.3)	Diff (②-①)/① (%)	Diff (③-①)/① (%)
Class 1: 0.25×0.25×0.05×0.05	x_{sc} (m)	-0.0591	-0.0619	-0.0624	4.706	5.584
	y_{sc} (m)	-0.0591	-0.0619	-0.0624	4.706	5.584
	k_{xx}	0.4684	0.4397	0.4349	-6.124	-7.152
	k_{yy}	0.4684	0.4397	0.4349	-6.124	-7.152
Class 3: 0.25×0.25×0.02×0.02	x_{sc} (m)	-0.062	-0.0624	-0.0629	0.645	1.452
	y_{sc} (m)	-0.062	-0.0624	-0.0629	0.645	1.452
	k_{xx}	0.4294	0.4222	0.4174	-1.682	-2.795
	k_{yy}	0.4294	0.4222	0.4174	-1.682	-2.795
Class 4: 0.25×0.25×0.01×0.01	x_{sc} (m)	-0.0624	-0.0625	-0.0629	0.120	0.801
	y_{sc} (m)	-0.0624	-0.0625	-0.0629	0.120	0.801
	k_{xx}	0.4217	0.4197	0.4149	-0.482	-1.613
	k_{yy}	0.4217	0.4197	0.4149	-0.482	-1.613

Table 8
Shear center and shear correction factors of Channel section

B×H×t_f×t_w(m)	Parameter	①ANSYS (μ=0)	②Present (μ=0)	③Present (μ=0.3)	Diff (②-①)/① (%)	Diff (③-①)/① (%)
Class 1: 0.3×0.5×0.05×0.05	x_{sc} (m)	-0.1947	-0.1987	-0.2025	2.050	4.006
	k_{xx}	0.3974	0.3668	0.3962	-7.710	-0.302
	k_{yy}	0.3837	0.3642	0.3674	-5.070	-4.248
Class 3: 0.3×0.5×0.03×0.03	x_{sc} (m)	-0.1976	-0.1990	-0.2028	0.720	2.632
	k_{xx}	0.3789	0.3622	0.3914	-4.402	3.299
	k_{yy}	0.3738	0.3630	0.3661	-2.881	-2.060
Class 4: 0.3×0.5×0.01×0.01	x_{sc} (m)	-0.199	-0.1992	-0.203	0.095	2.010
	k_{xx}	0.365	0.3600	0.389	-1.380	6.575
	k_{yy}	0.3658	0.3624	0.3655	-0.922	-0.082

Table 9
Shear correction factors of Z-shape section

B×H×t_f×t_w(m)	Parameter	①ANSYS (μ=0)	②Present (μ=0)	③Present (μ=0.3)	Diff (②-①)/① (%)	Diff (③-①)/① (%)
Class 1: 0.3×0.5×0.06×0.06	k_{xx}	0.4862	0.4567	0.5077	-6.060	4.422
	k_{yy}	0.4392	0.4221	0.4019	-3.897	-8.493

Class 3: 0.3×0.5×0.03×0.03	k_{xx}	0.4649	0.4485	0.4992	-3.535	7.378
	k_{yy}	0.4281	0.4185	0.3985	-2.233	-6.914
Class 4: 0.3×0.5×0.015×0.015	k_{xx}	0.4503	0.4485	0.4949	-0.407	9.905
	k_{yy}	0.4206	0.4185	0.3969	-0.490	-5.635

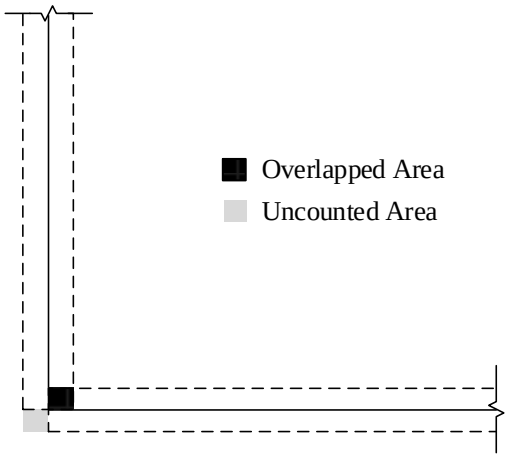

Fig. 11 The overlapped effect induced from the one-dimensional element modelling

5.3. Example 3 – Typical closed sections

This example investigates the shear center and shear correction factors of several commonly used steel close sections such as rectangular, circular and elliptic hollow sections as illustrated in Fig. 12. Poisson's ratio is taken as 0 and 0.3 for all sections. The value of 0.3 represents steel material. Three different plate thicknesses are studied for each section shape. For circular and elliptic hollow sections, several straight elements are used instead of curved element. For comparison purpose, the results from ANSYS using Plane82 element are also presented. The shear correction factors and shear centers obtained from the present method are listed in Table 10 to Table 12 against the results from ANSYS.

It can be concluded that as the plate thickness decreases, the difference tends to be smaller. It may be caused not only by the assumption of ignoring the nonuniform shear stress along the plate thickness but also the overlapped effect by using the one-dimensional warping element. The overall agreement between the proposed method by assuming Poisson's ratio as 0 and ANSYS can be observed within 5% difference which meets the engineering requirements. It also indicates that a relatively large difference may occur if ignoring the Poisson's ratio. Thus, ANSYS may not provide accurate shear correction factors for some cross sections.

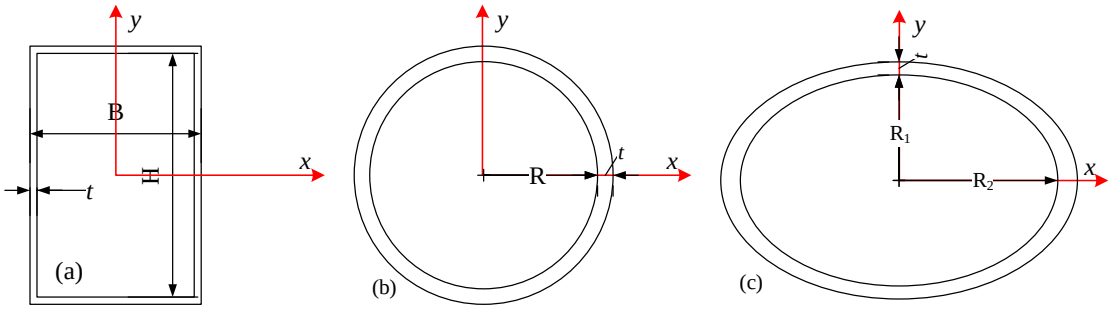

Fig. 12 Hollow sections: (a) Rectangular; (b) Circular; and (c) Elliptic

Table 10
Shear correction factors of rectangular hollow sections

B×H×t(m)	Parameter	①ANSYS (μ=0)	②Present (μ=0)	③Present (μ=0.3)	Diff (②-①)/①(%)	Diff (③-①)/①(%)
0.8×0.4×0.02	k_{xx}	0.2289	0.2235	0.2416	-2.377	5.548
	k_{yy}	0.6158	0.6107	0.6278	-0.834	1.949
0.8×0.4×0.008	k_{xx}	0.2255	0.2232	0.2413	-1.024	7.007
	k_{yy}	0.6127	0.6105	0.6277	-0.353	2.448
0.8×0.4×0.005	k_{xx}	0.2245	0.2232	0.2412	-0.597	7.439
	k_{yy}	0.6118	0.6105	0.6277	-0.209	2.599

Table 11
Shear correction factors of circular hollow sections

R×t (m)	Parameter	①ANSYS (μ=0)	②Present (μ=0)	③Present (μ=0.3)	Diff (②-①)/①(%)	Diff (③-①)/①(%)
0.2×0.02	k_{xx}	0.5023	0.5009	0.5316	-0.274	5.833
	k_{yy}	0.5023	0.5009	0.5316	-0.274	5.833
0.2×0.008	k_{xx}	0.5004	0.5001	0.5308	-0.052	6.075
	k_{yy}	0.5004	0.5001	0.5308	-0.052	6.075
0.2×0.002	k_{xx}	0.5	0.5000	0.5306	0.002	6.120
	k_{yy}	0.5	0.5000	0.5306	0.002	6.120

Table 12
Shear correction factors of elliptic hollow sections

$R_1 \times R_2 \times t$ (m)	Parameter	①ANSYS (μ=0)	②Present (μ=0)	③Present (μ=0.3)	Diff (②-①)/①(%)	Diff (③-①)/①(%)
0.4×0.2×0.02	k_{xx}	0.7131	0.7107	0.7359	-0.331	3.197
	k_{yy}	0.249	0.2476	0.2721	-0.559	9.277
0.4×0.2×0.008	k_{xx}	0.709	0.7101	0.7353	0.159	3.709
	k_{yy}	0.2458	0.2458	0.2701	0.020	9.886
0.4×0.2×0.002	k_{xx}	0.7187	0.7100	0.7351	-1.208	2.282
	k_{yy}	0.2335	0.2455	0.2698	5.154	15.546

5.4. Example 4 – Large stiffened box girder section

This example illustrates the accuracy of the presented one-dimensional warping element method in calculating the shear correction factors of large stiffened thin-walled steel box sections which is widely used in the bridge structures. Compared with the overall dimensions of the section, the plate thickness is much small. It causes high-density mesh when using the traditional warping area element method for this kind of sections.

In this paper, a stiffened steel box section as shown in Fig. 13 is studied, which is extensively adopted as the main girder in the large-span cable-supported bridges. Generally, many stiffeners are required to prevent local plate buckling and to achieve an economic design without use of thick plate. Two types of stiffeners are used in this box section, i.e. the closed U-ribs for flanges and flat-bar ribs for webs. Poisson's ratio is taken as 0 and 0.3. The shear center and shear correction factors from present study are shown in Table 13 against the results from traditional warping area element method allowing Poisson effect while ANSYS cannot consider this effect. It can be seen that the results from present study agree well with the warping area element method.

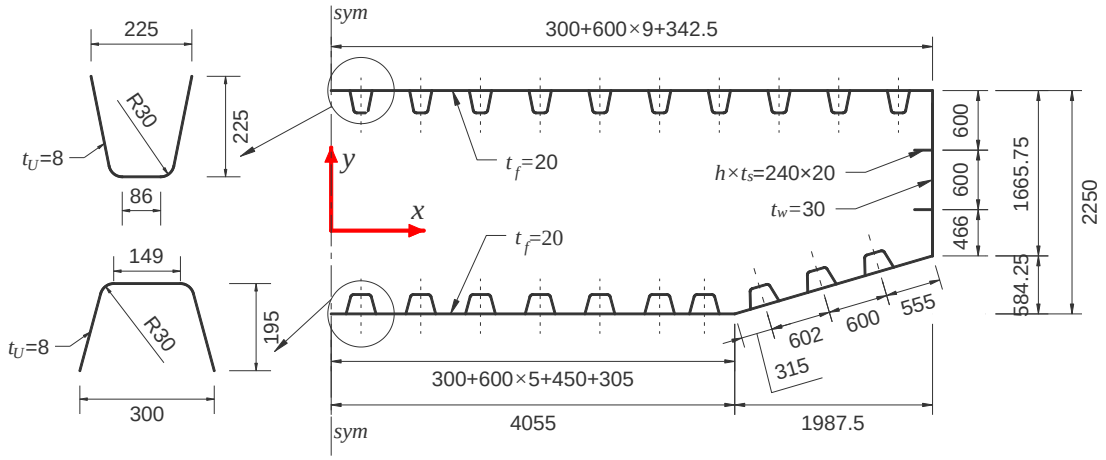

Fig. 13 Layout and dimensions of stiffened steel box section (unit: mm)

Table 13
Shear center and shear correction factors of stiffened steel box section

Parameter	①ANSYS (μ=0)	②Present (μ=0)	Diff (②-①)/①(%)	③Warping area element (μ=0.3)	④Present (μ=0.3)	Diff (④-③)/③(%)
y_{sc} (mm)	-212.9627	-213.9041	0.442	-213.6453	-227.0532	6.276
k_{xx}	0.5971	0.5966	-0.089	0.6079	0.6065	-0.230
k_{yy}	0.0463	0.0463	0	0.0526	0.0523	-0.570

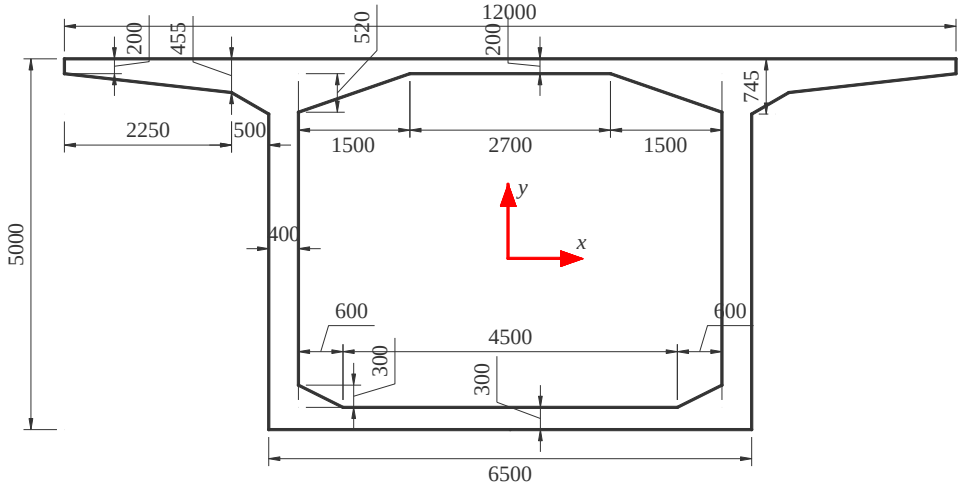

Fig. 14 Dimension of bridge box section

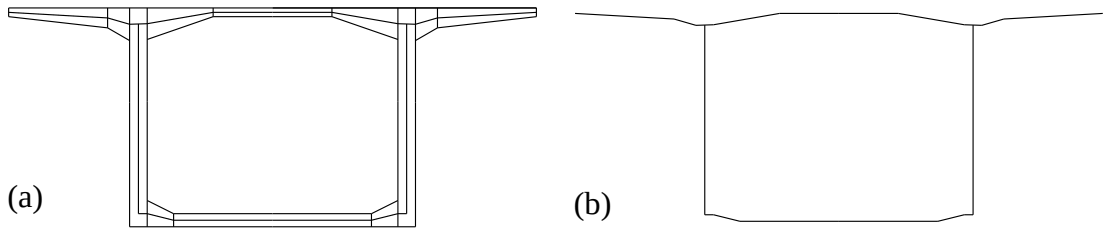

Fig. 15 Modelling of bridge box section: (a) Distribution of taper thicknesses; and (b) 1D warping elements

Table 14
Shear center and shear correction factors of bridge box section

Parameter	①ANSYS (μ=0)	②Present (μ=0)	Diff (②-①)/①(%)	③Warping area element (μ=0.2)	④Present (μ=0.2)	Diff (④-③)/③(%)
y_{sc} (mm)	-625.0437	-662.6341	6.014	-648.2929	-622.3806	-3.997
k_{xx}	0.4297	0.4081	-5.046	0.4368	0.4141	-5.191
k_{yy}	0.3545	0.3209	-9.470	0.3602	0.3250	-9.773

5.5. Example 5 – Large box section with non-uniform thickness

This example is to validate the performance of the proposed method in the calculation of the shear correction factors of the sections with non-uniform thickness. A box section with taper portions at the corners is investigated using the proposed one-dimensional warping element method. As seen in Fig. 15, this kind of box sections are widely used in rail and highway bridges. For economic design with less material as well as reduction of self-weight, the section with taper segments is most welcome. Poisson's ratio is assumed as 0.2 in this example. The modelling for the non-uniform thickness distribution is shown in Fig. 15(a) while the 1D element model by the proposed method is shown in Fig. 15(b). The shear center and shear correction factors from present study are shown in Table 14 against the results from traditional warping area element method allowing for Poisson effect.

From Table 14, it can be observed that the difference for y_{sc} and k_{xx} are less than 5% while k_{yy} is around 10%. The difference may come from the ignorance of the nonuniform shear stress along the plate thickness and the overlapped areas in the intersection points. This example demonstrates the simplicity in modelling and computational efficiency of the proposed method for practical engineering application.

5.6. Example 6 – Built-up double-channel sections

This example shows the application of the presented one-dimensional warping element method in calculating the shear correction factors of thin-walled built-up sections. A double-channel section with configuration listed in Table 15 is investigated. The influence of the distance l_f between two channels and the spacing l_{sp} of fasteners along the longitudinal axis is studied.

Table 15
Parametric study of double-channel section

Section profile	Parameter	Range
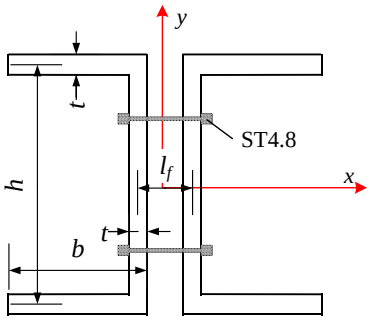	b (mm)	50
	h (mm)	75
	t (mm)	1
	l_f (mm)	2, 5, 10
	l_{sp} (mm)	100, 150, 200
	L/l_{sp}	2 to 11

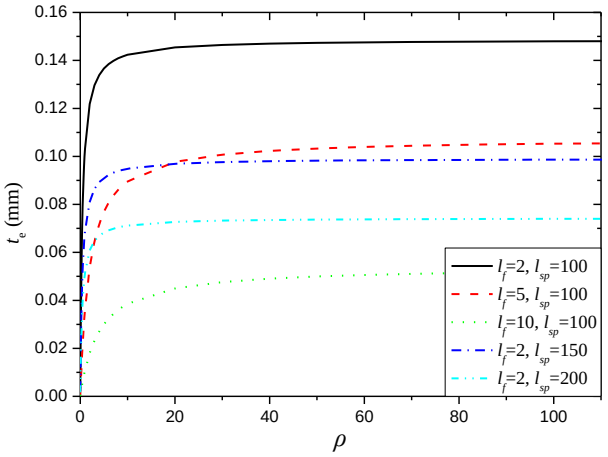

Fig. 16 Influence of rigidity coefficient ρ on the equivalent thickness t_e

The influence on the equivalent plate thickness t_e as given in Eq. (51) due to fixing condition (i.e. rigidity coefficient ρ), distance l_f and spacing l_{sp} is shown in Fig. 16. It can be seen that the equivalent plate t_e decreases with increase of l_f and l_{sp}. It is also noted when the sufficient constraint ($\rho \geq 20$) is provided, t_e approaches $t_{e,max}$ in Eq. (52). In other words, the equivalent plate thickness t_e is significantly affected by the rigidity coefficient ρ ranging from 0 to 20.

As there are few research carried out on the determination of the shear correction factors of built-up sections, no direct results are available for validation of the proposed method. Thus, a finite solid element model for a cantilever beam is employed here for comparison.

Assuming that the shear correction factor k for a general cross section is known, the deflection at the free end of a cantilever beam can be calculated by (Timoshenko 1949):

$$\delta=\delta_b+\delta_s=\frac{PL^3}{3EI}+\frac{PL}{GAk} \tag{61}$$

where, δ_b is due to the bending action; δ_s is due to shear effect.

As shown in Fig. 17(a), a cantilever beam using the built-up double-channel section is studied using the 4-node element SOLID45 in ANSYS. No contact behavior between the surfaces of the adjacent webs of the channels is considered. Only linear elastic analysis is performed. The tip deflection from ANSYS is denoted as δ_{FEM}.

To study the contribution of shear deformation on the total deflection, an indicator β is introduced as below:

$$\beta=\frac{\delta_{FEM}-\delta_b}{\delta_b}=\left(\delta_{FEM}-\frac{PL^3}{3EI}\right)\Big/\frac{PL^3}{3EI} \tag{62}$$

Specifically, δ_{FEM} is the deflection δ_x and δ_y along the x-axis and y-axis respectively as shown in Fig. 17 (b) and (c). The results of β against L/l_{sp} ratio in related to δ_x and δ_y are shown in Fig. 18 and Fig. 19 respectively accounting for different distances l_f and spacings l_{sp}. It is clear that the shear deformation will significantly affect the total deflection of the cantilever beam for $L/l_{sp}<5$ and therefore the shear correction factors should be carefully determined for further global structural analysis, especially in the direct analysis in which the structural responses should be well captured so that the effective length method for stability design is not needed.

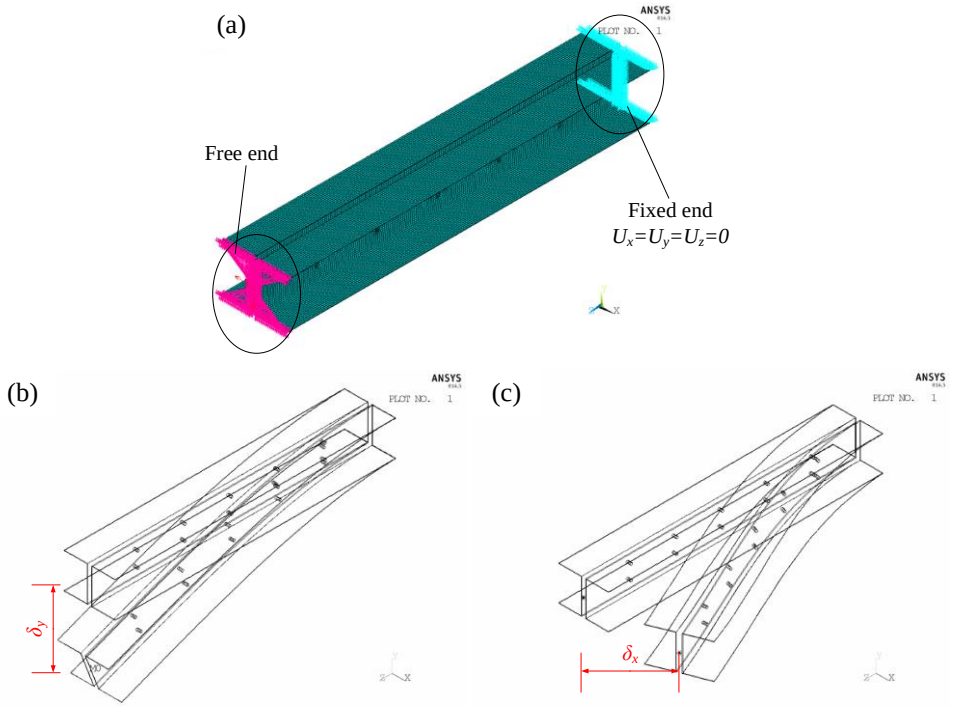

Fig. 17 Finite solid element model for cantilever beam with double-channel section: (a) boundary conditions; (b) vertical deformed shape; and (c) horizontal deformed shape

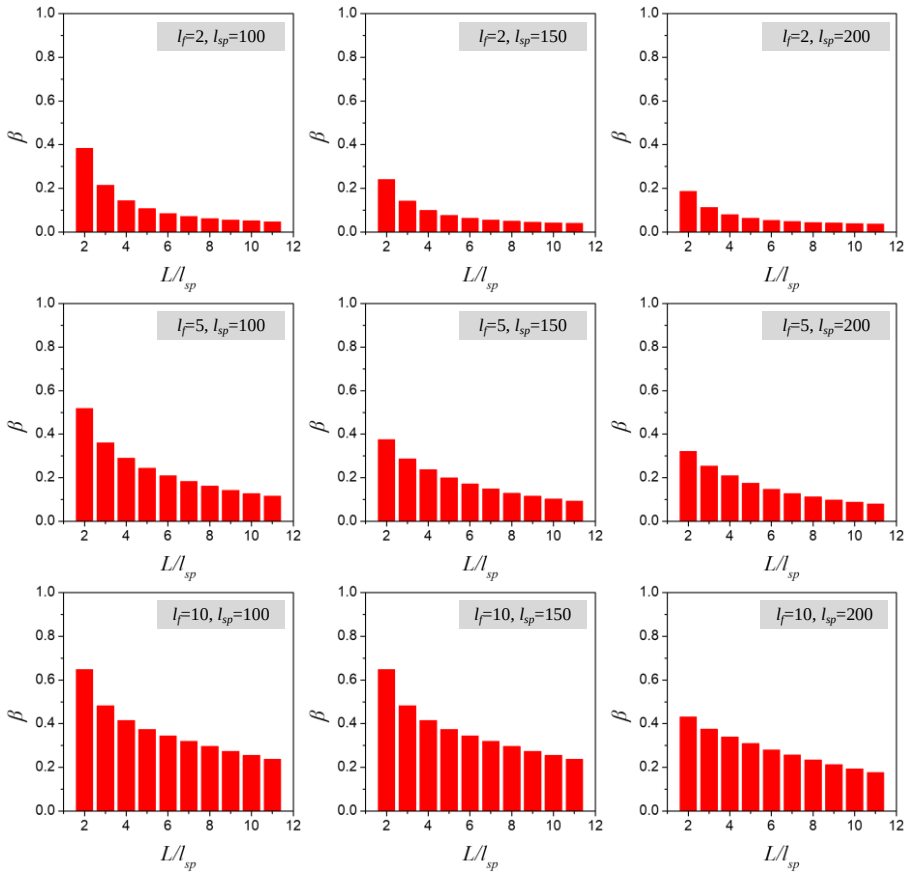

Fig. 18 Change of β in related to δ_x for the cantilever beam

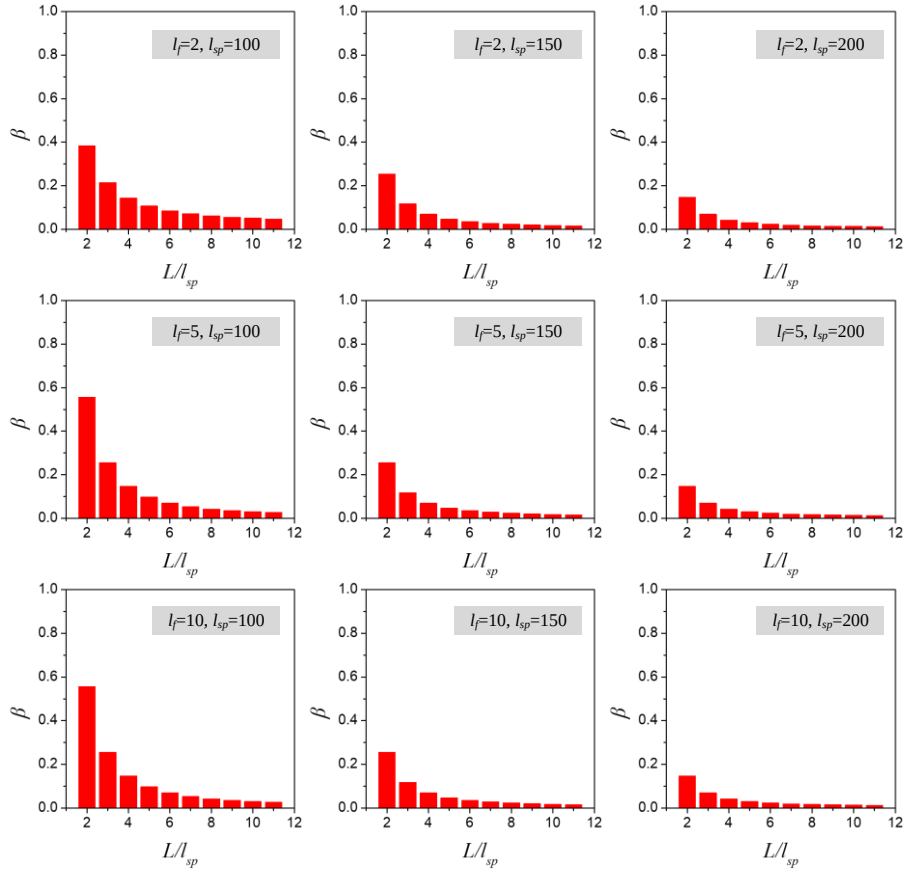

Fig. 19 Change of β in related to δ_y for the cantilever beam

The shear correction factors k_{xx} and k_{yy} of the double-channel sections are calculated by the proposed method and listed in Table 16 and Table 17 respectively. Several fixing conditions (i.e. rigidity coefficient ρ) as well as different distances l_f and spacings l_{sp} have been studied.

From Table 17, it can be found that the shear correction factor k_{yy} along the y-axis of double-channel section is close to the single channel section. The deflections δ_y obtained from the solid finite element model and the analytical solution are listed in Table 18. It can be also seen that there is only slight contribution of composite action along y-direction. Thus, the shear correction factor k_{yy} along the y-axis of the built-up section is almost equal to that of single channel section.

For the shear correction factor along the x-axis, it can be found from Table 16 that the rigidity coefficient ρ shows significant influence on k_{xx}.

Table 16
Shear correction factor k_{xx} of the double-channel sections

ρ	l_f=2			l_f=5			l_f=10		
	l_{sp}=100	l_{sp}=150	l_{sp}=200	l_{sp}=100	l_{sp}=150	l_{sp}=200	l_{sp}=100	l_{sp}=150	l_{sp}=200
($t_{e,max}$)	0.2549	0.2471	0.2397	0.1992	0.1712	0.1501	0.1070	0.0799	0.0637
($t_{e,min}$)	0.1043	0.0595	0.0372	0.0069	0.0031	0.0018	0.0018	0.0008	0.0005
0.01	0.1441	0.1166	0.0979	0.0027	0.0018	0.0013	0.0003	0.0002	0.0002
0.1	0.2368	0.2223	0.2094	0.2368	0.0163	0.0124	0.0033	0.0022	0.0017
1	0.2529	0.2443	0.2363	0.1147	0.0878	0.0711	0.1147	0.0179	0.0136
10	0.2547	0.2468	0.2393	0.1856	0.1564	0.1351	0.0817	0.0593	0.0465
100	0.2548	0.2470	0.2397	0.1978	0.1696	0.1484	0.0817	0.0772	0.0614
Single channel section: k_{xx}=0.4191									

Table 17
Shear correction factor k_{yy} of the double-channel sections

ρ	l_f=2			l_f=5			l_f=10		
	l_{sp}=100	l_{sp}=150	l_{sp}=200	l_{sp}=100	l_{sp}=150	l_{sp}=200	l_{sp}=100	l_{sp}=150	l_{sp}=200
($t_{e,max}$)	0.3276	0.3277	0.3277	0.3260	0.3263	0.3265	0.3249	0.3253	0.3255
($t_{e,min}$)	0.3279	0.3279	0.3279	0.3270	0.3270	0.3270	0.3260	0.3260	0.3260
0.01	0.3279	0.3279	0.3279	0.3270	0.3270	0.3270	0.3260	0.3260	0.3260
0.1	0.3277	0.3278	0.3278	0.3277	0.3270	0.3270	0.3260	0.3260	0.3260
1	0.3276	0.3277	0.3278	0.3267	0.3268	0.3269	0.3267	0.3259	0.3259
10	0.3276	0.3277	0.3277	0.3262	0.3265	0.3266	0.3253	0.3255	0.3256

100	0.3276	0.3277	0.3277	0.3260	0.3264	0.3265	0.3253	0.3253	0.3255
Single channel section: k_{yy}=0.3343									

Keeping the spacing l_{sp} as constant (l_{sp}=100), the deflections δ_x obtained from the solid finite element model and the analytical solution are plotted in Fig. 20 to Fig. 22 for l_f = 2, 5 and 10 mm respectively. Clearly, the analytical results with assumption of $t_e = t_{e,max}$ and $t_e = t_{e,min}$ are almost same as the finite element result when l_f = 2mm. It means that when the two channels are too close flexural behavior of the cantilever beam can be well predicted using $t_{e,max}$ or $t_{e,min}$ to compute the shear correction factor.

With the increase of the distance between the two channels (l_f = 5 and 10 mm), the analytical results assuming $t_e = t_{e,min}$ in related to lowest rigidity always predict large displacement than others while the assumption of $t_e = t_{e,max}$ in related to infinite rigidity provides the smallest displacement. The two assumptions are essentially two extreme cases. In reality, the connected details such as plate thickness, bolt size, distance l_f and spacing l_{sp} make the actual rigidity in between the two extreme cases. In this example, ρ = 0.1 and ρ = 1 provide the excellent results with the finite element model for l_f = 5 mm and l_f = 10 mm respectively. In principle, once the rigidity coefficient ρ is determined, the shear correction factors of the built-up section can be obtained. To exactly determine the shear correction factors of built-up sections, more works will be carried out in our future study. This paper aims to provide a good start in the field in which few research was done in previous works.

Table 18
Comparison of deflection along *y*-axis: δ_y

L/l_f	l_f=2, l_{sp}=100				
	①*	②*	③*	Diff (②-①)/① (%)	Diff (③-①)/① (%)
2	0.0573	0.0588	0.0573	-2.622	-2.605
3	0.1558	0.1573	0.1558	-0.915	-0.896
4	0.3376	0.3385	0.3376	-0.267	-0.246
5	0.6305	0.6303	0.6305	0.039	0.061
6	1.0624	1.0601	1.0624	0.220	0.241
7	1.6611	1.6556	1.6611	0.333	0.355
8	2.4545	2.4444	2.4545	0.411	0.433
9	3.4702	3.4541	3.4702	0.466	0.488
10	4.7363	4.7124	4.7363	0.507	0.529
11	6.2804	6.2468	6.2804	0.538	0.560

*: ① δ_y obtained from FEM; ② δ_y obtained by Eq. (61) with t_e=$t_{e,min}$; ③ δ_y obtained by Eq. (61) with t_e=$t_{e,max}$.

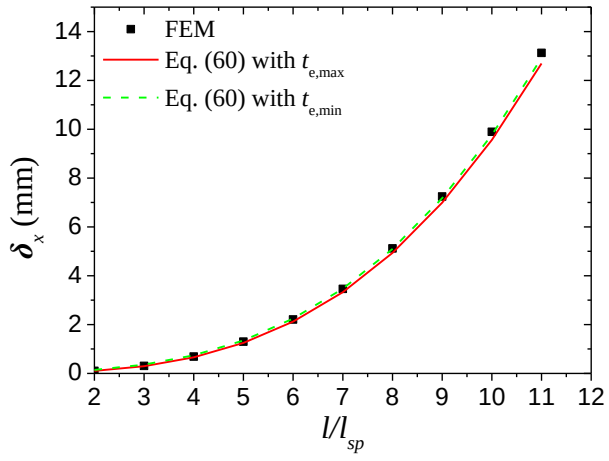

Fig. 20 δ_x of the cantilever with double-channel section: l_f=2 & l_{sp}=100

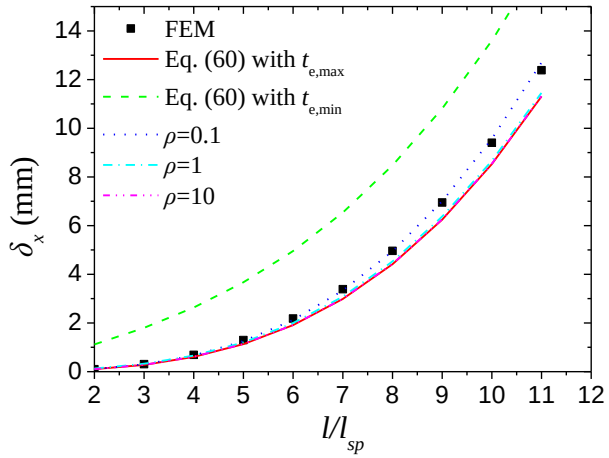

Fig. 21 δ_x of the cantilever with double-channel section: l_f=5 & l_{sp}=100

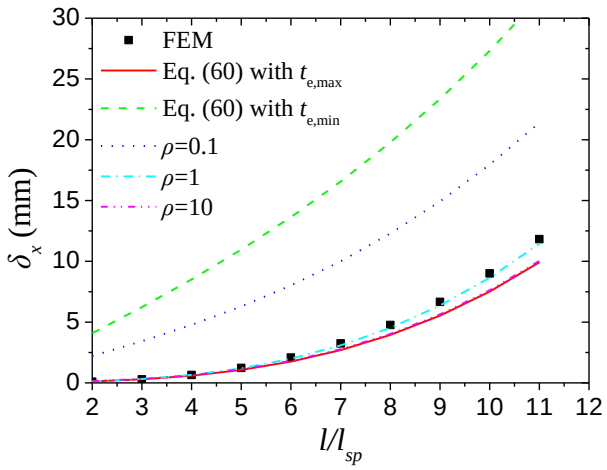

Fig. 22 δ_x of the cantilever with double-channel section: l_f=10 & l_{sp}=100

5.7. Example 7 – Influence of shear deformation in Direct Analysis of steel structures

A single steel member with two different boundary conditions reflecting practical engineering conditions, as shown in Fig. 23 (a) and (b), is studied to demonstrate the influence of shear deformation in the structural analysis of steel structures by using the Direct Analysis Method with consideration of geometric nonlinearity. The steel beam adopts ASTM standard W14x48 section with a length of 8.53 m. The two cases studied are introduced as below:

Case 1: the beam is simply supported with a uniformly distributed load over the length along gravity direction and a concentrated axial force applied at the end of the beam.

Case 2: the beam is fixed at one end and subjected to concentrated forces at the free end.

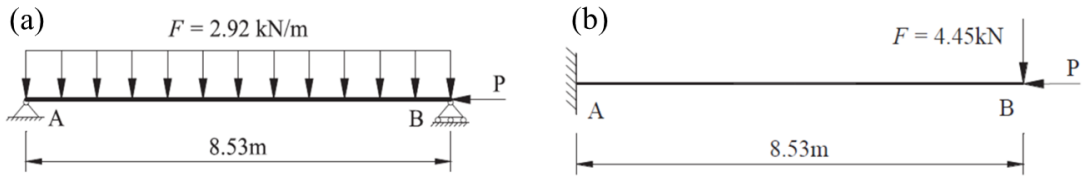

Fig. 23 A single steel member: (a) Case 1 - simply supported; (b) Case 2 - cantilevered

Table 19
Mid-span moment M_{mid} and displacement Δ_{mid} – Case 1

Response	Method	Number of elements	Axial Force, P(kN)			
			0	667	1334	2001
M_{mid} (kN·m)	AISC (2016)	-	26.6	30.5	35.7	43.0
	Du *et al*. (2019)	2	26.56	30.45	35.62	42.89
	SAP2000	2	26.56	30.38	35.46	42.48
		10	26.56	30.45	35.51	42.6
		20	26.56	30.45	35.51	42.6
	Present study (k_{yy} = 0)	1	26.56	26.56	26.56	26.56
	Present study (k_{yy} = 0.3328)	1	26.56	30.44	35.59	42.78
	ANSYS	2	26.558	30.341	35.098	41.259
		10	26.558	30.433	35.583	42.754
		20	26.558	30.437	35.601	42.813
		40	26.558	30.438	35.606	42.828
Δ_{mid} (mm)	AISC (2016)	-	5.13	5.86	6.84	8.21
	Du *et al*. (2019)	2	5.11	5.83	6.80	8.16
	SAP2000	2	5.11	5.82	6.76	8.06
		10	5.11	5.84	6.79	8.11
		20	5.11	5.84	6.79	8.11
	Present study (k_{yy} = 0)	1	5	5.68	6.59	7.85
	Present study (k_{yy} = 0.3328)	1	5.11	5.83	6.79	8.12
	ANSYS	2	5.1065	5.6869	6.416	7.3621
		10	5.1065	5.8256	6.7803	8.109
		20	5.1065	5.8306	6.794	8.1385
		40	5.1065	5.8319	6.7974	8.146

In both cases, the beam is simulated by one advanced beam-column element proposed by Tang *et al*. (2022) with consideration of both initial imperfection and shear deformation. To use this advanced element, the shear correction factor is required and will be calculated by the proposed one-dimensional element method in this paper.

The results are compared with those from AISC (2016), software SAP2000 and ANSYS, and the flexibility-based element from Du *et al*. (2019). The results without consideration of shear deformation (i.e. k_{yy} = 0) are also reported here for demonstration of the influence of shear effect.

Table 19 shows the mid-span moment and mid-span displacement of Case 1. The results are also plotted in Fig. 24 and Fig. 25 for comparison.

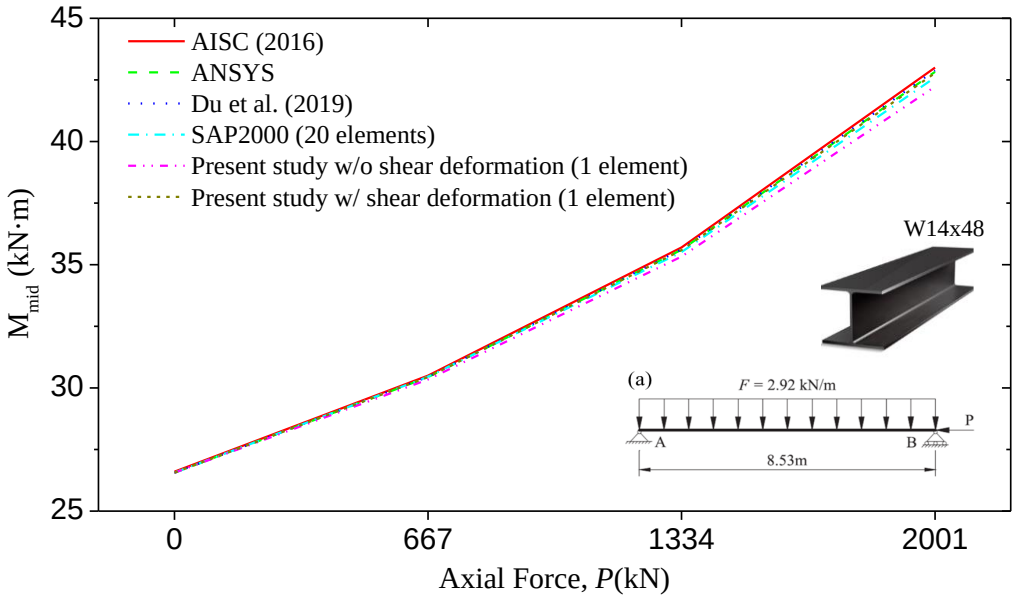

Fig. 24 Moment at mid-span: M_{mid} (kN·m) – Case 1

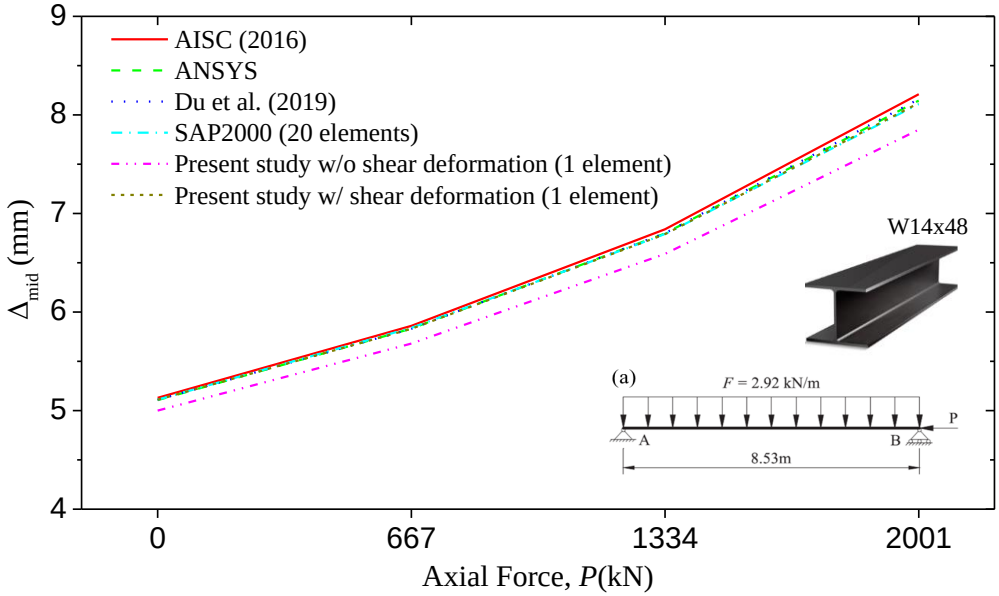

Fig. 25 Displacement at mid span: Δ_{mid} (mm) – Case 1

Table 20
Fixed end moment M_{end} and free end displacement Δ_{end} – Case 2

Response	Method	Number of elements	Axial Force, P(kN)			
			0	667	1334	2001
M_{end} (kN·m)	AISC (2016)	-	38.0	53.2	68.1	97.2
	Du *et al*. (2019)	2	37.96	53.12	67.98	97.37
	SAP2000	2	37.96	53.06	67.71	96.19
		10	37.96	53.10	67.89	96.66
		20	37.96	53.10	67.89	96.66
	Present study (k_{yy} = 0)	1	37.96	52.95	67.49	95.63
	Present study (k_{yy} = 0.3328)	1	37.96	53.10	67.85	96.64
	ANSYS	2	36.06	51.422	66.581	96.695
		10	37.009	52.414	67.619	97.841
		20	37.484	52.9	68.117	98.365
		40	23.1	34.2	45.1	66.6
Δ_{end} (mm)	AISC (2016)	-	23.01	34.08	45.03	66.78
	Du *et al*. (2019)	2	23.01	33.99	44.65	65.39
	SAP2000	2	23.01	34.04	44.86	65.96
		10	23.01	34.04	44.86	65.96
		20	22.85	33.72	44.30	64.83
	Present study (k_{yy} = 0)	1	23.01	34.04	44.84	65.96
	Present study (k_{yy} = 0.3328)	1	23.287	34.664	45.936	68.379
	ANSYS	2	23.287	34.67	45.954	68.431
		10	23.287	34.672	45.958	68.444
		20	38.0	53.2	68.1	97.2
		40	37.96	53.12	67.98	97.37

Table 20 shows the fixed end moment and free end displacement of Case 2. The results are also plotted in Fig. 26 and Fig. 27 for comparison.

It can be observed from both cases that with the axial force increasing, the second-order effect becomes unneglectable and increases exponentially for both moments and displacements. As shown in Fig. 24 to Fig. 27, the difference brought by whether the shear deformation is considered or not becomes more conspicuous and mainly influences the displacement of the structure. It is also noted that the model without consideration of shear deformation will be different from others. The shear deformation adversely impacts structural safety and is thus critical in the Direct Analysis of the structures. In addition, compared with the results from SAP2000 and ANSYS, the proposed one-dimensional method combined with the advanced element proposed by the authors achieves high accuracy while using only one element per member, bringing both modeling and computational efficiency.

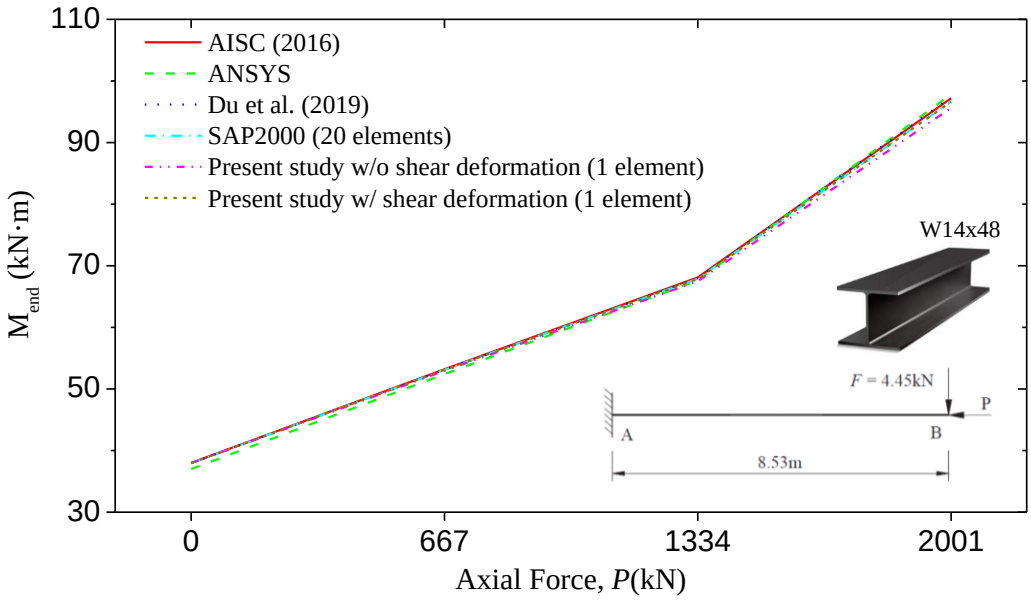

Fig. 26 Moment at fixed end: M_{end} (kN·m) – Case 2

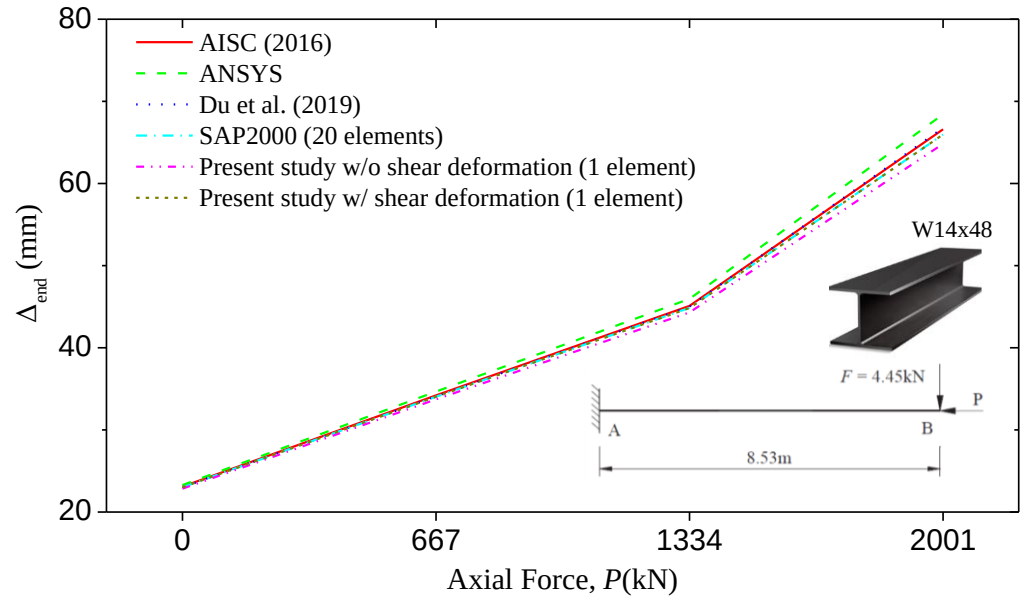

Fig. 27 Displacement at free end: Δ_{end} (mm) – Case 2

6. Conclusions

The shear correction factors of cross sections are required for consideration of shear deformation in global structural analysis such as Direct Analysis Method (DAM) based on beam-column theory. However, there is lack of a general method to determine the shear correction factors of thin-walled cross-sections in various shapes and as a result DAM cannot be applied to the structures adopting these cross-sections. To fill this gap, an innovative one-dimensional warping element model method is proposed to determine the shear correction factors of arbitrary thin-walled sections. The verification examples demonstrate the accuracy and efficiency of the proposed method against the analytical solution, conventional warping area element method and section analysis in ANSYS. The following conclusions can be made from this study:

(1) A one-dimensional warping element model method is proposed to determine the shear correction factors as well as the shear center of the thin-walled cross sections. Only one warping degree of freedom for each end of the proposed element.

(2) The non-uniform plate thickness between the two ends of the element has been taken into account in the element formulation. Thus, the element can be used to find the shear correction factors of the taper sections or the sections with taper portions.

(3) The proposed method can be applied to arbitrary thin-walled sections such as single open and closed sections. The modelling efforts can be significantly reduced for the sections with heavy stiffeners while the computational efficiency can be greatly enhanced.

(4) An equivalent plate thickness method is proposed for the determination of the shear correction factors of built-up sections composed of several single sections. The fixing conditions, distance between individual sections and the spacing of fasteners have been studied.

For the built-up sections, the upper bound and the lower bound of shear correction factors can be obtained by the proposed method. However, as the connected details such as plate thickness, bolt size, distance l_f and spacing l_{sp} will affect the actual rigidity, more research works will be carried out in our future study. Although the influence due to shear deformation on the I-shape section has been preliminarily investigated, more thin-walled members with complicated section shapes will be studied by using the Direct Analysis Method as a future work.

Acknowledgments

The authors are grateful for financial support from the Research Grant Council of the Hong Kong SAR Government on the project "Joint-based second order direct analysis for domed structures allowing for finite joint stiffness (PolyU 152039/18E)", Innovation, Technology Fund for the project “A new membrane-flood gate system for extreme weather hazardous mitigations for use in Hong Kong and worldwide (K-ZPD1)”, the Guangdong

Basic and Applied Basic Research Foundation (No. 2022A1515110289), and the China Postdoctoral Science Foundation (No. 2021M691071).

References

[1] Bai L H, Shen R L, Yan Q S, et al. Progressive-models method for evaluating interactive stability of steel box girders for bridges – Extension of progressive collapse method in ship structures[J]. Structures, 2021, 33:3848-3861.
[2] Shen R L, Bai L H, Zhang S H. Ultimate capacity of narrow type steel box section for railway self-anchored suspension bridge under bias compression. Advanced Steel Construction[J], 2019, 15(2):173–84.
[3] Ljubinkovic F, Martins J P, Gervasio H, et al. Experimental behavior of curved bottom flanges in steel box-girder bridge decks[J]. Journal of Constructional Steel Research, 2019, 160(9):169–188.
[4] Liu S W, Ziemian R D, Liang C, et al. Bifurcation and large-deflection analyses of Thin-walled beam-columns with non-symmetric open-sections. Thin-Walled Structures, 2018, 132:287-301.
[5] Saritas A, Filippou F C. Numerical integration of a class of 3d plastic-damage concrete models and condensation of 3d stress–strain relations for use in beam finite elements[J]. Engineering Structures, 2009, 31(10):2327-2336.
[6] Dikaros I C, Sapountzakis E J, Argyridi A K. Generalized warping effect in the dynamic analysis of beams of arbitrary cross section[J]. Journal of Sound & Vibration, 2016:119-146.
[7] Ding R, Nie X, Tao M X. Fiber beam-column element considering flange contribution for steel links under cyclic loads[J]. Journal of Structural Engineering, 2018, 144(9).
[8] Franza A, Acikgoz S, Dejong M J. Timoshenko beam models for the coupled analysis of building response to tunnelling[J]. Tunnelling and Underground Space Technology, 2020, 96(2):103160.
[9] Wang Y H, Nie J G, Fan J S. Fiber beam-column element for circular concrete filled steel tube under axial–flexure–torsion combined load[J]. Journal of Constructional Steel Research, 2014, 95(4):10-21.
[10] Tao M X, Nie J G. Fiber Beam-column model considering slab spatial composite effect for nonlinear analysis of composite frame systems[J]. Journal of Structural Engineering, 2014, 140(1):04013039.
[11] MSC. Marc Version 2007r1 [Computer software]. MSC, Software Corporation, Santa Ana, CA.
[12] Zhuge H, Xie X. Hysteresis model for fiber elements in effective damaged zone of square-section steel piers considering local instability effect of steel plates[J]. Journal of Structural Engineering, 2020, 146(8):04020156.
[13] Bai R, Hajjar J F, Liu S W, et al. A mixed-field Timoshenko beam-column element for direct analysis of tapered I-sections members[J]. Journal of Constructional Steel Research, 2020, 172:106157.
[14] Du Z L, Ding Z X, Liu Y P, et al. Advanced flexibility-based beam-column element allowing for shear deformation and initial imperfection for direct analysis[J]. Engineering Structures, 2019, 199(15):109586.
[15] Tang Y Q, Ding Y Y, Liu Y P, et al. Innovative displacement-based beam-column element with shear deformation and imperfection[J]. Steel and Composite Structures, 2022, (accepted).
[16] Chan S L, Liu Y P, Zhou Z H. Limitation of effective length method and codified second-order analysis and design[J]. Steel and Composite Structures, 2005. 5(2-3):181-192.
[17] Chan, S L, Zhou Z H. Pointwise equilibrating polynomial element for nonlinear analysis of frames[J]. Journal of Structural Engineering, 1994, 120(6), 1703-1717.
[18] Paolo D R, Daniela A, Filip C. Filippou. Mixed 3D Beam Element with Damage Plasticity for the Analysis of RC Members under Warping Torsion[J]. Journal of Structural Engineering, 2018, 144(6), 04018064.
[19] Daniela A, Paolo D R, Gabriele C. Enriched beam finite element models with torsion and shear warping for the analysis of thin-walled structures[J]. Thin-Walled Structures, 2021, 159:107259.
[20] Timoshenko S P. On the correction for shear of differential equation for transverse vibrations of bars of prismatic bars[J]. Philosophical Magazine, 1921, 41(5):744-746.
[21] Timoshenko S P, Goodier J N. Theory of elasticity[M]. McGraw-Hill, 1970.
[22] Love A E. A treatise on the mathematical theory of elasticity (4th ed.)[M]. Dover Publishing, New York, 1944.
[23] Herrmann L R. Elastic torsional analysis of irregular shapes[J]. Journal of the Engineering Mechanics Division, 1965, 91:11-19.
[24] Cowper, G.R. The shear coefficient in Timoshenko's beam theory[J]. Journal of Applied Mechanics, 1966, 33(2):335–340.
[25] Stephen N G. Timoshenko's Shear coefficient from a beam subjected to gravity loading[J]. Journal of Applied Mechanics, 1980, 47(1):121-127.
[26] Stephen N G. Discussion: "Shear coefficients for Timoshenko beam theory" (Hutchinson, J. R. 2001, ASME J. Appl. Mech. 68, pp. 87-92)[J]. Journal of Applied Mechanics, 2001, 68(6).
[27] Hutchinson J R. Shear coefficients for Timoshenko beam theory[J]. Journal of Applied Mechanics, 2001，68(1):87-92.
[28] Krahula J L, Lauterbach G F. A finite element solution for Saint-Venant torsion[J]. AIAA Journal, 1969, 7(12):2200-2203.
[29] Karan S Surana. Isoparametric elements for cross-sectional properties and stress analysis of beams[J]. International Journal for Numerical Methods in Engineering, 1979.
[30] Schramm U, Kitis L, Kang W, et al. On the shear deformation coefficient in beam theory[J]. Finite Elements in Analysis & Design, 1994, 16(2):141-162.
[31] Friedman Z, Kosmatka J B. Torsion and flexure of a prismatic isotropic beam using the boundary element method[J]. Computers & Structures, 2000, 74(4):479-494.
[32] Gruttmann F, Wagner W. Shear correction factors in Timoshenko's beam theory for arbitrary shaped cross-sections[J]. Computational Mechanics, 2001, 27(3):199-207.
[33] Gruttmann F, Sauer R, Wagner W. Shear stresses in prismatic beams with arbitrary cross-sections[J]. International Journal for Numerical Methods in Engineering, 1999, 45:865-889.
[34] Dong S B, Çarbas S, Taciroglu E. On principal shear axes for correction factors in timoshenko beam theory[J]. International Journal of Solids and Structures, 2013, 50:1681-1688.
[35] Dong S B, Alpdogan C, Taciroglu E. Much ado about shear correction factors in timoshenko beam theory[J]. International Journal of Solids & Structures, 2010, 47(13):1651-1665.
[36] Fialko S Y, Lumelskyy D E. On numerical realization of the problem of torsion and bending of prismatic bars of arbitrary cross section[J]. Journal of Mathematical Sciences, 2013, 192(6):664-681.
[37] Puchegger S, Bauer S, Loidl D, et al. Experimental validation of the shear correction factor[J]. Journal of Sound and Vibration, 2003, 261(1):177-184.
[38] NIDA. User's Manual, Nonlinear Integrated Design and Analysis. NIDA 10 HTML Online Documentation (http://wwwnidacsecom); 2021.
[39] Timoshenko S P, Maccullouoh G H. Elements of strength of materials (3rd ed.)[M]. van Nostrand Co., New York, 1949.

Advanced Steel Construction – Vol. 19 No. 3 (2023) 242–253
DOI:10.18057/IJASC.2023.19.3.5

NONLINEAR FINITE ELEMENT ANALYSIS OF ALL-STEEL BUCKLING RESTRAINED BRACES

Prachi Mishra [1, *] and Arvind Y. Vyavahare [2]

[1] *PhD Scholar, Visvesvaraya National Institute of Technology, Nagpur 440022, India*
[2] *Associate Professor, Visvesvaraya National Institute of Technology, Nagpur 440022, India*
** (Corresponding author: E-mail: dt19amc001@students.vnit.ac.in)*

ABSTRACT

Buckling restrained braces are gaining popularity in earthquake-resistant designs these days. These braces give stable hysteretic behaviour with a non-buckling steel core encased in a steel tube, that is filled with concrete or mortar. However, in the last few years, researchers have observed that these braces do not need any filler material and can be all-steel. This study aims to carry out a parametric study on All-Steel Buckling Restrained Braces (ASBRBs) by varying the restraining mechanism, the amount of gap between the core and the restrainer, and loading protocols. This paper presents a parametric study conducted on 12 proposed ASBRBs through non-linear finite element analysis. The proposed models have identical inner steel core cross-sections, but the restraining mechanism differs in each case. This paper also includes an experimental study on two small-scale ASBRB specimens. In addition, a finite element study on the effect of variation in stiffness of the transition portion of the core on different performance parameters is carried out. The parameters investigated include hysteretic response, energy dissipation, compression adjustment factor, and strain hardening adjustment factor. The results indicated that the global buckling behaviour of ASBRBs is significantly influenced by the restraining mechanism. In addition, this study also revealed that the global buckling behaviour does not significantly depend on the spacing of the restrainers. It was also observed that BRBs with unstiffened cores show stable hysteretic behaviour up to 2% strain, which deteriorates with further increase in the strain.

ARTICLE HISTORY

Received: 6 September 2022
Revised: 24 April 2023
Accepted: 10 May 2023

KEYWORDS

ASBRB;
Hysteretic behavior;
Restraining mechanism;
FE analysis;
Steel

Copyright © 2023 by The Hong Kong Institute of Steel Construction. All rights reserved.

1. Introduction

Buckling Restrained Braces (BRBs) represent a cutting-edge seismic device widely utilized in contemporary construction practices for steel and reinforced concrete (RC) buildings located in earthquake-prone regions. These innovative devices serve as effective energy dissipators, surpassing the seismic performance achieved by conventional bracing systems. Unlike conventional braces, which demonstrate unstable hysteretic behavior and fail to dissipate energy under compression, BRBs leverage a robust restraining mechanism that induces buckling prior to yielding, allowing for substantial energy dissipation during seismic events. Fig. 1 illustrates the contrasting hysteretic behavior between a BRB and a conventional brace. BRBs exhibit improved performance in both tension and compression, making them a noteworthy modification to conventional bracing systems. The fundamental concept revolves around restraining brace buckling by employing a metal core encapsulated within a buckling restraining mechanism, effectively preventing core buckling. This restraining mechanism consists of a steel outer cover enveloping the steel core, which is subsequently filled with a filler material such as mortar or plain concrete. The filler plays an important role in the energy dissipating behavior of BRBs [1]. Furthermore, the core is coated with a non-adhesive substance to prevent the restrainer from adhering to the inner metal core, thereby averting the transfer of axial load from the restrainer to the core. In contemporary practice, All-Steel Buckling Restrained Braces (ASBRBs) have gained preference over conventional filler BRBs due to their advantageous characteristics, including reduced weight, simplified installation, handling, and maintenance. Moreover, ASBRBs can be disassembled and inspected following seismic events, facilitating replacement if necessary. Fig. 2 presents a visual representation of a typical all-steel BRB concept.

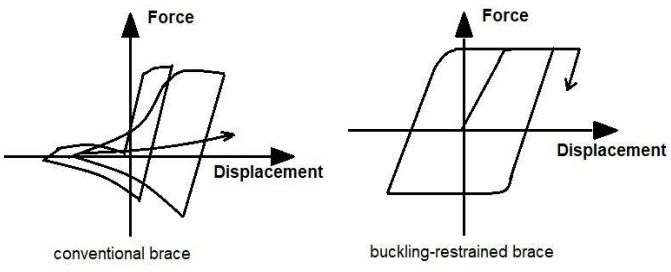

Fig. 1 Hysteretic behavior of a conventional brace and a BRB

The concept of BRBs originated in Japan, with Wakabayashi et al. [2] being the pioneers who conducted experiments on panel BRBs. Subsequently, Kano et al. [3] conducted a numerical study on the elastoplastic behavior of BRBs, while Kimura et al. [4] proposed the idea of fabricating BRBs to address the degradation of bearing capacity and stiffness. These proposed BRBs also addressed the requirements of reducing ductility and enhancing energy dissipation capacity in ordinary steel braces under compression. Mochizuki et al. [5, 6] conducted research to tackle the overall stability issues of steel braces surrounded by reinforced concrete.

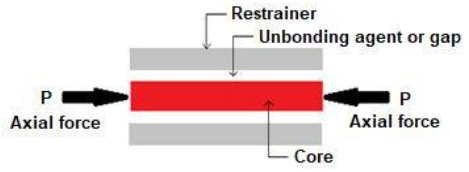

Fig. 2 Concept of all-steel BRB

Despite the positive responses and numerous research conducted on BRBs, they were not included in the design recommendations of the Architectural Institute of Japan (AIJ) until 1996. Fujimoto et al. [7] carried out research on BRBs with steel cores encased in steel tubes filled with concrete or mortar. In 1989, these BRBs were first practically applied in two steel-framed office buildings [8], and since then, they have been employed in approximately 160 buildings in Japan [9]. By 1990, more than a hundred buildings in Japan had adopted and utilized BRBs, with the majority of them being taller than 15 stories. Additionally, Wada et al. [10] introduced a new concept called "damage tolerant" design, where BRBs were utilized as energy dissipating elastoplastic dampers within an elastic mainframe. The acceptance and implementation of BRBs in Japan significantly increased, particularly after the 1995 Kobe earthquake.

After demonstrating successful performance in Japan, the technology of BRBs was transferred to the United States (US). A significant turning point in seismic research for steel structures in the US was the Northridge earthquake in 1994. Prior to this event, it was widely believed that special moment-resisting frames were effective solutions for earthquake-resistant design. However, the brittle failure of beam-to-column moment connections in numerous multi-story steel buildings during the earthquake compelled researchers to reassess and revise the seismic design provisions.

The first practical application of BRBs in the US occurred in 1998 with the construction of a building at the University of California (UC) Davis, followed

by testing at UC Berkeley in 2000. Subsequently, several projects utilizing BRBs were executed within a span of a few years. Black et al. [11] conducted component testing on the braces and observed repeating symmetrical hysteretic behavior. The seismic behavior of these braces was extensively investigated by Sabelli et al. [12]. Consequently, with the inclusion of design guidelines for BRB frames in the Seismic Provisions for Structural Steel Buildings [13], numerous buildings incorporating BRBs were constructed across the US. Fahenstock et al. [14] conducted large-scale pseudo-dynamic numerical analyses on the braces, further enhancing understanding of their behavior. The design standards for these braces are provided by AISC 341-10 [15], which establishes the guidelines for their implementation.

Numerous numerical models have been developed to accurately simulate the behavior of BRBs. In the present study, a comprehensive parametric analysis was conducted on 12 ASBRBs. Each ASBRB is characterized by a distinct restraining mechanism, varying gap sizes between the core and the restrainer, different core configurations (stiffened and unstiffened), and diverse loading protocols. The primary objective is to examine the influence of these parameters on the hysteretic behavior of all-steel BRBs. The study aims to identify the most cost-effective ASBRB configuration that maximizes energy dissipation under different loading conditions. By assessing these factors, valuable insights can be gained into optimizing the performance of ASBRBs in structural applications.

2. Basic concept

2.1. Concept

BRB is based on a very simple concept that is to restrict buckling and thereby show symmetrical and stable hysteretic behavior. This improves the energy absorption capability of the brace. A BRB is made up of the following components:

I. A metallic core placed centrally to yield,
II. A buckling-restraining mechanism to encase the core and restrain its global buckling, and
III. An un-bonding agent between the encasing restraint and the core so as to allow for the free expansion of the core element under cyclic loading and also to restrict the adhering of the core and the restraint.

2.2. Stability analysis

There are three major buckling modes under which BRB is to be identified [11].

1. Global buckling of the brace under axial compression.
2. Local buckling of the metallic core
3. Torsional buckling of the portion of the extended part of the core

The global stability of the brace can be found directly from Euler's theory of buckling which states that the critical load of the brace, P_{cr} is simply the Euler buckling load of the outer tube, P_e. Hence, when the Euler buckling load of the tube, P_e is greater than the yielding load of the inner metallic core, P_y, the brace is ensured in its global stability. Here,

$$P_e = \frac{\pi^2 EI_{tube}}{KL^2} \tag{1}$$

$$P_y = \sigma_y A_{core} \tag{2}$$

Where, EI_{tube} is the flexural rigidity of the outer tube, KL is the effective length of the entire brace, σ_y is the yield stress of the inner metallic core, and A_{core} is the cross-section area of the core.

Hence, for the global stability criteria, the ratio of the Euler load of the tube to the yield load of the core should be greater than 1. i.e.

$$\frac{P_e}{P_y} > 1 \tag{3}$$

For the local buckling mode, Wada et al. [10] came up with an equation for the critical load for the local buckling of the inner core as

$$P_{cr} = 2\sqrt{\beta E_i I_i} \tag{4}$$

Where, E_iI_i is the flexural rigidity for the inner steel core and β is the distributed spring constant.

It was observed that the efficiency of the brace can be enhanced when the buckling of the inner core along the restrained length does not take place.

High order buckling of the inner steel core can be avoided when,

$$P_{cr} \geq \sigma_y A_i \tag{5}$$

Which requires,

$$\beta \geq \frac{\sigma_y^2 A_i^2}{4E_i I_i} \tag{6}$$

Where, A_i is the cross-section area of the inner core. It was also observed that in higher modes, the critical load of the inner steel core does not depend upon the end conditions of the core [16].

The portion of the core that extends from the casing may undergo torsional buckling, which is the third and most critical mode of buckling for BRB. Many research [17, 18, 19] have been made, and some are still in progress, on the torsional buckling behavior of BRBs. Researchers have proven that the critical load causing torsional buckling of the extruded part in BRB does not depend upon the length of the extension [11]. However, the seismic performance of the brace depends on the length of the connectors [20].

3. Experimental study

3.1. Description of specimens fabricated

In order to study the actual behavior of ASBRBs, two small scale specimens of proposed ASBRBs are prepared and tested experimentally. The ASBRB specimens fabricated are similar to the proposed BRB models used for parametric study in the latter section. The core part of specimen 1 is made up of a rectangular steel plate of 15 mm x 3 mm size, and specimen 2 is of 18 mm x 3 mm plate size. Both plates have a yield strength of 250 MPa. The specimens are restrained with bolted connections. Both specimens have a different core cross-section but an identical restraining arrangement. The overall length of the specimens is 500 mm, with a yielding core length of 400 mm. The detailed dimensions and properties of both specimens tested are given in Table 1. Detailing of both ASBRBs is shown in Fig. 3.

Table 1
Properties of parts of specimens fabricated

Specimen	Parts	Dimension	Elastic Modulus (GPa)	Density (kg/m^3)
1.	Core plate	15 mm x 3 mm	210	7780
	Restrainer	Four ISA 35x35x5	210	7760
	Filler plates	10 mm x 3 mm	210	7760
2.	Core plate	18 mm x 3 mm	210	7780
	Restrainer	Four ISA 35x35x5	210	7760
	Filler plates	10 mm x 3 mm	210	7760

Four angle sections are used for restraining the core plate for both specimen 1 and specimen 2. Two filler plates are provided along the length of the core plates to facilitate bolting of the restrainer angle sections. A gap of 2 mm is kept between the filler plates and the core plate. A 1 mm thick sheet of polyflurotetraehtylene (PTFE) is coated on the core plate to avoid friction between the angle restrainers and the core part. The restrainers are connected to each other by bolted connections. 6 mm diameter bolts are provided at a centre-to-centre spacing of 40 mm.

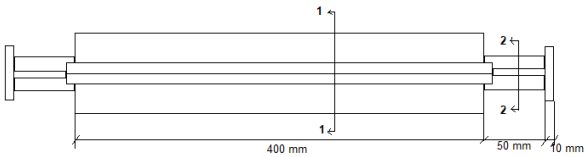

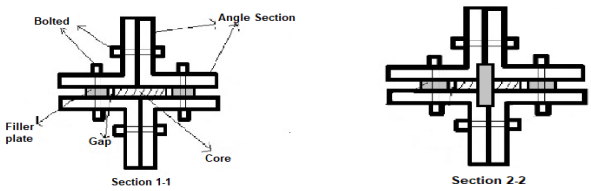

Fig. 3 Cross-sectional details of specimens

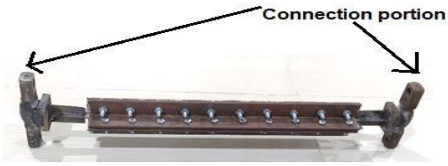

Fig. 4 Specimen 1

3.2. Loading protocol and experimental setup

The loading protocol for both specimens is according to the AISC provisions [13], i.e. $\pm\Delta_y$, $\pm 0.5\Delta_{bm}$, $\pm\Delta_{bm}$, $1.5\pm\Delta_{bm}$ and $\pm 2.0\Delta_{bm}$, but the number of cycles in each level is being increased to get more accurate results. The yield displacement, Δ_y for both specimens is found out to be 0.5 mm, and the ultimate displacement, Δ_{bm} is assumed to be 1% axial strain, which is 4 mm. Fig. 5 depicts the loading pattern, which consists of 5 sets of displacement levels with each level having 4 cycles. The specimens are tested in a shock absorber testing machine, and cyclic loading is given in five steps with four cycles each.

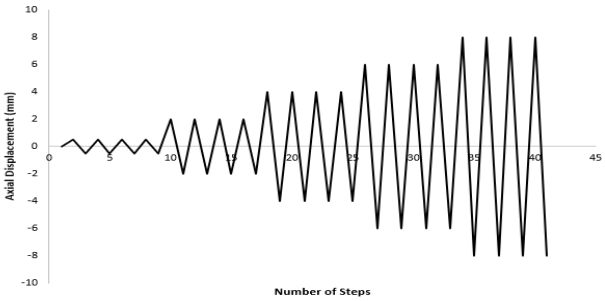

Fig. 5 Loading protocol

Both specimens are welded to end plates of size 50 mm x 35 mm x 10 mm on either end of the core plate. Further, the end plates are welded to the connection portion to enable the specimens to be installed in the testing machine. Fig. 4 shows the fabricated view of specimen 1. The specimens are fixed to the testing machine with the respective connecting parts. Fig. 6 shows the test setup for both specimens. The upper end of the specimen is kept fixed while the displacement cycles are applied through the lower part. Required inputs are given to the testing machine, and a force versus displacement plot is received as an output. A test frequency of 0.5 hertz is given for each displacement level as obtained from the loading protocol. Testing strokes are given as ±0.5 mm, ±2 mm, ±4 mm, ± 6 mm and ±8 mm for respective five displacement levels.

3.3. Experimental results

The hysteretic behavior of the two specimens tested can be plotted with force-displacement values received as an output from the shock absorber machine. It was observed that both showed symmetrical hysteretic behavior with optimum energy dissipation (Fig. 7). It is observed from the hysteretic behavior of both specimens that specimen 2 dissipated more energy than specimen 1. The failure pattern observed in the core parts of both specimens is shown in Fig. 8.

Specimen 1

No global buckling was observed in specimen 1, as expected, since the restrainer provided was as per Euler's global buckling criteria (explained in 2.2). Local buckling was observed along the yielding length of the core. The specimen dissipated a considerable amount of energy, but shear failure occurred at the transition portion on reaching 2% axial strain loading.

Specimen 2

Specimen 2 showed local buckling along with a little lateral bucklng about the weaker plane. A desirable amount of energy dissipation was observed with no global buckling, and hence it can be considered that the specimen can be further loaded after 2% axial strain.

Fig. 6 Test setup

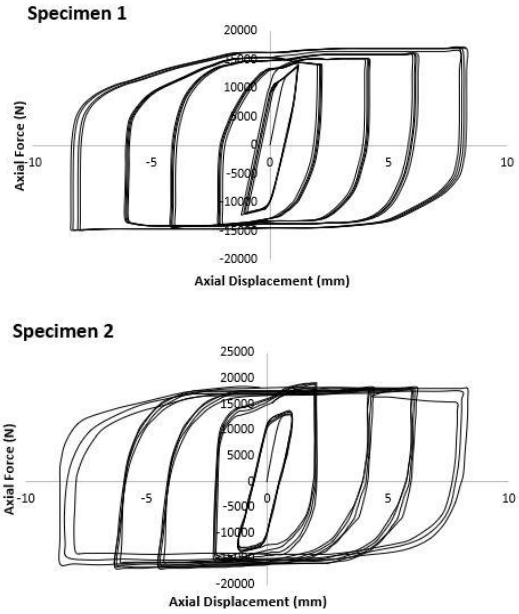

Fig. 7 Hysteretic response of the specimens tested

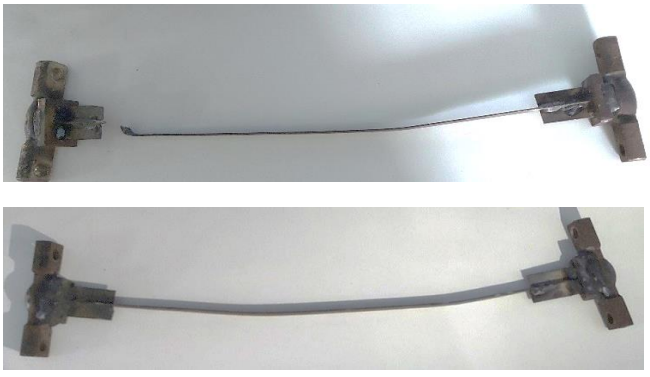

Fig. 8 Failure pattern of core part for specimen 1 (above) and specimen 2 (below)

4. Finite element modelling and validation

Over the past few decades, extensive numerical research and investigations have been conducted to assess the effectiveness and performance of BRBs. Researchers have employed 3D finite element analyses to study BRBs with various

configurations and material properties. Fahenstock et al. [14] conducted nonlinear dynamic analyses on BRB frames using scaled ground motion records at different seismic hazard levels. Takeuchi et al. [21] performed nonlinear analyses to understand the local buckling mechanism of the outer tube. Their findings indicated that larger gaps between the core and the outer tube, along with thinner tube thickness, resulted in a significant increase in tube strain rate. The length of the core member was found to have no effect on the brace's performance.

Korzekwa and Tremblay [22] conducted nonlinear analyses involving cyclic loading on all-steel BRBs, analyzing the nature of contact forces between the core member and the outer tube. They observed that these forces were resisted by tension in bolts and flexure in the tube. As a result, longitudinal frictional forces developed, leading to the generation of compressive loads acting axially in the outer tube during displacement cycles imposed on the brace. Dusicka and Tinker [23] investigated ultra-lightweight BRBs consisting of aluminium cores and bundled glass fibre-reinforced polymer pultruded tubes as restrainers. These BRBs were effective in resisting global buckling stability and weighed significantly less (27% of conventional filler-type BRBs and 41% of all-steel BRBs).

Further studies have also been conducted on all-steel BRBs. Anniello et al. [24] theoretically investigated the performance of dismountable all-steel BRBs through finite element analysis with the aim of upgrading existing RC buildings. Hoveidae and Rafezy [25, 26] performed finite element analyses on all-steel BRBs to study their overall and local buckling behavior. Karimi et al. [27] conducted finite element analysis on a three-story steel frame incorporating BRBs, investigating the seismic response of the frame under impact load and conducting dynamic analysis. Rossi [28] numerically examined BRBs using the isotropic hardening rule. Hosseinzadeh and Mohebi [29] compared the performance of all-steel BRBs with ordinary braces through finite element models and cyclic analysis. Almeida et al. [30] presented a case study on retrofitting an existing reinforced concrete school building with all-steel BRBs, demonstrating the effectiveness of BRBs in strengthening existing structures.

In addition, researchers have explored the integration of BRBs as energy dissipating devices in damped-outrigger systems [31]. Rahnavard et al. [32] proposed a method for accurately modelling and constructing a simple BRB model using finite element modelling with ABAQUS software. Avci-Karatas et al. [33] developed finite element models of BRB specimens based on full-scale experimental data [34], identifying key factors influencing the hysteretic behavior of BRBs. Alborzi et al. [35] proposed a hybrid BRB composed of multiple plates with different stress-strain behavior and compared its performance with conventional BRBs using time-history analysis. Jamkhaneh et al. [36] introduced a new type of all-steel BRB with corrugated edges, investigating its behavior through finite element modeling. They found that the corrugated and ribbed edges enhanced the buckling resistance of the braces. Naghavi et al. [37] numerically studied different types of concentrically braced frames and BRB frames using non-linear pushover analysis and time-history analysis.

In this study, 20 finite element analyses are conducted and studied on 12 all-steel BRB specimens with different restraining mechanisms, gaps, loading protocols, and core portions to study the effect of these parameters on the hysteretic behavior and energy dissipating capacity of all-steel BRBs.

4.1. Validation of finite element model

4.1.1. From literature available

With the aim of investigating the numerical behavior of the proposed BRB models, ABAQUS 6.13 software is used for non-linear finite element (FE) analysis. Beforehand, a BRB model based on past experimental research by Tabatabaei et al. (2014) is validated for its experimental and numerical results by performing finite element analysis on it. The loading protocol applied to the BRB model is as per Tabatabaei et al. [38]. Two cycles each for $\pm\Delta_{by}$, 0.5 $\pm\Delta_{bm}$, $\pm\Delta_{bm}$, 1.5 $\pm\Delta_{bm}$, and 2 $\pm\Delta_{bm}$ are applied as shown in Fig. 10. Here, Δ_{by} is the brace yield displacement, which is 1.7 mm, and Δ_{bm} is the axial displacement of the brace for the designed story drift, which is 27.7 mm. The material and geometric properties assigned to the model are the same as described in the literature [38]. The core is considered to be 80 mm in width and 10 mm in thickness, with a yield and ultimate strength of 235 MPa and 365 MPa, respectively. The end portions of the core are stiffened with two trapezoidal plates of 200 mm length, 80 mm width, and 10 mm thickness. The yield length of the core part is taken to be 1100 mm. The core is encased between two steel plates of 180 mm width and 10 mm thickness made from the same steel material as the core. The encasing plates are reinforced with square structural steel sections of 60 mm size and 5 mm thickness for out-of-plane action. The encasing plates are bolted with a filler plate along the length of the core. The core is further welded at both ends with square endplates of 300 mm size and 30 mm thickness. The modelling properties are also similar, with some minor changes. The identical parts were modelled and assembled as shown in Fig. 9, but somewhat finer meshing is used so as to obtain accurate results. 5 mm meshing is taken for all the parts,

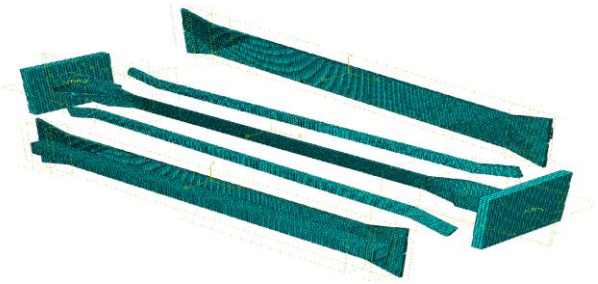

Fig. 9 Meshed parts of the model

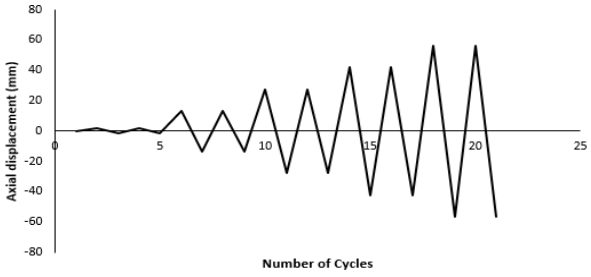

Fig. 10 Loading Protocol

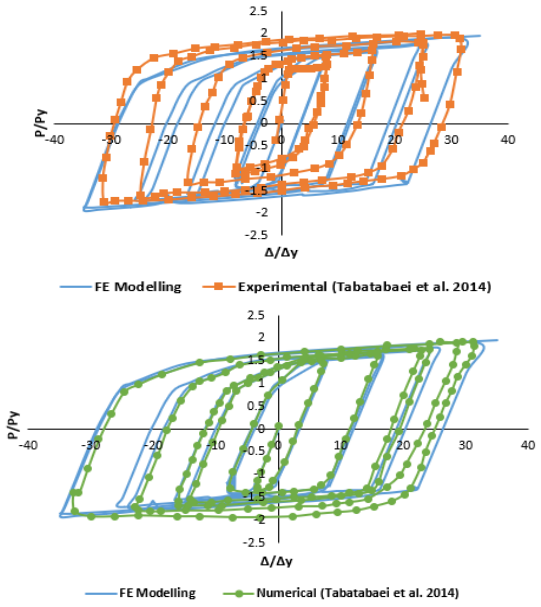

Fig. 11 Hysteretic curves obtained by FE modelling compared with experimental and numerical curves

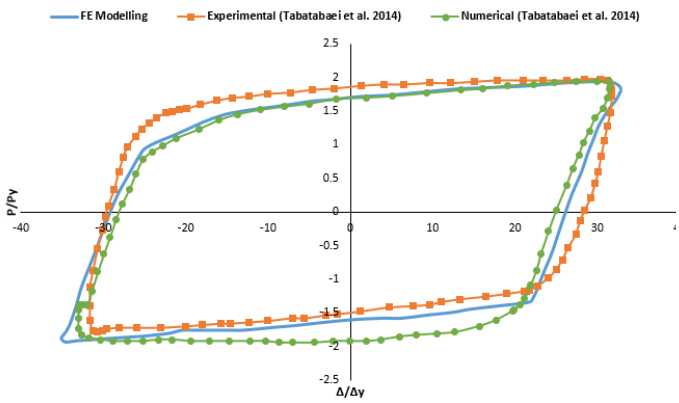

Fig. 12 Validation of hysteretic loop from FE modelling with experimental and numerical

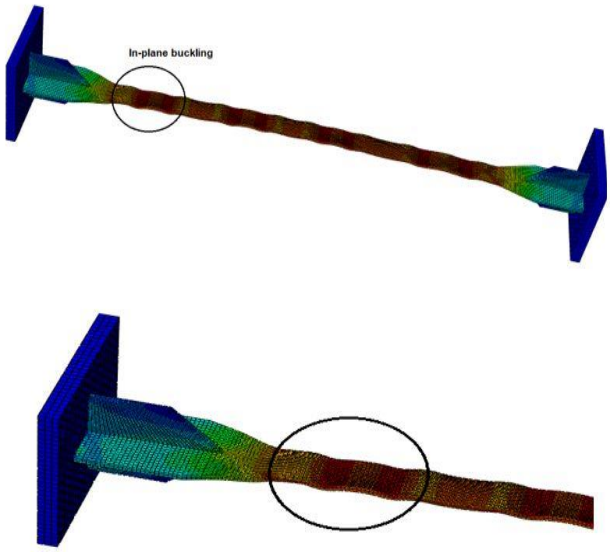

Fig. 13 Failure pattern observed

including the core, restraining plates with square hollow structural steel sections, filler plates, and endplates. A damping factor of 2E-4 is also introduced in the cyclic step to avoid the convergence problem. The hysteretic curve obtained with FE simulation is compared with that of the experimental and numerical one as shown in Figs. 11 and 12. A good correlation is observed between them. The failure pattern observed is also identical to the experimental result, as shown in Fig. 13. In-plane buckling and local buckling are observed along the yield length of the modelled BRB.

4.1.2. From experimental results

The specimens tested are also numerically investigated with ABAQUS 6.13 software. Both specimens are assigned their respective geometric and material properties as described in Section 2.1. The specimens are modelled using eight-node solid (C3D8R) elements with a reduced-integration technique and with 3D linear solid elements having three translational degrees of freedom per node. Nonlinear material modelling is done for core plates in both models and both elastic and plastic properties are assigned. A non-linear combined isometric and kinematic hardening rule with cyclic hardening is assigned for core parts in each model. The restrainer parts are assigned an elastic property only and are considered to remain elastic during the analysis. A friction coefficient of 0.1 is provided between the steel core plate surface and the angle restrainer surface to simulate the PTFE sheet in between. Finer meshing is done on the core parts of both models than on their respective restrainer parts (Fig. 14).

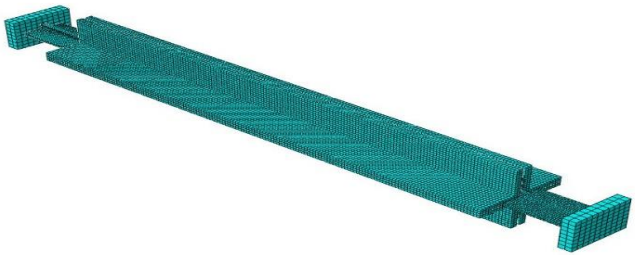

Fig. 14 Meshed FE models of specimen 1

The parts are prepared and assembled in the assembly by providing the required contact interaction. The combined hardening parameters assigned, including cyclic hardening, are material yield stress at zero plastic strain = 250 MPa, kinematic hardening parameter C = 10 GPa, Gamma1 = 48, rate factor b =4 and Q_∞ = 45 MPa [22]. An initial imperfection of L/400 is given to both models before the cyclic step, where L is the yielding length of the core.

The hysteretic curves obtained for specimen 1 are plotted with their FE results for each displacement level, as shown in Fig. 15. Each displacement level consists of four cycles of different frequencies. It can be seen that the hysteretic curves obtained for the specimen for experimental and numerical analysis are nearly identical for every displacement level. The hysteretic response of specimen 2 for all 5 displacement levels is also validated for its FE response (Fig. 16). The failure pattern obtained is also similar. Fig. 17 compares the failure pattern of specimen 2 for its experimental and FE results. Furthermore, the energy dissipated by the specimens at each level is calculated from the hysteretic loop obtained from the experimental and FE results and compared. Table 2 gives the energy dissipation comparison for both specimens.

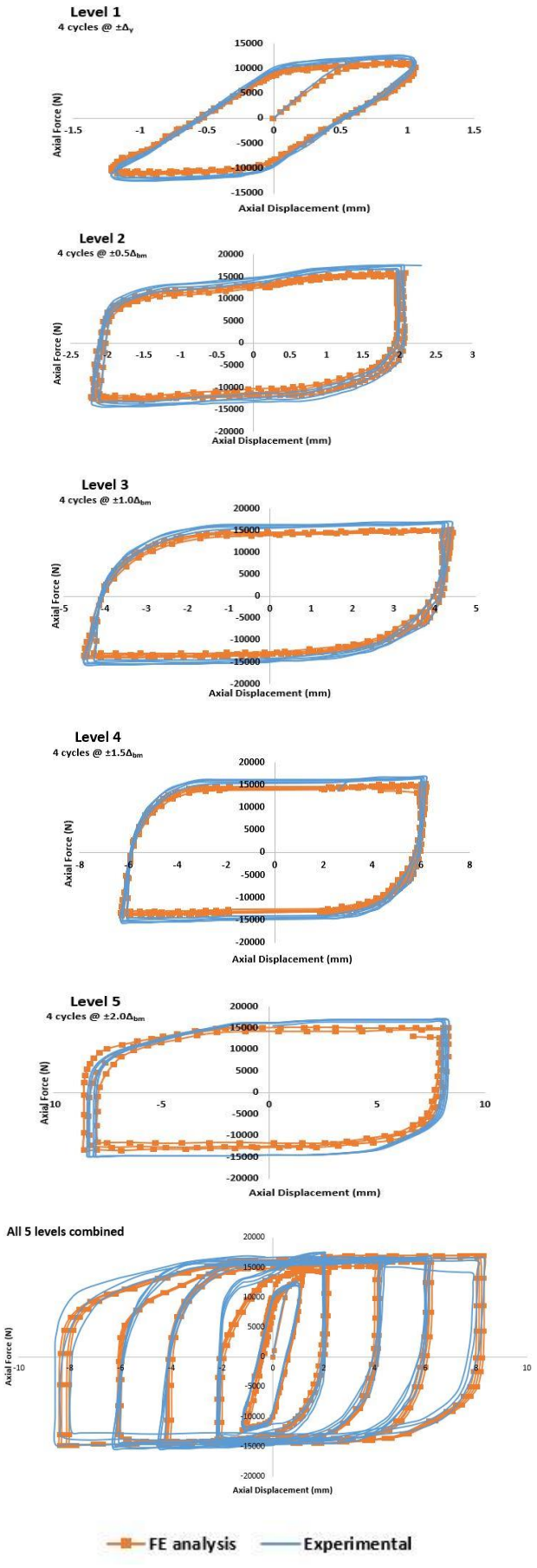

Fig. 15 Validation of experimental and FE results for specimen 1

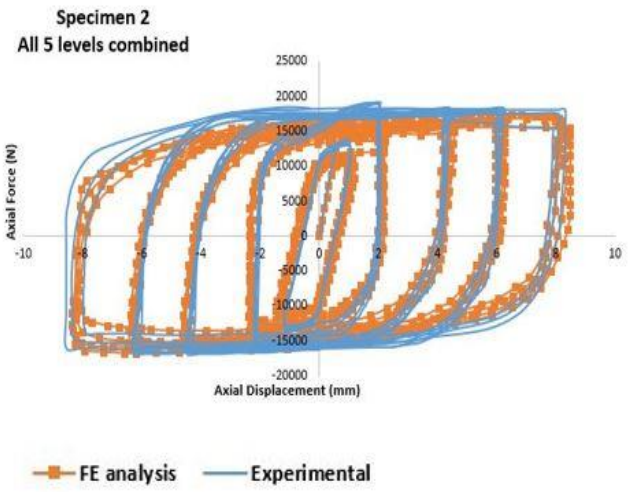

Fig. 16 Validation of experimental and FE results for specimen 2

Table 2
Energy dissipation by tested specimens

Specimen	Displacement Level	Energy dissipated (kN-mm)		Percentage difference (%)
		Experiment	FE analysis	
1.	1.	21.8	20.75	5.1
	2.	90.5	87.5	3.5
	3.	207.6	200	3.8
	4.	310	298	4.2
	5.	498	475	4.8
2.	1.	25.6	24.9	2.7
	2.	108.6	105	3.4
	3.	247.7	240	3.2
	4.	361.5	342.7	5.5
	5.	578	546.25	5.8

Fig. 17 Failure pattern observed in specimen 2 (experimental and FE)

4.2. Description of modelled parts

The finite element analysis for all the specimens was achieved with the help of the FE software ABAQUS 6.13. All the specimens are all-steel and have different parts that are assembled and then simulated. The specimens are grouped into two series depending on the restrainer used for the encasement of the core member, namely: (a) Series I and (b) Series II. The specimens with angle sections as restrainers are grouped in Series I, while the specimens with channel sections as restrainers are grouped in Series II. Both series are further subdivided into specimens, with the core having a stiffened transition portion and a non-stiffened transition portion. Table 1 gives a brief description of the specimens. The model name of the BRB specimens is in the form of codes ABRBij and CBRBij where, the indexes i and j represent the number of the model and type of specimen, whether stiffened or unstiffened, with letters S and U, respectively. ABRB stands for BRBs with angle sections used as restrainers, and CBRB stands for BRBs with channel sections used as restrainers. The different parts are assigned different material properties that are discussed in the next section.

4.3. Geometric and material properties

The geometric properties assigned to the specimens are briefly described in Table 3. A total of 20 finite element analyses are performed on 12 specimens that are divided into two series. All the specimens have the same core size of 40 mm x 8 mm. Series I includes six specimens, each having four angle sections with two filler plates as restrainer. Further, the size of the angle restrainer is different for every specimen. Each BRB is further divided into two types: the one with a stiffened transition portion and the other with an unstiffened one. Similarly, Series II has BRBs with two channel sections and two filler plates as restrainer, with each BRB having different sizes of channel sections for each specimen. The specimens are also subdivided on the basis of the stiffening of the transition portion. The filler plates are provided along the length of the core plates to prevent strong axis buckling. Further, a gap of 2 mm is provided between the filler plates and the core plate for Series I BRBs, and a gap of 1 mm is provided for Series II BRBs. A friction coefficient of 0.1 is provided between the restrainer and the core member so as to act as an unbonding agent. Fig. 18 explains the typical model of the proposed BRB specimens for both series.

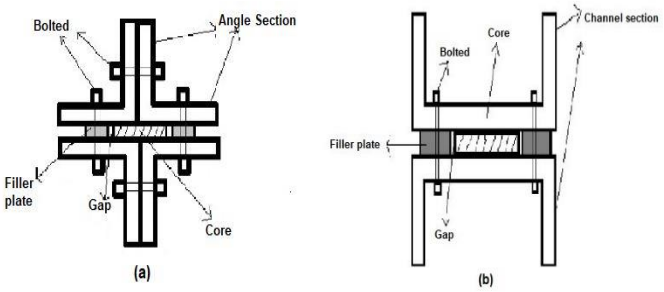

Fig. 18 Typical cross-section of proposed (a) Series I BRBs and (b) Series II BRBs

Table 3
Geometric properties of specimens

Series	Model name	Core dimensions (mm)	Restrainer dimensions (mm)	Area of core (mm^2)	Gap (mm)
I	$ABRB_{1S}$	40 x 8	4 ISA (50x50x3) + 2 filler plates	320	2
	$ABRB_{1U}$	40 x 8	4 ISA (50x50x3) + 2 filler plates	320	2
	$ABRB_{2S}$	40 x 8	4 ISA (55x55x5) + 2 filler plates	320	2
	$ABRB_{2U}$	40 x 8	4 ISA (55x55x5) + 2 filler plates	320	2
	$ABRB_{3S}$	40 x 8	4 ISA (60x60x5) + 2 filler plates	320	2
	$ABRB_{3U}$	40 x 8	4 ISA (60x60x5) + 2 filler plates	320	2
II	$CBRB_{4S}$	40 x 8	2 ISMC 100 + 2 filler plates	320	1
	$CBRB_{4U}$	40 x 8	2 ISMC 100 + 2 filler plates	320	1
	$CBRB_{5S}$	40 x 8	2 ISMC 125 + 2 filler plates	320	1
	$CBRB_{5U}$	40 x 8	2 ISMC 125 + 2 filler plates	320	1
	$CBRB_{6S}$	40 x 8	2 ISMC 150 + 2 filler plates	320	1
	$CBRB_{6U}$	40 x 8	2 ISMC 150 + 2 filler plates	320	1

The core plate is assigned the material properties of structural steel with a yield strength of 250 MPa. The core plate is also assigned plastic properties in addition to the elastic ones. The filler plates are simple structural steel plates. The restrainer angle sections and channel sections are assigned their respective properties on the steel table. The material properties assigned to core and filler plates are given in Table 4.

Table 4
Material properties of specimens

Parts	Density (kg/m^3)	Elastic Modulus (GPa)	Poisson's Ratio	Yield Strength (MPa)
Core	7780	210	0.3	250
Filler Plates	7760	210	0.3	-

4.4. Combined hardening parameters

A combined isotropic and kinematic hardening rule with cyclic hardening is used to analyze all the proposed models. Certain parameters need to be defined for such analyses in ABAQUS. These parameters include the kinematic hardening modulus *C*, the kinematic hardening rate parameter γ, the isotropic hardening magnitude for cyclic hardening Q_∞, and the isotropic hardening rate parameter *b* for cyclic hardening. Fig. 19 depicts the stress-plastic strain curve for steel and explains the variation of parameters *C* and γ for kth backstress.

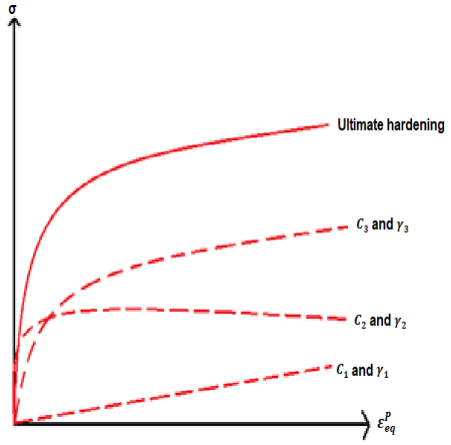

Fig. 19 Stress-plastic strain curve of steel

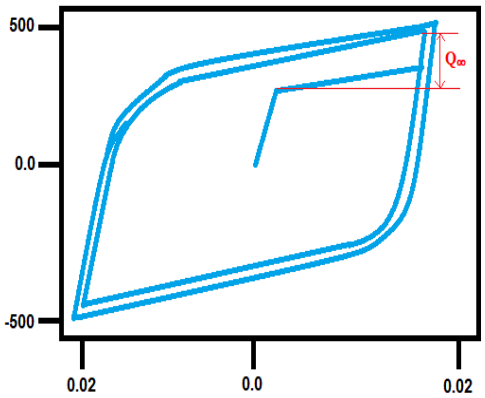

Fig. 20 True stress-strain curve for a metal

The uniaxial kinematic hardening modulus for the material can be given as [39]

$$H_u^{'} = \sum_k \left(C_k e^{-\gamma_k \varepsilon^P_{eq}} \right) \tag{7}$$

Here, C_k is the kinematic hardening modulus and γ_k is the kinematic hardening rate parameter for k^{th} backstress, respectively. The stress of the material for which the stress-strain curve is presented in Fig. 19 can be given as

$$\sigma = \frac{C}{\gamma}\left(1 - e^{-\gamma \varepsilon^P_{eq}}\right) \tag{8}$$

Here, γ is the rate at which *C* decreases with increasing equivalent plastic strain ε^P_{eq} [39]. The yield stress of the material can be given by

$$\sigma_y = \sigma_{y0} + Q_\infty \left(1 - e^{-b\varepsilon^P_{eq}}\right) \tag{9}$$

Where, σ_{y0} is the initial yield stress. Here, Q_∞ represents the maximum change in yield surface size in the true stress-strain plot (Fig. 20) and *b* defines the rate at which Q_∞ changes with increasing equivalent plastic strain.

These parameters are the material properties and can be found in the stress-strain curve of the core material. However, approximate values of such parameters are suggested by some researchers [40, 22]. Hartloper et al. [39] have proposed these parameters for structural steel in their research. For FE modelling purposes, these parameters can be assumed depending on the material selected and the values suggested in past research.

4.5. Modelling assumptions

Finite element models of all 12 specimens are developed using ABAQUS 6.13 software. All the specimens are modelled using eight-node solid (C3D8R) elements with a reduced-integration technique. The models are made in parts and then assembled to perform cyclic analysis. Every part is modelled using 3D linear solid elements with three translational degrees of freedom per node. Non-linear material modelling is done for the core plates in each model and is assigned both elastic and plastic properties. A non-linear combined isometric and kinematic hardening rule with cyclic hardening is assigned for core parts in each model. However, the restrainer parts are assigned an elastic property only and are considered to remain elastic during the analysis. The core part and the filler part are provided with a gap of 1 to 2 mm. The interaction property between the angle or channel section parts and the core parts is assigned a surface-to-surface contact property with tangential behavior. The frictional coefficient should be assumed carefully as the increase in the value of this coefficient increases the amount of axial force transmitted to the restrainer part. This further results in an increase in bending moment in the restrainer due to the P-Δ effect, and consequently, the global buckling load of the entire ASBRB may change. Hence, a friction coefficient of 0.1 is provided between the steel core plate surface and the restrainer surface to simulate a greasy, smooth surface between the core and the restrainer. The assumption of the friction coefficient is as per Chou et al. [41]. However, to simulate a rough and dry surface between the restrainer and the core element, the value of the frictional coefficient may be adopted as 0.3 [22].

Normal behavior as hard contact is also assigned between the core and the restrainer with nonlinear properties. The filler plate and the angle or channel restrainers are assumed to be connected with bolted connections along the length, and hence, to simulate this, the restrainer parts are connected to each other using a tie constraint. The full Newton-Raphson method was employed to solve the non-linear analysis. A fine mesh is employed for both the core plate and restrainer parts. For core plates with stiffened transition segments, partitioning of the plate is done to achieve a uniform and desired mesh. (Fig. 21).

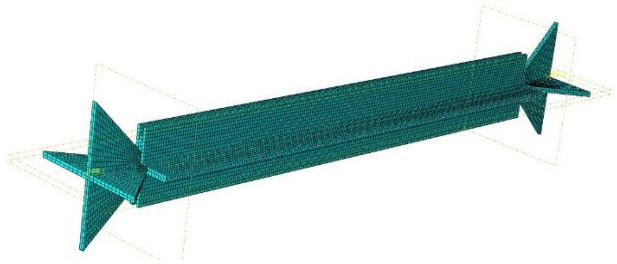

Fig. 21 Finite element model of $ABRB_{1S}$

The parameters used for a combined isometric and kinematic rule with cyclic hardening are material yield stress at zero plastic strain = 250 MPa, kinematic hardening parameter *C* = 10 GPa, Gamma1 = 48, rate factor *b* =4 and Q_∞ = 45 MPa [22]. An initial imperfection with a linear perturbation is also assigned as the initial step before the cyclic step. The initial geometric imperfection can be assigned in three ways: imperfection based on eigenmode data; imperfection based on static analysis data; and by directly defining the imperfection. In this analysis, an initial imperfection of 1 mm is assigned based on the first mode of buckling pattern. The first five buckling modes for the core plate with a stiffened transition portion can be seen in Fig. 23. An automatic stabilization with a damping coefficient of 1E-4 is applied to avoid convergence problems.

4.6. Loading protocols

Two different types of loading protocols are considered in this analysis. All 12 specimens are analyzed for the Type I loading protocol, which is shown in Fig. 20. In this loading protocol specimens are cyclically loaded at 8 different axial displacement levels, which are $1/3\Delta_y$; $2/3\Delta_y$; $1.0\Delta_y$; 0.33 Δ_{bm} (0.33%), $0.5\Delta_{bm}$ (0.5%), $1.0\Delta_{bm}$ (1%), $1.5\Delta_{bm}$ (1.5%), and $2\Delta_{bm}$ (2%). Two cycles of loading were applied at each displacement level, where Δ_y is the displacement that corresponds to the yielding of the core and Δ_{bm} is the axial deformation of the brace corresponding to the design story drift. In this study, Δ_{bm} was set to 10 mm, which corresponds to the axial strain of 1% in the core, and the core yielding displacement, Δ_y, was calculated as 1.27 mm based on the material characteristics. Hence, the ultimate axial displacement demand of the brace during cyclic loading was determined as $2\Delta_{bm}$=20 mm, which corresponds to a core strain of 2%. A similar loading pattern was considered by Eryasar [42] in his research. Eight specimens ($ABRB_{1S}$, $ABRB_{1U}$, $CBRB_{4S}$, $CBRB_{4U}$, $ABRB_{2S}$, $ABRB_{3S}$, $CBRB_{5S}$, and $CBRB_{6S}$) are also analyzed for the Type II loading protocol, which consists of two cycles at each deformation of an axial strain of 0.5, 1, 1.5, 2, 2.5, 3, and 3.5% with an increment of 0.5% after every two cycles. This type of loading pattern was considered by Sahoo and Ghowsi [43] in their experimental research. (Fig. 22).

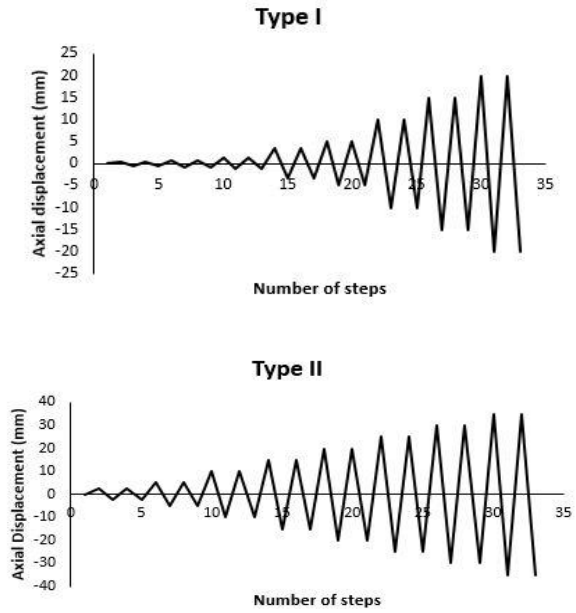

Fig. 22 Loading Protocols

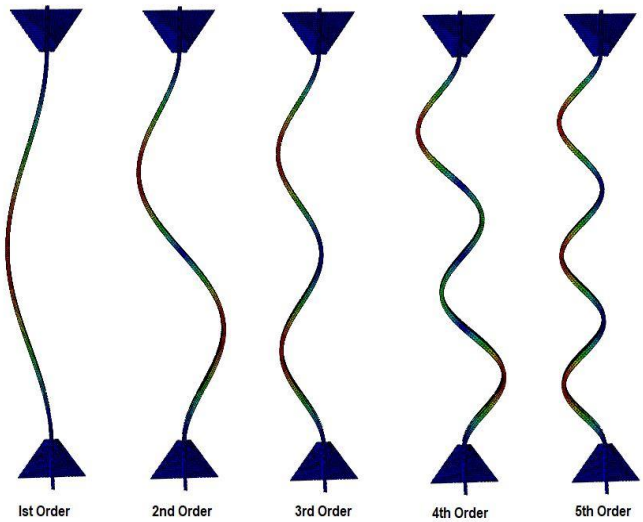

Fig. 23 First five buckling modes for core plate with stiffened transition portion

5. Results

5.1. Hysteretic loops

The hysteretic response of all 12 specimens for 20 different analyses is presented in Figs. 25 and 26. Normalized values for force and displacement are found for each specimen for plotting the curves to give a better understanding and comparison of the specimens. The compressive adjustment factor (β) and strain adjustment factor (ω) for all the specimens are calculated using equations (10) and (11) respectively.

$$\beta = \frac{C_{max}}{T_{max}} \tag{10}$$

$$\omega = \frac{T_{max}}{F_C A_C} \tag{11}$$

Where, F_c is the yield stress of the core plate, and A_c is the cross-section area of the core plate. β and ω values for all the modelled specimens are given in Tables 5 and 6 for both the loading types. It can be observed that these values are greatest for $ABRB_{4S}$ and are satisfactory for all other specimens. The β and ω values depend upon the type of contact and gap between the core and the restrainer member. β values are greater for direct contact because of high frictional forces generated at the core and the restrainer interface. The use of unbonding material or a gap between the core and the restrainer is therefore strongly recommended. All the specimen models in this study are thus provided with some gap between the core and the restrainer. β and βω values can also be found from the backbone curve of the ASBRB specimens, as shown for specimens $CBRB_{4S}$ and $ABRB_{3S}$ in Fig. 24. The strain adjustment values are needed for calculating the adjusted ASBRB strengths for design purposes. The energy dissipated by all the specimens is also calculated from their hysteretic responses for both loading types, as given in Table 7.

Table 5
Comparison of strength adjustment parameters for loading protocol Type I

Specimen	T_{max} (kN)	C_{max} (kN)	β	ω	βω
$ABRB_{1S}$	87	87	1.00	1.09	1.09
$ABRB_{1U}$	85	86	1.01	1.06	1.07
$ABRB_{2S}$	87	87	1.00	1.09	1.09
$ABRB_{2U}$	85	86	1.01	1.06	1.07
$ABRB_{3S}$	87	88	1.01	1.10	1.11
$ABRB_{3U}$	85	86	1.01	1.06	1.07
$CBRB_{4S}$	87	87	1.00	1.09	1.09
$CBRB_{4U}$	85	86	1.01	1.06	1.07
$CBRB_{5S}$	87	87	1.00	1.09	1.09
$CBRB_{5U}$	85	86	1.01	1.06	1.07
$CBRB_{6S}$	88	96	1.09	1.10	1.20
$CBRB_{6U}$	82	87	1.06	1.02	1.09

Table 6
Comparison of strength adjustment parameters for loading protocol Type II

Specimen	T_{max} (kN)	C_{max} (kN)	β	ω	βω
$ABRB_{1S}$	121	140	1.15	1.51	1.74
$ABRB_{1U}$	87	88	1.01	1.09	1.10
$ABRB_{2S}$	104	106	1.02	1.30	1.33
$ABRB_{3S}$	104	108	1.04	1.30	1.35
$CBRB_{4S}$	104	105	1.00	1.30	1.30
$CBRB_{4U}$	87	88	1.01	1.09	1.10
$CBRB_{5S}$	100	102	1.02	1.25	1.28
$CBRB_{6S}$	103	105	1.01	1.29	1.30

Table 7

Energy dissipated by the specimens

Specimen	Energy dissipated (kN-mm)	
	Type I	Type II
$ABRB_{1S}$	580	1300
$ABRB_{1U}$	440	950
$ABRB_{2S}$	520	1400
$ABRB_{2U}$	420	-
$ABRB_{3S}$	540	1400
$ABRB_{3U}$	460	-
$CBRB_{4S}$	520	1500
$CBRB_{4U}$	460	900
$CBRB_{5S}$	520	1400
$CBRB_{5U}$	440	-
$CBRB_{6S}$	900	1500
$CBRB_{6U}$	420	-

5.1.1. Type I loading

Specimens $ABRB_{1S}$ and $ABRB_{1U}$

It was observed from the hysteretic loops obtained from both these specimens that the specimen with an unstiffened transition portion, $ABRB_{1U}$ gives satisfactory performance up to 2% strain loading, and the energy dissipated is not much less than that by the specimen with a stiffened transition part, $ABRB_{1S}$. However, the specimen with a stiffened transition portion dissipates more energy and shows a better hysteretic response. The β and ω values for the former and latter are found to be 1.01 and 1.06; and 1.00 and 1.09, respectively.

Specimens $ABRB_{2S}$ and $ABRB_{2U}$

Both specimens whether with a stiffened transition core portion or without, show satisfactory hysteretic behavior and dissipate a comparable amount of energy, with a difference of 19%. The hysteretic curve obtained for specimen $ABRB_{2S}$, which dissipated a greater amount of energy, is somewhat better with more loops, which means stress distribution is more uniform. The β and ω values for both specimens are found to be 1.00 and 1.09; and 1.01 and 1.06, respectively, similar to the specimens discussed in the previous section.

Specimens $ABRB_{3S}$ and $ABRB_{3U}$

Specimen $ABRB_{3U}$ dissipated 0.85 times the energy dissipated by $ABRB_{3S}$, and both showed symmetrical hysteretic behavior. The β and ω values for both are found to be 1.01 and 1.10; and 1.01 and 1.06, respectively. No global buckling is observed, with some minor local buckling in both specimens.

Specimens $CBRB_{4S}$ and $CBRB_{4U}$

Stable hysteretic curves are obtained for both the BRBs. The energy dissipation is higher for $CBRB_{4S}$ when compared with $CBRB_{4U}$ as expected but by only 11%. The hysteretic loops are also better for $CBRB_{4S}$. The β and ω values for both are found to be 1.00 and 1.09; and 1.01 and 1.06, respectively. There is no global buckling observed in both BRBs.

Specimens $CBRB_{5S}$ and $CBRB_{5U}$

Both specimens dissipated a decent amount of energy with stiffened one dissipating more. Stable and symmetrical hysteretic behavior is observed in both the BRBs. The β and ω values for both are found to be 1.00 and 1.09; and 1.01 and 1.06, respectively. No global buckling is observed; however, in-plane buckling is observed in the specimen $CBRB_{5U}$.

Specimens $CBRB_{6S}$ and $CBRB_{6U}$

Specimen $CBRB_{6S}$ dissipated a considerable amount of energy, showed stable hysteretic behavior up to 2% strain, and further dissipated energy at higher strain levels. The specimen showed higher energy dissipation than any other specimen. The hysteretic curve formed by the specimen is symmetrical with some degradation. Specimen $CBRB_{6U}$ showed stable hysteretic behavior and dissipated satisfactory energy, though quite less than that by the specimen with a stiffened transition core portion. The β and ω values for both are found to be 1.09 and 1.10; and 1.06 and 1.02, respectively.

5.1.2. Type II loading

Specimens $ABRB_{1S}$ and $ABRB_{1U}$

A large amount of energy is dissipated by specimen $ABRB_{1S}$ compared to specimen $ABRB_{1U}$. Local buckling is observed in the specimen after a 2.5% strain rate. The specimen showed quite satisfactory hysteretic behavior with the hysteretic curve having a number of loops. The curve obtained is quite symmetrical up to 2.5% strain, and then degradation is visible with further strain loading. Specimen $ABRB_{1U}$ experienced in-plane buckling after 2% of the strain rate and stopped dissipating further energy after 2.5% strain loading. However, it showed stable hysteretic behavior. The β and ω values for the former and latter are found to be 1.15 and 1.51; and 1.01 and 1.09, respectively.

Specimens $CBRB_{4S}$ and $CBRB_{4U}$

Specimen $CBRB_{4S}$ experiences local buckling along the yield length of the core. Global buckling is not seen, but markable stress is induced in the restrainer portion, which can be seen in Fig. 25 (b). The hysteretic loop obtained is symmetric, as expected. For $CBRB_{4U}$, the energy dissipation is less when compared with $CBRB_{4S}$. It was observed that $CBRB_{4S}$ dissipates quite a higher amount of energy than the specimen $CBRB_{4S}$, but experienced local buckling for Type II loading. The β and ω values for both are found to be 1.1 and 1.3; and 1.01 and 1.09, respectively.

Specimens $ABRB_{2S}$ and $ABRB_{3S}$

Quite stable and symmetrical hysteretic behavior is obtained for specimen $ABRB_{2S}$ up to 3.5% strain with some degradation at the compression side, but a considerable amount of energy is dissipated by the specimen. Local buckling is observed along the yielding core length. A perfect symmetrical hysteretic curve is obtained for the specimen $ABRB_{3S}$, during the entire loading. The energy dissipated is satisfactory and similar to that of the former specimen. In-plane buckling is observed along the core length in the specimen. The β and ω values for both are found to be 1.02 and 1.3; and 1.04 and 1.3, respectively.

Specimens $CBRB_{5S}$ and $CBRB_{6S}$

The hysteretic curve obtained for the specimen $CBRB_{5S}$ is uniform and symmetrical up to 3% strain, and then degradation is observed on further loading. Energy dissipation is, however, satisfactory with local buckling along the yielding length of the core. A stable and symmetrical hysteretic curve is obtained for specimen $CBRB_{6S}$, with a higher amount of energy dissipation than the former specimen. The β and ω values for both are found to be 1.0 and 1.25; and 1.01 and 1.29, respectively.

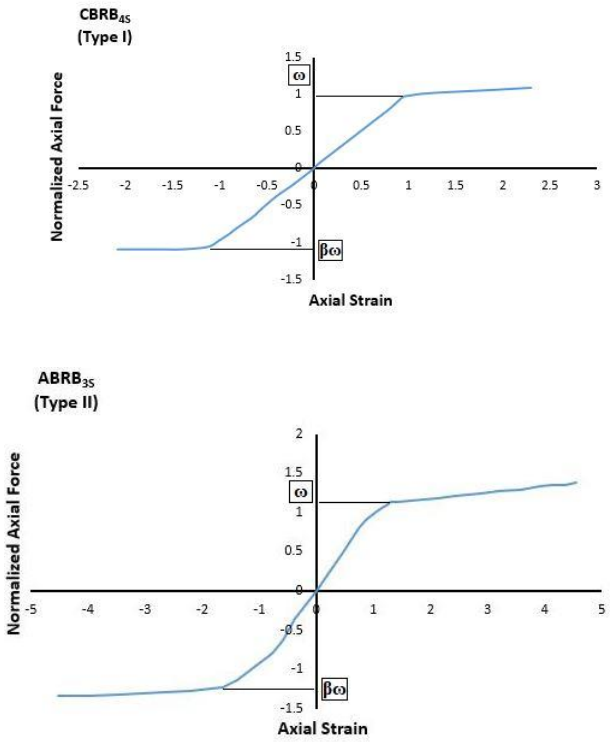

Fig. 24 Backbone curves for modelled ASBRBs

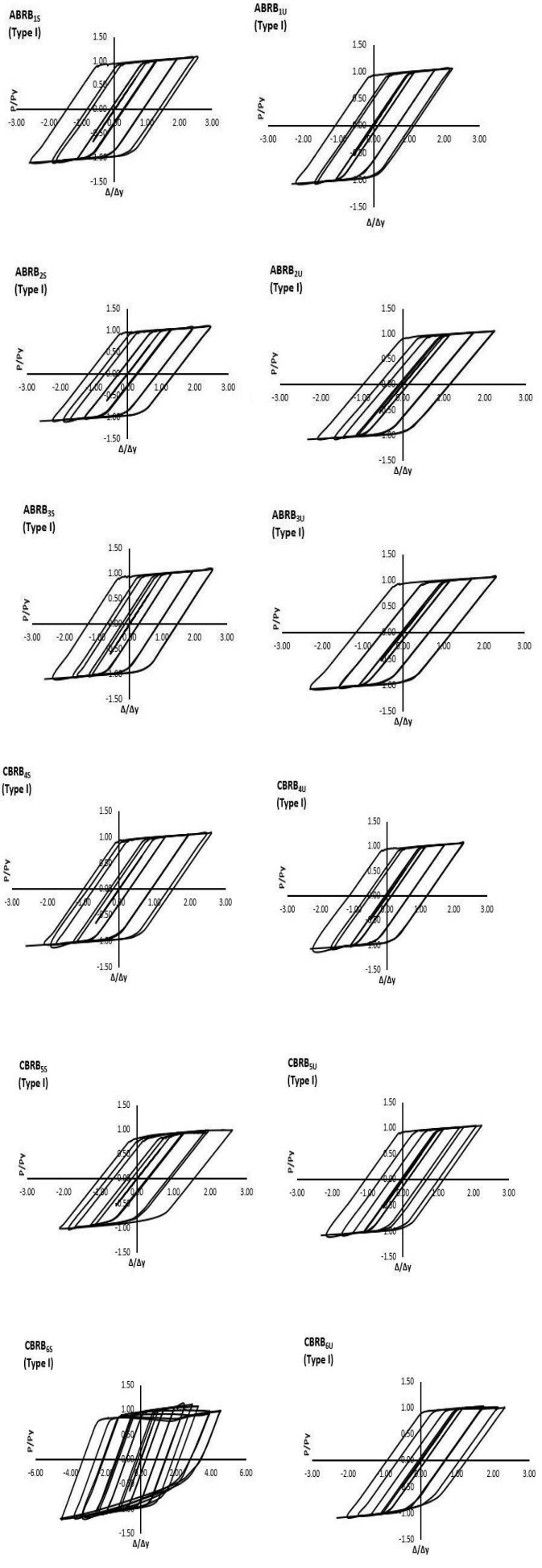

Fig. 25 Hysteretic responses for Type I loading protocol

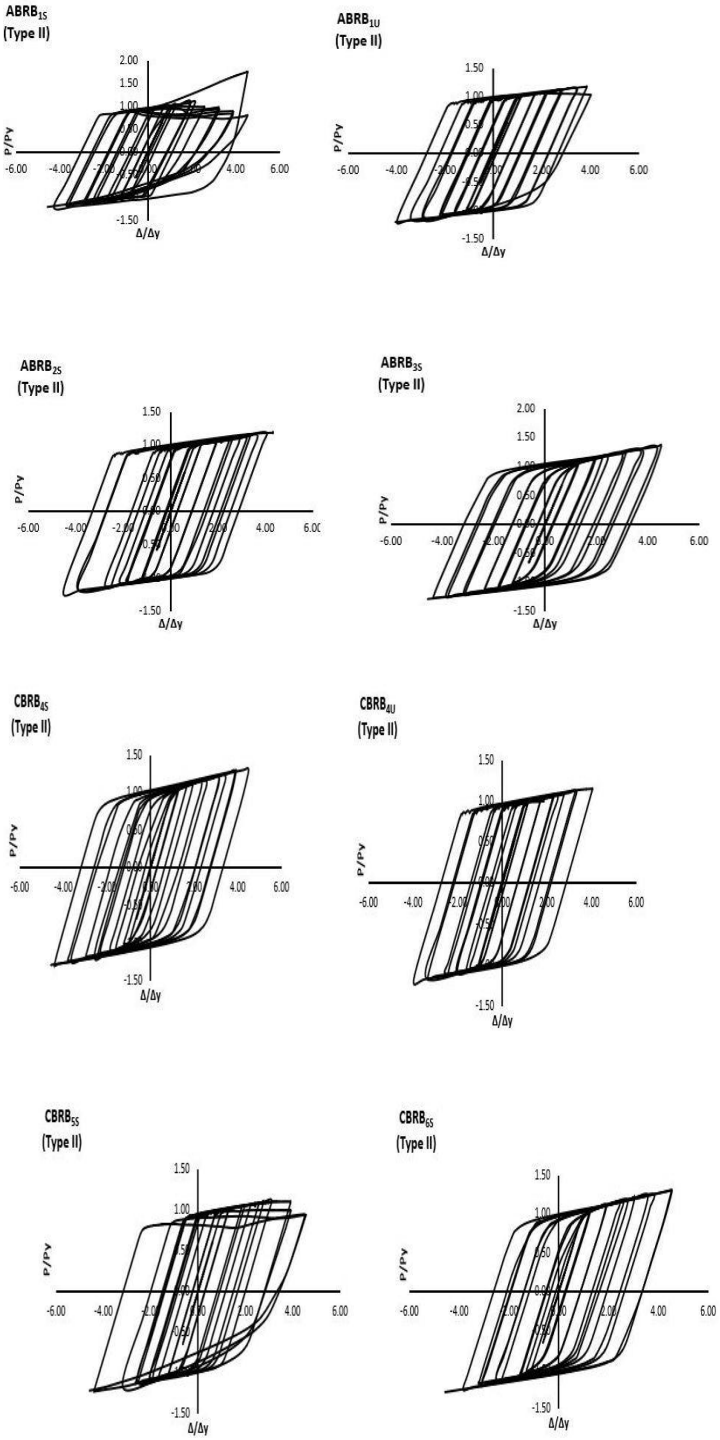

Fig. 26 Hysteretic responses for Type II loading protocol

5.2. Failure patterns

All the specimens showed a good hysteretic response and satisfactory energy dissipation for both types of loading patterns. For Type I loading, only in-plane buckling is observed in most of the specimens, with some minor local buckling along the core length. No global buckling is observed in any of the specimens for Type I loading. The specimens with unstiffened transition core portions performed well enough as compared with the specimens with stiffened transition core portions. However, for the Type II loading pattern, the specimens with stiffened transition portions performed much better. Local buckling is observed in almost all the specimens for Type II loading. Overall buckling is not seen in the specimens of this loading, but considerable stress is induced in the restrainers, which can be observed in some of the specimens. Fig. 27 shows the failure pattern and stress distribution pattern in the specimen $CBRB_{4S}$ for the Type II loading pattern.

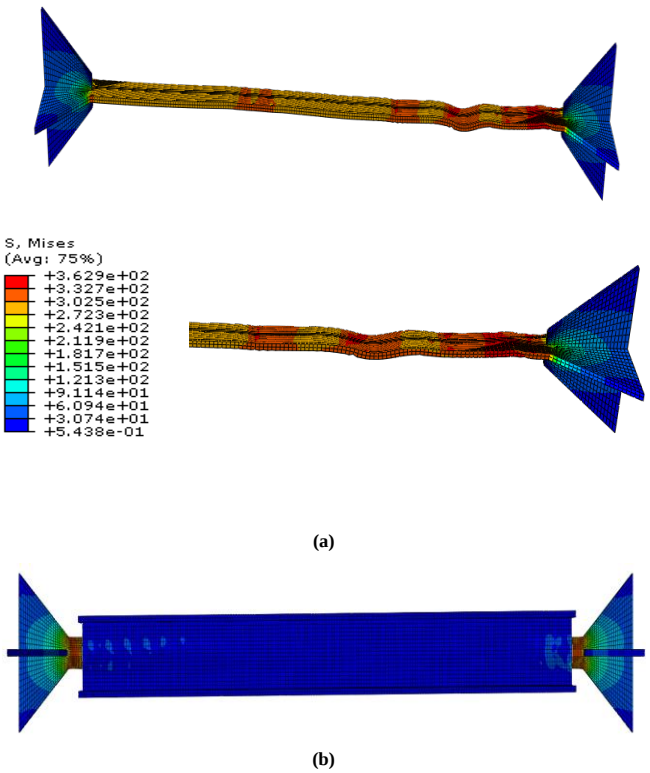

Fig. 27 Von-Mises Stress distribution in $CBRB_{4S}$ (a) core part and (b) entire BRB for Type II loading protocol

6. Conclusions

In a comprehensive study, a series of non-linear finite element analyses were conducted on 12 proposed All-Steel Buckling Restrained Brace (ASBRB) specimens. Prior to these analyses, two small-scale ASBRB specimens were subjected to cyclic testing to validate the experimental and finite element (FE) results. These specimens had different core cross-sections but utilized the same restraining arrangements, and they exhibited symmetrical hysteretic behavior. The dissipated energy of the tested specimens was compared between experimental and FE results. Additionally, the FE method used was validated by comparing the obtained results with literature from past research.

Subsequently, 20 non-linear FE analyses were performed on the proposed ASBRB specimens, considering various parameters. Based on these analyses, the following conclusions were drawn regarding the influence of these parameters:

Gap between Core and Restrainer: The size of the gap between the core and the restrainer was found to have a significant effect on the behavior of ASBRBs. Larger gaps resulted in increased energy dissipation capacity and improved overall performance.

Restrainer Material: The material used for the restrainer (steel or aluminium alloy) affected the behavior of ASBRBs. The choice of material influenced the stiffness and energy dissipation characteristics of the brace.

Core Stiffening: Stiffened and unstiffened types of core portions were investigated. It was observed that the inclusion of stiffening elements within the core enhanced the buckling resistance and energy dissipation capacity of ASBRBs.

Loading Protocols: Different loading protocols were examined to assess their impact on ASBRB behavior. The loading rate and sequence were found to influence the hysteretic response and energy dissipation characteristics of the braces.

By systematically varying these parameters and analyzing their effects, valuable insights were gained regarding the optimal configuration and design of ASBRBs. These findings contribute to the ongoing development and improvement of ASBRB technology, enhancing its effectiveness as an energy dissipating device in seismic-resistant structures.

6.1. Restraining mechanism

In the analyzed specimens, global buckling failure was not observed due to the strong restraining mechanism employed. The occurrence of global buckling failure depends on the ratio of the Euler buckling load of the restrainer to the yield load of the core part. If this ratio is greater than 1, the brace will not experience global buckling failure. All the specimens in the study had a ratio greater than 1, ensuring their resistance to global buckling.

However, it was found that the braces with channel restrainers outperformed the ones with angle restrainers in terms of energy dissipation. This suggests that the choice of restrainer design significantly influences the energy dissipation capacity of ASBRBs. It was also observed that local buckling occurred in the braces when the strain rate exceeded 2%.

To prevent global buckling, it is recommended to select restraining mechanisms with a value greater than 1.5, indicating that light sections can be chosen instead of heavy sections. Interestingly, the ASBRB with ISMC 150 as a restrainer, which is the heaviest restrainer among the proposed ASBRBs, achieved the maximum energy dissipation for both loading types.

These findings indicate that careful selection of the restrainer design, considering factors such as weight and the ratio of Euler buckling load to yield load, is crucial for optimizing the performance and energy dissipation capacity of ASBRBs.

6.2. Amount of gap

In the study, ASBRBs with angle restrainers had a 2 mm gap between the core member and the restrainer, while those with channel restrainers had a 1 mm gap. Surprisingly, the performance of the braces was found to be independent of the specific gap size (1 mm or 2 mm) in this study. The braces exhibited different behavior regardless of the gap size.

However, it is recommended to maintain a gap of 1 to 2 mm between the core member and the restrainer. This gap helps to prevent the transfer of axial load from the restrainer to the core and minimize the compression adjustment factor value. It is important to note that a larger gap can lead to undesirable consequences such as increased local buckling amplitudes and higher contact forces on the restrainer surface. These factors can ultimately result in a decrease in the strength of the ASBRB.

Therefore, while the specific gap size did not significantly affect the performance of the braces in this study, it is still necessary to maintain a suitable gap (1 to 2 mm) to ensure proper functioning and avoid potential issues related to strength and buckling.

6.3. Loading pattern

In this study, two different types of loading patterns were used: Type I loading, which followed the provisions prescribed by AISC (American Institute of Steel Construction), and Type II loading, which was based on the approach proposed by Sahoo et al. (2017). It was observed that ASBRB specimens could withstand higher strain rates than those prescribed in the AISC provisions.

The ASBRBs with stiffened transition portions exhibited good performance, particularly under higher strain rates. They were able to dissipate a significant amount of energy and exhibited a high number of symmetrical hysteretic loops during Type II loading.

The ratio of the yield load of the core part to the Euler buckling load of the restrainer (P_e/P_y) remained less than 1.5 for Type I loading. For Type II loading, this ratio increased for some ASBRBs but still remained below 2. It is worth noting that local buckling failure was observed in most cases during Type II loading, indicating the occurrence of localized buckling phenomena.

Overall, the study showed that ASBRBs have the capability to withstand higher strain rates and exhibit satisfactory performance, especially when equipped with stiffened transition portions. However, local buckling failures were observed in some cases during Type II loading.

6.4. Stiffening of the transition segment

Based on the simulations and findings of this research, ASBRBs without stiffened transition portions exhibited symmetrical hysteretic behavior for Type I loading. These braces performed satisfactorily and were able to dissipate energy up to a 2% strain rate. Although they dissipated less energy compared to ASBRBs with stiffened transition portions, they showed satisfactory performance, especially in buildings that are less prone to seismic attacks.

By not stiffening the transition portion of the core in ASBRBs used in such buildings, designers can achieve cost-cutting and material savings. It is recommended to use lightweight restrainers for ASBRBs, as they are replaceable and easy to handle. A gap of 1 to 2 mm between the core and the restrainer is sufficient to avoid transferring axial load and minimize compression adjustment factor values.

For structures with lower design story drift, ASBRBs with unstiffened transition portions in the core can be employed as cost-effective replaceable fuses. However, it is important to note that experimental validation of the finite element simulations conducted in this research is necessary. The authors plan to conduct such experimental validation in the future to further validate their findings.

Acknowledgment

The manuscript was developed at the Visvesvaraya National Institute of Technology (VNIT) in Nagpur, India. The authors acknowledge and express gratitude to VNIT for the support provided to the first author during her doctoral research. Additionally, the authors extend their thanks to the Motibagh Workshop of South East Central Railways (SECR) for their assistance in executing the experimental research conducted for the study.

Conflict of interest

There was no conflict of interest in the preparation of this manuscript.

References

[1] Yue Y. C., Bai Y. T., Wang Y., Ma X. F., Wang Y. H. and Li X. H., Experimental behavior and design of rectangular concrete filled tubular buckling-restrained brace, Advanced Steel Construction, 2021,Vol. 17 No. 4, pp. 366–375. DOI: 10.18057/IJASC.2021.17.4.5.

[2] Wakabayashi M., Nakamura T., Kashihara A., Yokoyama H., and Morizono T., Experimental study on the elasto-plastic behavior of braces enclosed by precast concrete panels under horizontal cyclic loading (Part 1 and Part 2) (1973), Summaries of Technical Papers of Annual Meeting of Architectural Institute of Japan Kinki Branch-Structural section I 1973; 6:121–8 (in Japanese).

[3] Kano Y., Kuwabara T., Seki Y. and Yoshino T., Experimental study on shear wall with braces (Part 1), Annual Research Meeting Architectural Institute of Japan, Kanto area, Japan, September; 1971. (in Japanese).

[4] Kimura K., Yoshioka K., Takeda T., Furuya N. and Takemoto Y., Tests on braces encased by mortar in-filled steel tubes, Annual Research Meeting Architectural Institute of Japan, Tokai area, Japan, October; 1976. (in Japanese).

[5] Mochizuki N., Murata Y., Ando N. and Takahashi S., Experimental study on buckling of unbonded braces under axial compressive force (Part 1 and Part 2), Annual Research Meeting Architectural Institute of Japan, Tokai area, Japan, September; 1979. (in Japanese).

[6] Mochizuki N., Murata Y., Ando N. and Takahashi S., Experimental study on buckling of unbonded braces under axial compressive force (Part 3), Annual Research Meeting Architectural Institute of Japan, Kinki area, Japan, September; 1980. (in Japanese).

[7] Fujimoto M., Wada A., Saeki E., Watanabe A. and Hitomi Y., A study on brace enclosed in buckling-restrained mortar and steel tubes (Part 2). Annual Research Meeting Architectural Institute of Japan, Kanto Area, Japan, October; 1988. (in Japanese).

[8] Fujimoto M., Wada A., Saeki E., Takeuchi T. and Watanabe A., Development of unbonded brace, 1990, Quarterly column no. 115, pp. 91-96.

[9] Takeuchi T., Wada A., Matsui R., Silter B., Lin P. C., Sutcu F., Sakata H. and Qu Z., Buckling-Restrained Braces and Applications, Japan Society of Seismic Isolation, 2017.

[10] Wada A., Connor J. J., Kawai H., Iwata M. and Watanabe A., Damage tolerant structures, Proceedings of first U.S.-Japan workshop on the improvement of building structural design and construction practices, September 8-10, 1992, San Diego, California.

[11] Black C. J., Makris N., and Aiken I. D., Component Testing, Stability Analysis, and Characterization of Buckling Restrained Braces, 2002, Univ. of California, Berkeley, CA.

[12] Sabelli R., Mahin S. and Chang C., Seismic demands on steel braced frame buildings with buckling-restrained braces, Eng. Struct., 2003, pp. 655–666.

[13] AISC 341-05. Seismic provisions for structural steel buildings. Chicago, IL, USA: American Institute of Steel Construction; 2002.

[14] Fahnestock L. A., Ricles J. M. and Sause R., Experimental evaluation of a large-scale buckling-restrained braced frame, J. Struct. Eng., 2007.

[15] AISC (American Institute of Steel Construction). Seismic provisions for structural steel buildings, Chicago, IL; 2010.

[16] Wu B., and Mei Y., Buckling mechanism of steel core of buckling-restrained braces, Journal of Constructional Steel Research, 2015, 107, pp. 61–69.

[17] Black C. J., Makris N., and Aiken I. D., Component Testing, Seismic Evaluation and Characterization of Buckling Restrained Braces, J. Struct. Eng., 2004, 130(6): pp. 880-894.

[18] Xie Q., State of the art of buckling-restrained braces in Asia, J. Constr. Steel Res., 2005, pp. 727–748.

[19] Wang C., Li T., Chen Q., Wu J., and Ge H., Experimental and Theoretical Studies on Plastic Torsional Buckling of Steel Buckling-restrained Braces, Advances in Structural Engineering, 2015, Vol. 17 No. 6, pp. 871-880.

[20] Yin Z. Z., Feng D. Z., Yang B. and Pan C. C., The seismic performance of double tube buckling restrained brace with cast steel connectors, Advanced Steel Construction, 2022, Vol. 18 No. 1, pp. 436–445. DOI: 10.18057/IJASC.2022.18.1.2.

[21] Takeuchi et al., Estimation of cumulative deformation capacity of buckling restrained braces. Journal of Structural Engineering, 2008, Vol. 134, No. 5, pp. 822– 31.

[22] Korzekwa A. and Tremblay R., Numerical simulation of the cyclic inelastic behavior of buckling restrained braces, In: 6th Int. Conf. on Behaviour of steel structures in seismic areas (STESSA 2009), Philadelphia, The Netherlands,

[23] Dusicka P. and Tinker J., Global Restraint in Ultra-Lightweight Buckling-Restrained Braces, J. Compos. Constr., 2013, 17(1), pp. 139-150.

[24] Aniello M., Corte G. D. and Landolfo R., Finite Element Modelling and Analysis of "All-Steel" Dismountable Buckling Restrained Braces, The Open Construction and Building Technology Journal, 2014, 8, (Suppl 1: M4), pp. 216-226.

[25] Hoveidae N. and Rafezy B., Overall buckling behavior of all-steel buckling restrained braces, J. Constr. Steel Res., 2012, pp. 151–158.

[26] Hoveidae N. and Rafezy B., Local Buckling Behaviour of Core Plate in All-Steel Buckling Restrained Braces, International Journal of Steel Structures, 2015, 15(2), pp. 249-260.

[27] Karimi M. R. B., Yaghin M. A. L., Nezhad R. M., Sadeghi V. and Aghabalaie M., Seismic Behavior of Steel Structure with Buckling-Restrained Braces, International Scholarly and Scientific Research & Innovation 9(4) 2015.

[28] Rossi P. P., Importance of Isotropic Hardening in the Modeling of Buckling Restrained Braces, J. Struct. Eng., 2015, 141(4): 04014124.

[29] Hosseinzadeh Sh. and Mohebi B., Seismic evaluation of all-steel buckling restrained braces using finite element analysis, Journal of Constructional Steel Research, 2016, 119, pp. 76–84.

[30] Almeida A., Ferreira R., Proenca J. M. and Gago A. S., Seismic retrofit of RC building structures with Buckling Restrained Braces, Engineering Structures, 2017, 130, pp. 14–22.

[31] Lin P. C., Takeuchi T. and Matsui R., Seismic performance evaluation of single damped-outrigger system incorporating buckling-restrained braces, Earthquake Engng Struct Dyn., 2018, 47, pp. 2343–2365.

[32] Rahnavard R., Naghavi M., Aboudi M. and Suleiman M., Investigating modeling approaches of buckling-restrained braces under cyclic loads, Case Studies in Construction Materials, 2018, 8, pp. 476–488.

[33] Avci-Karatas C., Celik O. C. and Eruslu S. O., Modeling of Buckling Restrained Braces (BRBs) using Full-Scale Experimental Data, KSCE Journal of Civil Engineering, 2019, 23(10), pp. 4431-4444.

[34] Avci-Karatas C., Celik O. C., and Yalcin C., Experimental investigation of aluminum alloy and steel core buckling restrained braces (BRBs), Int. J. Steel Struct., 2018, Vol. 18, No. 2, pp. 650-673.

[35] Alborzi M., Tahghighi H. and Azarbakht A., Numerical comparison on the efficiency of conventional and hybrid buckling-restrained braces for seismic protection of short-to-mid-rise steel buildings, International Journal of Advanced Structural Engineering, 2019, 11, pp.439–454.

[36] Jamkhaneh M. E., Ebrahimi A. H. and Amiri M. S., Investigation of the Seismic Behavior of Brace Frames with New Corrugated All-Steel Buckling Restrained Brace, International Journal of Steel Structures, 2019, https://doi.org/10.1007/s13296-018-00202-2.

[37] Naghavi M., Rahnavard R., Thomas R. J. and Malekinejad M., Numerical evaluation of the hysteretic behavior of concentrically braced frames and buckling restrained brace frame systems, Journal of Building Engineering, 2019, 22, pp. 415–428.

[38] Tabatabaei S. A. R., Mirghaderi S. R. and Hosseini A., Experimental and numerical developing of reduced length buckling-restrained braces, Engineering Structures, 2014, (77), pp. 143–160.

[39] Hartloper A. R., Sousa A. C. and Lignos D. G., Constitutive Modeling of Structural Steels: Nonlinear Isotropic/Kinematic Hardening Material Model and Its Calibration, J. Struct. Eng., 2021, 147(4): 04021031. DOI: 10.1061/(ASCE)ST.1943-541X.0002964.

[40] Tremblay R., Bolduc P., Neville R. and DeVall R., Seismic testing and performance of buckling restrained bracing systems. Can J Civ Eng 2006;33(1): pp. 183-98.

[41] Chou C. and Chen S., Sub-assemblage tests and finite element analyses of sandwiched buckling restrained braces. Eng Struct 2010;32:2108-21.

[42] Eryasar M., Experimental and numerical investigation of buckling restrained braces, A thesis submitted to the graduate school of natural and applied sciences of middle east technical university, 2009.

[43] Sahoo D. R. and Ghowsi A. F., Experimental Study of All-Steel Buckling-restrained Braces under Cyclic Loading, International conference on earthquake engineering and structural dynamics, 12-14 June 2017, Reykjavik, Iceland.

[44] Lopez W. A. and Sabelli R., Seismic Design of Buckling-Restrained Braced Frames, Structural steel education council, 2004.

Advanced Steel Construction – Vol. 19 No. 3 (2023) 254–261
DOI:10.18057/IJASC.2023.19.3.6

OPTIMIZATION OF STIFFNESS AND DAMPING COEFFICIENTS OF CONNECTION DAMPERS TO REDUCE THE DYNAMIC RESPONSE OF TRANSMISSION LINE STEEL TOWERS SUBJECTED TO WIND ACTION

Luiz Guilherme Grotto [1, *], Letícia Fleck Fadel Miguel [2] and João Kaminski Junior [3]

[1] *Postgraduate Program in Mechanical Engineering (PROMEC), Federal University of Rio Grande do Sul (UFRGS), Porto Alegre, Brazil, ORCID 0000-0002-1392-9033*

[2] *Department of Mechanical Engineering (DEMEC), Federal University of Rio Grande do Sul (UFRGS), Porto Alegre, Brazil, ORCID 0000-0001-9165-4306*

[3] *Department of Structures and Civil Construction (DECC), Federal University of Santa Maria (UFSM), Santa Maria, Brazil, ORCID 0000-0001-9912-0691*

** (Corresponding author: E-mail: luizgrotto@gmail.com)*

ABSTRACT

Tall and slender latticed steel towers, such as power transmission line towers, are very susceptible to vibrations imposed mainly by wind action. Thus, changing the design layout or making use of vibration control devices is often necessary to reduce vibration amplitudes and avoid the collapse of the structure. In this work, an alternative to the conventional types of commercial dampers is the use of elements in the connections of the structure, such as rubber rings working like connection dampers, so they can dissipate the energy of the system reducing the dynamic response of the tower. Thus, this work proposes a methodology for the optimization of stiffness and damping coefficients of connection dampers in structures of latticed steel towers of Transmission Lines (TL) that are subjected to the dynamic effects of wind. An illustrative example is presented. First, the structure is evaluated considering perfectly rigid connections; then the stiffness and damping coefficient of the connections are optimized in order to minimize the vibration amplitudes of the tower. Finally, the natural frequencies, damping ratios and maximum horizontal displacements are compared for situations of perfectly rigid and semi-rigid connections. The results show that the optimization process results in a structure with a fundamental frequency of vibration similar to that of the original tower, however a significant reduction in the horizontal displacements can be observed, since an increase in damping occurs, thus proving the capacity of the proposed methodology.

ARTICLE HISTORY

Received: 8 September 2022
Revised: 21 April 2023
Accepted: 10 May 2023

KEYWORDS

Latticed metallic tower;
Wind action;
Semi-rigid connection;
Dynamic analysis;
Optimization

Copyright © 2023 by The Hong Kong Institute of Steel Construction. All rights reserved.

1. Introduction

Structures such as towers have been the focus of study of many researchers, due to the fact that these structures are very sensitive to vibration effects caused by the wind and earthquakes. With the continuous expansion of the electric power generation and transmission system in Brazil and in the world, and the construction of new towers for telephone and internet services, new challenges are imposed on the designers.

Reduction in manufacturing, assembly and maintenance costs and, above all, the safety that these structures must have, are some of the main reasons for the greatest care in design and execution. The ruin of one of these structures can cause damage, such as the interruption of electricity transmission or telecommunications services. Besides, if they are built close to habitations, they could also cause fatalities.

A simplification that is normally used in the design of a structure is considering the connections between the elements as perfectly rigid or perfectly flexible. Muscolino et al. [1] mention that, in a practical way, if the moment transferred between the elements is sufficiently small – thus it can be neglected – the connections can be considered perfectly flexible. On the other hand, if the moment cannot be ignored, the connections are considered rigid.

However, in a real structure, observing these two extreme cases is practically impossible, since all connections allow some level of rotation and have some rigidity. In this sense, it is correct to state that the connections have a semi-rigid behavior. Zlatkov et al. [2] claim that underestimating the semi-rigidity of the connections and treating them as pinned has a negative impact on the costs of executing the structure, while overestimating, and treating them as rigid, produces results that do not match the reality and go against safety.

Usually, the actions used in the dimensioning of a latticed steel tower are the structure's self-weight, the weight of the transmission cables and antennas and, mainly, the wind action. As the design of towers becomes more and more slender, the natural frequency of vibration of these structures becomes smaller, which makes them more susceptible to wind actions. However, considering the semi-rigid behavior of the connections of a structure can help its dynamic response. Thus, as the semi-rigid connections represent more accurately the behavior of the structure, this is a topic researched by several authors.

Ye and Xu [3] investigated the static and dynamic responses of a steel frame with semi-rigid connections, simulated by a rotational spring of zero length. The authors noted that the resonance effect did not occur. They concluded that this happened due to the large power of dissipation capacity. Another conclusion of the work was that the frame with semi-rigid connections presented a greater resistance to collapse.

By analyzing the dynamic behavior, natural frequencies and vibration modes of a frame in an earthquake, Masoodi and Moghaddam [4] noted that the influence of the semi-rigidity of the connections for the highest acceleration peak values is important because they cause large variations in maximum displacement for rotational flexibility factor of connections close to zero (no rotation restriction). The authors also observed that, as the rotational flexibility approaches to rigid, for each of the analyzed acceleration peaks, the variation of the maximum displacement values becomes insignificant.

Similar results were achieved by Raftoyiannis and Polyzois [5], who studied the dynamic characteristics of a pole composed of two parts. The parts are joined with a resin, and the connection formed is considered semi-rigid. The authors performed a modal analysis and an experimental study exciting the structure. The results obtained showed that, as the stiffness of the connection increases, the influence of semi-rigidity on the dynamic characteristics decreases. This is due to the fact that after a certain level of rigidity, the connection starts to reach an almost perfect rigidity behavior.

Basiński and Kowal [6] performed a forced harmonic dynamic analysis on beams composed of the union of two bars with a semi-rigid connection and analyzed the displacement amplitudes in the middle of the beam. The effect of varying the rotational stiffness in the connection on the damping of the structure was also analyzed. The author demonstrated that, by reducing the rotational stiffness of the connections, the magnitude of the displacement amplitude also decreased. However, the author states that the increase in the stiffness of the connection leads to a decrease in damping, ushering the beam to reach greater displacement amplitudes in the harmonic excitation. Basiński and Kowal [6] also mention that, as semi-rigid connections regulate displacement amplitudes, they can act as vibration dampers for cyclical actions, such as wind gusts.

Daryan et al. [7] analyzed numerically a steel frame with two types of semi-rigid connections (top and seat angle with and without web angle) against an earthquake record. It has been shown that the top and seat angle with web angle reduced the relative displacement between the floors, and increased the structure's energy absorption capacity. The authors also concluded that the connection of a top and seat angle with a web angle is a suitable alternative for strengthening vibration-sensitive structures.

Wang et al. [8] also studied the effect of the semi-rigidity of connections against earthquakes and conducted an experimental study on tubular steel frames filled with concrete with bolted connections. The tests demonstrated excellent power dissipation capability.

Hao-Xiang He et al. [9] presented an experimental study in which it is inserted parts of low-yield-point steel in the connections of a structure. The low-yield-point steel proved to be more suitable than other types of ordinary steel in energy dissipation. Also, the authors concluded that it dissipates energy by deforming (protecting the main structure) and, after the dynamic force stops

acting, maintenance can be quickly performed.

In this sense, dampers are usually used to reduce problems related to excessive vibration. However, the use of industrial dissipation devices implies a higher cost in the work. As an alternative, some authors suggest the use of elements with high energy dissipation capacity in the structural connections in order to improve the dynamic response.

Zlatkov et al. [2] determined the matrices of beam elements with semi-rigid connections at both ends through the stationary potential energy function. Afterward, the authors conducted a numerical study applying an earthquake to a structure and varying the stiffness level of the connections. Results showed significant differences regarding the natural frequency of vibration, design forces and horizontal displacement. According to the authors, this demonstrates the importance of using the real stiffness of the connection in the calculation step for any engineering structure. Another configuration also used to consider semi-rigidity is to insert high flexibility elements in the connection or in some section of the structure. This alternative not only makes the connection semi-rigid, but also increases the structure's energy dissipation capacity.

Sekulovic et al. [10] studied the energy dissipation of a frame considering connections such as rotational springs and viscous rotational dampers. In that work, the stiffness matrix of the structure for this configuration was deduced and a parametric study was conducted. The authors demonstrated that frames with semi-rigid connections combined with connection dampers presented a more significant decay in displacement amplitude when compared to rigid connections.

Cacciola et al. [11] performed a deterministic and stochastic sensitivity analysis of the dynamic response of a frame with semi-rigid connections combined with connection dampers. Dampers are represented by elements whose behavior follows the Kevin-Voigt model. The authors noted that, in some situations, even with a small variation of the damping of the connection, the response can have large differences.

Attarnejad et al. [12] analytically evaluated the performance against a high-intensity earthquake of a structure with semi-rigid connections and energy dissipation elements. The authors observed that the greater the stiffness of the connection, the greater the initial overall stiffness of the structure. Furthermore, it was also observed that there is an optimal damping coefficient that can significantly reduce the dynamic response of frames with semi-rigid connections. The authors also point out that semi-rigid connections with connection dampers are significant in the design of structures resistant to earthquakes.

Yanxia Zhang et al. [13] and Meng-Yao Cheng et al. [14] presented an experimental study by adding columns with and without dampers in steel frames and observed that the structures with dampers perform better against dynamic action due to a better capacity of energy dissipation.

Köroğlu et al. [15] also studied connection dampers as an option to reduce the effects of seismic loads on the structural system. The results showed that, when loads and moments reached critical levels, the connection dampers acted and no damage was observed on the beam and column.

As already mentioned, the limitation of costs around the project requires that it has the best performance with the available resources. To achieve this, it employs the use of optimization, maximizing or minimizing a function, by applying computational simulations.

In order to use the device in the best possible way, that is, with lower cost and greater power dissipation capacity, many authors have studied the optimization of these devices. The use of optimization aims at finding the properties of devices; and/or the best positions for the device within the structure; and/or the ideal number of devices to obtain the best scenarios they can provide, thus reducing the effect of dynamic actions and prolonging the service life of the structure in which they are installed. Singh and Moreschi [16] point out that even a small increase in damping can be relevant, as slender structures have an extremely low damping value.

Generally, studies related to damping optimization are carried out on commercial dampers. For example, Si et al. [17] studied the optimization of the position and properties of a Tuned Mass Damper (TMD), in order to reduce the dynamic effects in an offshore wind power generation tower. The study showed that, by applying adequate properties and positioning the TMD above water, it is possible to reduce the effects caused by dynamic actions moderately, while improving the effectiveness of energy generation. Other examples of TMD optimization in different types of structures subjected to different types of dynamic excitation can be found in [18-27].

Mensah and Dueñas-Osorio [28] analyzed a Tuned Liquid Column Damper (TLCD) to provide greater reliability for wind power towers against excessive wind-induced vibrations. Results showed that the shock absorber used is a viable possibility, since it is cheaper and able to provide greater safety, as well as a useful life for these towers.

Zhang et al. [29] also analyzed vibrations in wind energy towers, and studied dampers to reduce the effects of vibration on turbine blades. The aim of the study was to optimize the damper mass, frequency, coefficient of friction and position. Results showed that the best conditions to achieve vibration reduction are to increase the damper mass and position it close to the free end of the structure.

Regarding friction dampers, the works by [30-38] can be highlighted, which propose different methodologies for optimizing these devices when applied to different structures subjected to different dynamic actions.

Ribakov and Reinhorn [39] presented a study based on the optimization of the damping of a structure by viscous dampers in a lever system. The authors conducted a numerical example and concluded that peak displacements were reduced to levels between 40% and 75%. Still, there was a notable gain in energy dissipation, thus indicating that the application of dampers can be an alternative for the recovery of structures sensitive to earthquakes.

As demonstrated in the works above, the use of optimization algorithms to assist in the design of external energy dissipation devices has been the focus of research by several authors, who propose modifications in the properties of dissipation devices in order to reduce the dynamic response of the structure to different excitations. However, there have been few studies on the optimization of the dynamic characteristics of structures with semi-rigid connections formed by less rigid elements, such as rubber rings, acting as an energy dissipation device (connection damper).

Thus, for the reasons mentioned so far, as well as for the lack of research on the subject, the present work proposes a methodology for the optimization of connection dampers inserted in the connections of a steel transmission line tower subjected to the dynamic action of synoptic winds (EPS winds), aiming to reduce the maximum displacement of the structure, that is, to improve its dynamic response.

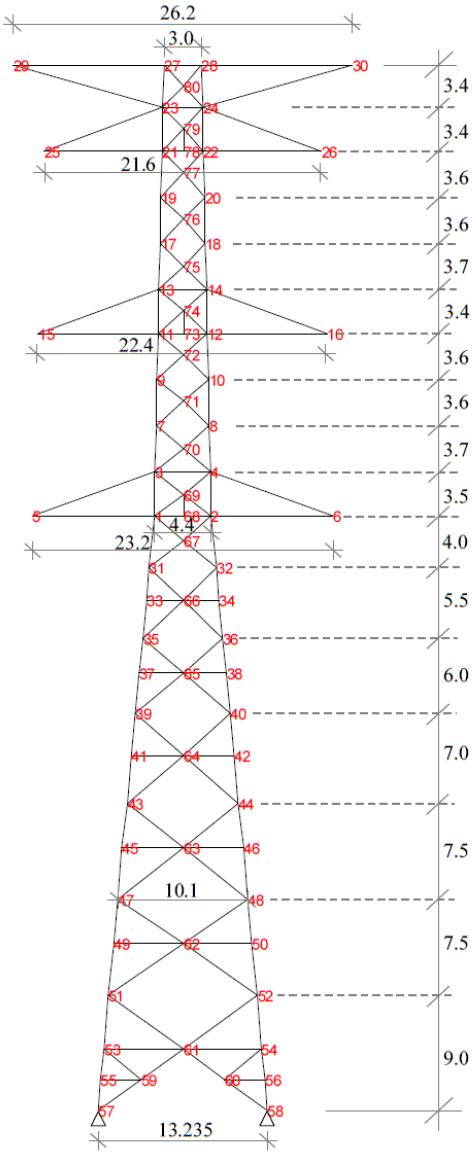

Fig. 1 Transmission tower - dimensions (in meters) and number of nodes. [41]

2. Definition of the structure

To illustrate the methodology proposed in this work, a real power transmission line tower (Fig. 1) damaged during a typhoon in Japan is studied. This structure has already been studied by Murotsu et al. [40] and Miguel and Fadel Miguel [41] in different contexts.

The structure is a silhouette of an 82-meter-high tower, with a base of 13.235 meters, and it is formed by angle profiles. The tower is modeled with 80 nodes and 163 2D frame elements. The representation of the tower with its nodes and dimensions is presented in Fig. 1.

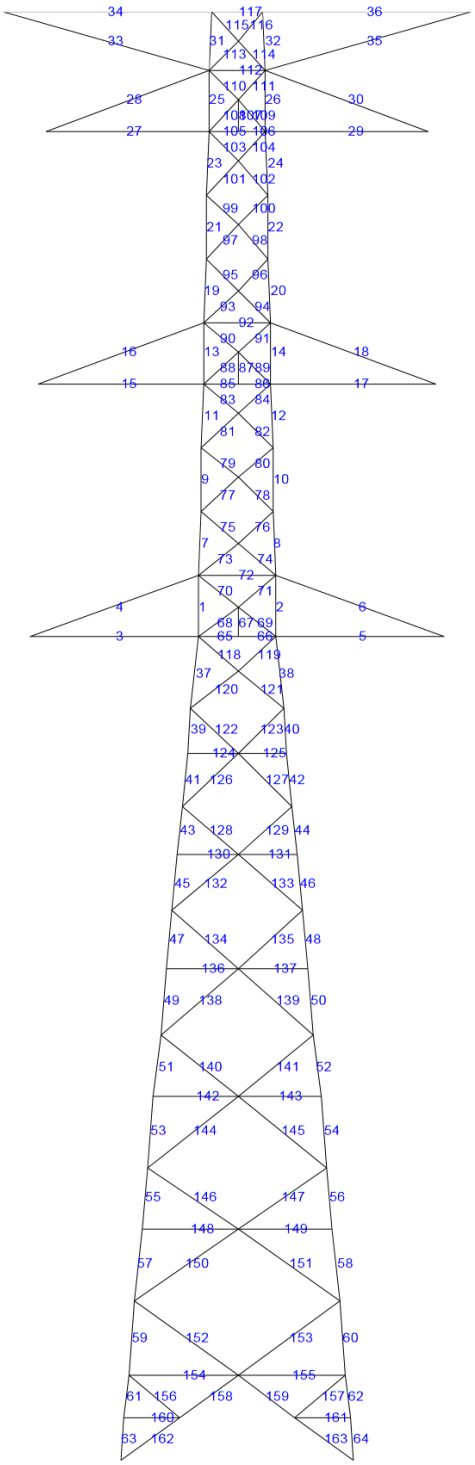

Fig. 2 Transmission tower - number of elements. [41]

In this study, it is assumed that: (i) the tower is located in the city of Chuí (RS, Brazil), unlike the original structure, located in Japan; (ii) the structure has a completely rigid base; (iii) the presence of cables is simulated by adding masses in some nodes of the structure. The corresponding mass value and the nodes where they are added were given by [40] and [41] and are presented in Table 1.

Table 1
Nodal masses added to the structure

Nodes	Mass (kg)
5, 6	1550
15, 16	1550
25, 26	1550
29, 30	130

The tower is formed by 11 different angle profiles, which have been adapted to Brazilian commercial angle profiles taken from [42], and the material used in the profiles of the structure is steel ASTM A36. The geometrical properties of the angle profiles are presented in Table 2 and the profile used in each element of the structure is presented in Table 3. The number of each element is presented in Fig. 2.

Table 2
Geometrical properties of the angle profiles

Number	Profile (mm)	Area (cm^2)	Moment of inertia (cm^4)
1	20.32 x 20.32 x 1.905	73.81	2901.1
2	20.32 x 20.32 x 1.588	62.9	2472.4
3	12.70 x 12.70 x 0.952	23.29	362
4	10.16 x 10.16 x 0.794	15.48	154
5	15.24 x 15.24 x 1.270	37.09	828
6	15.24 x 15.24 x 1.588	45.86	1007
7	15.24 x 15.24 x 1.905	54.44	1173
8	5.08 x 5.08 x 0.952	8.76	20
9	6.35 x 6.35 x 0.794	9.48	35
10	10.16 x 10.16 x 0.635	12.51	125
11	4.445 x 4.445 x 0.794	6.45	11.2

Table 3
Angle profile of each element used in the structure

Number	Element
1	1-8, 15-18, 27-30, 33-36
2	9-12, 65-67, 72, 85-87, 92, 105-107, 112, 117
3	13, 14, 19, 20
4	21-26, 31, 32
5	37-46
6	47-54
7	55-64
8	68-71, 73-84, 88-91, 93-104, 108-111, 113-116, 118-131, 136, 137, 142, 143, 148, 149, 156, 157
9	132-135, 138-141, 146, 147, 154, 155, 158, 159, 162, 163
10	144, 145, 150-153
11	160,161

The damping matrix is considered proportional to the mass and stiffness matrices, according to Eq. (1), and a damping ratio of 0.5% is considered for the first two modes.

$$C_M = \alpha M_M + \beta K_M + CM \tag{1}$$

in which M_M , C_M and K_M are the mass, damping coefficient and stiffness matrices of the structure, respectively, CM is the global damping coefficient matrix of the connections dampers and α, β are constants.

Two configurations of connections are studied in this paper. The first one considered that all bolted connections are perfectly rigid. The second one considered that all bolted connections with connection dampers have a semi-rigid behavior. The configurations are called rigid and semi-rigid, respectively. For both configurations, the bolted connections between elements that represent the main legs of the tower are considered rigid.

3. Definition of the connection damper

The connection damper is represented by an element with zero length, and it works as a connection between two 2D frame elements. As it is a 2D element, the connection damper has stiffness and damper coefficient in all three degrees of freedom and it can be exemplified as a system of spring and damper. Therefore, it can be depicted by two translational parts that represent the horizontal and vertical displacements, and one rotational part that represents the angular displacement. The depiction of the connection damper's parts is presented in Fig. 3.

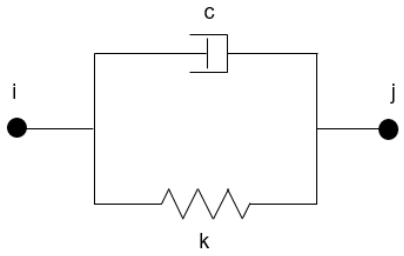

(a) Translational part

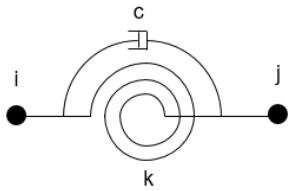

(b) Rotational part

Fig. 3 Connection damper

As the length of the connection damper is zero, the end node of the first 2D frame element is superimposed (same position) with the start node of the second 2D frame element that makes up the connection. Furthermore, as the mass of this element is insignificant compared to the mass of the structure, its addition can be ignored.

Each element has stiffness in all three degrees of freedom. If it is necessary for the connection to have a perfectly rigid behavior, it assumes a very high value for the spring stiffness. If the connection has a perfectly flexible behavior, the spring assumes a stiffness equal to zero.

The stiffness matrix of the spring part of the element used in this study is defined by Eq. (2).

$$KM = \begin{bmatrix} KU_X & 0 & 0 & -KU_X & 0 & 0 \\ & KU_Y & 0 & 0 & -KU_Y & 0 \\ & & KROT_Z & 0 & 0 & -KROT_Z \\ & & & KU_X & 0 & 0 \\ & sym & & & KU_Y & 0 \\ & & & & & KROT_Z \end{bmatrix} \quad (2)$$

in which KU_X and KU_Y are the translational stiffness in relation to the X and Y axis, respectively. Also, $KROT_Z$ is the rotational stiffness in relation to the Z axis.

The stiffness values for the three degrees of freedom are already calculated and applied in relation to the global coordinates, so the coordinate transformation matrix is unnecessary.

The damping coefficient matrix of the damper part of the element used in this study is defined by Eq. (3).

$$CM = \begin{bmatrix} CU_X & 0 & 0 & -CU_X & 0 & 0 \\ & CU_Y & 0 & 0 & -CU_Y & 0 \\ & & CROT_Z & 0 & 0 & -CROT_Z \\ & & & CU_X & 0 & 0 \\ & sym & & & CU_Y & 0 \\ & & & & & CROT_Z \end{bmatrix} \quad (3)$$

in which CU_X and CU_Y are the translational damping coefficient in relation to the X and Y axis, respectively. Also, $CROT_Z$ is the rotational damping coefficient in relation to the Z axis.

Like the stiffness matrix, the damping coefficient matrix already has its coefficients in global coordinates, and the coordinate transformation matrix is unnecessary. Besides, if the connection is not responsible for any part of the damping ratio of the structure, it assumes that the damper part is null. On the other hand, if the connection assists the damping of the structure, the damper part is not null.

The stiffness and damping coefficient matrices are the matrix of the element CONBIN40, the spring element from ANSYS [43].

For the connection dampers to be considered to be made of the same material, the translational stiffness in both X and Y axes must be the same for any inclination of the structure bars. To do so, the values of KU_X and KU_Y must be equal. In relation to the damping coefficients, it is considered that the material has the same energy dissipation capacity for each of the degrees of freedom analyzed. Therefore, the values of CU_X , CU_Y and $CROT_Z$ are also identical.

When the connections of the structure are considered rigid, the CM matrix is considered null. In the second case, which considers the semi-rigid behavior of the connections, the CM matrix assumes the values of the damping coefficients of the connection dampers.

4. Definition of wind action

The structure is evaluated as if it were installed in Brazil, in the state of Rio Grande do Sul, in the city of Chuí, in a place with flat and open terrain, with few obstacles and isolated. The tower is planned to support transmission lines to the city, and its collapse does not affect people's safety, once it is located in a land with few obstacles.

The city of Chuí was chosen as the location for the installation of the structure because this is the region with one of the highest mean wind velocities in Brazil.

The wind action is subdivided into two parts: the mean static portion and the floating one. Before proceeding to the calculation of forces, it is interesting to determine both static and floating portions of wind velocity, then determine the definitive wind forces that are acting on the structure. Once the velocities are determined, the process of calculating the forces is identical for the static and floating portions.

To determine the mean static wind velocity acting on the structure of a latticed tower, the procedure described in NBR 6123/1988 [44] is used. To simulate the floating portion of the wind, the Davenport power spectrum is used and the Shinozuka and Jan method [45], also known as the spectral representation method, is used to simulate a random process through a series of cosines to produce the sample functions. This function is used as the basis for generating the spectral density sample.

To determine the floating components, the method proposed by Miguel et al. [46] is employed. The frequency range of the analysis is from 0.01Hz to 5Hz, with an interval Δf of 0.01Hz; and the time range is from 0s to 100s, with an interval Δt of 0.02s.

Furthermore, to calculate the floating wind velocity at different heights, it is necessary to determine the correlation length. Eq. (4) by [46] empirically relates the correlation length with the height of the studied structure. This equation is estimated through a linear regression obtained in relation to different heights and surface roughness presented in Fig. 4.

$$a = 0.93z + 29.3 \quad (4)$$

in which a is the correlation length and z is the height above the ground.

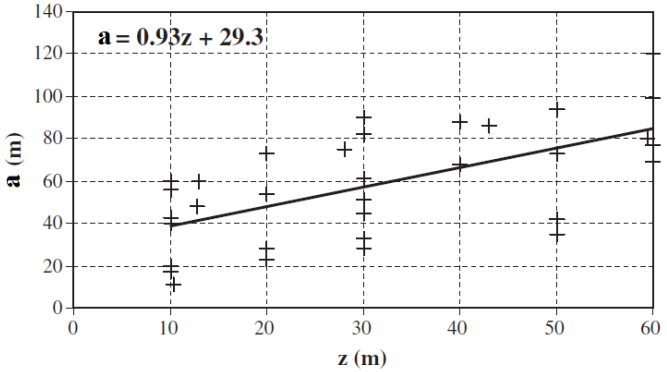

Fig. 4 Vertical correlation length [46]

Thus, it is possible to generate the floating components at points spaced apart by a correlation length and the intermediate components by means of interpolation according to Eq. (5).

$$V_f(z, f) = V_1(t) + \frac{V_2(t) - V_1(t)}{a} z \tag{5}$$

in which $V_1(t)$ and $V_2(t)$ are the wind velocity in height zero and a , respectively.

In possession of the velocity field for both mean static and floating parts, the total wind velocity is given by Eq.(6).

$$V_t(z,t) = V_S(z) + V_f(z,t) \tag{6}$$

in which $V_S(z)$ and $V_f(z,t)$ are the mean static wind velocity and the floating one, respectively.

As this study analyzes a 2D frame structure, an area might be supposed to generate the wind force profile. It is assumed that the lateral silhouette of the structure is the same as the front silhouette without the braces. Fig. 5 features a front and side view layout for some nodes.

After determining the influence area for all the different heights, it is possible to calculate the drag forces applied in the structure according to NBR 6123/1988 [44].

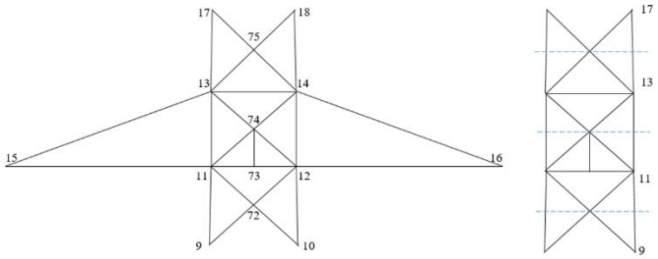

(a) Frontal view (b) Lateral view

Fig. 5 Example of a section's frontal and lateral views

5. Optimization process

In this study, the objective function is to minimize the maximum horizontal displacement at the top of the structure. The design variables are the stiffness and damping constants of the elements inserted in the connections (connection dampers). To carry out the optimization proposed in this work, the Whale Optimization Algorithm (WOA) developed by Mirjalili and Lewis [47] is implemented.

The optimization study is carried out on the structure so that it has the smallest maximum horizontal displacement possible. For this, the stiffnesses KU_X , KU_Y and $KROT_Z$, and damping constants CU_X , CU_Y and $CROT_Z$ of the connection damper are modified for each optimization step. As previously mentioned, the stiffnesses KU_X and KU_Y are identical, as are the damping constants CU_X , CU_Y and $CROT_Z$. Therefore, optimization is performed by modifying three parameters.

A flowchart of the optimization process is presented in Fig. 6.

6. Proposed methodology

At first, the structure is studied without the connection dampers, and its connections are considered rigid. A modal analysis is performed and its natural frequencies of vibration are determined. Then, an EPS wind (a synoptic wind) is applied to the structure, and the horizontal displacements during the entire period of action and the damping ratios related to each of the structure's natural frequencies are determined. Fundamental natural frequency, damping ratio and maximum horizontal displacement data are stored for future comparison.

Subsequently, connection dampers are inserted into the structure's connections. At this moment, through the optimization process, the stiffness and damping coefficient of the connection dampers are optimized so that the maximum horizontal displacements are minimized. The natural vibration frequency, the damping ratio and the maximum horizontal optimized displacements are compared to that of the previous situation, in which the structure does not have the added damping from the connection dampers.

But it is important to note that not all the connections receive the connection dampers. The connections between the elements of the main legs are considered rigid in both configurations. All the other connections (diagonal bracing – main leg, diagonal bracing – horizontal bracing, diagonal bracing – diagonal bracing, horizontal bracing – main leg, horizontal bracing – horizontal bracing, cross arm – main leg and cross arm – cross arm) are considered semi-rigid with a connection damper between the elements.

The optimization of the connection dampers is carried out by using the WOA (metaheuristic algorithm programmed in MATLAB), and the natural frequencies and the vibration modes are obtained through an algorithm elaborated using the finite element method, solving the eigenproblem of the system. For the structure with perfectly rigid connections, the damping ratio used for the first two modes of vibration is 0.5%, as a function of the structure's natural damping, while for the structure with connection dampers, the damping ratio is calculated by the equations of uncoupled motion. The generation of the wind field velocities and forces, as well as the calculation of the structure's dynamic response, which allows the determination of the maximum horizontal displacement, are performed in computational routines developed in this work. The dynamic response of the structure is determined by using the Newmark method. All calculations and algorithms are developed in MATLAB language.

To impose a limit on the allowable displacement, the maximum horizontal displacement value during the entire application of wind action on the structure must not exceed 1% of the total height of the structure. The reference value applied in this work was used by [48] to define the maximum transverse or longitudinal displacement for the service limit state of a latticed metal tower of transmission lines.

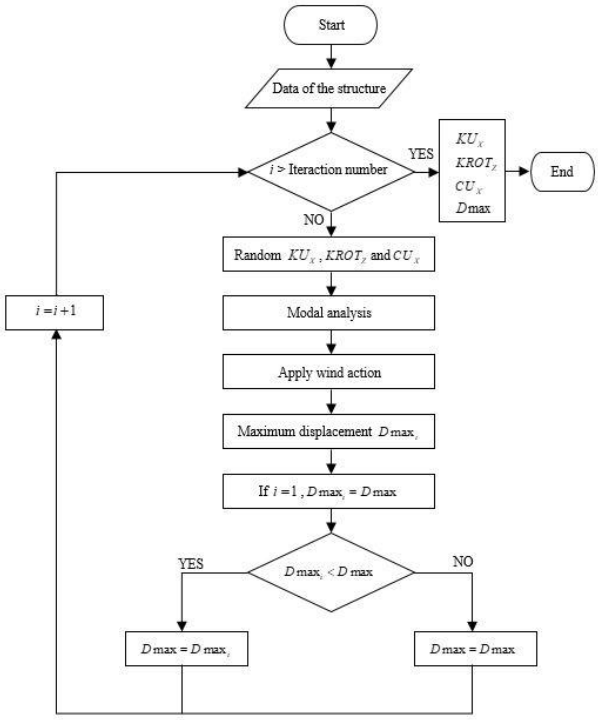

Fig. 6 Flowchart of the optimization process

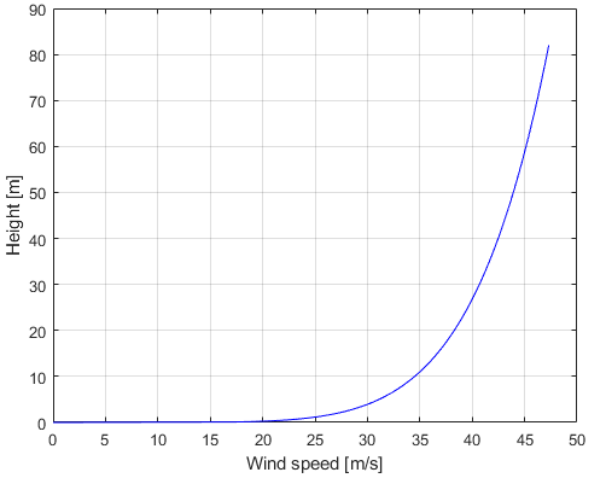

Fig. 7 Mean static wind velocity

7. Results and discussion

7.1. Wind force

The mean static wind velocity for all heights of the structure, determined by the procedure of NBR 6123/1988 [44], is presented in Fig. 7.

Knowing that the height of the structure is 82 meters and using Eq. (4), the correlation length becomes $a = 105.56m$.

As the correlation length is higher than the tower's height, only two signals generated by the spectral representation method are necessary to create the floating wind velocity field: one for the height of zero (ground), and the other for the height of the correlation length (105.56m). All floating wind velocities for the intermediate points are given by Eq. (5).

With the mean static and floating wind velocities portions, it is possible to determine the total wind velocity acting on each node of the tower. For instance, Fig. 8 shows the wind velocity at node 27 throughout the analysis period.

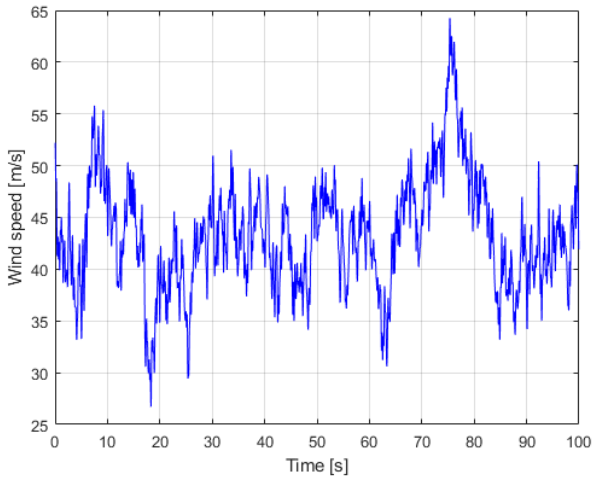

Fig. 8 Wind velocity at node 27

With the total wind velocity for all heights of the structure and the influence areas for all nodes, the total drag forces can be calculated according to NBR 6123/1988 [44]. For instance, Fig. 9 shows the drag force at node 27 throughout the analysis period.

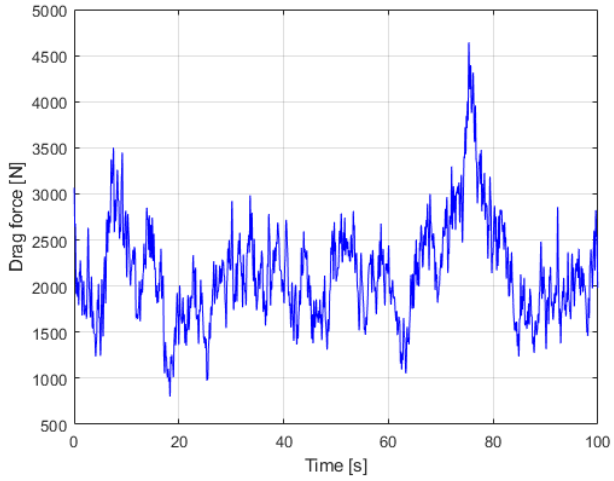

Fig. 9 Drag force at node 27

7.2. Structure with rigid connections

The modal analysis is conducted on the structure presented in Fig. 1, which was modeled in a program developed in MATLAB. As the developed program has a connection element in all points that bracing meets the main legs, for the perfect rigid connections without connection dampers, the stiffness in all degrees of freedom has a big value and the damping coefficient is null, as presented in Table 4.

Table 4
Stiffness and damping coefficient for rigid connections

Degree of freedom	Stiffness	Damping coefficient
U_X	1E12 $N{\cdot}m^{-1}$	0 $N{\cdot}s{\cdot}m^{-1}$
U_Y	1E12 $N{\cdot}m^{-1}$	0 $N{\cdot}s{\cdot}m^{-1}$
ROT_Z	1E12 $N{\cdot}m{\cdot}rad^{-1}$	0 $N{\cdot}s{\cdot}m{\cdot}rad^{-1}$

The value used in the stiffness for the three degrees of freedom is enough for the connections to be considered perfectly rigid. This value is validated by comparing the results obtained with the ANSYS program, simulating the same structure with rigid connections without connection elements.

The natural frequencies for the first three mode shapes, as well as the structure damping ratios, are presented in Table 5. The structure damping ratio, as already mentioned, is 0.5% for the first two vibration modes.

Table 5
Natural frequency and damping ratio for rigid connections

Vibration mode	Natural Frequency (Hz)	Damping ratio (%)
1	0.6187	0.5
2	2.0167	0.5
3	3.8458	0.79

Subsequently, the wind action is applied to the structure and, through the Newmark method, a dynamic analysis is performed. The wind force profile on the structure was determined in Section 7.1. Fig. 10 shows the horizontal displacements at the top of the structure (node 27).

As can be seen in Fig. 10, the maximum displacement at the top of the tower (node 27) with rigid connections is 0.9173m ($D\max = 0.9173m$).

7.3. Structure with semi-rigid connections

In this step, the connections are considered semi-rigid and, via the optimization process, the values of stiffness and damping coefficient of the connection dampers are defined. The objective function is to minimize the maximum horizontal displacement of the structure, changing the stiffness and damping coefficient of the connection dampers. The wind action applied to the structure was the same that was already applied to the configuration of rigid connections.

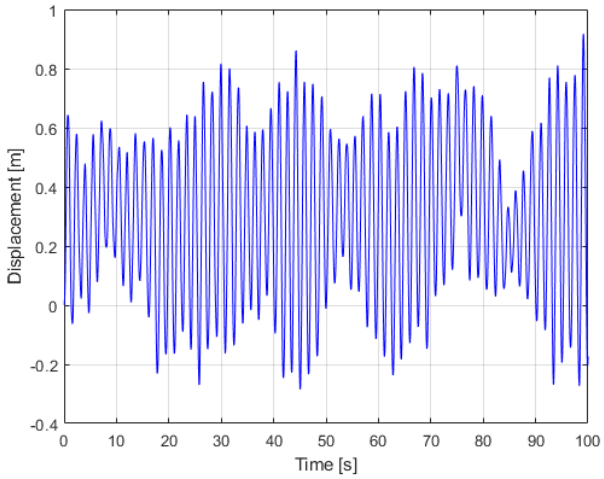

Fig. 10 Horizontal displacement at node 27 with rigid connections

The convergence curve of the optimization process is shown in Fig. 11, in which can be seen that the maximum displacement at the top of the tower (node 27) converges to its minimum value of 0.7056m ($D\max = 0.7056m$), in iteration number 67.

The results of the stiffness and damping coefficient of the connection dampers obtained in the optimization process are given in Table 6.

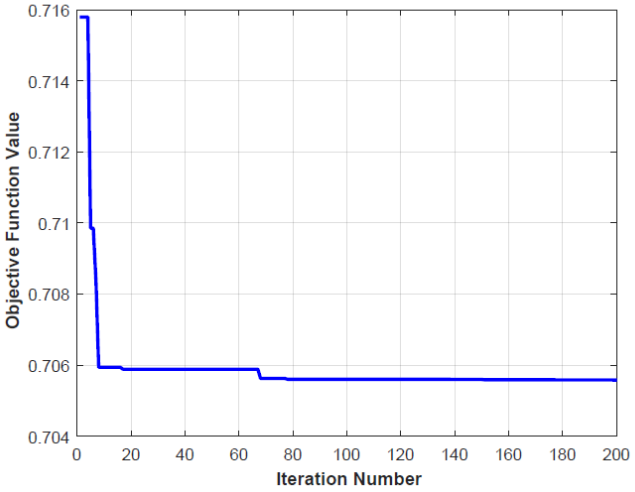

Fig. 11 Convergence curve

Table 6
Stiffness and damping coefficient for semi-rigid connections

Degree of freedom	Stiffness	Damping coefficient
U_X	6.7035$E7$ $N{\cdot}m^{-1}$	4.264$E7$ $N{\cdot}s{\cdot}m^{-1}$
U_Y	6.7035$E7$ $N{\cdot}m^{-1}$	4.264$E7$ $N{\cdot}s{\cdot}m^{-1}$
ROT_Z	1.4633$E7$ $N{\cdot}m{\cdot}rad^{-1}$	4.264$E7$ $N{\cdot}s{\cdot}m{\cdot}rad^{-1}$

With the optimum configuration of connection dampers, a modal analysis is conducted in the same way for the case of the structure with perfectly rigid connections. The first three natural frequencies as well as the structure damping ratios are presented in Table 7.

Then, the wind action is applied to the structure and a dynamic analysis is conducted. The wind force profile is the same applied in the configuration of rigid connections.

Table 7
Natural frequency and damping ratio for semi-rigid connections

Vibration mode	Natural Frequency (Hz)	Damping ratio (%)
1	0.6011	7.44
2	1.7096	115
3	2.8061	336

The horizontal displacements at the top of the structure (node 27) are shown in Fig. 12, in which can be seen that the maximum displacement at the top of the tower (node 27) with semi-rigid connections is 0.7056m ($D\max = 0.7056m$).

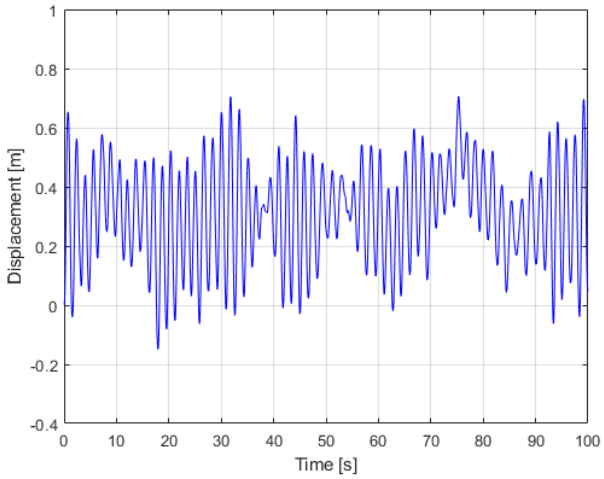

Fig. 12 Horizontal displacement at node 27 with semi-rigid connections

7.4. Comparison of results

The comparison of results for both rigid and semi-rigid connections is presented in Table 8, and the comparison of the horizontal displacements at the top of the structure (node 27) is presented in Fig. 13.

Table 8
Comparison of results for both rigid and semi-rigid connections

Data	Rigid	Semi-rigid	Difference
Fundamental frequency (Hz)	0.6187	0.6011	-2.84%
Damping ratio $(\%)$	0.5	7.44	1388%
Maximum horizontal displacement (m)	0.9173	0.7056	-23.08%
KU_X and KU_Y $(N{\cdot}m^{-1})$	1E12	6.7035E7	-
$KROT_Z$ $(N{\cdot}m{\cdot}rad^{-1})$	1E12	1.4633E7	-
CU_X , CU_Y $(N{\cdot}s{\cdot}m^{-1})$	0	4.264E7	-
$CROT_Z$ $(N{\cdot}s{\cdot}m{\cdot}rad^{-1})$	0	4.264E7	-

As can be seen in Table 8, comparing the results obtained, it is possible to notice that, by inserting a semi-rigidity in the connection, there is a small reduction (2.84%) in the fundamental frequency of the structure, however the damping ratio increases considerably (1388%), causing the maximum horizontal displacement at the top of the tower to be reduced by 23.08%.

Initially, the structure did not meet the maximum horizontal displacement requirements at the top of the Brazilian standard NBR8850/2003 [48], exceeding it by approximately ten centimeters (11.87%). However, after adding the connection dampers to the structure, the maximum horizontal displacement decreased by approximately twelve centimeters (13.95%) in relation to the standard limit [48].

Still, looking at Fig. 13, it is possible to visually notice that all horizontal displacements decreased. This indicates that the presence of the connection dampers also helps to reduce the displacement amplitude throughout the period of application of the wind force.

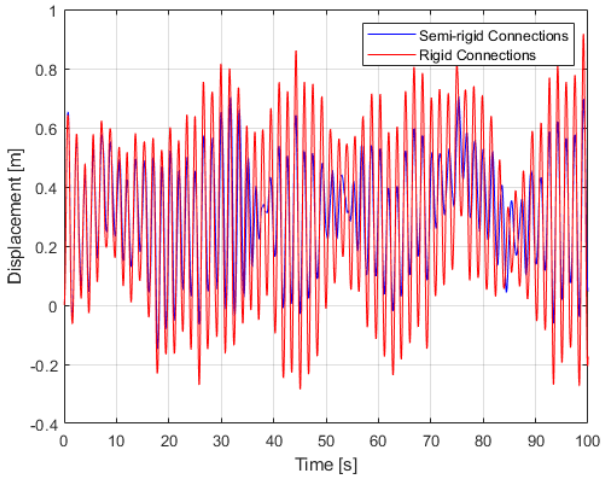

Fig. 13 Comparison of displacement at node 27 for both rigid and semi-rigid connections

8. Conclusions

The use of energy dissipation devices to minimize the effect of high displacements on structures susceptible to vibrations is widely studied. However, the vast majority of these studies are related to the addition of active or passive external dampers in the original structure. On the other hand, few studies focus on the research of the semi-rigidity of connections by inserting connection dampers to improve energy dissipation.

Thus, in order to reduce the dynamic response of a steel tower, in the present work, the insertion of connection dampers was proposed. A methodology to optimize the stiffness and damping constants of the connection dampers was proposed, minimizing the dynamic response of the structure.

Regarding the fundamental frequency of vibration, it was possible to notice that the frequency remains very similar to the one of the original structure, even with the decrease in translational and rotational rigidity, not allowing the dynamic action of the wind to be amplified.

Through the evaluation of the damping ratio in these two connection

configurations, it was possible to notice a huge increase in relation to the original damping (1388%). This indicates that the presence of connection dampers in the structure improves the energy dissipation of the system.

Regarding the maximum horizontal displacement values, there was an important decrease in these values. The damping coefficient inserted in the connections was responsible for decreasing the maximum horizontal displacement at the top of the structure by approximately 23%.

Initially, the structure did not meet the maximum horizontal displacement requirements at the top required by the technical standard and exceeded it by approximately 12%. However, after adding the connection dampers, the maximum horizontal displacement decreased by approximately 14% in relation to the stipulated maximum limit, and 23% in relation to the horizontal displacement with rigid connections.

Comparing the results obtained for the structure with rigid and semi-rigid connections, it was possible to perceive that the structure has improved its performance against wind action, with more flexible elements in the connections.

Thus, it is believed that the methodology proposed in this work can be an excellent alternative to reduce the dynamic response of steel structures.

Acknowledgments

The authors are grateful for the financial support of CNPq and CAPES.

References

[1] Muscolino G., Palmeri A. and Recupero A., “Seismic analysis of steel frames with a viscoelastic model of semi-rigid connections”, Proceedings of the 13th World Conference on Earthquake Engineering (WCEE 2004), Vancouver, British Columbia, Canada, Paper Number 2783, 2004.

[2] Zlatkov D., Zdravković S., Mladenović B. and Stojić R., “Matrix formulation of dynamic design of structure with semi-rigid connections”, Facta Universitatis, series: Architecture and Civil Engineering, 333(5), 89-104, 2011.

[3] Ye J. and Xu L., “Member discrete element method for static and dynamic responses analysis of steel frames with semi-rigid joints”, Applied Sciences, 7(7), 714, 2017.

[4] Masoodi A. R. and Moghaddam S. H., “Nonlinear dynamic analysis and natural frequencies of gabled frame having flexible restraints and connections”, KSCE Journal of Civil Engineering, 19(6), 1819-1824, 2015.

[5] Raftoyiannis I. G. and Polyzois D. J., “The effect of semi-rigid connections on the dynamic behavior of tapered composite GFRP poles”, Composite Structures, 81(1), 70-79, 2007.

[6] Basiński W. and Kowal Z., “Analysis of oscillatory motion of SIN girders with semirigid joints”, Architecture Civil Engineering Environment, 9(4), 55-65, 2016.

[7] Daryan A. S., Sadri M., Saberi H., Saberi V. and Moghadas A. B., “Behavior of semi-rigid connections and semi-rigid frames”, The Structural Design of Tall and Special Buildings, 23(3), 210-238, 2014

[8] Wang J. F., Wang J. and Wang H., “Seismic behavior of blind bolted CFST frames with semi-rigid connections”, Structures, 9, 91-104, 2017.

[9] Hao-Xiang H., Li-Can L. and Shi-Tao C., “Damping performance experiment and damage analysis of replacement connection with low-yield-point steel”, Adv. Steel Constr., 17 (2), 169-180, 2021.

[10] Sekulovic M. S., Salatic R. M. and Mandic R. S., “Seismic analysis of frames with semi-rigid eccentric connections”, Proceedings of the 12th World Conference on Earthquake Engineering (WCEE 2000), Auckland, New Zealand, 2000.

[11] Cacciola P., Colajanni P. and Muscolino G., “Stochastic sensitivity of steel frames with connection dampers by modal analysis”, Proceedings of the 20th International Modal Analysis Conference (IMAC 2002), Los Angeles, California, USA, 2002.

[12] Attarnejad R., Ghareshiran M. R. and Pirmoz A., “Seismic performance of semi-rigid frames with connections dampers”, Proceedings of the 8th National Congress on Civil Engineering (8NCCE), Babol, Iran, 2014.

[13] Zhang, Y.X., Lui, A.R., Zhang, A.L. and Liu, X.C., “Seismic performance analysis of a resilient prestressed steel frame with intermediate column containing friction dampers”, Adv. Steel Constr., 13 (3), 241-257, 2017.

[14] Meng-Yao Cheng et al., “Experimental study of hysteretic behavior of resilient prefabricated steel frames with and without intermediate columns”, Adv. Steel Constr., 18 (3), 715-727, 2022.

[15] Köroğlu M. A., Köken A. and Dere Y., “Use of different shaped steel slit dampers in beam to column connections of steel frames under cycling loading”, Adv. Steel Constr., 14 (2), 251-273, 2018.

[16] Singh M. P. and Moreschi L. M., “Optimal placement of dampers for passive response control”, Earthquake Engineering & Structural Dynamics, 31, 955-976, 2002.

[17] Si Y., Karimi H. R., Gao H., “Modelling and optimization of a passive structural control design for a spar-type floating wind turbine”, Engineering Structures, 69, 168-182, 2014.

[18] Brandão F da S, Miguel LFF. Vibration control in buildings under seismic excitation using optimized tuned mass dampers. Frattura ed Integrità Strutturale 2020;14(54):66-87. https://doi.org/10.3221/IGF-ESIS.54.05

[19] Brandão F da S, de Almeida AK, Miguel LFF. Optimum design of single and multiple tuned mass dampers for vibration control in buildings under seismic excitation. International Journal of Structural Stability and Dynamics 2022; 2250078 (27 pages). https://doi.org/10.1142/S021945542250078X

[20] Brito JWS, Miguel LFF. Optimization of a reinforced concrete structure subjected to dynamic wind action. Frattura ed Integrità Strutturale 2022; online. https://doi.org/10.3221/IGF-ESIS.59.22

[21] Fadel Miguel, LF, Lopez RH, Miguel LFF, Torii, AJ. A novel approach to the optimum design of MTMDs under seismic excitations. Structural Control and Health Monitoring 2016a;23(11): 1290-1313. https://doi.org/10.1002/stc.1845

[22] Fadel Miguel, LF, Lopez RH, Torii, AJ, Miguel LFF, Beck AT. Robust design optimization of TMDs in vehicle–bridge coupled vibration problems. Engineering Structures 2016b;126:703-711. https://doi.org/10.1016/j.engstruct.2016.08.033

[23] Miguel LFF, Santos GP. Optimization of multiple tuned mass dampers for road bridges taking into account bridge-vehicle interaction, random pavement roughness, and uncertainties. Shock and Vibration 2021;2021 (6620427):1-17. https://doi.org/10.1155/2021/6620427

[24] Ontiveros-Pérez SP, Miguel LFF. Reliability-based optimum design of multiple tuned mass dampers for minimization of the probability of failure of buildings under earthquakes. Structures 2022;42:144-159. https://doi.org/10.1016/j.istruc.2022.06.015

[25] Rossato BB, Miguel LFF. Robust optimum design of tuned mass dampers for high-rise buildings subject to wind-induced vibration. Numerical Algebra, Control & Optimization, 2022; online. http://dx.doi.org/10.3934/naco.2021060

[26] Vellar LS, Ontiveros-Pérez SP, Miguel LFF, Fadel Miguel LF. Robust optimum design of multiple tuned mass dampers for vibration control in buildings subjected to seismic excitation. Shock and Vibration 2019;2019(9273714):1-9. https://doi.org/10.1155/2019/9273714

[27] Wen-Tao Qiao et al., “Study on dynamic behaviors and vibration reduction techniques on cable-supported ribbed beam composite slab”, Adv. Steel Constr., 15 (1), 73-81, 2019.

[28] Mensah A. F. and Dueñas-Osorio L., “Improved reliability of wind turbine towers with tuned liquid column dampers (TLCDs)”, Structural Safety, 47, 78-86, 2014.

[29] Zhang Z., Li J., Nielsen S. R. K. and Basu B., “Mitigation of edgewise vibrations in wind turbine blades by means of roller dampers”, Journal of Sound and Vibration, 333, 5283-5298, 2014.

[30] Miguel LFF, Fadel Miguel LF, Lopez RH. Robust design optimization of friction dampers for structural response control. Structural Control and Health Monitoring 2014;21(9):1240-1251. https://doi.org/10.1002/stc.1642

[31] Miguel LFF, Fadel Miguel LF, Lopez RH. A firefly algorithm for the design of force and placement of friction dampers for control of man-induced vibrations in footbridges. Optimization and Engineering 2015;16:633-661. https://doi.org/10.1007/s11081-014-9269-3

[32] Miguel LFF, Fadel Miguel LF, Lopez RH. Simultaneous optimization of force and placement of friction dampers under seismic loading. Engineering Optimization 2016a;48(4):582-602. https://doi.org/10.1080/0305215X.2015.1025774

[33] Miguel LFF, Fadel Miguel LF, Lopez RH. Failure probability minimization of buildings through passive friction dampers. The Structural Design of Tall and Special Buildings 2016b;25(17):869-885. https://doi.org/10.1002/tal.1287

[34] Miguel LFF, Fadel Miguel LF, Lopez RH. Methodology for the simultaneous optimization of location and parameters of friction dampers in the frequency domain. Engineering Optimization 2018;50(12):2108-2122. https://doi.org/10.1080/0305215X.2018.1428318

[35] Ontiveros-Pérez SP, Miguel LFF, Fadel Miguel LF. Optimization of location and forces of friction dampers. REM - International Engineering Journal 2017a;70(3):273-279. https://doi.org/10.1590/0370-44672015700065

[36] Ontiveros-Pérez SP, Miguel LFF, Fadel Miguel LF. Robust simultaneous optimization of friction damper for the passive vibration control in a Colombian building. Procedia Engineering 2017b;199:1743-1748. https://doi.org/10.1016/j.proeng.2017.09.430

[37] Ontiveros-Pérez SP, Miguel LFF, Fadel Miguel LF. A new assessment in the simultaneous optimization of friction dampers in plane and spatial civil structures. Mathematical Problems in Engineering 2017c;2017(6040986):1-18. https://doi.org/10.1155/2017/6040986

[38] Ontiveros-Pérez SP, Miguel LFF, Riera JD. Reliability-based optimum design of passive friction dampers in buildings in seismic regions. Engineering Structures 2019;190:276-284. https://doi.org/10.1016/j.engstruct.2019.04.021

[39] Ribakov Y. and Reinhorn A. M., “Design of amplified structural damping using optimal considerations”, Journal of Structural Engineering, 129, 1422-1427, 2003.

[40] Murotsu Y., Okada H. and Shao S., “Reliability-based design of transmission line structures under extreme wind loads”, Proceedings of 13th International Conference on Structural Safety and Reliability (ICOSSAR 93), Rotterdam, Netherlands, 3, 1675-1681, 1994.

[41] Miguel L. F. F. and Fadel Miguel L. F., “Assessment of modern metaheuristic algorithms-HS, ABC and FA-in shape and size optimization of structures with different types of constraints”, International Journal of Metaheuristics, 2, 256-293, 2013.

[42] Gerdau, Equal leg angle profile catalog, online, Available in <https://www2.gerdau.com.br/produtos/cantoneira-gerdau>, 2021.

[43] Ansys® Academic Research Mechanical, Release 2021 R2, Help System, Combin40 Element Description, ANSYS, Inc 2021.

[44] Brazilian Association of Technical Standards (ABNT), NBR 6123: Wind loads on edifications, Rio de Janeiro, 1988.

[45] Shinozuka M. and Jan C. M., “Digital simulation of random processes and its applications”, Journal of Sound and Vibrations, 25, 111-128, 1972.

[46] Miguel L. F. F., Fadel Miguel L. F., Riera J. D., Kaminski Jr. J. and Menezes R. C. R., “Assessment of code recommendations through simulation of EPS wind loads along a segment of a transmission line”, Engineering Structures, 43, 1-11, 2012.

[47] Mirjalili S. and Lewis A., “The whale optimization algorithm”, Advances in Engineering Software, 95, 51-67, 2016.

[48] Associação Brasileira de Normas Técnicas (ABNT), NBR 8850: Execução de suportes metálicos treliçados para linhas de transmissão - Procedimento, Rio de Janeiro, 2003.

Advanced Steel Construction – Vol. 19 No. 3 (2023) 262–272
DOI:10.18057/IJASC.2023.19.3.7

DISTRIBUTION OF RESIDUAL STRESS IN THE SPHERE-PIPE CONNECTION WELDS OF WELDED HOLLOW SPHERICAL JOINTS

Ren-Zhang Yan [1, 2], Chang-Long Zhang [1, 2], Shuai Wang [3], Jia-Qi Liu [2] and Tao Sun [4, *]

[1] *State Key Laboratory of Mountain Bridge and Tunnel Engineering, Chongqing Jiaotong University, Chongqing 400074, China*
[2] *School of Civil Engineering, Chongqing Jiaotong University, Chongqing 400074, China*
[3] *Chongqing Aerospace Polytechnic College, Chongqing 400021, China*
[4] *Department of Military Facility, Army Logistics Acadmy of PLA, Chongqing 401331, China*
[*] *(Corresponding author: Email: 372322119@qq.com)*

ABSTRACT

Welded hollow spherical joint is widely used in large-span spatial structures due to its simple structure, clear mechanical behavior and convenient connection. However, a large number of sphere-pipe connection welds at the joints will inevitably produce complex welding residual stress, which will have adverse effects on the stiffness of the joints and the overall safety of the structure. Focusing on the sphere-pipe connection welds on the hollow spherical joints, this paper keeps track of the whole process of sphere-pipe welding, analyzes and summarizes the distribution law and specific distribution mode of welding residual stress on the joints and parametrically analyzes the influence trend of the configuration dimension of joints on the distribution of welding residual stress. Studies have found that the circumferential welding residual tensile stress is mainly concentrated in and near the weld, while the compressive stress is concentrated in the outer area of the weld. The longitudinal residual stress shows the obvious bending features of external compression and internal tension along the wall thickness direction near the weld; The configuration dimension of the hollow spherical joint mainly affects the influence range of welding residual stress, that is, with the change of dimension, the welding heat-affected zone on steel pipes will vary within the area with a distance to the weld 0.6~1.35 times the diameter, and the heat-affected zone on spherical joints will vary within the area with a distance to the weld no more than 0.5 times the diameter. The above-mentioned refined research on the residual stress of the hollow spherical joint can lay a foundation for the accurate evaluation of the stiffness and overall safety of the welded hollow spherical joints.

ARTICLE HISTORY

Received: 12 October 2022
Revised: 27 April 2023
Accepted: 10 May 2023

KEYWORDS

Welded hollow spherical joint;
Welding residual stress;
Experiment;
Refined numerical simulation

Copyright © 2023 by The Hong Kong Institute of Steel Construction. All rights reserved.

1. Introduction

The welded hollow spherical joint is composed of a core hollow sphere welded with multiple steel pipes. Due to its simple structure, reliable force transmission, and convenient construction, it is widely used in large-span spatial grid structures. As we all know, since the welded hollow spherical joints are mainly made of steel [1], when the steel is welded, the welding area is under the action of highly concentrated heat, and the local steel will successively produce plastic expansion due to thermal compression and lead to uneven shrinkage deformation. At the same time, the microstructure and properties of the material have also changed greatly, and welding defects such as welding residual stress and residual deformation will inevitably occur in the welds and heat-affected zone [2]. These defects adversely affect on the stiffness, stability, brittleness and corrosion resistance of steel structure connections and joints [3], and even become the key factors restricting the selection of weld connection methods. The influence of welding residual stress on the connection of steel structures has been a hot topic of scholars. Osgood [4] first started to study welding residual stress and deformation in the 1920s and 1930s. Subsequently, scholars at home and abroad studied the distribution law of welding residual stress of welded joints and its influence on joint performance by combining experimental research and numerical simulation. Brar [5] precisely captured the residual stresses in heat affected zone of cruciform welded joint of hollow sectional pipes through finite element simulation. Wang [6] analyzed and clarified the high-temperature residual stress of the welded section of high-strength steel. Yang [7] studied the residual stress of high-performance steel after welding through experiments, and proposed a simple yet accurate method for determining the residual stress. Xu [8] compared and analyzed the residual stress of high-performance steel and high strength steel after welding. Mirzaee-Sisan [9] measured the circumferential and axial residual stresses of steel pipe butt welding. It can be seen from the above research results that, when the steel structure is welded, the distribution law of welding residual stress at the welded joint is relatively complex, and the influence on the connection performance of the steel structure cannot be ignored. Moreover, as the weld hollow spherical joint is a collection of multiple steel pipes, a large number of sphere-pipe welds are gathered. The influence of welding residual stress on the mechanical properties of hollow spherical joints is far worse than that of common welded joints. Sometimes the sphere-pipe joint weld becomes the cause of the overall collapse of the structure. For example, statistics of steel structure collapse accidents at home and abroad show that 19%~27% of the accidents are caused by joint failure [10]. The failure of the weld connection between the member pipe and the welded hollow sphere is one of the main reasons for the failure of the joint [11]. Therefore, in recent years, scholars at home and abroad have carried out a large number of studies on the mechanical properties of welded hollow spherical joints, such as stiffness, bearing capacity and influencing factors. Zang [12] analyzed the influence of the external ribs on the bearing capacity of welded hollow spherical joints. YU [13] studied the ultimate bearing capacity of ribbed hollow spherical joints and relationship with various influencing factors. CHEN [14] studied the ultimate bearing capacity and failure mechanism of welded hollow spherical joints through experiments. Some scholars studied the structural performance and ultimate bearing capacity of hollow spherical joints connected by rectangular steel pipes [15]. In terms of the stiffness research of welded hollow spherical joints, Liao [16], Liu [17], Lopez [18], Wang [19], Yan [20,21] have studied the stiffness calculation and analysis methods of welded hollow spherical joints. In addition, Liu [22,23] and Lu [24] studied the bearing capacity of welded hollow spherical joints after fire and high temperature action. Zhao [25~27] studied the influence of corrosion on the bearing capacity of welded hollow spherical joints. The above studies on the performance of welded hollow spherical joints do not consider the influence of welding residual stress. Only Zhao [28] analyzed the influence of welding residual stress on the mechanical behavior of hollow spherical joints through numerical simulation, but the material properties and welding process are simplified. The compression failure of welded hollow spherical joints is the stability failure of thin shells, and the welding residual stress will reduce the stiffness and stability of weldments. Therefore, the residual stress produced by the sphere-pipe weld has a significant influence on the stiffness and bearing capacity of the joints and furthermore, the overall safety of the spatial structure. In this paper, the commonly used welded hollow spherical joints in engineering are selected to study their variation laws of temperature field in the dynamic process of welding and determine the final distribution pattern of welding residual stress by combining experiment and numerical simulation, laying foundation for the fine analysis of mechanical properties of welded hollow spherical joints.

2. Design of welded hollow spherical joint sample

Hybrid structure of suspendome with stacked arch has been adopted in Chiping Gymnasium, Shandong, and the upper reticulated shell is in the form of welded hollow spherical joints. Complex residual stress tends to be generated in the hollow spherical joints due to lots of sphere-pipe welds, which greatly influences the stiffness and ultimate bearing capacity of the joints. In this paper, based on the project of suspendome in Chiping Gymnasium, Shandong, the

frequently used welded hollow spherical joints and circular steel pipes in the upper reticulated shell are selected as the research objects. Besides, in order to investigate the influence laws of the hollow spherical diameter D, the wall thickness t and the steel pipe diameter d, the wall thickness δ on the distribution pattern of residual stress in the joints, 9 sets of specimens are designed on the basis of Orthogonal experimental design method and the specification of *Technical specification for space frame structures* for the numerical simulation and experimental research. The specific geometric configuration dimensions of samples are demonstrated in the Table 1.

Table 1
Geometric configuration dimension table of samples

Sample Number	Geometric Configuration Dimensions of Samples			
	D / mm	t / mm	d / mm	δ / mm
FEA1	280	8	89	6
FEA2	300	8	89	6
FEA3	300	8	114	6
FEA4	300	8	140	6
FEA5	300	10	114	6
FEA6	300	12	114	6
FEA7	300	12	114	8
FEA8	300	12	114	10
FEA9	350	8	89	6

3. Numerical models and analytical methods

3.1. Numerical models

In order to improve the computational efficiency, the 1/2 model of sphere-pipe weld connection joint has been established according to the symmetry of the hollow spherical joint. The geometric structure of the joint can be seen in Fig. 1. In order to investigate the influence scope of welding temperature on the steel pipe and eliminate the influence of steel pipe end restraint, 1.5 d is selected for the length of steel pipe to establish the finite element model of ANSYS. In order to ensure the calculation accuracy, the division method of mapped meshing is chosen to achieve the discretization of finite element model. A total of 19683 finite elements and 32344 joints have been divided, and the dimension of each element is less than 1/10 of the model dimension except for the wall thickness direction.

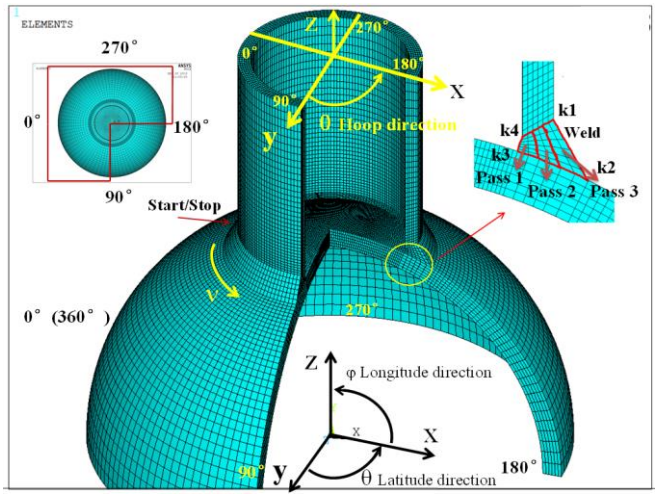

Fig. 1 Schematic diagram of calculation model of the sphere-pipe weld connection joint

3.2. Thermal-structural indirect coupling numerical simulation analytical method

The welding process of the welded hollow spherical joints includes the coupling effects of many physical processes such as heat, force and material phase-change, etc. With the analytical function of thermal-structural coupling of ANSYS, the tracking analysis for temperature field of welds and their heat-affected zone in the welding process can be conducted, and the temperature field can also be precisely adopted on the structural models to obtain the uneven temperature effects after welding. To achieve thermal-structural coupling analysis, all elements will be defined as SOLID70 in the thermal analysis during the welding simulation, and then they will be converted into SOLID185 in the analysis of structural stress. It is assumed that both the welding material and the base material are made of Q235 with the same properties. The material properties are defined according to the curve of material properties changing with temperature [29]. Specifically, several characteristic temperature such as 25°C, 100°C, 200°C, 300°C, 400°C, 500°C, 600°C, 700°C, 750°C, 800°C, 850°C, 900°C, 950°C, 1000°C, 1100°C, 1200°C, 1420°C and 1460°C were selected according to the distribution of the curve. Since the selected characteristic temperature are close to each other, the material properties between adjacent temperature are close to linear changes, the linear interpolation method is used to calculate the temperature and material properties between adjacent temperature in finite element. Due to the large number of temperature points, only the properties of the material at partial temperature are listed in Table 2.

Table 2
Table of the material properties changes with the welding temperature

Temperature/°C	20	250	500	750	1000	1500	1700	2500
Thermal Conductivity/[W/(m·°C)]	50	47	40	27	30	35	45	50
Density/$\times10^3$kg/m^3	7.82	7.70	7.61	7.55	7.490	7.35	7.30	7.09
Specific Heat Capacity/$\times10^2$J/(kg·°C)	4.6	4.8	5.3	6.8	6.7	6.6	7.8	8.2
Poisson's ratio	0.28	0.29	0.31	0.35	0.4	0.49	0.5	0.5
Linear Expansion Coefficient /$\times10^{-5}$m·°C	1.1	1.22	1.39	1.48	1.34	1.33	1.32	1.31
Elastic Modulus /$\times10^6$Pa	205000	187000	150000	70000	20000	0.002	0.0015	0.001
Yield Strength/$\times10^6$Pa	220	175	80	40	10	0.1	-	-

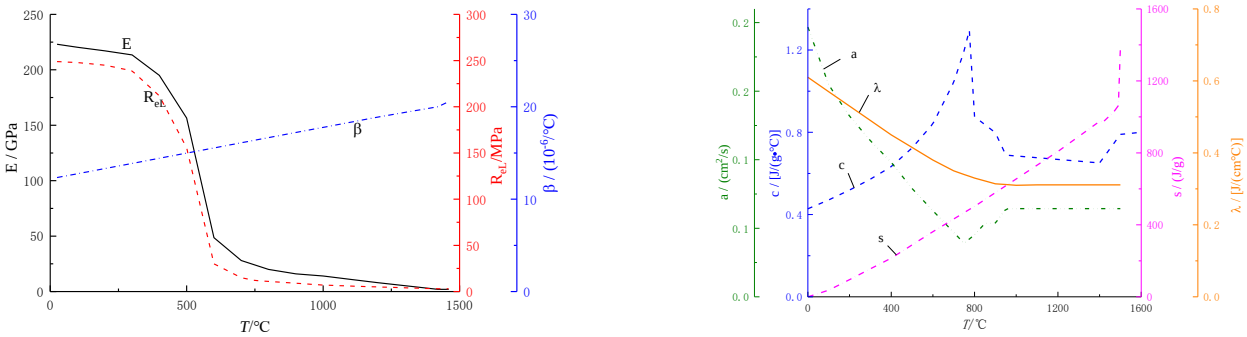

Fig. 2 Curve of material properties changing with temperature

For the boundary conditions of the model, the initial temperature and the room-temperature are set as 25℃ in the thermodynamic analysis; the symmetric planes of the model and the end faces of the steel pipe are the adiabatic plane, the others are set as convective heat transfer surfaces, and the convective heat transfer coefficient is taken as 30J/(m^2•s•℃). In the structural mechanics analysis, symmetric constraints are imposed on the symmetric planes of the hollow sphere.

In order to simulate the manual arc welding used in sphere-pipe welding, the heat generation rate heat source model shown in formula (1) is used. According to the practice of on-site construction, the arc voltage U=15V, the welding current I=160A, and the welding speed v=5mm/s, and the welding thermal efficiency K=0.7. The sphere-pipe butt welds are divided into 3 layers, and the layer of welding beads is numbered from the inside to the outside (See Fig. 1)). Each layer is divided into 80 equal parts in the circumferential direction, and each single element functions as a heat generator.

$$HENG = \frac{K \cdot U \cdot I}{A_i \cdot D \cdot T_i \cdot y} \tag{1}$$

among them, $DT_i = \frac{L_i}{80}$

In this formula, Ai is the cross-sectional area of the welds of each layer; DTi is the welding time of each element, L_i is the length of the welds of each layer; i=1, 2, 3.

Element “birth and death” technology is used to simulate weld formation during welding, as well as localized heating. The specific process is as follows: At the initial moment, all weld elements are set to the "dead" state; Then from the starting point of welding, each weld element is activated one by one from the first layer to the third layer. When a weld element is activated, the welding heat source is moved by applying a heat generation rate to the element, and removing the heat generation rate load from the previous activated element.

There are 240 load steps in the welding process, with a total duration of (80×ΣDT_i). After all weld elements are activated, the cooling phase of the weld comes. In the cooling stage, the model exchanges heat with the outside until the whole model returns to room-temperature of 25°C. The cooling time of 80 minutes in total is divided into 20 load steps with a step length of 240 s; The heat generation rate of the last weld element is removed in the first cooling load step. So far, the thermodynamic analysis of the sphere-pipe connection weld in the welding process is completed, then the model elements will be converted into mechanical analysis elements, and a symmetric constraint is applied on the symmetric plane of the hollow sphere for mechanical analysis.

4. Analysis of temperature field change law during welding

The uneven temperature rises and fall in the welding process is the main cause of welding residual stress. Therefore, clarifying the temperature field change law of welds and their heat-affected zone during welding can qualitatively test the accuracy and effectiveness of the subsequent simulation of the sphere-pipe welding process. Due to space limitation, sample FEA7 is taken as an example to track the 3-layer welding process of the sphere-pipe single butt seam and analyze its temperature field.

4.1. Nephograms of temperature field distribution

During the welding of sphere-pipe welds, the welding heat source moves counterclockwise from the position of 0° on the weld bead, then passes through 90°, 180°, 270° and 360°, and circulates 3 times in turn. The temperature field distribution nephograms of the FEA7 model at the moment when the welding heat source of the first layer of weld passes through 90° and that of the third layer of weld passes through 270° are extracted respectively, as shown in Fig. 3. It can be seen from Fig. 3 that the highest temperature is in the molten pool during welding, and gradually spreads to the rest of the joints with the progress of welding. The temperature distribution presents a crescent shape, and the temperature gradient gradually increases along the welding direction, which conforms to the characteristics of local instantaneous high temperature of welds during welding. After cooling, the overall temperature of the model is restored to room-temperature of 25°C.

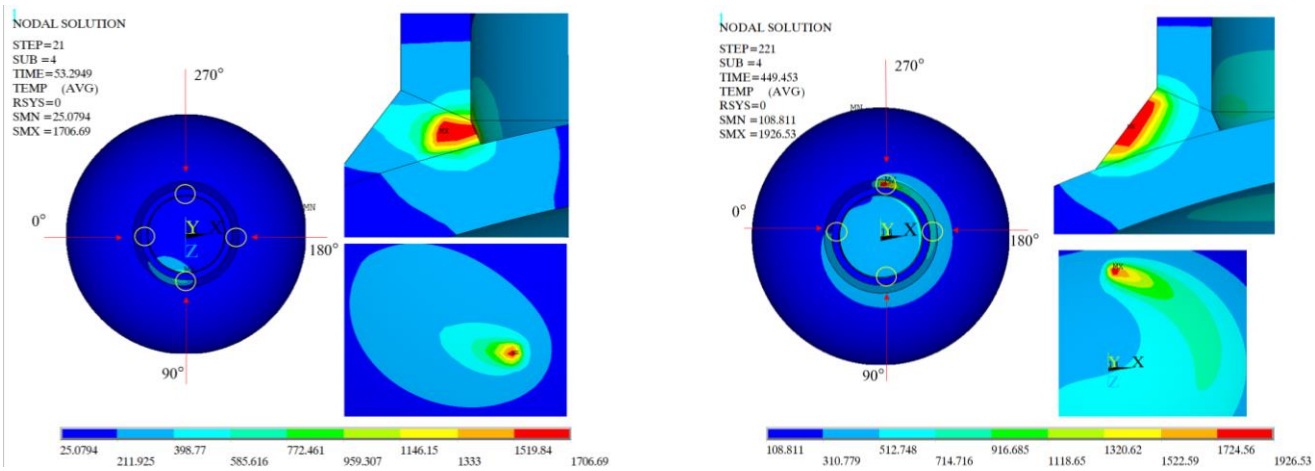

(a) Welding through 90° (b) Welding through 270°

Fig. 3 Temperature distribution nephograms of hollow spherical joints during welding (Unit: °C)

4.2. Variation law of temperature of key weld joints with welding process

In order to more intuitively observe the variation of local temperature of welds with time in the welding process more intuitively, the temperature variation curve of key points at the position of welds is drawn, as shown in Fig. 4. Four points on the initial welding section that can be in direct contact with the heat source are selected as key points (See Fig. 1). The key points 4 and 3 are in direct contact with the heat source during the welding of the first layer, while the key points 1 and 2 are in direct contact with the heat source during the welding of the third layer. It can be seen from Fig. 4 that each key point has undergone 3 heating processes, which directly reflects that the weld has gone through the process of 3 layers of welding. Key points 3 and 4 reach temperature extremes during welding at the first layer, while key points 1 and 2 reach temperature extremes during welding at the third layer, which conforms to the welding sequence from inside to outside. When the key points are in direct contact with the heat source, their temperature exceeds the melting point of the steel (usually 1538°C). And after cooling, the temperature of each key point returns to room-temperature.

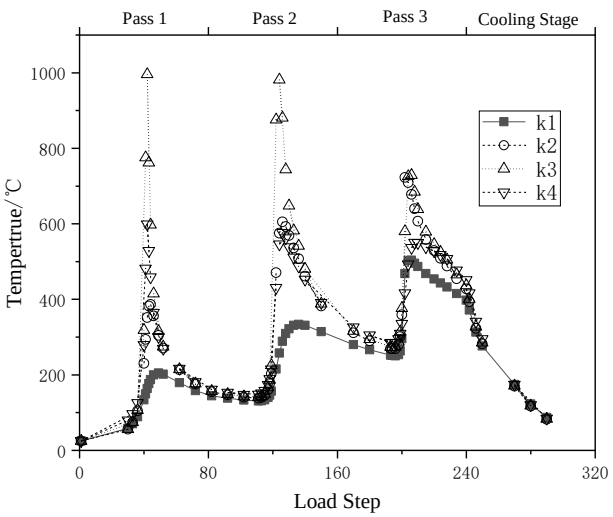

Fig. 4 Temperature variation curve of key points

Based on the temperature characteristics of the above finite element model, it can be seen that the finite element model established in this paper can effectively simulate the sphere-pipe welding process of hollow spherical joints, and then it can be considered that the residual stress of the joints after the completion of cooling can be regarded as the welding residual stress.

5. Calculation results of welding residual stress in different directions

Since the temperature field in the welding process presents three-dimensional characteristics in the joints, the welding residual stress in the joints also presents three-dimensional characteristics. According to the analysis, it is found that the geometric configuration dimension of the joints will affect the numerical value of the welding residual stress, but will not have a great impact on its distribution law. Therefore, the FEA7 model is still taken as an example to introduce the distribution law of the welding residual stress of sphere-pipe connection welds of the welded hollow spherical joints.

5.1. Distribution nephograms of welding residual stress in different directions

According to the coordinate system established in Fig. 1, the residual stress nephogram in each direction after welding are drawn (See Fig. 5). It can be seen from Fig. 5 that the residual stress in each direction is mainly distributed near the welds, and is relatively uniform along the circumferential direction of the steel pipe.

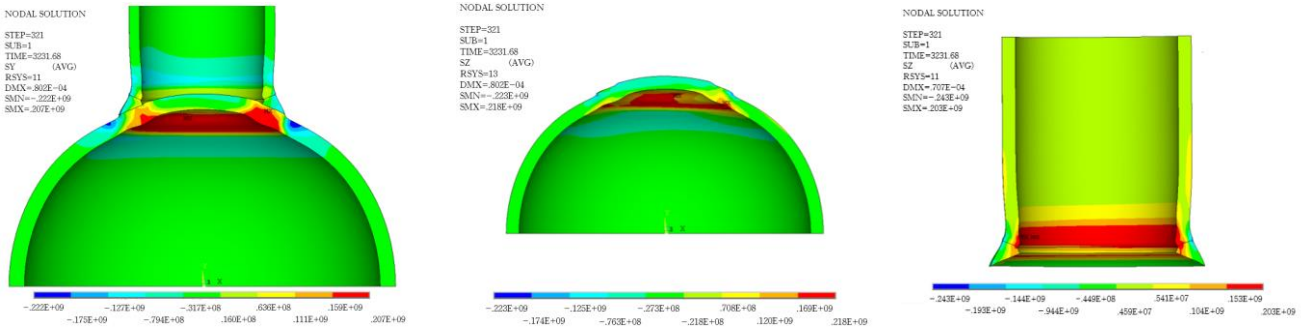

(a) Circumferential residual stress σ_θ (b) Longitudinal residual stress σ_φ (c) Axial residual stress σ_z

Fig. 5 Welding residual stress nephograms (Unit: Pa)

It can be seen from Fig.5-a) that the shrinkage of the welds along the length direction leads to the corresponding necking of the steel pipe and hollow sphere on both sides of the welds, which can partially release the circumferential residual stress. Moreover, due to the relatively weak constraint of the steel pipe, the necking of the steel pipe is more obvious than that of the hollow sphere. Therefore, the circumferential residual stress σ_θ on the hollow sphere is generally greater than that of the steel pipe. In addition, the area directly in contact with the weld on the hollow ball, the heat dissipation condition is the worst, welding weld heat will be directly into this area. However, the heat will be finally cooled after the heat dissipation of the welds during cooling, so it will be constrained by the outer surface that is cooled first, resulting in the stress in this area being tensile on the inner surface and compressed on the outer surface. The maximum circumferential residual compressive stress is -222MPa at a certain distance from the outer surface of the hollow sphere to the weld toes, and the maximum circumferential residual tensile stress is 207MPa inside the hollow sphere under the welds.

As can be seen from Fig. 5-b) and Fig. 5-c), the necking of steel pipe and hollow sphere is also caused by the shrinkage of welds along the direction of length, so that the steel pipe and hollow sphere near the welds show obvious bending characteristics along the wall thickness direction respectively. Therefore, near the welds, the longitude residual tensile stress of the hollow sphere and the axial residual tensile stress of the steel pipe are distributed in their inner areas, with the maximum values of 218 MPa and 203 MPa respectively; the longitude residual compressive stress of the hollow sphere and the axial residual compressive stress of the steel pipe are distributed in the outer area, with the maximum values of -223 MPa and -243 MPa respectively at the weld toes. In the outer area of welds, the residual stress values of the steel pipe and the hollow sphere in the thickness direction are relatively low, which are less than 30MPa except at the weld junctions.

5.2. Distribution law of welding residual stress in different directions

5.2.1. Distribution law of σ_θ

In order to clarify the distribution law of welding residual stress in hollow spheres, the 180° section of FEA7 model is still selected to analyze the distribution law of residual stress at different wall thickness positions of hollow spheres. Fig. 6 shows the distribution curve of circumferential residual stress σ_θ along the longitudinal direction at different wall thickness positions of the hollow sphere along the longitudinal direction. The angles on the spherical surface corresponding to the weld toe are 18.6° and 26.1° respectively. Hollow sphere is divided into three areas: the inside of the circumferential weld, the weld area in direct contact with the circumferential weld and the outside of the circumferential weld. It can be seen from Fig. 6 that the tensile stress is mainly concentrated in the weld and adjacent areas, while the compressive stress is concentrated in the outside of the weld.

The distribution laws of σ_θ along the longitudinal direction at different wall thickness positions of the hollow sphere are similar along the longitudinal direction. The tensile stress in the weld area gradually decreases towards the inside and outside of the circumferential weld, and then develops to the compressive stress direction until a critical position and then to the tensile stress direction.

In addition, combined with Fig. 5-a) and Fig. 6, it can be seen that the maximum circumferential residual compressive stress on the hollow spherical surface occurs at the position of φ=5.6° from the outer weld toe in the outer area encircling the weld on the exterior surface of the hollow sphere. The maximum residual tensile stress occurs at the position of φ=20.8° and R=0.144m inside the hollow spherical wall thickness.

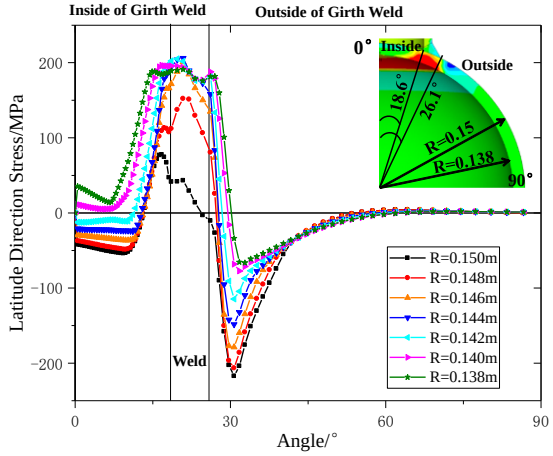

Fig. 6 Distribution curve of σ_θ at different wall thickness

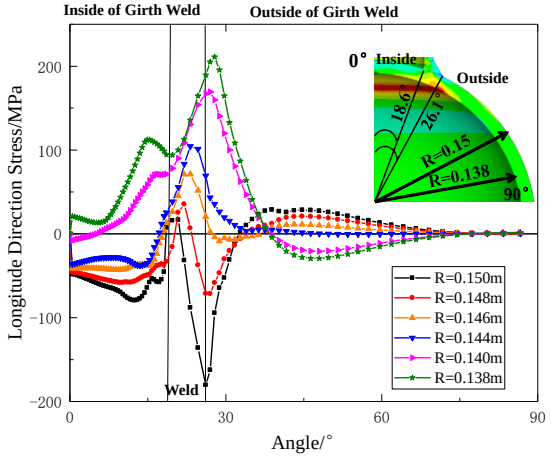

Fig. 7 Distribution curve of σ_φ at different wall thickness

5.2.2. Distribution law of σ_φ

Fig. 7 shows the distribution curve of σ_φ along the longitudinal direction of hollow spheres at different wall thicknesses along the longitudinal direction of hollow spheres. As can be seen that from φ=0°~36°, σ_φ gradually changes from tensile stress to compressive stress from the inner surface to the outer surface of the hollow sphere; from φ=36°~90°, the opposite is true.

Specially, on the outer wall of the hollow sphere(R=0.15m), σ_φ obtains the maximum compressive stress of -180.3 MPa at φ=26.1°, then decreases with the increase of φ and reaches 0 at φ=32.6°; then, with further increase of φ, σ_φ turns into tensile stress and obtains the extreme value of 28.6MPa at φ=38.9°. On the inner wall of the hollow sphere (R=0.138m), σ_φ obtains the maximum tensile stress of 205.1MPa at φ=27°, then gradually decreases with the increase of angle φ. It obtains the same value of 23.1MPa at the outer wall of φ=36.2°, and then reaches 0MPa at 38.4°. As the angle decreases, it turns into compressive stress and obtains an extreme value of 29.4 MPa at φ=48°.

In addition, by comparing σ_θ and σ_φ at the same position of welds, it can also be found that σ_φ is always greater than σ_θ, which indicates that the steel is more likely to yield along the longitudinal direction at the weld, that is, the axial direction of the welded hollow spherical joints, especially for the compressed joints, the superposition of residual compressive stress and external load will lead to the failure of joint extraction. In the range of 15mm~20mm from the weld, σ_θ will reach the peak, which is extremely unfavorable to the bending of joints.

6. Experimental studies and verification of welding residual stress

Although the distribution of residual stress in the welded hollow spherical joints can be obtained comprehensively by numerical simulation, the accuracy and reliability need to be verified because the welding heat source and material phase-changing are properly assumed in the calculation process. Therefore, in order to verify the reliability of the numerical simulation results, two sets of equal-scale samples S-1 and S-2 are designed with reference to the FEA7 model, and the magnetic measurement method is used to test and analyze the welding residual stress on the surface of the hollow sphere. The geometric dimensions and welding process of samples S-1 and S-2 are exactly the same as those of FEA7 model. Specific structural dimensions can be seen in Table 1.

6.1. Basic principle and test overview of magnetic measurement method

The magnetic measurement method is used to measure the initial stress inside steel based on the magneto strictive effect of ferromagnetic materials [30]. In the plane stress state, the current difference output in the principal stress direction and the principal stress difference have a single-value linear relationship shown in Formula (2).

$$(I_1 - I_2) = \alpha(\sigma_1 - \sigma_2) \tag{2}$$

In this formula, σ_1 and σ_2 are the maximum and minimum principal stresses respectively, in MPa; I_1 and I_2 are the current output values in the direction of maximum and minimum principal stresses respectively, in mA; α is the sensitivity coefficient, in mA/MPa.

Since the direction of principal stress is unknown, the direction angle of principal stresses and the differences of principal stresses can be determined by Formula (3) and Formula (4) respectively.

$$\theta = -\frac{1}{2}tan^{-1}\left(\frac{2I_{45}-I_0-I_{90}}{I_{90}-I_0}\right) \tag{3}$$

$$(\sigma_1 - \sigma_2) = \frac{I_{90}-I_0}{a\cos 2\theta} \tag{4}$$

In the above formula, θ is the included angle between σ_1 and the vertical direction of the shaft network; I_0, I_4 and I_{90} are the measured current values in three directions of 0°, 45° and 90° respectively.

After the principal stress difference and direction angle are calculated according to the above formula, the principal stress can be separated by the shear stress difference method, and the stress component of any point P can be calculated according to Formulas (5) ~ (7).

$$(\sigma_x)_P = (\sigma_x)_0 - \int_0^P \frac{\partial \tau_{xy}}{\partial y}dx \tag{5}$$

$$\left(\sigma_y\right)_P = (\sigma_x)_P - (\sigma_1 - \sigma_2)_P \sin 2\theta_P \tag{6}$$

$$\left(\tau_{xy}\right)_P = \frac{(\sigma_1-\sigma_2)_P}{2}\sin 2\theta_P \tag{7}$$

In this formula, $(\sigma_x)_0$ is the known stress value of the boundary point, and the $(\sigma_x)_0$ of the free boundary is set as 0. In calculation, increment is used to replace differentiation.

When the magnetic measurement method is used, after the samples are welded and cooled to room-temperature, an auxiliary grid is established at the measuring point on the surface of the hollow sphere, and the measuring points are represented by square grid joints and numbered, as shown in Fig. 8. The coordinate system corresponds to the spherical coordinate system shown in Fig. 1.

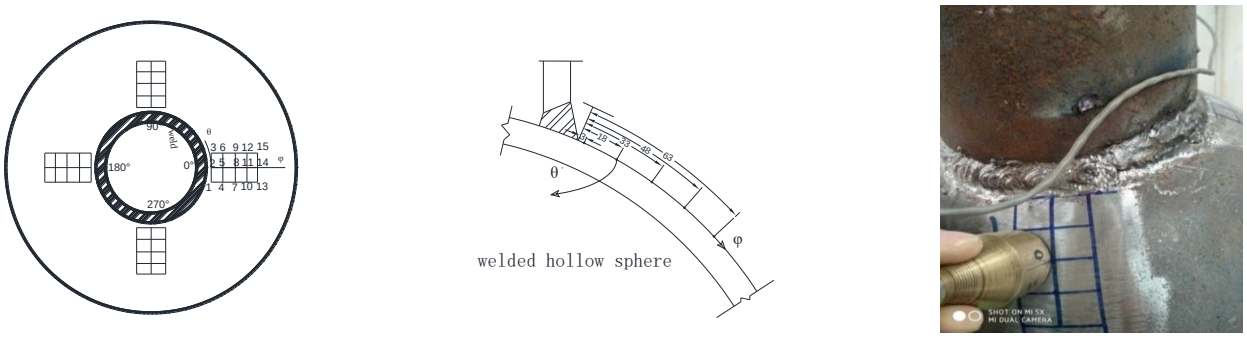

(a) Vertical view (b) Section (c) Real picture

Fig. 8 Layout of residual stress measuring points

In order to be representative, a test area is set every 90° along the circumferential direction from the welding starting point. Five measuring points are evenly arranged along the longitudinal direction in each measuring area, and three measuring points are arranged along the circumferential direction. During measurement, the average value of the three measuring points in the circumferential direction is taken as the stress value of the longitude position. SC21B three-dimensional stress distribution magnetic instrument is used for measurement. The measuring instrument and process are shown in Fig. 9.

Fig. 9 Measurement process of residual stress

6.2. Comparative analysis of test results and numerical simulation results

σ_θ and σ_φ of samples S-1 and S-2 at measuring points can be measured by magnetic measurement method, and compared with the finite element calculation results in Section 5.1, as shown in Figs. 10 and 11.

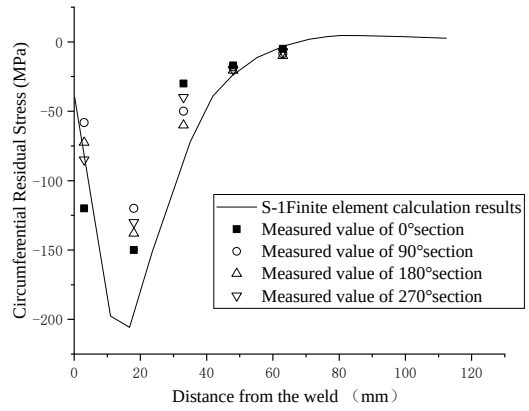

(a) S-1

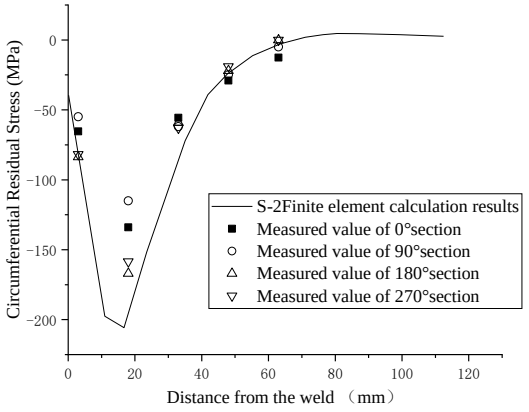

(b) S-2

Fig. 10 Comparison of σ_θ by testing and finite element calculation

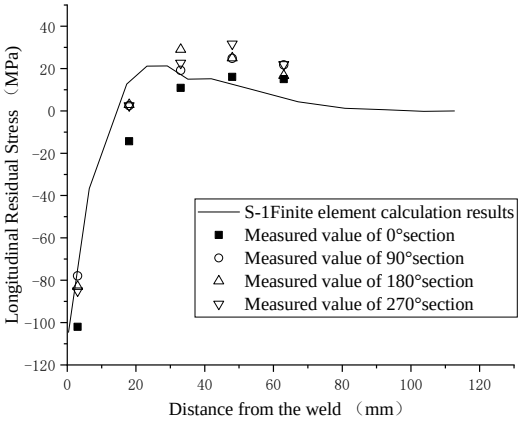

(a) S-1

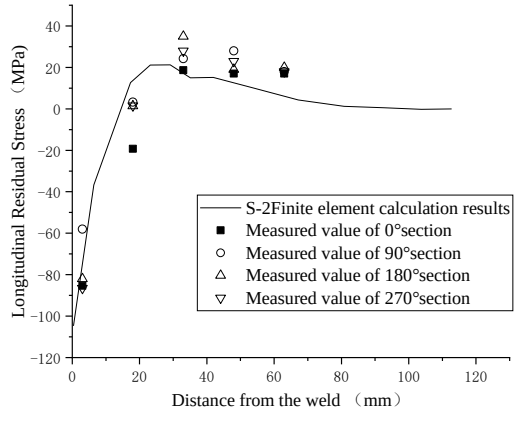

(b) S-2

Fig. 11 Comparison of σ_φ by testing and finite element calculation

It can be seen from Fig. 10 and Fig. 11 that the distribution law and change trend of welding residual stress of samples S-1 and S-2 are in good agreement with the finite element calculation results of FEA7.

It can be seen in Fig. 10 that the σ_θ of samples S-1 and S-2 increases gradually from weld toe and reaches peak value at the measuring point that is 18mm away from weld. This value is 6.44% and 7.83% different from the finite element calculation respectively, which indicates that the test results are in good agreement with the finite element calculation results. Specifically, the maximum σ_θ of sample S-1 is -150MPa, 27.4% smaller than the peak value calculated through the finite element method; of sample S-2, the value of maximum σ_θ is -167MPa, 17.73% smaller than that than the peak value calculated through the finite element method.

It can also be seen from Fig. 11 that for samples S-1 and S-2, the maximum σ_φ is reached at the weld toe and decreases with the distance from the weld growing, which is the same as the result through the finite element calculation. Specifically, the maximum σ_φ of sample S-1 is -102MPa, which is only 2.86% smaller than the value by the method of finite element calculation. The maximum σ_φ of sample S-2, the maximum is -85.7MPa, which is 30.6% smaller than that through the finite element method.

From the analysis above, the finite element calculation results of FEA7 are always larger than the test values of S-1 and S-2. it is known that for FEA7, the result by the method of finite element calculation is always larger than the testing value of samples S-1 and S-2. As for reasons for this conclusion, on the one hand, it is difficult to measure the peak value of an accurate point because the magnetic measurement method measures the average stress at the probe; on the other hand, the actual result is the stress at the center of the probe. For the 3cm range (probe diameter) close to the weld, the probe is hard to reach due to the obstruction of steel pipe forming a dead angle. However, the similarity between the changing trends of the test results and the finite element calculation results can still verify the reliability of the above-mentioned numerical model to a certain extent.

7. Calculation result of Von Mises equivalent welding residual stress

From the analysis above, it can be seen that the residual stress of the welded hollow spherical weld and its heat-affected zone is in complex stress condition. The unidirectional stress state is difficult to describe the actual working state, so it is necessary to extract the equivalent stress that can characterize the complex stress state according to actual yield criterion.

7.1. Nephograms of Von Mises equivalent welding residual stress distribution

By comparing the test result and finite element result, it is known that the meticulously-organized numerical model is reliable to some extent. Therefore, the Von Mises equivalent stress nephographs of the joint (See Fig. 12) is extracted from the FEA1 model as an example to analyze its complex stress state. It can be seen from Fig. 12-a) that the extreme value of Von Mises equivalent residual stress at joints has reached 220MPa, which is close to the yield strength of the material. Hence, the weld and its adjacent area will become the weak areas. With the distance from the weld growing, the welding residual stress gradually decreases until it dissipates, which conforms to the physical law in Fig. 3 that the temperature and temperature gradient decrease as the distance from the weld grows. The smaller the temperature gradient is, the smaller local constraint is, and the stress is smaller. In addition, it can be seen from Fig. 12-a) that in the area near the weld, along the circumferential direction of the steel pipe, the welding residual stress is basically at the same level except for the starting point of welding. While the residual stress at the welding start and its adjacent areas is obvious difference. The reason for this difference is that the weld is a circular closed weld, and the start of welding is both the arcing point and the stopping point of arc welding. Each layer experiences two instantaneous high temperatures, resulting in complex and irregular stress in this area.

7.1.1. Calculation results of welding residual stress in steel pipe

According to Fig. 12-b), the maximum Von Mises equivalent stress of steel pipe, 216MPa, is in the direct contact between the pipe and the weld. From the stress distribution on the section, along the direction of thickness, the welding residual stress at the inner and outer boundaries is larger than the internal stress of the steel pipe, showing a pattern that is high on both sides and low inside. At the same horizontal height of the steel pipe, the stress value is basically the same. The minimum stress of the steel pipe is 1.19MPa, so the stress on the pipe can be ignored after a certain distance from the weld, which indicates that the influence area of welding on the steel pipe has a certain range.

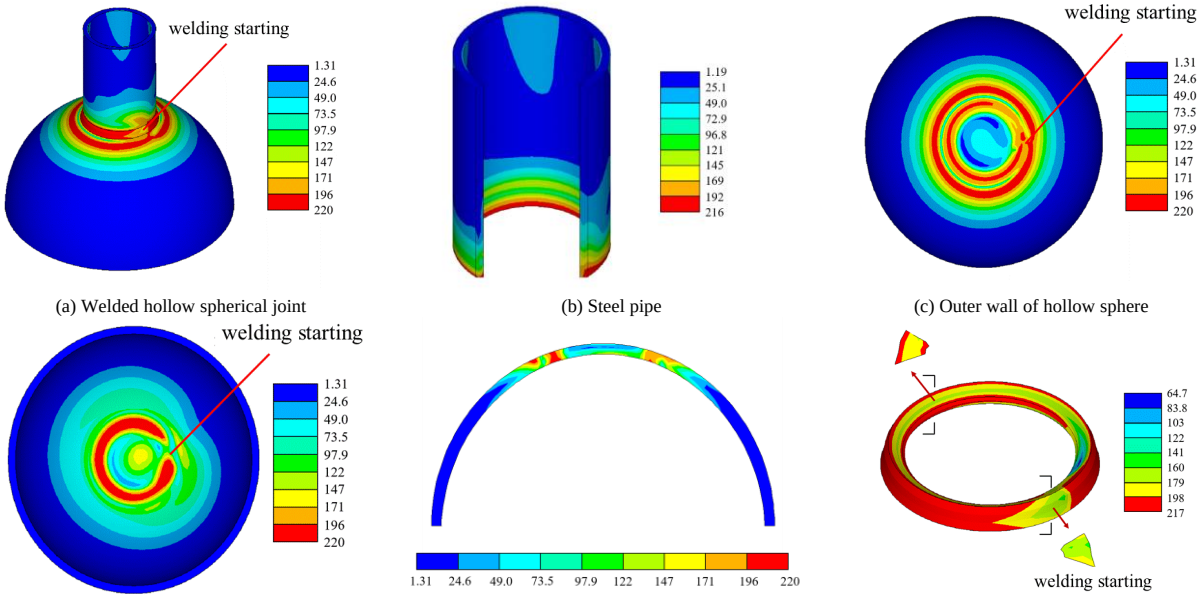

(a) Welded hollow spherical joint (b) Steel pipe (c) Outer wall of hollow sphere

(d) Inner wall of hollow sphere (e) Section of welding start (f) Weld

Fig. 12 Nephograms of welding residual stress of welded hollow spherical joint (Unit: MPa).

7.1.2. Calculation results of welding residual stress in hollow sphere

It can be seen from Fig. 12-c) and Fig. 12-d) that the maximum welding residual stress in the hollow sphere is 220MPa and the minimum is 1.31MPa. The difference between the welding residual stress at the starting position of welding and the stress at other positions at the same latitude is more obvious on the hollow sphere.

Similarly, there is also a certain welding influence area on the hollow sphere, which is similar to the stress distribution on steel pipe. Beyond this area, the welding residual stress can be ignored; moreover, the welding residual stress on the outer wall of the hollow sphere in contact with air is larger than that on the inner wall. The welding residual stress along the direction of thickness is also high on both sides and low inside.

It is worth mentioning that the maximum welding residual stress on the inner wall of the hollow sphere appears below the corresponding position of the weld, while the maximum of the outer wall appears on both sides of the direct contact of the weld. This proves that thermal boundary condition has an influence on the welding residual stress of joints, and the residual stress on a boundary has a larger value. That is, the boundary condition is the reason for the distribution of welding residual stress in the thickness direction of "high on both sides and low inside" and the difference of stress distribution on the inner and outer walls of the hollow sphere.

7.1.3. Calculation results of welding residual stress in weld

It can be seen from Fig. 12-f) that the welding residual stress of sphere-pipe weld is relatively large, with the maximum of 217MPa and minimum of 64.7MPa. Similarly, the stress on the boundary in contact with air is larger than that in the interior not in contact with air. Except for the start of welding, the distribution of stress on the weld is approximately similar. Generally, in the process of welding, a heat-affected zone is formed at the hollow spherical joint. Within this zone, the closer to the weld, the larger the residual stress is, and the influence of welding outside this zone can be ignored. Since the start of welding experiences one more heating than the other positions on the same circumference, the residual stress here is different from that of the other positions.

7.2. Distribution pattern of the welding residual stress

To make clear the specific zone influenced range of welding residual stress, a simplified distribution mode of welding residual stress based on Von Mises yield criterion is concluded according to the above calculation results. It is assumed that the welding residual stress along the direction of thickness remains unchanged, and the resultant stress along the direction is taken as the welding residual stress at this position. To this end, nine paths are established on the same circumference as the welded hollow spherical joint (See Fig. 13). The paths are selected according to the interval of element division. Within the weld， paths are separated by one element, while the others by two elements.

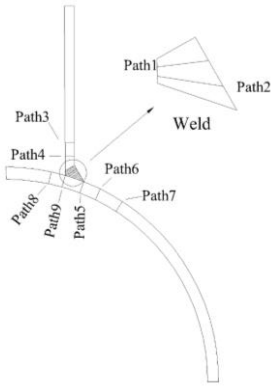

Fig. 13 Schematic diagram of the description paths of welding residual stress on the section

According to the above method, the welding residual stress distribution curve of the 9 paths shown in Fig. 13 are drawn (See Fig. 14). The curves adopt polar coordinate system, and the angle of the start of welding is set to 0°. The circumference is specified as the zero- stress point. The closer to the center of the circle, the greater the stress value.

It is clear that welds and areas adjacent to them on the hollow sphere have relatively larger residual stress by comparing the welding residual stress distribution curves of each path. Meanwhile, combined with the nephograms of stress in Fig. 12, it is obvious that the repeated temperature rise and fall at the start of welding has a great impact on the distribution of welding residual stress in this area. Specifically, the repeated heating rise at the starting position has the largest impact on the steel pipe, resulting in the largest stress fluctuation area on Path3 (Fig. 14-c)) and Path4 (Fig.14-d)), at about -45°~45°. The second largest is on Path1 (Fig. 14-a)) and Path2 (Fig. 14-b)) in the weld, with a region of -13.5 ° ~45 °; And the paths on the hollow sphere have the smallest, about -18 ° ~18 °.

On the other hand, in terms of specific fluctuation range, the variation rules of each region are also different: the fluctuation amplitude of Path1 and Path2 in the weld is the largest, while the fluctuation amplitude of the paths on the steel pipe and hollow sphere is relatively small. The reason may be that the direct contact between the weld and the high-temperature heat source is instantaneous, while influence on the steel pipe and hollow sphere is continuous because the propagation of temperature needs a certain time. Moreover, from the stress distribution curves of each path, it is also apparent that the extreme value of stress is not at the starting position of welding since when the start experiences high temperature again, the weld there melts again, and the weld areas generated already are no longer constrained by the material there. As a result, the welding residual stress in the adjacent areas will be partially released, and dips shown in Fig. 14 appear on the stress curves.

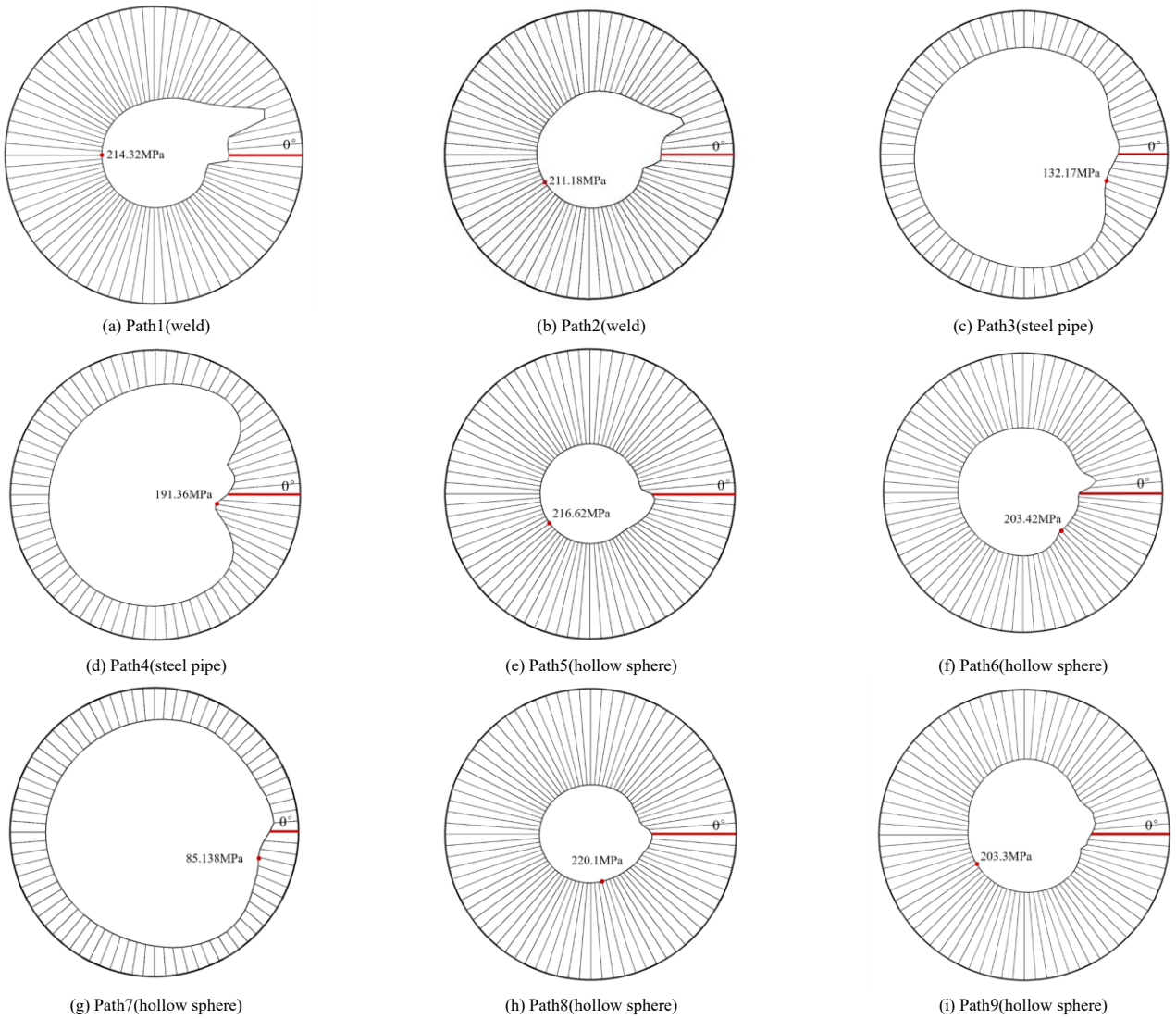

Fig. 14 Curves of welding residual stress distribution of the paths.

7.3. Determination of the welding heat-affected zone

Fig. 14 actually shows the stress distribution curve of the weld and its surrounding area along the circumferential direction. In engineering practice, more attention is paid to the stress distribution pattern along the vertical section. From Fig. 14, we can also notice a significant feature of the circumferential distribution of stress, that is, for the same circumferential path, except the start of welding, the stress distribution curves of other positions except the start of welding, are close to a concentric circle, and their stress values are almost equal. Therefore, combined with the good plastic characteristics of steel, it can be assumed that the stress of the paths in Fig. 14 is completely evenly distributed along the circumferential direction. A fixed stress value is taken along the circumference to ensures that the value ensures that the resultant force along the circumference is equal to the actual stress. Taking Path1 as an example, its stress curve is drawn through the Cartesian coordinate system, and then its simplified stress value is obtained based on the basis that the areas formed by the curve and the x-axis are equal in dimension (See Fig. 15). Hence, a simplified distribution model is obtained. It shows the welding residual stress on the section of hollow spherical joint according to Von Mises yield criterion (See Fig. 16).

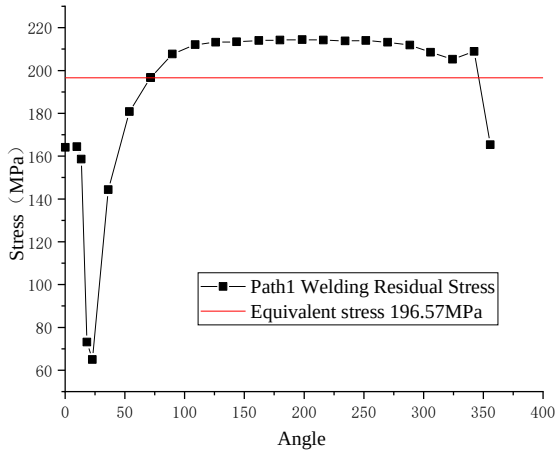

Fig. 15 Example of the simplified method for welding residual stress on the same circumference

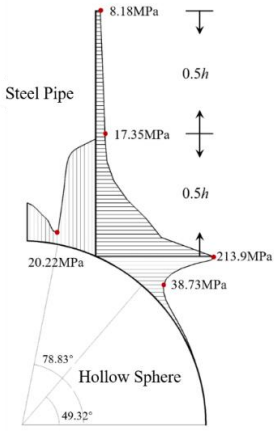

Fig.16 Simplified distribution pattern of welding residual stress on spherical section

It is known from Fig. 16 that on the vertical section of joints, the maximum welding residual stress is 213.9MPa, which is only 6.1MPa different from the accurate value of 220MPa by the method of finite element calculation in Section 7.1. The difference is within the acceptable range; and the variation law of residual stress is completely consistent with the analytical results in Section 6.1, that is, the residual stress decreases as the distance from the weld grows. Therefore, the more obvious Fig. 16 can be used to analyze the heat-affected zone of joints.

Specifically, at the 1/2 height of the steel pipe in Fig. 16, the welding residual stress reduces to 17.35MPa, 91.89% lower than the peak stress; at the latitude φ=49.32° on the hollow sphere, the residual stress decreases to 38.73MPa, 81.89% lower than the peak. The stress has reduced to a relatively small value. If 5% of the yield strength of the material is taken as the basis of whether the welding residual stress can be ignored to judge the stress influence area of welding. The welding influence area of each finite element model is shown in Fig. 17.

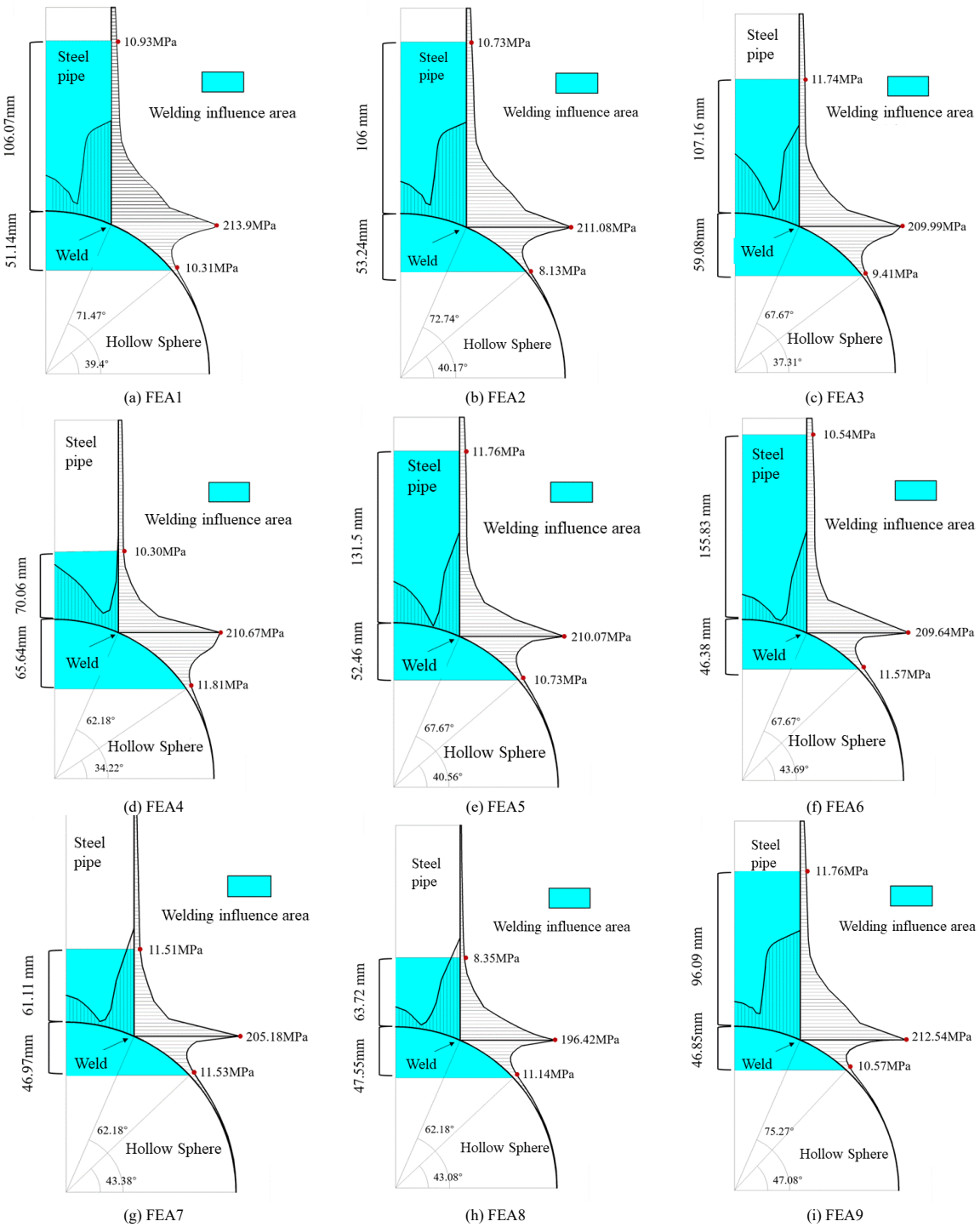

Fig. 17 Simplified distribution model of welding residual stress of the sections of the models

By comparing the models in Fig. 17, it can be seen that the distribution law of welding residual stress in each model is exactly the same, indicating that this kind of hollow spherical joint has the same distribution pattern of welding residual stress. The dimension of hollow spherical joint doesn't have a big impact on the maximum welding residual stress. The maximum of each model is about 210MPa, but it will affect the range of welding influence zone.

7.4. Effects of configuration dimension of joint on welding heat-affected zone

To more clearly analyze the influence law of each parameter of dimension on the welding influence zone, the trend charts that show the variation of the maximum welding residual stress of the joint and the proportion of the welding influence zone on the steel pipe and hollow sphere as a single parameter varies are drawn (See Fig. 18). Among them, the proportion of the influence area on the steel pipe is the ratio of the length of the influence area on the steel pipe to the total length of the pipe, and the proportion of the influence area on the hollow sphere is the ratio of the central angle of the influence area on the 1/4 arc section of the hollow sphere to 90 °.

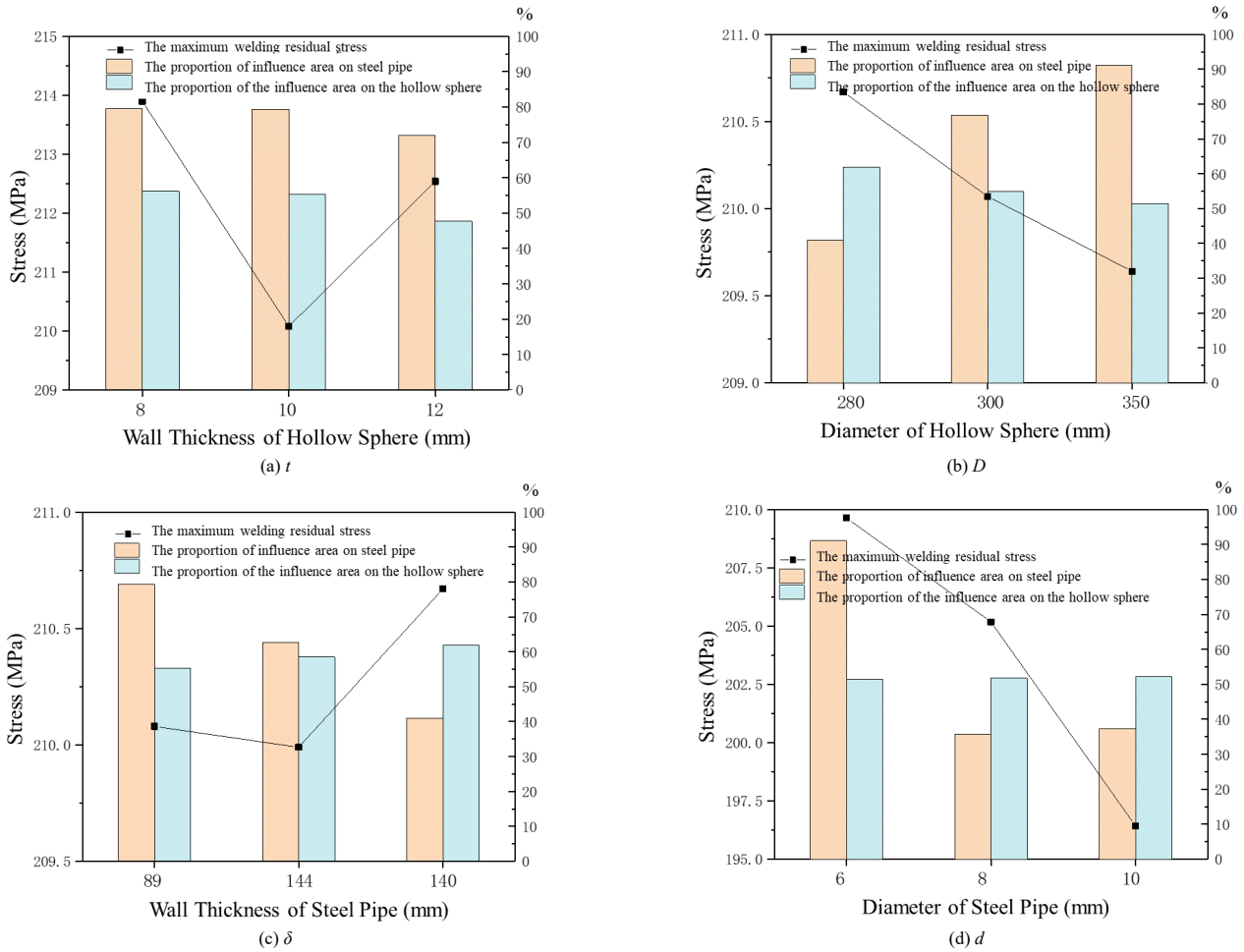

Fig. 18 Effects of dimension parameter on welding residual stress on joints

According to Fig. 18, the wall thickness of steel pipe δ has the greatest effect on the maximum welding residual stress. When the thickness increases, the maximum residual stress decreases; In addition, the maximum also falls with the increase of the diameter of the hollow sphere D, but compared with the wall thickness of steel pipe t, the reduction is very small. The influence of steel pipe diameter d and hollow sphere wall thickness t on the welding residual stress is characterized as the pattern of "V", which means there is an optimal dimension to minimize the welding residual stress of the whole joint.

Comparing the influence areas of welding residual stress of different configuration dimensions in Fig. 18, it is not difficult to find that in general, when the configuration dimensions of joints change, the influence areas on the hollow sphere change a little. It can be seen from Fig. 18-a) and 18-b) that with the increase of t and D, the influence areas on the hollow sphere decrease slightly, and the influence areas on the steel pipe also have some change larger than those on the sphere; from Fig. 18-c) and 18-d) it is known that as δ and d increase, the influence areas on the pipe decrease gradually, while those on the hollow sphere change a little. Reasons for these rules are that the dimension of weld is jointly determined by δ, d, and D. On the one hand, the larger δ is, the wider the weld is, and a large section of weld may make transition of the sections at welds tend to be smooth, which can reduce stress concentration at the weld so as to reduce the maximum welding residual stress and the range of influence zone on the steel pipe to some extent; on the other hand, the larger d is, the longer the weld is, but meanwhile, growing surface area in contact with the weld makes larger the heat dissipation area on the weld. Therefore, the influence area on the pipe may be reduced. Similarly, the contact area between the weld and the hollow sphere increases with the rise of D, which will also make transition of the sections of welds tend to be smooth. Moreover, this will also enlarge the heat dissipation area and reduce the influence area of the hollow sphere.

Specifically, the influence area on the steel pipe of FEA7 model is the smallest, at 35.74%. The largest, 91.13%, is on FEA6 model. Thus, the influence area on the steel pipe is 0.6d~1.35d from the weld. The model with the smallest proportion of influence area on the hollow sphere is FEA9, with an influence area of 47.69%, and the largest is 61.98% on FEA4. In the direction vertical to the weld, the influence area is roughly 0.5d from the weld, the range of change is smaller than that of the steel pipe.

8. Conclusions

The residual stress in the directions is mainly distributed near the circumferential weld. The maximum residual stress on the steel pipe is the axial residual stress of 243MPa and that on the hollow sphere is the longitudinal residual stress of 223MPa. Through the analysis, the circumferential residual stress along the longitude of the sphere was converted from a tensile stress to a compressive stress. After reached the extreme value, the residual stress gradually reduced. And the axial residual stress reached the extreme value at the weld and then gradually dissipated as away from the weld. Except for the start position of welding of repeated temperature rise and fall, stress values are almost the same; therefore, in integral analysis of the structure, it can be assumed that stress is completely evenly distributed along the circumferential direction, which means a fixed stress can be taken along the circumference to ensure that the resultant force along the circumference is equal to that of the actual stress.

The longitudinal residual stress at the same position of welds is always larger than the circumferential residual stress, indicating that steel is easier to yield along the longitudinal direction at the weld. Therefore, the superposition of residual compressive stress and external load is easier to cause the compression joint failure; however, in the range of 15mm~20mm from the weld, the circumferential residual stress will reach the peak, which is extremely unfavorable to the bending of the joint.

The influence of the geometric dimension of welded hollow spherical joints on the welding residual stress of joints is complex. The influence area on the steel pipe is about 0.6d~1.35d from the weld, and the area on the sphere is about 0.5d from the weld; When the wall thickness of steel pipe δ or the diameter of hollow sphere D increases, the maximum welding residual stress decreases. The influence of steel pipe diameter d and hollow sphere wall thickness t on the welding residual stress is characterized as the pattern of V, which means there is an optimal dimension to minimize the welding residual stress of the whole joint. The research found, the dimension parameter of the joint mainly affects the range of the welding influence zone on the joint, and the extreme value of welding residual stress is not affected much.

Funding acknowledgments

This work was supported by 2022 Technology Innovation and Application 531 Development Project of Nanan District, Chongqing (2022), and the Projects of Postgraduate Research Innovation in Chongqing(2020S0007).

Reference

[1] Zhongwei Zhao, Hongwei Zhang, Lina Xian, Haiqing Liu. Tensile strength of Q345 steel with random pitting corrosion based on numerical analysis. Thin-Walled Structures. 2020;148, 106579.

[2] ZHANG Yanhua. Principles of Welding Mechanics and Structural Integrity. Architecture & Building Press. 2007; China: Beijing.

[3] Farajian, M. Welding residual stress behavior under mechanical loading. Welding in the World. 2013; 57 (2), 157-169.

[4] Osgood W F. Mechanics[M]. Crawford: Crawford Press, 2007.

[5] Brar, G. S., and Singh, C. S. Fea of residual stress in cruciform welded joint of hollow sectional tubes. Journal of Constructional Steel Research. 2014;102, 44-58.

[6] W. Y. Wang, G. Q. Li, Y. Ge. Residual Stress Study on Welded Section of High Strength Q460 Steel After Fire Exposure. Advanced Steel Construction. 2015;11(2), 150-164.

[7] Bo Yang, Shidong Nie, Shao-Bo Kang, Gang Xiong, Ying Hu, Jubo Bai, Weifu Zhang, Guoxin Dai. Residual Stress Measurement on Welded Q345GJ Steel H-Sections by Sectioning Method and Method Improvement. Advanced Steel Construction. 2017;13(1), 78-95.

[8] Yong-Lei Xu, Yong-Jiu Shi, Yi-Ran Wu, Ling-Ye Meng. Residual Stress of Welded I Sections Fabricated from High Performance Steel: Experimental Investigation and Modelling. Advanced Steel Construction, 15(1), 1-8, 2019.

[9] Mirzaee-Sisan and A. Welding residual stresses in a strip of a pipe. International Journal of Pressure Vessels and Piping. 2018;159, 28-34.

[10] GUO Zhengxing, ZHU Zhangfeng, NIU Meng. Case Analysis and Warning of Installation Collapse Accidents of Steel Structure. Construction Technology. 2010;39 (07): 35-39.

[11] Ding Y., Qi L., Li Z.X. Mechanical calculation model for welded hollow spherical joint in spatial latticed structures. Advanced Steel Construction. 2011;7(4), 330-343.

[12] Zang Qian, LIU Hongbo, LI Yanbo, CHEN Zhihua, LI Xinghao. Mechanical properties of welded hollow spherical joints reinforced with external ribs under axial tension. Spatial Structures. 2022;28 (01): 71-78.

[13] YU Kequan, YU Jiangtao, TANG Bo. Experimental And Finite Element Analysis on The Ultimate Bearing Capacity of Hollow Spherical Joints with Ribbed Stiffener. Industrial Construction. 2011;41 (08): 85-90.

[14] CHEN Zhihua, WEN Suolin, LIU Hongbo, WANG Xiaodun, HU Hongzhi, HAN Ruijing. A Study on the Mechanical Properties of Large-Size Welded Hollow Spherical Joints of Beijing Daxing International Airport. Progress in Steel Building Structures. 2022;24 (01): 15-23.

[15] Li X. Load-carrying Capacity and Practical Design Method of Welded Hollow Spherical Joints in Space Latticed Structures. Advanced Steel Construction. 2010;6(4), 976-1000.

[16] Liao, J., Zhang, Y., Wu, J. Short-member model of reticulated shell with semi-rigid welded hollow spherical joints for elastic-plastic analysis. World Earthquake Engineering. 2010; 26 (3), 37-42.

[17] LIU Haifeng, LUO Yaozhi, XU Xian. Rigiditty of Welded Hollow Spherical Joints on Finite Element Analysis Precesion of Reticulated Shells. Engineering Mechanics. 2013;30 (01): 350-358+364.

[18] Lopez A, Puente l, Aizpurua H. Experimental and analytical studies on the rotational stiffness of joints for single-layer structures. Engineering Structures. 2010;33 (3): 731-737.

[19] Wang, X., Wang, F. Stiffness analysis of welded spherical joints with rib stiffeners. Applied Mechanics and Materials. 2011;71-78, 3756-3759.

[20] YAN Xiangyu, ZHANG Qiwu, QI Guocai, CHEN Zhihua. Study on bending stiffness of welded hollow spherical joints based on bending loading states. Journal of Experimental Mechanics. 2019; 34 (06): 945-953 .

[21] Yan X, Zhang Y, Chen Z, Liu H, Zhang Q. Flexural capacity and bending stiffness of welded hollow spherical joints with H-beams. Advances in Structural Engineering. 2021;24(5):1024-1039.

[22] Liu Hongbo, Gao Haotian, Chen Zhihua. Research on reinforcing method for welded hollow spherical joints. Journal of Constructional Steel Research. 182, 2021.

[23] Hong-bo Liu, Ying-jie Zhang, Lan Wang, Zhi-hua Chen. Mechanical Performance of Welded Hollow Spherical Joints at Elevated Temperatures. Advanced Steel Construction. 2020;16(1), 1-12.

[24] Lu J, Chen Z, Liu H, Guo Z. Behavior of eccentrically loaded welded hollow spherical joints after elevated-temperature exposure. Advances in Structural Engineering. 2019;22 (6):1352-1367.

[25] ZHAO Zhongwei, WU Gang. Random Compression Capacity of Corroded Whsjs. Engineering Mechanics. 2021;38 (05): 219-228+238.]

[26] Zhao Zhongwei, Dai Bozhi, Xu Hao, Li Tianhe. Bending capacity of corroded welded hollow spherical joints with considering interaction of tension force and bending moment. Structures. 34, 2021.2656-2664

[27] Zhongwei Zhao, Pingyi Zhang, Song Zhou, Xiongtao Fan. Collapse pressure of randomly corroded spherical shell. Ocean Engineering. 2022;246, 110604.

[28] Zhao Zhong Wei, H. Zhu, Z. H. Chen. Mechanical behavior of single-layer reticulated shell connected by welded hollow spherical joints with considering welding residual stress. Welding in the World. 2016;60(1), 61-69.

[29] LIU Mingjiong. Manual of practical mechanical Engineering materials. 2004; China: Liaoning.

[30] LIU Xiaoyu. Magnetic Measurement Method to Test Steel Bridge Welding Residual Stress. Journal of Chongqing Jiaotong University (Natural Science). 2010;29 (01): 38-41+84.

Advanced Steel Construction – Vol. 19 No. 3 (2023) 273–292
DOI:10.18057/IJASC.2023.19.3.8

RESEARCH ON SEISMIC BEHAVIOR OF L-SHAPED CONCRETE-FILLED STEEL TUBES COLUMN FRAME-BUCKLING RESTRAINED STEEL PLATE SHEAR WALLS

Amer Mohammed [1], Zhi-Hua Chen [1, 2], Yan-Sheng Du [1, *], W. A. H. Mashrah [3], Yu-Tong Zhang [1] and Mu-Wang Wei [4]

[1] *School of Civil Engineering, Tianjin University, Tianjin, 300072, China*
[2] *State Key Laboratory of Hydraulic Engineering Simulation and Safety, Tianjin 300072, China*
[3] *Dali Construction Group Co., Ltd, Hangzhou 310000, China*
[4] *School of Civil Engineering and Architecture, Wuyi University, Wuyishan, Fujian Province, China*
** (Corresponding author: E-mail: duys@tju.edu.cn)*

ABSTRACT

Frame buckling restrained steel plate shear walls (BRSPSWs) have been widely used in high-rise residential buildings. L-shaped concrete-filled steel tube (CFT) columns were used in the frame in this research to investigate the impact of the frame members type in the BRSPSWs system. A nonlinear finite element model (NFEM) was generated to examine the seismic performance of BRSPSWs with various types of connections to the frame elements. The NFEM results were compared to test results to make them more reliable, and the comparison showed that the NFEM can predict the seismic behavior of BRSPSWs. Then based on the validated NFEM results, several parameters were analyzed in parametric studies to assess their impact on the performance of BRSPSWs, including leg's length, column's width-to-thickness, axial compression ratio, and height-to-thickness of the steel plate, concrete panel's thickness, and bolt arrangement. The effect of these parameters on lateral resistance and yield stiffness was reported and discussed. A theoretical model has also been proposed based on modified plate-frame interaction (MPFI) to calculate the yield lateral resistance of BRSPSWs. The outcomes of MPFI were validated through testing and NFEM findings, and the comparison revealed reasonable concurrence.

Copyright © 2023 by The Hong Kong Institute of Steel Construction. All rights reserved.

ARTICLE HISTORY

Received: 18 October 2022
Revised: 17 April 2023
Accepted: 10 May 2023

KEYWORDS

Buckling restrained steel plate shear walls;
L-shaped CFT columns;
Nonlinear finite elements model;
Seismic performance;
Connection forms;
Modified plate-frame interaction

1. Introduction

Steel-plate-shear-walls (SPSWs) structures have been greatly utilized in high-rise buildings to resist earthquakes and wind loads [1-6]. A few decades ago, different types of SPSWs were proposed and studied, and it was found that the form of connecting the frame member to steel plates have a considerable impact on the overall behavior of SPSWs.

Astaneh et al. [7, 8] suggested and examined the effectiveness of SPSWs, consisting of precast concrete panels containing thin steel plates joined by the shear bolt (see Fig.1). Additionally, the objective of utilizing concrete panels is to prevent steel plates' buckling thereby improving the overall structure's lateral stability and energy absorption capacity. However, when these panels touch the boundary frame, the edges of the concrete panels often become deformed due to the force exerted on them. Consequently, the constraining effect of the concrete panels on the thin steel plate is diminished. Accordingly. A novel SPSWs system proposed by Astaneh et al. [9], making a gap between the boundary elements and concrete panels. Similarly, the lateral resistance will be impacted marginally by concrete panels, improving the steel plate's buckling resistance. After that, scholars concluded that the concrete panels get partly deformed causing by shear bolts and nuts, leading to shear deformation. According to the Astaneh's model, an improved buckling-restrained steel plate shear wall was suggested by Guo et al [10], which placed oval holes on the concrete panels to prevent huge damage to panels around shear connectors. The main function of sandwiching the inner steel plate by concrete is to constrain the local buckling and out-plan deformation. According to the research findings, the BRSPSWs have exhibited remarkable lateral resistance and seismic performance [10].

Conversely, research indicates that the connections linking frame elements and the stiffness of the framework significantly impacted the seismic performance of SPSW. Thus, academics have put forth various types of connections as potential solution such as low yield light-gauge and point SPSW [11, 12], perforated SPSW panels [13], partially connected to beam only SPSW [14], steel plate slits SPSW [15], buckling-restrained steel SPSW with inclined-slots [16] bound-columns with buckling-restrained SPSW [17], and partially connected bucking SPSW [18] to overcome steel plate's local buckling and to minimize the stiffness of vertical boundary elements (VBEs). In contrast, the manufacture and construction of these linkages involve intricate processes, which lead to the use of suboptimal materials and reduced economic efficiency. Furthermore, a group of scholars has proposed a new type of partial connection inner BRSPSW as a solution to generate a robust system capable of withstanding lateral forces while requiring low stiffness requirements for VBEs [19-22].

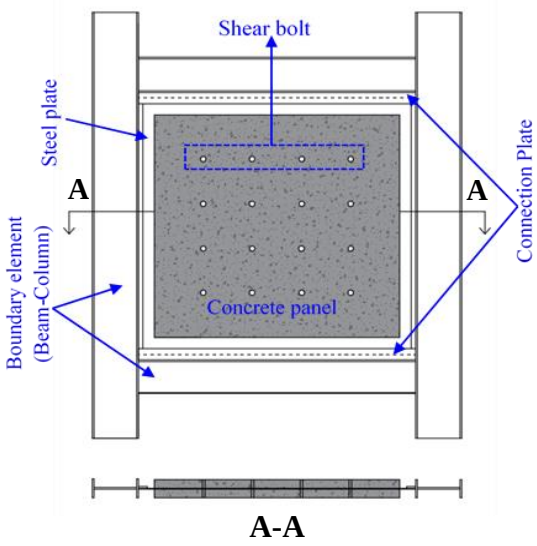

Fig. 1 Strip model of steel plate shear walls [2]

The seismic performance of buckling-restrained SPSWs with four side connections was well examined [23-27]. Buckling-restrained SPSWs showed better lateral stiffness, lateral resistance, and energy consumption than unconstrained SPSW. The transferred force from boundary columns to SPSWs in four-sided buckling-restrained SPSWs may cause early deformation on columns [26]. Diagonal local buckling and fracture at the corner steel plates always happened. Also, the size of buckling-restrained SPSWs should be a little large to build the four-side connections steel plate to connect it with the boundary frames [25, 26]. Buckling-restrained SPSWs with two-side connections were designed and studied to exceed the premature deformation of columns. It was found that the buckling-restrained SPSW with two-side connections has an excellent deformation capacity. Still, the lateral resistance and energy consumption were less than BRSPSW with four-side connections [14, 24, 28, 29].

Furthermore, several studies were carried out in SPSW using various VBEs such as H-section and CFT columns [18, 22, 30, 31]. Chen et al. [32-34] suggested and studied axial behavior and presented a superposition approach for determining ultimate capacity [35-37]. To boost the application of CFT columns, Zhou et al [38]. carried out a test and FE modeling study on a special-shaped CFT column frame shear wall and inspected the effect of the

compression load ratio on the stiffness of the frame. The findings presented that the frame has good seismic performance with lateral resistance, ductility.

This paper firstly conducted an experimental program on BRSPSWs under lateral cyclic loads. Then three-dimensional NFEM was established using a commercial finite element application ABAQUS CAE to simulate the seismic performance of BRSPSWs. Based on validated NFEM, parametric analyses were generated to evaluate the impact of critical aspects, including leg's length, width-to-thickness of column, compression load, the steel plate's height-to-thickness of, thickness of the concrete panel, and bolt arrangements. All parameters were discussed based on lateral resistance and stiffness. Finally, a modified calculation approach has been suggested for calculating the lateral resistance at yield point, and it was validated against the test and parametric models' results.

2. Test program

An experimental program [22] with three specimens was included in this research paper to prove the accuracy of numerical simulation on the seismic performance of frame-buckling restrained steel plate shear walls (BRSPSWs).

2.1. Specimens' design

Three of 1/2 scale specimens with one bay and two floors were designed to study the seismic behavior of BRSPSWs with various types of connections between boundary members, as illustrated in Fig.2. The methodology and geometric configuration were obtained from an engineering endeavor in China. H-section beam and L-shaped CFT columns manufactured horizontal and vertical boundary elements, respectively. To create the L-shaped CFT columns, three square steel tubes were linked with two vertical plates by welding connection, as shown in Fig.3. Additionally, to link the columns and beams, Vertical stiffeners were employed to connect the L-shaped CFT column to the beam, as depicted in Fig. 4.

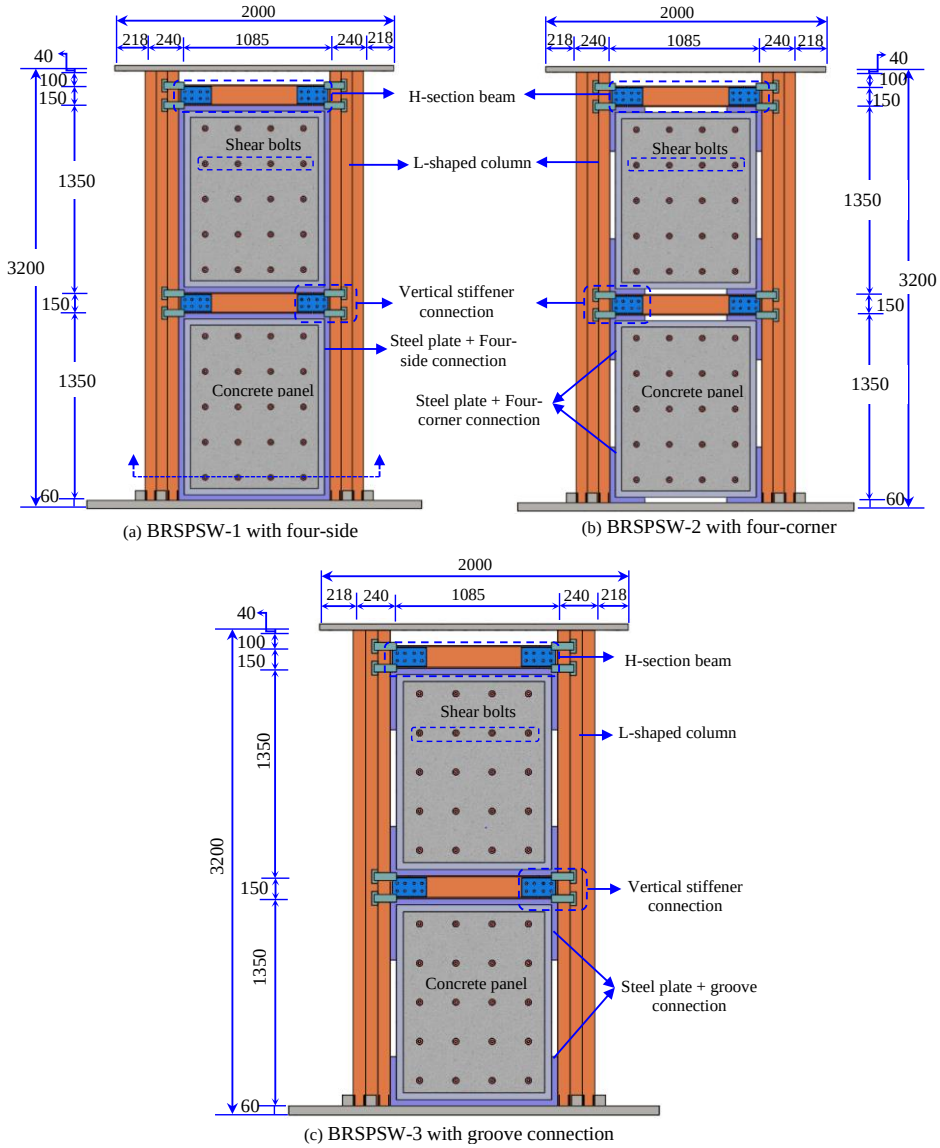

(a) BRSPSW-1 with four-side

(b) BRSPSW-2 with four-corner

(c) BRSPSW-3 with groove connection

Fig. 2 Elevation view of specimens

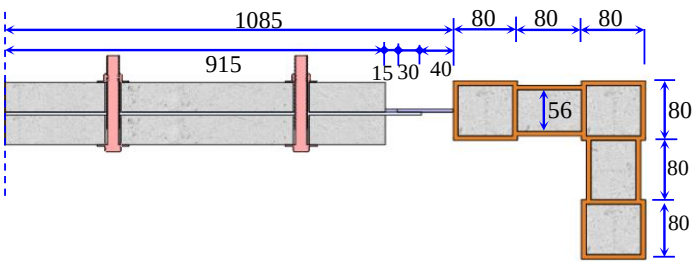

Fig. 3 Top view of column-shear wall connection

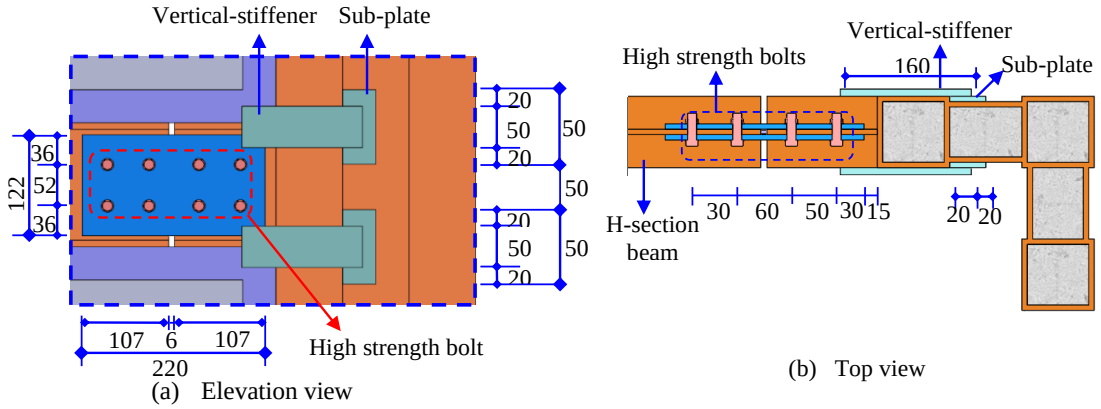

Fig. 4 Beam-column connection

Three kinds of connections have been utilized to link the steel plates to the frame members, namely four-side, four-corner and groove connections corresponding to the subsequent specimens, BRSPSW-1, BRSPSW-2 and BRSPSW-3. In greater details, the four-side indicates that the inner steel plate was completely linked with the frame members Fig. 5(a), since the four-corner was partly linked by 320mm and 250mm to the columns and beams, as seen in Fig. 5(b). Likewise, the beams were entirely connected to the inner steel plate while partially with columns (see Fig. 5(c)). The two concrete panels sandwiched steel plate using high-strength bolts to constrain its early buckling. Besides, the concrete panels were two-way reinforced with HPB235 by a one sheet.

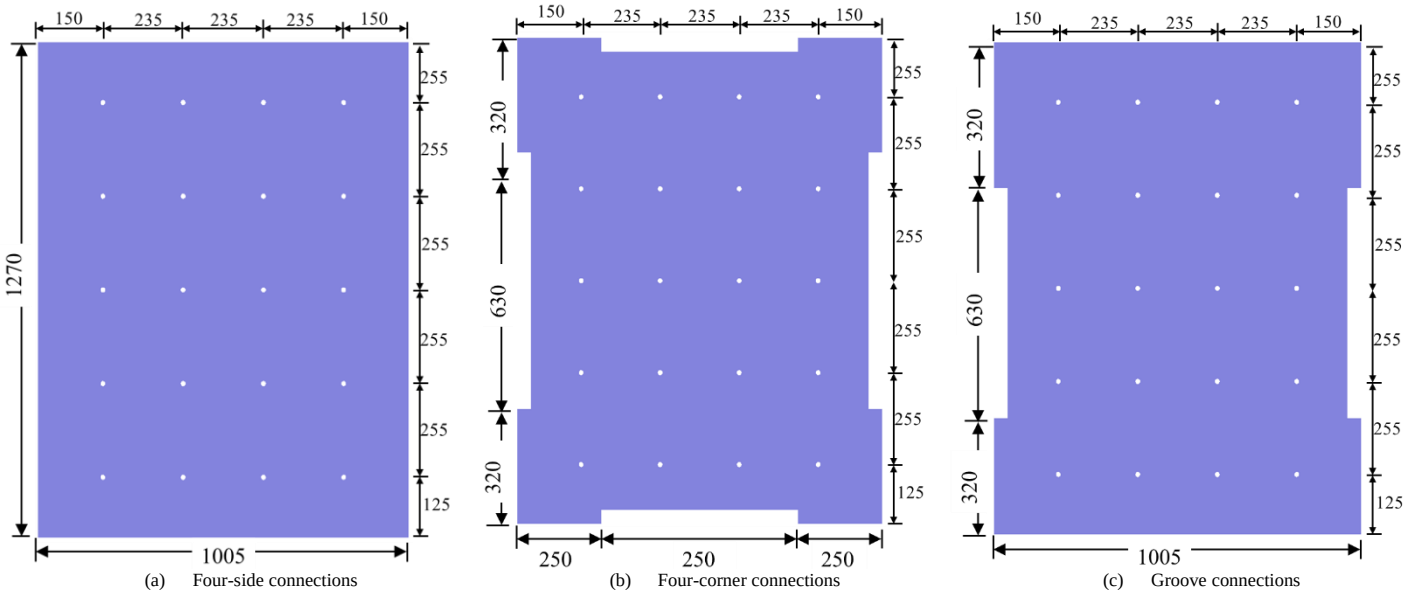

Fig. 5 Details of buckling steel plates

2.2. Material properties

All steel tubes, H-section beams, and steel plates were manufactured using Q235 steel. A tensile coupon test was conducted on different material types and thicknesses to determine the mechanical properties based on the Chinese guidelines GB/T 228.1–2010 [39], as seen in Fig.5(a). Engineering stress-strain relationships acquired from the steel material testing are illustrated in Fig. 5(b). The outcomes of each coupon's mean yield and ultimate strength, the elasticity of modulus, and fracture of strain are listed in Table 1. Notable, thickness has an impact effect on strength and stiffness.

Concrete panels and infill are both constructed using normal-grade C40 concrete. Six cubes **100 × 100 × 100 mm** concrete cube was designed and tested in accordance with the GB/T50081-2019 [40] guidelines to determine the mechanical properties. The mean values of elasticity of modulus and compressive strength were 236 GPa and 41.59 MPa.

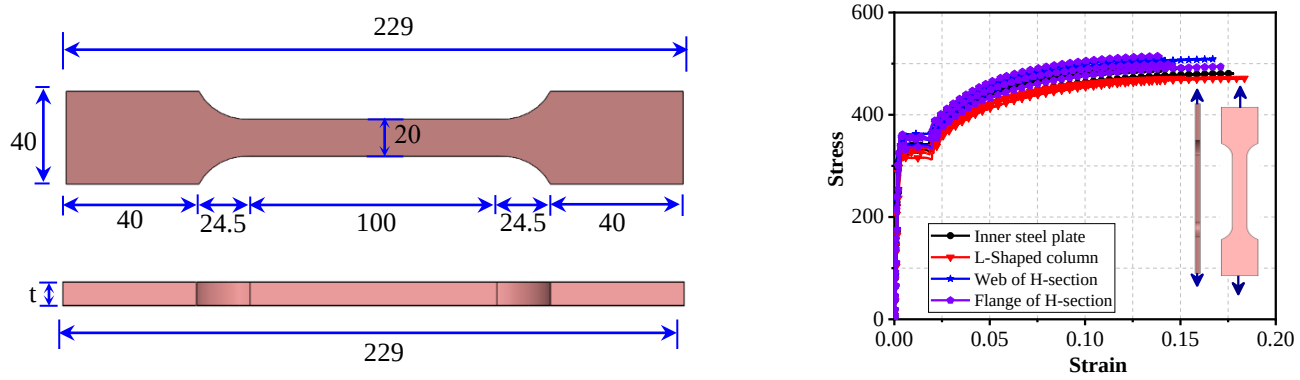

Fig. 6 Steel material test

Table 1
Test results of steel material properties

Elements	Thickness (mm)	f_y (MPa)	f_u (MPa)	E (MPa)	f_y/f_u	ε_f
Steel tubes for L-Shaped column	6	306	469	168	0.65	0.141
Web of H-section	6	338	502	176	0.67	0.169
Flange of H-section	8	339	508	176	0.67	0.168
Inner steel plates	4	327	488	172	0.67	0.165

Note: f_y yield strength, f_u refers ultimate strength, E is elasticity of modulus, ε_f is the fracture strain

2.3. Test setup and loading protocol

The specimens were positioned on the rigid floor and linked to it by high-strength bolts to approach fixed ends, as illustrated in Fig. 7. The specimens underwent lateral cyclic loading using a 300-ton bi-directional hydraulic actuator that was connected to the loading beam on the top plate. Besides, to consider the impact of the slab restraints in the horizontal orientation of the actual buildings, steel tubes were put at the top of each story.

Fig. 8. illustrates the recorded horizontal loading data for BRSPSWs, which was obtained by applying the Chinese standard JGJ 101-2015 [41]. The loading progression was classified into the force-control phase and displacement-control phase. During the load-control phase, one cycle with a 20 % interval from the yield load ($\boldsymbol{P_y}$) was adopted to apply the loading-control phase. Subsequently, the displacement-control phase took over from the load-control phase, where the displacement increments for each level were determined by the yield displacement (Δ_y), and three uniform cycles were executed for each level, as seen in Fig.8. Finally, the loading procedure was interrupted in two scenarios; firstly, when the lateral resistance had declined to eight five percent after reaching the maximum resistance, and secondly, once the samples had undergone complete damage.

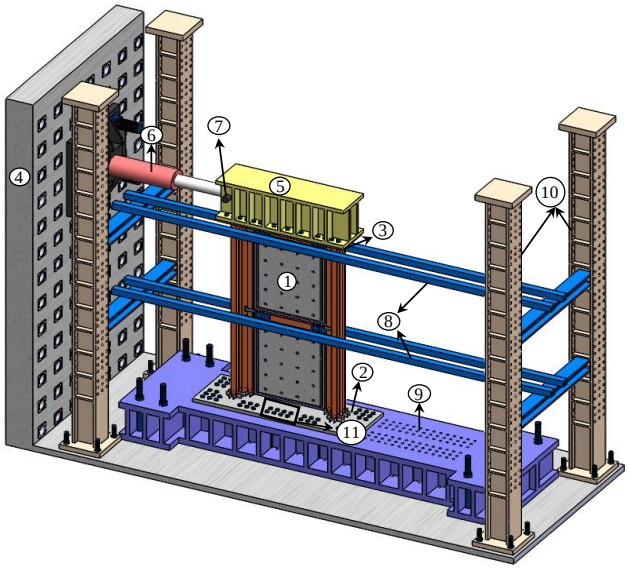

1. Specimen; 2. Bottom plate; 3. Top plate; 4. Reaction wall; 5. Loading beam; 6. Hydraulic actuator; 7. Hinged joint; 8. Square steel tubes; 9. Foundation; 10. Reaction frame; 11. High strength bolts

Fig. 7 Test setup of BRSPSWs under lateral cyclic loads

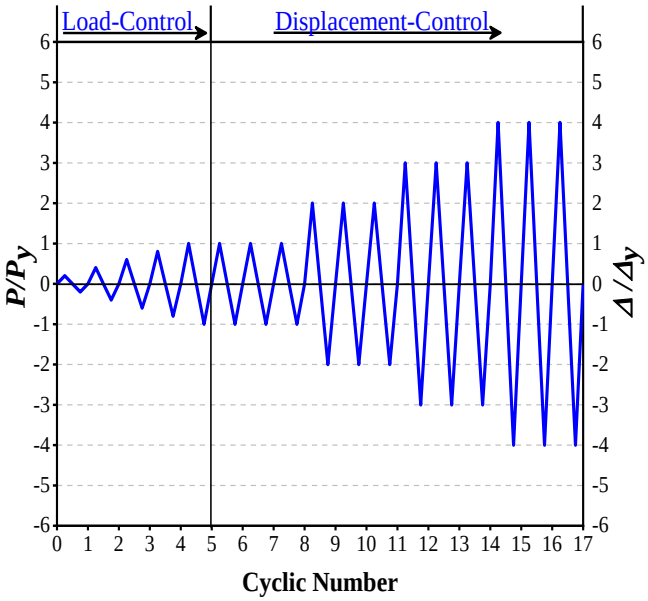

Fig. 8 Time-history of loading BRSPSW

3. Finite element model

As mentioned above, the main target of the tests was to validate the accurateness of the numerical outcomes. Even though the test program revealed valuable investigation, the results are inadequate for further analysis of BRSPSWs. Thus, generating nonlinear finite element models (NFEM) is mandatory to deeply understand the performance of BRSPSWs with critical parameters obviating conducting a new additional testing program [42].

3.1. General

ABAQUS explicit/solver was adopted to build more FE models. Additionally, to obtain high accuracy in the explicit/solver, geometrical, material nonlinearities, meshing convergence, complicated contact pairs, loading rate, and boundary conditions were considered during simulation.

3.2. Material models

All steel components were modeled using nonlinear isotropic/kinematic hardening. Q235 steel components was undergoing cyclic loading and unloading according to a five-stage uniaxial stress-strain model, as shown in Fig. 9. and Eq (1). The mechanical properties acquired from the material test were inserted during modeling. In addition, shear and ductile damage were employed to replicate steel materials' tearing and fracture behavior in modeling [43].

$$\sigma_s = \begin{cases} E_s\varepsilon_s & ,\varepsilon_s \le \varepsilon_e \\ -A\varepsilon_s^2 + B\varepsilon_s + C & ,\varepsilon_e \le \varepsilon_s \le \varepsilon_{e1} \\ f_y & ,\varepsilon_{e1} \le \varepsilon_s \le \varepsilon_{e2} \\ f_y[1+0.6(\varepsilon_s-\varepsilon_{e2})/(\varepsilon_{e3}-\varepsilon_{e2})] & ,\varepsilon_{e2} \le \varepsilon_s \le \varepsilon_{e3} \\ 1.6f_y & ,\varepsilon_s \le \varepsilon_{e3} \end{cases} \quad (1)$$

where E_s is steel elastic modulus, σ_s and ε_s denote the stress and strain of steel respectively; f_y indicates the yield strength of steel; $\varepsilon_e, \varepsilon_{e1}$, and ε_{e2} represents the medium strain; ε_{e3} is the ultimate strain; A, B and C are constant. All strain values and constants can be calculated as follows.

$$\varepsilon_e = 0.8\frac{f_y}{E_s};\quad \varepsilon_{e1} = 1.5\varepsilon_e;\quad \varepsilon_{e2} = 10\varepsilon_{e1};\quad \varepsilon_{e3} = 100\varepsilon_{e1} \quad (2)$$

$$A = 0.2\frac{f_y}{(\varepsilon_{e1}-\varepsilon)^2};\quad B = 2A\varepsilon_{e1};\quad C = 0.8f_y + A\varepsilon_e^2 - B\varepsilon_e \quad (3)$$

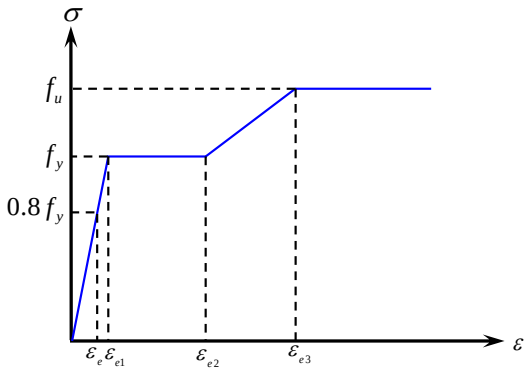

Fig. 9 Stress-strain model for steel materials

The concrete infill and panels were simulated using the concrete damage plasticity model. Two failure mechanisms were assumed to accurately model infill concrete and precast concrete's behavior, which are compressive and tensile behavior. On the other hand, Han's stress-strain relationship was adopted to categorize the plastic behavior of the concrete [44]. The following mathematical equations can express the stress-strain relationship.
For concrete compressive behavior,

$$y=\begin{cases}2x-x^2 & ,x\le 1\\ \dfrac{x}{\beta_0(x-1)^{1.6+1.5/x}+x} & ,x>1\end{cases}\qquad x=\frac{\varepsilon_c}{\varepsilon_{c0}};y=\frac{\sigma_c}{\sigma_{c0}} \tag{4}$$

In which

$$\sigma_{c0}=\left[1+(-0.0135\xi+0.1\xi)\left(\frac{24}{f_c^{'}}\right)^{0.45}\right]f_c^{'} \tag{6}$$

$$\varepsilon_{c0}=[(1300+760(\frac{f_c^{'}}{24}-1)]\xi^{0.2}\times 10^6 \tag{7}$$

$$\varepsilon_0=(1300+12.5f_c^{'})\times 10^6 \tag{8}$$

$$\beta_0=\begin{cases}\dfrac{(f_c^{'})^{0.1}}{1.35\sqrt{1+\xi}} & ,\xi\le 3\\ \dfrac{(f_c^{'})^{0.1}}{1.35\sqrt{1+\xi}(\xi-2)^2} & ,\xi>3\end{cases} \tag{9}$$

$$\xi=\frac{A_s f_y}{A_c f_{ck}} \tag{10}$$

For concrete tensile behavior,

$$y=\begin{cases}1.2x-0.2x^6\\ \dfrac{x}{0.31\sigma_{t0}(x-1)^{1.7}+x}\end{cases} \tag{11}$$

In which

$$x=\frac{\varepsilon_t}{\varepsilon_{t0}};y=\frac{\sigma_t}{\sigma_{t0}} \tag{12}$$

$$\sigma_{t0}=0.26(1.25f_c^{'})^{2/3} \tag{13}$$

$$\varepsilon_{t0}=0.0000431\sigma_{t0} \tag{14}$$

where $\sigma_{c0},\varepsilon_{c0}$ are compressive stress and strain of concrete, respectively f_y and A_s denote the yield strength of steel tubes and cross-sectional area; f_{ck} and A_c indicate compressive strength of concrete and its cross-sectional area; $f_{ck}=0.67f_{cu}$ for normal concrete; $f_c^{'}$ and f_{cu} are cylinder and cube of concrete's compressive strength, the elastic modulus elasticity of concrete could be determined according to ACI-318 code as $E_c=4730\sqrt{f_c^{'}}$ [45]; Poisson's ratio $\nu=0.2$ for concrete. Additionally, $\varepsilon_{t0},\sigma_{t0}$ refer to the tensile strain and stress of concrete, respectively.

3.3. Elements and meshing convergence

Each deformable part's three-dimensional simulation was carried out using hex-structured mesh controls, including a linear brick with eight nodes, hourglass-shaped and reduced integration control element of type C3D8R. A sequence of meshing convergence was take into account during simulation to make an equilibrium between the accuracy of numerical modeling and computing efficiency. Figs. 10(a) and (b) present the assemble and meshing dimension of all elements of the structures.

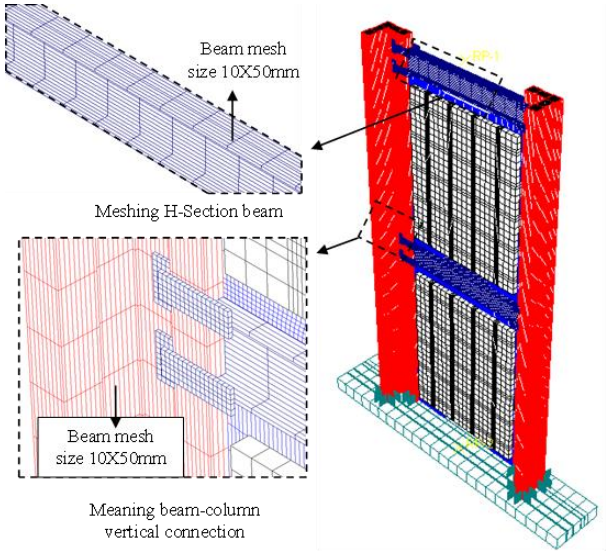

(a) Meshed element model

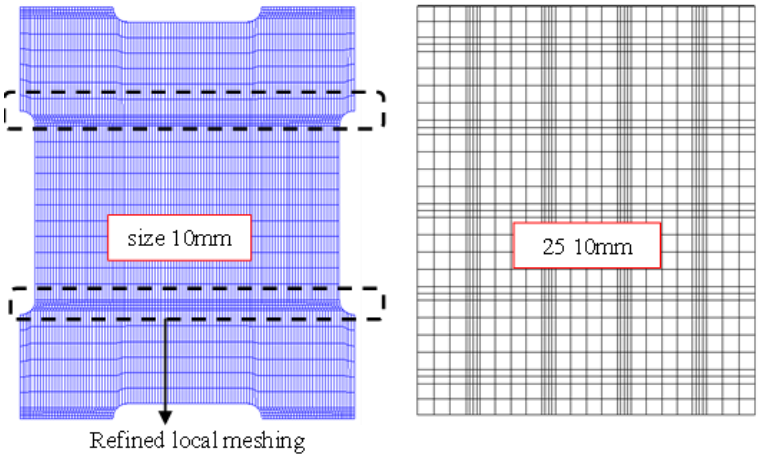

(b) Refined Meshing of inner steel plate and concrete panel

Fig. 10 Typical meshing of finite element model

3.4. Interactions and boundary conditions

All steel members were tied together to simulate welding performance, including lower boundary plate, frame elements, and steel plates. Due to the complex interaction among bolts, concrete panel, and steel plates, the concrete panels were tied to the steel plates at specific positions, as illustrated in Fig. 11. These specific positions chosen at the concrete panels and tied to the steel plates could simulate the bolt functions in the tested specimens regarding connecting the concrete panels to the steel plate (see Figs. 2-3). To establish how the concrete panels and steel components interact, a surface-to-surface

contact algorithm was utilized. A hard contact method was employed in the perpendicular direction, while a penalty friction model with a coefficient of 0.6 was implemented in the parallel directions [46, 47]. The slave and master surfaces were determined based on the relative hardness of the materials.

Fig. 11. demonstrates the simulation of loading and boundary conditions. The top surfaces of the columns were coupled to a reference loading point, and then the lateral load was applied as displacement loading. Four constrained beams with fixed ends were launched on both upper sides of each story to simulate square steel tubes for the tests, and these beams were restrained in both displacement and rotations. The test also restrained displacement and rotation for emulating fixed support. To account for initial defects and the buckling modal of steel plates during simulation, the first eigenmode was chosen as the buckling modal allocation.

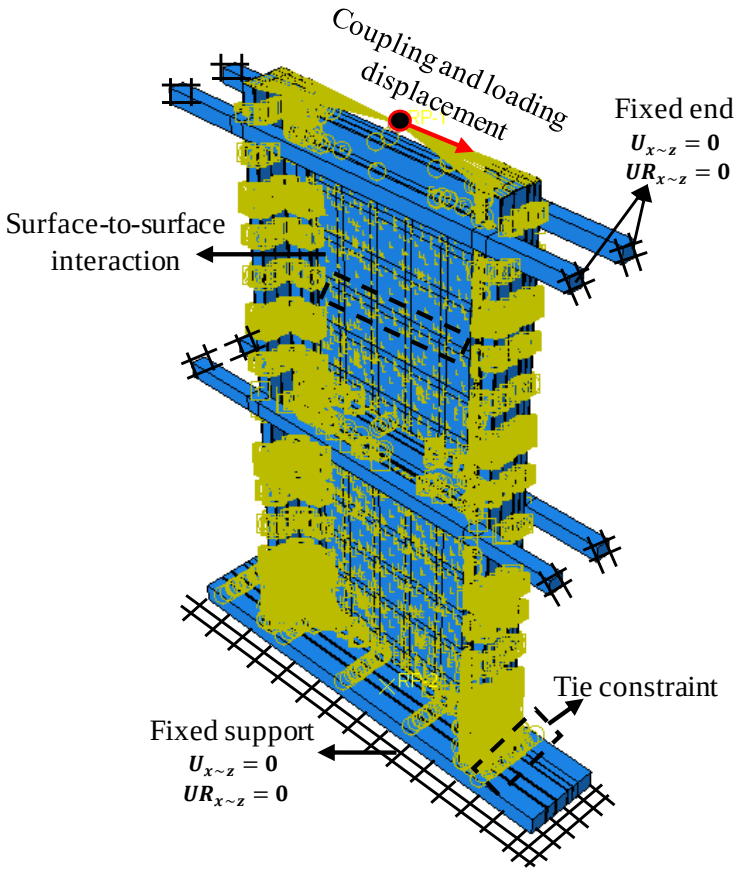

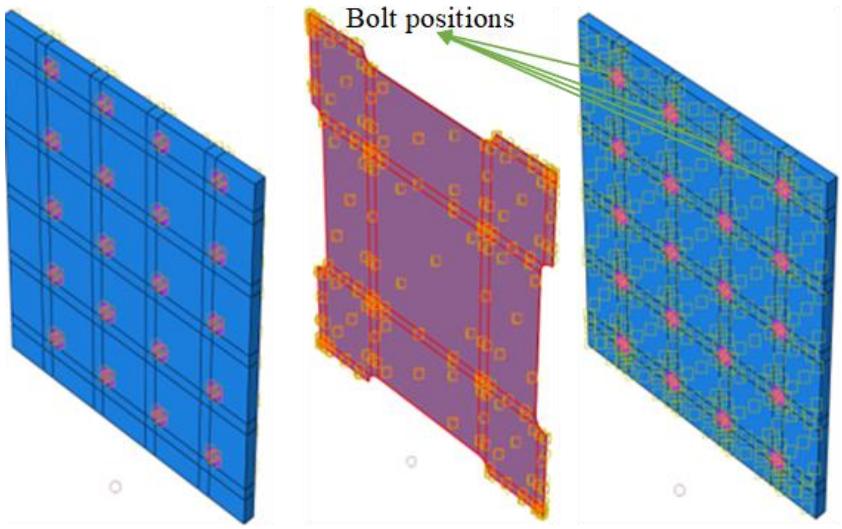

Fig. 11 Numerical simulation details in interactions and boundary conditions

3.5. Validations

3.5.1. Comparison of failure modes

Fig. 12. compares the FE simulation with an experimental program of deformation shapes and failure modes of BRSPSW-1, 2 and 3. It noticed that the FE simulations could accurately predict the failure patterns of BRSPSWs. Firstly, the manifestation of damage on BRSPSW-1 is assigned to the occurrence of concrete crackling at the intersection of the concrete panels, coupled with the fracturing and impairment of the column. Furthermore, it has been observed that the lateral resistance of BRSPSW-1 deteriorated sharply to less than 85%, and the lower section of the boundary columns in BRSPSW incurred extensive damage, primarily owing to the adverse fully connected of the steel plate to the frame members, as displayed in Fig. 12(a). Secondly, the BRSPSW-2 system effectively detected both inner steel plates' local buckling and concrete cracking at the corners of the panels owing to its distinct configuration of separating the inner steel plate and concrete panels, as seen in Fig. 12(b). Conversely, the boundary columns remained undamaged even though the effective connected area of the frame to steel plates between the

was reduced. Finally, Fig. 12(c). depicts the comparison of deformation shaped between FE-simulation and test phenomenon. BRSPSW-3 experienced multiple failures, including local buckling of the steel plate, cracking of concrete panels, and fractures and tears in both the frame members and inner steel plate. Subsequently, considering the high accuracy and adequacy of NFEM, elaborating parametric studies is suitable and recommended.

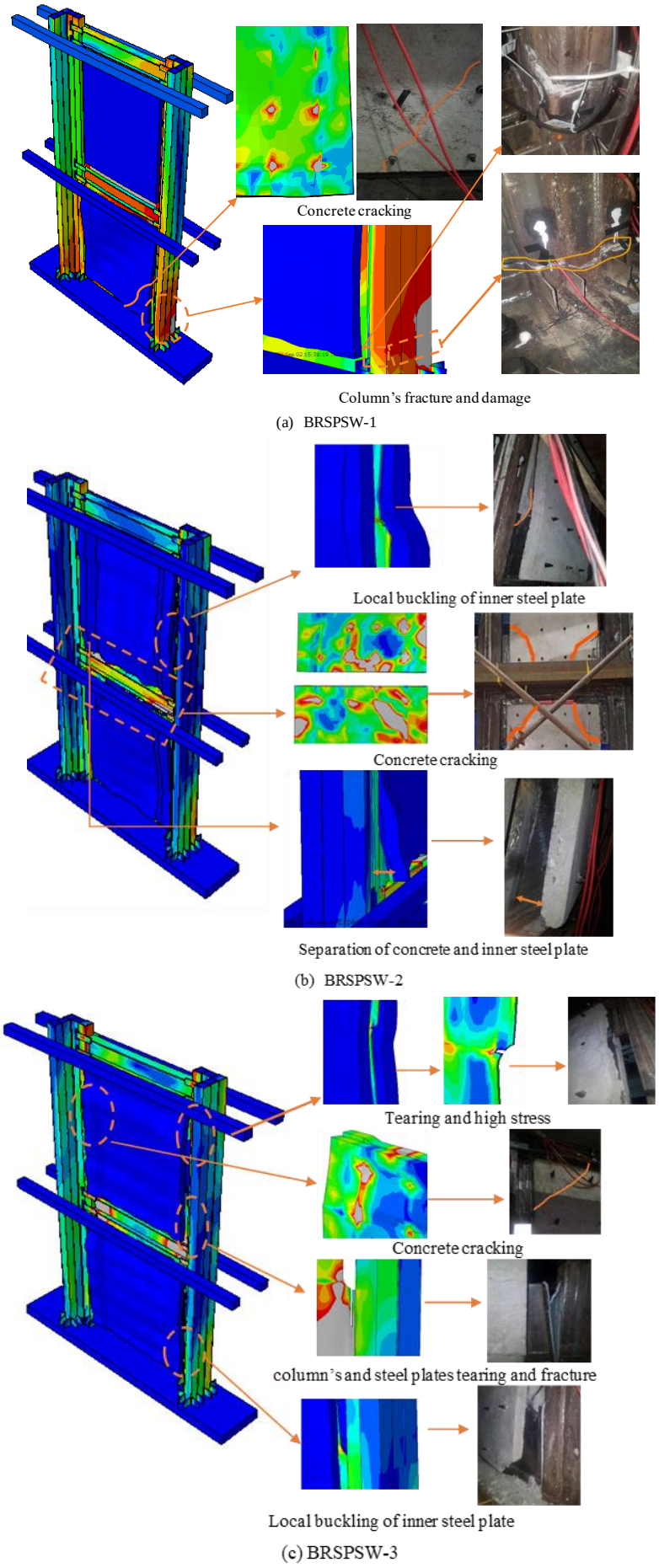

Fig. 12 Validation of failure modes between experiments and numerical simulations

3.5.2. Comparison of hysteretic and skeleton curves

Fig. 13(a-c). compares the experimental load versus displacement $(P-\Delta)$ curves with FE-simulation results. It shows that the FE simulations can precisely simulate the hysteresis and skeleton curves of BRSPSWs. The behavior of both hysteretic and skeleton curves remains the same for both test and FE modeling results. Besides, the pinching effect in the hysteretic curves was observed in both the test and FE models outcomes, and it shows that the pinch behavior is mainly affected by connection forms. In BRSPSW-3, the pinch behavior appeared clearer than others due to the steel plates' local buckling, while the BRSPSW-1 is the fullest among them, according to Fig. 13 and Table 2. A comparison was made between the test results and the corresponding FE predictions for yield, peak lateral resistance, and yield stiffness in both positive and negative directions. The mean value of test-to-FE simulations of yield and peak lateral resistance was (1.02 & 0.99) with standard deviations (0.05, 0.04). The average lateral yield stiffness is (0.97) with std.v (0.03). Consequently, FE simulation could predict the performance of BRSPSWs subjected to lateral cyclic load.

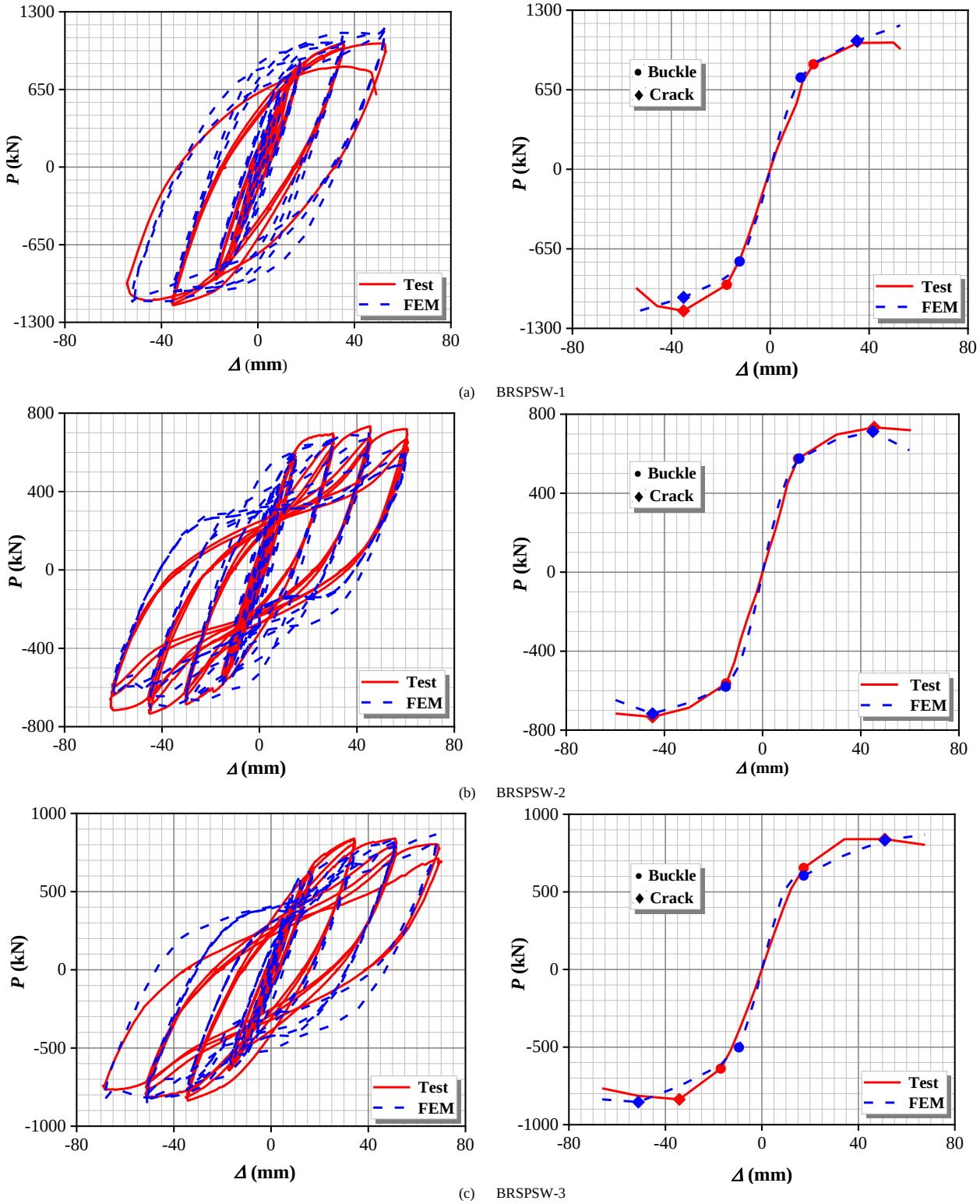

Fig. 13 Comparisons of load-displacement relationship of tests-to-FE-models

Table 2
Comparison test-to-prediction ratios for P_y, P_m and K_y

items	$P_{y,Test}$ (kN)	$P_{y,FE}$ (kN)	$\frac{P_{y,Test}}{P_{y,FE}}$	$P_{m,Test}$ (kN)	$P_{m,FE}$ (kN)	$\frac{P_{m,Test}}{P_{m,FE}}$	$K_{y,Test}$ $(\frac{kN}{mm})$	$K_{y,FE}$ $(\frac{kN}{mm})$	$\frac{K_{y,Test}}{K_{y,FE}}$

	+	878.00	922.00	0.95	1038.90	1176.30	0.88	43.25	46.33	0.93
BRSPSW-1	-	-956.10	-949.00	1.01	-1156.90	-1155.30	1.00	49.80	47.21	1.05
	Avg	**917.05**	**935.50**	**0.98**	**1097.90**	**1165.80**	**0.94**	**46.52**	**46.77**	**0.99**
	+	590.80	595.20	0.99	733.70	712.80	1.03	35.38	36.97	0.96
BRSPSW-2	-	-585.20	-595.50	0.98	-733.30	-717.10	1.02	32.69	34.62	0.94
	Avg	**588.01**	**595.35**	**0.99**	**733.50**	**714.95**	**1.03**	**34.03**	**35.80**	**0.95**
	+	694.40	620.50	1.12	840.00	869.40	0.97	36.17	31.34	1.15
BRSPSW-3	-	-670.10	-645.80	1.04	-873.20	-853.80	1.02	33.84	32.13	1.05
	Avg	**682.25**	**633.15**	**1.08**	**856.60**	**861.60**	**0.99**	**35.01**	**31.73**	**1.10**
Mean value				1.02			0.99			0.97
Std.v				0.05			0.04			0.03

Note: $P_{y,Test}$, $P_{y,FEM}$, $P_{m,Test}$, $P_{m,FEM}$, $K_{y,Test}$ and $K_{y,FEM}$ signify test value of yield, peak resistance, and yield stiffness gained from experiments and FE-modeling, respectively. The yield stiffness can be calculated as follows K_y P_y/Δ_y. The general yield moment method is adopted to calculate yield point, as seen in Fig. 14.

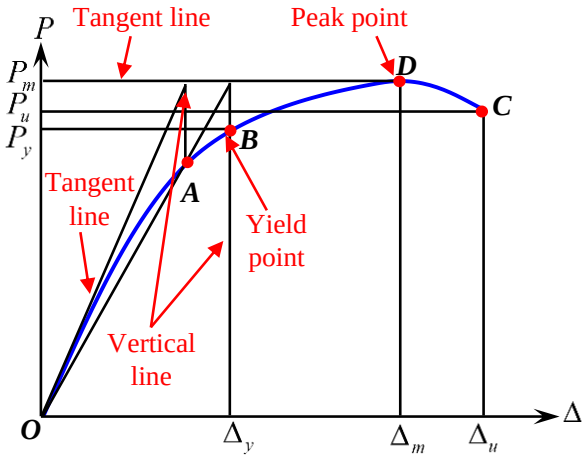

Fig. 14 Yield point determinations diagram

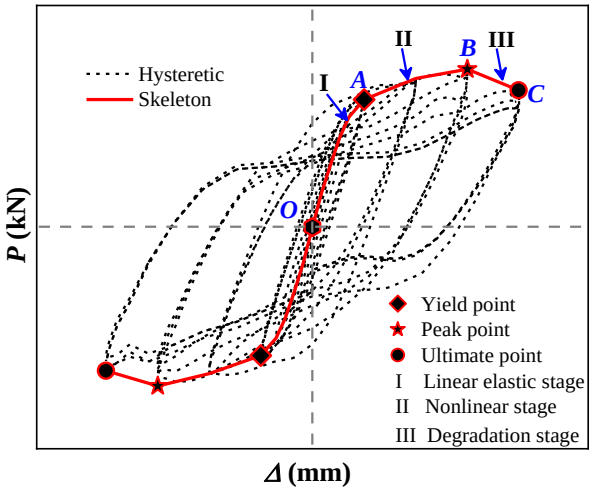

Fig. 15 General classification of hysteretic and skeleton curves

4. Numerical parametric studies on BRSPSW

4.1. General behavior

Fig. 15. plots P-Δ (hysteretic and skeleton) curves. From the test and FE-simulated results in (Fig. 13(a-c)), it can be observed that all P-Δ curve has three stages, including linear, nonlinear and degradation stages. As seen in Fig. 15, at linear stage (I), (i.e., *OA)*, the cyclic load of the BRSPSWs increase linearly with the increasing lateral displacement. At the end of the linear stage, the yield point of BRSPSWs was achieved. Nonlinear with pinch behavior is observed during the nonlinear stage (II), (i.e., curve *AB* in Fig. 15.) owing to of inner steel plates' local buckling resistance, and the peak point was achieved at the end of this stage. After the samples reached their peak points, the degradation stage (II) started. When the lateral resistance reached 85% of peak lateral resistance, the models achieved their ultimate points (i.e., *BC* in Fig. 15.)

4.2. Failure modes

Generally, high stress on bolts' positions was appeared on the concrete panels, indicating cracking on the concrete panels stared from bolts holes due to buckling on inner steel plates, as shown in Fig. 16(a). With increasing the lateral displacement, the local buckling of steel plates started from their edges and developed with appearing diagonally. As seen in Fig. 16(b), it appeared diagonally in the nonlinear phase. after that, due to the large local buckling of steel plate, concrete separation and out-plane deformation was obvious, indicating less buckling resistance by concrete panels (see Fig.16 (a&b)). In the degradation stage, the concrete panels were severely damaged, and the inner steel plate was torn because of their instability to resist the overall buckling (see Fig. 16(b)). Finally, the column was buckled at the bottom, as shown in Fig.16(c).

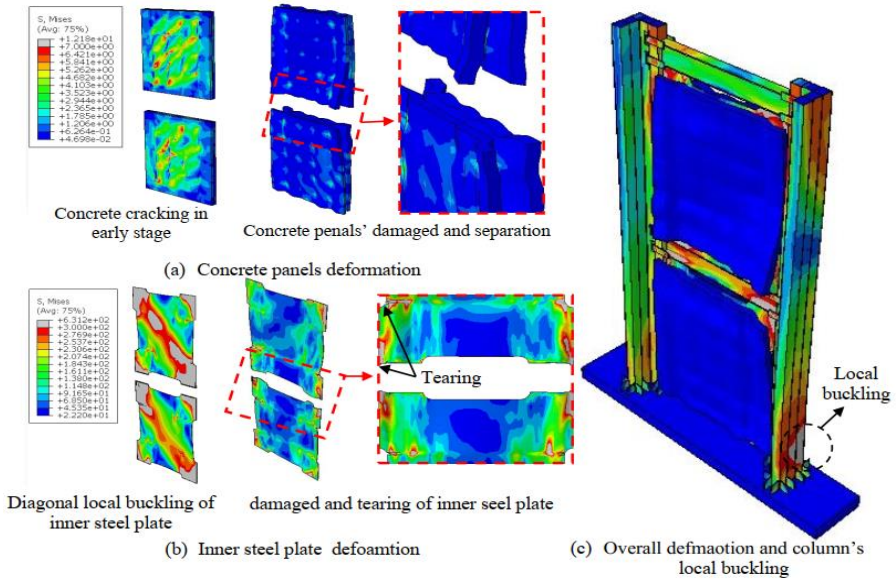

Fig. 16 Overall FE-failure modes of BRSPSW

4.3. Details of cases in the parametric studies

After verifying the numerical results via comparing them with experimental results of BRSPSWs under cyclic loading, numerical parametric investigations were executed to explore the impact of crucial factors, including leg's length (L_p), columns' width-to-thickness (D/t), axial compression ratio (n_d), the inner steel plates' height-to-thickness ratio, thickness of the concrete panels (t_c), and bolt arrangements ($B(RxC)$), as listed in Table 3. Besides, BRSPSW-2 was chosen as a reference to study all these parameters. The yield and peak lateral resistance (P_y & P_m) and lateral yield stiffness (K_y) was used to analyze the behavior of BRSPSWs. The lateral yield stiffness can be determined as the following equation.

$$K_y = \frac{P_y}{\Delta_y} \tag{15}$$

in which K_y is the ratio of yield lateral resistance P_y to its corresponding yield displacement Δ_y .

Table 3
Details of different cases of parametric studies

Samples	Models' ID	L_p (mm)	D/t (%)	n_d (%)	t_s (mm)	t_c (mm)	$B(RxC)$ #
Impact of leg's length	L_P=150	**150**	13.33	0 %	4	40	B(4x5)
	L_P=200	**200**	13.33	0 %	4	40	B(4x5)
	L_P=250	**250**	13.33	0 %	4	40	B(4x5)
	L_P=300	**300**	13.33	0 %	4	40	B(4x5)
	L_P=350	**350**	13.33	0 %	4	40	B(4x5)
	L_P=400	**400**	13.33	0 %	4	40	B(4x5)
Impact of column's width-to-thickness	D/t=20	250	**20.0**	0 %	4	40	B(4x5)
	D/t=16	250	**16.0**	0 %	4	40	B(4x5)
	D/t=13.3	250	**13.3**	0 %	4	40	B(4x5)
	D/t=11.4	250	**11.4**	0 %	4	40	B(4x5)
	D/t=10	250	**10.0**	0 %	4	40	B(4x5)
Impact of axial compression ratio	n_d=0 %	250	13.33	**0 %**	4	40	B(4x5)
	n_d=25 %	250	13.33	**25 %**	4	40	B(4x5)
	n_d=50 %	250	13.33	**50 %**	4	40	B(4x5)
	n_d=75 %	250	13.33	**75 %**	4	40	B(4x5)
	n_d=100 %	250	13.33	**100 %**	4	40	B(4x5)
Impact of Height-to-thickness ratio	t_s=2	250	13.33	0 %	**2**	40	B(4x5)
	t_s=3	250	13.33	0 %	**3**	40	B(4x5)
	t_s=4	250	13.33	0 %	**4**	40	B(4x5)
	t_s=5	250	13.33	0 %	**5**	40	B(4x5)
	t_s=6	250	13.33	0 %	**6**	40	B(4x5)
Impact of concrete panel's thickness	t_c=20	250	13.33	0 %	4	**20**	B(4x5)
	t_c=30	250	13.33	0 %	4	**30**	B(4x5)
	t_c=40	250	13.33	0 %	4	**40**	B(4x5)
	t_c=50	250	13.33	0 %	4	**50**	B(4x5)
	t_c=60	250	13.33	0 %	4	**60**	B(4x5)
Impact of bolt arrangements	B(4x5)	250	13.33	0 %	4	40	**B(4x5)**
	B(4x3)	250	13.33	0 %	4	40	**B(4x3)**
	B(4x2)	250	13.33	0 %	4	40	**B(4x2)**
	B(2x3)	250	13.33	0 %	4	40	**B(2x3)**
	B(2x2)	250	13.33	0 %	4	40	**B(2x2)**

Note: L_p denotes the leg's length of steel plate connection; D/t denotes column's width-to-thickness; n_d denotes the axial compression ratio; t_s denotes the thickness of the steel plate; t_c denotes the concrete panel's thickness; *B(RxC)* denotes the number of bolts arrangements

4.3.1. Influence of leg's length of steel plate

The behavior of BRSPSWs under cyclic load is greatly affected by the connection form of the inner steel plate with the boundary elements [18]. Therefore, the FE-model of the BRSPSW-2 was selected as a reference model in which leg's length $L_p = 250mm$ was adopted (see Fig. 5(b)). Then other FE-models were simulated with different leg's length values (*150mm,200mm,300mm,350mm and 400mm*). The comparison load-displacement curves (hysteretic and skeleton) are represented in Fig. 17 (a-b). It can be noticed that the leg's length did not greatly influence initial stiffness and ductility. Fig. 17(c) plots the yield, peak lateral resistance, and lateral yield stiffness, showing that the lateral resistance increased with the leg's length. However, yield and peak lateral resistance slightly increased when the leg's length was 150, 200, and 250 Fig. 17(c). Then they dramatically increased when the legs were 300mm,350mm, and 350mm. Besides, the lateral yield stiffness showed a slight growth when leg's length was less than 250mm, but when the leg's length was more than 300mm, the stiffness suddenly jumped.

Then it almost remained stable. Consequently, it can be concluded that the leg's length greatly influenced the yield and peak lateral resistance. Still, it is not recommended when the leg's length is less than 250mm due to its negative effect on ductility.

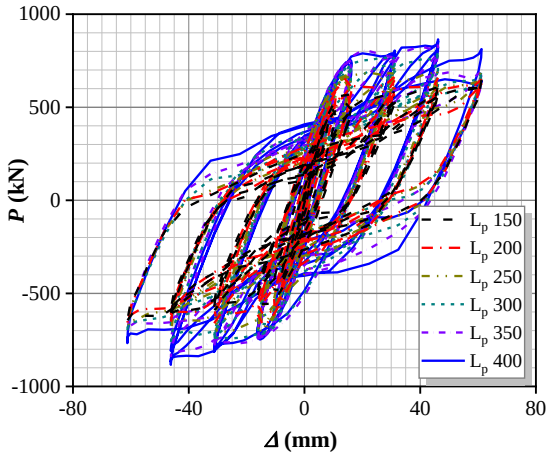

(a) Comparison of hysteretic curves

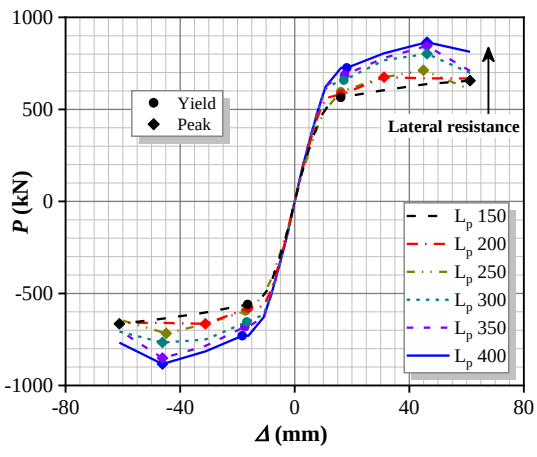

(b) Comparison of skeleton curves

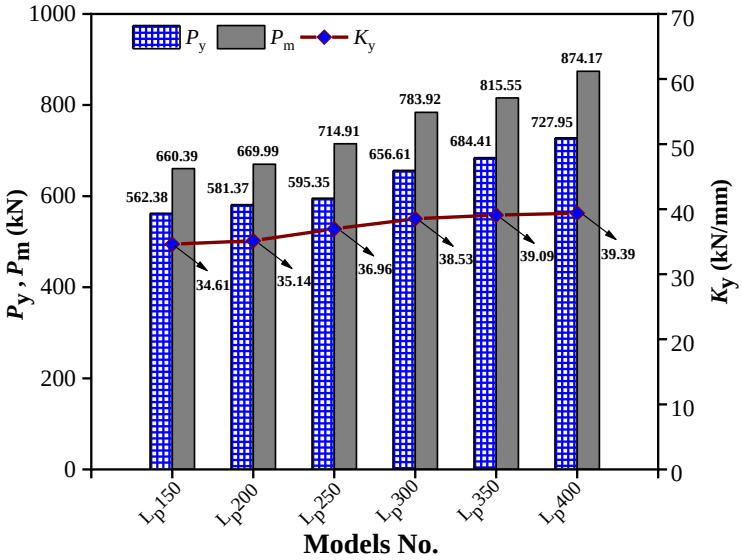

Fig. 17 Impact of length of leg connected to steel plate on lateral resistance and yield stiffness of BRSPSWs

4.3.2. Influence column's width-to-thickness ratio

During applying the lateral cyclic load on steel tubes infilled by concrete, the section's webs are parallel to the loading direction, and the flanges are perpendicular to the loading direction (see Fig. 18). Thus, the flanges will be under high stress and are more probably to buckle during the loading process. The width-to-thickness obviously influenced the seismic behavior of BRSPSWs. According on AISC-360, the CFT columns is classified as a compact section when the ratio is $D/t < 2.26\sqrt{E_s / f_y}$, indicating that the steel section tends to yield before bucking and provide a good confinement to the concrete infill. Therefore, all cases in this section belong to a compact section.

The FE-model of BRSPSW-2 was taken as the basic model the width-to-thickness ratio is $\boldsymbol{D/t = 13.3\%}$. However, various FE models have different D/t values as follows: *10%, 11.4, 13.3, 16%* and *20%* by changing the column's thickness. The comparison of hysteretic and skeleton curves is illustrated in Fig. 19(a-b). It is noted that initial stiffness and ductility remained almost stable. Fig. 19(c) represents the effect of D/t ratio on the lateral resistance and yield stiffness. Both yield and peak lateral resistance showed a slight increase with decreasing the D/t ratio. Also, it can be noticed that the ratio of yield-to-peak lateral resistance tended to decline when D/t was reduced. On the other hand, the lateral yield stiffness declined within reducing D/t ratio due to less resistance offered by steel tubes. Finally, D/t ratio shows a minor effect on the cyclic behavior of BRSPSWs.

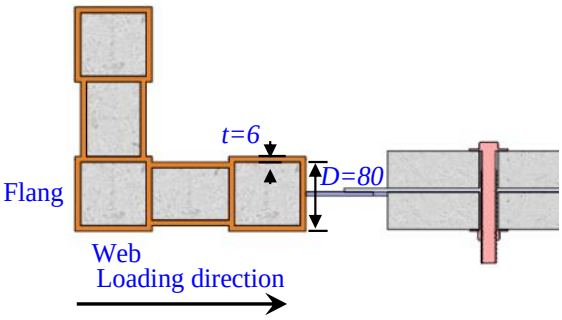

Fig. 18 Column's section and loading direction

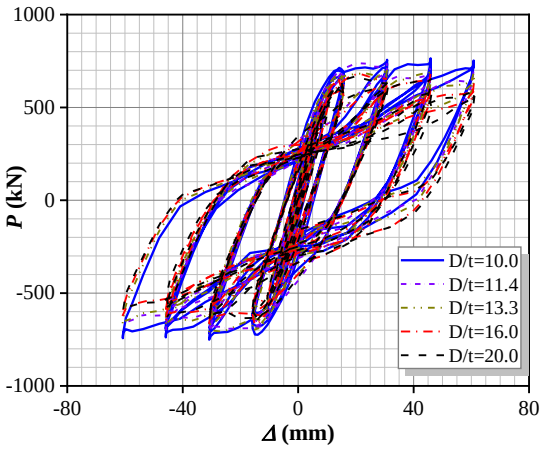

(a) Comparison of hysteretic curves

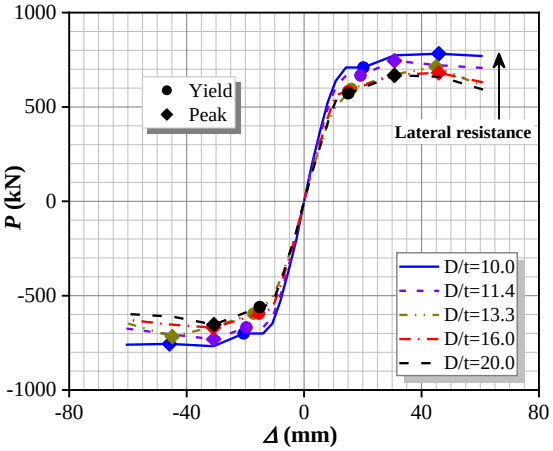

(b) Comparison of skeleton curves

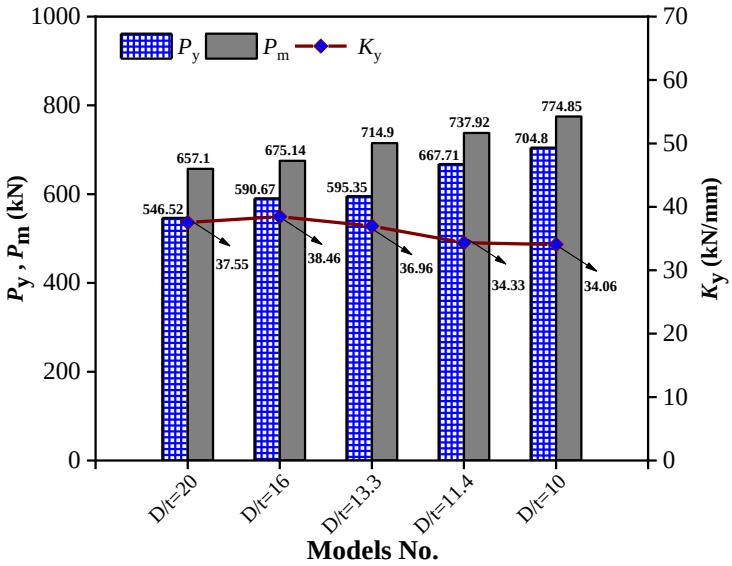

(c) Comprehensive comparison of lateral resistance and yield stiffness

Fig. 19 Impact of width-to-thickness ratio of column on lateral resistance and yield stiffness of BRSPSWs

4.3.3. Influence of axial compression ratio

Regarding the test program, the initial step includes the applying of axial compression load, which is then pursued by horizontal loading. Noticeable, it was found in the literature that the cyclic behavior of wall structures is significant by axial compression ratio [48-50]. Due to the limitation of equipment in the laboratory, there was no axial compression ratio (n_d) applied. Thus, the axial compression ratio was considered during FE-simulation with *0%*, *25%*, *50%*, *75%* and *100%* axial compression.

Fig. 20 (a-b). compares the load-displacement responses, involving hysteretic and skeleton with varying axial compression ratios. It is clear that the models behaved linearly in the initial stage, and the ductility was greatly affected by the axial compression ratio. When the axial compression ratio was 100%, the model was exposed to hard damage, so it could not complete to the end. In contrast, yield and peak lateral showed an enormous decreased trend when the axial compression ratio increased, as illustrated in Fig. 20(c). Besides, the ratio of yield-to-peak resistance went up with rising the axial compression ratio. Similarly, the yield stiffness was declined with rising the axial compression ratio. Finally, the cyclic behavior of BRSPSW is dramatically influenced by the axial compression ratio.

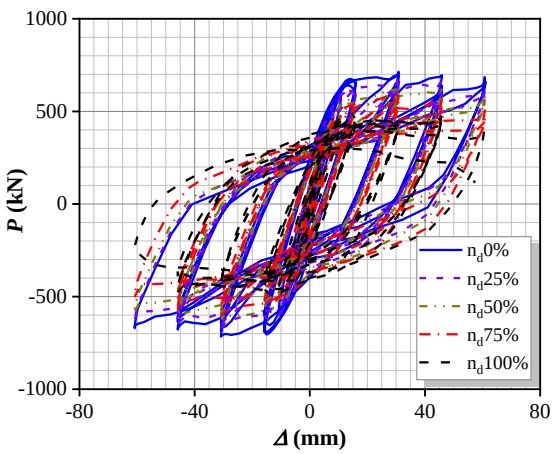

(a) Comparison of hysteretic curves

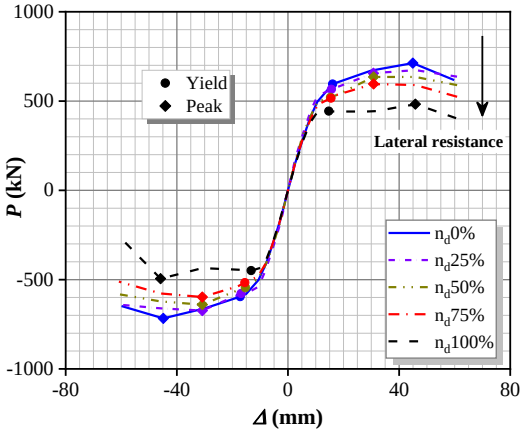

(b) Comparison of skeleton curves

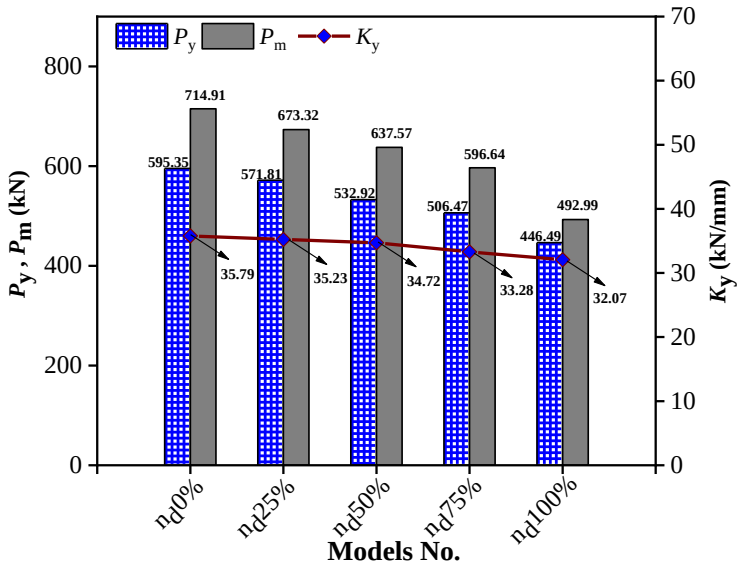

(c) Comprehensive comparison of lateral resistance and yield stiffness

Fig. 20 Impact of axial compression load ratio on lateral resistance and yield stiffness of BRSPSWs

4.3.4. Influence of height-to-thickness ratio of inner steel plate

The size of the inner steel plate has an important impact in determining not only the occurrence of local buckling but also the seismic behavior of BRSPSWs in their entirety. The categorization of BRSPSWs into thick and thin types is determined by the ratio of their inner steel plate's height to their thickness (H_p/t_s), as seen in Fig. 21. When the H_p/t_s ratio of the inner steel plate is small, thicker steel plate tend to buckle after yield, and fully utilize their lateral stiffness. Oppositely, thin steel plate has a bigger height-to-thickness ratio, they tend to buckle earlier than reaching their yield point. According to JGJ/J 380-2015 [51], the H_p/t_s ratio of BRSPSW should be between $100 < H_p / t_s\sqrt{235/f_y} < 600$. As the tested sample has a thickness of 4mm, it can be categorized as a thin steel plate, which tends to undergo buckling prior to exhibiting yielding behavior.

During the test and FE-analysis, it was found out that the local buckling appeared diagonally in the tension field and developed into overall buckling (see Fig. 16). To investigate the impact of the height-to-thickness ratio, five models were conducted with different thicknesses of inner steel plate (t_s=*2 mm ; 3 mm ;4 mm ; 5 mm* and *6 mm*). Fig. 22(a-b). The graph illustrates the modified thicknesses of the inner steel plate by plotting both hysteretic and skeleton responses, dramatically affecting the initial stiffness. Besides, it observed that the ductility declined with reducing the thickness of inner steel plates of because of damaged inner steel plates when the thickness of the inner steel plates is smaller. The hysteretic also could not complete all loops compared with the larger thickness. In addition, the inner steel plates' thickness also has a considerable consequence on lateral resistance and stiffness, as displayed in Fig. 22. the yield and peak lateral resistance were increased sharply with rising the thickness of inner steel plates, while the ratio of yield-to-peak was declined (see. Fig. 22(c)). In the same vein, the lateral yield stiffness showed a sharp increment. Consequently, the heigh-to-thickness ratio significantly impacts the overall seismic performance BRSPSWs.

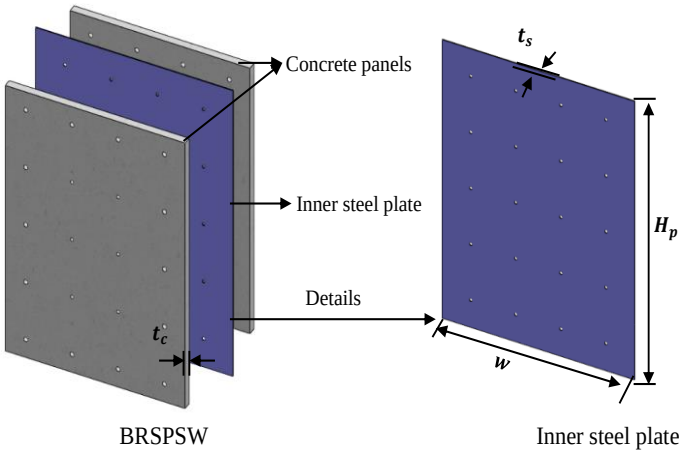

Fig. 21 Details of inner steel plate

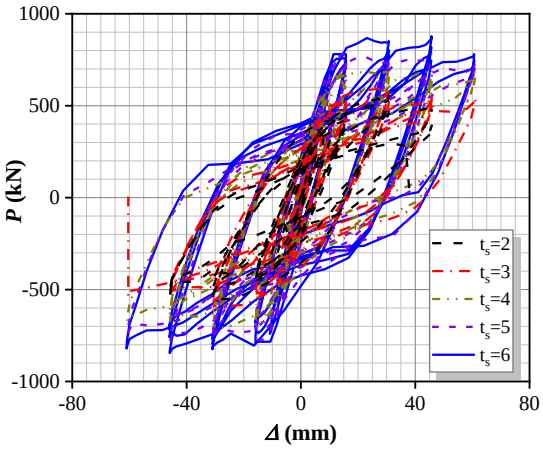

(a) Comparison of hysteretic curves

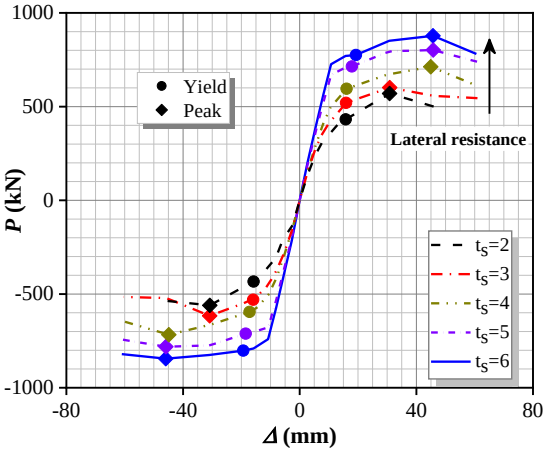

(b) Comparison of skeleton curves

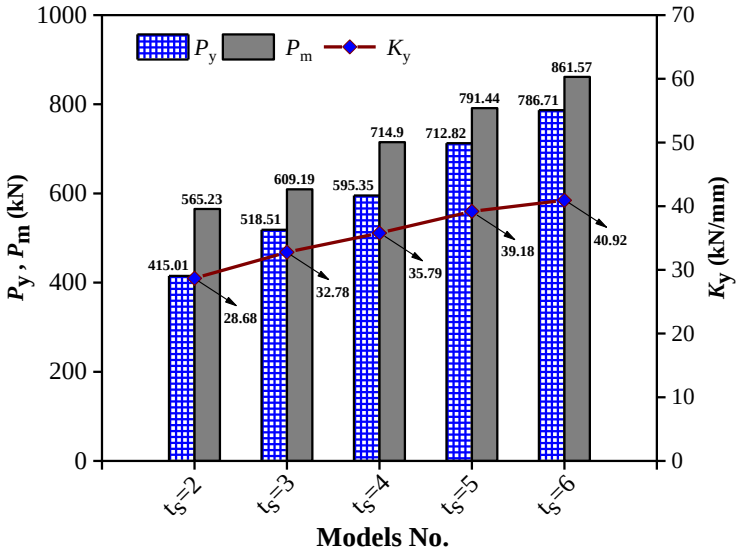

(c) Comprehensive comparison of lateral resistance and yield stiffness

Fig. 22 Impact of height-to-thickness of inner steel plates ratio on lateral resistance and yield stiffness of BRSPSWs

4.3.5. Influence concrete panel's thickness

In the tested specimens, the concrete panel thickness was considered as ($t_c = 40mm$), and it was observed the concrete panel's thickness contributed greatly to reducing local buckling of inner steel plates. For this reason, five concrete panel's thicknesses from 20mm to 100mm with 20 intervals were modeled to study the impact of this parameter. The results showed that the concrete panel's thickness impacted minimally on the initial stiffness and ductility. Rising the thickness of concrete panels increased the initial stiffness and decreased ductility, and the pinch behavior of hysteretic curves tended to be less with increasing the lateral displacement due to limiting of inner steel plate's buckling, as demonstrated in Fig. 23(a-b). Additionally, the lateral resistance and yield stiffness went up steadily, increasing the thickness of concrete panels, as seen in Fig. 23(c). Besides, there was no change in yield-to-peak lateral resistance. Thus, rising the of concrete panels's thickness increased the lateral resistance and stiffness but reduced the ductility. Accordingly, concrete thickness has a minor factor in the overall seismic behavior of BRSPSWs.

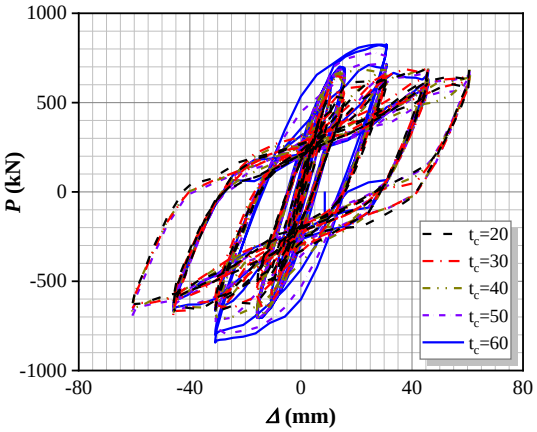

(a) Comparison of hysteretic curves

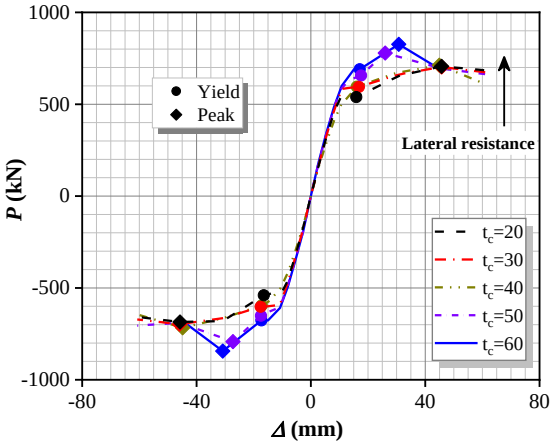

(b) Comparison of skeleton curves

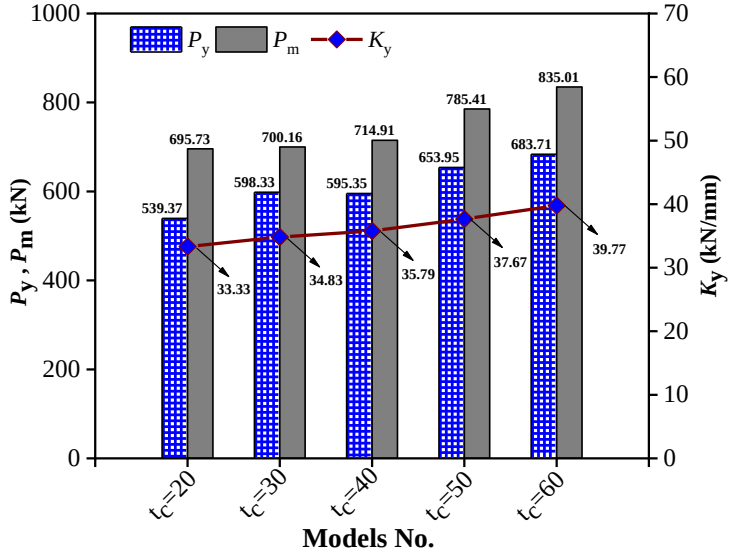

(c) Comprehensive comparison of lateral resistance and yield stiffness

Fig. 23 Effect concrete panels' thickness on lateral resistance and yield stiffness of BRSPSWs

4.3.6. Influence of bolt arrangements

During the fabrication process, the inner steel plates were connected to concrete panels using high-strength bolts arranged in four rows and five columns (B4x5) at equal intervals (see Fig. 21). Based on test and FE-simulation results, concrete cracking appeared firstly on the concrete panels' holes, followed by buckling on inner steel plates. Therefore, five models were established in FE simulation to investigate the effect of bolt arrangements (*B4x5; B4x3; B4x2; B2x3;* and *B4x2*). The result showed that various bolts with different arrangements have approximately no effect on initial stiffness and ductility (see Fig. 24). On the other hand, this factor greatly affected the overall steel plates' buckling and the cracking of concrete panels. Increasing the number of row of bolts can obviously restrain the out-plane buckling of inner steel plates and concrete panels while increasing the number of columns of bolts could not resist, as shown in Fig. 25(a-e). To sum up, the bolt arrangements do not have a great effect on lateral resistance, stiffness and ductility, but it has a substantial impact on the buckling behavior of the inner steel plates and cracking of concrete.

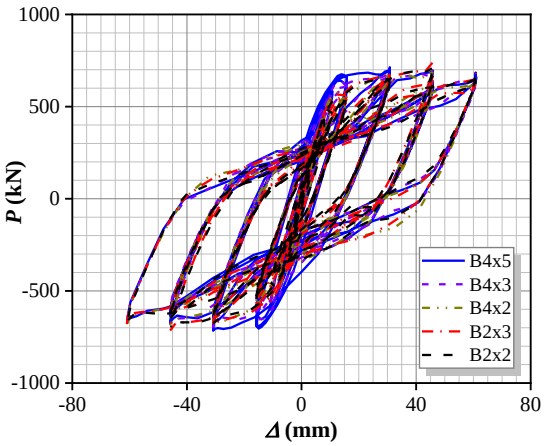

(a) Comparison of hysteretic curves

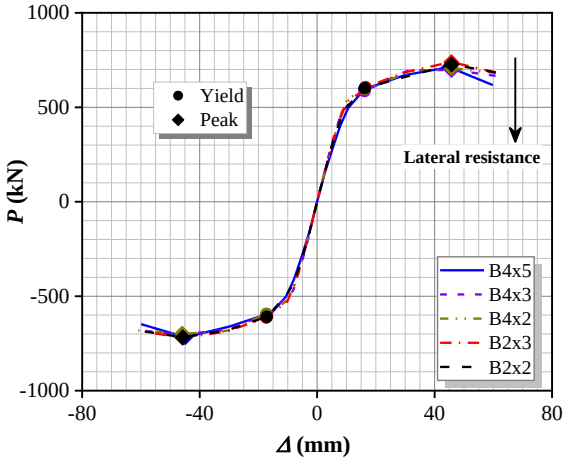

(b) Comparison of skeleton curves

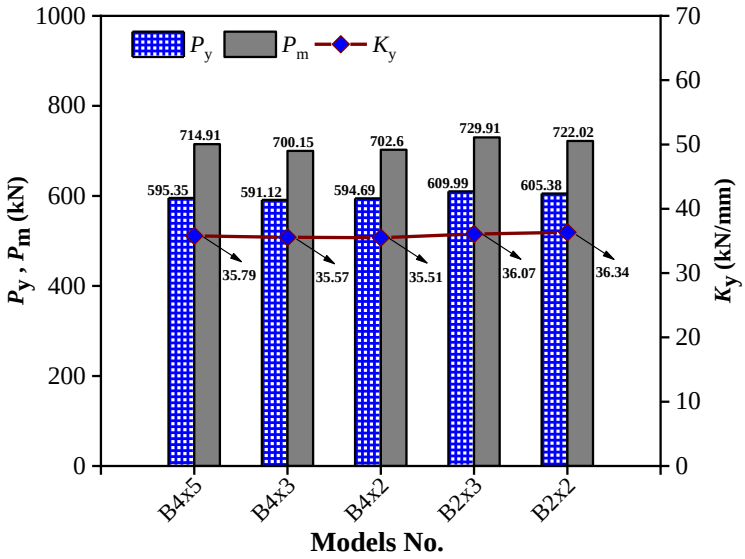

(c) Comprehensive comparison of lateral resistance and yield stiffness

Fig. 24 Effect bolts arrangments thickness on lateral resistance and yield stiffness of BRSPSWs

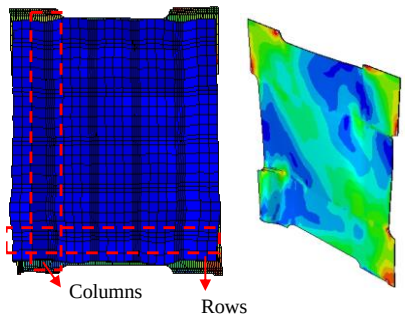

(a) B4x5

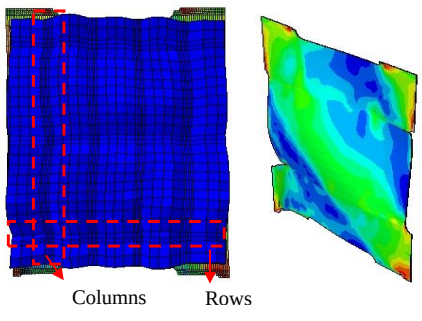

(b) B4x3

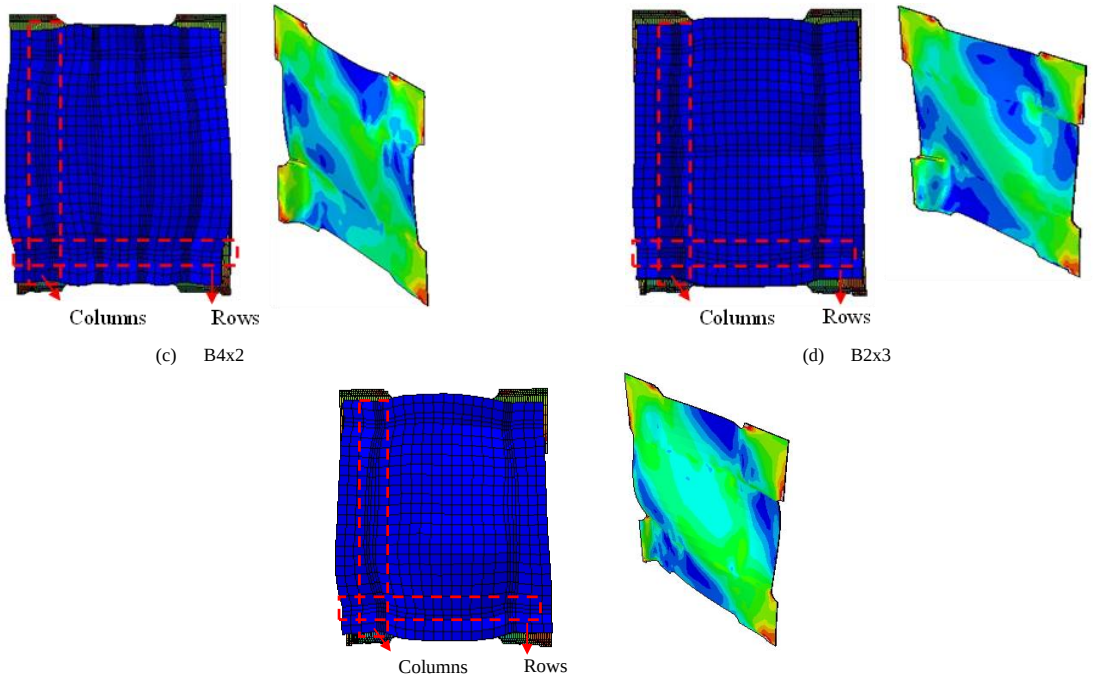

(c) B4x2 (d) B2x3

(e) B2x2

Fig. 25 Effect of bolt arrangements on out-plane deformation of BRSPSWs

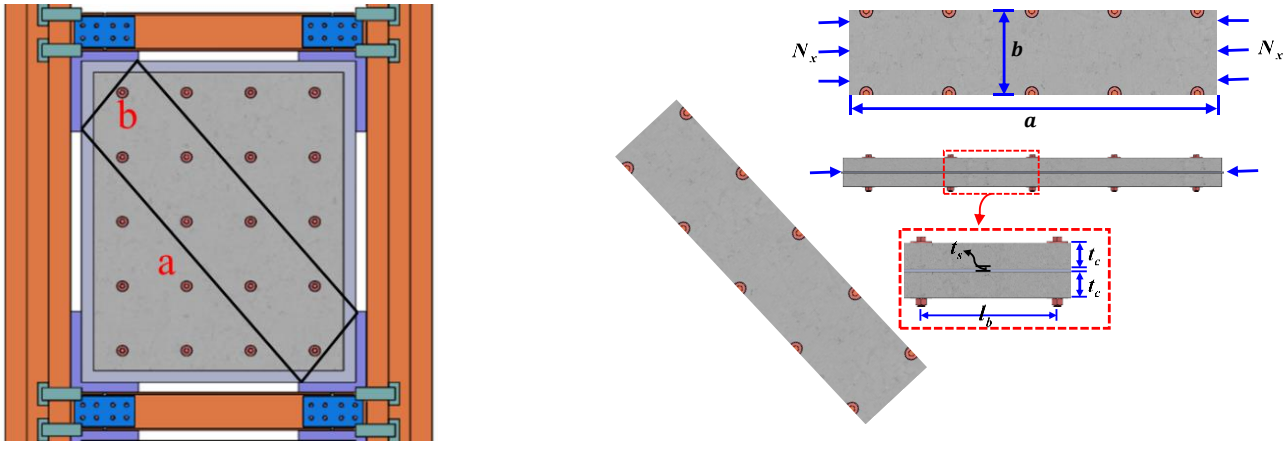

(a) Partially connected BRSPSW (b) Simplified method for calculating the lateral resistance

Fig. 26 Buckling response of the inner steel plate and simplified calculation lateral resistance

4.4. Discussions

The parametric analyses represent that [1] modifying the length leg that connected to the steel plate increases the yield and peak lateral resistance 28 %, and 30%. It also reduces the yield stiffness by roughly and 18%. [2] By raising the column's width-to-thickness ratio from 10% to 20%, there is an improvement in both yield and peak lateral resistance by approximately 26% and 16%, respectively. However, this change leads to a reduction in the yield stiffness by about 5%. [3] increasing the axial compression ratio from 0% to 100% results in a decrease of approximately 25% in the yield, 31% in the peak lateral resistance, and 10% in the yield stiffness. [4] By elevating the thickness of the steel plate from 2 mm to 6 mm, there is a substantial increase in both the yield and peak lateral resistance by approximately 62% and 42%, respectively, along with a boost in the yield stiffness by about 34%. [5] Changing the concrete panel's thickness of the from 20 mm to 60 mm, there is an increase in both the yield and peak lateral resistance by approximately 24% and 20%, respectively, along with an increase in the yield stiffness by about 18%. [6] Changing the bolts arrangement does not affect lateral resistance and yield stiffness but it greatly affects the inner steel plates' buckling behavior.

Accordingly, the most efficient method for enhancing the lateral resistance and yield stiffness is by increasing steel plate's thickness. In contrast, the leg's length of the steel plate and concrete thickness have a less significant factor on improving the lateral resistance and yield stiffness compared to the thickness of the steel plate. On the other hand, expanding the axial compression ratio resulted in reduction on the lateral resistance and yield stiffness. The width-to-thickness ratio has an excellent contribution on improving lateral resistance but reducing yield stiffness value but reducing. Finally, the steel plate's buckling behavior is improved by the configuration of bolts that connects the concrete panels and inner steel plates.

5. Theoretical model on the lateral resistance of BRSPSWs

In accordance with test and FE modeling findings, it was founded that the bearing capacity was mainly calculated by steel plate and frame. Therefore, a calculation approach was suggested to estimate the lateral resistance based on plate-frame interaction theory, which was firstly introduced by Sabouri et al. [52]. This method predicted the lateral resistance for SPSW with L-shaped columns in ref [47]. The previous research on PFI theory only considered the contribution of the steel plate and frame elements; however, the parametric studies in this paper showed that the inner steel plate's buckling-restrained using concrete panels has a minor effect on the wall's lateral resistance. Subsequently, the calculation equations were assumed based on PFI theory, and then it was modified to consider the buckling restrained by the concrete panels. On the other hand, the effect of bolt arrangements is ignored due to approximately zero effect based on FE analysis. Therefore, the following assumption can be drawn:

$$P_{MPFI} = P_s + P_f \tag{16}$$

where P_{MPFI} indicates the peak lateral resistance of the BRSPSWs, P_s and P_f denote the peak lateral resistance of the inner steel plate and frame, respectively.

(1) As the inner steel plate's local buckling happened diagonally, it can be simplified as length (a) and width (b), as illustrated in Fig. 26. In accordance with stability of the steel plate, the buckling strength can be determined as

$$N_x = \frac{\pi^2 D_s}{a^2}(m + \frac{1}{m}\frac{a^2}{b^2})^2 \tag{17}$$

In this context, the variable " N_x " represents the amount of compressive load per unit height applied to the "b" side, "m" denotes the quantity of half-wavelengths of buckling in the "a" direction, and " D_s " refers to the out-of-plane flexural rigidity of the steel plate, expressed as

$$D_s = \frac{E_s t_s^3}{12(1-\nu_s^2)} \tag{18}$$

where E_s stands for modulus of elasticity; t_s stands for steel plates' the thickness; ν_s is the Poisson's ratio.

It is noteworthy to mention that the steel plate exhibited diagonal buckling with a longer wavelength, which is primarily influenced by the bolt spacing and the types of the connection linking the frame elements to steel plates. However, the buckling response will reproduce to a short wavelength since it reduces with increasing compressive force, as shown in Fig. 27. Consequently, the bending moment of the steel plate and plastic hinges form at the wave peak. The longitudinal and transversal displacement, (γ and δ) can be drawn in term of the buckling wave rotation as follows:

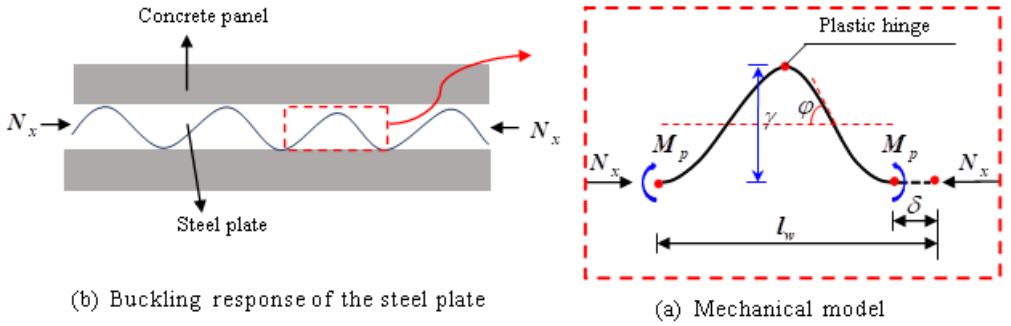

Fig. 27 Equavilent model of steel plate's buckling

$$\delta = \frac{8\gamma^2}{l_w} \tag{19}$$

where l_w refers to the inner steel plate's half-wavelength of buckling; φ is buckling wave's the rotation angle. The compressive resistance of the steel plate's the buckling is illustrated in Fig. 27. And it can be expressed as:

$$N_x = \frac{2\sqrt{2}M_p}{bl_w}\frac{1}{\sqrt{\varepsilon_s}} \tag{20}$$

where ε_s stands for the nominal strain of the steel plate; M_p stands for the plastic moment of the steel plate which is determined as follows.

$$M_p = \frac{bt_s^2}{4} f_y \tag{21}$$

In Fig. 28, the steel plate and concrete panels were simplified to equivalent braces. To apply the lateral load at the pinnacle of the equal braced framework, the following expression can be utilized.

$$P_s = (f_y + \sigma_x)A_e \cos\alpha \tag{22}$$

where f_y refers to the yield strength of the inner steel plate $\sigma_x = N_x/t_s$ refers to the high-order buckling the resistance of the inner steel plate, $A_e = (\sqrt{L_p^2 + H^2}/4)t_s$ is the efficient region of equivalent braces (see Fig. 28). The AISC-360 code [53]can be utilized to calculate the angle of inclination (α) for the tension field and as follows:

$$tan\alpha = \sqrt{\frac{1+\frac{t_s L_p}{2A_c}}{1+t_s H(\frac{1}{A_b}+\frac{H^3}{360I_c L_p})}} \tag{23}$$

where t_s is the thickness of plate, L_p is the leg's length, A_c is the equivalent area of the column, h refers to floor's height of the, A_b refers to beam's the cross-sectional, I_c is the moment of inertia of the column.

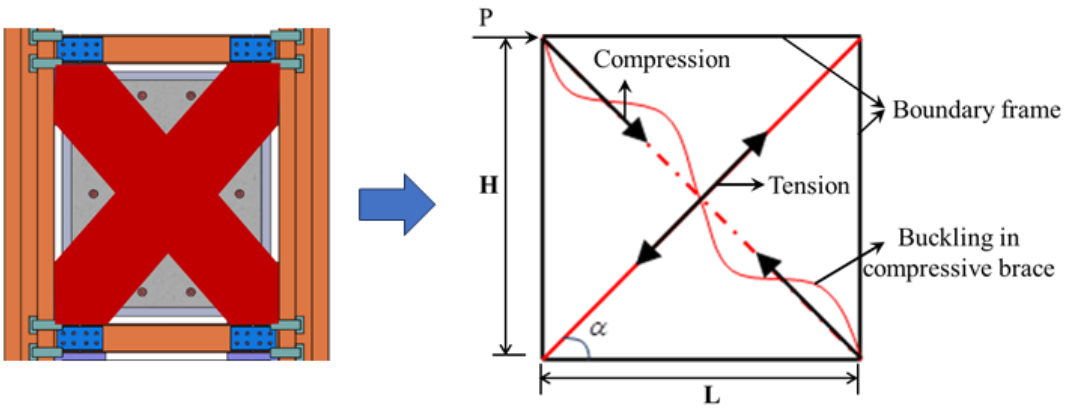

Fig. 28 Simplified and Equivalent model for the frame buckling-restained steel plate shear wall

(2) The lateral resistance of the frame can be computed using the following formula.

$$P_f = \frac{4(M_f - \varphi n_d N_d e)}{H} \quad (24)$$

where M_f is the plastic moment, and it can be calculated using the equation presented in Ref [54]; φ is coefficient factor (0.75) in the case; n_d is the axial compression ratio; N_d is the design compression load; e is the eccentric distance based on neutral axis as shown in Fig. 29.

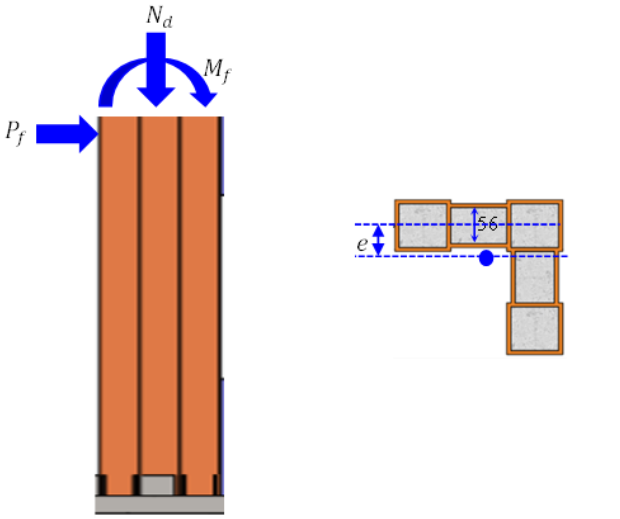

Fig. 29 Calcaution diagram of frame's columns subjected to combained compression and horizontal load

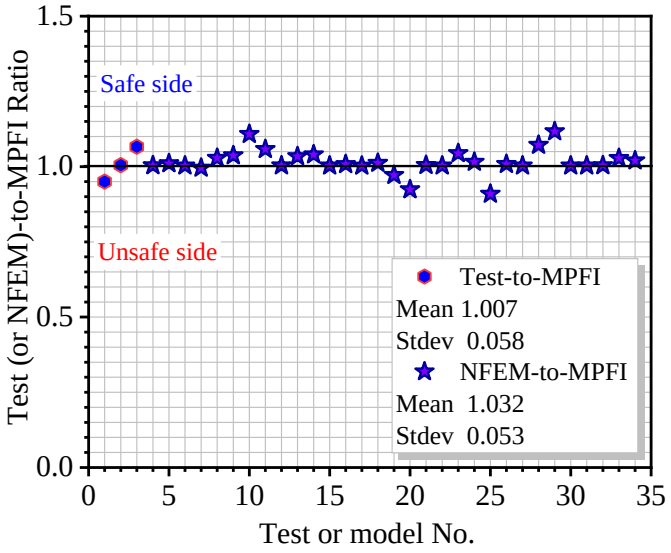

Fig. 30 Scatter of test and NFEM to MPFI predication ratio

5.1. Verification

The calculation method results for yield lateral resistance of BRSPSWs were firstly compared with test results and then with numerical results. The MPFI prediction showed high agreement with the test and numerical results, as shown in Fig. 30. Besides, most of the MPFI results were on the safe side, ramming this method could be used for the design approach of BRSPSWs with L-shaped CFT columns.

6. Conclusion

This paper firstly developed nonlinear finite element models (NFEM) for L-shaped CFT columns frame-buckling-restrained steel plate shear walls (BRSPSWs). After verifying the FE models, through parametric studies, the effect of various factors on the lateral resistance and yield stiffness was assessed. Then based on plate-frame interaction (PFI) theory, a modified MPFI was proposed to calculate the yield lateral resistance. The main conclusions of this study can be drawn as follows:

(1) The seismic performance of frame BRSPSWs was investigated through FE models. Failure modes, hysteretic and skeleton curves were compared with tested results, and the FE models could accurately predicate the seismic behavior of BRSPSWs. In addition, the test-to-FE prediction ratio showed high accuracy for yield, peak lateral resistance, and yield stiffness.

(2) Increasing the leg's length from 150 mm to 400 mm leads to about 28 %, 30 % and 18% increase in yield, peak lateral resistance, and yield stiffness. On the other hand, rising the thickness of the steel plates from 2 mm to 6 mm takes increment by about 62 %, 42 % and 34 %, yield and peak lateral resistance and yield stiffness. Therefore, modification on steel plates significantly affects the overall behaviors of BRSPSWs, whether in leg length or thickness.

(3) The yield and peak lateral resistance and yield stiffness were reduced by roughly 25 %, 31 % and 10%, with declining the axial compression ratio increases from 0% to 100%. Thus, the axial compression ratio minimally affects the lateral resistance and stiffness. However, increasing the width-to-thickness ratio of the columns raises the yield and peak lateral resistance and yield stiffness by about 26 %, 16 %, but it declines the stiffness by about 25 %. Thus, this parameter can be ignored during the design of the BRSPSWs.

(4) Changing the concrete panel's thickness from 20 mm to 60 mm booms the yield and peak lateral resistance and stiffness by about 24 %, 20 % and 18 %, respectively, and it greatly impacts lateral displacement ductility, which is uncoverable on seismic design of BRSPWS system. Thus, the concrete thickness slightly impacts the structural behavior of BRSPSWs. Oppositely, the lateral resistance and stiffness of concrete panels connected to steel plates remain unaffected by the number of bolts used. However, buckling can be prevented by increasing the number of rows of bolts.

(5) A modified plate-frame interaction approach has been suggested to estimate the yield lateral resistance. Then the predicted outcomes are verified to the test and FE models' results to verify it, and they showed a good agreement against FE results.

Acknowledgment

This work is sponsored by the National Key Research and Development Project (Grant No. 2019YFD1101005). The Guangdong Basic and Applied Basic Research Foundation (Nos. 2020A1515110304）

Nomenclature

f_y	yield strength of steel	L_p	leg's length
f_u	ultimate strength of steel	n_d	axial compression ratio
E_s	steel elastic modulus	H_p / t_s	height-to-thickness ratio of inner steel plates
σ_s	stress of steel	t_c	concrete panels' thickness
$\varepsilon_e, \varepsilon_{e1}, \varepsilon_{e2}$	intermediate strain	$(B(RxC))$	bolt arrangements
ε_{e3}	ultimate strain	P_{MPFI}	prediction of peak lateral resistance
A_s	cross-sectional of steel	P_{ms}	lateral resistance of the steel plate

f_{cu}, f_c	cube and cylinder compressive strength of concrete	P_{mf}	lateral resistance of the frame
E_c	concrete elastic modulus	A_e	equivalent area of braces
A_c	cross-sectional of concrete	N_x	high order buckling resistance of the steel plate
σ_{c0}	compressive stress concrete	α	inclination angle of the tension filed
ε_{c0}	strain of concrete at f_c	**Abbreviation**	
ν	Poisson's ratio	BRSPSWs:	Buckling-restrained steel plate shear walls
σ_{t0}	tensile stress concrete	SPSWs:	Steel plate shear walls
ε_{t0}	strain of concrete at σ_{t0}	PFI:	Nonlinear finite element model
P_y	yield lateral resistance	NFEM:	Plate-frame interaction
P_m	peak lateral resistance	MPFI:	Modified Plate-frame interaction
K_y	yield lateral stiffness	CFT:	Concrete-filled steel tube
Δ_y	yield displacement	CDPM:	Concrete damage plasticity model
D/t	columns' width-to-thickness		

Reference

[1] Y. Takahashi, Y. Takemoto, T. Takeda, and M. Takagi, "Experimental study on thin steel shear walls and particular bracings under alternative horizontal load," in *Preliminary Report, IABSE, Symp. On Resistance and Ultimate Deformability of Tsructures Acted on by Well-defined Repeated Loads, Lisbon, Portugal*, 1973.

[2] L. Thorburn, G. Kulak, and C. Montgomery, "Analysis of steel plate shear walls, Structural Engineering Report No. 107," *Edmonton, Alberta: University of Alberta, Department of Civil Engineering*, 1983.

[3] E. W. Tromposch and G. L. Kulak, "Cyclic and static behaviour of thin panel steel plate shear walls," 1987.

[4] V. Caccese, M. Elgaaly, and R. Chen, "Experimental study of thin steel-plate shear walls under cyclic load," *journal of Structural Engineering*, vol. 119, no. 2, pp. 573-587, 1993.

[5] R. Driver, "Seismic behavior of steel plate shear walls [Dissertation of Ph. d.]," *D. Department of Civil and Environmental engineering, University of Alberta, Alberta, Canada*, 1997.

[6] H.-G. Park, J.-H. Kwack, S.-W. Jeon, W.-K. Kim, and I.-R. Choi, "Framed steel plate wall behavior under cyclic lateral loading," *Journal of structural engineering*, vol. 133, no. 3, pp. 378-388, 2007.

[7] A. Astaneh-Asl, *Seismic behavior and design of steel shear walls*. Structural Steel Educational Council Moraga, CA, 2001.

[8] A. Astaneh-Asl, *Seismic behavior and design of composite steel plate shear walls*. Structural Steel Educational Council Moraga, CA, 2002.

[9] Q. Zhao and A. Astaneh-Asl, "Cyclic behavior of traditional and innovative composite shear walls," *Journal of Structural Engineering*, vol. 130, no. 2, pp. 271-284, 2004.

[10] L. Ye, L. Guoqiang, and S. Feifei, "Experimental study on buckling-restrained composite steel plate shear wall with large aspect ratio," *Progress in Steel Building Structures*, vol. 11, no. 2, pp. 18-27, 2009.

[11] S.-J. Chen and C. Jhang, "Cyclic behavior of low yield point steel shear walls," *Thin-walled structures*, vol. 44, no. 7, pp. 730-738, 2006.

[12] J. W. Berman and M. Bruneau, "Experimental investigation of light-gauge steel plate shear walls," *Journal of Structural Engineering*, vol. 131, no. 2, pp. 259-267, 2005.

[13] T. M. Roberts and S. Sabouri-Ghomi, "Hysteretic characteristics of unstiffened perforated steel plate shear panels," *Thin-Walled Structures*, vol. 14, no. 2, pp. 139-151, 1992.

[14] I.-R. Choi and H.-G. Park, "Steel plate shear walls with various infill plate designs," *Journal of structural engineering*, vol. 135, no. 7, pp. 785-796, 2009.

[15] T. Hitaka, C. Matsui, and J. i. Sakai, "Cyclic tests on steel and concrete-filled tube frames with Slit Walls," *Earthquake engineering & structural dynamics*, vol. 36, no. 6, pp. 707-727, 2007.

[16] S. Jin, J. Ou, and J. R. Liew, "Stability of buckling-restrained steel plate shear walls with inclined-slots: theoretical analysis and design recommendations," *Journal of Constructional Steel Research*, vol. 117, pp. 13-23, 2016.

[17] Q. Liu, G. Li, and Y. Lu, "Experimental and theoretical study on the steel bound-columns with buckling restrained steel plate shear wall," in *Proceedings of the EUROSTEEL, 7th European conference on steel and composite structures, Italy*, 2014.

[18] M.-W. Wei, J. R. Liew, Y. Du, and X.-Y. Fu, "Seismic behavior of novel partially connected buckling-restrained steel plate shear walls," *Soil Dynamics and Earthquake Engineering*, vol. 103, pp. 64-75, 2017.

[19] M.-W. Wei, J. R. Liew, M.-X. Xiong, and X.-Y. Fu, "Hysteresis model of a novel partially connected buckling-restrained steel plate shear wall," *Journal of Constructional Steel Research*, vol. 125, pp. 74-87, 2016.

[20] M.-W. Wei, J. R. Liew, and X.-Y. Fu, "Panel action of novel partially connected buckling-restrained steel plate shear walls," *Journal of Constructional Steel Research*, vol. 128, pp. 483-497, 2017.

[21] M.-W. Wei, J. R. Liew, D. Yong, and X.-Y. Fu, "Experimental and numerical investigation of novel partially connected steel plate shear walls," *Journal of Constructional Steel Research*, vol. 132, pp. 1-15, 2017.

[22] Y. Du, Y. Zhang, T. Zhou, Z. Chen, Z. Zheng, and X. Wang, "Experimental and numerical study on seismic behavior of SCFRT column frame-buckling restrained steel plate shear wall structure with different connection forms," *Engineering Structures*, vol. 239, p. 112355, 2021.

[23] Y. Guo and Q. Dong, "Static behavior of buckling-restrained steel plate shear walls," in *Tall Buildings: From Engineering to Sustainability*: World Scientific, 2005, pp. 666-670.

[24] W.-Y. Liu, G.-Q. Li, and J. Jiang, "Mechanical behavior of buckling restrained steel plate shear walls with two-side connections," *Engineering Structures*, vol. 138, pp. 283-292, 2017.

[25] H. Gao and G. Li, "Experimental and theoretical study on composite steel plate shear walls," Master's Dissertation, Tongji University, Shanghai, China, 2007.

[26] F. Sun, H. Gao, and G. Li, "Experimental research on two-sided composite steel plate walls," in *Proceeding of the 4th technical seminar on steel structure for Cross-Strait and Hong Kong. Tongji University Press, Shanghai, China*, 2006.

[27] Z.-S. Huang, Z.-Z. Yin, and B.-Y. Song, "STUDY ON SEISMIC BEHAVIOR OF TRAPEZOIDAL CORRUGATED STEEL PLATE SHEAR WALL STRUCTURE WITH PEC COLUMN," *ADVANCED STEEL CONSTRUCTION*, vol. 19, no. 2, pp. 157–165, 2023.

[28] L. Guo, Q. Rong, X. Ma, and S. Zhang, "Behavior of steel plate shear wall connected to frame beams only," *International Journal of Steel Structures*, vol. 11, no. 4, pp. 467-479, 2011.

[29] A. Pirmoz, "Beam-attached steel plate shear walls," *The Structural Design of Tall and Special Buildings*, vol. 21, no. 12, pp. 879-895, 2012.

[30] M. Wang, W. Yang, Y. Shi, and J. Xu, "Seismic behaviors of steel plate shear wall structures with construction details and materials," *Journal of Constructional Steel Research*, vol. 107, pp. 194-210, 2015.

[31] B. Jkta, A. Xhz, N. B. Xin, A. Yhw, and W. A. Kang, "Experimental and numerical investigation of cross-shaped buckling-restrained SPSWs with composite structure," *Journal of Building Engineering*, vol. 47 (2022) 103873, 2021.

[32] C. Zhihua, "New-Type special-shaped column by steel structure and composite " *Steel Construction*, vol. 2, pp. 27-29, 2006.

[33] Q.-Q. Xiong, W. Zhang, Z.-H. Chen, T. Zhou, and J.-H. Qian, "EXPERIMENTAL STUDY ON THE BEHAVIOUR OF L-SHAPED COLUMNS FABRI-CATED USING CONCRETE-FILLED STEEL TUBES UNDER ECCENTRIC LOADS," *ADVANCED STEEL CONSTRUCTION*, vol. 18, no. 2, pp. 528-535, 2022.

[34] T.-F. Ma, Z.-H. Chen, K. Khan, and Y.-S. Du, "EXPERIMENTAL AND NUMERICAL ANALYSIS OF L-SHAPED COLUMN COMPOSED OF RECYCLED AGGREGATE CONCRETE-FILLED SQUARE STEEL TUBES UNDER ECCENTRIC COMPRESSION," *ADVANCED STEEL CONSTRUCTION*.

[35] Z.-h. Chen, Z.-y. Li, B. Rong, and X.-l. LIU, "Experiment of axial compression bearing capacity for crisscross section special-shaped column composed of concrete-filled square steel tubes," *Journal of Tianjin University*, vol. 39, no. 11, pp. 1275-1282, 2006.

[36] Z.-h. Chen, B. Rong, and A. Fafitis, "Axial compression stability of a crisscross section column composed of concrete-filled square steel tubes," *Journal of Mechanics of Materials and Structures*, vol. 4, no. 10, pp. 1787-1799, 2010.

[37] Z.-H. Chen, R. Ma, Y.-S. Du, and M. Lian, "Experimental and Theoretical Research on Rcft Beam-Columns Fabricated with Q420b High-Strength Steel Subjected To Eccentric Load," *ADVANCED STEEL CONSTRUCTION*, vol. 16, no. 4, pp. 287-296, 2020.

[38] T. Zhou, Y. Jia, M. Xu, X. Wang, and Z. Chen, "Experimental study on the seismic performance of L-shaped column composed of concrete-filled steel tubes frame structures," *Journal of Constructional Steel Research*, vol. 114, pp. 77-88, 2015.

[39] "GB/T 228.1-2010 Tensile testing of metallic materials - Part 1: room temperature test method[S], Standards press of China, Beijing," 2011 (In Chinese).

[40] *GB/T 50081, Ordinary Concrete Mechanices Performance Test Method Standard, 2019*. (In Chinese).

[41] *JGJ/T101, Specification for Seismic Test of Building, 2015, (in Chinese)*.

[42] D. S. Simulia, "ABAQUS 6.13 User's manual," *Dassault Systems, Providence, RI*, vol. 305, p. 306, 2013.

[43] F. H. Aboutalebi and A. Banihashemi, "Numerical estimation and practical validation of Hooputra's ductile damage parameters," *The International Journal of Advanced Manufacturing Technology*, vol. 75, no. 9-12, pp. 1701-1710, 2014.

[44] *Concrete Filled Steel Tubular Structures-Theory and Practice (Third Edition)* L. Han, Beijing: Sicence press, 2016 (in Chinese).

[45] A. A. Standard, "Building Code Requirements for Structural Concrete (ACI 318-11)," in *American Concrete Institute*, 2011.
[46] Z. Wang, J.-B. Yan, and X.-M. Liu, "NUMERICAL AND THEORETICAL STUDIES ON DOUBLE STEEL PLATE COMPO-SITE WALLS UNDER COMPRESSION AT LOW TEMPERATURES," *ADVANCED STEEL CONSTRUCTION*, 2019.
[47] K. Wang, M.-N. Su, Y.-H. Wang, J.-K. Tan, H.-B. Zhang, and J. Guo, "Behaviour of buckling-restrained steel plate shear wall with concrete-filled L-shaped built-up section tube composite frame," *Journal of Building Engineering*, vol. 50, p. 104217, 2022.
[48] B. Zhao *et al.*, "Experimental seismic behavior of SCFRT column chevron concentrically braced frames," *Journal of Constructional Steel Research*, vol. 133, pp. 141-155, 2017.
[49] Z. Chen, H. Xu, Z. Zhao, X. Yan, and B. Zhao, "Investigations on the mechanical behavior of suspend-dome with semirigid joints," *Journal of Constructional Steel Research*, vol. 122, pp. 14-24, 2016.
[50] Z. Zhao, Z. Chen, X. Yan, H. Xu, and B. Zhao, "Simplified numerical method for latticed shells that considers member geometric imperfection and semi-rigid joints," *Advances in Structural Engineering*, vol. 19, no. 4, pp. 689-702, 2016.
[51] "JGJ/T 380, Technical specification for steel plate shear walls, 2015 (in Chinese)."
[52] S. Sabouri-Ghomi, C. E. Ventura, and M. H. Kharrazi, "Shear analysis and design of ductile steel plate walls," *Journal of Structural Engineering*, vol. 131, no. 6, pp. 878-889, 2005.
[53] A. Committee, "Seismic provisions for structural steel buildings (AISC 341-10)," *American Institute of Steel Construction, Chicago-Illinois*, 2010.
[54] L.-H. Han, "Flexural behaviour of concrete-filled steel tubes," *Journal of Constructional Steel Research*, vol. 60, no. 2, pp. 313-337, 2004.

Advanced Steel Construction – Vol. 19 No. 3 (2023) 293–307
DOI:10.18057/IJASC.2023.19.3.9

EXPERIMENTAL STUDY ON MECHANICAL PERFORMANCE OF BUCKLING-RESTRAINED BRACE ON FRAMES WITH HIGH-STRENGTH CONCRETE-FILLED SQUARE STEEL TUBE COLUMNS

Chuan-Zheng Ma *, Guo-Chang Li and Zhe-Yuan Wang

Department of Civil Engineering, Shenyang Jianzhu University, Shenyang 110168
** (Corresponding author: E-mail: 502699131@qq.com)*

ABSTRACT

Using buckling-restrained braces (BRBs) in frames with high-strength concrete-filled square steel tube columns(HSCFSSTC) can solve issues such as brittle failure and low lateral stiffness. To investigate the mechanical performance of buckling-restrained brace frames(BRBFs), an experiment study was conducted. The investigation involved the design and analysis of a frame system composed of BRBs, HSCFSSTC and H-shaped steel beams. Sub-structures at a 1/3 scale with two types of connections, welded and pin connections, were subjected to pseudo-static tests. The influence of BRBF connection types on the plastic hinge formation mechanism, load-bearing capacity, energy dissipation capacity and stress magnitude of the connection gusset plates was examined. After the test, ABAQUS software was used for finite element analysis of the specimen, and the simulation results were in good agreement with the experimental results.Based on the results, both the welded and pin-connected specimens formed plastic hinges at column bases and the beam ends, which ensured the energy dissipation performance of BRBs. Pin connections were found to exhibit noticeable slippage during loading due to the presence of holes. However, the study found that the plastic hinge formation mechanism, load-bearing capacity, and lateral stiffness of the frames with the two connection types were similar. Furthermore, there was no significant difference in the load-bearing capacity, stress distribution, and magnitude between the two connection types. Nevertheless, welded connections demonstrated a greater potential for broader application as they allowed the BRB to resist horizontal seismic forces earlier than pin connections.

ARTICLE HISTORY

Received: 25 April 2023
Revised: 30 May 2023
Accepted: 20 June 2023

KEYWORDS

Buckling-restrained brace;
High-strength concrete;
Pseudo-static test;
Welded connection;
Pin connection

Copyright © 2023 by The Hong Kong Institute of Steel Construction. All rights reserved.

1. Introduction

High-strength concrete-filled square steel tube columns are characterized by their small cross-sectional dimensions and lightweight, which have contributed to their widespread use in high-rise and super high-rise structures[1-4]. The reduction in column cross-section decreases the lateral stiffness of the structure, which can lead to increased story drift in the frame and make it difficult to meet seismic design requirements. Therefore, the use of BRB in frames can enhance the lateral stiffness of the system, dissipate seismic energy, as well as improve its overall seismic performance. [5-8]. The BRB in a frame with HSCFSSTC can mitigate the brittleness of high-strength concrete and fully utilize its performance, enhancing the safety and economy of the structure. With promising prospects for application and promotion, ensuring the connection reliability of BRBF connections is one of the key factors to consider.

Connections between BRBs and steel frames usually adopt three forms: bolted, welded and pin connections[9]. Bolted connections offer the advantages of simple construction methods but have drawbacks such as requiring more bolts and higher installation precision during construction, the transition segments （unrestrianed non-yielding segments） of BRB are longer, and the in-plane and out-of-plane bending stiffnesses are relatively smaller, making them prone to out-of-plane instability failure. For example, Keh-Chuuan Tsai et al. [10, 11] performed quasi-dynamic tests on a three-story concrete-filled tubular steel (CFST) structure with three full-size holes and bolted connections between the BRB and the structure. It was found that for a ply drift angle of 0.025 rad, the torsional deflection of the reinforcement leads to out-of-plane instability of the BRB. Similarly, Wang Jingfeng[12] and Li Beibei[13] conducted pseudo-static tests on five different types of connections used between BRBs and steel frames under cyclic loading conditions. In bolted connection specimens, out-of-plane deformation of the BRBF connection segment and reduced load-bearing capacity occurred when the story drift angle was around 1%. Mingming Jia et al. [14] performed the pseudo-static test on a two-story steel structure and a scaled-down passageway bolted between the BRB and the structure. When the drift angle is 0.026 rad, out-of-plane instability failure occurred in the BRBF connection portion, ending the experiment.

Pin connections offer advantages such as ease of construction and not transfering bending moments. However, when the connection shaft and gusset plate processing precision are insufficient, the BRB may not be able to bear horizontal shear forces at smaller story drift angles. Keith D. Palmer et al.[15] conducted pseudo-static tests on a 2-story single-bay spatial frame with pin connections between the BRB and the frame under bidirectional loading. The results showed that under bidirectional loading, the BRB could withstand large plastic deformations. However, due to the gap between the gusset plate and the pin shaft, the BRB core was not loaded during the transition between tension and compression, resulting in a horizontal slippage plateau on the axial force-displacement curve of the BRB. Junda E.[16] conducted cyclic tests on three diagonally braced frame sub-structures under cyclic loading and found that all three specimens with pin connections exhibited noticeable horizontal slippage plateau in the hysteresis curves. Similar slippage phenomena were observed in the experimental studies by Wang Jingfeng[12], Li Beibei[13], and others[17, 18].

Keh-Chyuan Tsai et al.[19] conducted a comparative analysis of welded connections and bolted connections in BRBFs. The results demonstrated that the transition segments of welded BRBs was shorter than that of bolted BRBs, which reduces their susceptibility to out-of-plane instability failure. The frames with welded connections had smaller story drift compared to the frames with bolted connections. Wang Cuihong[20] conducted static and dynamic elastoplastic analyses on three 8-story BRBFs, examining the behavior of beam-to-column connections that were either welded and bolted. The results indicated that both welded and bolted connections in the BRBF exhibited good ductility, leading to a global failure mechanism. The BRBF with welded connections at the first-story exhibited significantly higher load-bearing capacity and lateral stiffness compared to those with bolted connections. Sheng Pei et al.[21] performed pseudo-static tests on two single-story single bay BRBFs that had welded connections. The experimental results revealed that the BRBF with welded connections exhibited superior ductility and energy dissipation capability. Studies[19-21] on the welded BRBF connections have indicated that the structural performance of frames with welded connections was superior to those of bolted connections. However, few comparative analyses have been conducted on the structural performance of BRBFs with welded and pin connections. The limited understanding of the advantages and features of welded connections among designers is impeding the promotion and adoption of this connection type.

To investigate the structural performance of BRBFs with welded connections between BRBs and HSCFSSTC, this study designed two single-story single-bay planar frames with H-shaped steel beams. The BRBF adopted two connection methods: welded and pin connections. These two test frameworks were tested quasi-statically in the laboratory. After conducting the experiments, a comparative analysis of the structural performance of the two frames was carried out. In addition, the specimens were modeled using ABAQUS finite element software, facilitating a comparative analysis of the experimental results against the simulation results.

2. Experimental overview

2.1. Design of the prototype structure

In order to determine the parameters of the specimen, MIDAS was used for structural design. A 16-story 3×5 span space frame structure with BRB consisting of square steel columns filled with high-strength concrete and H-beams was designed. The total height of the structure is 58.2 meters, with the first floor at 4.2 meters and the second through sixteenth floors at 3.6 meters each. The columns in the structure were constructed using 450mm wide, 10 mm thick square steel tubes of Q460 steel and C100 concrete. The beam cross-section dimensions were H450×9×280×14 mm, and all steel beams used Q345 steel. The BRB core segment used Q235 steel. The structural plan layout is shown in Fig. 1, with a longitudinal span of 5×6=30 m and a transverse span of 3×6=18 m.

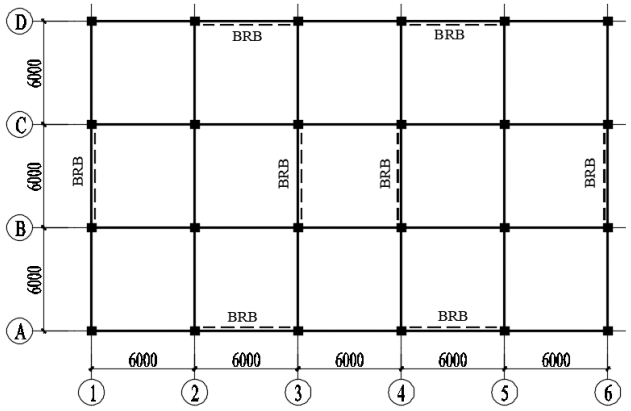

Fig. 1 Structural plan layout

The main design parameters of the prototype structure were as follows: a seismic fortification intensity of 7 degrees, earthquake grouping of groups 3, class 4 site, site characteristic period T_g=0.9s, and design basic seismic acceleration of 0.15g. The floor had a dead load of 4.5 kN/m^2 and a live load of 3 kN/m^2. The seismic performance of the frame met the relevant requirements of "Building Seismic Design Code" (GB50011-2010)[22] and "Building Energy Dissipation and Vibration Reduction Technical Code" (JGJ 297-2013)[23].

2.2. Design of the sub-structure

To investigate the seismic performance of a BRBF with HSCFSSTC and H-shaped steel beam, a single-story single-span specimen containing BRBs was selected from the bottom of the prototype structure as a sub-structure, and pseudo-static tests under cyclic loading were conducted.

The specimens were designed and processed at a 1/3 scale according to the prototype frame, with specimen numbers SP1-Test and SP2-Test. The schematic diagrams and key cross-sectional dimensions are shown in Figs. 2-5. In the SP1-Test frame, the BRB (referred to as BRB1) was connected to the beam-column using butt welds, while in the SP2-Test frame, the BRB (referred to as BRB2) used pin connections, with all other parameters remaining the same. Steel beams are connected to CFST columns through external flange plates, the width of which is designed according to FEMA-350 [24], and references for design and calculation of BRB and frame angles and ribs are given in [25, 26].

To secure the test frame, a steel beam with high rigidity was welded at the bottom of the column. The detailed parameters of the beams, columns and BRBs are shown in Table 1.

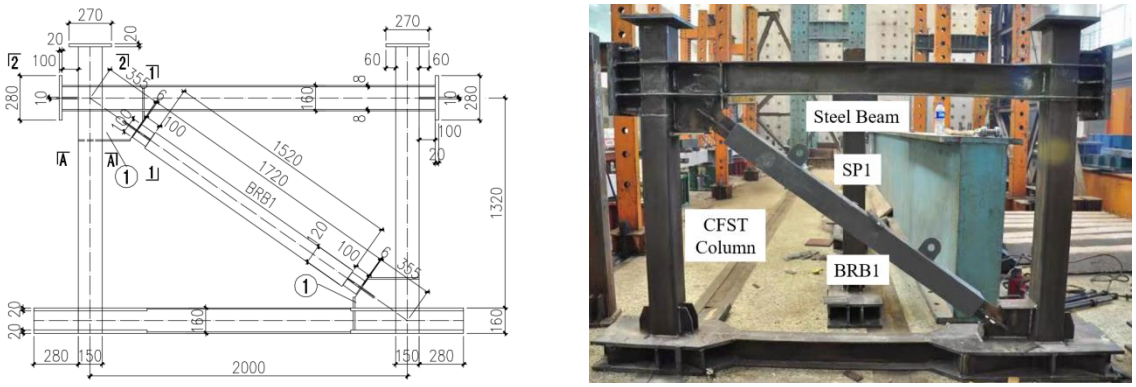

Fig. 2 Schematic diagram of specimen SP1

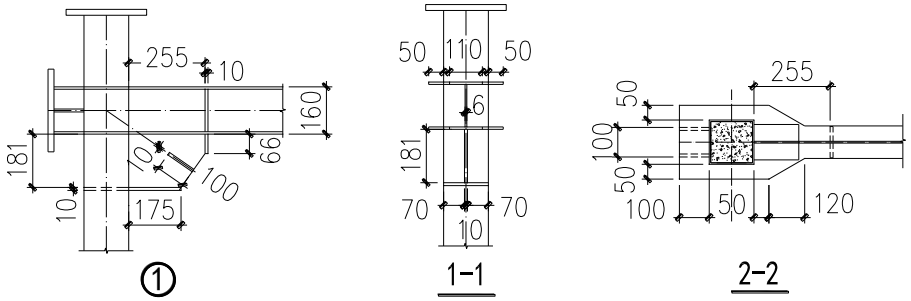

Fig. 3 Key cross-sectional dimensions of specimen SP1

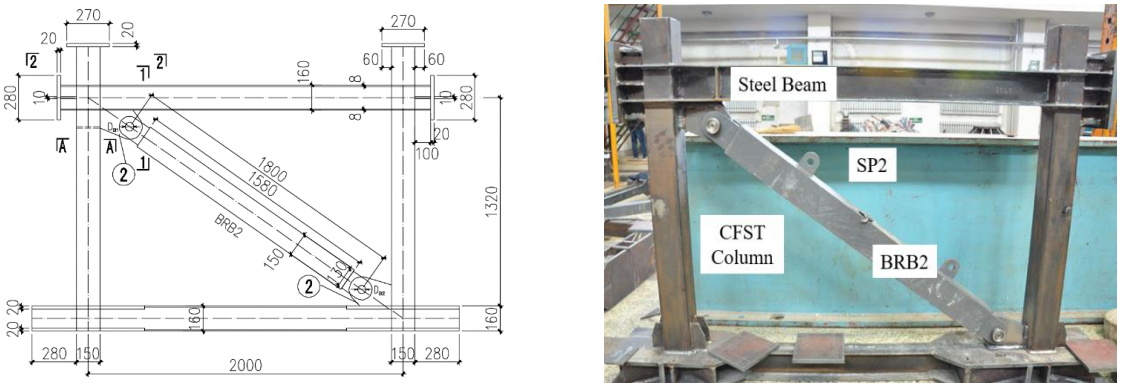

Fig. 4 Schematic diagram of specimen SP2

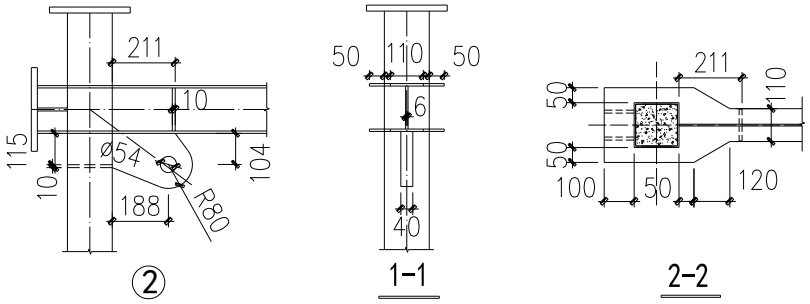

Fig. 5 Key cross-sectional dimensions of specimen SP2

Table 1
Frame design parameters of specimens

Specimen number	SP1	SP2
Connection method of BRB with beam and column	Butt-welded connection	Pin connection
Column (cold-formed square steel tube Q460)	□150×150×5 mm	□150×150×5 mm
Concrete strength grade	C100	C100
Specimen length, width	2000×1400	2000×1400
Beam (Q345)	H-160×110×6×8mm	H-160×110×6×8mm

2.3. Specimen parameters

The buckling-restrained braces of the test specimens were designed and manufactured by Shanghai Lanke Building Damping Technology Co., Ltd., and were designed to bear 60% of the total shear force of the frame. The core segment of the BRB was made of Q235 steel, while the transition segment were made of Q345 steel. The transition segment of the BRB1 specimen utilized a cross-shaped plate that was connected to the frame using double-sided fillet welds, while the BBR1 itself was connected to the gusset plate via butt fusion welds. In addition, the inner partition is welded to the end column of the pinch plate, and the reinforcing rib is welded to the supporting column to strengthen the stress concentration area and prevent premature failure of the node area. The BRB2 is mounted on the 40mm thick gusset plate with steel shafts. The gusset plate was connected to the column and the beam of the frame using fusion welds, and an internal partition was welded inside the column at the gusset plate end, with stiffeners welded on the beam web. The specific parameters of the BRBs are shown in Table 2.

Table 2
Design parameters of BRB

Number	BRB1	BRB2
BRB total length (L_1)	1720	1930 (center-to-center distance of holes1800)
BRB restrained segment length (L_2)	1580	1600
BRB core segment length (L_3)	1120	1120
BRB transition segment length (L_4)	300	405
Cross-sectional dimensions of BRB transition segment (Q345)	+100×100×10 mm	=130×25 mm
Cross-sectional dimensions of BRB restrained segment (Q345)	□120×120×10 mm	□150×120×10 mm
Cross-sectional dimensions of BRB core segment (Q235)	-41×25 mm	-41×25 mm
A_{gsc} (mm^2)	1025	1025
ϖ	1.5	1.5
β	1.15	1.15
P_y (kN)	261	261
ϖP_y (kN)	392	392
$\varpi\beta P_y$ (kN)	450	450
Hole diameters of BRB transition segment D_{B1}, D_{B2}	-	54
Pin diameters D_1, D_2	-	53.5
Hole diameters of BRBF gusset plate D_{E1}, D_{E2}	-	54

β= BRB compression strength adjustment factor; ϖ=BRB tension overstrength factor; P_y=axial yield load

The columns used cold-formed steel tubes filled with C100 concrete. The concrete cubic compressive strength recorded during testing was 97.1MPa. The steel beams were fabricated by welding, and the connection between the beams and columns was made using external plate welding method. In addition, a column cap made of 20 mm thick steel plate is welded to each column. The strength of the steel in the specimen was determined by tensile tests, which were conducted in accordance with the "Metal Materials Room Temperature Tensile Test Method" (GB/T 228-2002)[27], and the yield strength, tensile strength of the BRB yielding section, gusset plate, steel tube, and steel beam web and flange are presented in Table 3.

Table 3
Material properties of specimens SP1 and SP2

Steel type	f_y (material yield strength)	f_u
Steel tube (Q460)	434.6	543.7
Beam flange (Q345)	349.6	497.3
Beam web (Q345)	356.4	508.5
BRB core steel (Q235)	254.5	422.8
Gusset plate (Q345)	371.3	515.2

2.4. Test device and measurement scheme

The tests were finished at the structural laboratory of Shenyang Jianzhu University. The test loading device is illustrated in Fig. 6. A steel beam with high stiffness was welded to the bottom of the SP1-Test and SP2-Test columns. Prior to the test, the specimens were secured on the rigid ground using four steel beams with high stiffness and ground anchor bolts. During the test, two hydraulic cylinders exert an axial force of 400 kN on the top of the test structure. The jacks were affixed to the rigid crossbeam of the reaction frame through free sliding supports, which allowed simultaneous movement with the column when applying horizontal displacement. The end of the beam, which was fastened to the loading end plate of the beam, received horizontal displacement from an MTS actuator. The actuator had a maximum loading capacity of 500kN and a stroke of ±250mm. The test device is shown in Fig. 7.

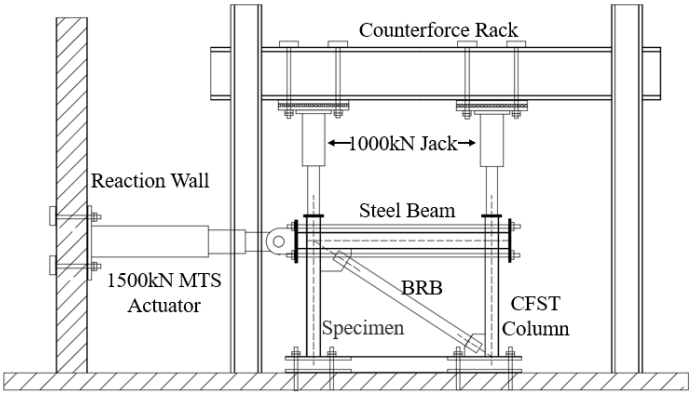

Fig. 6 Schematic diagram of test loading device

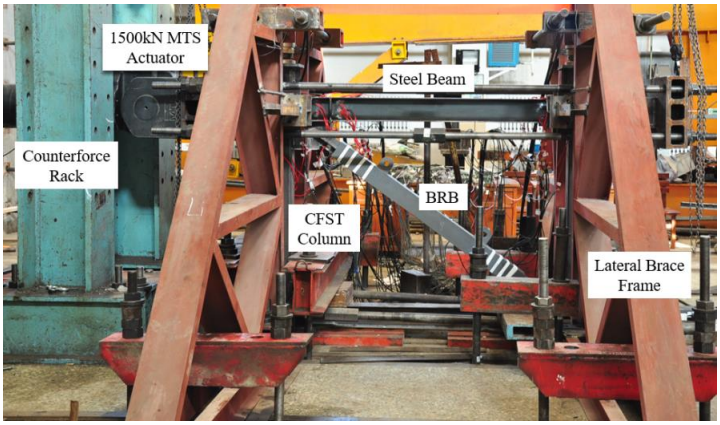

Fig. 7 Test loading device

Steel trusses were positioned on both sides of the specimen and secured to the rigid ground. To prevent out-of-plane instability of the specimen during the test procedure, a sliding device was inserted between the specimen and the steel trusses, with the top support placed at the junction of the beam and column of the test frame.

The test measurements consisted of three parts: load, displacement and strain. The configuration of strain gauges and displacement meters during the test is shown in Fig. 8. The horizontal reaction force and horizontal displacement of the test frame were automatically recorded by the MTS actuator. To measure the strain values of the beam and columns of the test frame, strain gauges were fastened to the bottom of the columns, the core area of the beam-to-column joint, the upper and lower flanges, and the web of the beam sections. At the two ends of the specimen, displacement meters W3 and W4 measured the axial displacement of the BRB, and the average value of the two measurements served as the axial displacement. Strain gauges were attached along the axial direction of the BRB yielding section and the exposed connection portion to measure the strain values. The loading displacement was controlled by the displacement meter W1 arranged at the beam end. During the experiment, all test instruments were synchronized with the MTS system for data acquisition.

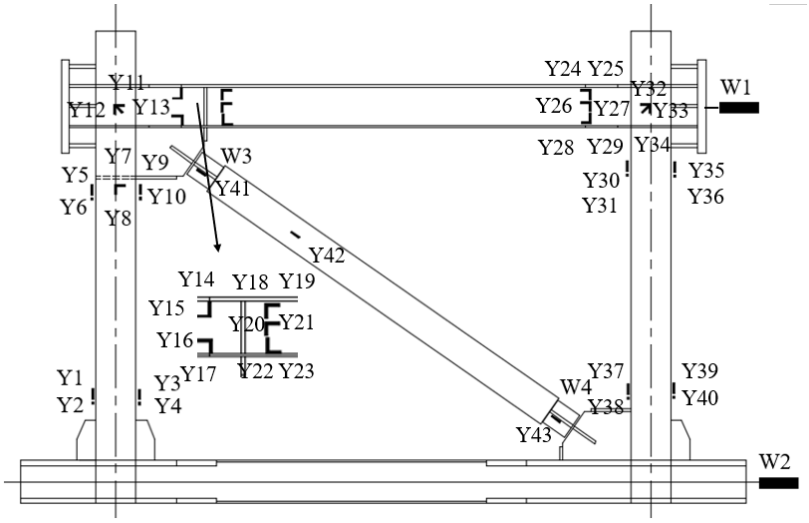

(a) SP1 strain gauge and displacement meter layout

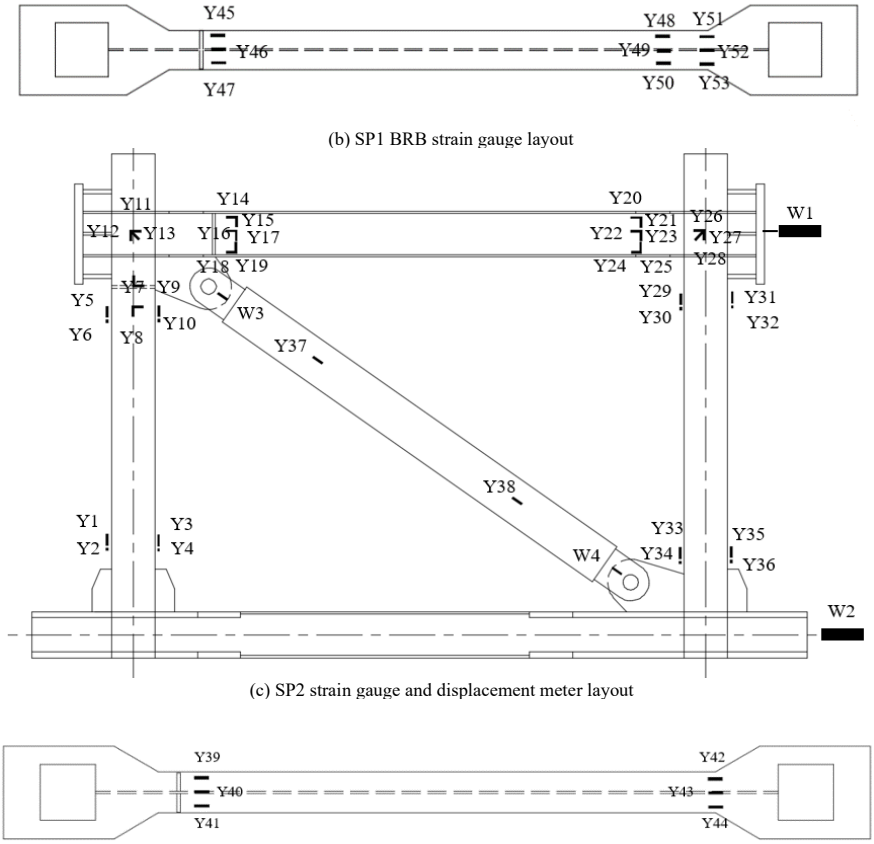

(b) SP1 BRB strain gauge layout

(c) SP2 strain gauge and displacement meter layout

(d) SP2 BRB strain gauge layout

Fig. 8 Specimen strain gauge and displacement meter layout

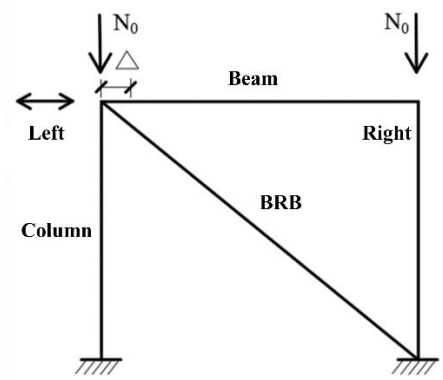

Fig. 9 Test loading schematic

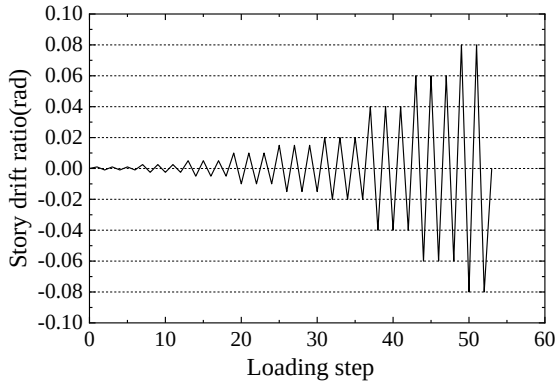

Fig. 10 Test loading procedure

2.5. Loading protocol

The test loading protocol followed the specifications outlined in the American Institute of Steel Construction (AISC) 2010 standard[25]. The loading schematic is presented in Fig. 9, and the test loading procedure for displacement control is seen in Fig. 10. The test was conducted using displacement control, with $\triangle_1$=±1.4mm (θ_1=0.001rad); $\triangle_2$=±3.5 mm (θ_2=0.0025 rad); $\triangle_3$=±7 mm (θ_3=0.005rad); $\triangle_4$=±14 mm (θ_4=0.01 rad); $\triangle_5$=±21 mm (θ_5=0.015 rad); $\triangle_6$=±28 mm (θ_6=0.02 rad); $\triangle_7$=±56 mm (θ_7=0.04 rad); $\triangle_8$=±84 mm (θ_8=0.06 rad) for three cycles; $\triangle_9$=±112 mm (θ_9=0.08 rad); $\triangle_{10}$=±140 mm (θ_{10}=0.1 rad) for two cycles. The loading continued until the specimen became unstable and failed, or until the load decreased to 85% of the ultimate load. It should be noted that $\triangle=\theta\times h$.

3. Test phenomena and failure characteristics

3.1. Experimental observations

3.1.1. Specimen SP1-Test

The Finite Element Simulation stress units in Figs. 11and 13 are MPa, Strain unit dimensionless.

When loading the specimen, it is specified that loading to the left side is positive loading. At the first cycle of the 7th loading level (4% rad), the positive loading reached 40mm (2.9% rad), causing yielding on the left side of the beam noticeable buckling of the lower flange, as shown in Fig. 11c. When the loading reached 45mm (3.2% rad), the upper flange of the right side of the beam buckled, as shown in Fig. 11c. At a loading of 56mm (4% rad), web buckling was observed at both ends of the beam. Additionally, the left column (referred to as column SP1-T-left) displayed local buckling at the base of the steel tube, as illustrated in Fig. 11i. The right column (referred to as column SP1-T-right) experienced local buckling at the steel tube near the end of the BRB1 gusset plate. When the negative loading reached -50mm (-3.6% rad), local buckling appeared on the steel tube beneath the left column joint, as shown in Fig. 11c. After the test, the steel pipe was cut and some cracks were found in the left column joint concrete, and the concrete at position 1 on the right side was locally broken, as shown in Fig. 11e.

During the first cycle of the 8th loading level (6% rad), the negative loading reached -65mm, causing out-of-plane instability of the beam. The right loading was stopped, and the negative left loading was completed for the first cycle of the 8th loading level. After the first cycle, a non-through crack measuring 0.5mm in width and 7mm in length was found on the outer side of the joint weld where BRB1 was connected to the right column gusset plate, as shown in Fig. 11h. To measure the ultimate load of specimen SP1, the second cycle of the 8th loading

level was continued. The specimen was loaded to the right up to 65mm and then the left up to -66mm (-4.6% rad). At this point, the load dropped sharply to around 400kN (55% of the maximum load). A loud "bang" sound was heard, and although the displacement continued to increase slightly, the horizontal load did not increase. It was concluded that the core reinforcement of BRB1 could break due to tensile loading, which would cause BRB1 to lose its load-bearing capacity, so the tests were stopped.

After the test, the Steel Casing of BRB1 and the columns were cut open. Observations from the images of the cut-open BRB1 revealed that its core segment experienced both compressive buckling and tensile fracture during the test, confirming that the core steel was broken under tension at around -66mm (-4.6% rad) as depicted in Figs. 12a, b and c. After inspecting the beam, column and BRB1 joint area, no cracks or crushing damage in the concrete were found (see position 2 in Fig. 11e). The gusset plate and stiffeners increased the stiffness of the joint, thereby preventing any yielding or failure in this area throughout the loading process. It can be seen from Figs. 11i to 11p that the concrete damage at the base of the left column SP1-T-left was more severe than that at the base of the right column SP1-T-right.

3.1.2. BRB1 test observations

Prior to loading to 6% rad, no cracks were observed in the joint weld connecting the ends of BRB1 to the gusset plates. However, during the second cycle at 6% rad, a non-through crack measuring 0.5mm wide and 7mm long was found on the outer side of the joint weld where BRB1 was connected to the column SP1-T-right gusset plate, as shown in Fig. 11h. Throughout the entire test, no apparent yielding or failure phenomena such as cracking in welds, local buckling or out-of-plane instability was observed in the laminated panels tested in SP1.

During the test, when the SP1-Test 's horizontal displacement reached -3.2mm (or an story drift angle of-0.23% rad), the axial displacement of BRB1 reached -2.1mm (with negative displacement indicating tension in BRB1), causing BRB1 to yield under tension. The axial displacement of BRB1 was measured using displacement sensors fixed at the transition segments of BRB1, and the yielding of BRB1 was determined using strain gauges attached to the yielding section of BRB1. The yield load of BRB1 under tension was 265kN, which is close to its design yield load of P_y = 261kN, calculated using the strain values from the strain gauges attached to the connection portions of BRB1. When the horizontal displacement reached 3.6mm to the right (or an story drift angle of 0.26% rad), the axial displacement of BRB1 reached 2.2mm, causing BRB1 to yield under compression. The corresponding yield load was 274kN, which is 5% higher than the design yield load of P_y = 261kN. Moreover, the compressive yield load-bearing capacity of BRB1 was 3% higher than the tensile yield load-bearing capacity.

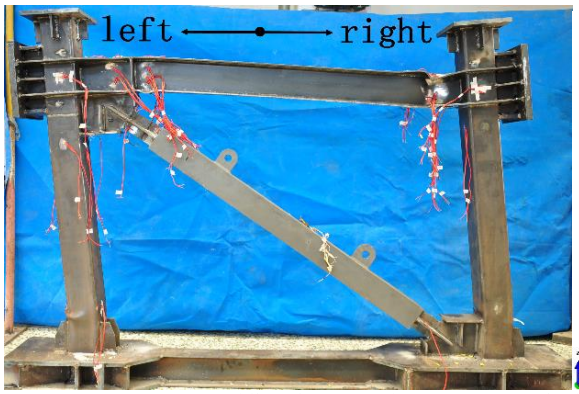

a. Post-test failure phenomena of SP1-Test

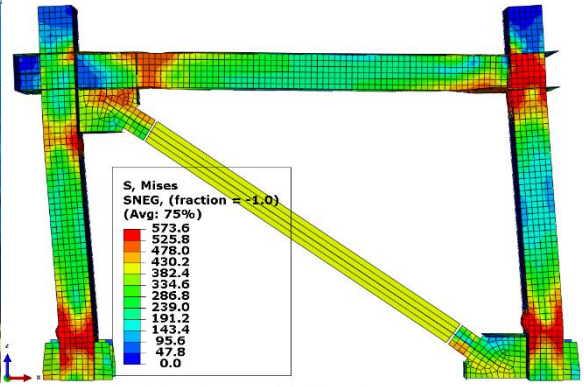

b. Finite element simulation of SP1-Model failure phenomena

c. Left-side beam-column joint (test)

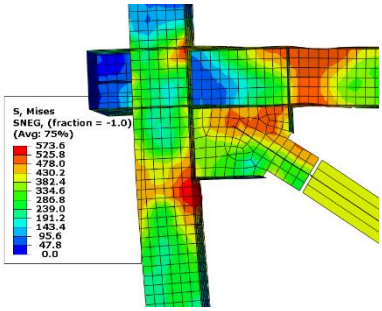

d. Left-side beam-column joint (FEM)

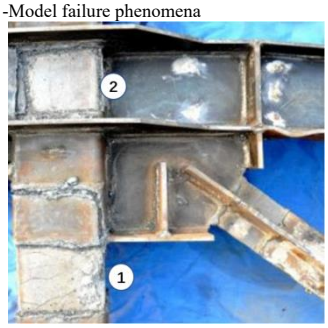

e. Left-side beam-column joint concrete

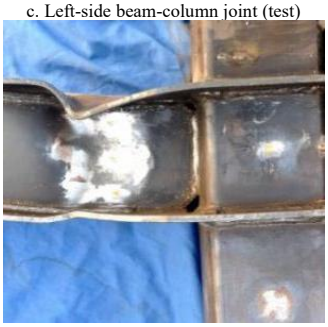

f. Right-side beam-column joint (test)

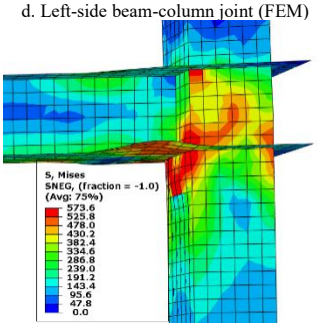

g. Right-side beam-column joint (FEM)

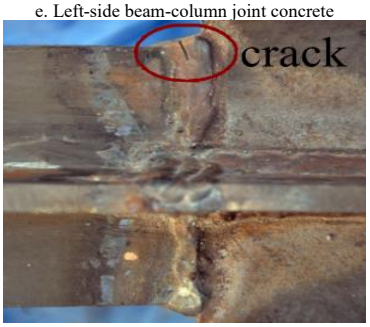

h. Crack in BRB1 butt-weld

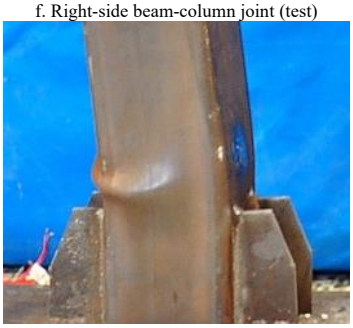

i. Left-side column base (test)

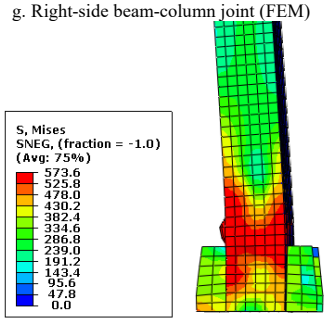

j. Left-side column base (FEM)

k. Left-side column base concrete

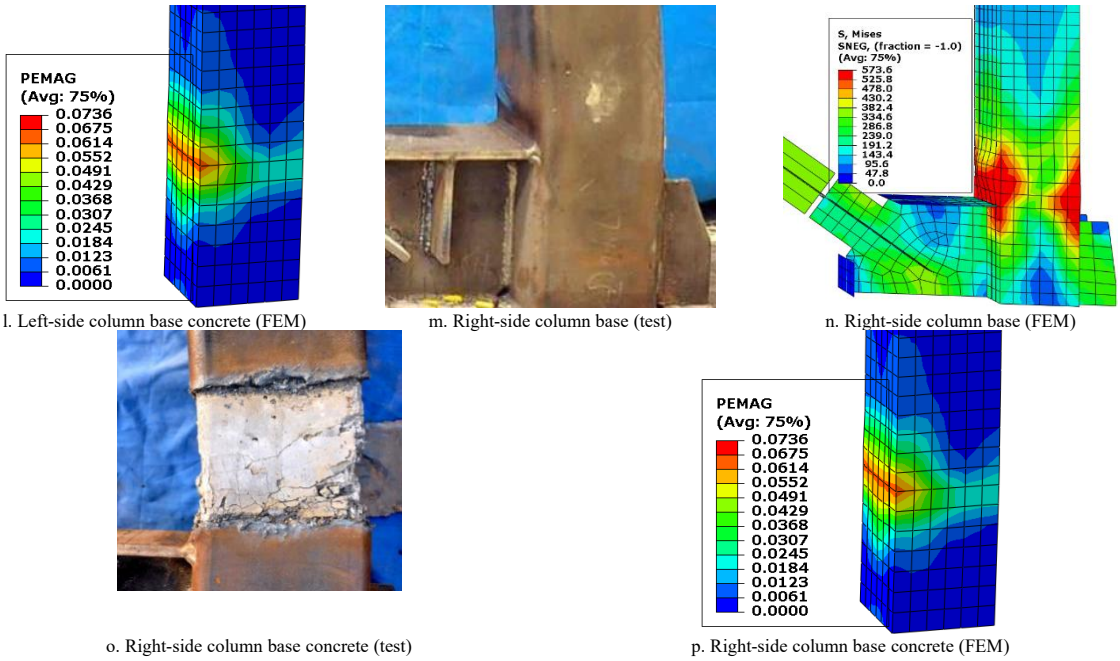

l. Left-side column base concrete (FEM) m. Right-side column base (test) n. Right-side column base (FEM)

o. Right-side column base concrete (test) p. Right-side column base concrete (FEM)

Fig. 11 Failure phenomena of specimen SP1

a. BRB1 core segment b. Core segment fracture c. Core segment buckling

Fig. 12 Failure phenomena of BRB1

3.1.3. Specimen SP2-Test

Following the loading protocol, displacement loading was carried out incrementally. At the first cycle of the 6th load level (2% rad), when the forward load reached about 28 mm (2% rad), local buckling happened at the lower flange of the left end of the beam, as shown in Figs. 13c and 13d. Additionally, local buckling was observed at the lower flange of the right end of the beam, as shown in Figs. 13e and 13f.

During the first cycle of the 7th loading level (4% rad), as the positive loading reached 35mm (2.5% rad), the upper flange and web of the beam at the left end, where it connected to BRB2, buckled as shown in Fig. 13c. The buckling of the right end of the beam also occurs at the flange and web (see Fig. 13e). The steel plate of the column connected to the lower flange of the beam experienced tensile buckling and delamination from the concrete, as shown in Fig. 13e. When the load is -42mm (-3%rad) to the left, the weld of the outer flange plate at the right end of the beam and the column cracks, causing deformation of the lower flange at the right end of the beam and the beam becomes more pronounced. Furthermore, the web of the beam buckled, and the base of the left column of specimen SP2-Test (referred to as column SP2-left) experienced bulging, as shown in Figs. 13h and 13i. Simultaneously, the steel plate at the base of the right column of specimen SP2 (referred to as column SP2-T-right) buckled, as depicted in Figs. 13j and 13k.

During the first cycle of the 8th loading level (6% rad), when the loading reached 42mm (3% rad) to the right, out-of-plane instability occurred in the beam, and the loading to the right was stopped. To determine the maximum load when loading to the left, the loading was continued to the left. When the loading reached 84mm (6% rad), no evidence of tensile rupture in the core segment of BRB2 was observed. At this point, there was no need to continue loading, and the loading was immediately stopped. The test of specimen SP2-Test was concluded. Throughout the entire test, no cracks or fractures were observed in the butt weld joint between BRB2 and the gusset plates.

3.1.4. BRB2 failure behavior

During the testing process, when the load was applied to the right and reached a displacement of about 5.6mm (0.4%), BRB2 underwent compressive yielding, resulting in an axial displacement of 1.8mm. The yielding force was measured to be approximately 273kN, which is 5% higher than the design value P_y=261 kN. Similarly, when the load was applied to the left and reached a horizontal displacement of about -6mm (-0.43%), BRB2 underwent compressive yielding, resulting in an axial displacement of -1.9mm. The yielding force was measured to be approximately 280kN, which is 7% higher than the design value P_y=261 kN. The axial displacements at which BRB2 experienced tensile and compressive yielding were relatively close, and the differences in the yielding forces were not significant. The methods used to determine the yielding of BRB2, as well as to obtain its axial displacement and yielding force, were consistent with those for BRB1. Additionally, no cracks or fractures were observed in the butt welds between BRB2 and the gusset plates throughout the testing process.

3.2. Comparison of test observations between specimens SP1-Test and SP2-Test

The results of specimen SP2-Test showed that the steel beam exhibited earlier yielding and buckling failure occurred at both ends of the steel beam, compared to the same locations in specimen SP1-Test. Comparing the yield buckling behavior of the left and right flanges of the sp2 test and the sp1 test steel beam, the left flange of the sp2 test steel beam buckling buckling failure occurs at the lower deflection angle of 2.0% rad, while the sp1 test lags behind at 2.9% radian. Likewise, in the sample sp2 test, the right flange of the steel beam buckled and formed a plastic hinge at a story dip of 2.1% rad; while for the SP1 test sample, this occurred at a higher story drift angle of 3.2% rad.

From Figs. 11 and 13, it can be seen that the damage at the left end of the steel beam in specimen SP2-Test is much more severe than that in specimen SP1-Test. Fig. 13g provides a clear illustration of the damage observed in specimen SP2-Test. It can be seen from the figure that when the sample reaches the sheet deflection angle of 2.9% rad, cracks appear in the weld seam between the outer plate of the right lower flange and the column. When the load was increased to 3.3% rad, the outer plates connecting the bottom flanges of the steel beams fractured. During the test, specimen SP1-tested steel beam formed a plastic hinge at both ends and no weld cracking or plate tearing occurred.

The testing process demonstrated that the failure at both ends of the steel beam in specimen SP2-Test occurred earlier than in specimen SP1-Test, and the

extent of the damage was more severe in specimen SP2-Test. Instability out-of-plane happened earlier in the specimen SP2-test than in the specimen SP1-test.

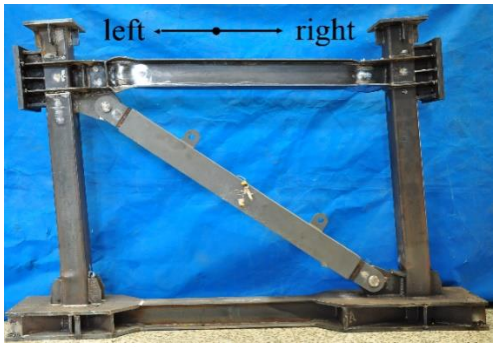

(a) Damage phenomenon of SP2-Test after the experiment

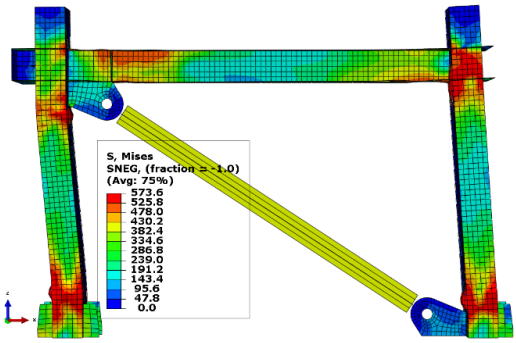

(b) Finite element simulation of SP2-Model damage phenomenon

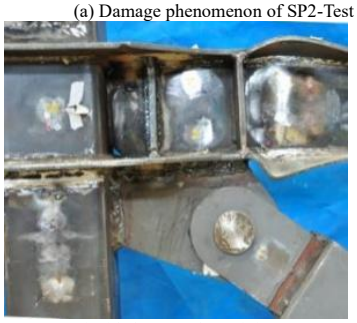

(c) Left-side beam-column joint (test)

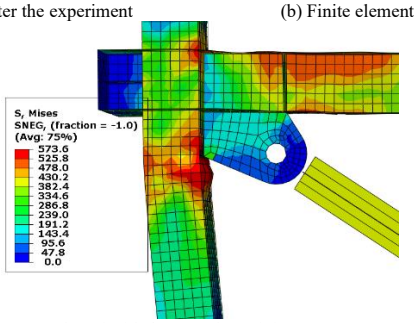

(d) Left-side beam-column joint (FEM)

(e) Right-side beam-column joint (test)

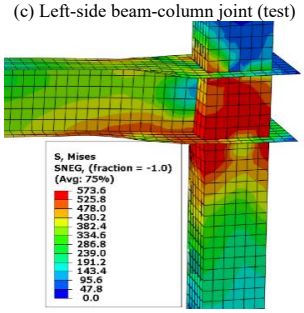

(f) Right-side beam-column joint (FEM)

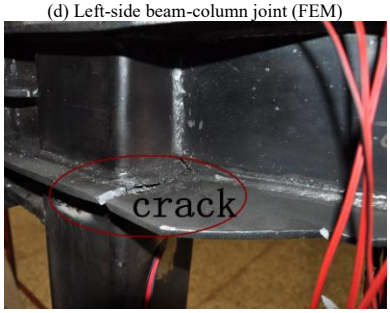

(g) Crack in the lower flange weld of the right-side external plate

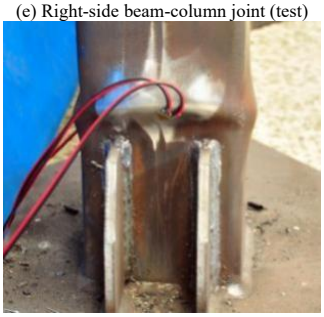

(h) Left-side column base (test)

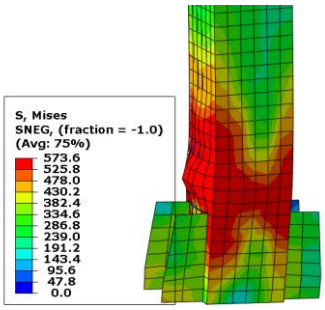

(i) Left-side column base (FEM)

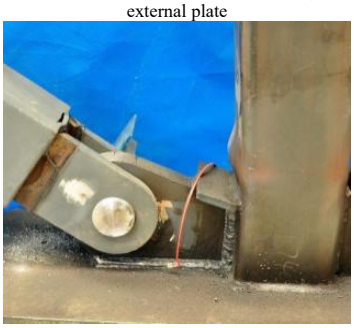

(j) Right-side column base (test)

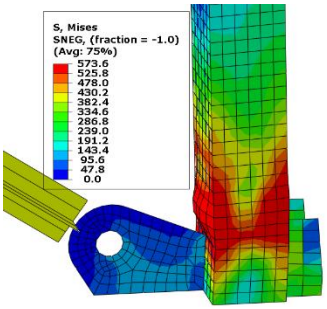

(k) Right-side column base (FEM)

Fig. 13 Failure Phenomenon of Specimen SP2

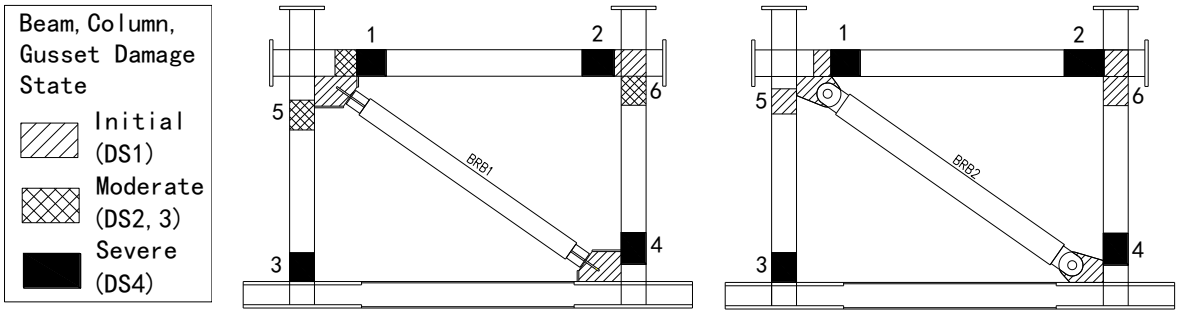

(a) Specimen SP1-Test (b) Specimen SP2-Test

Fig. 14 Schematic of the plastic hinge location during the specimen test process

As shown in Figs. 11 and 13, the left column of the specimen SP1-Test exhibited yielding and plastic hinge formation at the lower portion of the gusset plate, accompanied by the appearance of cracks within the concrete of the steel tube. Contrary to the behavior of the left column in the specimen SP1-test, the left column of specimen SP2-Test did not yield or form a plastic hinge in the same area, suggesting that the pin connection is beneficial in mitigating the bending moment transferred from the BRB transition segments to the column. Nevertheless, according to the test results, the overall stress distribution and damage of specimen SP1-test were significantly better than that of specimen SP2-test.

Fig. 14 illustrates the progression of yielding, plastic hinge formation, and damage extent and location in the beams, columns, gusset plates and other components of specimens SP1-Test and SP2-Test throughout the testing process. Initially, plastic hinges develop at the ends of the beams with BRB connections and subsequently at the ends of the beams without BRB connections. Subsequently, plastic hinges appear on column bases without BRB connections and finally on column bases with BRB connections. During the whole test process, the beam-to-column connection and the core area of the BRBF gusset plate were not damaged and were in an elastic state.

4. Analysis of experimental results

4.1. Hysteresis curves

The hysteresis curves for specimens SP1-Test and SP2-Test are illustrated in Fig. 15. Both specimens exhibited full hysteresis loops, with no pinching phenomena detected, and the ultimate load capacities for both specimens are relatively close. While the curve for specimen SP1-Test remains consistently smooth, the curve for specimen SP2-Test demonstrates an abrupt transition in proximity to the zero load, as indicated by the 'pin slip' in Fig. 15b. Upon further analysis, this sudden change observed in the test results can be attributed to two primary factors. Firstly, prior to the tests, measurements were taken of the gusset plate hole diameters and pin shaft diameters of BRB2. The pin shaft diameters were found to be approximately 0.7mm smaller than the BRBF connection gusset plates hole diameters, resulting in a gap between them. Consequently, when the core segment of BRB2 changed from compression to tension, or vice versa, it was almost unloaded, and the horizontal load was entirely supported by the beam and columns. Secondly, to facilitate the installation of BRB2, there was a clearance of approximately 1.0 mm between the two connecting plates of BRB2. When the frame was loaded in the positive direction, this gap caused BRB2 to undergo minor out-of-plane deformations, which affected the effective transfer of horizontal loads to BRB2.

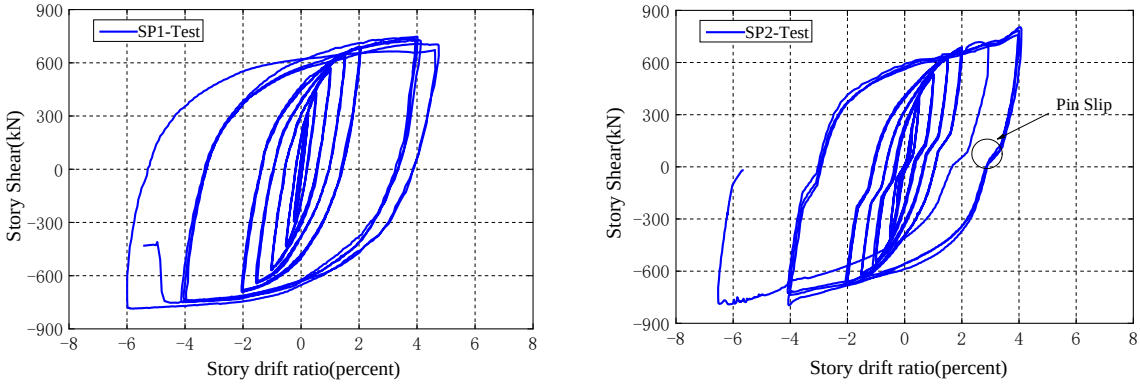

（a）SP1-Test （b）SP2-Test

Fig. 15 Load-Displacement Curve of the Test Specimen

4.2. Energy dissipation

In order to evaluate the energy dissipation capacity of the test specimen, this paper introduces two parameters: the equivalent viscous damping coefficient, denoted as ζ_e, and the energy dissipation coefficient, denoted as E. The expressions for the equivalent viscous damping coefficient ζ_e and energy dissipation coefficient E of the hysteresis loop, as converted based on Fig. 16, are shown below.

$$\zeta_e = \frac{1}{2\pi} \cdot \frac{S_{ABC}+S_{CDA}}{S_{\Delta OBE}+S_{\Delta ODF}} \tag{1}$$

$$E = 2\pi\zeta_e \tag{2}$$

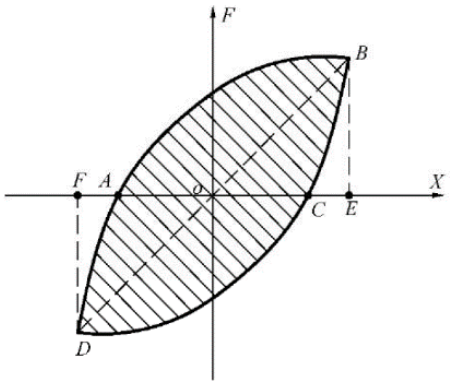

Fig. 16 Percentage of shear force carried by the BRB (experiment)

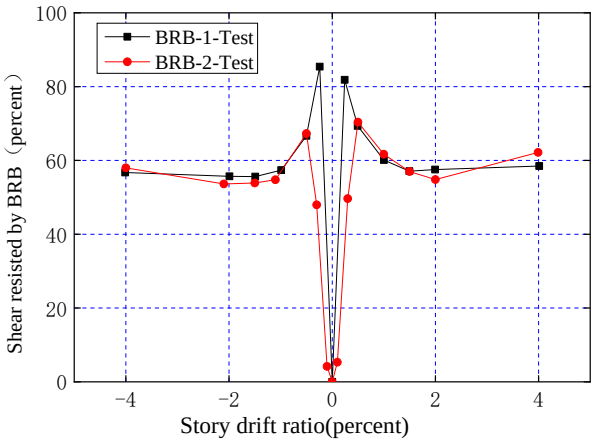

Fig. 17 Percentage of Shear Force Carried by BRB (experiment)

Table 5
Energy dissipation indicators of specimens

Specimen ID	Total energy dissipation (kN·mm)	Equivalent viscous damping coefficient ζ_e	Energy dissipation coefficient E
SP1	569177	0.349	2.192
SP2	487415	0.299	1.878

Using Equations (1) and (2), the total energy dissipation, equivalent viscous damping ratio ζ_e, and energy dissipation ratio E of each specimen at the ultimate state can be calculated, as presented in Table 5. The total energy dissipation, equivalent viscous damping ratio ζ_e, and energy dissipation ratio E of specimen SP1-Test with welded connections are all greater than those of specimen SP2-Test with pin connections.

4.3. Energy-dissipation capacity of BRB

The shear force ratios of BRB1 and BRB2 during the testing process are illustrated in Fig. 17. It is observed that under rightward loading, when the story

drift angle increases from 0 to 0.5% rad, a substantial difference exists between the shear forces carried by BRB1 and BRB2. As the inter-story displacement angle increases from 0 to 0.25 % rad, the proportion of shear force borne by BRB1 to the total frame shear force increases from 0 % to a peak of about 82%. In this phase, the axial load of BRB1 exhibits a linear relationship with the story drift angle, and BRB1, in both tension and compression begins to yield when the story drift angle approaches 0.25% rad.

After exceeding 0.25 % rad inter-story displacement angle, the proportion of horizontal shear force borne by BRB1 to the total frame shear force decreases as the inter-story displacement angle continues to increase. As the inter-story displacement angle increases from 0 to 0.5 % rad, the proportion of shear force borne by BRB2 to the total frame shear force increases from 0 % to a peak of about 70 %. At an angle of interlaminar displacement of 0.5 % rad, BRB2 starts to yield in both tensile and compressive states. When the inter-story displacement angle exceeds 0.5 % rad, the proportion of horizontal shear force borne by BRB2 to the total frame shear force decreases with the increase of inter-story displacement angle. Moreover, within the range of 0.5% to 4% rad story drift angle, the shear forces carried by both BRB1 and BRB2 contribute to approximately 60% of the total story shear force, which is in relatively close agreement with the design expectation. In the initial loading stage (0 to 0.3% rad), gaps between the connecting pin shafts, gusset plate holes and BRB2 connecting plate holes prevent the effective transmission of shear force to BRB2 during low loading displacements. As a result, the shear force carried by BRB2 is minima during this initial loading stage, leading to a significant deviation from the ideal state.

The energy dissipation capacity of buckling-restrained braces can be evaluated through the cumulative ductility demand μ_c, as specified in AISC (2010) [25].

$$\mu_{max}=\Delta_{max}/\Delta_{by} \quad (3)$$

$$\mu_c=(\sum\Delta_{plastic})/\Delta_{by} \quad (4)$$

in which, $\sum\Delta_{plastic}$ represents the cumulative plastic deformation of the BRB, and Δ_{max} represents the maximum deformation of the BRB.

When the story drift of specimen SP1-Test reached 4% rad, the maximum ductility demand of BRB1 μ_{max} was 21, the cumulative ductility demand μ_c was 518.2, which was comparable to the value reported in reference [8]. The cumulative ductility demand μ_c increased to 671.2 at the point of BRB1 tensile fracture, which exceeded the value reported in reference [8]. It also surpassed the requirement of cumulative ductility demand μ_c greater than 200 specified in AISC (2010) [25].

When the story drift of specimen SP2-Test reached 4% rad, the maximum ductility demand of BRB2 μ_{max} was 20.8, which was comparable to the value reported in reference [8]. The cumulative ductility demand μ_c was 406.6, which was lower than the value reported in reference [8], but it still exceeded the requirement of cumulative ductility demand μ_c greater than 200 specified in AISC (2010) [25].

5. Finite element simulation

5.1. Constitutive model of materials

The steel model for columns and beams is an ideal bilinear model without accounting for strain hardening. The plastic damage model defined in ABAQUS is used for concrete materials, and the stress-strain relationship is calculated using the material model [28] proposed in the literature, while considering the confinement effect of steel pipes on the concrete core. For the BRB core, the steel material model uses the Combined Hardening model in ABAQUS, which considers both isotropic hardening and kinematic hardening. The specific parameters are determined based on reference [29].

5.2. Element types and meshing

The meshing of the specimen is shown in Fig. 18. The steel tubes, H-shaped steel, stiffeners and the BRB are modeled using S4R shell elements. The column grid is 25 mm, the beam grid is 25 mm, and the grid on the gusset plates and stiffeners is 20 mm. Chung-Che Chou and Jia-Hau Liu [30] modeled the BRB core using truss elements T3D2 (two-node) to avoid core buckling,in order to eliminate the BRB restraining members from the model. Tsai KC [19]and Yu YJ [31] recommend that the BRB of frame can be conveniently replaced by a truss element in a BRBF analytical model. The BRBs were modeled by Li Jiaqi [32] using S4R shell elements which the out-of-plane displacement is set to zero to avoid core buckling.In this paper, the BRBs are modeled using S4R shell elements. The number of elements for the BRB core along the length direction is set to one to avoid core buckling. The concrete is modeled using C3D8R eight-node linear hexahedral elements. The contact relationship between concrete and steel pipe is defined as normal hard contact. Considering tangential friction, the Coulomb coefficient of friction is 0.6 [33]. The sample SP1 model (scaled finite element model of SP1 test) uses connection constraints to connect the BRB to the frame, and the sample SP2 model (scaled FE model of SP2 tests) uses hinge constraints for pin connections and gussets are relative in the plane of the frame rotate.

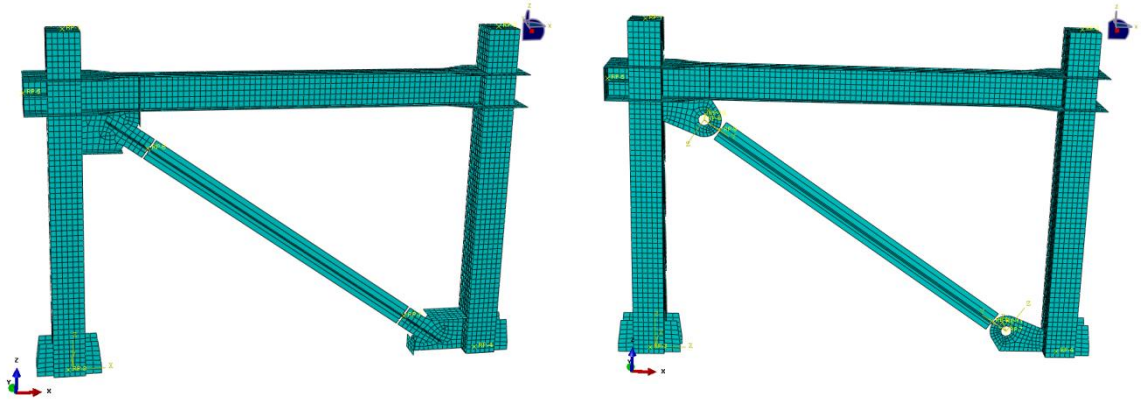

(a) Schematic diagram of mesh division and contact relationship for SP1-Model

(b) Schematic diagram of mesh division and contact relationship for SP2-Model

Fig. 18 Mesh division of test specimens

5.3. Model boundary conditions and loading method

The finite element model has the same boundary conditions as the test frame, the bottom of the column is fixed, the vertical concentrated force is applied at the top of the column during the simulation, as shown in Fig. 9 (test loading diagram). During the test, the lateral support is used to limit the out-of-plane instability of the specimen, the out-of-plane horizontal displacement at the top of the column is set to zero during the simulation.

Furthermore, the loading method is in alignment with the test frame, the in-plane horizontal displacement was loaded at the left end of the beam , with each level of loading displacement and number of cycles consistent with the test frame loading method.

5.4. Comparison and analysis of experiment and finite element results

As can be seen from Figs. 19-23, the finite element simulation results of the specimen SP1-model show excellent agreement with the experimental results. However, the hysteresis loop shape of the finite element simulation results for specimen SP2-Model slightly deviates from the experimental results, primarily due to the unaccounted processing errors in the pin shaft diameter and gusset plate hole diameter of BRB2 during modeling. Nevertheless, as shown in Fig. 23, the backbone curve of the SP2-model agrees well with the results of the experiment.

Based on the results of experiments and simulations (refer to Figs. 17 and 24), the shear force ratios of BRB1 and BRB2 remain very close throughout the entire loading period. As the story drift angle increases from 0 to ±0.25%, the

shear force ratios of BRB1 and BRB2 rise from 0 to a maximum value of 80%. For the inter-story displacement angles between 0.25 % and 1.5 % and between - 0.25 % and -1.5 %, the proportion of the horizontal shear force borne by BRB1 and BRB2 to the total shear force of the frame decreases with the increase of the inter-story displacement angle. Finally, when the story drift angle falls within the range of 1.5% to 4% and -1.5% to -4%, the shear force ratios of BRB1 and BRB2 are within the interval of 55-60%.

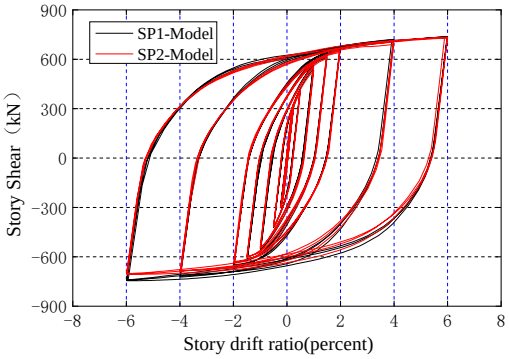

Fig. 19 Load-displacement curves of the specimens (FE simulation)

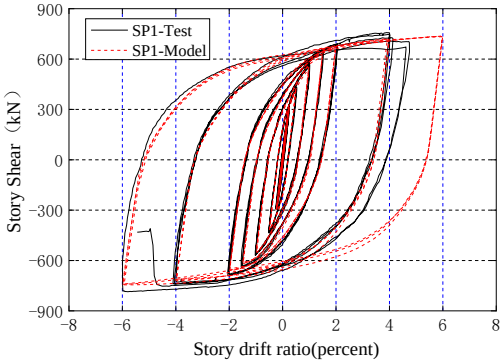

Fig. 20 Load-displacement relationship of specimen SP1

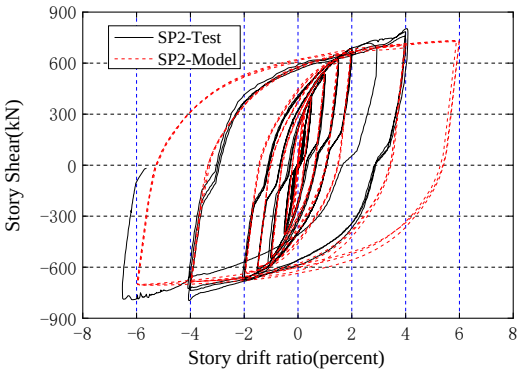

Fig. 21 Load-displacement relationship of specimen SP2

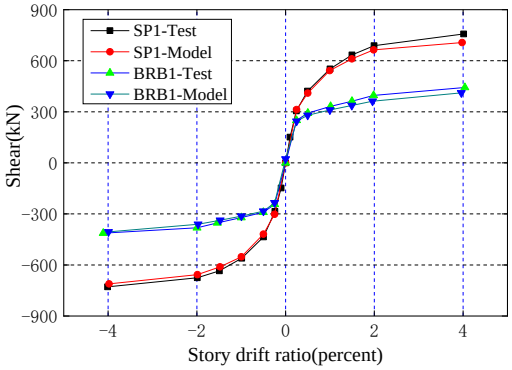

Fig. 22 Shear force-deflection curve for specimen SP1

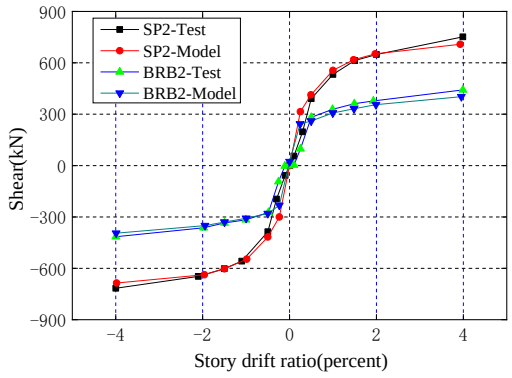

Fig. 23 Shear force-deflection curve for specimen SP2

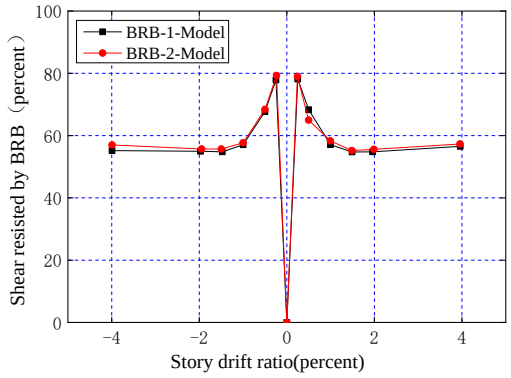

Fig. 24 Percentage of Shear Force Carried by BRB (FE Simulation).

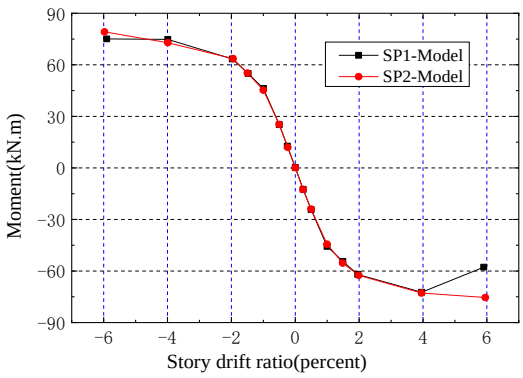

Fig. 25 Moment-rotation relationship of left beam end at 1-1 section.

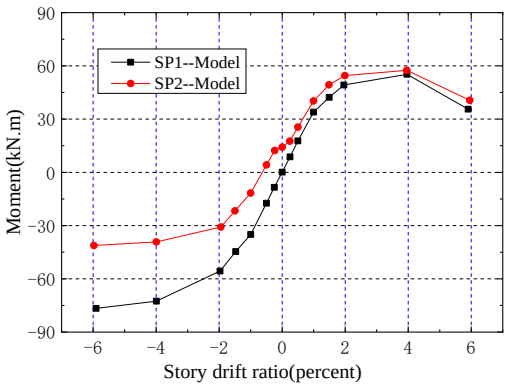

Fig. 26 Moment-rotation curves of left column end A-A section

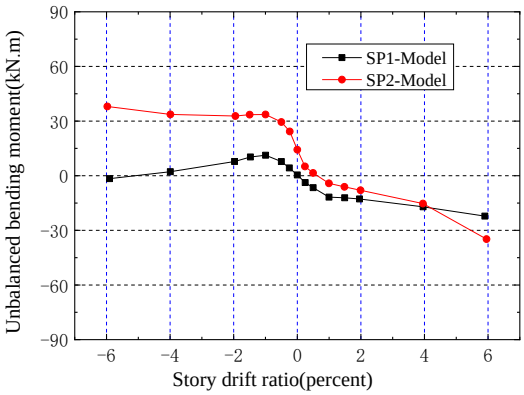

Fig. 27 Unbalanced bending moment and rotation curves at the beam-end and column-end

5.5. Analysis of forces on the beam and column ends of the frame

The relationship between the bending moment at the left beam end of the specimen and the turning angle can be observed in Fig. 25. It is evident that, with story drift angles ranging from 0 to 4% rad, both the BRB welded frame model SP1-Model and BRB hinged frame model SP2-Model exhibit yielding at the same location of the left beam-end, with very similar beam-end moments at that specific location.

The relationship between the left column-end moment and rotation at section A-A can be seen in Fig. 26. When loaded to the right, the column-end moments of the BRB welded frame model SP1-Model and BRB hinged frame model SP2-Model are moderately close. However, when loaded to the left, the column-end moment of SP1-Model is twice that of SP2-Model.

The unbalanced moments at the beam end and column end can be observed in Fig. 27 as a function of the angle of rotation. It can be seen that when loaded to the right, the unbalanced moments of both SP1-Model and SP2-Model are relatively close. However, when loaded to the left, the unbalanced moment of SP2-Model is greater, accounting for approximately 50% of the beam-end moment. This portion of unbalanced moment is generated due to the axial force of the BRB not passing through the intersection of the beam-column axis during loading. In contrast, the unbalanced moment of SP1-Model is smaller.

From the above moment diagrams, it can be seen that, throughout the entire loading process, the beam-end moment and column-end moment of SP1-Model remain relatively similar, and the unbalanced moment is small. The use of a welded connection between the BRB and the frame does not increase the beam-end moment or amplify the limit moment of the joint.

5.6. Sectional stress analysis of beam and column ends

Section 1-1, located at the plastic hinge at the left beam-end of specimens SP1-Model and SP2-Model, and section A-A at the plastic hinge at the left column-end, as shown in Fig. 2, have been selected for stress analysis. Figs. 28-30 respectively show the Mises stress distribution in these sections. Since the stress magnitude and distribution in these beam and column sections are almost unaffected by leftward and rightward loading, only the stress distribution for rightward loading is presented. From Fig. 28, it can be observed that when the story drift is less than 1.5%, the stress magnitude at section 1-1 for both SP1-Model and SP2-Model is smaller than the material yield stress of 345 MPa. The stress amplitude at this section is comparable for both specimens across different load levels. Furthermore, Figs. 29 and 30 indicate that for story drift below 1.0%, the stress magnitude at column section A-A for both SP1-Model and SP2-Model is smaller than the material yield stress of 345 MPa. The stress distribution patterns and stress amplitude magnitudes at this section are also quite similar for both specimens across different load levels. It can be seen that the welded and pin connection between the BRB and the frame have a minor impact on the stress distribution patterns and stress amplitude magnitudes at the beam-end and column-end joints.

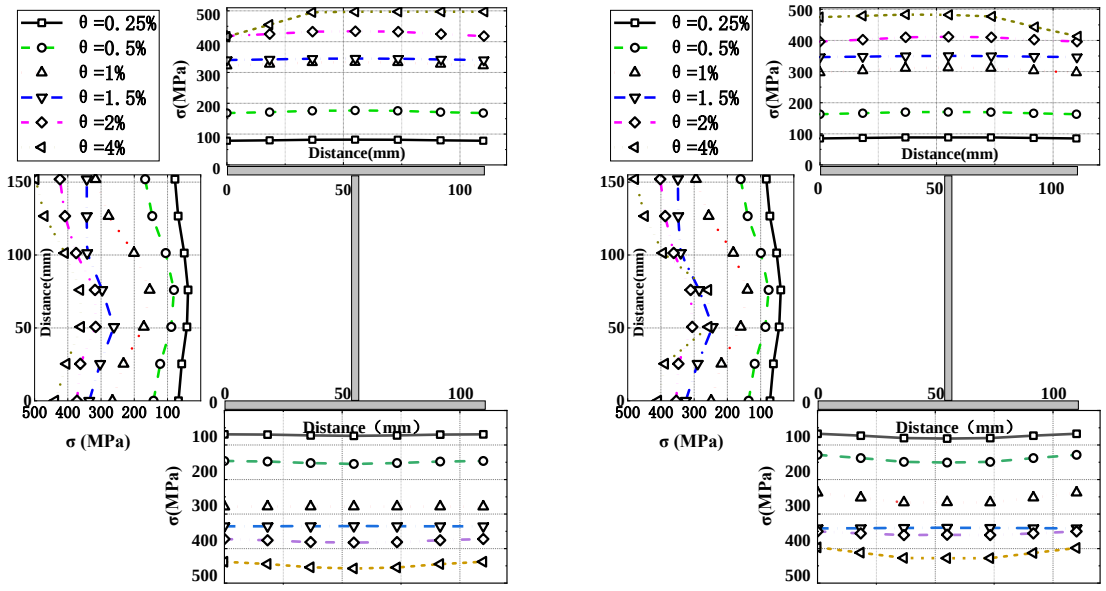

(a) Specimen SP1-Model (b) Specimen SP2-Model

Fig. 28 Mises stress distribution at steel beam section 1-1 under rightward loading for specimen

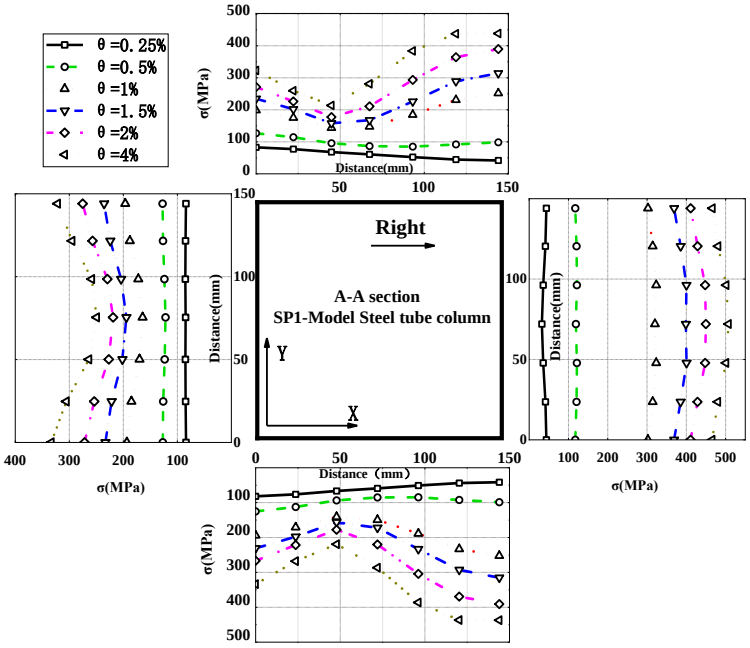

Fig. 29 Mises stress distribution at column section A-A for specimen SP1-Model under rightward loading

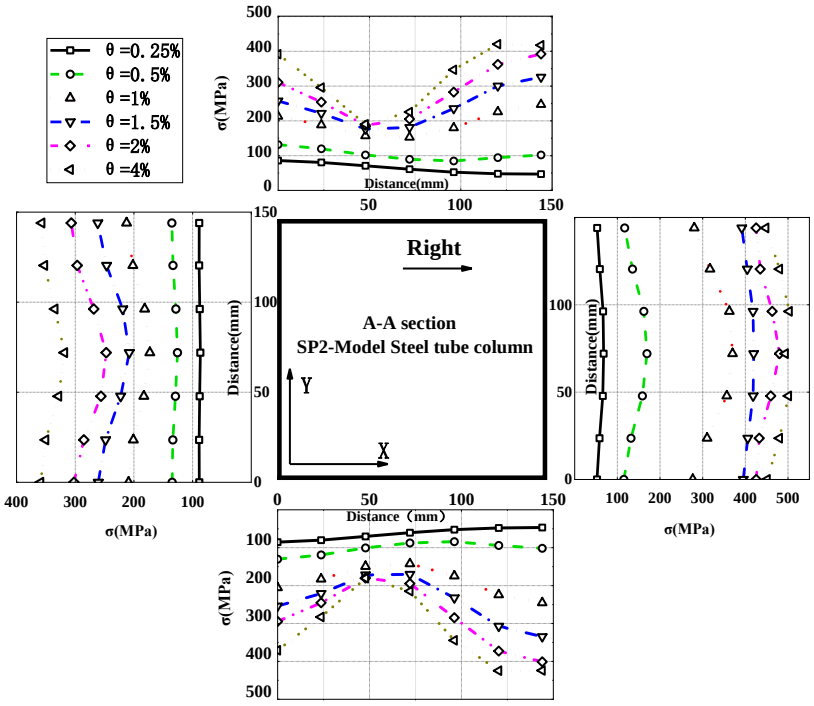

Fig. 30 Mises stress distribution at column section A-A for specimen SP2-Model under rightward loading

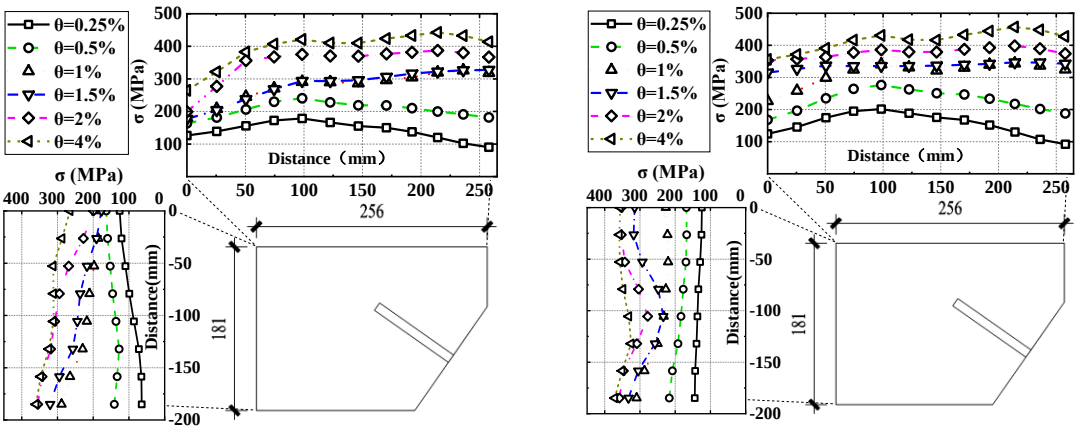

(a) Loading to the right (b) Loading to the left

Fig. 31 Mises stress distribution at the left joint weld of specimen SP1-Model

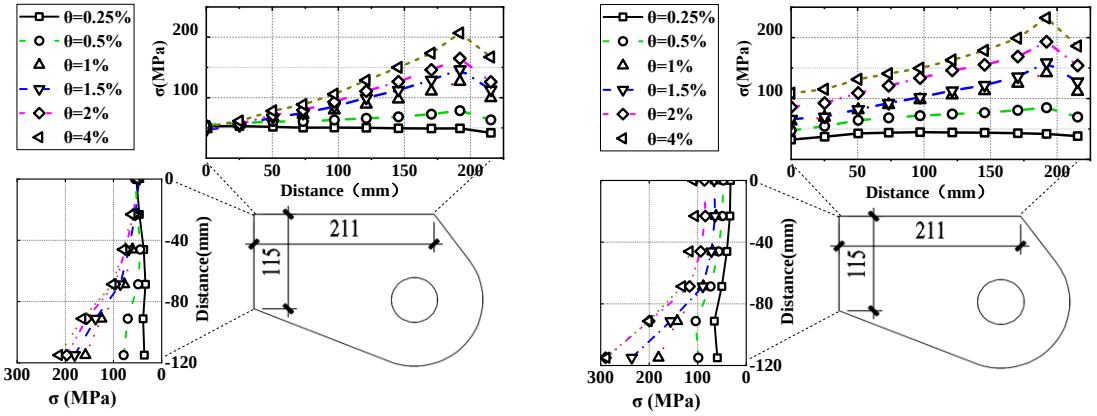

(a) Loading to the right (b) Loading to the left

Fig. 32 Mises stress distribution at the left joint weld of specimen SP2-Model

5.7. Analysis of weld stress at joints

In specimens SP1-Test and SP2-Test, the gusset plates were welded to the beams and columns using full penetration welds. On the other hand, in the finite element model, the gusset plates are 'merged' ideally to the beams and columns. The welds at the gusset plates are susceptible to failure due to concentrated forces. To understand the stress condition at the welds, the Mises stress at the joint welds at the maximum displacement angle of the first cycle during cyclic loading is selected, as shown in Figs. 31 and 32. When the story drift is less than 1.5%, the tensile and compressive stresses in the horizontal and vertical welds of the left joint of SP1-Model are all less than the yield stress of 345 MPa. Once the story drift reaches 2%, the maximum tensile and compressive stresses in the horizontal and vertical welds are both less than 400 MPa. Although the loading direction changes, the stress magnitude does not change significantly.

The stress at the left joint welds of SP2-Model is shown in Fig. 32. When the story drift angle is less than 4%, both the tensile and compressive stresses in the horizontal and vertical welds are less than 250 MPa, which is lower than the steel yield stress of 345 MPa. Similarly, the stress magnitude does not change significantly with the loading direction.

Upon comparing Figs. 31 and 32, it can be observed that the weld stress in the pin connection is significantly lower than that in the welded connection. This is because the gusset plate used in the pin connection has a thickness of 40 mm, while the gusset plate used in the welded connection has a thickness of 10 mm. At the weld location, the steel cross-sectional area at the pin connection gusset plate is approximately twice that of the welded connection gusset plate. The difference in stress is not due to the type of connection used but rather the cross-sectional area of the gusset plates.

6. Conclusion

This paper employed experimental and finite element simulation methods to compare and analyze the mechanical performance of frames featuring HSCFSSTC with buckling-restrained braces (BRBs) using both welded and pin connections under cyclic loading. Based on the analysis, the following conclusions were reached:

(1) The hysteresis loops of the BRBFs with welded and pin connections were relatively full, which satisfied the code[22] requirements for story drift limits.

(2) During the experimental failure, the plastic hinge appeared in the following order: beam ends, column base, and column ends, indicating a reasonable design. Moreover, the use of welded or pin connections in BRBFs did not significantly affect the failure mechanism of the BRBFs, the formation of plastic hinges, the energy dissipation capacity of the BRBs, the load-bearing ratio of the BRBs, or the seismic performance of the BRBFs.

(3) The result of ABAQUS analysis shows that the stress distribution patterns and magnitude at the welds of the gusset plates connecting the BRBs to frames' beams and columns, as well as the beam ends and column ends, were quite similar for both connection types. The experimental results and ABAQUS analysis results show that the BRBFs with welded and pin connections exhibit good seismic resistance and energy dissipation capabilities.

(4) When using pin connections in the BRBFs, it is important to increase the manufacturing accuracy, reduce dimensional deviations, and minimize the clearances between the pin and the connection gusset plates and connecting plates of BRBs. This helps to minimize installation errors and improve the performance of the BRBs, which ensures the seismic performance of the frames. On the other hand, welded connections overcome the drawbacks of pin connections, exhibit better performance of the BRBs, and are considered safer and more reliable. As such, welded connections have great potential for widespread application.

Acknowledgments

The authors gratefully acknowledge the financial support provided by the Key Projects of National Natural Science Foundation of China, China (51938009), the Educational Department of Liaoning Province, China (LJKMZ20220929) , the Department of Science & Technology of Liaoning province, China(2023JH6/100100053) and Shanghai Lanke Building Damping Technology Co., Ltd..

References

[1] Li Guochang, Chen Bowen, Yang Zhijian, et al. Experimental and numerical behavior of eccentrically loaded square concrete-filled steel tubular long colmns made of high-strength steel and concrete[J]. Thin-Walled Structures, 2021, 159(2):107289
[2] Li Guochang, Chen Bowen, Yang Zhijian, et al. Axial behavior of high-strength concrete-filled high strength square steel tubular stub columns. [J] Advanced Steel Construction, 2021, 17(2):158–168
[3] Saad Younas1, Ehab Hamed, Dongxu Li, Brian Uy. Eccentrically loaded concrete-filled steel tubes made with high strength materials. [J] Engineering Structures, 2023, 275
[4] Saad Younas, Ehab Hamed, et al. Effect of creep on the strength of high strength concrete-filled steel tubes. Journal of Constructional Steel Research 2023, 201
[5] Uang CM, Nakashima M, Tsai KC. Research and application of buckling-restrained braced frames[J]. Steel Structures 2004; 4(4):301–313.
[6] Atsushi Watanabe. Design and Applications of Buckling-Restrained Braces. International Journal of High-Rise Buildings. September 2018, Vol 7, No 3, 215-221.https://doi.org/10.21022/IJHRB.
2018.7.3.215
[7] Yun Zhou, Hetian Shao, Yongsheng Cao, Eric M. Lui. Application of buckling-restrained braces to earthquake-resistant design of buildings: A review. Engineering Structures 246 (2021) 112991
[8] Wang Bo,Wang Jingfeng, et al. Experimental study on seismic behavior of assembly CFST composite frames with bucking restrained braces. China Civil Engineering Journal, 2018, Vol. 51 No. 6 (in Chinese)
[9] Wigle Victoria R., Fahnestock Larry A. Buckling-restrained braced frame connection performance[J]. Journal of Constructional Steel Research, 2010，66(1)： 65-74.
[10] Keh-Chyuan Tsai, Po-Chien Hsiao.Pseudo-Dynamic Tests of a Full-Scale CFT/BRB Frame—Part I Specimen design, experiment and analysis[J]. Earthquake Engineering and Structural Dynamics 2008; 37: 1081-1098
[11] Keh-Chyuan Tsai, Po-Chien Hsiao. Pseudo-Dynamic Tests of a Full-Scale CFT/BRB Frame—Part II Seismic performance of buckling-restrained braces and connections[J]. Earthquake Engineering and Structural Dynamics 2008; 37: 1099-1115
[12] Wang Jingfeng, Gao Xiang, Li Beibei, et al. Seismic performance tests and analysis of connections between buckling restrained braces and steel frame. China Civil Engineering Journal, 2019，Vol. 52 No. 8 (in Chinese)
[13] Beibei Li, Jingfeng Wang, Yuanqing Wang. Subassemblage test and gusset rotation response of buckling-restrained braced steel frames. Structures 33 (2021) 3417–3432
[14] Mingming Jia, Kai Liu, et al. Experimental research of seismic performance of buckling-restrained braced frame with ductile connections[J]. Structures 41 (2022) 908–924
[15] Keith D. Palmer, Charles W. Roeder, et al. Experimental Performance of Steel Braced Frames Subjected to Bidirectional Loading[J]. Journal of Structural Engineering. 2013.139：1274-1284.
[16] Junda E., Leelataviwat S., Doung P. Cyclic testing and performance evaluation of buckling-restrained kneebraced frames. Journal of Constructional Steel Research 148 (2018) 154–164
[17] Wang Jingfeng ,Wang Xinle, et al. Experimental studies on seismic performance of prefabricated concrete frame structures with buckling-restrained braces. China Civil Engineering Journal,2018, Vol. 51 No. 12 (in Chinese)

[18] Jingfeng Wang, Fei Lu, Beibei Li. Subassemblage tests and analysis of buckling-restrained braced reinforced concrete frames with various gusset connections. Structures 39 (2022) 39–56
[19] Keh-Chyuan Tsai, et al, Welded end-slot connection and debonding layers for buckling-restrained braces[J]. Earthquake Engng Struct. Dyn. (2014) DOI: 10.1002/eqe
[20] Wang Cuihong. Study on Seismic Resistance and Seismic Demand Performance of BRBF Structure with Rigid Joint and Bolt Joint. Guilin university of technology.2020 (in Chinese)
[21] Sheng Pei. Experimental study on seismic performance of ultrahigh strength steel frames with buckling restrained braces[J]. Archives of Civil and Mechanical Engineering (2021) 21:164
[22] Ministry of Housing and Urban-Rural Development of the People's Republic of China, General Administration of Quality Supervision, Inspection and Quarantine of the People's Republic of China. Code for seismic design of buildings: GB 50011—2010[S]. Beijing: China Architecture & Building Press, 2010. (in Chinese)
[23] Ministry of Housing and Urban-Rural Development of the People's Republic of China. Technical specification for seismic energy dissipation of buildings: JGJ 297—2013[S]., 2013. (in Chinese)
[24] FEMA-350. Recommended Seismic Design Criteria for New Steel
[25] AISC. (2010). "Seismic provisions of structural steel building." ANSI/AISC 341-10, Chicago.
[26] Lin PC, Tsai KC, Roeder CW. Seismic design and hybrid tests of a full-scale three-story buckling-restrained braced frame using welded end connections and thin profile[J]. Earthquake Engineering and Structural Dynamics 2012; 41(5):1001–1020.
[27] Metallic materials- Tensile testing—Part 1: Method of test at room temperature. (in Chinese)
[28] Wang Wenda, Han Linhai. Nonlinear finite element analysis on mechanical performance of concrete-filled steel tubular frame structure[J]. Journal of Building Structures.2008, 29(6):75-83. (in Chinese)
[29] Shi Yongjiu, Wang Jiaojiao et al. Mechanical performance of low-yield-point steel LYP225 under cyclic loading. Journal of Southeast University (Natural Science Edition). 2014, Vol.44(6):1260-1265. (in Chinese)
[30] Chung-Che Chou, Jia-Hau Liu. Frame and Brace Action Forces on Steel Corner Gusset Plate Connections in Buckling-Restrained Braced Frames [J]. Earthquake Spectra, Volume 28, No. 2, pages 531–551, May 2012
[31] Yu YJ, Tsai KC, Li CH, Weng YT, Tsai CY. Earthquake response analyses of a full-scale five-story steel frame equipped with two types of dampers. Earthquake Engineering and Structural Dynamics 2013; 42(9):1301–1320.
[32] Li Jiaqi ,Li Guochang. Study of effect of axial compression ratio and steel core cross-section area on aseismic behaviour of buckling restrained brace-concrete frame [J].Industrial Construction 2017, 47(3)
[33] Li Guochang, Yan Hailong, Chen Bowen. Finite Element Analysis on Mechanical Behavior of the High Strength Concrete-Filled High Strength Square Steel Tube Stub Column Under Axial Compressive Loading. Journal of Shenyang Jianzhu University (Natural Science).2015, Vol.31(5):847-855 (in Chinese)

Advanced Steel Construction – Vol. 19 No. 3 (2023) 308–320
DOI:10.18057/IJASC.2023.19.3.10

STABILITY PERFORMANCE AND WIND TUNNEL TEST OF STEEL HYPERBOLIC COOLING TOWER CONSIDERING SKINNED EFFECT

Hui-Huan Ma [1, 2, 3], Yu-Qi Jiang [4, *], Zong-Yu Li [4] and Zhi-Wei Yu [5, *]

[1] *School of Civil Engineering, Sun Yat-Sen University, Guangzhou, PR China*
[2] *Southern Marine Science and Engineering Guangdong Laboratory (Zhuahai)*
[3] *Guangdong Research Center for Underground Space Exploitation Technology*
[4] *Harbin Institute of Technology, 150090, China*
[5] *School of Civil Engineering, Guangzhou University, Guangzhou, P. R. China*
* *(Corresponding author: E-mail: 120828422@qq.com; yuzhiwei@gzhu.edu.cn)*

ABSTRACT

With the development of industry, cooling towers play a very important role in thermal power generation, and steel cooling towers are being used more widely. The surface of cooling towers is covered with profiled panels, and the skinned effect on the mechanical performance and stability of the structure should be considered. At present, most studies on steel cooling towers have not considered the skinned effect. In steel cooling towers, the skin panels are usually connected to members by self-tapping screws., the shearing test of self-tapping screw connection is carried out considering different screw diameters and plate thicknesses to obtain the shear stiffness of the screws. Then, three FE models of steel hyperbolic cooling towers are established and compared: in Mode–1, the skin panel is not considered; in Model–2, the panel and the member node are rigidly connected; in Model–3, the spring elements are established to simulate the shearing and tension stiffness of self-tapping screws connecting skin panel and members. Based on the finest Model–3, a parametric analysis is done to investigate the effect of the skinned effect on the overall structural stability. Considering different landform types and the roughness of the inner and outer surfaces, a total of 18 measurement conditions are tested in the wind tunnel to study the outer and internal wind pressure coefficients. Furthermore, based on the wind tunnel test, the wind-induced response analysis of steel hyperbolic cooling towers is performed.

ARTICLE HISTORY

Received: 2 November 2022
Revised: 18 April 2023
Accepted: 10 May 2023

KEYWORDS

Steel hyperbolic cooling tower;
Skinned effect;
Static stability;
Shear stiffness;
Tension stiffness

Copyright © 2023 by The Hong Kong Institute of Steel Construction. All rights reserved.

1. Introduction

The cooling tower is a large-scale building currently widely used in the power industry and machinery industry, as shown in Fig. 1. At the beginning of the 20th century, the worldwide first cooling tower was built in the Netherlands. In the following decades, many cooling towers have been built successively in various countries, and the height of the tower has continued to increase. By the end of the 20th century, Germany and France have built very large cooling towers with a height of nearly 200m [1-3].

(a) Reinforced concrete structure (b) Steel structure

Fig. 1 The cooling tower structures

As the height of cooling towers becomes higher and higher, steel cooling towers has shown great potential, especially in areas with a high incidence of strong earthquakes and geological hazards, and the research on Steel Cooling Towers (SCT) has drawn more and more attention from the researchers. For the SCTs, the beam-column frame system and reticulated shell system are the two common systems. The SCTs belong to large-span spatial structures, and the stability behavior of SCTs is a prominent problem needed to be investigated in detail. A 120m SCT structure with a straight-cone-straight shape was studied [4], and the results showed that the SCT structure with the shape has good performance and can be used for the higher structures. The nonlinear behavior of single and double-layer SCTs with different latticed shell types was compared and the optimum type was suggested for the structures with different heights [5, 6]. A linear analysis was carried out on an SCT structure with and without stiffening rings [7]. The results showed that the stiffening rings help save material, and SCTs show good performance during earthquakes. The elasto-plastic buckling behavior under earthquake, dead and wind loads was studied [8-10], and the study found that the forces in members and construction cost are decreased be using the buckling-restrained members. The influence of initial imperfections on the nonlinear stability of SCTs with five structural systems was studied [11,12], and an imperfection value of H/300 was suggested as the reasonable limit for SCT design.

Another challenging issue for SCTs is the joints for connecting members in the beam-column frame system and reticulated shell system. Normally, the joints used in SCTs are welded or bolted joints, as shown in Fig. 2. The bolt joints for connecting members in steel structures have the advantage of easy installation. However, the bolted joints used in the actual SCTs are assumed to

be pin joints because of the weak bending stiffness. To solve this problem, a series of new joint types were developed [13-15], and the mechanical behavior of the new joints was investigated experimentally and numerically. The results showed that the new joints have good stiffness and bending carrying capacity, which is suitable for SCT structures.

(a) The 181 m high cooling tower with welded joints (b) The 124 m high cooling tower with bolted joints

Fig. 2 Steel cooling towers and joints in China

The SCTs are high-rise light self-weight structures, which belong to the wind-sensitive structures. Many studies have focused on the wind-induced response of the structures. The dynamic performance of SHCTs under wind load was studied in detail through field measurement, wind tunnel tests, and the CFD method [16-18]. The wind-reduced response and the effect of stiffening rings on the dynamic performance were discussed. The formation mechanism of non-Gaussian fluctuating wind pressures for the SCT structure was studied [19], and the forming mechanism of fluctuating wind pressure distribution was investigated in detail. The wind-induced inner and outer pressure of cylindrical-conical type SCT structure was studied [20], and a reference for wind resistance design of SCTs was obtained.

The outer surface of SCTs is covered with profiled panels. The skinned effect can strengthen the overall performance of the structure. When the structure is designed, the skin effect is only used as a reserve for stiffness and strength. Related studies by scholars have shown that the behavior of structures will be optimized under the consideration of the skinned effect, and it has been found that considering the skinned effect can help save structural costs by about 10% [21]. At present, most of the actual engineering design does not consider the strengthening effect due to the skinned effect on the structure. This design method is considered safe. However, when the skinned effect is significant, there may be skin panels may fail under normal load before the structure [22], and the study pointed out that there is still no practical design discipline for considering the skinned effect. The skinned effect of single-layer spherical aluminum alloy reticulated shell structures was studied [23], and it was obtained that the skin effect can change the buckling mode and critical load of the structure. One of the stability bearing capacities increased form 0.7 kN/m^2 to 2.96 kN/m^2, and the effect of the aluminum plates should be considered for future structural design.

According to the summary of previous studies, it can be found that most of the research on SCT structures focuses on static analysis, elasto-plastic stability analysis, and seismic analysis, and they have not considered the skinned effect on the mechanical performance of cooling towers. Therefore, three finite element models of the SCT structure were established in this paper considering the skinned effect, conducted wind tunnel tests, and studied the wind vibration response analysis and stability analysis.

2. Shear performance test of self-tapping screw connection

In actual engineering projects, the skin panel and purlins fixed on the structural members are connected by self-tapping screws. In order to establish a FE model of SCT structures considering the skinned effect, the shearing test was performed to obtain the load-deformation curve of the self-tapping screws. The test specimens were made according to the recommended method in the code for the fastener test [24]. The steel sheet and the aluminum sheet were overlapped by self-tapping screws. The dimensions of the connection sheet are shown in Fig. 3. The steel grade is Q345 and the aluminum alloy grade is 6061-T6. The surface of the sheets is smooth and flat. The types of self-tapping screws are ST5.5 and ST6.3, in which 5.5 and 6.3 mean the screw diameter (mm). The test was controlled by force, and the loading speed was set to 1kN/min according to the specifications. The test mainly considered two types of parameters: plate thickness and self-tapping screw specifications. The parameter setting and the numbering rules are shown in Table 1 and Fig. 4.

Table 1
Detailed information on specimens

Numbering	t_1 (mm)	t_2 (mm)	Screw type	Screw diameter (mm)
L2-G5-5.5	2.0	5.0	ST5.5	5.5
L2-G5-6.3	2.0	5.0	ST6.3	6.3
L3-G5-5.5	3.0	5.0	ST5.5	5.5
L3-G5-6.3	3.0	5.0	ST6.3	6.3
L4-G5-5.5	4.0	5.0	ST5.5	5.5
L4-G5-6.3	4.0	5.0	ST6.3	6.3
L5-G5-5.5	5.0	5.0	ST5.5	5.5
L5-G5-6.3	5.0	5.0	ST6.3	6.3

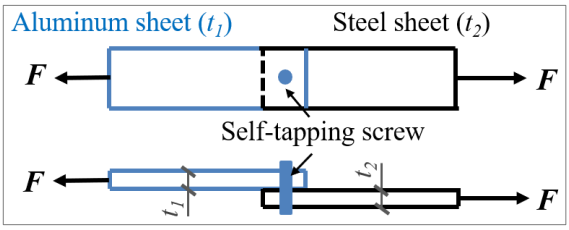

Fig. 3 Connection sheet test chart

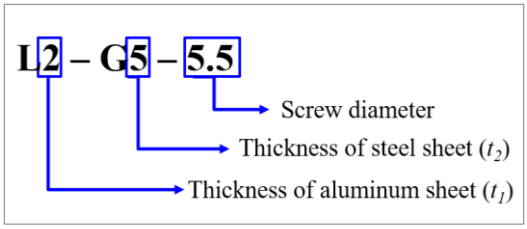

Fig. 4 Numbering rules for specimens

There are three failure modes of the specimens:

i) Failure mode 1 belongs to a kind of ductile failure modes. The screw in specimens was severely deformed, and finally was cut off. The aluminum sheet warped a little, and the screw hole on aluminum sheet was damaged, as shown in Fig. 5. This type of damage occurred in specimens L2-G5-5.5, L3-G5-5.5, and L4-G5-5.5. The load (L)-displacement (Δ) curves with failure mode 1 are divided into four stages: elastic stage, elasto-plastic stage, plastic stage and destruction stage, as shown in Fig. 6.

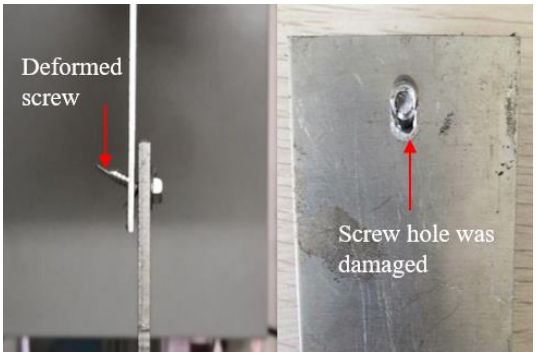

Fig. 5 Picture of failure mode 1

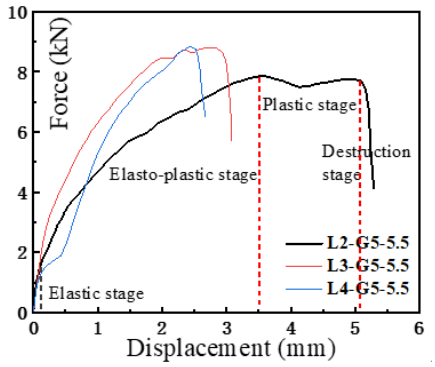

Fig. 6 *L-Δ* curves of specimens with failure mode 1

ii) Failure mode 2 also belongs to a kind of ductile modes. The screw hole was cracked. There was little deformation occurred in screw, and the aluminum sheet was flat, as shown in Fig. 7. This type of damage occurred in specimen L2-G5-6.3. The *L-Δ* curve for the specimen with failure mode 2 can be divided into four stages that are similar to specimens with failure mode 1, as shown in Fig. 8.

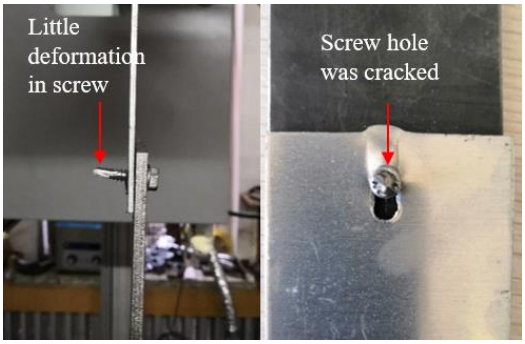

Fig. 7 Picture of failure mode 2

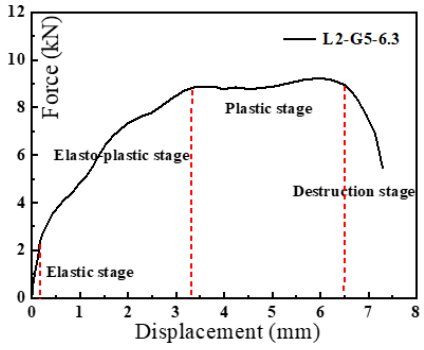

Fig. 8 *L-Δ* curves of specimens with failure mode 2

iii) Failure mode 3 is a kind of brittle failure mode. The screw in the specimens was cut suddenly, and the aluminum sheet was slightly wrapped. The screw hole remained intact, as shown in Fig. 9. This type of damage occurred in specimens L3-G5-6.3, L4-G5-6.3, L5-G5-5.5 and L5-G5-6.3. The *L-Δ* curves for the specimen with failure mode 3 are divided into three stages, as shown in Fig. 10.

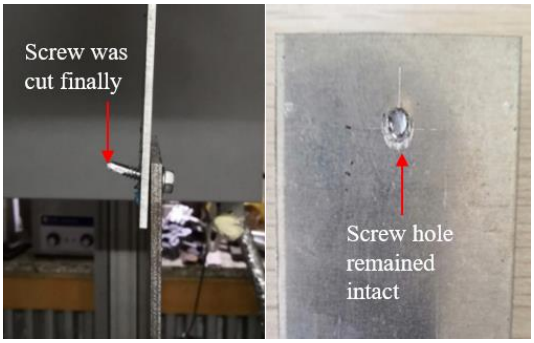

Fig. 9 Picture of failure mode 3

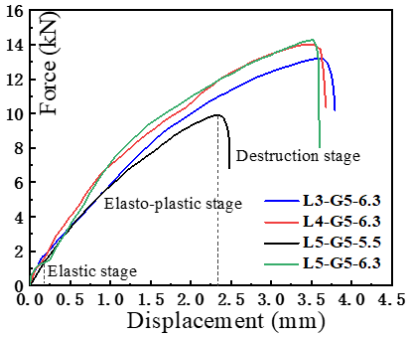

Fig. 10 *L-Δ* curve specimens with failure mode 3

3. Static stability of SCT structures considering the skinned effect

3.1. Simulation method for self-tapping screw connections

The main structure of the SCTs is mainly composed of longitudinal, circle members, diagonal members, and outer surface skin panels, as shown in Fig. 11. In this paper, three FE models of SCT structures were established to investigate the skinned effect on the stability behavior. In Model 1, the skin panel is not considered in the model; In Model 2, the aluminum skin panel is considered in the model, while the aluminum skin panel is fixed on the members through coupling the nodes of the skin plate and members. That is, the aluminum skin panels and the member nodes are rigidly connected; Model 3 is the finest model in which the spring elements are established to simulate the connection stiffness according to the actual situation between aluminum skin panels and members. In the three models, the Beam188 element is used for the longitudinal, circle and diagonal members, and the panel is simulated using the shell181 element. The panel is generally an aluminum alloy profiled plate, which is directly connected to the member by self-tapping screw at a distance of 200 mm. Since the self-tapping screw connections in structures are mainly subjected to tensile and shear forces, the self-tapping screw is simulated by establishing three combin39 spring elements in three directions of *x*, *y*, and *z*, as shown in Fig. 12. The combin39 spring elements are established between the connection nodes on skin panel (1, 2, 3, etc.) and on members (1', 2', 3', etc.). The Nodes 1 and 1' are at the same coordinates in the numerical model of SCTs. Nodes 2 and 2', nodes 3 and 3', nodes 4 and 4', etc. are the same. The three combine39 elements at the connection point simulate the shear stiffness of self-tapping screws in the *x* and *y* directions and the tensile stiffness of screws in the *z* direction, respectively.

In ANSYS software, the *L-Δ* curves of the connections are entered by setting the real constants. Two types screws, ST5.5 and ST6.3, were used during the structure analysis. According to the results of the shear tests on self-tapping screw connections, when the thickness of aluminum and steel plate is 5 mm (specimens L5-G5-5.5 and L5-G5-6.3), the screws in specimens are cut, and the screw hole remains intact. The influence of the plates is ruled out. Therefore, the load-deformation curves of self-tapping screw specimens L5-G5-5.5 and L5-G5-6.3 can be used as the shear stiffness curves of the screws in the FE models of SCT structures, as shown in Fig. 13. The tension stiffness of the screws in the FE models of SCT structures are calculated based on the experimental study [25], as shown in Fig. 14.

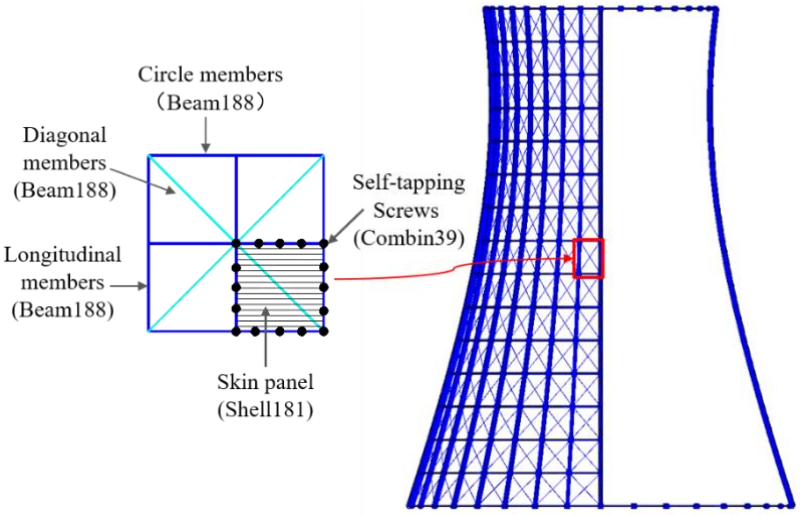

Fig. 11 Members in SCT structure

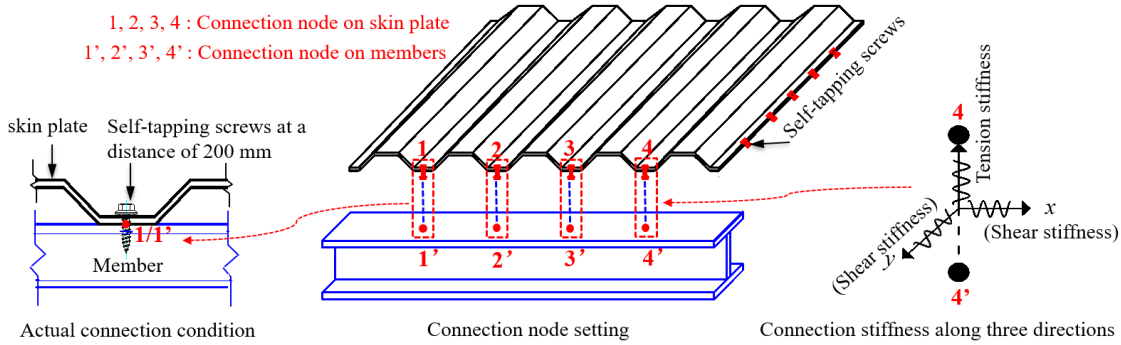

Fig. 12 Simulation method for self-tapping screw connections

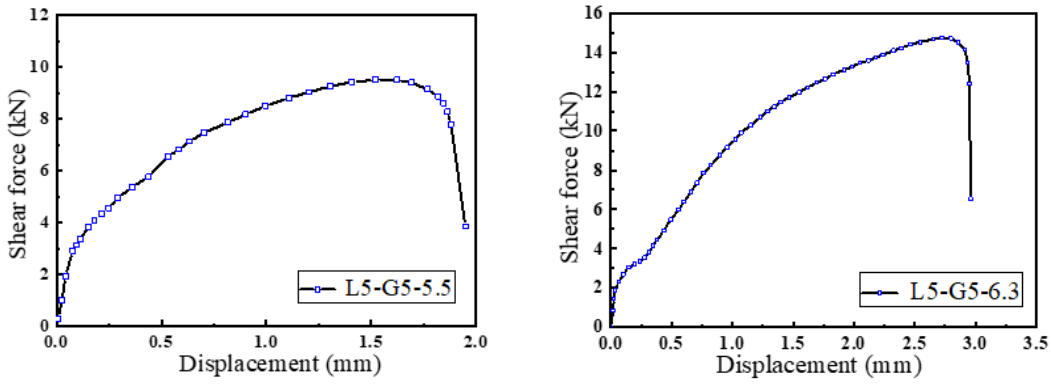

(a) ST5.5 self-tapping screw (b) ST6.3 self-tapping screw

Fig. 13 Shear stiffness of self-tapping screws

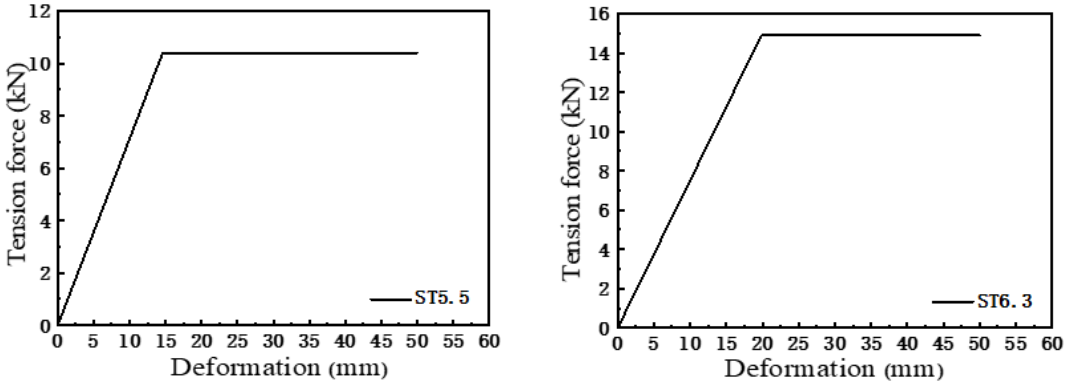

(a) ST5.5 self-tapping screw (b) ST6.3 self-tapping screw

Fig. 14 Tension stiffness of self-tapping screws

3.2. Equivalent method of aluminum skin panel

In the real project, the surface skin panel of SCT structures is generally a profiled aluminum plate. During the parametric analysis of SCT structures, a simplified model of skin panels was established to improve computational efficiency. The shear membrane of the deck panels of a high-story steel structure was considered in the finite element analysis [26-27]. The shell element was used to simulate the cold-formed deck, which was treated as an orthogonal anisotropic deck. Based on the equivalent stiffness in three directions, an anisotropic flat plate is used instead of the isotropic profiled plate, as shown in Fig. 15.

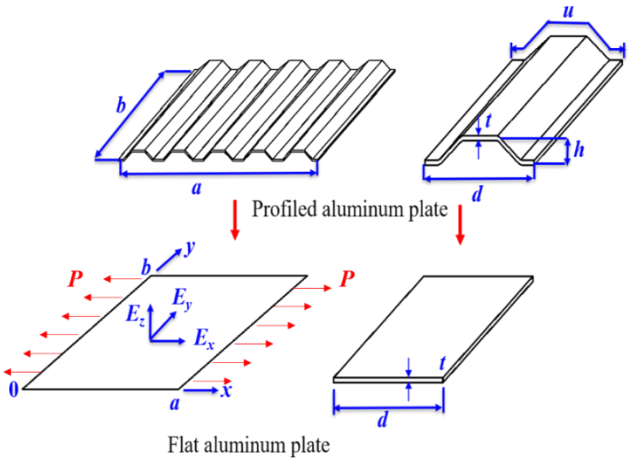

Fig. 15 Equivalent principle of the aluminum plate

The equivalent principles of the profiled plate and flat plate are: the area, length, width, and thickness of the two plates are same; the same deformation is obtained when the two plates are under same force. The material characteristics of the profiled plate and flat plate are shown in Table 2. As shown in Fig. 15, if there is a uniformly distributed tensile force P in the direction of the plate monopod, the elongation of the profiled plate is Δ_1, and the elongation of the equivalent plate is Δ_1', such that $\Delta_1 = \Delta_1'$, the modulus of elasticity of the profiled plate E' can be determined. The principal Poisson's ratio μ_y of the equivalent plate is the same as the Poisson's ratio of the profiled plate.

Table 2
Material characteristics of the profiled plate and flat plate

Plate type	E_x (MPa)	E_y (MPa)	v_{xy}	v_{yx}	G	$f_{0.2}$ (Mpa)
Profiled plate	63305	63305	0.3	0.3	260	180
Flat plate	1408	75966	6.46×10^{-5}	0.3	1300	180

3.3. Grid mesh method and load calculation

The hyperbolic SCT structures are usually composed of a latticed shell tower and a bottom support structure, as shown in Fig. 16. The grid size is associated with the longitudinally divided number of N_h and the circular divided number N_r. N_h equals H_1 divided by L_h, which H_1 is the height of the latticed shell tower, and L_h is longitudinal grid height; N_r is equal to 360º divided by θ. θ is the angle occupied by a grid around the circle. The latticed shell which is covered with profiled aluminum panels is the main study object. D_1, D_2 and D_3 are the diameter of the air inlet, throat and air outlet of the SCT structure, and h_1, h_2 and h_3 are the elevation of them. C is a coefficient determining the structural shape. The geometric dimension parameters of the hyperbolic SCTs are designed according to the requirements of the cooling tower design code [28], and all parameters should be set to meet the requirements of thermal calculation results. One hyperbolic line is used to generate the hyperbolic SCT structures. The equation of hyperbolic line is shown in Eq. (1).

$$\frac{X^2+Y^2}{(D_2/2)^2}-\left(\frac{Z-h_2}{C^2}\right)^2=1 \quad (h_1 \le Z \le h_3) \tag{1}$$

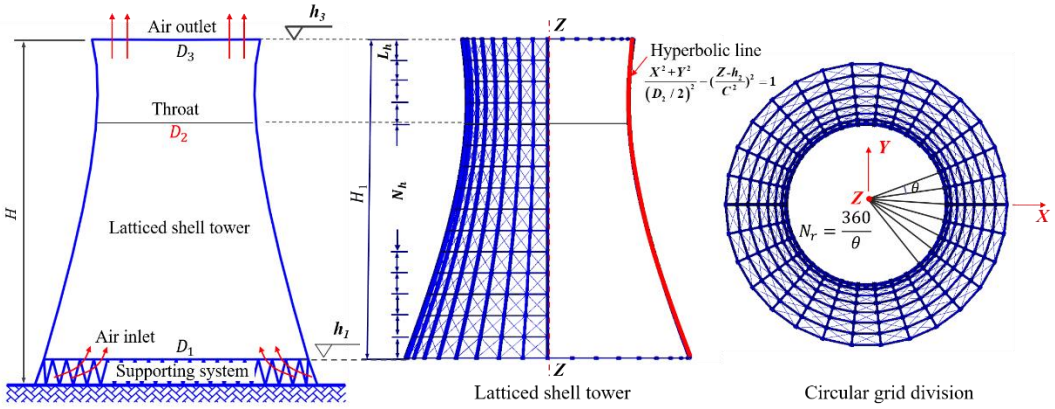

Fig. 16 Cooling tower structure diagram

During the analysis of SCT structures, the wind load and the self-weight load (steel members and aluminum skin panels) of the cooling tower considered as the main control loads were researched. The schematic diagram of the wind load was given in Fig.17. In FE Model 1 of the SCT structure without aluminum skin panel, the wind pressure is calculated and applied to the nodes of the structure; In FE Model 2 and Model 3 of the SCT structure with aluminum skin panels, the wind load is applied to the surface of aluminum skin panel as a surface load.

According to the code[29], the standard value of the equivalent wind load on the surface is calculated by Eq. (2). $\omega_{(Z,\theta)}$ is the standard equivalent wind load (kPa) of the outer surface of the cooling tower; β = 1.9 is the wind vibration factor. C_g = 1.0 is the interference coefficient between the towers. Eq. (3) is the formula for calculating $C_p(\theta)$, the average wind pressure distribution coefficient. μ_z is the height variation coefficient of wind pressure. the basic wind pressure ω_0 equals 0.55 kPa. α_k and k are the coefficients for calculating $C_p(\theta)$, which are calculated according to the requirements of the cooling tower design code [29]. At the same time, the SCT structure has an internal wind pressure effect, and Eqs (4) and (5) are the formula for calculating the standard value of the internal wind suction. In the equations. ω_i is the standard value of internal suction load (kPa). The internal suction coefficient C_{pi} equals -0.5. $q_{(H)}$ and μ_H are the design value and the height variation coefficient of wind pressure at the top of the tower.

$$\omega_{(Z,\theta)} = \beta \cdot C_g \cdot C_p(\theta) \cdot \mu_z \cdot \omega_0 \tag{2}$$

$$C_p(\theta) = \sum_{k=0}^{m} \alpha_k \cdot \cos k\theta \tag{3}$$

$$\omega_i = C_{pi} \cdot q_{(H)} \tag{4}$$

$$q_{(H)} = \mu_H \cdot \beta \cdot C_g \cdot \omega_0 \tag{5}$$

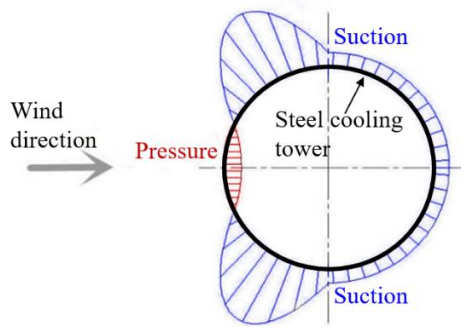

Fig. 17 Wind pressure diagram

3.4. Comparison of the three FE models

Two-height single-layer rectangular SCTs are selected for analysis considering the geometric and material nonlinearity to show the effect of the simulation method of self-tapping screw connection and the stressed-skin on the stability behavior of SCT structures. Three FE models of 90 m and 220 m SCT structures are established respectively. In Model–1, the skin panel is not considered. In Model–2, the panel and the member node are rigidly connected. In Model–3, the spring elements are established to simulate the connection stiffness according to the actual situation between skin panel and members. The full process *L-Δ* curves are shown in Fig. 18.

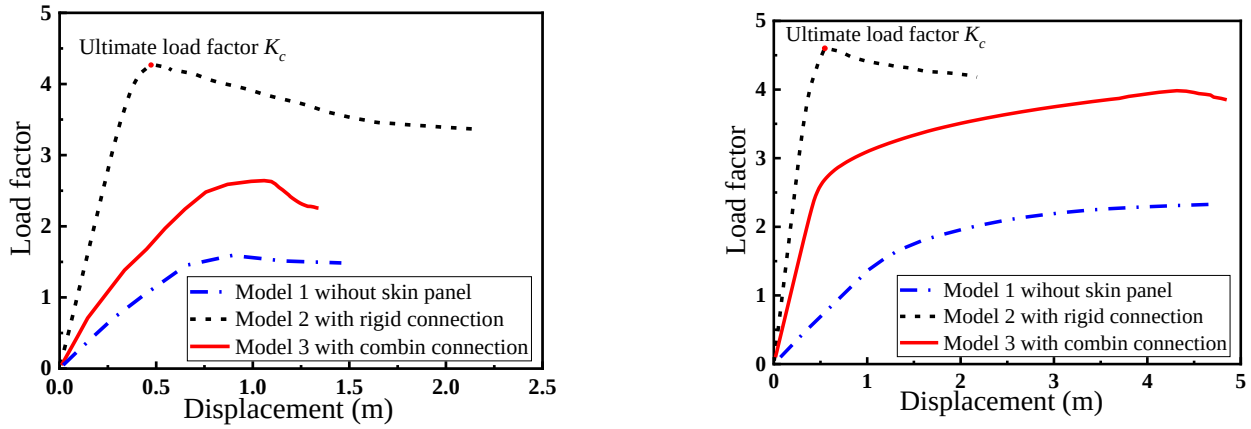

(a) H = 90 m (b) H = 220m

Fig. 18 Load-displacement curves

Comparing the results of the three models without skin panel, the rigid joint between skin panel and members, and spring connection. The stability behavior of the SCT structure can be significantly improved by considering the skin effect. Comparing with Model–1 without skin panel, the carrying capacities obtained by Models 2 and 3 are much higher. The ultimate load factor α_u of Model–3 of 90 m SCT structure with spring connections is 2.65, which is 1.67 times α_u of Model–1 without skin panel. α_u of Model–2 with rigid connections is 4.25, which is 2.67 times that of Model 1 without skin panel. The Model–3 of the SCT structure is the finest model, which reflect the actual situation of the real project by considering the self-tapping screw connection stiffness. The simplified Models 1 and 2 are easy to be established, but the results obtained by them cannot reflect the real mechanical behavior of SCT structures.

3.5. Parametric stability analysis of SCT structures considering the skinned effect

In order to comprehensively analyze the stability performance of the SCT structures considering skinned effect, four heights of 90 m, 130 m, 180 m, and 220 m are selected, and different grid sizes are designed. The specific size settings are shown in Table 3 below. For the SCT structures with different heights, six grid sizes (G_1~G_6) from small to large are considered. For the SCT structure with each height and grid size, the skinned and unskinned structural models are analyzed and compared. The finest Model–3 of the SCT structure is used to carry out the parametric analysis. The dual nonlinear stability analysis was carried out on 48 models with different heights and grid sizes.

3.5.1. Typical example analysis

Based on the finest Model–3 of SCT structure with 90 m height and G_2 grid size, the stiffness state of the screwed connections and stress state in the panels were studied. Three points are plotted on the *L-Δ* curves (Fig. 19) of SCT with 90 m height and G_2 grid size. Point 1 is the upper limit of the linear stage of the structure. Point 2 corresponds to the critical load factor. Point 3 is the end point of the calculation.

Fig. 20 shows the stress distribution of the panels of SCT corresponding to the three key points. It can be found that a large number of panels at bottom and a small number of panels in the middle of SCT yield at Point 1. At Point 2, the yield area in the middle expands to the suction area of the SCT. The local buckling that happens at Point 3 leads to the failure of the structure. As shown in Fig. 21, lots of self-tapping screw connections enter elastic stage due to shear force or tension force. The self-tapping screw connections enter elastic stage due to shear force mostly in the middle and bottom pressure area and side suction area of the structure. The self-tapping screw connections enter the plastic stage due to shear force is mostly in the middle and bottom pressure area.

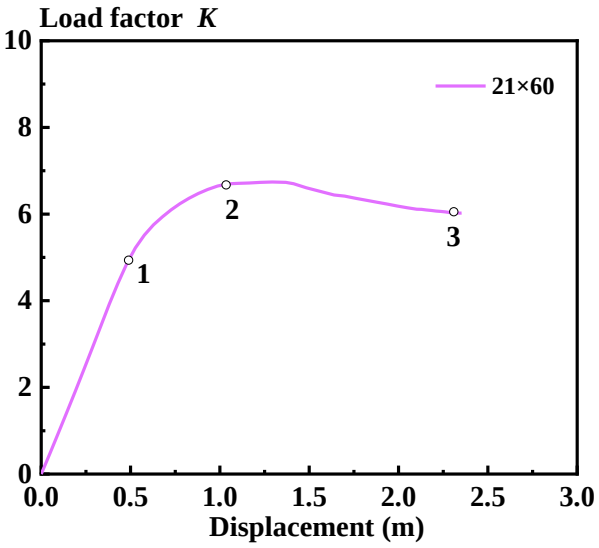

Fig. 19 Load-displacement curves of SCTs with 90 m height and G_2 grid size

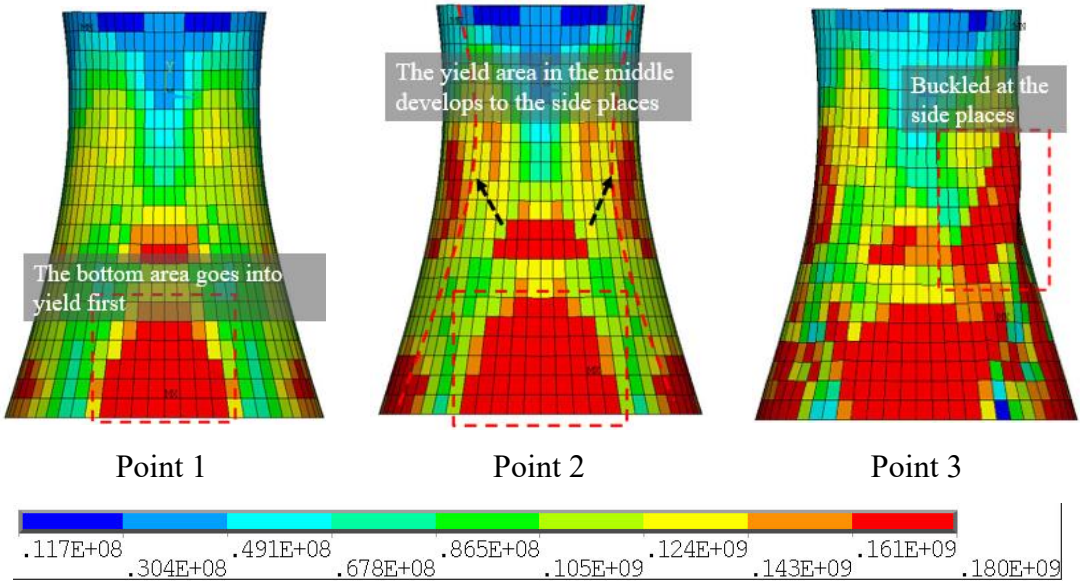

Fig. 20 Stress distribution of the panels of SCTs with 90 m height and G_2 grid size

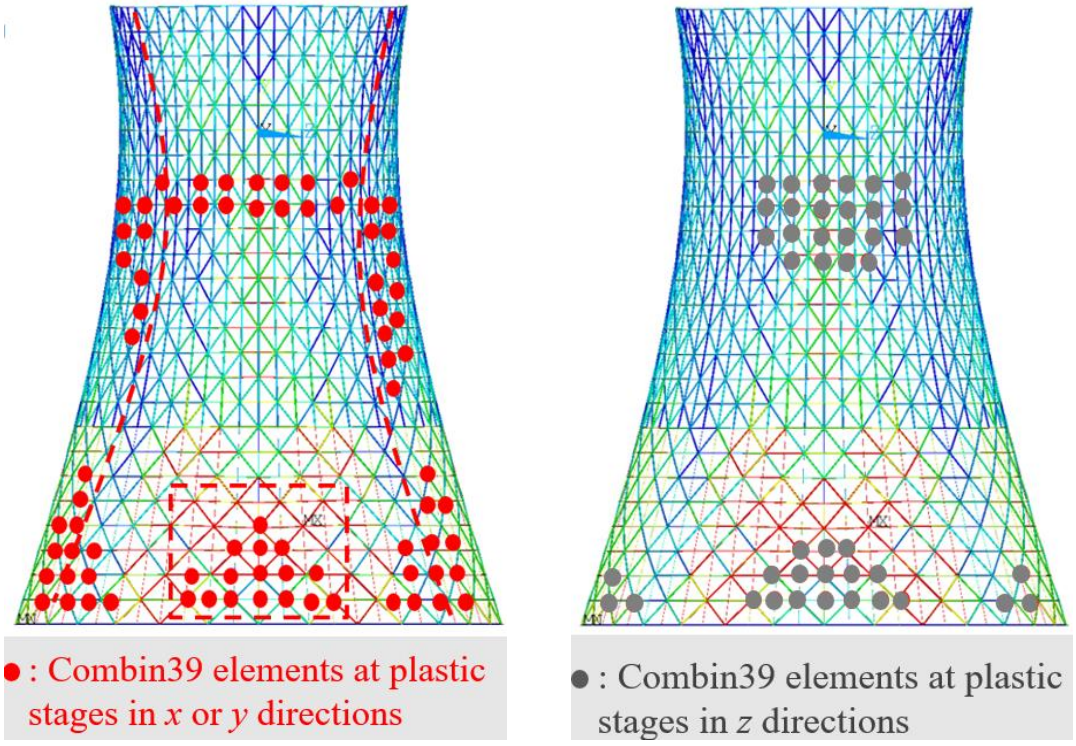

(a) Connections at the plastic stage because of shear force (b) Connections at the plastic stage because of tension force

Fig. 21 The self-tapping screw connections at plastic stage

3.5.2. Results of parametric stability analysis

The whole load-displacement curves are shown in Fig. 22. For each height grid size, two models with and without skin were calculated. The solid lines in the figures are obtained by Model 3 with skin panels, and the dashed line is obtained by Model 1 without skin panels. The ultimate bearing capacity of the skinned structure is represented by K_{cr}, and the ultimate bearing capacity of the unskinned structure is represented by K_{cr}', as shown in Fig. 23 and Table 4. The change law of K_{cr}/K_{cr}' which can reflect the skinned effect on the bearing capacity, as shown in Fig. 24.

Table 3
Parameter scheme for height and grid size

Height H(m)	Grid size	$N_h \times N_r$	Air inlet size (m^2)	Throat size (m^2)	Air outlet size (m^2)
90	G_1	25×72	3.37×2.89	3.37×1.69	3.37×1.81
	G_2	21×60	4.01×3.47	4.01×2.03	4.01×2.17
	G_3	17×40	4.95×5.21	4.95×3.05	4.95×3.26
	G_4	15×36	5.61×5.78	5.61×3.39	5.61×3.62

	G_5	13×30	6.48×6.94	6.48×4.06	6.48×4.34
	G_6	11×24	7.65×8.68	7.65×5.08	7.65×5.43
	G_1	35×72	2.9×2.96	2.9×2.10	2.9×2.20
	G_2	31×60	3.27×3.56	3.27×2.52	3.27×2.64
	G_3	27×50	3.76×4.27	3.76×3.01	3.76×3.17
130	G_4	25×40	4.06×5.34	4.06×3.79	4.06×3.96
	G_5	21×36	4.83×5.93	4.83×4.21	4.83×4.40
	G_6	17×24	5.97×8.89	5.97×6.31	5.97×6.60
	G_1	55×72	3.00×4.95	3.00×2.97	3.00×3.05
	G_2	45×60	3.67×5.94	3.67×3.56	3.67×3.66
	G_3	35×50	4.71×7.13	4.71×4.27	4.71×4.39
180	G_4	33×48	5.00×7.43	5.00×4.45	5.00×4.57
	G_5	25×40	6.60×8.91	6.60×5.34	6.60×5.49
	G_6	21×36	7.86×9.90	7.86×5.94	7.86×6.10
	G_1	45×80	4.21×6.91	4.21×5.45	4.21×5.60
	G_2	35×72	5.41×7.68	5.41×6.06	5.41×6.23
	G_3	33×60	5.74×9.22	5.74×7.27	5.74×7.47
220	G_4	29×50	6.53×11.06	6.53×8.73	6.53×8.97
	G_5	25×48	7.58×11.52	7.58×9.09	7.58×9.34
	G_6	21×40	9.02×13.83	9.02×10.91	9.02×11.21

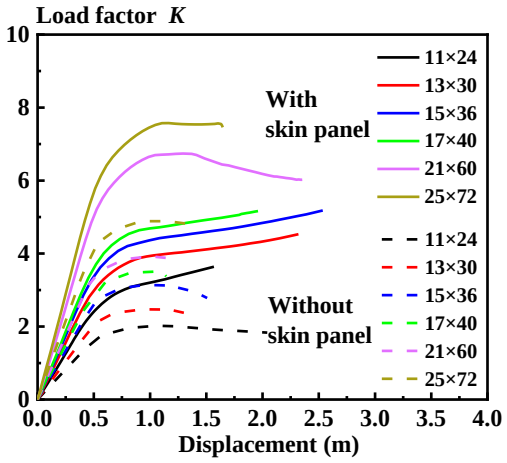

(a) H = 90 m

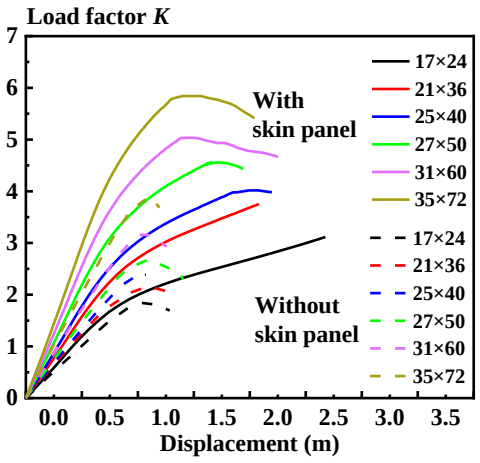

(b) H = 130 m

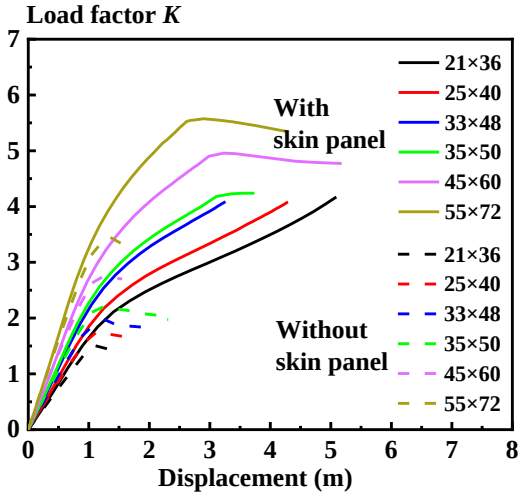

(c) H = 180 m

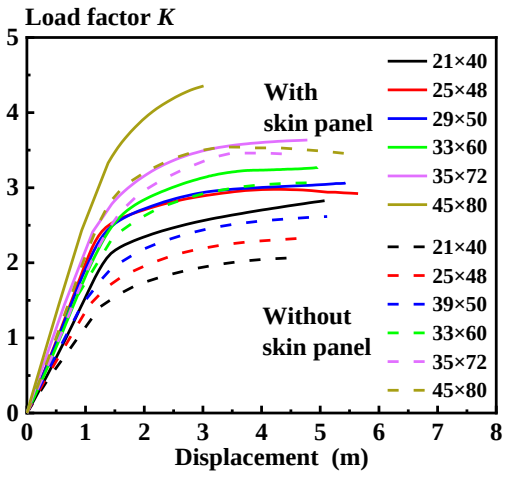

(d) H = 220 m

Fig. 22 Load-displacement curves of SCTs with different heights and grid sizes

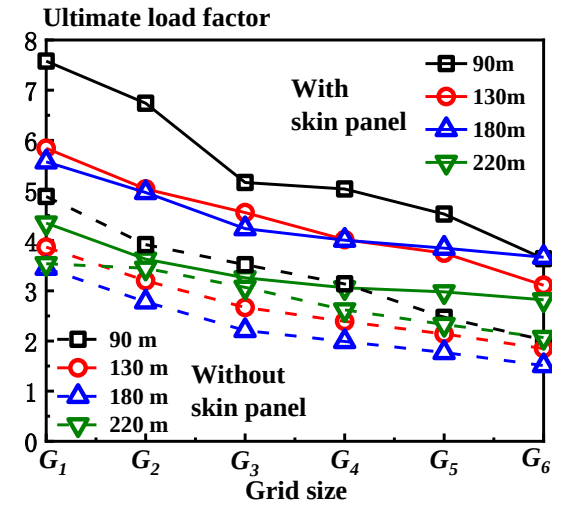

Fig. 23 Comparison of ultimate carrying capacity at different heights

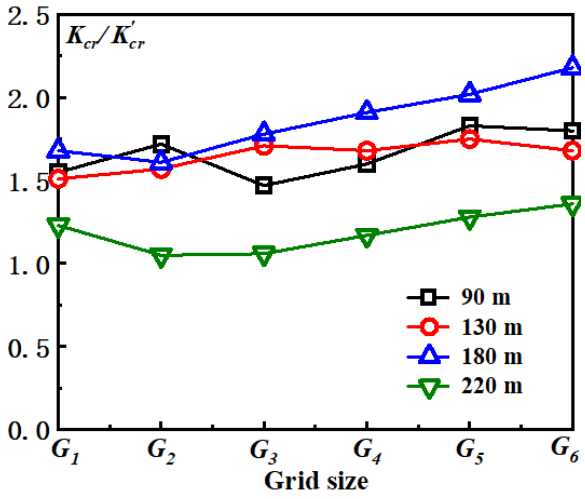

Fig. 24 Chang law of K_{cr}/K_{cr}'

It can be concluded that at the same height, as the grid size increases, K_{cr} and K_{cr}' decrease, and K_{cr}/K_{cr}' represents the skinned effect on the ultimate bearing capacity. The grid size becomes larger, and K_{cr}/K_{cr}' gradually increases, indicating that as the grid becomes larger, the skinned effect on the bearing capacity gradually increases.

Table 4
Ultimate bearing capacity of SCTs with different heights and grid sizes

Height H (m)	Grid size	$N_h \times N_r$	K_{cr}	K_{cr}'	K_{cr}/K_{cr}'
90	G_1	25×72	7.58	4.88	1.55
	G_2	21×60	6.74	3.92	1.72
	G_3	17×40	5.16	3.52	1.47
	G_4	15×36	5.03	3.14	1.60
	G_5	13×30	4.53	2.47	1.83
	G_6	11×24	3.64	2.02	1.80
130	G_1	35×72	5.84	3.87	1.51
	G_2	31×60	5.03	3.20	1.57
	G_3	27×50	4.56	2.67	1.71
	G_4	25×40	4.02	2.39	1.68
	G_5	21×36	3.75	2.14	1.75
	G_6	17×24	3.11	1.85	1.68
180	G_1	55×72	5.57	3.45	1.61
	G_2	45×60	4.96	2.78	1.78
	G_3	35×50	4.24	2.21	1.91
	G_4	33×48	4.01	1.99	2.02
	G_5	25×40	3.85	1.77	2.18
	G_6	21×36	3.67	1.51	2.43
220	G_1	45×80	4.35	3.54	1.23
	G_2	35×72	3.63	3.45	1.05
	G_3	33×60	3.26	3.07	1.06
	G_4	29×50	3.06	2.62	1.17
	G_5	25×48	2.98	2.33	1.28
	G_6	21×40	2.82	2.07	1.36

The following table 5 is the comparison of the maximum displacement of cooling towers with different grid sizes at the height of 90 m. It indicated that the maximum displacement of the structure decreased with decreasing grid size. However, the stiffness increased with decreasing grid size. Comparing the maximum displacement of skinned and non-skinned SCTs with the same grid, the maximum displacement of the skin structure is smaller than that of the non-skinned structure, because the overall skin panel on SCTs increases the stiffness and reduces the displacement. Compared with the reduction ratios of the maximum displacement, it can be seen that when the grid size is smaller, the reduction ratio of the maximum displacement is larger. As the mesh size becomes larger, the reduction ratio gradually decreases, indicating that the denser the mesh, the denser the skin panel, and the stronger the skinned effect, the greater the increase in structural stiffness.

Table 5
Comparison of maximum displacements of 90 m SCTs (m)

Models	Grid size					
	G_1	G_2	G_3	G_4	G_5	G_6
Skinned structure	1.65	2.01	3.34	4.61	4.74	4.97
Non-skinned structure	2.13	2.49	3.78	5.21	5.45	5.79
Reduction ratio	29.1%	23.1%	13.2%	13.1%	15%	16.5%

4. Wind tunnel test and wind-induced response analysis of hyperbolic SCT structures

4.1. Wind tunnel test

At present, the wind tunnel test is currently the most commonly used method for obtaining wind loads in the field of wind engineering. It is relatively easy to implement and measure and can provide a design basis before building construction. The wind tunnel test was conducted in the wind tunnel and wave trough joint laboratory of the HIT. The size of the test model was designed according to the actual parameters of the 220m SCT structure under design in Zhaozhuang, Shanxi province of China (see Fig. 25(a)). The scale ratio is 1: 250 according to the requirements of the wind tunnel laboratory. The wind tunnel test model is made of an acrylic sheet (Plexiglas sheet) and a plastic sheet, as shown in Fig. 25(b). Table 6 lists the specific dimensions of the cooling tower model and prototype.

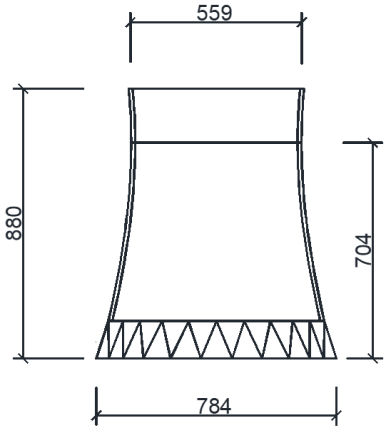

(a) The size of the test model

(b) Picture of the test model

Fig. 25 The test model

Table 6
Cooling tower prototype and model dimensions

SCT	H	h_1 (m)	D_1 (m)	h_2 (m)	D_2 (m)	h_3 (m)	D_3 (m)
Prototype	220	30.5	179.3	176	138.9	220	142.7
Test model	0.88	0.122	0.717	0.704	0.556	0.88	0.571

The arrangement of measuring points considers both external pressure and internal pressure. The external and internal pressure measuring points were evenly arranged along circumferential direction and the meridional direction of the test model. The total number of measurement points arranged on the test model was 372, as shown in Fig. 26.

In this paper, the Reynolds number effect was simulated by changing the surface roughness. There are mainly two simulation methods, one is sticking tape on the surface, and the other is sticking sandpaper on the surface. 36 pieces of tape or sandpapers at a distance of about 6mm were pasted on the outer surface of the cooling tower model, as shown in Fig. 27. At the same time, considering that the inner steel members of the SCT structure may have some influence on the internal pressure, a sponge bar was fixed to the internal surface of the test model to simulate the internal members. 6×16 strips with 1cm ×1cm specifications were arranged in the ring direction and the meridian direction, as shown in Fig. 28.

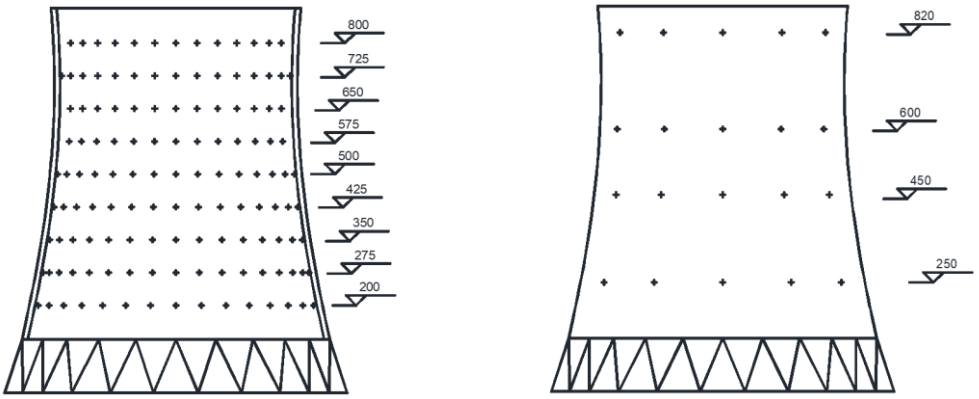

(a) External pressure measuring point (b) Internal pressure measuring point

Fig. 26 The measuring point layout on the test model

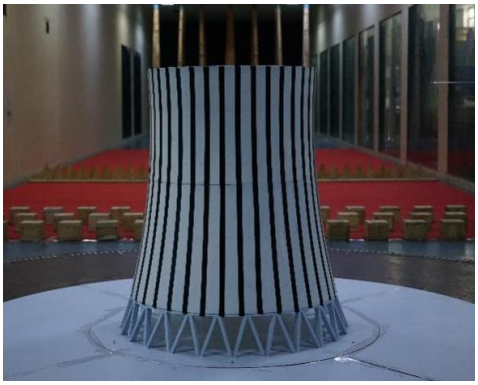

Fig. 27 Reynolds number effect simulation

Fig. 28 Internal member simulation

(a) A type (b) B type (c) C type

Fig. 29 Three planform types

In this test, three types of landforms, A type, B type, and C type, were considered. The passive simulation method was used for wind field simulation by placing spikes, baffles, rough elements, and carpets. The pictures of the three landform types are shown in Fig. 29. According to the landform type, the roughness of the inner and outer surfaces, and a total of 18 measurement conditions have been set, as shown in Table 7.

Table 7
Measurement conditions

Conditions	Landform type	Inner members	Outer roughness simulation
1	A	Yes	Smooth
2			Tapes
3			sandpapers
4		No	Smooth
5			Tapes
6			sandpapers
7	B	Yes	Smooth
8			Tapes
9			sandpapers
10		No	Smooth
11			Tapes
12			sandpapers
13	C	Yes	Smooth
14			Tapes
15			sandpapers
16		No	Smooth
17			Tapes
18			sandpapers

The wind pressure values at different heights under different working conditions were obtained. The average wind pressure coefficient of the test models with smooth surface, tapes on the surface, and sandpapers on the surface were compared with the standard curve in the cooling tower design code [29], as shown in Fig. 30. In order to compare the changes of wind pressure on the cooling tower surface under different wind speeds, three wind speed were carried out in the test. The model with adhesive tape on surface was taken as an example. The average wind pressure coefficients of the test model under different wind speeds were shown in Fig. 31. It can be obtained that: changing the surface roughness has a greater influence on the extreme value of the wind suction; the width of the wind suction area at the leeward side of the structure; the wind pressure coefficients obtained by the model setting surface tapes is closer to that in the cooling tower design code [29], and changing wind speed has little effect on the wind pressure coefficient.

Fig. 32 is a comparison diagram of the internal pressure at different heights under two working conditions: smooth inner surface and sponge surface. It can be obtained that the internal pressure coefficient obtained by the test is slightly larger than that in the cooling tower design code [29], and the internal pressure gradually increases with decreasing height. The internal pressure value at the bottom measurement point is more unstable, and the suction point appears on the leeward surface. By comparing the test models with smooth internal surface and internal surface sticking sponge strips, the internal sponge strip has a certain effect on the wind pressure value of the internal wind field, and it is not much different from the values in the cooling tower design code [29].

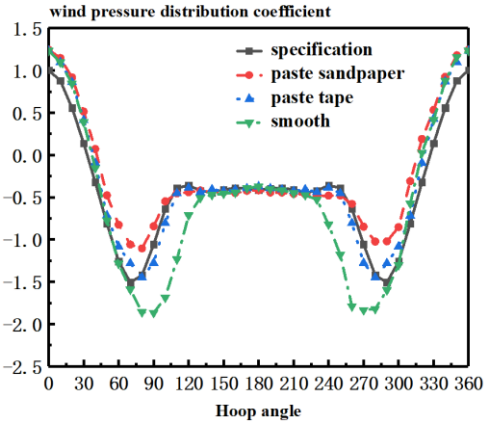

Fig. 30 Comparison of wind pressure coefficient at throat height

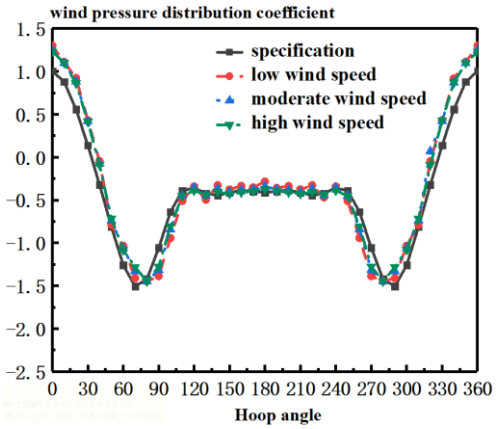

Fig. 31 Comparison of average wind pressure coefficients at different wind speeds

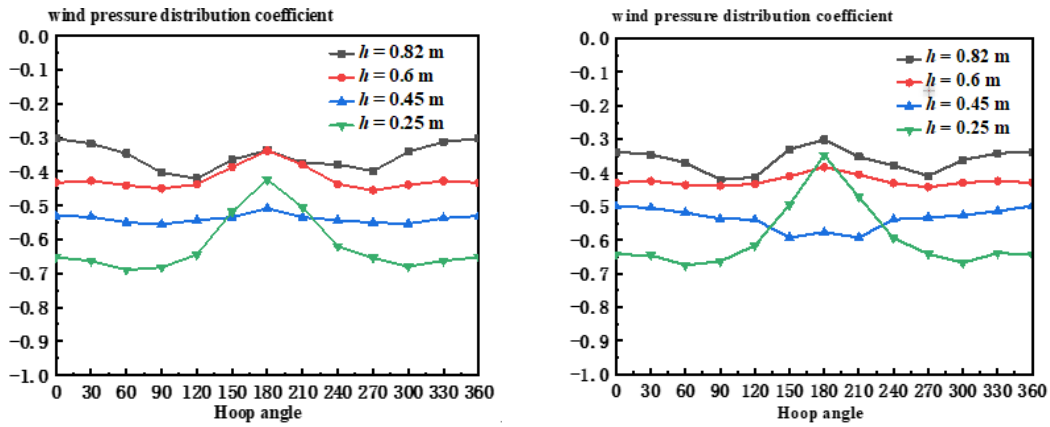

(a) Smooth inner surface (b) Inner surface with spongy strips

Fig. 32 Comparison of internal pressure at different heights

4.2. Wind-induced response analysis of SCT structures

First, the dynamic characteristics of the structure, including the mode shape and frequency, were analyzed. The SCT structure with H = 220 m, grid size 45 × 80, and panel thickness of 2 mm was taken as an example. The first 40 modes and frequencies of the structure were extracted according to the Model 3, established previously. The following Table 8 gives the main several mode shapes, frequencies, and mode characteristics of the SCT structure considering the skinned effect.

Table 8
Mode shapes and frequencies of SCT structures

Order	1, 2	3, 4	7, 8	11, 12	17, 18	33, 34
Frequency	0.67	0.70	0.92	0.98	1.17	1.66
Shape characteristics	4 toroidal harmonics	3 toroidal harmonics	4 toroidal harmonics; 3 vertical harmonics	Hoop compression	3 toroidal harmonics; 2 vertical harmonics tilt	Vertical compression
Mode shape	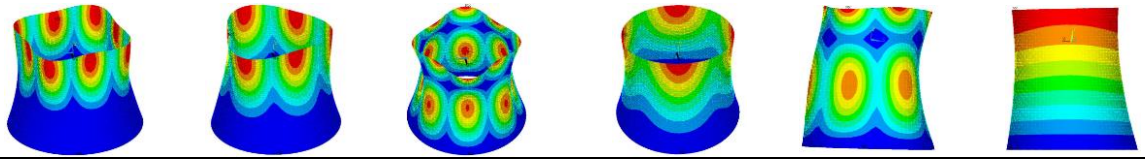					

The hyperbolic tower is symmetric, and the mode shapes of the structure appear in pairs. From the frequency results, the first few modes of the structure mainly show a combination of several ring harmonics and vertical harmonics; the first few modes are symmetrical deformation and lower frequency; more complex modes appear after the 15th order, and there is a lateral tilt under the combination of hoop harmonics and vertical harmonics; vertical compression modes appear only after the 30th order. It shows that the torsional stiffness and lateral stiffness of the hyperbolic cooling tower are small, while the vertical stiffness is large.

The wind load time-history data obtained from the wind tunnel test is interpolated and encrypted to investigate the wind-induced response of hyperbolic SCT structures. The wind load data is interpolated by the POD method based on the wind tunnel test points. The wind pressure data for a total of 3600 points are obtained, which is the same as the node number in the SCT structure model. The wind load data at each point position is imported into the model to carry out the transient dynamic analysis. The loading time interval is converted to 0.1s according to the sampling frequency of the wind tunnel test. The displacement time history of each node of the structure can be obtained. The displacement distribution of the nodes along the circular direction at the top of the tower and the nodes at 0° meridians along the height were plotted, as shown in Fig. 33. The above figures show that the displacement response of the tower top is the lagest and basically symmetrical along the horizontal axis. The displacement in the leeward area is small. Along the meridian direction, the displacement increases moderately with the increasing height, reaches a peak at the left and right positions of the throat, and then decreases a little.

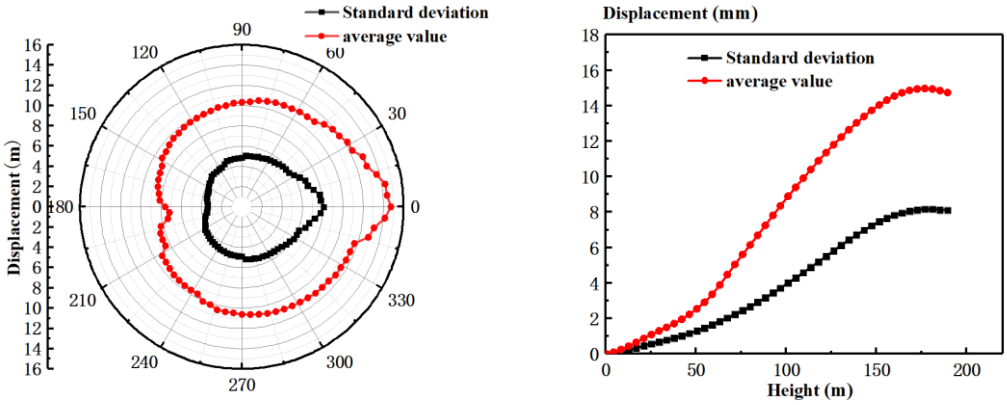

(a) Vertex displacement

(b) 0° meridian displacement along the height

Fig. 33 Distribution of ddisplacement response

The wind vibration factor is usually represented by the ratio of the structure's maximum response to its average response, which can reflect the amplification effect on the turbulent wind. This paper mainly solves the wind vibration factors, and defines the wind vibration factors of a point as the ratio of the maximal displacement response to the average displacement response of the point. After extracting the displacement time history of, the average and standard deviation of the displacement can be obtained. Therefore, the displacement wind vibration factor G_x can be obtained by the following formula:

$$G_x=\frac{X_{max}}{X_{ave}}=1+g\frac{\sigma_x}{X_{\text{ave}}} \tag{6}$$

among them, G_x is the displacement wind vibration factor at a certain position of the structure and X_{max}, X_{ave}, σ_x are maximum, average, and standard deviation vibration displacement response of the wind vibration displacement of the structural at position; g is the crest factor of the structural displacement response, which is generally taken as 3-4 according to related theories, and 3 is taken in this paper.

The SCT structure is more complex and has more nodes. This paper only gives the displacement wind vibration factors at several angles, as shown in Table 9 below. The meridional and annular directions are plotted to more clearly reflect the distribution of the wind vibration factors. The change law of the wind vibration factors along the vertical and circumferential direction of the SCT structure with a height of 220 m is shown in Fig. 34 which shows that the wind vibration factors are symmetric along the horizontal direction.

Table 9
Value of the wind vibration factor (H = 220 m)

Parameter	Height h (m)	Angle 0°	45°	90°	135°	180°
Wind vibration factor G	219.45	2.04	2.36	2.48	2.68	3.06
	173.14	1.89	2.28	2.46	2.78	3.07
	126.83	2.12	2.36	2.49	2.61	2.91
	84.73	2.25	2.55	2.66	2.83	2.73
	46.84	2.51	2.72	2.82	2.53	2.47

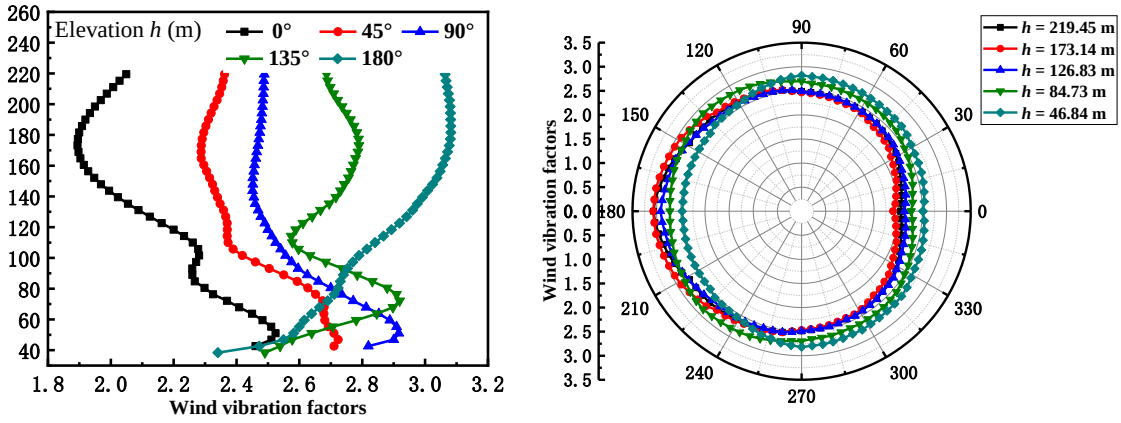

(a) Wind vibration factors the along height

(b) Hoop displacement wind vibration factors

Fig. 34 Wind vibration factors along the vertical and circumferential direction

5. Conclusions

A series of shearing tests was conducted on the self-tapping screwed connections to investigate the connection performance. The *L-Δ* curves of specimens with different plate thicknesses and screw diameters were obtained and analyzed. Two ductile failure modes and one brittle failure mode happened during the test.

Based on experimental shear stiffness curves of self-tapping screw connection, three FE models of steel hyperbolic cooling towers with and without skin panels were established. By comparing the results of the three models, it is found that the stability behavior of SCT structure obtained by threw modes is much different. The ultimate load factor α_u of Model–3 of 90 m SCT structure with spring connections is 2.65, which is about 2 times α_u of Model–1 without skin panels. α_u of Model–2 with rigid connections is 1.60 times that of Model–3 with a spring connection. Based on the parametric analysis of SCT structures, the stability behavior of SCT structure can be significantly improved by considering the skin effect, and as the grid size increases, the skinned effect on the ultimate bearing capacity increase gradually.

Based on the wind tunnel test, changing the surface roughness has a greater influence on the extreme value of the wind suction area and the width of the leeward suction area. The wind pressure coefficients obtained by the model setting surface tapes are closer to that in the cooling tower design code. Changing wind speed has little effect on the wind pressure coefficient. By comparing the test models with smooth internal surface and internal surface sticking sponge strips, the internal sponge strip has a certain effect on the wind pressure value of the internal wind field. The wind vibration factors are symmetric along the horizontal direction.

Acknowledgement

This research was supported by the National Key R&D Program of China (grant no. 2018YFC0705500, 2018YFC0705504)

References

[1] D. Busch, R. Harte, W. B. Krätzig, U. Montag. New natural draft cooling tower of 200 m of height. Eng. Struct. 2002; 24(12): 1509-1521.
[2] D. Busch, R. Harte, W. B. Krätzig, U. Montag. World's Tallest Natural Draft Cooling Tower, near Cologne, Germany. Struct Eng. Int. 2001; 11(2):107-109.
[3] R. Harte, W.B. Krätzig, Large-scale cooling towers as part of an efficient and cleaner energy generating technology, Thin-Walled Struct. 40 (7) (2002) 651–664, https://doi.org/10.1016/S0263-8231(02)00018-6.
[4] L. Kollar, Large reticulated steel cooling towers, Eng. Struct. 1985; 7 (4): 263–267
[5] H. Ma, S. Li, F. Fan, Static performance analysis of single-layer steel cooling tower, Structure 2019; 19: 322–332, https://doi.org/10.1016/S0141-0296(98)00138-2
[6] H.H. Ma, Z.Y. Li, S.Z. Li, B.B. San, F. Fan, Stability analysis and performance comparison of large-scale hyperbolic steel cooling towers with different latticed shell systems, J Constr Steel Res. 2019; 160: 559-578. https://doi.org/10.1016/j.jcsr.2019.05.042
[7] M. Izadi, K. Bargi. Natural draft steel hyperbolic cooling towers: Optimization and performance evaluation. Struct. Design Tall Spec. Build. 2014; 23:713-720.
[8] S. Kato, S. Nakazawa, S. Shimaoka, et al., Effectiveness of buckling restrained members for diagonal columns to reduce the seismic response of cooling towers, Natural Draught Cooling Towers, 2004.
[9] S. Kato, S. Shimaoka, H. Okada, et al., A study on buckling and earthquake-resistant capacities for steel cooling towers, J. Struct. Constr. Eng. (2005) 85–92.
[10] F. Pourshargh, F. P. Legeron, S. Langlois and K. Saoud. A simple method for a reliable modelling of the nonlinear behaviour of bolted connections in steel lattice towers. Advanced Steel Construction 2022, 18(1): 479-487.
[11] J. Wu, J.Y. Zhu, Y. Dong, Q.L. Zhang. Nonlinear stability analysis of steel cooling towers considering imperfection sensitivity, Thin-walled Struct 2020; 146: 106448. https://doi.org/10.1016/j.tws.2019.106448
[12] F. Wang, K. Zhou and S. Ke. Research on dynamic load carrying capacity of assembled internal stiffening wind turbine tower based on multi-scale modeling. Advanced Steel Construction 2023, 19(1): 86-90.
[13] H.H. Ma, Y. Zhao, F. Fan, Z.W. Yu, X.D. Zhi, Experimental and numerical study of new connection systems for a large-span hyperbolic steel cooling tower, Eng. Struct. 2019; 195: 452-468.
[14] H. Ma, C. Zhao, Y. Jiang, G. Zhou and Y. Wang, Rotational resistance test of a new aluminum alloy penetrating (AAP) joint system. Advanced Steel Construction 2023, 19(2): 121-129.
[15] Y. Jiang, H. Ma, G. Zhou and F. Fan. Parametric and comparison study of a new and traditional aluminum alloy joint systems. Advanced Steel Construction 2021, 17(1): 50-58.
[16] S.T. Ke, L.Y. Du, Y.J. Ge, L. Zhao. A study on the average wind load characteristics and wind-induced responses of a super-large straight-cone steel cooling tower. Wind Struct 2017; 25(5): 433-457
[17] J.F. Zhang, Y.J. Ge, S.T. Ke. Effects of stiffening rings on the dynamic properties of hyperboloidal cooling towers. Struct Eng Mech 2014; 49(5): 619-629.
[18] Y. Wang, S. Wang, X. Zhou, etc. Buckling behavior of the steel plate in steel – concrete – steel sandwich composite tower for wind turbine. Advanced Steel Construction 2022, 18(3): 699-706.
[19] Ke S, Wang H, GeY. Non-Gaussian characteristics and extreme distribution of fluctuating wind pressures on large cylindrical–conical steel cooling towers. Struct Design Tall Spec Build. 2017;26: e1403. https://doi.org/10.1002/tal.1403
[20] Ke S, Du L, Ge Y. Wind-induced internal pressure effect within a novel super-large cylindrical–conical steel cooling tower. Struct Design Tall Spec Build. 2018;27: e1510. https://doi.org/10.1002/tal.1510
[21] J.M. Davies，E.R. Bryan, Manual of Stressed Skin Diaphragm Design．New York：Granada Publishing, 1982．
[22] Y.L. Shi, X.L. Wang, Development and Research of Stressed Skin Diaphragms. Spatial Structures 2004; 19(4): 10-13. (in chinese)
[23] H.B. Liu, Z.H. Chen, S. Xu, et al. Structural Behavior of Aluminum Reticulated Shell Structures Considering Semi-Rigid and Skin Effect. Struct Eng Mech. 2015; 54(1): 121－133.
[24] Fastener test methods-Lap joint shear. GJB715.19-90.
[25] Y.Q. Li, Y.Q. Shuai, Z.Y. Shen, Y.F. Qin, Y.Q. Chen. Experimental study on tension behavior of self-drilling screw connections for cold-formed thin-walled steel structures. Journal of Building Structures 2015; 36(12): 143-152.
[26] H.Y. Wan, M. Wang, D. Zeng. Finite element analysis of high-story steel structure in case of shear-resistant membrane, Journal of Hefei University of Technology 2001; 24(2): 184-188 (in Chinese).
[27] A.H. Nilson, A.R Ammar. Finite Element Analysis of Metal Deck Shear Diaphragms. Proceeding of ASCE. Structure Division April, 1974．
[28] Code for design of cooling tower for industrial recirculating water, GB/T50102-2014.
[29] Code for design of steel structure. GB50017-2017.